

# **MICROBEAM ANALYSIS**

# **1983**

**Ron Gooley, *Editor***

Proceedings of the 18th Annual Conference  
of the  
Microbeam Analysis Society  
Phoenix, Arizona, 6-12 August 1983



*San Francisco Press, Inc.*

Box 6800, San Francisco, CA 94101-6800

*PUBLISHER'S NOTICE*

*The Microbeam Analysis Society (MAS) and its publisher since 1979, San Francisco Press, Inc., are not responsible for the information and views presented in this volume by the several contributors.*

*Back issues of MICROBEAM ANALYSIS are available as follows:*

<i>1974, 1975, 1976 (spiral bound)</i>	<i>\$25 each</i>
<i>1979, 1980, 1981</i>	<i>\$25 each</i>
<i>1982</i>	<i>\$42.50</i>
<i>1983 (the present volume)</i>	<i>\$30</i>

*Beginning with 1983 San Francisco Press, Inc., is also the publisher of the EMSA Proceedings (abstracts from the annual meeting of the Electron Microscopy Society of America), available at \$45.*

*MAS and EMSA members prepaying by personal check receive a 20% discount from the above prices. All overseas orders must be prepaid. California purchasers add sales tax.*

*San Francisco Press, Inc., is also publisher of L. Marton's EARLY HISTORY OF ELECTRON MICROSCOPY (\$5) and ANALYTICAL ELECTRON MICROSCOPY--1981 (\$25), papers from the special 1981 workshop in Vail, Colo.*

*Printed in the U.S.A.*

*ISSN 0278-1727*



## Table of Contents\*

Officers of the Microbeam Analysis Society. . . . .	vii
Sustaining Members' Information . . . . .	ix
J-1. FAILURE ANALYSIS IN MICROELECTRONICS . . . . .	1
Fritz, Laudate, Automated measurements of integrated circuit linewidths by electron microscopy . . . . .	1
Ward, Olson, Brewer, Johnson, Composition of aluminum stringers in VLSI . . . . .	5
Bolon, McConnell, Tong, Taylor, Voltage measurements of high voltage transistors using Auger electron spectroscopy . . . . .	11
1. MICROBEAM ANALYSIS IN GEOLOGICAL SCIENCE . . . . .	15
Raymond, Bardin, In situ elemental and mineralogic analysis of peat by SEM and petrographic techniques . . . . .	15
Andrejko, Raymond, Occurrence of detrital mineral matter in Okefenokee peats. . . . .	19
Snyder, Huggins, Specimen preparation and sizing by image analysis of respirable quartz particles collected on coal mine air-monitoring filters . . . . .	22
Minkin, Chao, Thompson, Wandless, Dulong, Larson, Neuzil, Submicroscopic mineral contents of vitrinites in selected bituminous coal beds . . . . .	27
Warren, Evidence for a tektosilicate structure and dominance of Fe(III) over Fe(II) in silicic volcanic glasses of the Nevada test site. . . . .	31
Sheridan, Wohletz, Origin of accretionary lapilli from the Pompeii and Avellino deposits of Vesuvius . . . . .	35
McCormick, Sheridan, Characterization of vapor-phase mineralogy from the green ignimbrite, Pantelleria . . . . .	39
Kortemeier, Sheridan, Role of grain type in quantitative surface morphology of pyroclasts from the Monte Guardia sequence on Lipari, Italy . . . . .	43
Smith, Launspach, Determination of the compositions of metal phases in chondritic meteorites . . . . .	47
Allen, Strope, Microcharacterization of basalt--Considerations for a nuclear waste repository. . . . .	51
Hinthorne, Minor and trace elements in hornblende, augite, and pyrope microprobe standards from Kakanui, New Zealand, by ion microprobe mass spectrometry. . . . .	54
Long, Strope, Composition of augite and pigeonite in basalt flows that are candidates for a nuclear waste repository . . . . .	57
Knowles, A microprobe study of silver in Northern Idaho . . . . .	61
Calvo, Guilemany, Structure and composition of complex pyrite ore from Sotiel (Huelva, Spain) . . . . .	65
2. QUANTITATIVE MICROBEAM ANALYSIS. . . . .	70
Thomas, Simultaneous electron and x-ray spectrometry in an STEM . . . . .	70
Murata, Cvikevich, Kuptsis, Thin-film analysis with a Monte Carlo simulation based on the Mott cross section . . . . .	79
Vander Wood, Pearson, Buseck, The dependence of bremsstrahlung emission on $\bar{Z}$ in compound samples . . . . .	85
Packwood, Brown, Remond, $\phi(\rho z)$ . . . . .	89
Hale, Packwood, Measurements of $\phi_0$ --The surface ionization coefficient from C-K $\alpha$ to Cu-K $\alpha$ . . . . .	97
3. LASER MICROBEAM MASS ANALYSIS. . . . .	101
Evans, Griffiths, Dingle, Southan, Ninham, Microanalysis of bulk samples by laser-induced ion mass analysis. . . . .	101
Lindner, Seydel, Laser microprobe mass analysis of single cells and cell components . .	106

\* An author index appears on p. 333.

4. COMPUTER-ASSISTED MICROBEAM ANALYSIS . . . . .	109
Chambers, Reproducibility considerations in an automated microprobe . . . . .	109
Russ, Hare, A self-educating classification scheme for particle and phase identification. . . . .	111
Sicignano, Friday, Postprocessing of x-ray maps . . . . .	115
5. MICROBEAM ANALYSIS OF METALS, CERAMICS, AND GLASS. . . . .	117
Mosley, Grain boundary cavitation and weld underbead cracking in DOP-26 iridium alloy .	117
Davidson, Electron metallography of 316 SS as related to unusual creep behavior (strain burst). . . . .	121
McConnell, Bolon, Grubb, Microprospecting for precious metals with an automated electron microprobe . . . . .	125
Jenson, Determination of xenon in irradiated nuclear fuel by means of a shielded electron microprobe. . . . .	128
6. SCANNING ELECTRON MICROSCOPY . . . . .	131
Wells, Coane, Aliotta, Measuring the field from a magnetic recording head in the SEM. .	131
Rosencwaig, Thermal-wave imaging in an SEM. . . . .	137
Joy, Farrow, Crystal lattice studies using electron channeling patterns . . . . .	143
Small, Newbury, Myklebust, The visibility of fibers in the SEM. . . . .	148
Jones, Landon, A diode array spectrograph and associated optics for cathodoluminescence measurements in an SEM. . . . .	151
7. ANALYTICAL ELECTRON MICROSCOPY/ELECTRON ENERGY LOSS SPECTROSCOPY . . . . .	153
Rez, Detection limits and error analysis in energy-loss spectrometry. . . . .	153
Pun, Ellis, Statistics of edge areas in quantitative EELS imaging: Signal-to-noise ratio and minimum detectable signal . . . . .	156
Leapman, Swyt, Electron energy loss imaging in the STEM: Systematic and statistical errors. . . . .	163
Newbury, Myklebust, Romig, Bieg, Observations on the determination of $\phi(\rho z)$ curves for thin films in the analytical electron microscope. . . . .	168
Johnson, Staudhammer, Reeves, Vesser, AEM/STEM analysis of vapor deposited multilayer laser targets. . . . .	171
Myklebust, The Si(Li) detector-specimen angles in an AEM. . . . .	174
8. MICROBEAM ANALYSIS OF PARTICLES. . . . .	177
Conley, Bradley, Giffin, Tomassian, Albee, Development of a miniature SEM for in-flight analysis of comet dust. . . . .	177
Post, Buseck, Energy-dispersive x-ray analyses of individual particles from two secondary iron foundries . . . . .	182
Bradley, Brownlee, Microanalyses of dispersed interplanetary dust particles . . . . .	187
Armstrong, Wasserburg, Individual particle microanalysis of exotic components in carbonaceous chondrite meteorites: A tool for unraveling the petrogenetic history of the early solar system . . . . .	191
Aden, Buseck, A minicomputer procedure for quantitative EDS analyses of small particles. . . . .	195
Isaacs, Limits to quantitation in particle analysis: Some empirical determinations. . .	202
Small, Norris, McKenzie, Fabrication of metals and metal alloys as particle standards .	209
9. MICROBEAM ANALYSIS IN BIOLOGICAL SCIENCE . . . . .	211
Warner, Myers, Taylor, Peakless continuum: Inaccuracies in biological quantification by means of the analytical microscope . . . . .	211
Nicholson, Chapman, Bremsstrahlung production in thin specimens and the continuum normalization method of quantitation. . . . .	215
Tormey, Improved methods for x-ray microanalysis of cardiac muscle. . . . .	221
Ingram, Ingram, Intracellular hydration measurement with freeze-dried, plastic-embedded biological soft tissue . . . . .	229
Warner, Wirfel, A comprehensive compute program for the quantitative analysis of thin biological sections . . . . .	231
Hook, Fiori, Elin, Imaging lymphocyte magnesium . . . . .	233

Cameron, Hunter, Smith, Validation of quantitative energy-dispersive electron-probe x-ray microanalysis of electrolytes in thin cryosections of erythrocytes. . . . .	237
Echlin, Hayes, McKoon, Analytical procedures for bulk frozen-hydrated biological tissues. . . . .	243
Shuman, Kruit, Somlyo, Quantitative electron energy loss spectroscopy of low concentrations of calcium in carbon containing matrices . . . . .	247
Griffith, Photoelectron microscopy of biological surfaces . . . . .	252
Izutsu, Johnson, Wang, Tamarin, Ensign, Goddard, Microbeam analysis of resting rat parotid gland. . . . .	257
Goddard, Calcium localization in mammalian skeletal muscle. . . . .	259
Crooker, Johnson, Mottet, Quantification of mercury losses during biological specimen preparation and x-ray microanalysis . . . . .	261
10. RAMAN MICROBEAM ANALYSIS. . . . .	265
Boyer, Raman microanalysis of defects in industrial materials . . . . .	265
Adar, Noether, Raman microprobe characterization of polymeric fibers: Orientation, crystallinity, and skin-core effects. . . . .	269
Couzi, Cruège, Martineau, Mallet, Paillet, Characterization of composite materials by means of the Raman microprobe. . . . .	274
Doyle, Alvarez, Micro-Raman analysis of Three Mile Island samples . . . . .	277
Barbillat, Delhay, Micro-Raman analysis with the use of multichannel intensified photodiode array detector . . . . .	280
Pineau, Audebrand, Fréour, Tessier, Faugère, Raman microprobe spectroscopy and study of the retention of air particles by the human respiratory system . . . . .	286
Purcell, White, A Raman microprobe study of phase-separated minerals. . . . .	289
Adar, Zorabedian, Raman microprobe measurements of local stress in laser recrystallized lateral epitaxial silicon films over silicon dioxide . . . . .	293
Tallant, Higgins, Stein, Raman microscopy through transparent materials . . . . .	297
Appendix: Conzemius, Simons, Shankai, Byrd, Laser mass spectrometry of solids: A bibliography 1963-1982. . . . .	301
Author index. . . . .	333



## Officers of the Microbeam Analysis Society (1983)

### *MAS Executive Council*

*President:* Roger D. Bolon, General Electric R&D Center  
*President-Elect:* David C. Joy, Bell Laboratories  
*Past President:* Robert L. Myklebust, National Bureau of Standards  
*Treasurer:* Mary C. Finn, Lincoln Laboratory  
*Secretary:* Charles E. Fiori, National Institutes of Health,  
Bldg. 13, Rm. 3W13, Bethesda, MD 20205  
(301) 496-2599

### *Directors*

John T. Armstrong, California Institute of Technology, Pasadena  
Constance K. Barsky, Owens-Corning, Granville, Ohio  
William F. Chambers, Sandia National Laboratories, Albuquerque, N.M.  
Roy H. Geiss, IBM Research Division, San Jose, Calif.  
Thomas R. McKee, Southern Clay Products, Gonzales, Tex.  
Fred Schamber, Tracor Northern, Inc., Middleton, Wis.

### *Honorary Members*

L. S. Birks, Naval Research Laboratory, USA  
I. B. Borovskii, Academy of Sciences, USSR  
Raymond Castaing, University of Paris (Orsay), France  
V. E. Cosslett, University of Cambridge, Great Britain  
Peter Duncumb, Tube Investments Research Laboratories, Great Britain  
Gunji Shinoda, Osaka University, Japan



## **Sustaining Members' Information**

### **AMRAY INC.**

160 Middlesex Turnpike  
Bedford, MA 01730

Contact: James Furlong, (617) 275-1400

Product Line: Largest manufacturer of scanning electron microscopes and accessories in the USA.

#### **Sales Offices:**

Warren Johnson, Cleveland, Ohio, (216) 579-0035  
George Bruno, New York State, (617) 275-8310  
Don Pollock, Lico, New England, (617) 275-8310  
Ken Benoit, New Jersey, (609) 662-3922  
Gene Werbick, Los Angeles, Calif., (714) 848-1940  
Dr. Bart Yatchmenoff, San Francisco, Calif., (415) 964-5900

### **BAUSCH & LOMB/ARL**

9545 Wentworth Street  
Sunland, CA 91040

Contact: (213) 352-6011

Product Line: Nanolab scanning electron microscopes, SEMQ scanning electron microprobe x-ray analyzer, Omnicon image analysis system.

#### **Sales Offices:**

9545 Wentworth St., Sunland, CA 91040, (213) 352-6011  
820 Linden Ave., Box 9189, Rochester, NY 14625, (716) 338-8209  
340 Melvin Dr., Northbrook, IL 60662, (312) 498-0400  
2131 Kingston Ct. SE, Marietta, GA 30067, (404) 952-9061  
2930 Baseline Rd., Nepean, Ont., Canada K2H 8T5, (613) 820-9437

### **CAMBRIDGE INSTRUMENTS INC.**

40 Robert Pitt Drive  
Monsey, NY 10952

Contact: Peter W. Boutell, (914) 356-3331

Product Line: Research scanning electron microscopes and accessories, research production beam microfabrication systems, image analysis equipment.

#### **Sales Offices:**

Joe Barrett, Arizona, New Mexico, Texas, (602) 991-9458  
John Pong, California, Nevada, Utah, Colorado, (714) 893-1609  
Mike Webber, Florida, Georgia, Alabama, Tennessee, Virginia, (404) 926-9636  
Brian Partridge, California, Washington, Montana, Idaho, (408) 734-2313  
T. Rodkin, Maine, Vermont, Mass., Connecticut, R.I., (603) 465-7888

### **CAMECA INSTRUMENTS INC.**

2001 West Main Street  
Stamford, CT 06902

Contact: Harry Rundall, (203) 348-5252

Product Line: CAMBAX/MICRO fully automated microprocessor controlled electron microprobe. IMS-3F second-generation ion microanalyzer.

Sales Offices:

Thomas Fisher, 416 Ohio Ave., West Springfield, MA 01089, (413) 734-0617  
R. Rattay, Dept. 559, Box 42999, Houston, TX 77042  
Ms. E. Flentye, Box 2994, La Jolla, CA 92038-2994

EDAX INTERNATIONAL, INC.

Box 135  
Prairie View, IL 60069

Contact: A. Devenish, (312) 634-0600

Product Line: Manufactures energy-dispersive x-ray analysis systems for x-ray microanalysis in SEMs, TEMs, and electron probes, as well as energy-dispersive x-ray fluorescence spectrometers. System configurations from basic qualitative to fully automated quantitative (with computer control and data processing) are available, including an automated WD/ED system with stage and spectrometer controls.

Sales Offices:

V. Balmer, 637 Sunnyside Rd., Vermilion, OH 44089  
E. Martin, Box 547, New Rochelle, NY 10802  
J. Moore, Box 2253, Boulder, CO 80306

EG&G ORTEC

100 Midland Road  
Oak Ridge, TN 37830

Contact: Charles Thomas, (615) 482-4411, Ext. 501

Product Line: Energy-dispersive systems for electron optical microscopes of all types. Wavelength-dispersive system electronics. Backscattered electron detection systems.

Sales Offices:

Joe Redmon, Box 6041, Boston, MA 02209  
Peeter Kark, 9401 Comprint Ct., Suite 101, Gaithersburg, MD 20760  
Robert G. Bardorf, Box 3355, Oak Ridge, TN 37930  
Dick Tischler, 21360 Center Ridge Rd., Rm. 304, Cleveland, OH 44116  
Earl Klugman, 310 Melvin Dr., Northbrook, IL 60062  
Val Johnson, Box 1678, Boulder, CO 80306  
Bill Tucker, 2104 Courland Circle, Carrollton, TX 75007  
John Telford, Bldg. 3, Suite 204, 300 120th Ave. NE, Bellevue, MA 98005  
Alan Welco, 22971 Triton Way, Suite C, Laguna Hills, CA 92653  
Ed Gooden, Box 14607, Albuquerque, NM 87919

GATAN, INCORPORATED

780 Commonwealth Drive  
Warrendale, PA 15086

Contact: Terry Donovan, (412) 776-5260

Product Line: Specializes in equipment for electron microscopy; these products are: electron energy loss spectrometer (EELS), ion beam milling equipment, image intensifier system, analytical stages of beryllium construction, general EM specimen preparation equipment.

HITACHI SCIENTIFIC INSTRUMENTS  
NISSEI SANGYO AMERICA, LTD.

460 E. Middlefield Road  
Mountain View, CA 94043

Contact: Rod Norville, (415) 961-0411

Product Line: Transmission and scanning electron microscopes, atomic absorption UV-Vis



spectrophotometers and liquid chromatographs.

Sales Offices:

TEM/SEM: 1300 Quince Orchard Blvd., Gaithersburg, MD 20878, (301) 849-1650

AAA/AA: 825 Third Avenue, Suite 2620, New York, NY 10022, (212) 755-2900

INTERNATIONAL SCIENTIFIC INSTRUMENTS, INC.

3255-6C Scott Boulevard

Santa Clara, CA 95051

Contact: Donald J. Evins, (408) 727-9840

Product Line: Scanning electron microscopes with a full complement of accessories, including WDX spectrometers. The ISI SEM line includes: SX-25, SX-30, SS-40, SS-60, LaB6-SS-130T, and DS-130. Also in the product line is our new wafer inspection SEM, the IC-130/5 and IC-130/6. A complete line of scanning electron microscopes suited for any application and budget.

Sales Offices:

Bill Maguire, Avon Park South, 20 Tower Lane, Bldg. 2, Avon, CT 06001, (203) 677-0016

John Fitzpatrick, c/o Santa Clara address, (713) 777-0321

Richard Feller, 800 Roosevelt Rd., Glen Ellyn, IL 60137, (312) 469-8111

JEOL U.S.A., INC.

11 Dearborn Road

Peabody, MA 01960

Contact: Robert Santorelli, (617) 535-5900

Product Line: Manufacturers and dealers of scanning electron microscopes, transmission electron microscopes, scanning transmission electron microscopes, electron probe micro-analyzers, scanning Auger microprobes, energy loss analyzers, and electron beam writing equipment.

Sales Offices:

John Bonnici, American Office Mall, 275 Route #18, East Brunswick, NJ 08816, (201) 254-5600 or 5603

Thayer Brickman, 1633 Bayshore Highway, Suite 245, Burlingame, CA 94010, (415) 697-9220

Jack Francis, 1402 Rambling Hills Dr., Cincinnati, OH 45230, (513) 232-7350

Thomas V. Gildea, 11 Dearborn Rd., Peabody, MA 01960, (617) 535-5900

Ray Gundersdorff, 6236 Gilston Park Rd., Catonsville, MD 21228, (301) 953-2959

Mike Hassel Shearer, 7586 Parkview Mountain, Littleton, CO 80123, (303) 979-0169

Richard Lois, One Kingwood Place, Suite 122B, 600 Rockmead Dr., Kingwood, TX 77339, (713) 358-2121

Lewis McDonald, 3223 G Post Woods Dr., Atlanta, GA 30339, (404) 434-9724

Jean-Pierre Slakmon, Soquelec Ltd., 5757 Cavendish Blvd., Suite 101, Montreal, Quebec, Canada H4W 2W8, (514) 482-6427

Robert Steiner, 640 Pearson St., Suite 102, Des Plaines, IL 60016, (312) 825-7164

KEVEX CORPORATION

1101 Chess Drive

Foster City, CA 94404

Contact: Robert P. Johnson, (415) 573-5866

Product Line: Analytical systems for x-ray energy spectrometry, wavelength-dispersive x-ray spectrometry, Auger, and electron energy spectrometry. Detector-cryostats and analytical spectrometer systems are compatible with all electron microprobe, SEMs, and TEMs in current production. Systems are available for both qualitative and quantitative analysis.

Sales Offices:

Blaise Fleischmann, 6436 Barnaby St., NW, Washington, DC 20015

Dana Kelley, 1101 Chess Dr., Foster City, CA 94404  
Frank Mannino, 627 Harvest Glen Dr., Richardson, TX 75081  
Ken Matz, 702 Main St., Collegeville, PA 19426  
Steve Miller, 602 S. Fairview, Park Ridge, IL 60068

#### KRISEL CONTROL, INC.

16 Farsta Court  
Rockville, MD 20850

Contact: Christos Hadidiacos, (301) 762-1790

Product Line: Automation equipment for electron microprobe/microscope, featuring on-line data acquisition and reduction using Alpha and ZAF correction schemes. Single-crystal automation system for on-line data collection, centering, calculation of orientation matrix, and refinement of cell parameters for an x-ray diffractometer.

#### LINK SYSTEMS (USA), INC.

3290 W. Bayshore Road  
Palo Alto, CA 94303

Contact: Nathan Schneider, (415) 856-2726

Product Line: Energy-dispersive x-ray microanalysis systems including interface with software support for electron energy loss spectroscopy (EELS), Auger, ESCA, and cathodoluminescence acquisition and processing. Simultaneous data acquisition and processing from energy-dispersive and wavelength-dispersive spectrometers including control of the microscope stage and spectrometers for fully automated analysis. Digital image processing systems for picture capture, enhancement, noise reduction and analysis, picture annotation, storage, and retrieval. Scan converters for interfacing digital image processors to electron microscopes and IR, RADA, and SONAR instruments.

#### Sales Offices:

Int'l Instrument Corp., 64 E. Main St., Marlton, NJ 08053, (609) 983-6550  
Pulcir, Inc., Box 357, Oak Ridge, TN 37830, (615) 483-6358  
The Buhrke Co., 1500 Old County Rd., Belmont, CA 94002, (415) 592-2904  
Barry Weavers, 7 Valley Forge Dr., North East, MO 21901

#### WALTER C. MCCRONE ASSOCIATES, INC.

2820 South Michigan Avenue  
Chicago, IL 60616

Contact: John Gavrilovic, (312) 842-7100

Product Line: Ultramicroanalytical services in chemistry and physics.

#### MICRON, INC.

Box 3536  
Wilmington, DE 19807

Contact: James F. Ficca Jr., (302) 998-1184

Product Line: Scanning electron microscopy, electron spectroscopy, electron probe x-ray analysis, transmission electron microscopy, quantitative image analysis, x-ray diffraction, x-ray fluorescence, optical microscopy and metallography, micro hardness, optical emission spectroscopy, differential scanning calorimetry, ultra microtomy, sample preparation.

#### MICROSPEC CORPORATION

265-G Sobrante Way  
Sunnyvale, CA 94086

Contact: Richard C. Wolf, (408) 733-3540

Product Line: WDX-2A wavelength-dispersive x-ray spectrometer systems. X-ray microanalysis systems for use as accessories on scanning electron microscopes and other electron beam instruments. Capable of x-ray analysis of all elements down to beryllium, atomic number 4. Unique design permits attachment to most SEM electron columns.

PHILIPS ELECTRONIC INSTRUMENTS, INC.

85 McKee Drive  
Mahwah, NJ 07430

Contact: John S. Fahy, (201) 529-3800

Product Line: Transmission analytical electron microscopes, scanning analytical electron microscopes, and analytical accessories for electron microscopes.

Sales Offices:

A. Hugo, 55 Virginia Ave., West Nyack, NY 10994  
D. Ahr, 6231 Executive Blvd., Rockville, MD 20852  
H. Ittner, 155 NE 100th St., Suite 403, Seattle, WA 98125  
T. Bates, 7094 Peachtree Industrial Blvd., Suite 220, Norcross, GA 30071  
B. Smick, Suite D45, 2525 East Oakton, Arlington Heights, IL 60005  
Ms. Jo Long, 7302 Harwin Dr., Suite 106, Houston, TX 77036  
S. Spiers, 3000 Scott Blvd., Suite 113, Santa Clara, CA 95050

PHYSICAL ELECTRONICS  
DIVISION OF PERKIN-ELMER CORP.

6509 Flying Cloud Drive  
Eden Prairie, MN 55344

Contact: John Green, (612) 828-6315

Product Line: Surface analysis instrumentation including Auger, ESCA, SIMS; also MBE.

Sales Offices:

John Callaghan, 415 W. Golf, Arlington Heights, Ill., (312) 228-0130  
Edward Graney, 5 Progress St., Edison, N.J., (201) 561-6530  
Leslie Holmes, 1011 S. Sherman St., Richardson, Tex., (214) 669-4400  
Dan Jean, 2 Taunton St., Plainville, Mass., (617) 695-7181  
Jude Koenig and Dixie Sinkovits, 151 Bernal Rd., San Jose, Calif., (408) 629-4343  
Guy Messenger, 7310 Ritchie Hwy., Glen Burnie, Md., (301) 761-3053  
Pete Seamans, 655 Deep Valley Dr., Rolling Hills, Calif., (213) 377-7750  
Jerry Rosenthal, 1382 Old Freeport Rd., Pittsburgh, Pa., (412) 963-6717  
Elm Sturkol, 6509 Flying Cloud Dr., Eden Prairie, Minn., (612) 828-6332

PRINCETON GAMMA-TECH, INC.

1200 State Road  
Princeton, NJ 08540

Contact: Douglas P. Skinner, (609) 924-8980

Product Line: Energy-dispersive x-ray spectrometers and SYSTEM-4 analyzer for electron column applications including energy-dispersive x-ray microanalysis, WDS automation, digital beam control, high-resolution digital image collection and processing, image analysis and EELS. Dedicated XRF systems for a variety of industrial applications are also available.

Sales Offices:

Joe Piersante, Rt. 2, Box 50-A16, Gainesville, GA 30501, (404) 887-9100  
Denny Cannon, Box 36157, Denver, CO 80236, (303) 978-0786  
Tom Griffin, 701 Morewood Pkwy., Rockey River, OH 44116, (216) 331-0120  
Jay Sylvester, 7111 Eckher Rd., San Antonio, TX 78238, (512) 680-3702  
Jake Brown, 556 Weddell Dr., Suite 3, Sunnyvale, CA 94086, (408) 734-8124  
Roland Marti, 5119 Edsel Ave., Los Angeles, CA 90066, (213) 823-1330  
Art Merkle, 1025 Old Mill Grove Rd., Lake Zurich, IL 60047, (312) 540-0555

Scientific System Sales Corp:

333 Jericho Turnpike, Jericho, NY 11753, (516) 822-4880  
203 Middlesex Turnpike, Burlington, MA 01803, (617) 273-1660  
14300 Gallant Fox Lane, Suite 212, Bowie, MD 20715, (301) 262-4104

SPI SUPPLIES

DIVISION OF STRUCTURE PROBE, INC.

535 E. Gay Street  
Box 342  
West Chester, PA 19380

Contact: Dr. John Stasny, (215) 436-5400

Product Line: SPI Supplies: Consumable supplies, film, and small instruments for EM labs. Specializing in innovative new products developed in Structure Probe's four East Coast labs: Plasma-Prep II, SPI-Sputter, Steadi-cool, field finder, immunological reagents. Structure Probe, Inc.: Analytical research services, electron microscopy, surface analysis, failure analysis, STEM, SEM, TEM, EDS, WDS, PSA.

Sales Offices:

535 E. Gay St., Box 342, West Chester, PA 19380, (215) 436-5400  
230 Forrest St., Metuchen, NJ 08840, (201) 549-9350  
63 Unquowa Rd., Fairfield, CT 06430, (203) 254-0000  
1015 Merrick Road, Copiague, NY 11726, (516) 789-0100

C. M. TAYLOR CORPORATION

289 Leota Avenue  
Sunnyvale, CA 94086

Contact: Dr. Charles M. Taylor, (408) 245-4229

Product Line: Various types of multi-element standards for microbeam analysis by SEM, microprobe, and ion probe using energy, wavelength, and mass spectrometers. The standards available exceed 175 different metals, alloys, glasses, compounds, or minerals. Bence-Albee standards are available. Also manufactures many types of sample holders, polishing jigs, and other types of equipment for sample preparation. Also offers analytical services to customers desiring electron-beam microprobe analysis using MAC-5 instrument. Have full ZAF correction capability for microprobe data, using FRAME B or Bence-Albee procedures.

M. E. TAYLOR ENGINEERING INC.

11506 Highview Avenue  
Wheaton, MD 20902

Contact: M. E. (Gene) Taylor, (301) 942-3418

Product Line: Scintillators for SEMs and microprobes, backscatter and secondary electron detectors of the quartz light pipe/scintillator design. Other products include Brimrose image intensifiers, ISI filaments and apertures, specimen mounts, adhesive tabs, vacuum pump oil, and foreline traps. SEM accessories on display and SEM services at Micro Source.

Sales Offices:

Agar Aids, 66A Cambridge Rd., Stansted, Essex, England, OM24 8DA  
Science Services, Badstr. 13, 8000 München 70, Federal Republic of Germany  
Micro Source, 620 Hungerford Dr., #12, Rockville, MD 20850, (301) 251-0642

TRACOR NORTHERN

2551 West Beltline Highway  
Middleton, WI 53562

Contact: Jim Aeschbach, (608) 831-6511

Product Line: Wide range of data processing instrumentation for qualitative and quantitative x-ray analysis. Products include data acquisition, reduction, and automation for electron microprobe, SEM, TEM, and STEM. Featuring simultaneous EDS/WDS acquisition/reduction, digital beam control allowing for digital mapping, line scans, and other digital image processing. Also particle location, sizing, and elemental characterization. Flexible packaging allows instrument to be used also for ELS, Auger, ESCA, SIMS, etc. Other products are used in nuclear, optical, signal-averaging, and medical applications.

Sales Offices:

345 E. Middlefield Rd., Mountain View, CA 94043, (415) 967-0350

3040 Holcomb Bridge Rd., Norcross, GA 30071, (404) 449-4165

Franklin Park Office, 134 Franklin Corner Rd., Lawrenceville, NJ 08648, (609) 896-1114

Suite 1458, Bldg. A, Miamisburg Centerville Rd., Dayton, OH 45459, (513) 439-3990



## J-1 Failure Analysis in Microelectronics

### AUTOMATED MEASUREMENTS OF INTEGRATED CIRCUIT LINEWIDTHS BY ELECTRON MICROSCOPY

G. S. Fritz and A. T. Laudate

Because of the great advances in integrated-circuit (IC) technology in recent years, chips have become more densely packed and IC lines have become smaller. At present, most IC linewidths are measured by optical systems, the best of which can only measure linewidths down to 0.5  $\mu\text{m}$  under ideal conditions. As IC lines approach submicron sizes, with the use of techniques such as electron-beam lithography, optical systems will no longer be able to measure the lines accurately and reproducibly. For these geometries, the shorter wavelengths of the scanning electron microscope (SEM) provide much better precision than optical systems.

In designing a linewidth measurement system for the semiconductor industry, the major needs are based on precision or reproducibility, accuracy, and high throughput. The relative importance of these needs depends on the application: the needs of researchers engaged in product development are quite different from those of manufacturing facilities. In manufacturing, reproducibility has high priority, to insure that a process remains the same from one production line to another. High throughput is also of prime concern to manufacturing, so provision should be made for the SEM stage to be automatically positioned to predefined areas of interest. In the research laboratories, accuracy is the most important consideration, since absolute dimensions are important in obtaining a targeted device performance. The problem of accurate measurements has not been totally solved, since a universally accepted definition of the edge of a line has not been established. A measurement system should therefore have some method of minimizing this effect.

The paper describes an automated linewidth measurement system designed, in conjunction with the SEM, to meet the coming needs of the IC industry. Both the hardware and software of the system are described.

#### *System Description*

The computer for the system is either an LSI-11/2 or LSI-11/23 (trademarks of Digital Equipment Corp.). To meet the need for high throughput, the system includes a full stage automation package consisting of axis positioners and stepping motors. Up to 100 stage positions (X, Y, and Z) can be indexed relative to a reference position and can then be stored on disk for later recall. Once a specific set of stage positions has been recalled from disk and the reference position for the present wafer has been indexed, the analysis can be started. The stage is automatically moved to each defined position and selected IC lines are measured in each field manually or automatically. If a different type of stage movement and analysis is required, the operator can write his own simple "schedule" of commands to perform the desired type of analysis. This "schedule" may also be stored on disk for later recall. For the SEM with a beam blanking device such as a beam deflector, the system is equipped with a latch bit that can blank the beam under computer control when measurements are not being made, so that beam damage to the wafer is minimized.

Linewidth measurements are made with a digital scan generator to control the position of the electron beam of the SEM and monitor its video signal. The digital scan generator consists of a video processor and an X-Y scan controller. The video processor includes an 8-bit analog-to-digital converter (ADC) capable of dividing the SEM video signal into 256 distinct gray levels. Multiple samples may be obtained at a single pixel at a rate of 1  $\mu\text{s}$  per sample and summed into a 20-bit accumulative register. In addition, a 12-bit digital-to-analog converter (DAC) allows the computer to output a video signal to the SEM CRT displays.

---

Author Fritz is at Tracor Northern, Inc., 2551 W. Beltline Hwy., Middleton, WI 53562; author Ladaute, at JEOL-USA, Inc., 11 Dearborn Road, Peabody, MA 01960.

The programmable X-Y scan controller consists of two 12-bit DACs for positioning the SEM beam and a joystick module. The joystick module is used for selective control of the X-Y cursors superimposed on the digital raster. The positions of the cursors can be read by the computer and used to index areas to be analyzed. Several utility programs are available that provide control of beam positioning, video signal acquisition, and output to the SEM CRT for graphics information.

### *Discussion*

The method of analysis used for linewidth measurements consists of acquiring video profiles across the IC line of interest either horizontally or vertically. Once acquired, the linewidth measurements are made manually by the adjustment of cursors on the video profile or by one of several automatic methods. The automatic methods include peak-to-peak, minimum-to-minimum, maximum-slopes, peak-percentage, and video-thresholding techniques. The reason different methods are employed is that one can obtain several types of profiles when examining photoresists, aluminized lines, metallic lines, and the same lines at different stages of manufacturing. Two of the automatic techniques are illustrated in Fig. 1. Peak-to-peak measurement is shown in Fig. 1(a). In the peak percentage technique the program locates the peaks and then determines the point at which the designated peak intensity percentage is found. In Fig. 1(b) a peak percentage of 50% was used to determine the edges of the line.

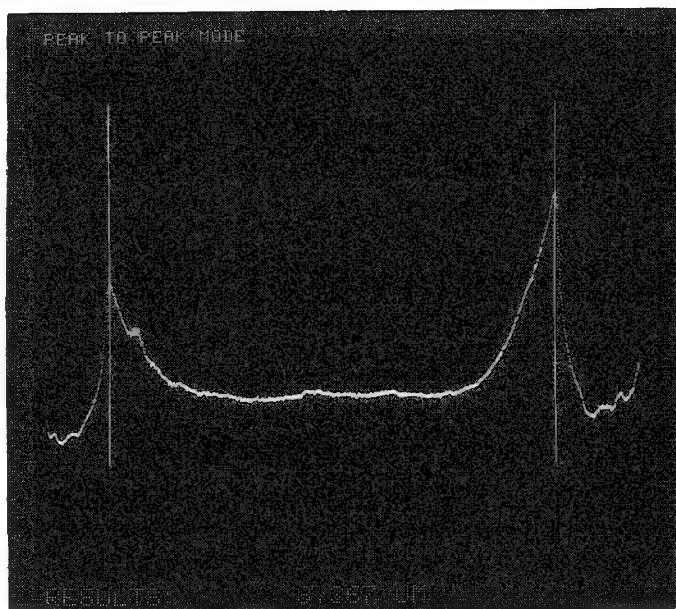
Several advantages are realized in this method of analysis. First, by using an automated process to determine the linewidths, the operator is removed from the decision-making process, so that operator bias is removed and reproducibility is enhanced. Second, video profiles (which are acquired digitally, in contrast to analog methods) can be signal averaged at each point for any specified period of time. This procedure improves the signal-to-noise ratio and the measurement statistics. Figure 2 illustrates this effect of signal averaging. In the profile of Fig. 2(a), 5 video samples were used at each point; in Fig. 2(b), 1000 video samples. One could also take multiple scans across the region of interest and average the scans together; however, it is difficult to assure that the electron beam remains at the same position during multiple scans because of sample-beam interactions. The system does allow the measurements of multiple scans to be averaged and a standard deviation to be obtained, but that is not the same as acquiring several scans to obtain one signal-averaged scan and making a measurement on that resultant scan.

The third advantage of this system is the computer-controlled acquisition of the video profiles. The beam is digitally positioned to each point in the scan and allowed to settle before the actual video signal is acquired. Most SEM scan generators use analog electronics, which may produce a nonlinear image at video rates. Systems that employ a marker bar or cross hairs on the SEM image, at video rates, to measure the linewidths are particularly subject to this nonlinearity. Adjustment of the bar or cross hairs at slow scan rates is extremely cumbersome. The nonlinearity of the image at video scan rates is due to the response time of the scan coils of the SEM, so that some SEMs may perform better than others in this regard. However, it is likely that any SEM will have some nonlinearity at video rates.

A fourth advantage is the ability to minimize the effect of defining the edge of a line and also the calibration of the SEM magnification. The system allows the operator to calibrate the scan in both the X and Y directions independently to a known "standard." The operator simply measures the "standard" line using the type of automatic measurement that will be used on the unknowns and then supplies the computer with the "true" value. Using this technique, where the standard and unknown are measured in the same manner, one can minimize the effect of the question: Where do we define the edge?

One of the major questions about any linewidth measurement system is, what precision and accuracy can be expected? This is not a trivial question, since many factors affect precision and accuracy. One is the level of noise on the video profile. A study was performed in which an 8  $\mu\text{m}$  IC line was measured at a magnification of 5400 $\times$  in the peak-to-peak mode. The video profiles for this study were acquired at different levels of signal averaging. The relative uncertainty in the video signal at a point in the center of the video profile line versus the amount of signal averaging performed is shown in Fig. 3. As expected, the uncertainty in the video signal declines as  $1/\sqrt{n}$ , where  $n$  is the number of samples averaged in the measurement. The precision of the linewidth measurements versus





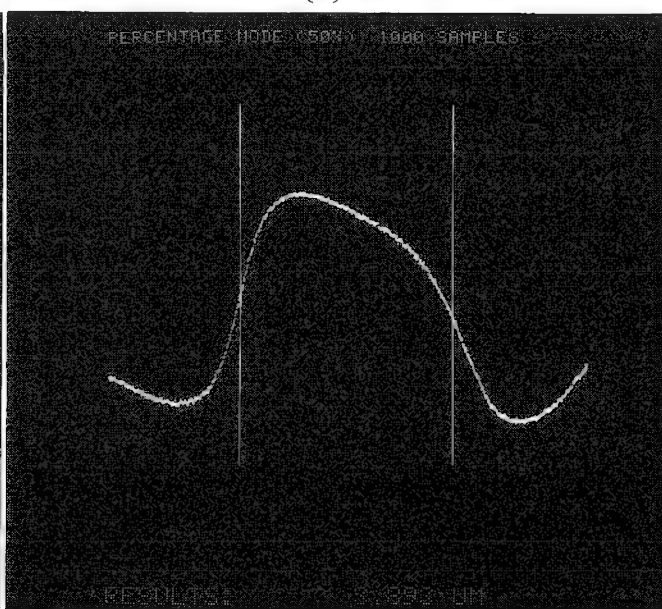
(a)



(a)



(b)



(b)

FIG 1.--(a) Example of peak-to-peak linewidth measurement displayed on SEM CRT screens: video profile is shown along with two vertical lines depicting the peaks as determined by the software; (b) peak percentage linewidth measurement: point at which intensity is 50% of peak is defined as edge of line.

FIG. 2.--(a) Video profile across IC line in which 5 video samples at each point in profile were used to determine average video signal: line measured with a peak percentage analysis set as 50% of peak; (b) profile across same line with 1000 video samples.

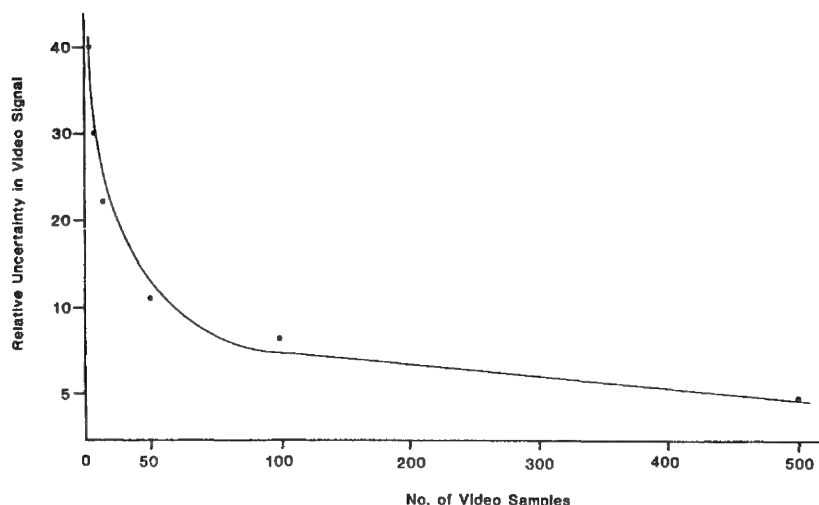


TABLE 1.--Correlation of video uncertainty in linewidth measurement of 8  $\mu$ m line

No. of Video Samples	Relative Uncertainty of Video	Uncertainty in Linewidth Measurement
500	4%	.008 m
100	8%	.015 m
50	11%	.019 m
10	22%	.035 m
5	30%	.051 m
2	39%	.102 m

FIG. 3--Relationship of uncertainty of video signal at the center of 8  $\mu$ m IC line with amount of signal averaging performed.

the amount of signal averaging and thus the level of noise on the signal is shown in Table 1. The uncertainty in the video level evidently affects the uncertainty of the measurement. With a relative video uncertainty of 4% we were able to obtain linewidth measurements with an uncertainty of 0.008  $\mu$ m.

Among other factors that affect the precision and accuracy of the measurements, the effect of the dynamic range of the video profile and the rate of change in the video signal at the edge of the line must be examined if one is to obtain a better understanding of what precision and accuracy can be expected under differing conditions.

#### Summary

A computer-based system has been described that measures IC linewidths automatically by use of video profiles. The system includes a package to allow fast registration of wafers to selected areas of analysis.

Although electron microscopes are not widely used for the measurement of linewidths, this application will become increasingly more important as the lines of ICs become smaller and optical means can no longer provide the precision and accuracy necessary.

#### References

1. Mitchell Rose, "Photometry: A better look at masks and wafers," *Test and Measurement World*, Feb.-Mar. 1982.
2. Mitchell Rose, "Masks and wafers: Linewidth measurements in a submicron industry," *Test and Measurement World*, Sept. 1982.
3. Peter Singer, "Linewidth measurement: Approaching the submicron dimension," *Semiconductor International*, March 1983.

## COMPOSITION OF ALUMINUM STRINGERS IN VLSI

C. M. Ward, R. R. Olson, R. Brewer, and S. G. Johnson

Metallization systems for advanced VLSI (very large scale integration) continue to receive a great deal of scrutiny. The interconnects must meet stringent dimensional, physical, and metallurgical requirements. Once the system is developed, the technique must be adapted into a fabrication process that meets very high standards for quality and reliability. As line widths and pitches have grown smaller, many minor problems have become major. One is the problem of metallization stringers; that is, small, hard-to-etch metal residue that runs parallel to steps on the wafer surface. These stringers are left after dry metallization etch processes and can short out adjacent metal lines.

Etch processes must be anisotropic to prevent undercutting the aluminum beneath the resist. Organic resists have been successfully combined with plasma etching in efforts to achieve an anisotropic etching process, but they can leave stringers. Various experiments have been reported in which good anisotropic etches have been obtained by use of standard photoresists, but it has proved difficult to achieve anisotropy with nonorganic masks such as  $\text{SiO}_2$  and  $\text{Si}_3\text{N}_4$ .<sup>1</sup> Models of the stringer phenomenon have been proposed, but few direct measurements of their composition have been made to check the models. This study is aimed at analyzing stringers as they form to obtain a better understanding of the process.

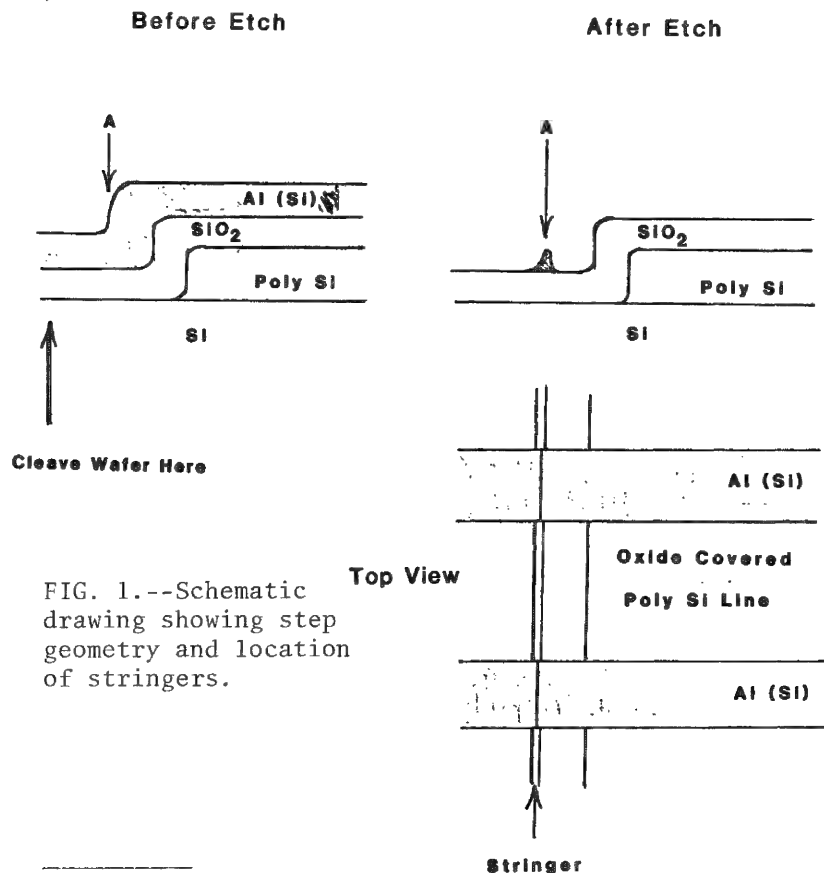


FIG. 1.--Schematic drawing showing step geometry and location of stringers.

### Experimental

The test structure for this investigation is a standard metallization pitch pattern, which gives an array of contact grooves overlain with aluminum. The base wafers have start oxidation and are then overlaid with  $1\text{ }\mu\text{m}$  of 6% low-pressure CVD phosphosilicate glass. The glass is patterned to form the grooves and then  $1\text{ }\mu\text{m}$  of aluminum (1% silicon) is sputter deposited at low temperature. A standard organic resist is used to delineate the lines and etching is done in a D&W etcher with  $\text{CCl}_4$ .

Samples were removed and evaluated at every step of the process from metallization to passivation. Analysis was performed on a PHI Model 600 high-resolution scanning Auger microprobe. The extensive sample manipulation capability and SEM resolution permit a full analysis to be performed in the same system. This procedure eliminated problems due to contamination and

The authors are with Perkin-Elmer, Physical Electronics Division, 6509 Flying Cloud Drive, Eden Prairie, MN 55344. They wish to thank D. F. Paul and C. T. Hovland for their support. (Please direct inquiries to R. R. Olson.)

area relocation. Figure 1 is a representation of stringers. All analyses were done at the same array location.

### *Results*

Figures 2 and 3 are typical areas at the end of processing. The stringers can be clearly seen and exhibit their most interesting property of not being on the wall but below the original location of the outer surface of the aluminum. In some cases a web of material is visible all the way back to the glass. Auger spectra taken from the top of the array show the stringers to be high in oxygen and carbon and show a strong aluminum oxide structure.

Figure 4 shows a similar area after metal deposition, resist application, exposure, and developing, but before etching. The aluminum has an oxide structure and shows a small amount of carbon. Depth profiles comparing the top of the metal-covered oxide finger and bottom of the trough between the fingers on the array indicate carbon less than 25 Å thick and an oxide layer about 50 Å thick. The layer is slightly thicker in the bottom of the trough.

Figure 5 shows the aluminum immediately after the oxide clear step in the reactor. Islands of uncleared oxide are apparent. An Auger spectrum shows a substantial increase in carbon along with chlorine and fluorine. The fluorine is unexpected and probably results from a leak in one of the reactor valves. Auger images of oxygen and aluminum oxide delineate the edges of the grooves (Figs. 6 and 7); carbon shows a relatively uniform distribution. Chlorine and fluorine are completely uniformly distributed. Depth profiles at the top and bottoms of the grooves indicate that carbon is now 25-50 Å thick, whereas the oxide remains between 50-75 Å thick.

The sample was then fractured through one of the grooves to expose the side wall (Fig. 8). Large unetched areas are visible on the side walls. Spectra were taken at five points (Figs. 9-14). Point 1 is on the aluminum that was exposed by the cleave going through the edge of the side wall. The next points are on the bottom of the groove, in the notch at the bottom of the side wall, on the side wall, and on top. The side walls show the highest oxygen. A small amount of contamination is also noted in the notch. Oxygen and carbon maps verify that the unetched areas are oxidized aluminum with some carbon. Depth profiles on the side wall show carbon to be 25 Å thick with oxygen now at 100 Å.

At 6 min into the etch cycle the aluminum is near clearing. A cross section at this point shows the stringers to be clearly forming (Fig. 15). Surveys and depth profiles show the side-wall composition to be unchanged with a thin carbon layer and 100 Å of oxide. Maps of oxygen and aluminum oxide taken at a view normal to the surface show that the highest concentrations are at the forming stringers.

### *Discussion*

This analysis of the stages of dry plasma etching shows that the oxidized aluminum noted in the final stringers is not an artifact of the exposure of thin aluminum to air but represents the real cause of the problem. As deposited, the aluminum has a native oxide and a thin layer of carbon. During the etching process carbon is deposited on side walls as well as the surface. But more important, the native oxide is not removed from the vertically oriented side walls.

In the plasma etcher, positively charged ions impinge on the wafer with their momentum directed normal to the surface of the wafer. The vertically oriented side wall, which is not subject to the energetic ion flux, exhibits a lower etching rate when it is covered with a thin oxide. On the horizontal surface the oxidation is removed and etching proceeds anisotropically, eventually going behind the vertical oxide wall and leaving a stringer.

Oda and Hirata proposed that carbon deposited on side walls, which they saw as films in the SEM, explained the anisotropic behavior of plasma-etched Al.<sup>1</sup> Sato and Nakamura investigated this further and concurred.<sup>2</sup> They noted that positive ions in the plasma are directed vertical to the surface and propose that these ions break up the polymer films on the surface, permitting Cl radicals to continue the attack on the surface but not on the side walls. Zarowin emphasizes that the degree of anisotropy of a plasma etching process is dominated more by the directionality of ion transport from the plasma to the wafer surface than by passivation effects.<sup>3</sup>



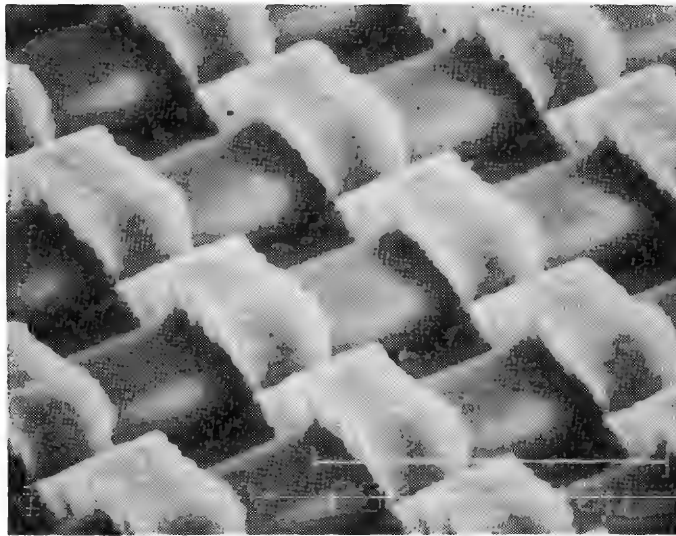


FIG. 2.--SEM image of stringers.

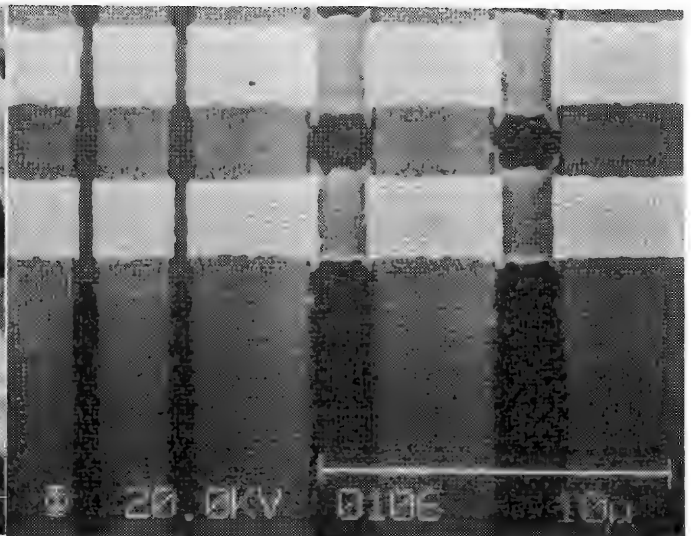


FIG. 3.--SEM image of stringers.



FIG. 4.--SEM image of test structure before plasma etching.

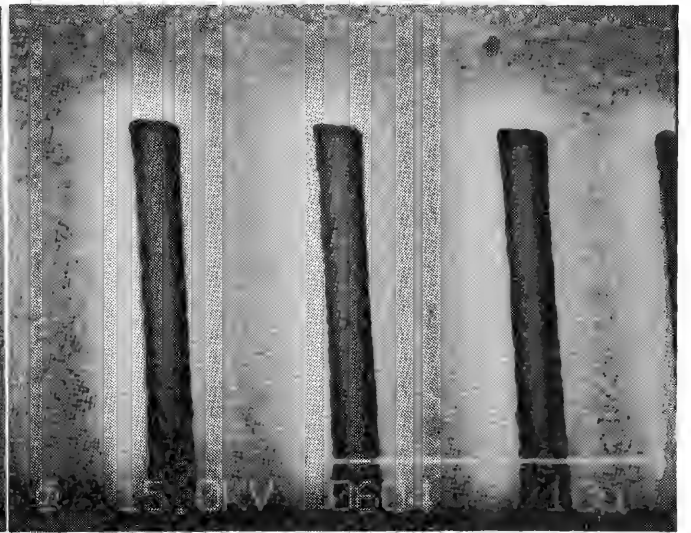


FIG. 5.--SEM image of test structure after oxide-removal step of plasma-etching sequence.

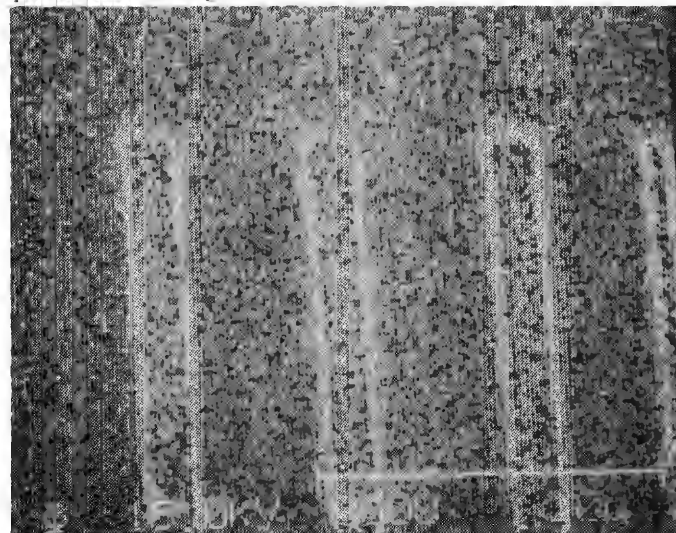


FIG. 6.--Auger image of oxygen on same area as Fig. 5.

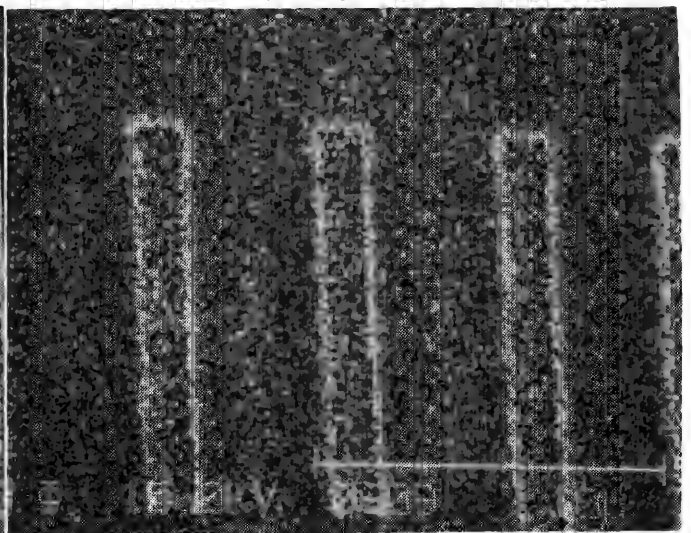


FIG. 7.--Auger image of aluminum oxide on same area as Fig. 5.

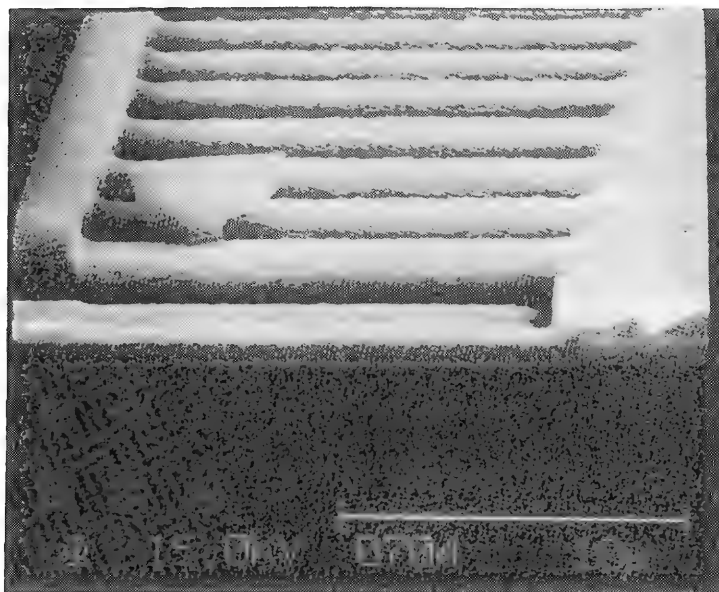


FIG. 8.--SEM image of edge of cleaved wafer.

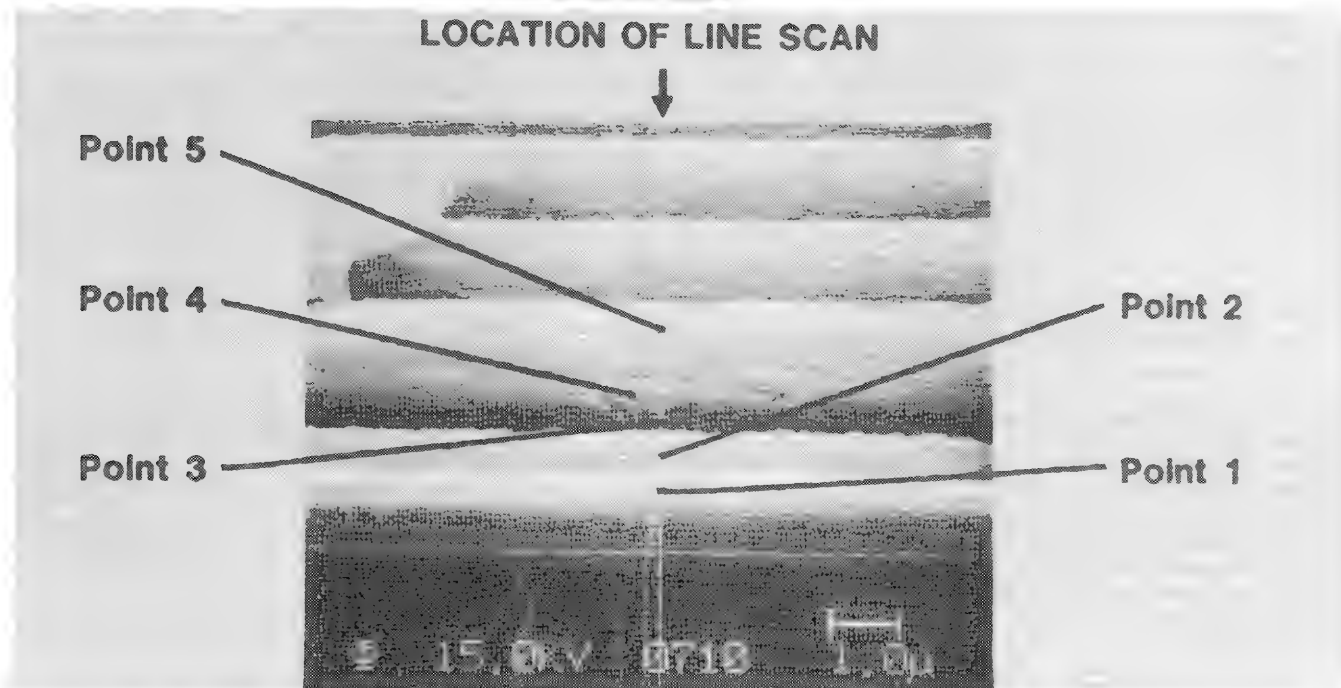
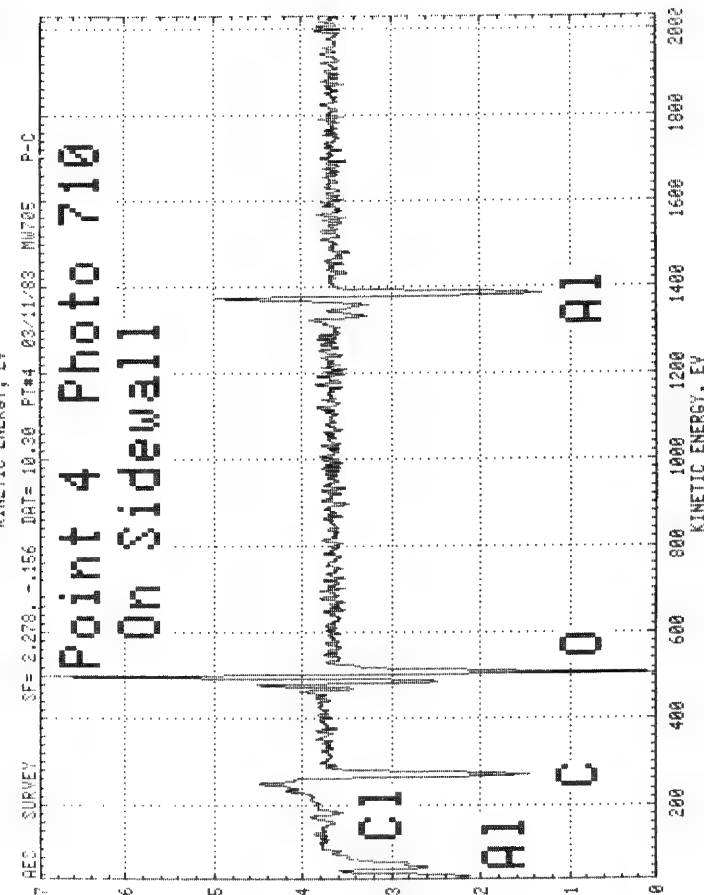
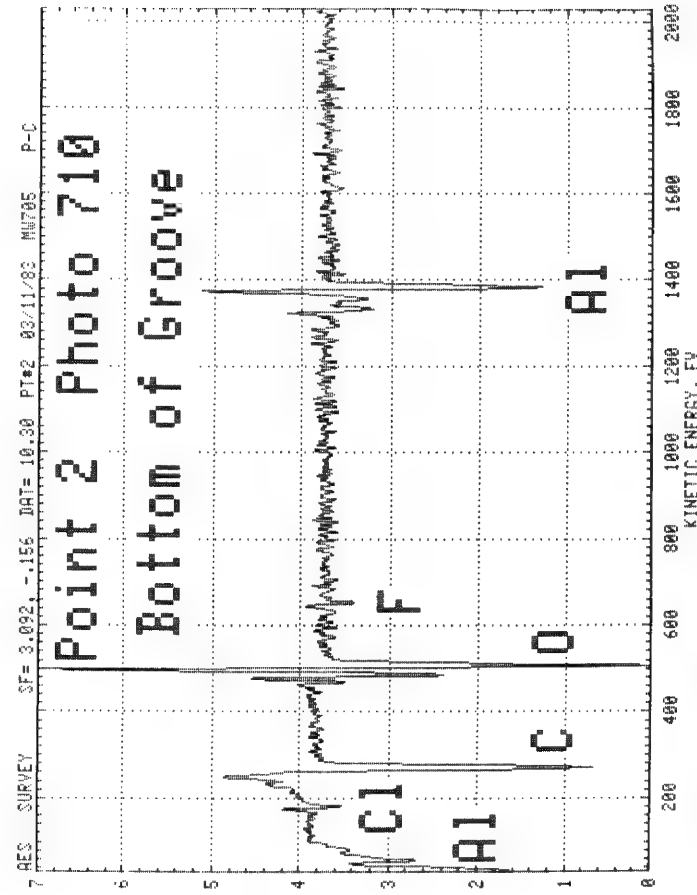
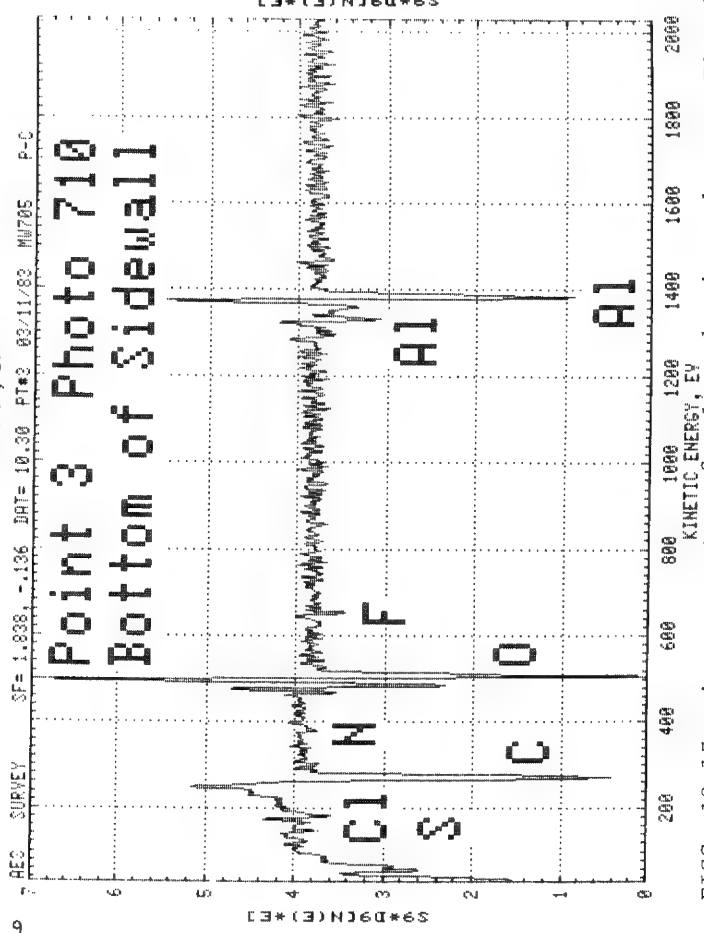
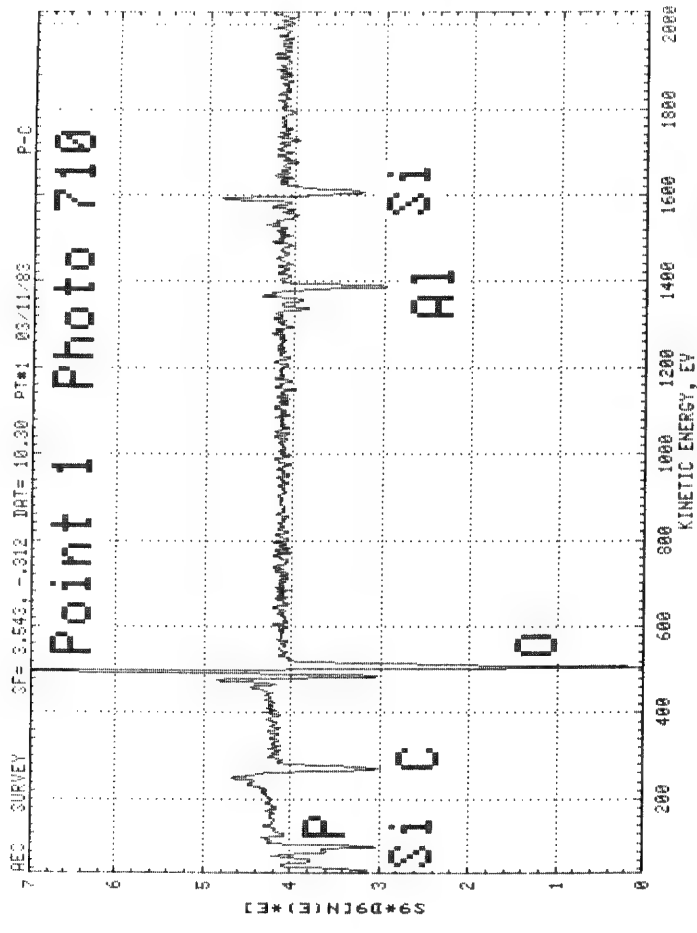


FIG. 9.--Higher magnification SEM image of area in center of Fig. 8, showing locations of point AES analysis.

This study shows that not only is carbon deposited but the side-wall native oxide is not etched as rapidly in the etch initialization step leading to the appearance of stringers. Clearly the challenge of creating small configurations without stringers must involve elimination of the native oxides with an isotropic etch prior to the regular cycle.

#### References

1. M. Oda and K. Hirata, *Jpn. J. Appl. Phys.* 19: 1405, 1980.
2. M. Sato and H. Nakamura, *J. Electrochem. Soc.* 2522, Nov. 1982.
3. C. B. Zarowin, *J. Electrochem. Soc.* May, 1982.



FIGS. 10-13.--Auger spectra of selected points shown on Fig. 9.

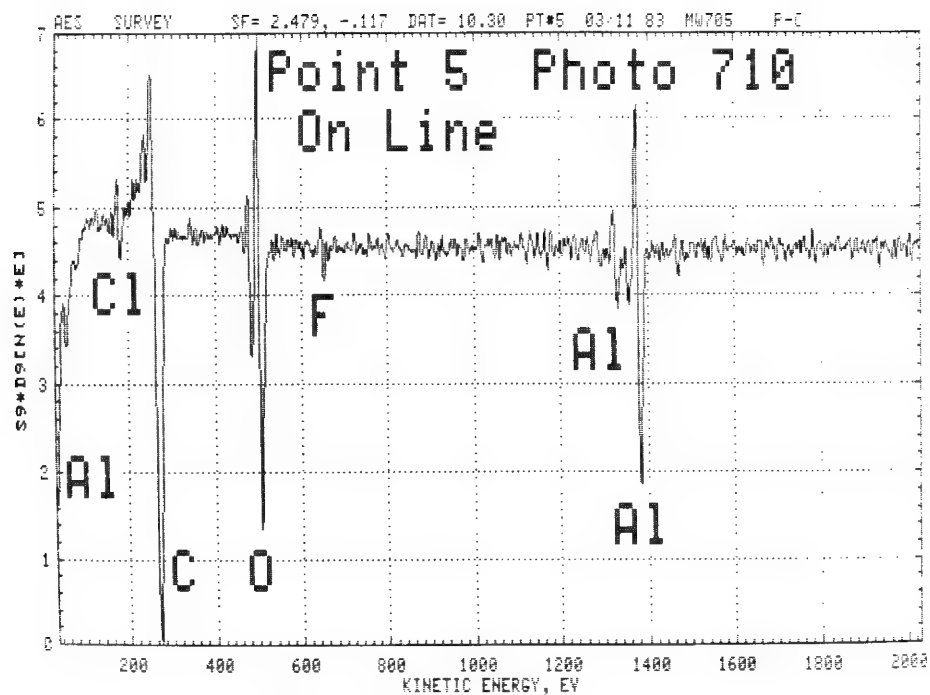


FIG. 14.--Auger spectrum of selected point shown on Fig. 9.

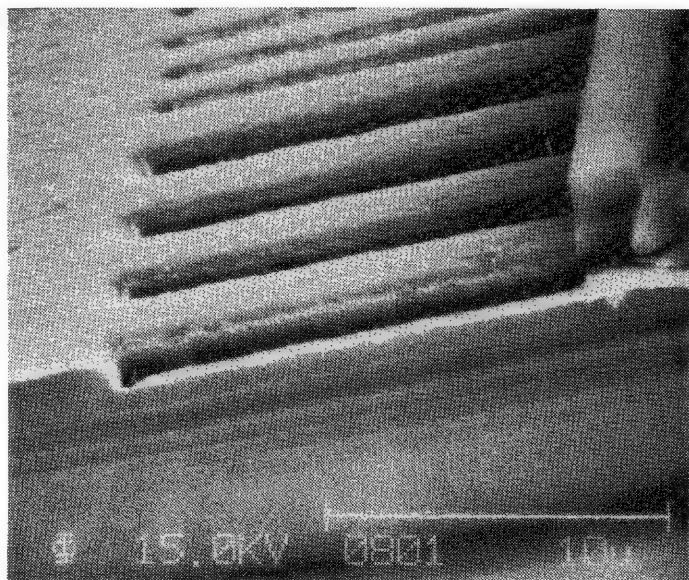


FIG. 15.--SEM image of cleaved wafer which was removed from plasma-etching system at 6 min into etch cycle. (Note forming stringers.)



## VOLTAGE MEASUREMENTS OF HIGH VOLTAGE TRANSISTORS USING AUGER ELECTRON SPECTROSCOPY

R. B. Bolon, M. D. McConnell, D. W. Tong, and D. M. Taylor

Measurements of the shift in energy of Auger lines due to local potentials has been found to be the preferred method for measuring the voltage profiles across reverse-biased junctions in high-voltage transistors with passivated coatings.

Scanning electron microscopy is a widely used alternative to fine metal contact probes for characterizing voltages on integrated circuits and other semiconductor devices. The advantages are superior spatial resolution and the ability to distinguish voltage differences beneath surface passivating films,<sup>1,2</sup> provided of course that the beam has sufficient energy to penetrate the film. The effect of local voltages on a sample are generally observed as variations in SEM image contrast. The mechanisms for this are described by Wells<sup>3</sup> and include shifts and distortions of the emitted electron spectrum as well as deflections in their trajectories caused by field gradients above the sample. The combined result is a change in the number of electrons collected by the secondary-electron detector. A more quantitative measure can be obtained by energy analysis of these emitted electrons.

In the early days of the development of Auger electron spectroscopy, attempts were made to augment the capabilities of the SEM by adding electron energy analyzers. MacDonald<sup>5</sup> found that all samples showed essentially only carbon, a consequence of oil contamination in the poor SEM vacuum. He then proposed that relative voltages could be determined by a measurement of the shift in the carbon Auger peak, which would be equal to the applied voltage. Unfortunately even the best cylindrical mirror analyzers (CMA) have an energy resolution of only 1 eV or more, which is inadequate to determine voltage gradients through active regions on discrete low-voltage devices. Instead, most current workers use the voltage shift observed in the low-energy secondary-electron peak. Although voltage differences of the order of 100 mV are claimed, there are complications due to spectral changes caused by surface topography, compositional differences, and charging of portions of the sample as well as various components within the specimen chamber.

In the case of high-voltage devices, the field gradients are so great that the secondary electron peak either cannot be detected or is so badly distorted that it cannot be used. Fortunately the Auger peaks such as oxygen KLL at 508 eV, are sufficiently energetic that they can be used with local potentials of over 700 V. In this range, the 1 or 2 eV resolution of the detector is more than adequate to describe the corresponding gradients. By measuring the shift in selected Auger lines of elements in the surface of high voltage transistors, we were able to map out the surface potential distribution under reverse-bias conditions. Furthermore, it was demonstrated that measurements could be made through surface passivation layers, provided that the beam had sufficient energy to penetrate the coating completely and render it conductive through ionization.

In this current study we have applied this technique to 1kV high-voltage NPN power transistors. Such devices require special design and construction to avoid local voltage gradients sufficient to initiate breakdown. Highly doped field spreading rings around the base region are used to control the gradient. The base collector junction is passivated with layers of semi-insulating polycrystalline silicon (SIPOS) and silicon nitride. Until now, due to the small dimensions and necessary passivating top layer, there has been no suitable experimental method for actually measuring these profiles. Instead, investigators have relied on computer models to predict them. A primary goal of this study was to test the accuracy of the computer model predictions.

---

Authors Bolon, McConnell, and Tong are with General Electric Corporate Research and Development, K1, GE R&D Center, Schenectady, NY 12303. Author Taylor is with the School of Electronics Engineering Science, University College of North Wales, Bognor, Gwynedd, Great Britain LL57 1UT.

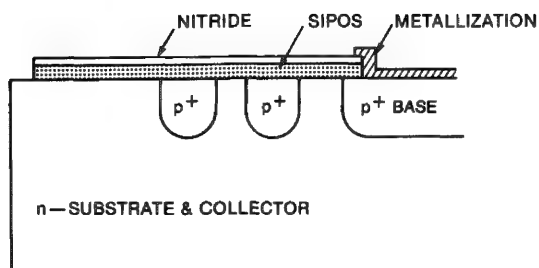


FIG. 1.--Cross-section diagram of base-collector junction.

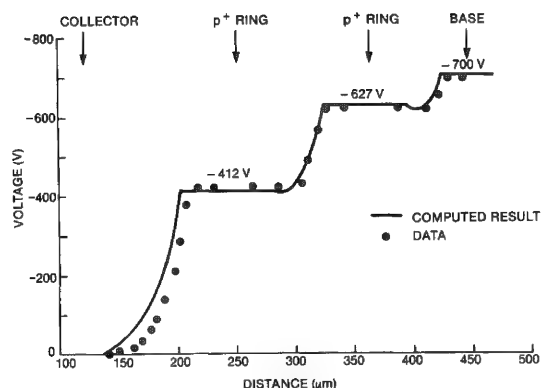


FIG. 2.--Experimental and computed surface potential.

### Method

The measurements were carried out in a PHI 590 SAM. The transistors were isolated from the sample stage with a simple insulating holder and the active elements of the passivated Si 1kV NPN power transistor wired to existing BNC connectors for power. Figure 1 illustrates the device structure in the high-field base-collector region where measurements were made under reverse bias. Two  $p^+$  field spreading rings are adjacent to the base region and the device passivated with a 2000Å nitride layer over a 4500Å SIPOS layer.

The instrument was operated with a beam energy of 8 kV. Various voltages up to -1000 V were applied to the PN base collector junction with one side (generally the collector) grounded. Data were then collected with the oxygen KLL Auger electrons. (Oxygen was a contaminant on the nitride coating.) Two methods were used. The first was to position the beam point by point through the junction region and then read the energy of the shifted Auger peak. However, this method tended to be tedious, so the scanning capabilities were also utilized. In this mode the analyzer would be set to a given energy above an isolated peak. Whenever the local potential shifted the peak into the window, the resulting signal would be recorded on the image. The result was an equal potential map for that energy. The actual surface potential is simply this value minus the value of the Auger line. By periodic adjustment of the analyzer during a scan, several bands of equipotential lines could be displayed on a single image.

### Results and Discussion

Figure 2 shows a comparison of a computer calculated surface potential to experimental data collected with a reverse bias of -700 V applied to the base-collector junction. The agreement between data and theory is sufficiently good to establish the validity of the model. Details of the computer program and model will be published elsewhere.

The accuracy of the experimental data was checked by measurement of the potential on the metallized contact against a calibrated power supply. This procedure established the accuracy at several volts, which was comparable to the width of the analyzer window used. Based on previous work,<sup>1,2</sup> it is believed that the voltage drop through the nitride layer is negligible, a finding that is further supported by the good agreement between the experimental data and theoretical calculations. Spatial resolution was of the order of 2 μm as judged in the imaging mode.

Figure 3(a) is a secondary-electron image of the region between the base and the collector. Figure 3(b) is the corresponding equipotential map obtained when the analyzer was periodically adjusted by predetermined amounts during the course of a scan, which resulted in the offset or stepped appearance of the image. The actual surface potential is the indicated analyzer value minus the oxygen Auger energy of 508 eV.

### References

1. D. M. Taylor, "The effect of passivation on the observation of voltage contrast in the SEM," *J. Phys.* Vol. D-11: 2443-2454, 1968.
2. D. M. Taylor et al., "Electron-beam-induced conductivity and related processes in

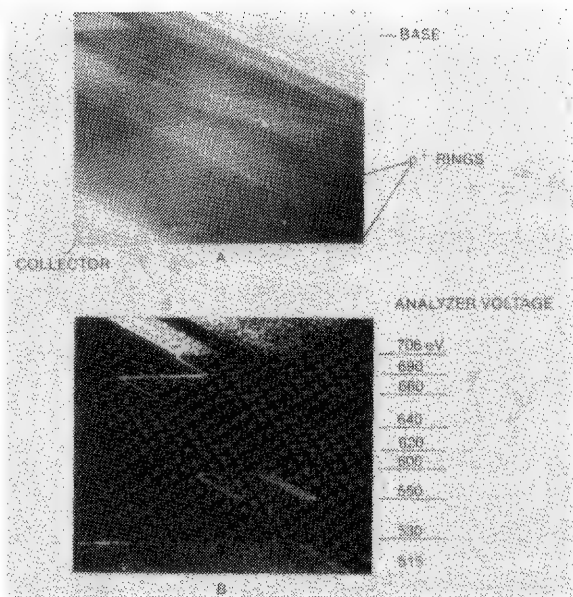


FIG. 3.--(a) SEM of base-collector;  
(b) SAM of biased base-collector

insulating films," *IEE Proc.* 128 (Pt. A): 174-182, 1981.

3. O. C. Wells, *Scanning Electron Microscopy*, New York: McGraw-Hill, 1974, 180-207.

4. R. E. Ogilvie et al., "An electron spectrometer for the SEM," *Proc. 4th Natl. Conf. EMA*, paper 63.

5. N. C. MacDonald, "Potential mapping using Auger electron spectroscopy," *SEM/1970*, 483-487.



# 1 Microbeam Analysis in Geological Science

## IN SITU ELEMENTAL AND MINERALOGIC ANALYSIS OF PEAT BY SEM AND PETROGRAPHIC TECHNIQUES

Robert Raymond Jr. and Sharon Bardin

A major problem with scanning electron microscope (SEM) analysis of elemental and mineralogical components of peats has been to identify the botanical constituents containing or associated with the substances being measured. Observations of these relationships can be an important first step in understanding the distribution, genesis, and diagenesis of mineral matter and elements in peat. Both freeze-drying and critical point drying techniques have produced nondessicated peat specimens suitable for SEM analysis. However, neither method allows one to identify the altered, decomposed plant materials that make up the bulk of most peats. Combining methods for producing oriented microtome sections of peat with those for critical point drying has resulted in a technique that allows one not only to carry out SEM analyses, but also to identify the botanical affinities of the associated plant materials.

### *Sample Preparation*

The method for preparation of oriented microtome peat sections for petrographic analysis is from Cohen,<sup>1</sup> and is a modification of techniques Johansen developed for plant studies.<sup>2</sup> In brief, an oriented sample of peat is sealed in a 2cm<sup>3</sup> box made from 100-mesh (150  $\mu$ m opening) copper screen. The sample is then "fixed" in a solution of alcohol, formaldehyde, acetic acid, and water. Next, the sample is gradually dehydrated in a series of ethanol and tertiary butyl alcohol solutions. In a vacuum oven, the dehydrated sample is impregnated with molten paraffin and later removed from the oven and allowed to cool. After the paraffin hardens, the copper box is removed and the impregnated cube is mounted with specific orientation on a wooden block for microtome sectioning. A 15 $\mu$ m-thick slice is cut with a sliding microtome and mounted on a 25  $\times$  75mm glass slide with Haupt's adhesive. Xylene is used to dissolve the paraffin from the mounted peat thin section, and before the xylene can evaporate, a permanent slide is made by securing a cover glass to the microscope slide with Canada balsam.

The preparation of peat thin sections for SEM analysis is similar to that above except that a 25 $\mu$ m-thick section is cut, and, after dissolution of paraffin with xylene, the wet slide is immediately placed in a critical point dryer and immersed in liquid CO<sub>2</sub>. The 25 $\mu$ m section of peat allows minerals greater than 15  $\mu$ m in diameter (e.g., large pyrite framboids) to remain in the peat section following microtoming. Placing the xylene-saturated sample in the critical point dryer insures that dessication features will not develop as a result of the xylene evaporating. Some authors, such as Hayat,<sup>3</sup> suggest an intermediate bath of pure acetone between the xylene baths and the critical point drying. This stage is recommended because of the total miscibility of acetone in liquid CO<sub>2</sub>. This intermediate bath has not been used for the samples shown in this text, but this step will be tested in future preparations. We follow critical point drying procedures as suggested by Ladd,<sup>4</sup> the manufacturer of our instrument. Following critical point drying, the samples are immediately coated with approximately 200 Å of gold palladium.

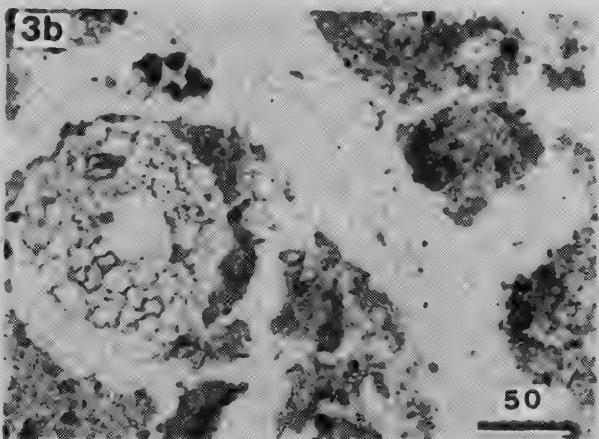
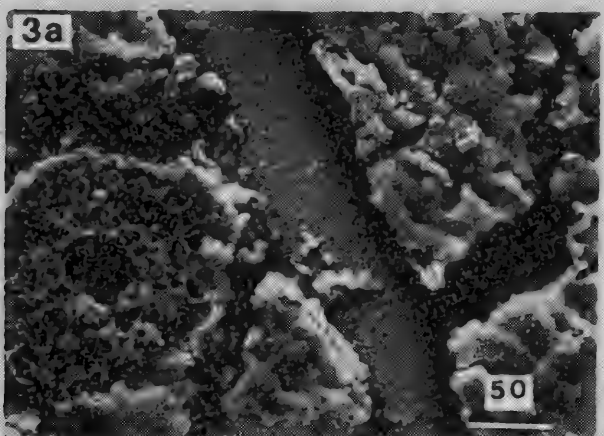
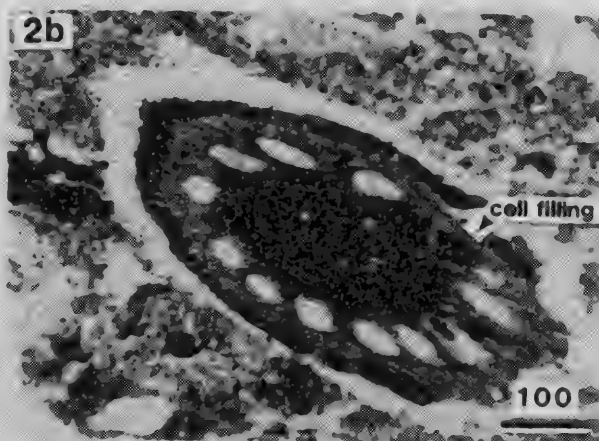
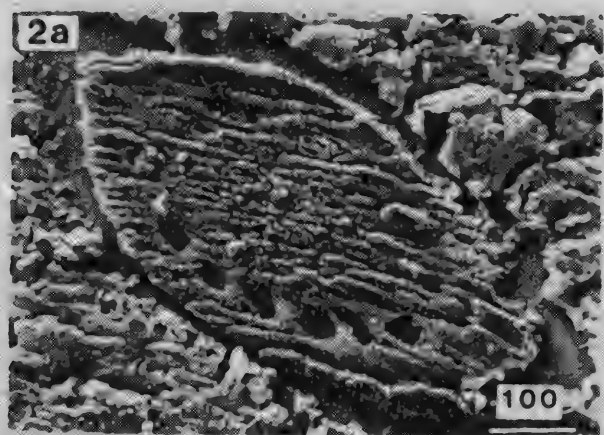
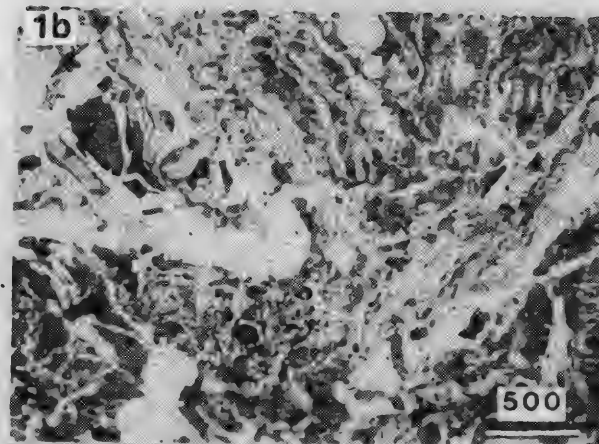
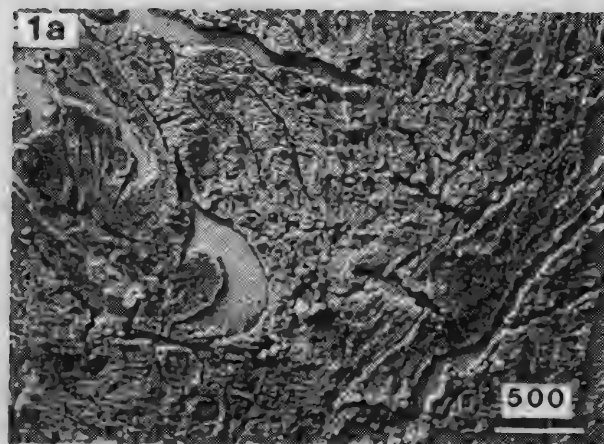
Petrographic and SEM sections can be made independently of each other. However, in order to improve correlation between the two, it is preferable to cut serial sections of 15 and 25  $\mu$ m thicknesses from the paraffin-embedded block, and mount the thinner section for light microscopy and the thicker adjacent section for SEM.

### *Analytical Results*

The photomicrographs of petrographic sections that follow are shown in black and white,

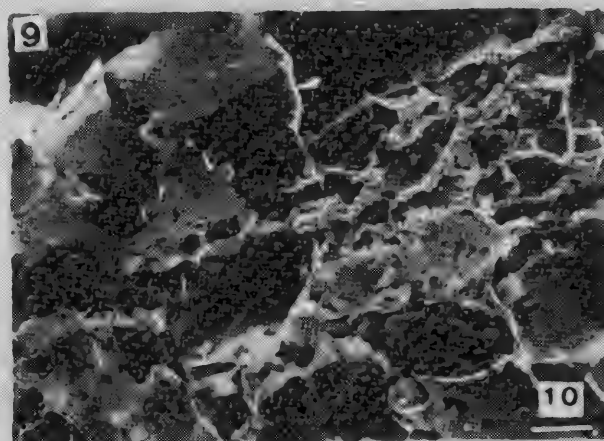
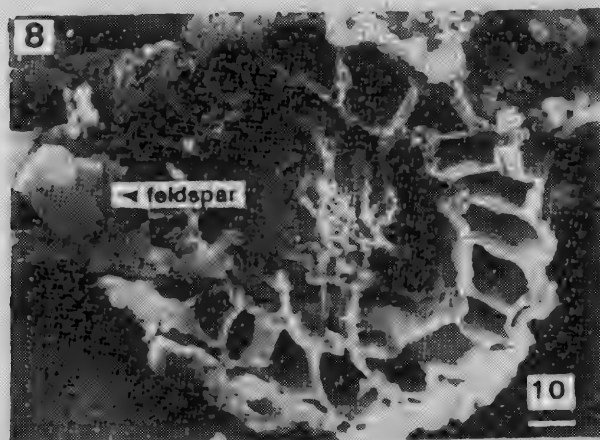
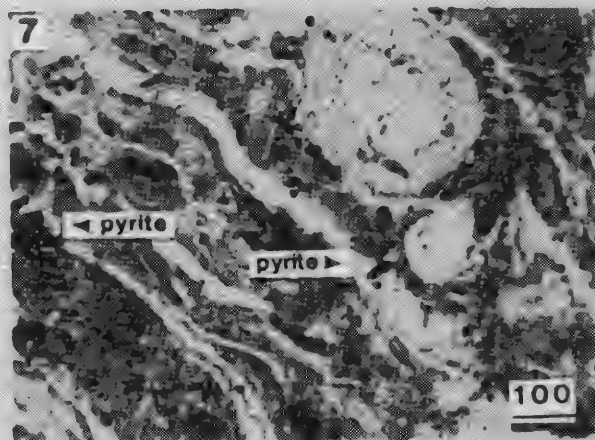
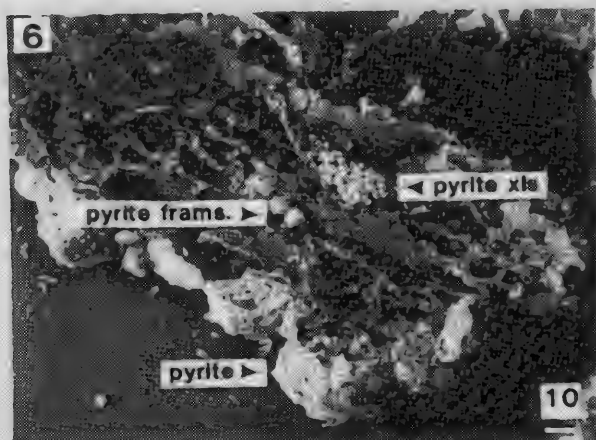
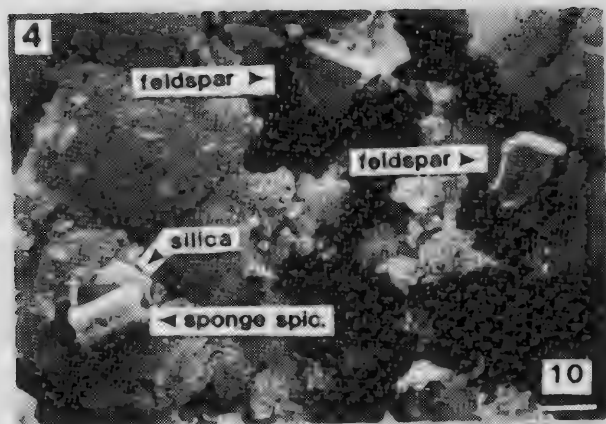
---

The authors are with the Earth and Space Sciences Division, Los Alamos National Laboratory, MS J978, Los Alamos, NM 87545. Supported by Department of Energy under Contract W-7405-ENG-36.



FIGS. 1-3.--Backscattered SEM (Figs. 1a, 2a, 3a) and transmitted-light, petrographic (Figs. 1b, 2b, 3b) photomicrographs of adjacent serial sections of peat samples cut with sliding microtome. Success of serial sectioning is evident in these figures. (Scale bar is in microns.)





FIGS. 4-9.--Backscattered SEM (Figs. 4, 5, 6, 8, 9) and transmitted-light, petrographic (Fig. 7) photomicrographs of peat samples. Note occurrence of mineral matter incorporated in organic material of peat, and structural integrity of samples following microtome sectioning. (Scale bar is in microns.)

which removes many distinguishing color features of plant components used by the peat petrographer during microscopic analysis. Nevertheless, it is still possible to demonstrate the advantages of this technique by comparing these photomicrographs with those taken with the SEM.

Figure 1(a) is a SEM photomicrograph covering nearly the same area as seen in the petrographic photomicrograph shown in Fig. 1(b). As is evident, there is no problem in identifying the same features in both figures. Figures 2(a) and 2(b) show a transverse section across a plant root as it appears both in the SEM and in the petrographic microscope. The open area around the root may be an artifact of sampling or of the petrographic thin-sectioning technique. Note the occurrence in both images of a cell filling in the upper right-hand corner of the root. This feature, along with those in Figs. 3(a) and 3(b) indicate the success of the serial sectioning. Portions of Fig. 3(a) are magnified in Figs. 4 and 5 to illustrate minerals incorporated in organic material of the peat. Energy-dispersive x-ray analysis shows these minerals to be potassium-aluminum-silicates (possibly feldspar) and titanium-iron-oxide (possibly illmenite). Other minerals present in Fig. 4 are small pieces of silica, one of which is a fragment of a sponge spicule.

Figures 6 and 7 show the relationships between pyrite and plant components. The SEM photomicrograph (Fig. 6) reveals the detailed relationships of single crystals of pyrite, framboids of pyrite, and plant materials. In the light photomicrograph, at lower magnification (Fig. 7), the pyrite particles appear only as black areas whose detailed relationships to surrounding plant components are not well defined.

In Fig. 8 a well-preserved cross section of a root demonstrates that the critical point drying technique allows its hollow cells to be preserved with a minimum of shriveling or collapse. If any mineral matter had been present as infillings of the cells, it would have been easily observable. For example, in Fig. 9 very thin layers of a potassium-aluminum-silicate mineral (most likely a clay) are shown as a partial filling of a cellular structure similar to that shown in Fig. 8.

### Discussion

The method for making oriented microtome sections of peats for light microscopic observations has previously been described by Cohen.<sup>1</sup> The technique of critical-point drying of botanical specimens for SEM analysis is a common biological procedure. Thus the technique we are suggesting is not a new development in specimen analysis of botanical materials. Rather, it is (to our knowledge) the first time that anyone has combined these two techniques for study of serial sections of oriented pieces of peat. Combining these techniques has the potential to yield information that was previously unobtainable by using either technique alone.

### References

1. A. D. Cohen, "Obtaining more precise descriptions of peat by use of oriented microtome sections, testing of peat and organic soils," in P. M. Jarett, Ed., ASTM STP 820 (in press).
2. D. A. Johansen, *Plant Microtechnique*, New York: McGraw-Hill, 1940.
3. M. A. Hayat, *Introduction to Biological Scanning Electron Microscopy*, Baltimore: University Park Press, 1978.
4. *Operational Manual for Ladd Critical Point Dryer*, Cat. No. 28000.



## OCCURRENCE OF DETRITAL MINERAL MATTER IN OKEFENOKEE PEATS

M. J. Andrejko and Robert Raymond Jr.

Peat, the precursor of coal, is predominantly composed of partially decomposed plant debris along with varying amounts of inorganic material. This inorganic matter (often referred to as "ash") consists of a mixture of distinct mineral species and ionically bound or complexed inorganic compounds. The composition of this inorganic fraction is controlled by a variety of botanical and depositional environments and processes. The peats used in this study are from the Okefenokee Swamp, a low-sulfur, exclusively fresh-water analog of an ancient coal-forming environment. Unlike other peat deposits, the inorganic fraction of Okefenokee peats is primarily composed of silica, most of which consists of biologically derived, authigenic particles.<sup>1</sup> However, the peats do contain nonbiogenic mineral particles of both a silica and nonsilica composition. Our purpose was to determine grain textures and elemental compositions of the nonbiogenic particles through use of scanning electron microscopy (SEM) and energy-dispersive x-ray (EDX) analysis. Analytical results indicate that many of these mineral particles are detrital in origin.

### *Methods of Analysis*

Peat samples were collected using a piston coring device developed by Cohen and Spackman.<sup>2</sup> The cores (7.5 centimeters in diameter) were taken in sections 120 centimeters in length from two major peat-forming environments. These consisted of a marsh habitat located in Grand Prairie and a swamp-forest environment located near Minnie's Lake. At each site, the cores were sealed within aluminum coring tubes to await transportation to the laboratory.

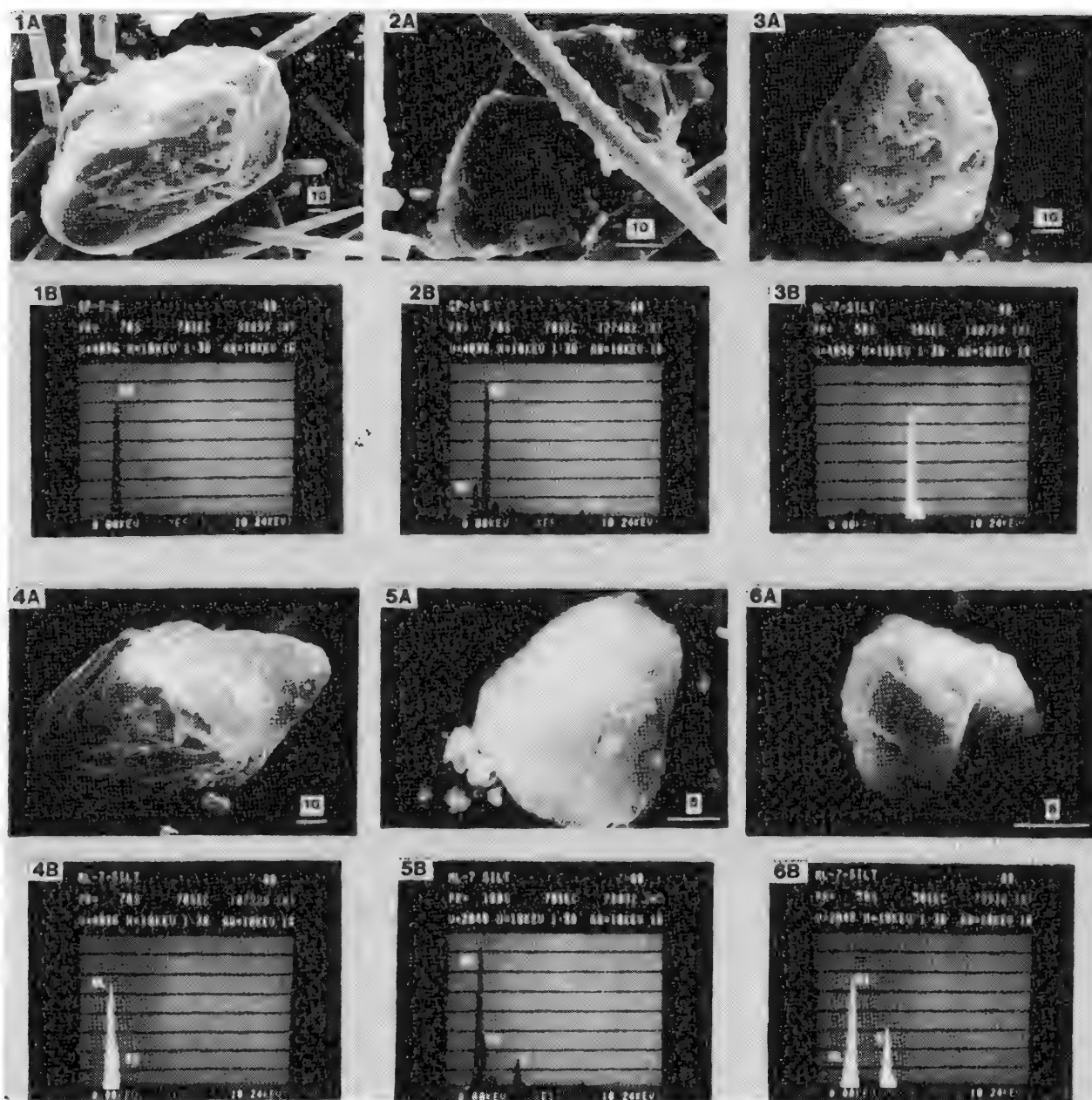
At the laboratory, the cores were cut open and separated into halves. After initial descriptions of macroscopic features were completed, the material inside the cores was sampled at intervals of 7.5 centimeters. One half of each sample was used for ash and mineralogical determination. Samples were placed in glazed porcelain crucibles (which were pre-fired and pre-weighed) and oven dried at 105°C for 16 hours. After moisture content was determined, the crucibles were placed in a temperature-regulated muffle furnace and ashed at 550°C for 16 hours to determine total ash content. The ashed material was digested in dilute HCl and filtered through ashless filter paper. Each filter paper was placed into the corresponding original crucible and ashed again at 550°C for 1 hour. The resultant residue was retained for analysis. The basal mineral sediments were also ashed and acidified prior to being processed for grain size analysis. The sand and silt size fractions were examined separately.

Each ash residue from the above process was split into equal sub-samples. One sub-sample was dispersed on an aluminum stub, sputtered-coated with gold palladium and examined with an ISI Model DS-130 scanning electron microscope. Qualitative elemental composition of the mineral particles within the inorganic residue was determined by use of a Kevex energy-dispersive x-ray analysis unit attached to the SEM.

### *Results*

Identification of mineral forms in the residue was based on observed elemental ratios and grain morphologies. Tentative identifications were then compared to mineral suites known to occur within the surface sediments of the Georgia Coastal Plain.<sup>3</sup>

Author Andrejko is affiliated with the Department of Geology, University of South Carolina, Columbia, SC 29208; present mailing address is Los Alamos National Laboratory, Earth and Space Sciences Division, MS-K586, Los Alamos, NM 87545. Author Raymond is with Los Alamos National Laboratory, Earth and Space Sciences Division, MS-J978. Funded in part by NSF Grant EAR-79-26382 and supported in part by the U.S. Department of Energy under Contract W-7405-ENG-36.



FIGS. 1-6.--SEM photomicrographs and respective energy dispersive spectra for detrital minerals from the Okefenokee Swamp. Particles in Figs. 1 and 2 are from a marsh peat from Grand Prairie. Particles in Figs. 3-6 are from mineral sediments at the base of the Minnie's Lake core. Presumed mineralogies of the particles shown in the figures are: (1) quartz; (2) amphibole; (3) rutile or leucoxene; (4) kyanite or sillimanite; (5) illite (clay mica); and (6) feldspar.

Figure 1(a) illustrates a residue from the marsh peat sampled in Grand Prairie. The majority of the background particles are biogenically derived siliceous sponge spicules. The large grain exhibiting frosted texture is composed exclusively of silicon oxide (Fig. 1b), probably in the form of quartz or chert. Occasionally other silicates were present within peat samples (Fig. 2a). Crystal structure and elemental ratios (Fig. 2b) suggest that this grain is an amphibole. However, nonsilica mineral grains formed an extremely small proportion of the nonbiogenic mineral matter within the peat.

Within the mineral sediments at the base of the Minnie's Lake core, nonsilica mineral matter constituted a relatively higher proportion than within the overlying peat. Observations indicated a greater abundance of these nonsilica particles in the silt size frac-

tion than within sand-sized material. Most of the basal materials exhibited weathered surface textures. Examples of weathered, nonsilica particles from the basal mineral sediment can be seen in Figs. 3-6. Figures 3(a) and (b) show a subrounded titanium oxide mineral, possibly rutile or leucoxene (a weathering product of illmenite). Examples of silicate particles included an aluminum silicate (Figs. 4 a,b) possibly kyanite or sillimanite, and potassium aluminum silicates, possibly illite (clay mica) (Figs. 5 a,b), and K-feldspar (Figs. 6 a,b).

### *Discussion and Conclusions*

There has long been a controversy regarding the origin of mineral matter in coals. Some researchers, such as Cecil,<sup>4</sup> have advocated an authigenic origin for most minerals. Others, such as Finkelman,<sup>5</sup> felt that although some minerals might have been authigenic in nature, there was strong evidence for substantial detrital input into the original coal-forming environment. Finkelman also felt that some minerals that might be considered by some as authigenic were actually diagenetic alterations of detrital material. However, such views are somewhat premature without detailed examination of the original minerals that occur within a modern coal-forming environment. In peat deposits, where there are considerable influxes of fluvial or marine mineral-rich sediments, it is rather easy to identify various mineral components by x-ray diffraction (XRD). However, in environments such as the Okefenokee where the occurrence of nonsilica minerals is rare, these minerals have been somewhat ignored owing to their small sample populations. However, by separating out (and thus concentrating) the inorganic residues from the peat, one can use SEM and EDX analysis to determine genesis of particles. Some of the mineral particles (e.g., Figs. 1a, 3a, and 4a) exhibited weathered textures possibly due to transportation by wind or water. In addition, the elemental composition in conjunction with the crystal forms of some of the grains (e.g., Figs. 2 and 3) are not compatible with an authigenic origin.

An advantage to EDX analysis in conjunction with SEM is that it permits nondestructive and simultaneous mineral determinations to be made while engaged in other SEM work. Such collaborative work has included identification and description of siliceous biogenic structures (e.g., diatoms, phytoliths, and sponge spicules).<sup>1</sup> The end result is that a more effective procedure, than for example XRD, is available for determining the mineralogy and geochemistry of minute individual particles in peat. In addition, SEM with EDX analysis allows for better documentation of the possible diagenetic alterations of residual minerals during peatification. This procedure permits greater insight into the development and conceptualization of more realistic depositional and geochemical models regarding the origin of mineral matter in coal. Subsequent refinements have demonstrated the versatility of the technique in that it can also be used for in situ studies of the mineral particles within thin-sections of peat.<sup>6</sup>

### *References*

1. M. J. Andrejko et al., "Scanning electron microscopy observation features on fresh-water sponge spicules," *SEM/1982 II*, 629-638.
2. A. D. Cohen and W. Spackman, "Methods of peat petrology and their application to reconstruction of paleoenvironments," *Geol. Soc. Am. Bull.* 83: 129-142, 1972.
3. F. L. Pirkle, "Evaluation of possible source regions of trail ridge sands," *Southeastern Geol.* 17: 93-114, 1975.
4. C. B. Cecil et al., "A geochemical model for the origin of mineral matter in coal," *Geol. Soc. Am. Abst. with programs*, 13: 424, 1981.
5. R. B. Finkelman, "Recognition of authigenic and detrital minerals in coal," *Geol. Soc. Am. Abst. with programs*, 13: 450, 1981.
6. R. Raymond Jr. and S. W. Bardin, "In situ elemental and mineralogical analysis of peat using SEM and petrographic techniques," *Microbeam Analysis--1983*, 15.

## SPECIMEN PREPARATION AND SIZING BY IMAGE ANALYSIS OF RESPIRABLE QUARTZ PARTICLES COLLECTED ON COAL MINE AIR-MONITORING FILTERS

J. G. Snyder and C. W. Huggins

Several quartz standards and respirable coal mine dust samples containing significant amounts of quartz were used to develop a method of quartz particle-size determination by image analysis. Data on the quartz particle size are crucial for the accurate determination of quartz (the cause of "silicosis") in respirable coal mine dusts collected on air-monitoring filters by the Mining Safety and Health Administration (MSHA). In the respirable dust range ( $< 10 \mu\text{m}$  diameter), particle size can significantly affect the response of x-ray diffraction (XRD) and infrared spectroscopy (IR), the techniques used at present by MSHA to determine quartz content on filters for enforcement purposes. To obtain accurate results, the particle-size distribution of the quartz reference standard must be similar to that of the mine samples. Joint studies by the Bureau of Mines and MSHA show that inaccuracy in quantitative quartz values may be as much as 30% when the particle size of the ground quartz standard does not match that of the sample. Results are biased because factors that affect x-ray peak intensity (absorption, x-ray scattering, particle orientation) are all particle-size dependent.<sup>1,2</sup> Similarly, measurements by IR are susceptible to variation with particle size. In the case of quartz particles in the respirable range, scattering reflection and retardation all increase with particle size.<sup>3,4</sup>

In this study, three pure ground quartz materials were chosen for particle-size distribution measurements: Minusil -5, Minusil -10, and Silver Bond B. Size distributions for the quartz standards were first determined manually by a Philips EM 100-B transmission electron microscope (TEM) as a basis for verification of the results from image analysis. Next, a specimen preparation technique was developed for image analysis. Particle-size analysis was done with a Cambridge Mark II scanning electron microscope (SEM) interfaced with a Tracor Northern 1310 image analyzer (IA) and a Tracor Northern 880 energy-dispersive x-ray spectrometer (EDS).

### *Specimen Preparation for Image Analysis*

Methods of specimen preparation for maximum dispersion of particles for SEM analysis have been published. In techniques that involve the production of pellets of particulate sample imbedded in resin,<sup>5</sup> such as barium methacrylate resin,<sup>6,7</sup> the specimens are polished to a flat surface and coated with carbon. Such techniques may allow the production of a uniform dispersion of particles, but because a flat surface is produced by polishing, particles are sliced randomly. Erroneous size distributions may result since particle diameters may not be truly represented. Techniques involving deposition such as centrifugation,<sup>8</sup> atomization by means of a spray mounter, and sprinkling powder onto double-stick tape may be inappropriate for size distribution studies because they may result in deposits that are not uniform. Chatfield and Dillon<sup>9</sup> outlined some aspects of filtration for specimen preparation of liquid, air, and bulk particulate samples with special reference to asbestos. Specifically, they mention the use of Nuclepore filters, which provide a relatively smooth, featureless, and continuous substrate for SEM analysis.

Specimens for the respirable coal dust study were prepared with Nuclepore filters in the following manner. We prepared quartz standards by weighing out 3mg portions of Min-

---

Authors Snyder and Huggins are at the Bureau of Mines, U.S. Department of the Interior, Avondale Research Center, 4900 LaSalle Road, Avondale, MD 20782. The authors acknowledge M. E. Taylor and others of the Central Facility for Electron Microscopy, University of Maryland, for assistance and use of equipment. T. Tomb and S. Goldberg of MSHA in Pittsburgh provided the respirable coal dust samples. G. Fritz and J. McCarthy of Tracor Northern, Inc., Middleton, Wis., provided useful suggestions and discussion. Reference to specific brand names throughout this paper is for information only and does not imply endorsement by the Bureau of Mines.

usil -5, Minusil -10, or Silver Bond B and suspending the quartz in 200 ml of isopropanol at 24°C to obtain a concentration of 15 µg/ml. In connection with centrifugation experiments,<sup>10</sup> isopropanol has been determined to be an excellent dispersing medium that minimizes agglomeration of particles. The suspensions were agitated ultrasonically at 80 kHz for 10 min to obtain complete dispersion, and cooled in an ice bath to 24°C to insure consistent volume in the liquid. An optimum mass loading of 5 µg/cm<sup>2</sup> for image analysis has been suggested to obtain the largest number of particles with minimum particle agglomeration.<sup>11</sup> To obtain this mass loading, 2 and 4ml aliquots of suspension were diluted with 50 ml of isopropanol and ultrasonified and filtered through 0.2µm pore size Nuclepore filters, which resulted in deposits of 30 and 60 µg of quartz over a filter area of about 10.5 cm<sup>2</sup>. Filter deposits of 30 µg were suitable for Minusil -5 and -10; however, a deposit of 60 µg was preferred for Silver Bond B, because its larger mean particle size yielded fewer particles per unit mass. In addition to providing a smooth substrate, 0.2µm pore openings in the Nuclepore filters minimize the loss of the very small particles present in samples.

Coal mine dust samples obtained from MSHA were collected on Bendix and MSA filters. Because the collection filters are too rough for direct analysis by image analysis, the samples were prepared by the low-temperature ashing of a small part of each collection filter. This process removes the organic-based filter and coal material. The ashed dusts were then suspended in isopropanol, ultrasonified at 80 kHz for 10 min, and redeposited on Nuclepore filters as above.

Squares approximately 1.5 × 1.5 cm were cut from each filter and attached to smooth SEM stubs, with carbon paint used as an adhesive. Latex spheres 1.0999 µm in diameter were placed next to the sample on each SEM stub for magnification calibration. These samples were gold-coated in a sputter-coater prior to analysis.

### *Image Analysis*

The SEM was operated at an accelerating voltage of 20 kV. The image analyzer utilizes gray-level differences in the video signal (Fig. 1a) to determine whether the electron beam is on a particle and to calculate particle size.<sup>12</sup> To facilitate image analysis, the back-scattered electron mode (BSE) of the SEM is used to provide the best contrast between particles and filter substrate. The contrast "threshold" level is set just above background to insure that all particles are located. Once the image analyzer has located a particle, it determines particle size by deflecting the electron beam in a series of horizontal, vertical, and diagonal movements (Fig. 1b). A minimum size of 0.3 µm was chosen for particle analysis to eliminate the possibility of the beam dwelling on slightly charged 0.2µm pore openings of the Nuclepore filter substrate. The off-point density, or the number of off-particle picture points per SEM CRT testline, was set at 100 for the 10cm CRT. The on-point density, or the number of on-particle picture points per 10 cm CRT testline, was set at 500. After a feature has been located, an x-ray spectrum is acquired at its geometric center. SEM specimen tilt of 15° was used to allow collection of x rays while minimizing image distortion. In this study, a suitable spectral acquisition time was 3 s.

The analysis was performed at 2100× on every fifth field of view. A minimum of 200 particles for the quartz standards and 100 particles for the coal mine dust samples were measured. Particles have been categorized by their x-ray spectra into two groups: "Quartz" (Si only) and "All types," which may include in addition to quartz clay minerals, carbonates, or ash present in the dust samples. The two groups were distinguished by the setting of windows in the EDS multichannel analyzer for the detection of the elements commonly present in respirable coal mine minerals, including Na, Mg, Al, Si, K, Ca, and Fe.

### *Results and Discussion*

*Validation.* Prior to image analysis, quartz standards were examined for particle size using the Philips EM 100-B at magnification ranging from 8000 to 11 000×. Specimens were prepared similar to a method described by Campbell et al.<sup>13</sup> except that particles were dispersed in a collodion/amylose acetate mixture used to form collodion substrates on copper TEM grids. Micrographs were taken on the TEM, and the negatives were subsequently enlarged 10×.

Particle size distributions determined by manual measurements on the TEM and by the SEM/IA for Minusil -5, Minusil -10, and Silver Bond B are given in Fig. 2. Average particle diameters determined by the two techniques are very similar. However, the SEM tech-

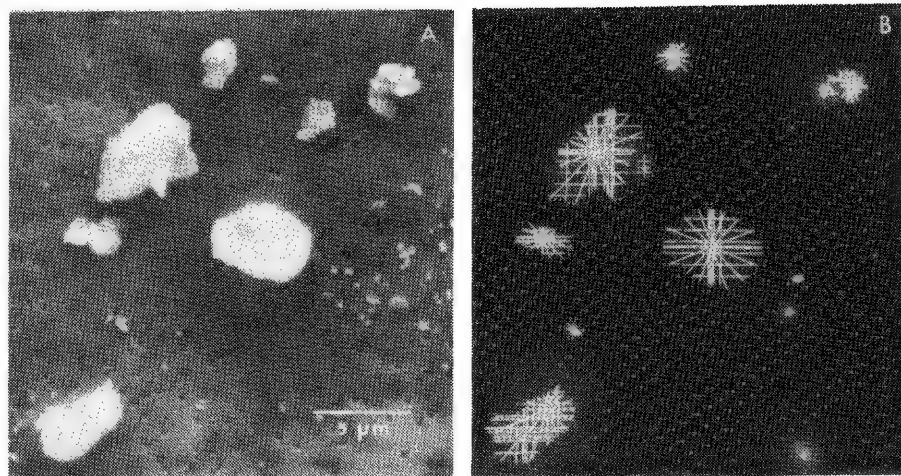


FIG. 1.--SEM micrographs showing image analysis of a respirable coal mine dust sample: (a) particles on a Nuclepore filter in BSE mode, (b) Particle size delineated by the electron beam in image analysis mode.

nique did not allow measurement of as many of the particles less than  $1\text{ }\mu\text{m}$  in average diameter. This bias has been introduced probably because SEM/IA was carried out at a much lower magnification than the TEM technique, which effectively obscured the ability to observe these smaller particles.

*Quartz in Coal Mine Dusts.* Histograms of average particle diameter in micrometers for all particles and for quartz particles found in three respirable coal mine dust samples are shown in Fig. 3. Most quartz particles are within the  $1\text{--}3\text{ }\mu\text{m}$  size range. As mentioned earlier, some smaller particles may have been missed due to the relatively low magnification used. In order to cover the possible ranges of particle size, the analysis should be completed at several magnifications. Also, the SEM operating conditions used did not allow for maximum resolution in the backscattered electron image. Specimen tilt of only  $15^\circ$  and an accelerating voltage of 20 kV caused the disadvantageous effect of electron penetration and intersection in the specimen. In this case, BSE resolution was approximately  $0.10\text{ }\mu\text{m}$ .

In addition, some particles smaller than  $1\text{ }\mu\text{m}$  may have gone undetected because the x-ray signal-to-noise ratio was too low to detect them.

### Conclusion

The quantitative analysis of quartz in respirable mine dust requires that the size distribution of the sample must closely match that of the quartz standard. The results of this limited investigation suggest that Minusil -5 may be the most suitable standard to use for these respirable coal mine dust samples.

This paper presents a practical method of sample preparation for image analysis of respirable-size particles. Further development will be necessary to address the problem of dispersing and detecting particles  $<1\text{ }\mu\text{m}$ . This method will be extended to the analysis of other coal mine dust air-monitoring samples. Of prime importance will be the determination of the extent of variation in quartz particle size among coal mine dust samples from different mining operations, such as from coal deposits of different grades, or from the use of different mining techniques. In addition, this work will be extended to provide ground work for the quantitative measurement of quartz in metal and nonmetal mines.

### References

1. J. W. Edmonds et al., "Particle size effects in the determination of respirable  $\alpha$ -quartz by x-ray diffraction," *Anal. Chem.* 49: 2196-2203, 1977.
2. H. P. Klug and L. E. Alexander, *X-ray Diffraction Procedures for Polycrystalline and Amorphous Materials*, New York: Wiley, 1954.
3. R. L. Henry, "The transmission of powder films in the infrared," *J. Opt. Soc. Am.* 38: 775-789, 1948.
4. M. V. Tuddenham and R. P. Lyon, "Infrared techniques in the identification and



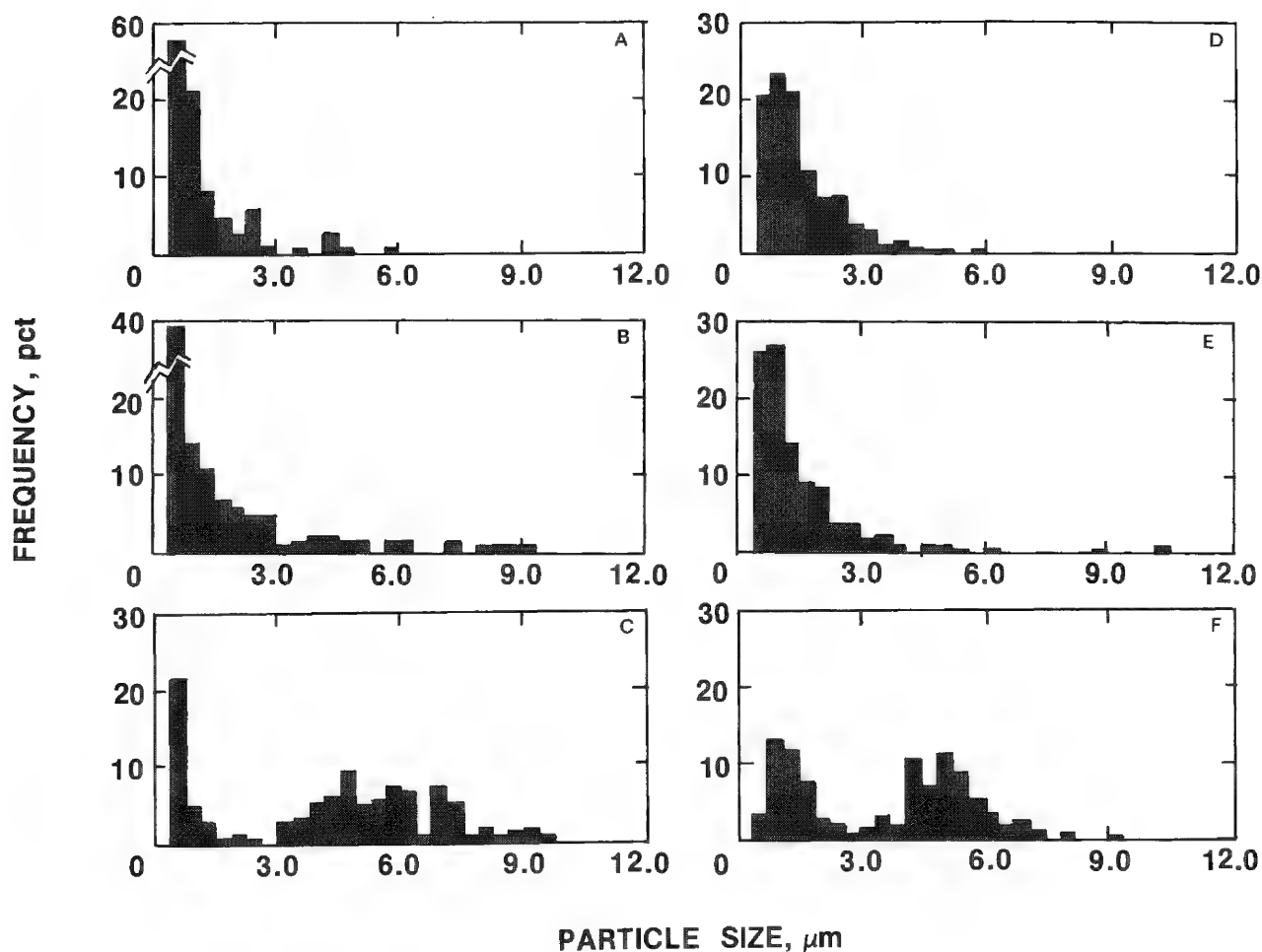


FIG. 2.--Comparison of particle-size distribution of pure  $\alpha$ -quartz standards determined by TEM (left) and SEM (right) with image analysis. A and D, Minusil -5; B and E, Minusil -10; and C and F, Silver Bond B.

measurements of minerals," *Anal. Chem.* 32: 1630-1634, 1960.

5. F. E. Huggins et al., "Scanning electron microscope-based automated image analysis (SEM-AIA) and Mössbauer Spectroscopy," in E. L. Fuller Jr., Ed., *Coal and Coal Products: Analytical Characterization Techniques*, ACS Symposium Series 205, Washington, D.C., 1982, 239-258.

6. A. K. Moza et al., "A mounting medium for coal particles," *SEM/1978 I*, 289-291.

7. A. K. Moza et al., "Inorganic element analysis of coal particles using computer evaluation of scanning electron microscope images," *SEM/1979 I*, 473-476.

8. E. J. Chatfield et al., "Analysis of water samples for asbestos: Sample storage and technique development studies," *Symp. Electron Microscopy of Microfibers*, Washington, D.C.: Food and Drug Administration, 1976.

9. E. J. Chatfield and M. J. Dillon, "Some aspects of specimen preparation and limitations of precision in particulate analysis by SEM and TEM," *SEM/1978 I*, 487-496.

10. S. L. Law et al., *Characterization of Steelmaking Dust from Electric Arc Furnaces*, Washington, D.C.: Bureau of Mines, RI 8750, 1983.

11. J. F. Kelly et al., "Automated characterization of fine particulates," *SEM/1980 I*, 311-322.

12. R. J. Lee and J. F. Kelley, "Overview of SEM-based automated image analysis," *SEM/1980 I*, 303-310.

13. W. J. Campbell et al., *Chemical and Physical Characterization of Amosite, Chrysotile, Crocidolite, and Nonfibrous Tremolite for Oral Ingestion Studies by the National Institute of Environmental Health Sciences*, Washington, D.C.: Bureau of Mines, RI 8452, 1980.

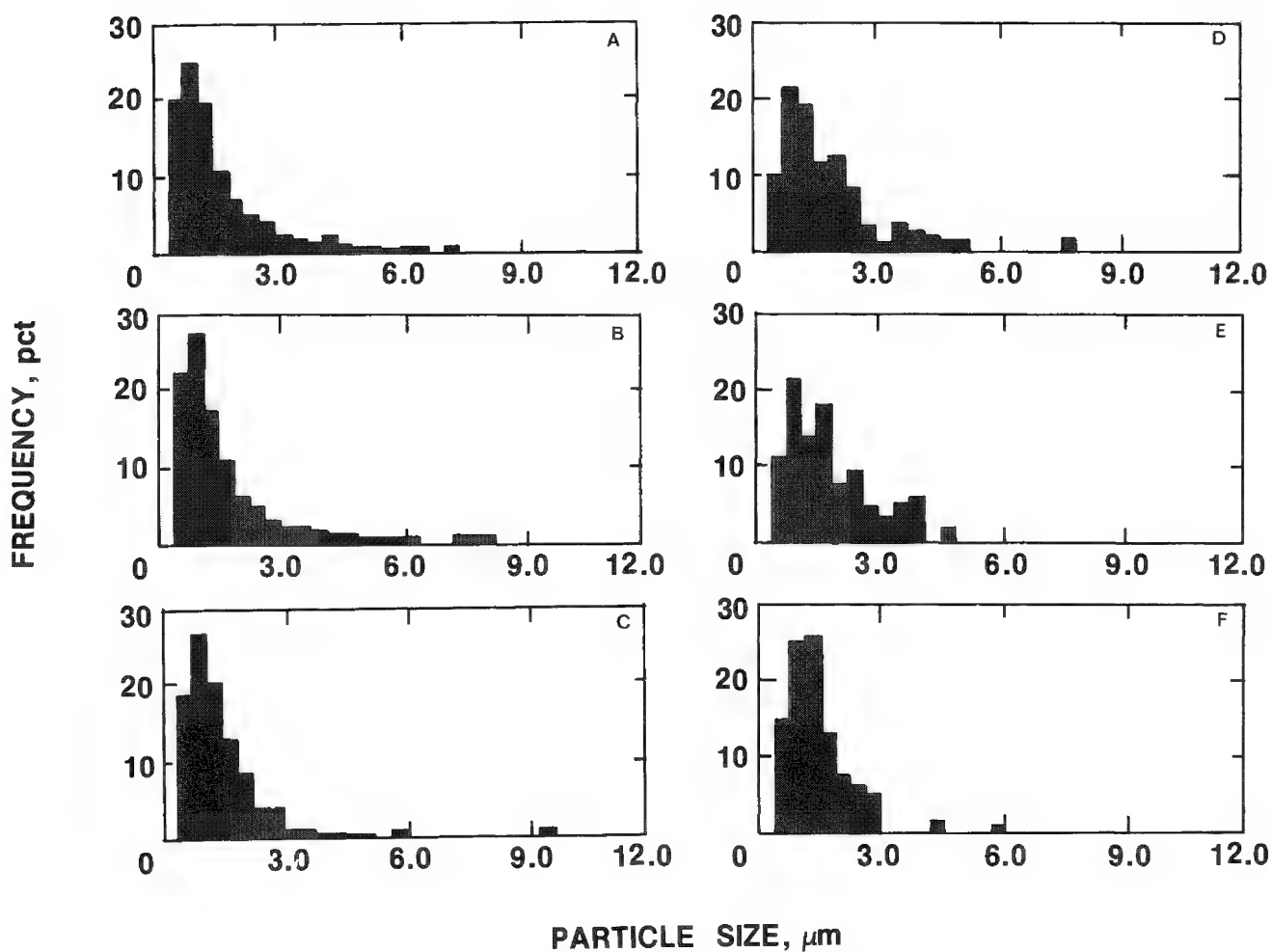


FIG. 3.--Particle-size distribution of "All types" (left) and "Quartz" (right) determined by SEM with image analysis for three respirable coal mine dust samples. A and D, Sample #44010829; B and E, Sample #18433385; C and F, Sample #44541494.



## SUBMICROSCOPIC ( $< 1 \mu\text{m}$ ) MINERAL CONTENTS OF VITRINITES IN SELECTED BITUMINOUS COAL BEDS

J. A. Minkin, E. C. T. Chao, C. L. Thompson, M.-V. Wandless, F. T. Dulong, R. R. Larson, and S. G. Neuzil

An important aspect of the petrographic description of coal is the characterization of coal quality, including chemical attributes. For geologic investigations, data on the concentrations, distribution, and modes of occurrence of minor and trace elements provide a basis for reconstructing the probable geochemical environment of the swamp material that was converted into peat, and the geochemical conditions that prevailed during and subsequent to coalification. Such data are also important for technological evaluation such as washability, pollution potential, and suitability for utilization in a synfuels program. We have been using electron (EPMA) and proton (PIXE) microprobe analytical methods<sup>1,2,3</sup> to obtain data on the chemical characteristics of specific coal constituents in their original associations within coal samples. In many maceral<sup>4</sup> grains that appear to be homogeneous under optical examination at magnifications as great as 500 $\times$ , some elemental concentrations are found by probe analysis to be quite variable at different locations within a single grain. We have inferred this variability to indicate the probable presence of discrete submicron-size mineral particles within the maceral grain. The present study is aimed at evaluation of the nature of mineral occurrences and heterogeneous elemental concentrations within vitrinites. Vitrinites are usually the most abundant, and therefore most important, maceral group in bituminous coal.<sup>4</sup>

### *Experimental*

Fragments of vitrain (a macroscopic unit of coal consisting essentially only of vitrinite<sup>5</sup>) were carefully selected and separated from two drill-core and three columnar samples collected from bituminous coal beds in the eastern and western United States. Each sample was studied by a combination of the following techniques:

1. Optical examination of doubly polished thin sections (PTS)
2. EPMA of PTS and PIXE analysis of companion polished chips
3. Scanning electron microscopy (SEM) with energy-dispersive analysis (EDX) of PTS
4. Scanning transmission electron microscopy (STEM) of ion-thinned PTS
5. Low-temperature ash residues (LTA) of companion chips
6. X-ray powder diffraction analysis (XRD) and STEM of LTA

LTA is widely used as a method for separating the mineral content from coal and retaining the mineral components in a relatively unaltered state.<sup>6</sup> In this study, chips of the vitrains to be examined microscopically were ashed at low temperatures to obtain an estimate of the abundance of mineral particles in these samples. As seen from Table 1, the percentage of LTA ranged from 0.7 to 6.4 wt. %. The three lower-ash vitrains were obtained from columnar samples of the Kentucky No. 9, Upper Freeport, and Herrin (No. 6) coal beds. On the basis of petrographic examination of slabs from the three samples, the plant precursors of the coal are interpreted by us as being of autochthonous origin. In contrast, the two higher-ash vitrains are from split drill-core samples of the I and J coal beds of the Ferron Sandstone Member of the Mancos Shale. We conclude from petrographic examination of several drill cores, and from field data, that the plant precursors of the coal in these beds are of allochthonous origin. (We use the terms autochthonous and allochthonous here as defined by Stach et al.<sup>7</sup>) Autochthonous coals are formed principally from plants which remain in place after death to form peat; i.e., these coals are formed in quiet waters.

---

Authors Minkin, Chao, Wandless, Dulong, Larson, and Neuzil are at the U.S. Geological Survey National Center, Reston VA 22092. Author Thompson, formerly of USGS, is now at CONOCO, Inc., Ponca City, OK 74601.

TABLE 1.--Analytical data for vitrains studied.

Sample	Wt. % LTA*	Wt. % organic S**	XRD Analysis of LTA†	STEM tentative identifications‡
Columnar sample K809, 37 m, Kentucky no. 9 coal bed, Webster County, Kentucky	0.66	0.65	N.D.	siderite
Columnar sample H2-42P-1, 8 cm, Upper Freeport coal bed, Indiana County, Pennsylvania	1.4	0.50	N.D.	unknown Fe-Al-Si-Ca, calcite, kaolinite
Block sample ISGS2, Herrin (no. 6) coal bed, East central Illinois	2.4	1.15	pyrite, quartz, calcite, kaolinite	pyrite, quartz, kaolinite, diopside, tephroite, calcite
Drill-core sample TRM1-42.57 m, I coal bed, Ferron Sandstone Member, Mancos Shale, central Utah	3.4	1.59	gypsum, kaolinite	calcite, kaolinite
Drill-core sample TRM1-40.475 m, J coal bed, Ferron Sandstone Member, Mancos Shale, central Utah	6.4	1.65	gypsum, quartz	calcite, possible garnet

N.D. = not determined.

\*S. G. Neuzil, analyst.

\*\*EPMA determinations, J. A. Minkin, analyst.

†Minerals listed in order of relative abundance; F. T. Dulong, analyst

‡Minerals listed in order of relative abundance; M.-V. Wandless, analyst.

On the other hand, most of the plant precursors of allochthonous coals were transported considerable distances from the site of growth to the site of deposition prior to coalification. The flowing waters which carried the plant material in the latter case transported mineral content as well.

Doubly polished thin sections of each vitrain sample were specially prepared for STEM analysis by being bonded to glass slides during preparation with an adhesive which is soluble in acetone. Each PTS was examined optically in reflected and transmitted light. Only a few discrete mineral grains (> 1  $\mu$ m size) were observed in any one sample. The mineral grains that were detected were limited to quartz, clays (principally kaolinite and illite), and isolated pyrite grains. The number of submicron-size grains on the surface of the areas surveyed with the SEM was also very limited.

Areas without optically observable minerals were selected for ion thinning prior to STEM analysis. A diamond object-marker accessory for the petrographic microscope was used to inscribe 3mm-diameter circles to designate the areas selected for analysis. A 3mm-diameter circular copper supporting grid was attached with a minimal amount of epoxy to each

inscribed area of the PTS. After curing of the epoxy, the PTS was removed from the glass slide by immersion in acetone (the epoxy attaching the copper grid to the PTS was unaffected by the acetone treatment). The grid-supported circular areas of the PTS were then ion thinned, and carbon coated to prevent charging in the electron beam.

### *Results and Discussion*

The results of STEM analysis of the vitrains studied to date are shown in Table 1 along with comparative XRD analyses of LTA of companion fragments. The minimum particle size of grains that can be analyzed routinely with the present STEM configuration at the U.S. Geological Survey laboratories in Reston, Va., is approximately 80 nm. The range of optimum crystallite size for XRD analysis is 0.2  $\mu\text{m}$  (200 nm) to 50  $\mu\text{m}$ .<sup>8</sup> We therefore cannot at this time identify mineral particles smaller than about 100 nm in diameter in vitrain samples. Most of the particles analyzed in this STEM study had a minimum dimension between 0.1  $\mu\text{m}$  (100 nm) and 1  $\mu\text{m}$  (1000 nm). In all samples, the distribution of the mineral particles is generally random. Many of the areas surveyed with the STEM contained no mineral grains, others contained widely dispersed single grains, and still others contained clumps of mineral particles of the same or varied compositions.

In the samples from the Kentucky No. 9 and Upper Freeport coal beds, the vitrains had relatively low ash contents, and there was not sufficient LTA from these samples to perform XRD analysis. In the Kentucky No. 9 sample, only two mineral grains, both identified as siderite (all STEM mineral identifications are based on elemental compositions, and therefore must be regarded as tentative), were observed in all the areas surveyed in the STEM study. An interesting aspect of the STEM analysis of the Upper Freeport vitrain was that, out of a total of seven grains analyzed, five submicron-size particles showed spectra with Al, Si, Ca, and Fe in varying amounts relative to one another. These are believed to be mineral assemblages, even at such small sizes.

Pyrite is the dominant mineral present in the Herrin (No. 6) vitrain sample, as determined by both XRD and STEM analyses. Of the vitrains studied so far, the Illinois sample is the only one in which quartz and pyrite were observed in the submicron size range, although both these minerals are seen in optically observable sizes in all the samples.

In the vitrains from the I and J coals of the Ferron Sandstone Member, calcite is the dominant mineral tentatively identified in the STEM study, but gypsum is the principal mineral determined by XRD analysis of LTA (Table 1). Of the five samples in this study, the I and J vitrains have the highest organic sulfur content (Table 1), and possibly for these samples the gypsum was formed during the LTA process by combination of calcium derived from calcite with the relatively large amounts of sulfur liberated from the vitrinite.

Evaluation of heterogeneity in the distribution of elemental concentrations in macerals was attempted through generation of x-ray maps by means of microbeam instruments. In an experiment in which a PIXE microprobe<sup>3</sup> was used, x-ray scans were generated for the distribution of S, Ca, and Fe in a polished block of vitrain from the Upper Freeport coal bed. The volume analyzed was 70  $\times$  100  $\times$  50  $\mu\text{m}$  thick (the thickness corresponds to the depth of penetration of the proton beam). The distribution of S was ascertained to be quite homogeneous, confirming the organic association of S. The x-ray maps for Ca and Fe, however, showed localized concentrations of both elements closely resembling each other in spatial distribution, possibly corresponding to the cellular arrangement in woody tissues which were the precursors of the vitrinite in this coal. In this initial experiment x-ray maps were not generated for elements such as Al and Si. Maps for these elements would have helped to evaluate the possibility of whether the Ca-Fe distribution was mineral (silicate)-related. It would also have been desirable to have made x-ray scans on a PTS rather than a polished block, so as to assess whether the area analyzed displayed a preserved cellular arrangement corresponding to the Ca and Fe distributions observed. Attempts to generate x-ray maps with electron bombardment in an SEM showed that the sensitivity of detection under the operating conditions was not adequate to obtain patterns of the nature of those produced with proton bombardment; the limit of detection with PIXE is routinely about 1-10 ppm for most elements, and with SEM-EDX about 0.1-0.5 wt.% (1000-5000 ppm). SEM-generated x-ray maps for a PTS of the Upper Freeport vitrain showed differences in concentration patterns only where obvious (larger) mineral inclusions were present. Further work with PIXE x-ray scans will be required for a better understanding and interpretation of the initial results.

### Summary and Conclusions

On the basis of the LTA and STEM data, vitrain in the allochthonous coals (from the I and J coal beds of the Ferron Sandstone Member) studied appears to be more enriched in submicroscopic minerals than is vitrain in the autochthonous coals (from the Kentucky No. 9, Upper Freeport, and Herrin No. 6 coal beds) of this sample suite. Most of the particles analyzed with STEM had a minimum dimension between 0.1 and 1  $\mu\text{m}$ . Information is generally still lacking on identification of minerals of the order of 0.1  $\mu\text{m}$  or less in size. Of the submicroscopic minerals identified in this study, calcite and kaolinite appear to be the most common. Submicron-size mineral aggregates containing Al, Si, Ca, and Fe were also observed. Submicroscopic illite was not apparent in any sample, and submicroscopic pyrite and quartz were observed only in the Illinois sample.

### References

1. J. A. Minkin et al., "Distribution of elements in coal macerals and minerals: Determination by electron microprobe," *American Chemical Society Division of Fuel Chemistry, Preprints*, 24 1, 242-249, 1979.
2. J. A. Minkin et al., "Arsenic- and selenium- bearing pyrite in Upper Freeport coal, Indiana County, Pennsylvania," *Comptes Rendu, Proceedings of the Ninth International Congress of Carboniferous Stratigraphy and Geology* (in press).
3. J. A. Minkin et al., "Proton microprobe determination of elemental concentrations in coal macerals," *SEM/1982 I*, 175-184.
4. R. W. Stanton and R. B. Finkelman, "Petrographic analysis of bituminous coal: optical and SEM identification of constituents," *SEM/1979 I*, 465-471.
5. E. Stach et al., *Stach's Textbook of Coal Petrology*, Berlin and Stuttgart: Gebrüder Borntraeger, 1982, 171-172.
6. H. J. Gluskoter, "Electronic low-temperature ashing of bituminous coal," *Fuel* 44: 285-291, 1965.
7. E. Stach et al., *ibid.*, 19-20.
8. J. W. Starbuck, "Introduction to powder diffraction," in E. F. Kaelble, Ed., *Handbook of x-rays*, New York: McGraw-Hill, 1967, 7-4.

## EVIDENCE FOR A TEKTOSILICATE STRUCTURE AND DOMINANCE OF Fe(III) OVER Fe(II) IN SILICIC VOLCANIC GLASSES OF THE NEVADA TEST SITE

R. G. Warren

More than 400 individual analyses have been obtained by electron microprobe for silicic glasses in 58 samples of tuff and lava from the Nevada Test Site (NTS). These samples comprise a wide range in chemical and petrographic types, including calc-alkaline and peralkaline rock types, and include most of the volcanic units of the NTS.<sup>1</sup> Locations and brief petrographic descriptions are given for representative samples in Table 1.

### *Analytical Procedure*

Each sample was examined under the petrographic microscope and areas most suitable for microprobe analysis of glasses were selected. All such areas must be free of alteration, dust, and microlitic inclusions within a  $40 \times 40 \mu\text{m}$  area. Several types of glass fragments may be present in each tuff sample, including small glass shards; pumice fragments; and large, rounded, or angular glass fragments (perlite). Several fragments of each type present were analyzed in each sample. Each analysis was performed using a  $40 \times 40 \mu\text{m}$  raster with a beam current of 10 nA. Under such conditions, consecutive analyses of the same area indicated negligible sodium loss. In some samples, such areas as large as  $40 \times 40 \mu\text{m}$  may not exist, and it is necessary to analyze by a  $10 \times 10 \mu\text{m}$  raster and to move the sample constantly beneath the beam. Such analyses are possible only for the often highly elongate walls of pumice tubes, which allow movement for hundreds of microns in a single direction. Even under such conditions, a small but consistent loss of sodium is evident and such analyses should be avoided, if possible. Feldspar standards were utilized for Na, K, Ca, Ba, Si, and Al analyses, ilmenite for Mn, and a clinopyroxene for Mg, Fe, and Ti. All analyses are corrected for differential matrix effects.<sup>3</sup>

### *Results*

Analytical totals for the 99 sets of averaged analyses from the 58 samples range from 89.7 to 98.1%.  $\text{SiO}_2$  contents (uncorrected for  $\text{H}_2\text{O}$  content) range from 65.8 to 75.8%. Representative analyses are shown in Table 2. In Table 3, elemental concentrations are represented as the number of molecules per 24 oxygens. For all samples, within the expected limits of analytical accuracy, the following relationships are found for the molecular concentrations:

$$[\text{O}] = 2[\text{Si} + \text{Ti} + \text{Al} + \text{Fe}]$$

$$[\text{Al} + \text{Fe}] = [\text{Na} + \text{K} + 2(\text{Ca} + \text{Ba} + \text{Mn})]$$

Median values and their standard deviations for the elemental sums above are listed in Table 4.

### *Discussion and Conclusions*

The above molecular relationships are valid throughout a wide range of glass type and chemistry (Tables 2 and 3) as well as rock type (Table 1), and apparently define a general relationship for natural glasses of silicic composition. We may explain this relationship most simply by postulating a tektosilicate structure for such glasses in which Si, Ti, Al, and Fe(III) occupy 4-coordinate (network-forming) sites. Occupancy of such sites by Al and Fe(III) produces a negative charge that is exactly balanced by the total positive

---

The author is at the Los Alamos National Laboratory, Los Alamos, NM 87545.

TABLE 1.--Locations and condensed petrographic descriptions for representative samples of NTS volcanic rocks.

Sample	Sample type <sup>a</sup>	Nevada State Coordinates(ft)		USGS <sup>b</sup> quad	Unit symbol <sup>c</sup>	Rock type <sup>d</sup>	Alteration <sup>e</sup>	% phenocrysts	
		N	E					felsic <sup>f</sup>	mafic <sup>g</sup>
RW19w-1	O	902610	606630	AT	TMR1	mwt	Gl	15	0.07 (Biot)
Ue19p-1261	C	912382	598307	DHF	TPCu	nwt	Gl	3.1	0.13 (Biot>Cpx>Hbld)
Ue19p-1461	C	912382	598307	DHF	TRPP	l	Gl	11	0.35 (Biot>>Cpx)
RW18a-9	O	887850	619510	AT	TRAU2	b	Gl	17	4.7 (Biot>Hbld>>Opx)
Ue19p-1790	C	912382	598307	DHF	TRAM	b	Gl	2.6	0.06 (Cpx>Hbld>>Opx)
U19ab-1930-1940	da	911400	599378	DHF	TRAM	b	Zc, mGl	4.3	0.03 (Hbld>Biot)
TTR-2	O	876600	488790	TC	TTT	vt	Gl, $\mu$ Gr	15	0.56 (Cpx<Ol>>Biot>Hbld)
RW18a-3	O	892040	614370	AT	TBG	b	Gl, mZc	0.00	0.00

<sup>a</sup>O = outcrop, C = core, da = drill cuttings that are representative of unit.

<sup>b</sup>AT = Ammonia Tanks 7.5', DHF = Dead Horse Flat 7.5', TC = Thirsty Canyon 15'.

<sup>c</sup>Symbols are for petrologic units of Warren.

<sup>d</sup>b = bedded tuff, t = ash-flow tuff (nw = nonwelded, mw = moderately welded, v = vitrophyric), l = lava.

<sup>e</sup>Gl = vitric, Zc = zeolitic (clinoptilolite),  $\mu$ Gr = microgranophyric, "m" indicates a minor amount of the indicated component.

<sup>f</sup>Felsic phenocrysts are quartz, sanidine, anorthoclase, and plagioclase.

<sup>g</sup>Mafic phenocrysts are biotite (Biot), hornblende (Hbld), clinopyroxene (Cpx), orthopyroxene (Opx), and olivine (Ol), present in the indicated relative concentrations.

TABLE 2.--Electron microprobe analyses of glass in representative samples of NTS volcanic rocks, weight per cent basis. (All n analyses of a particular glass type are averaged. Glass types are: s = shard, pu = pumice, pe = perlite, l = lava.)

Sample	n	SiO <sub>2</sub>	TiO <sub>2</sub>	Al <sub>2</sub> O <sub>3</sub>	Fe <sub>2</sub> O <sub>3</sub>	MnO	MgO	CaO	BaO	Na <sub>2</sub> O	K <sub>2</sub> O	Total
RW19w-1	3s	74.5	0.11	11.7	0.57		0.00	0.16	0.00	3.69	5.25	96.0
	3pu	73.7	0.13	11.9	0.40		0.00	0.28	0.00	3.68	5.30	95.4
Ue19p-1261	8s	73.5	0.09	11.8	0.87	0.12	0.00	0.25	0.00	4.30	4.62	95.6
	6pu	73.8	0.09	11.7	0.87	0.12	0.00	0.30	0.00	4.08	4.75	95.7
Ue19p-1461	4l	72.0	0.17	12.3	0.90		0.04	0.39	0.00	3.97	5.20	95.0
RW18a-9	3s	69.9	0.15	11.1	0.91	0.11	0.16	0.97	0.04	2.80	4.31	90.5
	2pu	70.1	0.17	11.2	0.92	0.07	0.16	1.01	0.07	2.84	4.33	90.9
Ue19p-1790	3pe	69.7	0.13	11.5	1.05		0.00	0.39	0.00	3.16	5.26	91.2
	3pu	69.1	0.09	11.4	1.09		0.00	0.37	0.00	3.01	5.28	90.3
U19ab-1930-1940	4pu	68.6	0.07	11.4	0.94		0.02	0.43	0.00	2.87	5.36	89.7
TTR-2	3s	65.8	0.46	15.1	3.90		0.28	0.87	0.07	5.52	6.05	98.1
	2pu	72.0	0.20	13.5	1.09		0.06	0.39	0.00	4.49	6.10	97.8
RW18a-3	4pu	68.3	0.22	10.1	3.59	0.09	0.00	0.14	0.00	4.64	4.68	91.8
	8s	68.1	0.22	10.1	3.47	0.07	0.00	0.15	0.00	4.92	4.39	91.4

TABLE 3.--Elemental contents for glass analyses of Table 2, calculated as the number of molecules per 24 oxygens. (Symbols for glass types are identical to those used in Table 2).

Assumed coordination number =		4				$\geq 6$				Summed values		
Sample	n	Si	Ti	Al	Fe	Mn <sup>a</sup>	Ca	Na	K	Cn=4	Al+Fe	charge Cn $\geq 6$
RW19w-1	3s	10.064	0.011	1.896	0.056	0.000	0.022	0.965	0.902	12.027	1.952	1.911
	3pu	10.025	0.013	1.900	0.038	0.000	0.040	0.967	0.915	11.976	1.938	1.961
Ue19p-1261	8s	9.991	0.008	1.892	0.088	0.012	0.036	1.134	0.799	11.979	1.980	2.029
	6pu	10.021	0.008	1.870	0.087	0.012	0.040	1.071	0.820	11.986	1.957	1.995
Ue19p-1461	4l	9.889	0.015	1.998	0.092	0.004	0.055	1.055	0.911	11.994	2.090	2.084
RW18a-9	3s	10.008	0.015	1.874	0.095	0.039	0.148	0.776	0.785	11.992	1.969	1.935
	2pu	9.999	0.015	1.889	0.096	0.032	0.150	0.782	0.785	11.999	1.985	1.931
Ue19p-1790	3pe	9.953	0.012	1.938	0.111	0.000	0.057	0.876	0.958	12.014	2.049	1.948
	3pu	9.964	0.008	1.938	0.116	0.000	0.055	0.839	0.971	12.026	2.054	1.920
U19ab-1930-1940	4pu	9.963	0.005	1.953	0.101	0.002	0.065	0.806	0.992	12.022	2.054	1.932
TTR-2	3s	9.074	0.046	2.449	0.403	0.057	0.125	1.473	1.062	11.972	2.852	2.899
	2pu	9.702	0.020	2.134	0.106	0.009	0.052	1.170	1.043	11.962	2.240	2.335
RW18a-3	4pu	9.841	0.022	1.706	0.385	0.009	0.020	1.294	0.858	11.954	2.091	2.210
	8s	9.837	0.022	1.713	0.375	0.007	0.020	1.376	0.806	11.947	2.088	2.276

<sup>a</sup>also includes Ba and Mg

TABLE 4.--Median values and standard deviations of summed values defined in Table 3 for complete sample set. (All values based on 24 oxygens. Complete sample set consists of 402 analyses from 58 samples.)

	Cn=4	Al+Fe	Charge Cn $\geq$ 6
Median summed value	11.992	1.957	1.949
$\pm 2\sigma$ { population	0.026	0.082	0.131
{ median	0.001	0.004	0.007

is clear that water does not greatly modify the glass structure, even though much of the water may be structurally bound, as in zeolites.

Laboratory studies of glasses from binary and multicomponent systems are consistent with the structural relationships hypothesized above. Infinitely branched silicates occur in binary mixtures of  $\text{SiO}_2$  and oxides of a network modifying cation (such as  $\text{Na}_2\text{O}$ ,  $\text{K}_2\text{O}$ ,  $\text{CaO}$ , etc.) when the mole fraction of  $\text{SiO}_2$  exceeds 0.44.<sup>4</sup> A pronounced viscosity maximum at  $\text{Al/Na} = 1$  was found for the  $\text{Na}_2\text{O-Al}_2\text{O}_3\text{-SiO}_2$  system, independent of  $\text{SiO}_2$  concentration.<sup>5</sup> This finding was attributed to existence of a network structure. Recent Mössbauer studies have shown that Fe(III) occupies a 4-coordinate site.<sup>6</sup>

The existence of a well-defined structure for natural silicic glasses is of great importance for three reasons:

1. The relationships among elements defined by the structure provides the microprobe analyst with a measure of the quality of natural silicic glass analyses. Due to absorption of variable amounts of water, the analytical total does not provide such a measure.

2. Earlier NTS workers have concluded that Si has been leached by groundwater from glasses of most NTS volcanic rocks, and therefore glass compositions have been substantially modified from magmatic compositions.<sup>7,8</sup> These conclusions are invalid because they are based on whole-rock chemical analyses of glassy tuffs, which contain ash that differs chemically from shards and other glass fragments.<sup>9</sup> However, it is possible that magma might contain excess Na and K, which are subsequently lost from glass during secondary hydration. The additional, nonbridging oxygen required in a structure containing excess Na and K would be replaced by two hydroxyl groups upon hydration. Such alteration, however, would not affect elements that occupy 4-coordinate sites and concentrations of such elements in the glass would reflect magma chemistry.

3. Clearly, the tendency for glasses to form a tektosilicate structure is very strong. Rocks that have chemical compositions represented almost entirely by tektosilicate normative components (albite, orthoclase, and quartz) are very abundant; their compositions define the "granite minimum." If natural silicic glasses indeed represent unaltered, quenched magmas, then it is probable that the structure of the silicate liquid plays a major role in guiding the evolution of silicate magmas toward the "granite minimum."

## References

1. F. M. Byers, Jr., et al., "Volcanic suites and related cauldrons of timber mountain--Oasis Valley Caldera Complex, Southern Nevada," *U. S. Geol. Surv. Prof. Paper* 919, 1976.
2. R. G. Warren, "Use of petrology and geochemistry to define petrologic units in drill holes Uel9p, Uel9p-1 and U19ab, Southeastern Pahute Mesa, Nevada Test Site," *Los Alamos National Laboratory Report* (in progress).
3. A. E. Bence and A. L. Albee, "Empirical correction factors for electron microanalysis of silicates and oxides," *J. Geol.* 76: 382-403, 1968.
4. P. C. Hess, "Polymer model of silicate melts," *Geoch. Cosmoch. Acta* 35: 289-306, 1971.
5. E. F. Riebling, "Structure of sodium aluminosilicate melts containing at least 50 mole %  $\text{SiO}_2$  at 1500°C," *J. Chem. Phys.* 44: 2857-2865, 1966.
6. "Structure of liquids and glasses," H. S. Yoder, Jr., *Annual Report of the Director, Geophysical Laboratory, Carnegie Institute*, 1982, 340-365.

7. P. W. Lipman, "Chemical comparison of glassy and crystalline volcanic rocks," *U. S. Geol. Surv. Bull.* 1201-D, 1965.
8. D. C. Noble, "Sodium, potassium, and ferrous iron contents of some secondary hydrated natural silicic glasses," *Am. Miner.* 52: 280-286, 1967.
9. R. B. Scott, "Chemical variations in glass shards and interstitial dust of ignimbrite cooling units," *Am. J. Science* 270:166-173, 1971.



## ORIGIN OF ACCRETIONARY LAPILLI FROM THE POMPEII AND AVELLINO DEPOSITS OF VESUVIUS

M. F. Sheridan and K. H. Wohletz

Accretionary lapilli from the Pompeii and Avellino Plinian ash deposits of Vesuvius consist of centimeter-sized spheroids composed of glass, crystal, and lithic fragments of submillimeter size. The typical structure of the lapilli consists of a central massive core surrounded by concentric layers of fine ash with concentrations of larger clasts and vesicles and a thin outer layer of dust. Clasts within the lapilli larger than 125  $\mu\text{m}$  are extremely rare. The median grain-size of the fine ash is about 50  $\mu\text{m}$  and the size distribution is well sorted. Most constituent particles of accretionary lapilli display blocky shapes characteristic of grains produced by phreatomagmatic hydroexplosions.

Spheroids of accretionary ash have been long recognized in the geologic literature.<sup>1-3</sup> Modern references have noted their occurrence in ash-fall and base-surge deposits of phreatomagmatic origin.<sup>4-6</sup> No recent detailed studies by modern techniques have been published on accretionary lapilli. We have used the scanning electron microscope (SEM) in conjunction with energy-dispersive spectral analysis (EDS) to investigate the textural and chemical variation along traverses from the core to the rim of lapilli from Vesuvius.

### *Method*

The accretionary lapilli were collected from hydromagmatic ash deposits produced by the last two major catastrophic eruptions of Vesuvius. Avellino (3500 years b.p.) samples were taken from stratigraphic sections measured at Cave l'Amendolare, Ottaviano, Palmenetto, and Vallegrande. Pompeii (A.D. 79) samples came from sections at Pompeii-Castellum and Oplontis. At all locations the accretionary lapilli were dispersed within the fine-ash of surge deposits that rest above thick (greater than 2 m) Plinian pumice-fall beds.

Photographs ( $\sim 1000\times$ ) were taken at discrete intervals from the core to the rim of epoxy-impregnated thin sections of the lapilli. Grain-size measurements were made directly from these photographs by visual inspection of approximately 1000 grains by means of a hand magnifier.

Bulk chemical analyses were made of 2700  $\mu\text{m}^2$  areas (200 s count, 15 keV beam potential) at four selected intervals from the core to the rim. Spectra were quantitatively analyzed by use of an internal standard with a ZAF correction routine (KEVEX). Precision was checked by repeated analysis of the same area as well as by change in the size of the analyzed area.

### *Results*

Accretionary lapilli from both the Avellino and Pompeii deposits have three distinct structural zones (Fig. 1): a massive (structureless) core (3 to 6 mm diameter) of fine ash, an intermediate zone with bands of bubbles and larger clasts, and a fine-grained rim (0.3 to 1.8 mm thick). Patches of bubbles (50 to 300  $\mu\text{m}$  in diameter) occur in the cores of some lapilli as well as bands and patches between the cores and the rims. The distribution of larger clasts (greater than 50  $\mu\text{m}$  in diameter) in the zone between the cores and the rims is either random or concentrated in one or two concentric bands. A matrix of fine dust (less than 1  $\mu\text{m}$  in diameter) has an irregular distribution, but in some lapilli it occurs as distinct layers.

Only a small fraction of the clasts from the accretionary lapilli have vesicles: for Pompeii lapilli about 2% and for Avellino lapilli about 5%. Most clasts are blocky with delicate projections; many corners have acute angles (Fig. 2). The median grain size

---

Author Sheridan is at Arizona State University (Department of Geology), Tempe, AZ 85287; author Wohletz is at Los Alamos National Laboratory (Earth and Space Science Division), Los Alamos, NM 87545.

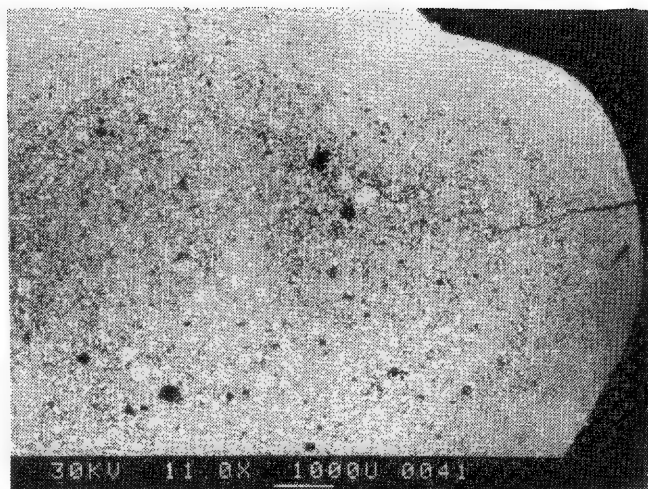


FIG. 1.--Accretionary lapillus from Avellino deposit at Cave l'Amendolare, Vesuvius. Note three concentric zones: (1) massive core without bubbles, (2) intermediate zone with concentric bands of bubbles and larger clasts, and (3) outer rim composed of fine dust.

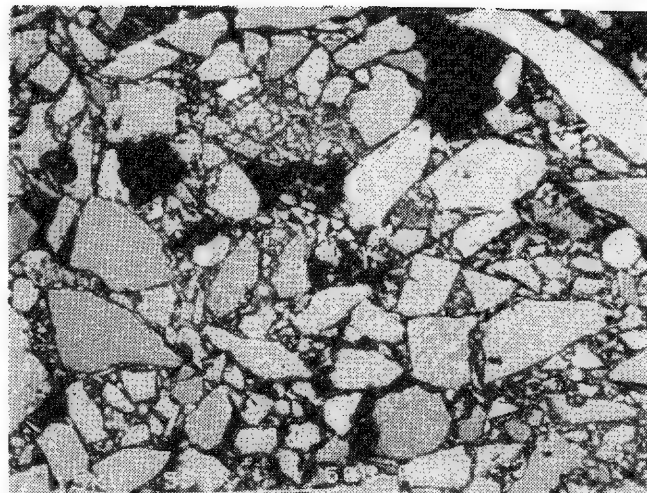


FIG. 2.--Detail of texture in rim zone of lapillus from the Avellino deposit at Vallegrande, Vesuvius. Note extremely angular clasts, fine dust matrix, and bubble voids. Backscatter image mode distinguishes crystals (bright) from glass (gray).

ranges from 3.7 to 5.4  $\phi$  (77 to 24  $\mu\text{m}$ ); the most common mode is about 45  $\mu\text{m}$ . The sorting is good ( $\sigma_\phi = 1.0$ ). The size and shape of these grains are characteristic of pyroclasts produced by hydroexplosions.<sup>6,7</sup>

Considerable chemical data exists for the ash deposits containing these lapilli. Major element analyses were made on bulk ash samples collected throughout the entire stratigraphic thickness (Plinian fall through overlying surge beds) of the Pompeii deposit.<sup>8</sup> In addition, pumice from the Avellino and Pompeii deposits as well as representative lavas of the post-caldera stage of Vesuvius have been analyzed.<sup>9</sup> Thus, the original magmatic composition is well known.

The fine-ash horizon above the pumice-fall bed of the Pompeii deposit has a significant change in composition<sup>8</sup> that reflects a general increase in contamination of the ash with carbonate xenolithic materials (Fig. 3). The general model for the Plinian eruptions of Vesuvius is based on the assumption that the carbonate walls of the magma chamber disintegrate and allow pulses of water to enter the chamber to create hydroexplosions.<sup>9,10</sup> The coupled wall-rock disintegration and water/magma interaction produces finer-grained products in an eruption plume that becomes progressively enriched in water (liquid and vapor) relative to magma. The compositions of analyzed pumice and lava give an approximation to that expected for uncontaminated ash. Figure 3 shows a linear decrease of CaO and MgO when plotted against SiO<sub>2</sub> that reflects the contamination trend for the Pompeii deposit.

If simple mixing of pyroclasts with comminuted wall-rock were true for the accretionary lapilli, their analyses should plot on a line that parallels the slope of the Pompeii surge ash analyses. This trend is in fact true for the spot analyses of the Avellino and Pompeii accretionary lapilli. However, the analyses plot above the line defined by the surge samples (Fig. 3). In addition, spot analyses from the core to the rim of individual lapilli also define lines that are parallel to the general trend.

### *Conclusions and Discussion*

Several conclusions may be drawn from textural evidence. (1) The structureless cores of the lapilli accreted rapidly in a zone of the eruption plume that did not experience appreciable turbulence. (2) Grain-size layering in the intermediate zone suggests rotation of the lapilli during their accretion in a portion of the eruption cloud containing grains of variable size. (3) The outer rim of fine dust suggests final accretion in a relatively low-energy environment. (4) The dispersal of lapilli throughout the fine-grained surge deposit suggests that they fell into a laterally moving surge cloud as discrete particles

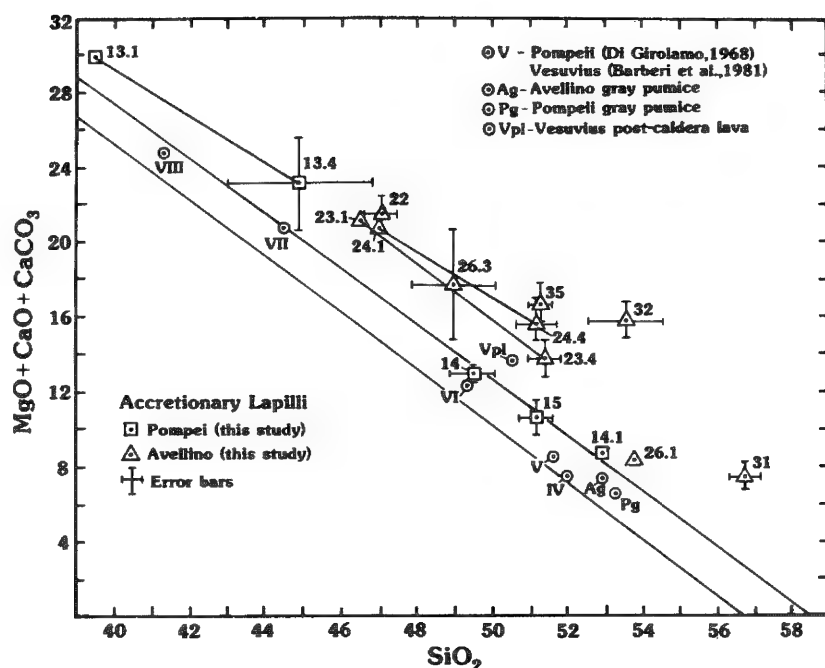


FIG. 3.--Plot of  $(\text{CaO} + \text{CaCO}_3 + \text{MgO})$  vs  $\text{SiO}_2$  for Plinian-fall and surge deposits (circles) and accretionary lapilli from Pompeii (squares) and Avellino (triangles) deposits. Whole numbers refer to lapilli from single level at specific locality. Decimal numbers indicate number of analyses in average of several areas on single lapillus. Error bars about these points represent standard deviation.

rather than as a pulsating rain that would have formed individual beds. (5) The unbroken spheroids show that they remained coherent during transport and deposition within the surge deposits of ash.

The bubbles provide evidence for local temperature and humidity conditions during growth of the lapilli. The presence of bubbles suggests either that water adhering to the particles was vaporized by the hot core or that the condensed water on the surface of lapilli was incorporated with a spherical shape due to surface tension. In either case, bubbles indicate that abundant water was present when the temperature in the cloud decreased below the vaporation point.

Chemical data provide additional constraints on the model of lapilli formation.

(1) The chemical trend ( $\text{CaO}$ ,  $\text{MgO}$ , and  $\text{SiO}_2$ ) for the lapilli is parallel to that for the Plinian (lapilli-fall plus surge) deposit as a whole. (2) The accretionary lapilli analyses fall above those of the associated surge deposit. (3) The Avellino lapilli analyses plot in a higher position than do the Pompeii lapilli. (4) Generally the rims of the lapilli are enriched in carbonate ( $\text{MgO}$  and  $\text{CaO}$ ) components. Sample 14, however, had the reverse trend. (5) The maximum amount of carbonate included is about 20 per cent.

#### *Model for Formation*

The above data and conclusions are compatible with a model for formation of the lapilli by rapid accretion of the cores in a high-temperature (above  $100^\circ\text{C}$ ) volcanic plume, which produced a massive core without bubbles. The core composition near that of the last-erupted magma is consistent with the hot central zone of the plume that is enriched in magmatic components and poorer in water vapor and xenolithic dust. As the lapilli move outward from the zone of laminar flowage in the central part of the erupted plume into the turbulent margins, the layered zone is accreted. The presence of bubbles in this zone indicates that the incorporated air from the atmosphere had cooled the vapor to the saturation temperature so that water could condense. This part of the plume also contains more carbonate ( $\text{CaO}$  plus  $\text{MgO}$ ), as would be expected from the increased load of chamber-wall clasts towards the margins of the conduit and hence in a corresponding position within the plume above. Little accretion occurs after the lapilli move out of the turbulent plume. Only a thin veneer of fine carbonate-rich dust deposited as a rim before the lapilli plunged down into the avalanching surge clouds. The plot of the lapilli analyses above those of the surge deposits in Fig. 3 suggests that the lapilli are enriched in glass (or depleted in crystals) relative to the base-surge clouds.

## References

1. G. P. Scrope, *Considerations on Volcanoes*, London: W. Phillips and G. Yard Pub., 1925.
2. A. LaCroix, *La Montagne Pelée et ses eruptions*, Paris: Masson, 1904.
3. H. T. Stearns, "The explosive phase of Kilauea volcano, Hawaii, in 1924," *Bull. Volcanol.* 5: 1-16, 1925.
4. J. G. Moore and D. L. Peck, "Accretionary lapilli in volcanic rocks of the western continental United States," *J. Geol.* 70: 182-193, 1962.
5. G. H. Heiken, "Tuff rings: Examples from the Fort Rock-Christmas Lake Valley basin, south central Oregon," *J. Geophys. Res.* 76: 5615-5626, 1971.
6. S. Self and R. S. J. Sparks, "Characteristics of widespread pyroclastic deposits formed by the interaction of silicic magma and water," *Bull. Volcanol.* 41: 196-212, 1978.
7. K. H. Wohletz, "Mechanism of hydrovolcanic pyroclast formation: size, scanning electron microscopy, and experimental studies," in M. F. Sheridan and F. Barberi, Eds., *Explosive Volcanism*, Elsevier, 1983.
8. P. di Girolamo, "Petrografia del Somma-Vesuvio: Le series piroclastiche," *Rend. Accad. Sci. Napoli* 35: 1-68, 1968.
9. F. Barberi, H. Bizouard, R. Clocchiatti, N. Metrich, R. Santacroce, and A. Sbrana, "The Somma-Vesuvius magma chamber: A petrological and volcanological approach," *Bull. Volcanol.* 44: 295-316, 1981.
10. M. F. Sheridan, F. Barberi, M. Rosi, and R. Santacroce, "A model for Plinian eruptions of Vesuvius," *Nature* 289: 282-285, 1981.

## CHARACTERIZATION OF VAPOR-PHASE MINERALOGY FROM THE GREEN IGNIMBRITE, PANTELLERIA

Tamsin McCormick and M. F. Sheridan

Scanning electron microscopy (SEM) and electron microprobe analysis of vapor-phase products in the green ignimbrite from Pantelleria were completed to provide information on the process of vapor-phase crystallization. While the volcanic rock cools, vapor-phase crystallization occurs by the growth of crystals in pores through the action of a hot vapor.<sup>1</sup> The actual role of the vapor and the extent of replacement of the glass by this process is not well understood.

### *Geologic Setting*

Pantelleria is a volcanic island located in the straight of Sicily midway between Sicily and Libya. The island is famous for its strongly peralkaline rhyolites (Pantellerites). The green ignimbrite is the youngest of several pantelleritic welded tuffs on the island. Some authors consider this unit to be an ash-flow tuff,<sup>2,3</sup> whereas others believe that it is a welded ash-fall unit.<sup>4-6</sup> However, all agree that the green ignimbrite is rheomorphic, meaning that it has undergone secondary flowage as a hot viscous body after its primary emplacement.

Although the green ignimbrite once completely blanketed the island of Pantelleria, subsequent domes, lava flows, and tephra cones now locally cover it, especially within the central caldera.<sup>3</sup> Erosion has produced numerous cliffs that expose a complete section of the unit. The large amount of vapor-phase aegirine gives the rock its characteristic green color. Although the petrochemistry of the lavas on Pantelleria has received much attention, a thorough study of the formation of vapor-phase minerals in the tuffs has not yet been undertaken. The purpose of this paper is to report on the morphology, composition, and development of vapor-phase minerals in the green ignimbrite as a first contribution to the better understanding of late-stage processes in peralkaline welded tuffs.

The studied section of green ignimbrite is exposed on the northern part of the island near Lago del Bagno. Phenocryst phases in the tuff include aegirine, aenigmatite, Ca-Fe pyroxene, iron oxides, and sanidine. Besides crystals the unit consists of lithic clasts and flattened pumice in a matrix of glass shards. Samples come from textural zones labeled A through E proceeding from the base to the top of a 7m-thick section (Fig. 1).

At the base of this section is a nonwelded Plinian-fall deposit, the upper part of which is weakly stratified. Unit A consists of a welded vitrophyre with conspicuous black fiamme composed of flattened pumice. A cross-stratified surge horizon separates units A and B. Unit B is a welded vitrophyre similar to A but somewhat thinner. Above it is another cross-bedded surge horizon. Then follows unit C, the vitrophyric base of a thick welded tuff. Units D and E from the lower and upper parts of this welded unit exhibit rheorphism and strong secondary crystallization. The degree of vapor-phase mineralization visibly increases upward in the section.

### *Vapor-phase Mineralization*

Vapor-phase mineralization in the lower part of the section is largely confined to the porous ash matrix. Needles of aegirine and/or riebeckite about 0.5  $\mu\text{m}$  thick and 10  $\mu\text{m}$  long are fairly abundant in parts of the matrix of Unit A. They locally occur on the walls of bubbles in the glassy pumice fragments.

In Unit B the aegirine and riebeckite needles have doubled in size and have been joined

---

Authors McCormick and Sheridan are at Department of Geology, Arizona State University, Tempe, AZ 85287. SEM and microprobe work were done at Los Alamos National Laboratory. Support of NSF grants EAR79-26375 and EAR81-211190 is acknowledged. G. Orsi provided the samples.

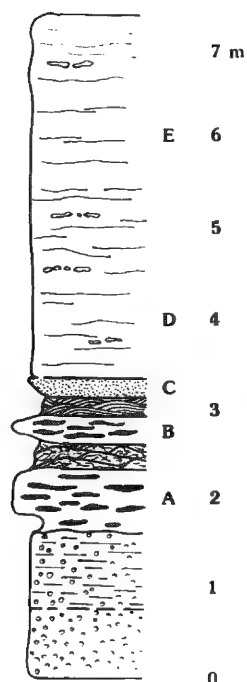


FIG. 1.--Stratigraphic section of green ignimbrite near Lago del Bagno showing the position of studied samples.

by crystals of rounded and pitted cristobalite, 25 to 30  $\mu\text{m}$  in diameter (Fig. 2a). Submicron blocky, iron-rich sanidine is also evident in the matrix. Vapor-phase products also occur in bubbles in the glassy pumice fragments. Here the cristobalite is not pitted, in contrast to its morphology in the matrix.

In Unit C the vapor-phase crystallization is further developed in this fashion. Aegirine and riebeckite needles of the order of 30  $\mu\text{m}$  long form a network throughout the matrix and occur as radiating clusters on the walls of cavities near pumice fragment boundaries (Fig. 2b). Unpitted cristobalite in this unit is recognized in bubble cavities, but it is not obvious in the matrix.

Pumice fragments in unit D are surrounded by a narrow, fine-grained dark rim which contains euhedral quartz crystals (Fig. 4b). The centers of these clasts are completely replaced by coarse crystals that obscure the original structure, although large cavities in these features mimic original vesicles. These areas contain tridymite plates and blocky sanidine crystals in addition to laths of aegirine and riebeckite (Fig. 3a).

The strongest development of vapor-phase mineralization is displayed near the top of the section in unit E. Although the pumice are now completely crystalline, their former vesiculated structure is still evident (Fig. 3b). Transparent feldspar crystals, dark green riebeckite, and pale green aegirine laths line the cavities. In addition, small euhedral quartz crystals and cristobalite occur in the cavities. Electron microprobe analyses of vapor-phase crystals in Units D and E show no significant variation in composition. Table 1 gives representative analyses.

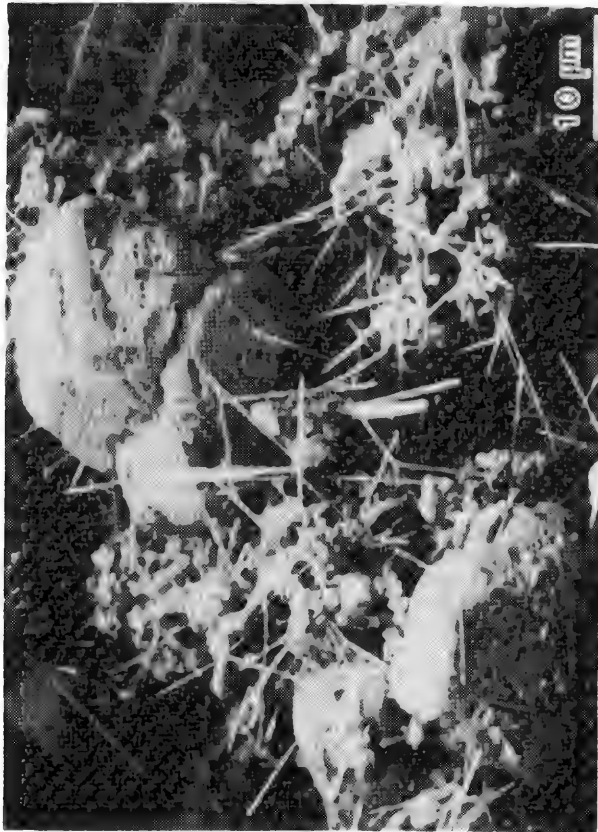
#### Discussion

It is apparent from the SEM micrographs that although initial vapor-phase crystals grew within pumice bubbles and in the matrix, the greatest development of these crystals accompanies replacement of glass in pumice clasts in the upper part of the sheet. Vapor-phase sanidines are slightly more potassic and substantially more iron-rich than phenocrystic sanidines. In addition, aenigmatite appears to be absent from the vapor-phase assemblages, being replaced by riebeckite. This suggests that the vapors were rich in alkalies and iron but poor in titanium.

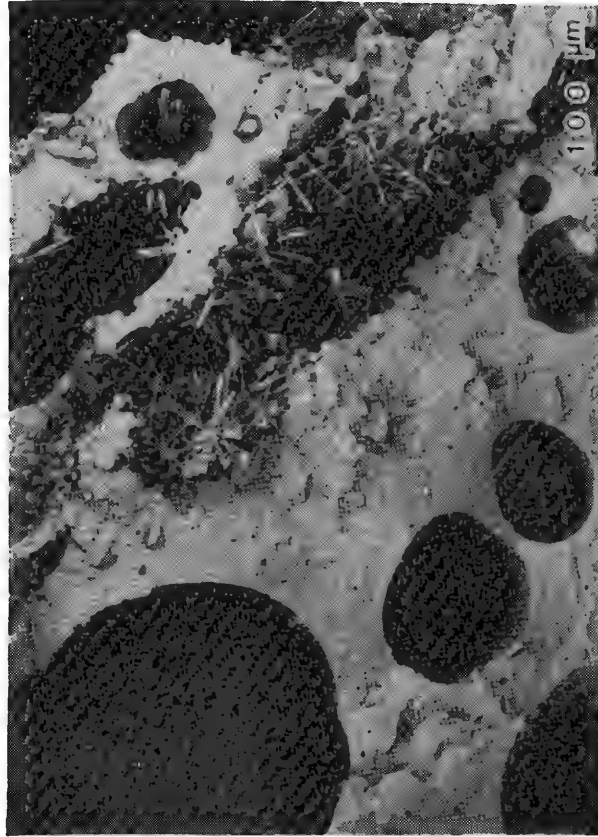
#### References

1. R. L. Smith, "Ash flows," *Bull. Geol. Soc. Am.* 71: 795-841, 1960.
2. L. Villari, "The island of Pantelleria," *Bull. Volcanol.* 38: 680-724, 1974.
3. Y. Cornette, G. Crisci, P. Y. Gillot, and G. Orsi, "Recent volcanic history of Pantelleria: A new interpretation," in M. F. Sheridan and F. Barberi, Eds., *Explosive Volcanism, J. Volcan. Geotherm. Res.* 17 (in press).
4. J. A. Wolff and J. F. Wright, "Rheomorphism of welded tuffs," *J. Volcanol.* 10: 13-34, 1981.
5. R. S. J. Sparks and J. F. Wright, "Welded air-fall tuffs," in C. E. Chapin and W. E. Elston, Eds., *Ash-flow Tuffs*, Geol. Soc. America Sp. Paper 180, 1979, 155-166.
6. J. V. Wright, "Stratigraphy and geology of the welded tuffs of Pantelleria, Italy," *Geol. Rundsch.* 69: 263-291, 1980.





(a)



(b)

FIG. 2.--(a) Vapor-phase minerals in ash matrix of Unit B. Visible are cristobalite (etched), aegirine, riebeckite, and sanidine. (b) Vapor-phase minerals in pumice of Unit C. Large spherical vesicles are present in fresh glass of pumice. Needles of aegirine and riebeckite (?) within vesicles and along margins of pumice.

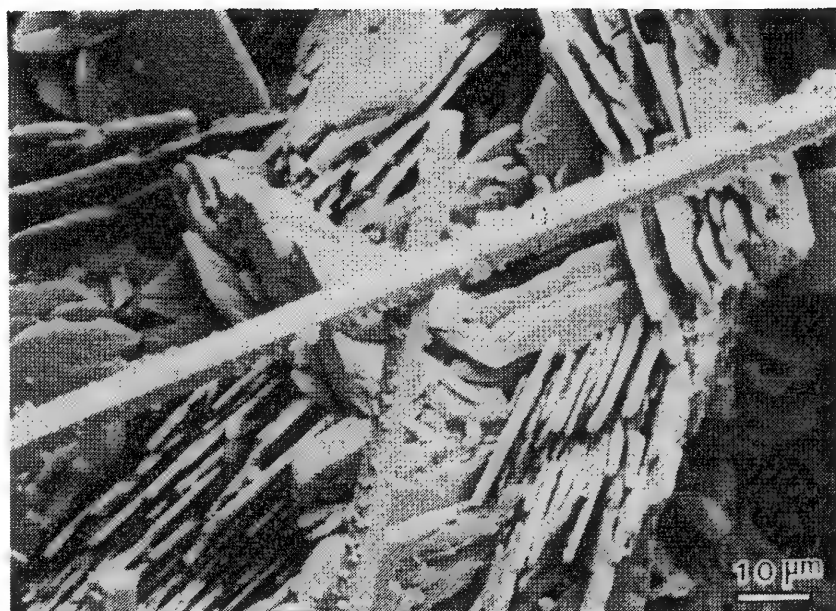


(a)



(b)

FIG. 3.--(a) Vapor-phase minerals of Unit D. Glass is completely replaced by crystals. Wedge-shaped tridymite, needles of aegirine and riebeckite, and platy sanidine are visible. (b) Vapor-phase minerals in pumice of Unit E. Outlines of spherical vesicles are preserved, but glass is completely replaced by secondary minerals. Laths of aegirine and riebeckite are visible. Sanidine forms blocky crystals and small granules in matrix. There are a few quartz grains.



(a)



(b)

FIG. 4.--(a) Vapor-phase minerals in Unit D. Platy sanidine and aegirine (?) needles. (b) Vapor-phase minerals, including quartz, sanidine plates, aegirine and riebeckite needles are near edge of pumice in Unit D.

TABLE 1.--Representative chemical data on phases.

	Aegirine Unit D	Sanidine Unit E	Riebeckite Unit E
SiO <sub>2</sub>	51.46	65.34	48.07
TiO <sub>2</sub>	1.42	0.00	1.35
Al <sub>2</sub> O <sub>3</sub>	0.34	13.77	0.28
Fe <sub>2</sub> O <sub>3</sub> *	29.15	7.35	---
FeO	1.32	0.00	34.01
MnO	0.77	0.00	2.18
MgO	0.54	0.02	0.50
CaO	3.52	0.00	0.52
Na <sub>2</sub> O	11.50	6.42	9.06
K <sub>2</sub> O	0.02	7.09	1.27
Total	100.01	100.00	97.23

\*Recalculated for aegirine and sanidine. Total Fe as FeO for riebeckite.



## ROLE OF GRAIN TYPE IN QUANTITATIVE SURFACE MORPHOLOGY OF PYROCLASTS FROM THE MONTE GUARDIA SEQUENCE ON LIPARI, ITALY

C. P. Kortemeier and M. F. Sheridan

This paper presents a new quantitative method for examining images of single grains of pyroclasts. The technique can be adapted for quantitative classification, discrimination, or interpretation of several types of pyroclastic deposits. An example is presented using the Monte Guardia sequence, a well-characterized deposit of base-surge origin on the island of Lipari.<sup>1</sup> Samples taken from different types of deposits at various distances from the source represent diverse depositional environments. Cluster analysis shows that clast type dominates over environmental factors in the correlation of grains based on their surface morphology.

### *Background*

Lipari is the largest island in the Aeolian arc located north of Sicily. The Monte Guardia sequence is a rhyolitic base-surge deposit that erupted between 22 600 and 16 800 years ago.<sup>1</sup> This unit contains four dominant pyroclast types: (1) pumice, (2) white non-vesicular glass, (3) black microcrystalline clasts, and (4) crystals.<sup>2</sup> Samples were taken from four distinctive types of deposits (sandwave, massive, and planar surge beds, and lapilli-fall deposits) at three distances (proximal, medial, and distal) to investigate the various factors that affect the development of surface textures on the grains. This paper reports on the variability of grain-surface features related to clast type.

### *Method*

The technique used to prepare the samples for this study follows that suggested by Sheridan and Marshall.<sup>3</sup> Grain-size analysis of 14 samples representing various deposit types and localities allowed the identification of principal subpopulations. Representative splits were chosen of two size populations that are generally present in all samples. The pyroclasts were cleaned in a dilute (10%) HCl solution and examined with a binocular optical microscope prior to mounting on an aluminum stub. Grains from each of four clast types were placed in rows on the stubs with their identity recorded so that they could be relocated for future analysis. The number of grains examined from each sample ranged from 20 to 50.

The magnification for SEM imagery was chosen to produce single-grain images. The average magnifications were approximately 50× for the coarser population and 150× for the finer size fraction. Thus the resolution of detail on grain surfaces is much greater for the fine pyroclasts.

Prior to quantification of any morphological features, a general reconnaissance was made to familiarize the operator with the variability of surface features displayed by the grains. Individual pyroclasts that were inappropriate for the study were eliminated at this stage.

Images in this study were compared directly to those in the textural atlas of Sheridan and Marshall.<sup>4</sup> Each grain was given a decimal ranking in proportion to the degree of development for each of the 8 morphological parameters. This standardized approach allows direct comparison of populations from widely different localities. The parameters chosen to characterize the pyroclasts in this study were: vesicularity, bubble shape, breakage, largest simple surface, glass coating, pitting, amorphous overgrowths, and crystalline overgrowths. A different selection of parameters may be appropriate for other studies.

Authors are at the Department of Geology, Arizona State University, Tempe, AZ 85287. Rosanna deRosa collected the samples and prepared the stubs. Support of NASA grant NAGW-245 is acknowledged.

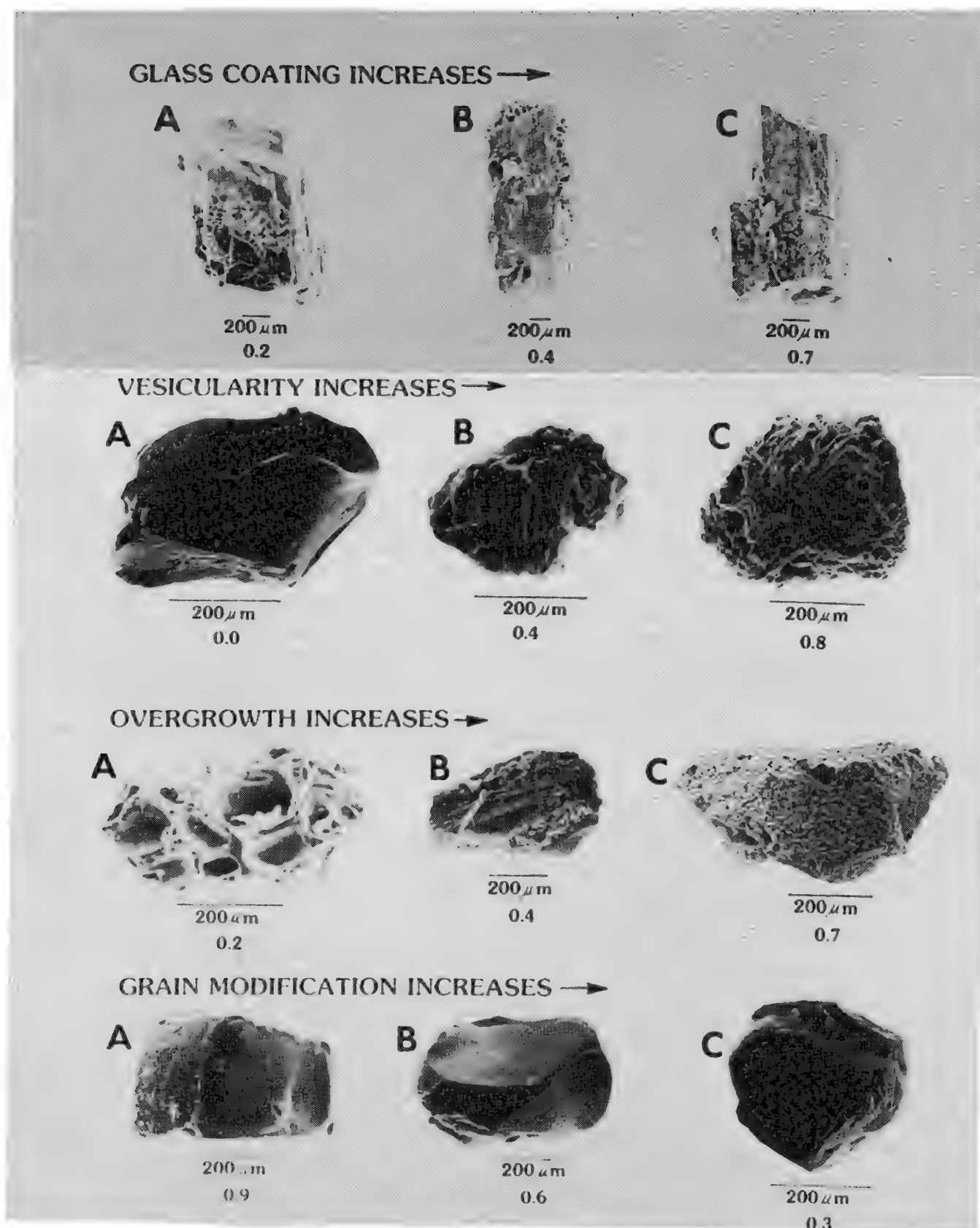


FIG. 1.--Examples of textural development. Numbers beneath scale bars give quantitative values of parameters.

Grains exhibiting four of these parameters are shown in Fig. 1.

Glass coated crystals appear in the first row of Fig. 1. Crystals free of glass have a value of 0.0; those completely coated have a value of 1.0. The glass layer is invariably vesicular. Therefore, as the thickness of the glass coating increases or the size of the crystal decreases, a morphological gradation exists between glass-coated crystals and porphyritic pumice.

The second row of Fig. 1 illustrates the vesicularity of grains. Bubble-free glassy particles have a value of 0.0 and vitric clasts exhibiting maximum vesicularity have a value of 1.0. This parameter does not represent the actual void space, but rather the ratio of vesicle surface area to area of intervesicle wall that is visible in the image.

The third row of Fig. 1 exhibits the range of secondary crystalline overgrowth. Secondary overgrowth may be amorphous, microcrystalline, or crystalline. A grain free of overgrowth has a value of 0.0. Grains with barely discernible crystalites have a value of 0.1. A completely overgrown grain whose largest secondary crystal approaches the size of the pyroclast has a value of 1.0.

The fourth row of Fig. 1 shows the degree of grain modification, represented by the largest simple surface. The size of the largest simple surface grades from 1.0 for the largest to 0.0 for the smallest. These values are relative in that the area of the face is compared with the size of the entire grain image. Resolution of the image becomes an important factor for very small faces. The size of the largest surface decreases logarithmically as the grain is modified by collisions. Therefore the scale for this parameter is not linear.

### Statistical Analysis

In order to use this method to resolve questions of textural modification by eruption, transportation, and diagenesis, the hierarchy of controls on grain morphology must be established. Because some grain types can be easily identified by inspection of SEM images,<sup>5</sup> grain type is the first level of discrimination to examine. The complete matrix of 8 parameters were used to test for similarity of grains of the same type within single populations and combinations of populations by using the cluster analysis program CLUSTAN.<sup>6</sup>

Dendrograms based on three or more eigenvalues were plotted for single samples and various combinations of samples to test the effect of grain type on clustering. Scatter diagrams based on eigenvalues were also made for comparison of the grouping of data by grain type. Figure 2 gives a representative dendrogram for the coarse grain size of a

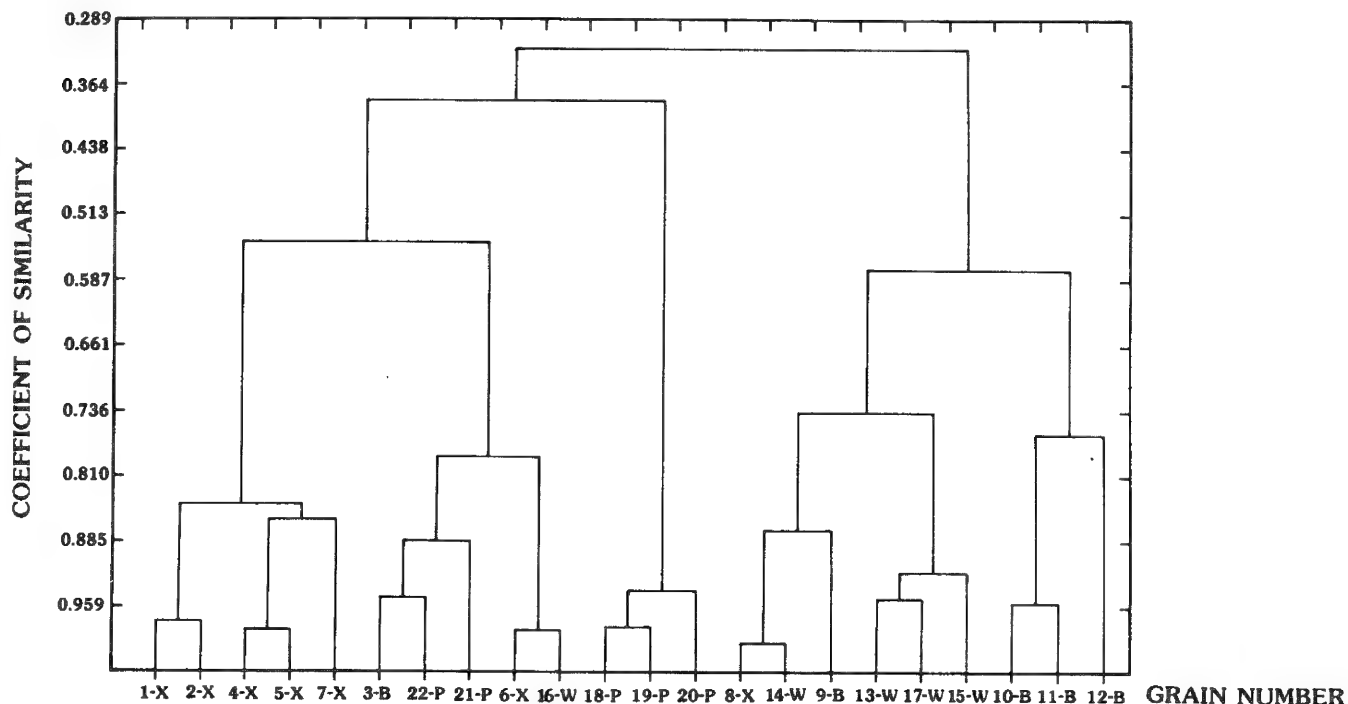


FIG. 2.--Dendrogram of all eight eigenvalues of pyroclast surface features on coarse grains from distal planar surge bed. X = crystals, P = pumice, B = black microcrystalline fragments, W = white vitric pyroclasts.

distal planar surge bed. Crystals, pumice, and glass are easily separated by this technique. Although the black microcrystalline fragments and white glassy pyroclasts are in the same major group, subclusters do separate these types. One of the major clusters contains grains of various types which apparently contain no strongly characteristic surface features. These grains may exhibit textures more characteristic of secondary processes.

### *Discussion*

Some difficulties may arise in the assignment of quantitative values for morphological parameters. Features related to secondary processes, such as overgrowths and pitting, may obscure primary features, such as vesicularity or glass coatings. Some primary features, like glass coatings, may be removed by chipping or fracturing during transport. In addition, certain features may combine to superficially resemble totally unrelated textures. For example, a finely vesiculated pumice with amorphous coating may resemble a crystal with secondary crystalline overgrowths, or the microcrystalline surface on lithic grains. High-resolution microscopy or energy-dispersive analysis may be required to resolve these uncertainties. In the worst case such ambiguous grains could be eliminated from the quantitative analysis since their number is small.

The method outlined in this paper appears to be useful as a first attempt to quantify surface textural features on pyroclasts. Grain type is the dominant factor in the development of the various surface textures examined, which means that in order to investigate the effects of eruption, transport, and diagenesis of this type of deposit, the images must first be regrouped into grain types. Then each type can be tested for variability according to eruption type, emplacement mode, modification during transport, and diagenesis after deposition.

### *References*

1. G. M. Crisci, R. DeRosa, G. Lanzafame, R. Mazzuoli, M. F. Sheridan, and G. G. Zuffa, "Monte Guardia sequence: A Late-Pleistocene eruptive cycle on Lipari (Italy)," *Bull. Volcanol.* 44: 241-255, 1981.
2. R. DeRosa and M. F. Sheridan, "Evidence for magma mixing in the surge deposits of the Monte Guardia Sequence, Lipari," in M. F. Sheridan and F. Barberi, Eds., *Explosive Volcanism, J. Volc. Geotherm. Res.* 17 (in press).
3. M. F. Sheridan and J. R. Marshall, "SEM examination of pyroclastic materials: Basic considerations," *SEM/1982* (in press).
4. M. F. Sheridan and J. R. Marshall, "Towards a quantitative analysis of pyroclastic grain-textural elements," in J. R. Marshall, Ed., *Characterization and Quantification of surface features on elastic and pyroclastic particles*, New York: Hutchinson Ross.
5. M. F. Sheridan and J. R. Marshall, "Interpretation of Pyroclast surface features using SEM images," *J. Volc. Geotherm. Res.* 17 (in press).
6. D. Wishart, *CLUSTAN User Manual*, Edinburgh: Program Library Unit, Edinburgh University, 3d ed., 1978, 1-175.

## DETERMINATION OF THE COMPOSITIONS OF METAL PHASES IN CHONDRITIC METEORITES

D. G. W. Smith and S. Launspach

Metal phases in chondritic and other meteorites are composed of major Fe and Ni, minor Co, and traces of other elements. Due to the different origins and thermal histories of meteorites the proportions of these elements vary greatly, not only from meteorite to meteorite but also in most instances from grain to grain and within grains. It has been recently shown that the pattern of variation, in combination with the average composition of the metal grains, may be distinctive for a particular meteorite and may thus provide a means of characterization or "fingerprinting," as well as offering insights into the meteorite's thermal history.<sup>1,2</sup>

Such characterization requires the analysis of several hundred points for each meteorite. This paper outlines the procedures that have been developed to acquire the data relatively quickly and conveniently by use of an automated electron microprobe fitted with both energy-dispersive and crystal spectrometers.

### *Analytical*

The equipment used in this work was initially an Applied Research Laboratories (A.R.L.) "EMX" microprobe fitted with three crystal spectrometers and an Ortec energy-dispersive spectrometer. Subsequently, full automation of the procedure was achieved on an A.R.L. "SEM-Q" microprobe, which has four crystal spectrometers and an Ortec "EEDS II" energy-dispersive system. Throughout the work an operating voltage of 15 kV was found to be very satisfactory when combined with a probe current of about 25 nA, measured by a Faraday cage in the sample position. Of the available crystal spectrometers it was necessary to use only the two that have LiF analyzing crystals.

No attempt was made to determine the trace element contents of grains investigated. That would require completely different and more time-consuming procedures. Thus, only the elements Fe, Ni, and Co were determined. These elements suffer from mutual interferences in energy-dispersive analysis (EDA) because of the relatively poor resolution of such systems. Only the Fe K $\alpha$  peak is essentially free of such interference. It was therefore decided that Fe should be determined by EDA; the LiF crystal spectrometers with their superior resolution were used to determine simultaneously Ni and Co.

Because the metal phases closely approach a binary system, since they are made up in nearly every instance of more than 97% Fe + Ni, the normal procedures for fully quantitative analysis, requiring peak and background measurements on both samples and standards as well as full ZAF corrections, need not be adopted. Instead, the "calibration curve" approach can be used without significant loss of accuracy provided that a series of standard materials covering the Fe-Ni composition range is available. The composition of standards used in this work are shown in Table 1.

Co determinations were made against a pure Co standard and the size of matrix corrections for Co in pure Fe and pure Ni were calculated by the ZAF subroutines of the program EDATA2.<sup>3</sup> Co K $\alpha$  radiation lies on the low-energy side of both the Fe and Ni K absorption edges and hence these corrections were found to be both small and very similar (0.976 and 0.995). A constant, average ZAF correction (0.985) was therefore applied to all Co determinations, irrespective of the Fe/Ni ratio calculated for that sample by the calibration curve technique. The background beneath the Co peak can be calculated from an expression based on determinations of the actual background at the Co peak position on various Fe-Ni samples of known composition. Thus it was found that in the concentration range Fe =

---

The authors are at the Department of Geology, University of Alberta, Edmonton, Alberta, Canada, T6G 2E3. Supported by operating grant A4254 from the Natural Sciences and Engineering Research Council of Canada to the first author.

TABLE 1

Standards used	
Fe (wt.%)	Ni (wt.%)
100.0	0.0
94.9	5.1
42.9	57.1
36.7	63.3
10.5	89.5
0.0	100.0

Note: pure Fe and Ni obtained from chemical supply house. All other Fe, Ni alloys were prepared at the INCO Labs. in Sterling Forest and were supplied courtesy Dr. A. Batt. The compositions are the averages obtained by 6 laboratories in the Metropolitan Probe Users' Group.

Fe, Ni, and Co on whatever sample points are to be analyzed. Twenty-second counting times were found to be sufficient to give acceptable accuracy.

These data provide the input for the FORTRAN IV program "FENICO," which first calculates third-order polynomial fits to the standard intensities for Fe and Ni. Sample data are processed next and the concentrations for Fe, Ni, and Co are determined and presented. These concentrations are presented again after recalculation to 100%. FENICO then calculates an average metal composition on the basis of the points analyzed and finally generates plots of frequency of occurrence vs Ni wt.% and Co wt.% vs Ni wt.%. Note that any analysis totaling less than 95% is automatically excluded from recalculation and plotting. Typically, only a few per cent of the results lie in this category; nearly all totals lie between 98% and 102% when the counting times specified above are used. As written at present the program processes data in batch form once they have been gathered. Minor modifications would be required to process data from each sample point at the time they are acquired and present the results immediately. Similarly, it would be possible to modify the program to calculate and update plots for display on the screen of an integrated energy-dispersive system as data are acquired, rather than, as is the case at present, having plots calculated once at the end of data acquisition and processing.

Selection of analytical points is as far as possible random, but inevitably some operator bias enters into the choice. Attempts were made to sample within grains randomly, although there is undoubtedly a tendency to avoid the extreme margins, a tendency that could in some circumstances possibly result in a slight distortion of the pattern of values found.

An added advantage of the simultaneous acquisition of an energy-dispersive spectrum (from which one obtains Fe determinations by reading the appropriate energy region of interest) is that errors in the choice of analytical points, such as selecting a grain of troilite in mistake for metal, are immediately apparent from casual inspection of the spectrum, and acquisition can then be aborted.

### Discussion of Results

Some typical results obtained by the procedures outlined here are shown in Fig. 1. It will be noted that not only are there very considerable spreads in the Fe, Ni, and Co values obtained but also that there are significant differences in the patterns of these elements between the chondrites investigated.

Since analytical points are chosen randomly and optical differences between grains, lamellae, or other intergrowths of different metal compositions are often insufficient to

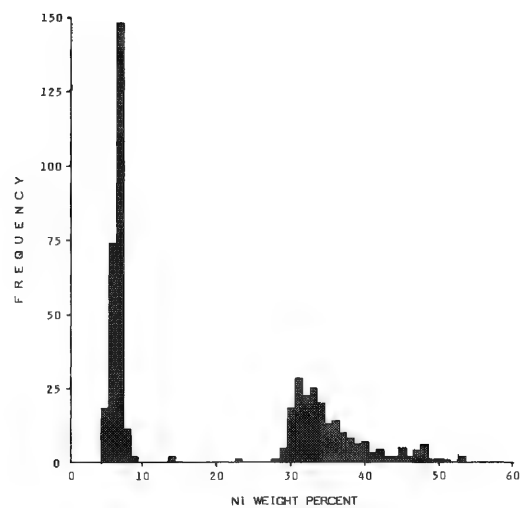
100 - 40 wt.% the background intensity B at the Co peak can be very closely approximated by the linear expression

$$B = (mX + c)I/C$$

where the slope  $m = 4.8333 \times 10^{-4}$ ,  $X$  = wt.% Fe present in the sample, the constant  $c = 0.64377$ ,  $I$  = Co standard net peak counts, and  $C$  = Co standard concentration in wt.%. At lower concentrations of Fe (seldom encountered in meteoritic metals) the relationship becomes noticeably nonlinear and a slightly different expression would be required to obtain the most accurate background values. This procedure for determining the Co background correction avoids possible problems of interference associated with the very weak Fe satellite line close to the Co K peak position.<sup>1,4</sup>

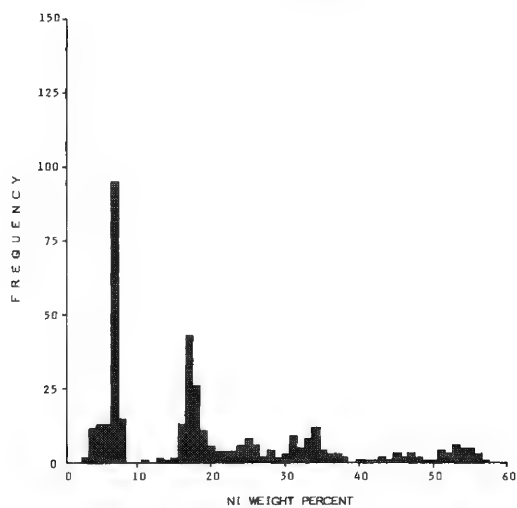
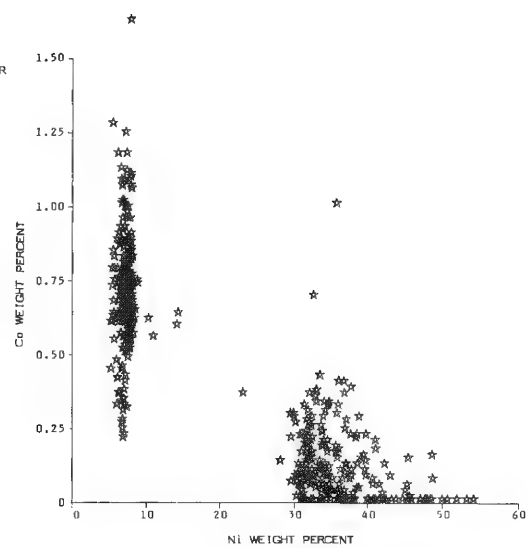
To determine the compositions of the metal phases in a chondritic meteorite, data are acquired first for each of the standard materials over 100s counting periods in each case. Typically, the following count rates are obtained (counts/s/percent/nA probe current): Fe: 0.52; Ni: 1.50; Co: 1.24. The approximate background (counts/s/nA probe current) for Co are: on Fe, 0.92; on Ni, 0.71.

Once standardization is complete, the procedure requires the determination of peak data (only) for elements



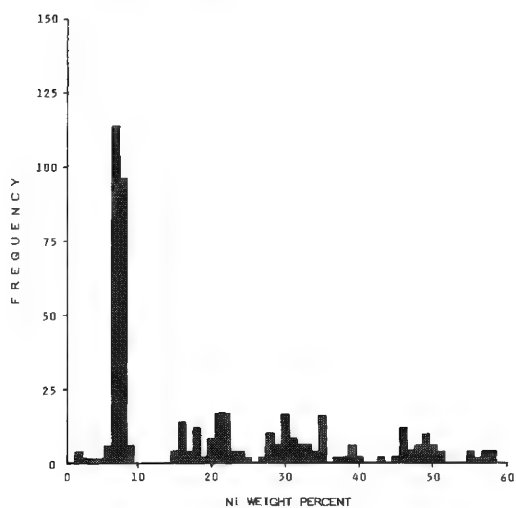
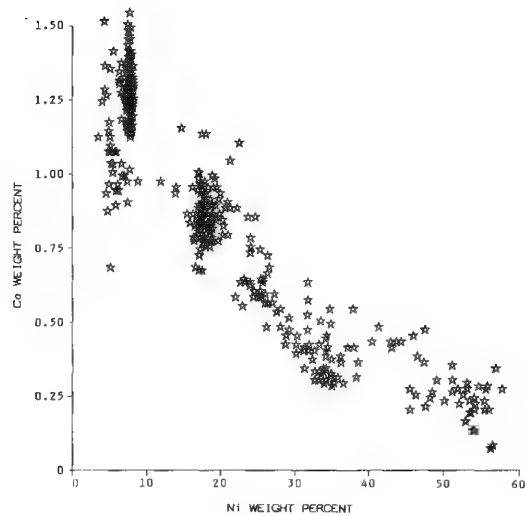
#### PEACE RIVER

Ave. Ni = 19.8%  
Ave. Fe = 79.8%  
Ave. Co = 0.44%



#### HOLBROOK

Ave. Ni = 20.0%  
Ave. Fe = 79.2%  
Ave. Co = 0.84%



#### L' AIGLE

Ave. Ni = 19.7%  
Ave. Fe = 79.6%  
Ave. Co = 0.67%

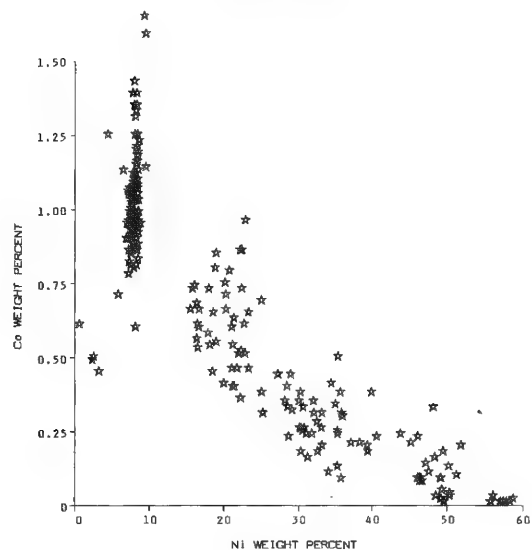


FIG. 1



delineate boundaries, it is inevitable that on some occasions an analyzed volume lies astride a boundary. The extent to which that happens varies according to the scale of the intergrowths; the most frequent occurrence is in fine-scale intergrowths such as plessite. An estimate of the importance of this effect can be obtained from the amount of broadening of the kamacite peak on its high-Ni side. When a substantial number of points have a Ni content in excess of approximately 8%, inadequate resolution of intergrowths can be suspected. However, if a fully focused beam less than 1  $\mu\text{m}$  in diameter is used, this situation is very rare. We therefore conclude that the effect is quantitatively unimportant in controlling the pattern of Fe, Ni, and Co concentrations found for metal phases.

An effect that must be considered, however, has to do with the exsolution of taenite from kamacite. With falling temperature the diffusion of Ni in taenite is sluggish and produces characteristic "M profiles" in which the marginal regions immediately adjacent to the kamacite have Ni contents that may be very significantly higher than the central taenite region. This disequilibrium situation may be "frozen" into the metals on final cooling. These concentration gradients in interface regions may produce, at least in part, the ranges of taenite values observed in the plots for many chondrites.

However, that does not appear to be the complete explanation. Plots for many chondrites exhibit a frequency maximum at about 50-55 wt.% Ni, probably corresponding to the tetrataenite phase. This phase is believed to be stable at temperatures below about 320°C,<sup>5</sup> and its presence in the chondrites may indicate prolonged mild reheating, perhaps during low temperature burial metamorphism. The points on the low-Ni flank of the kamacite peak, which are seen in the plots for most chondrites, may also represent kamacite interface regions depleted in Ni by low-temperature exsolution over long periods, although in this case it is also possible that they could represent original high-temperature, low-Ni kamacite, since the maximum Ni content of that phase increases with falling temperature to a value of about 6-8 wt.% at temperatures between 475 and 425°C (depending on the P content), then starts to decrease again and reaches values as low as 4.2 wt.% at 300°C.<sup>6</sup>

In addition to variations in the Fe/Ni ratio in the metal phases, there is a very clear trend in Co concentrations with low Co being in general associated with high Ni, and high Co with high Fe. It has been observed that chondrites with the most inhomogeneous metal phases also have the greatest variation in Co concentrations for any given Fe/Ni ratio.<sup>1</sup>

The results illustrated in Fig. 1 are from three chondrites that not only all belong to the abundant L group but also to the same petrologic type.<sup>6</sup> Yet there are significant differences between the average Co concentrations and the Fe-Ni-Co patterns that are obtained for these chondrites--differences that are, by and large, of similar magnitude as those observed between chondrites belonging to other groups and petrological types.<sup>1,2</sup> So far it has not been possible to demonstrate any obvious relationship between the average metal composition and/or Fe-Ni-Co patterns on the one hand and the group and/or petrologic type on the other. Thus it seems likely that the characteristics of the metal phases demonstrated by this work have not been acquired during the events that produced the different groups and types of chondrites but rather during lower-temperature processes of planetary accretion and burial metamorphism. If that is the case, they have the potential of revealing important information about accretion histories and the later thermal events affecting these meteorites.

## References

1. D. G. W. Smith, "The mineral chemistry of the Innisfree Meteorite," *Can. Min.* 18: 433-442, 1980.
2. Y. Miura, D. G. W. Smith, and S. Launspach, "The Ni, Fe and Co contents of metal phases in the Allende, Holbrook and Nuevo Mercurio chondrites," *Mem. Natl. Inst. Polar Res.*, Sp. Issue (in press), 1983.
3. D. G. W. Smith and C. M. Gold, "A scheme for fully quantitative energy dispersive microprobe analysis," *Advances in X-ray Anal.* 19: 191-201, 1976.
4. F. Affiatalab and J. T. Wasson, "Composition of the metal phases in ordinary chondrites: implications regarding classification and metamorphism," *Geochim. Cosmochim. Acta* 44: 431-446, 1980.
5. L. Billard and A. Chamberod, "On the dissymmetry of Mössbauer spectra in iron-nickel alloys," *Solid State Commun.* 17: 113-118, 1975.
6. A. D. Romig and J. I. Goldstein, "Determination of the Fe-Ni and Fe-Ni-P phase diagrams at low temperatures (700 to 300°C)," *Metall. Trans.* 11A: 1151-1159, 1980.



## MICROCHARACTERIZATION OF BASALT--CONSIDERATIONS FOR A NUCLEAR WASTE REPOSITORY

C. C. Allen and M. B. Strope

The National Waste Terminal Storage Program of the U.S. Department of Energy is assessing a number of rock types to determine their suitability for the disposal of nuclear waste. As a part of this effort, the Basalt Waste Isolation Project (BWIP) is investigating the Pasco Basin in southeastern Washington State as the possible site of a nuclear waste repository in basalt (NWRB). The microcharacterization work described in this paper results in a detailed identification of the minerals and other phase assemblages that provide the basis for a determination of the environment that acts to control geochemical conditions in an NWRB. Interactions between the basalt, groundwater, and proposed waste packages are being studied to insure that the final repository and waste package designs meet all requirements for safety and isolation.

The rock at the proposed repository location is a fine-grained tholeiite, containing crystals of plagioclase, pyroxene, and titaniferous magnetite plus a glass-rich mesostasis.<sup>1</sup> Partial reaction of this mesostasis with groundwater is thought to be the predominant source of most elements in the groundwater. The composition of the mesostasis and its reaction thus should affect the chemical environment of the waste packages. For this reason, microcharacterization of the mesostasis, particularly the glass phase, has been conducted by the BWIP in support of hydrothermal laboratory studies that provide data to geochemical and performance models.

### *Sample Preparation and Analysis*

Microanalysis was performed by a Leitz petrographic microscope, a Cameca electron microprobe, and a JEOL 200 CX scanning transmission electron microscope (STEM) with a Princeton Gamma-Tech Model 3000 energy-dispersive spectrometer (EDS). Rock samples were prepared as doubly polished thin sections (30  $\mu\text{m}$  thick) and carbon coated for microprobe analysis. Thin sections designated for STEM study were prepared with easily releasable crystalbond. The STEM samples were released from their mounting slides and cemented to slotted beryllium grids, ion thinned, and carbon coated.

The microprobe was calibrated with mineral standards, and the data were reduced by a ZAF correction routine. Crystals were analyzed with a point beam; glass analyses utilized a  $5 \times 5 \mu\text{m}$  area scan and short counting times to reduce alkali migration.

### *Results*

The Grande Ronde Basalt, which contains flows that are under consideration as candidate repository horizons, consists of basalt flows tens of meters thick. The dense interiors of many of these flows display two distinctive textural units, designated *colonnade* and *entablature*.<sup>2</sup> The colonnade, comprising the lower portion of a typical flow, is dominated by well-defined columnar jointing; the entablature above exhibits highly irregular fracturing. The two textural units apparently reflect different thermal histories in portions of a flow that were cooled simultaneously from the base and from the top.<sup>3</sup> Colonnade and entablature samples are identical in bulk chemical composition, but differ in detailed mineralogy.

The plagioclase crystals in both colonnade and entablature samples are sodic anorthites,

---

The authors are with the Basalt Waste Isolation Project, Rockwell Hanford Operations, Richland, WA 99352. Supported by U. S. Department of Energy under Contract DE-AC06-77RL01030. The authors wish to thank S. B. Kunkler and J. R. Smith for technical support and K. R. Fairchild for point counting data. Discussions with H. Babad, D. L. Lane, R. C. Edwards, and P. E. Long were valuable to our study.

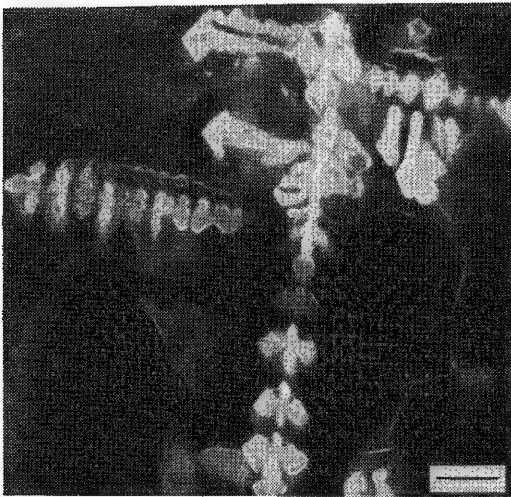


FIG. 1.--Titaniferous magnetite grains in entablature glass: secondary electron image. 10 $\mu$ m-scale bar.

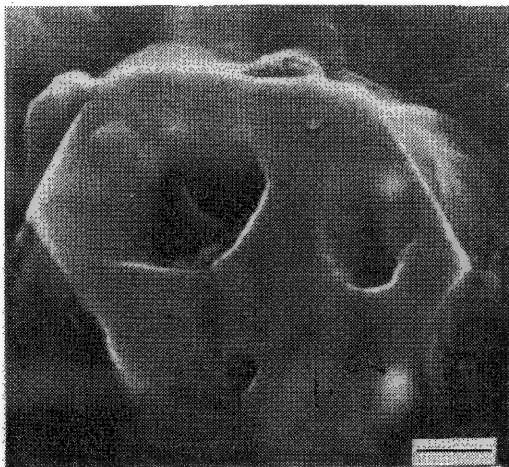


FIG. 2.--Cross section of hollow fluorapatite crystal in colonnade glass: secondary electron image. 1 $\mu$ m-scale bar.

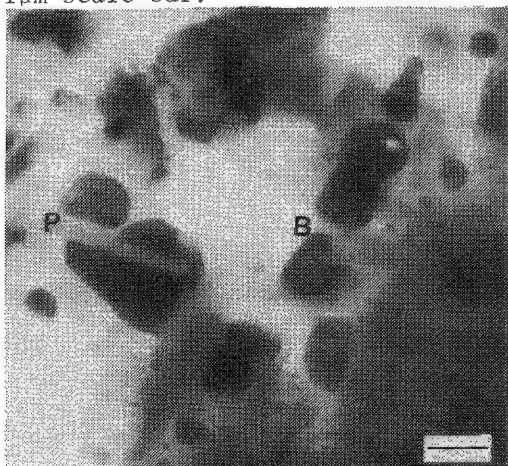


FIG. 3.--Entablature glass containing poorly crystallized blebs (B) and plagioclase microcrystals (P): scanning transmitted electron image. 1 $\mu$ m-scale bar.

with similar compositional ranges. The pyroxenes in both samples include augite and pigeonite. Augite in the colonnade samples may be rimmed by iron-rich pigeonite, whereas pigeonite is abundant in some entablature samples and rare in others. Titaniferous magnetite crystals in colonnade samples are blocky and subhedral, with characteristic dimensions of 50 to 100  $\mu$ m. In the entablature, metallic oxide with a similar composition occurs as trefoil-shaped grains a few microns across. These grains rim the larger plagioclase crystals in some samples, and in others they form delicate filagreed dendritic patterns in the mesostasis glass (Figure 1).

Optical microscopy and limited point counting indicate that mesostasis comprises 15 to 65 vol.%<sup>3</sup> of the samples studied and is systematically more abundant in the entablature than in the colonnade. The mesostasis represents the residual liquid left over after the crystallization of the major phases described above. Approximately half the mesostasis in a typical entablature sample consists of micron-scale plagioclase and pyroxene crystals; most of the remainder is glass. Mesostasis in the colonnade samples also contains rod-shaped fluorapatite crystals 20-40  $\mu$ m in length and 3-6  $\mu$ m in diameter. These crystals are hollow, with hexagonal cross sections (Figure 2). Apatite crystals are extremely rare or totally absent in the entablature.

Entablature mesostasis typically contains abundant rounded blebs, ranging in diameter from 1 to < 0.01  $\mu$ m (Figure 3). Microprobe and EDS analyses show that these blebs have a considerable range in chemical composition, but are generally rich in Si, Ca, Mg, and Fe, with minor K, Ti, and P. The STEM electron diffraction patterns indicate that the blebs are poorly crystalline, but that some of the larger ones contain ilmenite, maghemite, and apatite. Such blebs are relatively rare in samples of colonnade glass.

An optically amorphous glass phase constitutes approximately half the mesostasis volume in a typical sample. The average chemical composition of this glass (Table 1) differs significantly between analyzed samples of colonnade and entablature. Both glass compositions are silica rich, and the colonnade composition resembles that of a typical rhyolite.<sup>4</sup> The averaged compositions presented in Table 1 mask significant chemical heterogeneities on the scale of a few microns, particularly in entablature samples. Discrete amorphous phases that approach pure silica, potassium-feldspar, and hedenbergite in bulk chemical composition have been observed. Colonnade glass tends to be amorphous on the scale of electron diffraction interactions, but some entablature samples display diffraction rings that suggest microcrystalline ordering.

#### Discussion

Colonnade and entablature glass exhibit mineralogical differences related to their distinct cooling

TABLE 1.--Averaged electron microprobe analyses of mesostasis glass from Umtanum flow, Grande Ronde basalt.

	Colonnade (wt.%)	$\sigma$	Entablature (wt.%)	$\sigma$
SiO <sub>2</sub>	71.2	1.2	62.6	2.0
TiO <sub>2</sub>	0.8	0.1	1.6	0.5
Al <sub>2</sub> O <sub>3</sub>	12.4	0.9	13.7	0.7
FeO*	2.3	0.5	7.8	1.6
MgO	--	--	0.5	0.4
CaO	0.6	0.3	3.7	0.7
Na <sub>2</sub> O	3.0	0.6	4.6	0.4
K <sub>2</sub> O	5.5	0.6	2.6	0.3
P <sub>2</sub> O <sub>5</sub>	0.2	0.1	0.7	0.2
Total	96.0		97.8	
No. of points	57		60	

$\sigma$  = one standard deviation.

\*All Fe reported as FeO.

histories. Crystallization at relatively low cooling rates proceeded farther in the colonnade than in the entablature, as evidenced by the presence of iron-enriched rims on augite, fluorapatite crystals, large titaniferous magnetite grains, and a smaller percentage of mesostasis. This difference is also reflected in the more "evolved" chemical composition of the colonnade glass. The micron-scale blebs common in entablature glass represent poorly organized concentrations of material that solidified in a state intermediate between glassy and crystalline.

Two major considerations relevant to NWRB studies are highlighted by these results. First, recognition of the distinction between entablature and colonnade is necessary to proper prediction on the waste package-rock interactions. Second, mesostasis glass, particularly in entablature samples, is strikingly heterogeneous in terms of both chemical composition and mineralogy. An average chemical composition for this glass may not appropriately represent the glass phase most susceptible to alteration. The major elements are partitioned among multiple glass compositions plus other phases with varying degrees of crystallinity; each phase has unique kinetics of hydration and alteration. Studies of the effects of such factors on repository waste package design are currently under way within the BWIP.

The mineralogy, identified in this paper as a result of microcharacterization work, has provided a primary basis for understanding of the mineralogical characteristics of the repository environment. Interaction of water with the host rock is responsible for control of repository conditions such as Eh and pH. Reaction of the waste released from the waste form with the rock-water system provides a mechanism to control release from the engineered system in an NWRB.<sup>5</sup> The results of microcharacterization work allow the products from hydrothermal testing to be identified and that in turn facilitates a detailed understanding of the geochemical transformations taking place in the near- and far-field environments in an NWRB.

#### References

1. A. F. Noonan, C. K. Fredrickson, and J. Nelen, "Phase chemistry of the Umtanum basalt, a reference repository host in the Columbia Plateau," in J. G. Moore, Ed., *Scientific Basis for Nuclear Waste Management*, New York: Plenum, 1980, 3; 51-58.
2. A. Spry, "The origin of columnar jointing, particularly in basalt flows," *Geological Soc. Australia J.* 8: 191-216, 1962.
3. P. E. Long and N. J. Davidson, "Lithology of Grande Ronde basalt with emphasis on the Umtanum and McCoy Canyon flows," in C. W. Myers and S. M. Price, Eds., *Subsurface Geology of the Cold Creek Syncline*, RHO-BWI-ST-14, Richland, Wash.; Rockwell Hanford Operations, 1981, 5-1 to 5-55.
4. S. R. Nockolds, "Average chemical compositions of some igneous rocks," *Geol. Soc. Am. Bull.* 65: 1007-1032, 1954.
5. M. J. Apted and J. Myers, *Comparison of the Hydrothermal Stability of Simulated Spent Fuel and Borosilicate Glass in a Basaltic Environment*, Richland, Wash.; RHO-BW-ST-38 P, Rockwell Hanford Operations, 1982.

MINOR AND TRACE ELEMENTS IN HORNBLENDE, AUGITE, AND PYROPE MICROPROBE STANDARDS FROM KAKANUI, NEW ZEALAND, BY ION MICROPROBE MASS SPECTROMETRY

J. R. Hinthorne

Ion microprobe measurements of major elements and 17 minor elements present below the 1% level have been reduced by the use of working curves and the local thermal equilibrium (LTE) model.<sup>1</sup> Table 1 gives the results compared to the values recommended by Mason and Allen.<sup>2</sup>

*Data Acquisition*

The ion microprobe data were acquired on an Applied Research Ion Microprobe Mass Analyzer. A mass-analyzed primary beam of  $^{16}\text{O}^+$  at 17 keV and 5 na current into a 15 $\mu\text{m}$  spot

TABLE 1.--Ion microprobe analyses (IMMA) of megacrysts from Kakanui, New Zealand, compared to reference values.<sup>2</sup> [Values in atom percent (%) or ppma.]

	HORNBLENDE		AUGITE			PYROPE	
	IMMA	MASON <sup>2</sup>	IMMA	IMMA	MASON <sup>2</sup>	IMMA	MASON <sup>2</sup>
Li	2.0	-	2.8	2.7	-	.28	-
B	5.0	-	3.6	2.3	-	1.7	-
F	3800	-	140	120	-	38	-
P	16	-	22	21	-	19	-
Na	2.2%	1.9%	.82%	.82%	.89%	260	490
Mg	7.3%	7.0%	8.1%	8.1%	9.0%	9.3%	9.9%
Al	8.4%	6.5%	4.6%	4.4%	3.4%	11.1%	9.9%
Si	11.7%	14.9%	17.5%	17.2%	18.4%	14.3%	14.9%
K	1.2%	1.0%	30	26	50	14	45-69
Ca	4.8%	4.1%	6.9%	7.4%	6.1%	2.1%	2.0%
Ti	1.2%	1.2%	.22%	.24%	.20%	970	1390
Fe	3.2%	3.4%	1.7%	1.7%	2.0%	2.9%	3.2%
V	135	183	88	106	107	84	97
Cr	40	2.1	360	390	330	230	220
Mn	310	290	360	370	390	830	830
Co	110	34	21	26	15-21	20	16-25
Rb	4.5	3.7	-	-	.05	-	.05
Sr	120	107	17	20	15	3.4	3.5
Y	3.5	2.2	2.8	3.3	2.4	14	13
Zr	9.8	12	3.5	4.6	7.2	6.5	14
Nb	1.8	2.8	.13	.14	.09	.08	.09
Ba	49	27-43	.06	.28	.15-.20	.09	.07-.16

The author is in the Department of Geology, Central Washington University, Ellensburg, Wa 98926. Support of NASA and CWU Faculty Research Fund is acknowledged.

was used. The sample consisted of a polished grain mount, containing all three mineral types, prepared and carbon coated at the Smithsonian Institution for normal electron microprobe work. Positive secondary ions were detected in the ion counting mode for all peaks measured. A cold plate at liquid-nitrogen temperature was positioned about 1 cm above the sample's surface in a vacuum chamber at  $10^{-6}$  Torr.

Duplicate counts for 4 s each were made on the required mass peaks.  $^{30}\text{Si}^+$  was measured before and after each run; the maximum observed drift was -4% (on hornblende). After the individual peaks were counted, the analyzing magnet was set to four fixed positions and a group of mass peaks was integrated in a fast multichannel scaler mode (MCS).<sup>3</sup> By "peak stripping" these MCS data inferences on  $^{54}\text{Fe}^+$ ,  $^{85}\text{Rb}^+$ , and  $^{88}\text{Sr}^+$  could be eliminated, an internally consistent set of data on the light rare earth elements (REE) accumulated, and a prolonged integration for Th and U made.

### Data Reduction

The acquired peak intensities, adjusted from the MCS data, were corrected for deadtime (29 ns), isotopic abundance, and relative sensitivity to arrive at the values given in Table 1. For fluorine, the working curve of Hinthorne and Andersen<sup>4</sup> was used. (The working curve is based on numerous analyzed silicates, including 30 amphiboles.) The 38 ppma F content of the pyrope was checked in several locations and appears to be valid. This value implies that some water or (OH) will also be present. A detection limit of 1-2 ppm F, under the analytical conditions used, was established by analysis of lunar proxenes and olivines; only background count rates were observed at the  $^{19}\text{F}^+$  peak position.

For the cations, the relative sensitivity factor was calculated from the Saha-Eggert ionization equation,<sup>1</sup> where the relative sensitivity is computed as the ratio of singly charged to neutral atoms for each element under an assumed set of "plasma" conditions designated "temperature (T)" and "free electron density ( $N_e$ ).". On the basis of experience in analyzing more than a hundred silicated standards, a set of parameters, T and  $N_e$ , was chosen and used for all three Kakanui minerals. Because only *relative* sensitivity factors are calculated, it is necessary to introduce one additional item of information to convert relative atom abundances to concentrations; in these cases an assumed sum of the cations was used. For instance, in augite the cations total 40% of the atoms and the oxygen 60%, if all the sites are filled. Results based on allowing the LTE model to find a "best fit" solution for the major elements will be compared with Table 1.

### Discussion of Results

Few, if any, prior values have been published for Li, B, F, and P in these Kakanui minerals. The values presented are believed to be accurate enough for use in petrologic and geochemical modeling; in fact, they are as accurate as the remainder of the elements presented in Table 1. At these concentrations and beam currents counting statistics have to be considered; the *worst* case counting statistics were 1 sigma = 5% for the 1.7 ppma B in the pyrope.

The major and most minor elements correspond relatively well to "established" values. No specific reason could be found for the low Si found in the hornblende. Most of the low-level elements agree broadly with the summary by Mason and Allen;<sup>2</sup> however, there are some notable exceptions. K in the hornblende, and Na and K in the augite are close to accepted values, but K and Na in the pyrope are much lower than reported by other techniques. The probable reason for this difference is that all other techniques which can measure alkalis at these levels are *bulk* analysis methods in which there is great potential for accepting minute inclusions or alteration products or fracture fillings, which could be rich in Na or K, into the analyzed volume. The reported<sup>2</sup> value of 50 ppma K in the augite is greater than the ion microprobe value of 26-30 ppma probably for the same reason.

Experience has shown that Zr and Nb are underestimated by about a factor of 2 with the LTE model. This is approximately true for Zr in the Kakanui minerals, but the apparently good match of Nb is a puzzle. The problem for these elements is due to the large amount (50% or more) of the cations which remain bound to oxygen during the sputtering process. The same problem exists with the analysis of some other elements (e.g., Mo, REE's Hf, Ta, W, Th, and U) in an oxygen-rich sputtering environment.

The rare earth results for the hornblende are presented here as *relative* abundances

normalized to the chondritic meteorites: La 0.97; Ce 1.00; Pr 1.39; Nd 1.46; Sm 1.56 and Eu 1.20. Note that these light REE's show less than a 50% variation from the primitive chondritic pattern.

#### *References*

1. C. A. Andersen and J. R. Hinthorne, "A thermodynamic approach to the quantitative interpretation of sputtered ion mass spectra," *Anal. Chem.* 45: 1421-1438, 1973.
2. B. Mason and R. O. Allen, "Major and minor element abundances in augite, hornblende and pyrope megacrysts from Kakanui, New Zealand," *New Zealand J. Geol. Geophys.* 16: 935-947, 1973.
3. J. R. Hinthorne and R. L. Conrad, "The application of peak stripping to problems in ion probe microanalysis," *Proc. 10th Annual Conf. Microbeam Analysis Society*, Las Vegas, 1975, 74A-74D.
4. J. R. Hinthorne and C. A. Andersen, "Microanalysis for fluorine and water in silicates with the ion microprobe mass analyzer," *Am. Min.* 60: 143-147, 1975.

## COMPOSITION OF AUGITE AND PIGEONITE IN BASALT FLOWS THAT ARE CANDIDATES FOR A NUCLEAR WASTE REPOSITORY

P. E. Long and M. B. Strophe

Basalt flows underlying the Pasco Basin in southeastern Washington are being considered for construction of a mined geologic repository for high-level nuclear waste, as part of the U.S. Department of Energy's (DOE's) Basalt Waste Isolation Project (BWIP). These basalt flows were emplaced as widespread sheets of lava up to ~50 m thick, which subsequently crystallized, developing contraction fractures as they cooled. Many of the flows are characterized by distinct patterns of fractures in which well-defined polygonal columns (colonnade) make up the lower third of the flow. The colonnade is overlain by irregularly fractured basalt (entablature) in the central part of the flow, which is in turn overlain by a vesicular to brecciated flow top.<sup>1</sup> The fractures in these flows are virtually all filled with secondary clays, zeolites, and silica. Nevertheless, limited groundwater movement may still occur along the fractures, and hence it is important to understand the fracture patterns in order to evaluate the isolation capability of a nuclear waste repository in basalt (NWRB). Moreover, the cooling fractures are the principal planes of structural weakness in the rock and play an important role in determining the stability of mined openings at depth in an NWRB.

Petrographic textures of entablature and colonnade have been interpreted as indicating that the entablature cooled more rapidly than the colonnade. The higher rate of cooling in the entablature apparently accounts for its irregular fracture pattern<sup>1</sup> and has been attributed to quenching of the flow interior due to water influx from flooding of the partially molten flow.<sup>2</sup> The flooding was probably caused by disruption of drainage by the emplacement of the flow itself.

In this paper, we report data on compositional variation of augite and pigeonite in entablature and colonnade from two flows, the Cohasset and Umtanum, which are candidates for an NWRB. The data are consistent with the suggested difference in cooling rates between the entablature and colonnade. This work is part of an overall BWIP effort to both characterize the mineralogy of the basalts in order to understand geochemical reactions in an NWRB and to determine the extent and nature of fractures in the vicinity of an NWRB.

### *Methods*

The analyses were performed with an automated Cameca electron microprobe with three wavelength-dispersive spectrometers. The accelerating voltage was 15 kV with a 30 nA absorbed current and a 1  $\mu$  beam diameter. The samples were collected from surface exposures of the Cohasset and Umtanum flows at locations where entablature and colonnade could be readily identified. The samples were prepared as polished thin sections that were coated with 300 Å of carbon. A suite of appropriate mineral standards was used and the data reduced by a ZAF program.

### *Results*

Representative analyses of augite and pigeonite from two flows are given in Table 1, and comparison of analyses from two samples, one each from entablature and colonnade, is illustrated in Fig. 1. The augite analyses typically range from  $Wo_{40} En_{40} Fs_{20}$  to  $Wo_{30} En_{30} Fs_{40}$ , whereas the pigeonite analyses range from  $Wo_{10} En_{60} Fs_{30}$  to  $Wo_{10} En_{30} Fs_{60}$ . As illustrated in Fig. 1, the pigeonite grains in some entablature samples are tightly clustered with little iron enrichment. In other samples, especially from the colonnade,

---

The authors are with the Basalt Waste Isolation Project, Rockwell Hanford Operations, Richland, WA 99352. Supported by DOE under Contract DE-AC06-77RL01030.

TABLE 1.--Representative electron microprobe analyses of pyroxenes (wt.%) from the Cohasset and Umtanum flows.

Oxide	C9018 PX1-12 (entablature -augite)	C9018 PX1-36 (entablature -pigeonite)	C9017 PX1-5 (colonnade -augite)	C9017 PX1-45 (colonnade -pigeonite)
Cohasset flow				
Na <sub>2</sub> O	0.3	0.1	0.1	0.1
MgO	16.6	18.4	17.1	10.8
Al <sub>2</sub> O <sub>3</sub>	1.9	0.9	1.3	0.6
SiO <sub>2</sub>	52.0	52.2	53.1	49.8
CaO	18.0	5.4	16.8	4.3
TiO <sub>2</sub>	0.7	0.5	0.5	0.5
FeO	9.6	21.1	10.4	32.8
MnO	0.3	0.6	0.3	0.8
Total	99.3	99.3	99.9	99.9
Wo <sup>a</sup>	37	11	35	10
En <sup>b</sup>	47	54	49	33
Fs <sup>c</sup>	16	35	16	57
Umtanum flow				
Oxide	C8096 PX2-92 (entablature -augite)	C8096 PX2-25 (entablature -pigeonite)	C2251 PX1-55 (colonnade -augite)	C2251 PX1-23 (colonnade -pigeonite)
Na <sub>2</sub> O	0.2	0.1	0.3	0.1
MgO	14.0	19.7	12.9	19.5
Al <sub>2</sub> O <sub>3</sub>	1.7	0.8	1.6	0.8
SiO <sub>2</sub>	50.9	52.2	50.7	52.4
CaO	17.9	4.9	16.3	4.9
TiO <sub>2</sub>	0.9	0.5	0.98	0.5
FeO	13.3	21.1	14.8	21.8
MnO	0.4	0.5	0.3	0.5
Total	99.3	99.8	99.8	100.4
Wo <sup>a</sup>	38	10	37	10
En <sup>b</sup>	41	56	36	56
Fs <sup>c</sup>	21	34	26	34

<sup>a</sup>Wo = percentage wollastonite endmember.

<sup>b</sup>En = percentage enstatite endmember.

<sup>c</sup>Fs = percentage ferrosilite endmember.



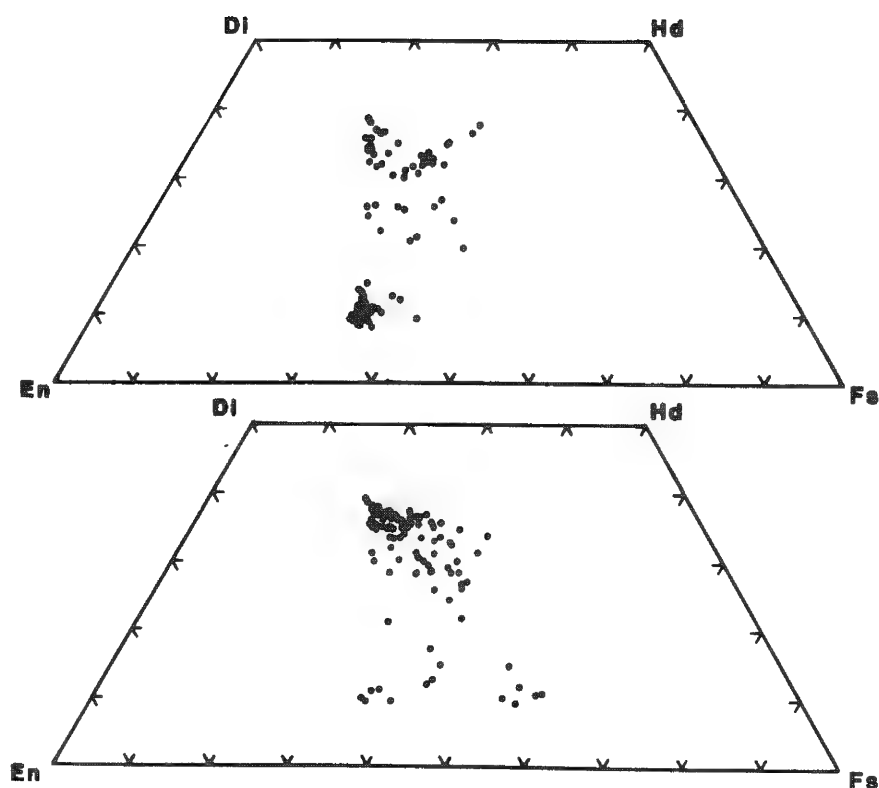


FIG. 1.--Comparison of pyroxene quadrilateral plots for (a) Umtanum entablature (Sample C8096) and (b) colonnade (Sample C2251). Pigeonite analyses plot in lower cluster in (a) and augite in the upper cluster. Di, diopside; Hd, hedenbergite; En, enstatite; Fs, ferrosilite.

as individual grains. Details of the textural and compositional relationships between pigeonite and augite suggest that the occurrence of pigeonite is controlled in at least two ways: (1) by composition of the residual liquid in late stages of crystallization, and (2) by preservation of early formed microphenocrysts of pigeonite due to relatively rapid cooling.

### Discussion

A previous study<sup>3</sup> has shown that primary microphenocrysts of pigeonite were present on eruption of the flows and that pigeonite is stable at high temperatures at one atmosphere, but may react to form augite as the basalt crystallizes. In the case of the Umtanum entablature, early-formed pigeonite was apparently preserved; that is, was not resorbed or did not react to augite. In the case of the colonnade, most of the abundant early-formed pigeonite apparently reacted out. More complete crystallization of colonnade relative to the entablature resulted in significant occurrence of late-formed iron-rich pigeonite.

Abundant pigeonite is not present in the entablature of the Cohasset flow but is present in the Cohasset colonnade in amounts and compositions similar to those in the Umtanum colonnade. Thus, in the Cohasset entablature, cooling conditions were such that microphenocrysts of pigeonite could react out but crystallization did not proceed far enough to develop iron-enriched pigeonite rims on augite.

The most reasonable explanation of the occurrence of abundant pigeonite in the Umtanum entablature is a high cooling rate, which prevented resorption or reaction of early-formed pigeonite and that may have suppressed nucleation of augite. In the Cohasset entablature, the cooling rate was somewhat lower, such that early-formed pigeonite was resorbed or reacted to augite; the cooling rate was high enough, however, to prevent formation of late-stage pigeonite. The apparent instability of intratelluric pigeonite microphenocrysts in

the pigeonites show strong iron enrichment. The relative proportion of augite and pigeonite are reversed in these particular samples of entablature and colonnade from the Umtanum flow (Fig. 1). In contrast, entablature samples from the Cohasset flow exhibit only minor pigeonite, whereas the colonnade samples have pigeonite abundances similar to Umtanum colonnade. These differences occur in spite of the virtually identical chemical composition of entablature and colonnade in a given flow. Compositions intermediate between the main groupings of augite and pigeonite also occur; presumably they represent either submicroscopically unmixed pigeonite or analyses where the beam intersected a boundary between augite and pigeonite.

Typical textural relationships among pigeonite and augite grains are illustrated in Fig. 2. Pigeonite occurs as rims on augite, as grains that are optically continuous with augite, and

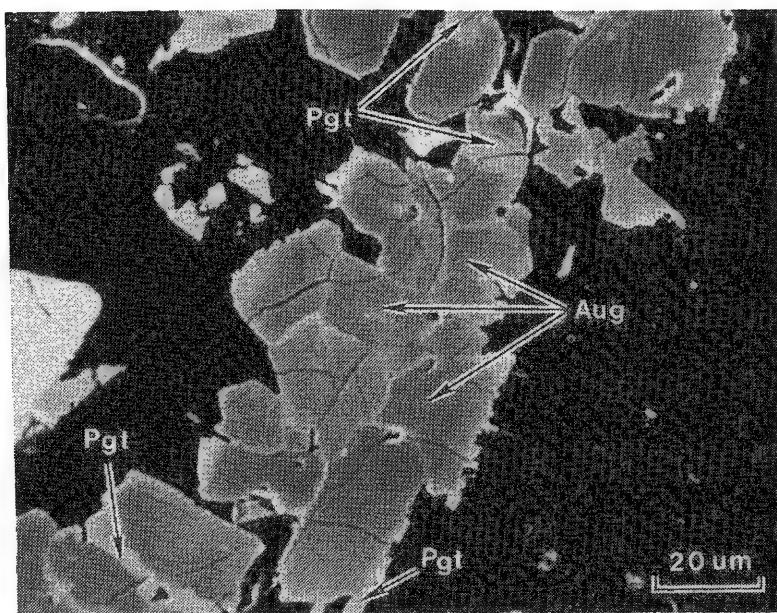


FIG. 2.--Secondary electron image of pyroxene in Umtanum entablature (Sample C8094) showing characteristic occurrence of pigeonite (Pgt) and augite (Aug).

out during crystallization of the flow and the extent to which late-stage pigeonite rims are developed. The preservation of pigeonite in the entablature of flows such as the Umtanum tends to corroborate the proposed origin of entablatures and their attendant fracture patterns by relatively rapid cooling of the interior of these flows.

#### References

1. P. E. Long and N. J. Davidson, "Lithology of Grande Ronde basalt with emphasis on the Umtanum and McCoy Canyon flows," in C. W. Myers and S. M. Price, Eds., *Subsurface Geology of the Cold Creek Syncline*, RHO-BWI-ST-14, Richland, Wash.: Rockwell Hanford Operations, 1981, 5-1 to 5-55.
2. B. J. Wood and P. E. Long, "Structures, textures and cooling histories of Columbia River basalts," *Geol. Soc. Am. Abstracts with Programs* 13: 584, 1981.
3. P. Schiffman and G. E. Lofgren, "Dynamic crystallization studies on Grande Ronde pillow basalts, central Washington," *J. Geology* 90: 49-78, 1982.

the Cohasset entablature may also partly reflect the slightly higher calcium content of the Cohasset relative to the Umtanum. Colonnade samples from both the Cohasset and Umtanum flows apparently cooled the slowest such that much of the early pigeonite reacted out and late-stage pigeonite was well developed. These general relationships of cooling rates approximately match those based solely on textural interpretations.<sup>1-2</sup>

#### Summary

The abundance and composition of pigeonite are variable within single flows of basalt in spite of uniform bulk composition. These variations are spatially related to the occurrence of entablature and colonnade, which in turn apparently reflect the cooling history of the flow. Differences from one flow to another in the occurrence of pigeonite may be explained by the extent to which early-formed microphenocrysts of pigeonite react

## A MICROPROBE STUDY OF SILVER ORE IN NORTHERN IDAHO

C. R. Knowles

An electron microprobe study was made on thirty-five ore samples from seven mines in the Coeur d'Alene mining district in the panhandle of northern Idaho, in the Bitterroot Mountains near the Montana border. The district is about 5 miles wide and 25 miles long. The region produces about half the silver in the USA and is also a producer of lead, zinc, antimony, and copper.<sup>1</sup> Only a few mines are still in production between Wallace and Kellogg, Idaho. These active mines (Lucky Friday, Galena, Coeur, and Sunshine) produce mostly silver, with lead, zinc, cadmium, antimony, copper, and gold as byproducts and co-products. These mines are among the deepest in the world, with shafts of over 2400 m (8000 ft). Because of high operating costs and poor market prices, two mines (Bunker Hill and Star-Morning) have closed recently.

Ore samples were collected from seven of these deep mines (Sunshine, Bunker Hill, Star-Morning, Lucky Friday, Galena, Page, and Atlas). Samples were collected from diverse regions within the mines, both vertically and laterally. The sample numbers in Table 1 show the depth (e.g., SM7700-106 is from the 7700ft level). The Page mine and the Atlas mine have been closed for years, and a single sample for each was obtained from a mine sample collection.

Geologists have believed that silver is present in solid solution with galena, PbS, in a relationship of 1% Pb correlated to 1 oz/ton (34 ppm) of Ag. If 1 oz/ton of Ag is in solid solution, a silver value of 0.3% mixed with galena would be expected. To test this hypothesis, samples of inclusion-free "pure" galena were examined with an ARL and a CAMECA electron microprobe to measure the quantity of Ag in the galena matrix. Both microprobes have a detection limit of less than 0.1% Ag. No Ag from any of the thirty-five samples could be detected in solid solution with galena.

However, silver was present in nearly all ore samples as discrete mineral grains. The most common mineral is argentiferous tetrahedrite,  $(\text{Cu,Ag})_{12}\text{Sb}_4\text{S}_{13}$ , with some small inclusions of polybasite,  $\text{Ag}_{16}\text{Sb}_2\text{S}_{11}$ , present. X-ray scan photographs show that in these silver-rich regions the tetrahedrite commonly forms a rim around sphalerite, ZnS grains. The silver minerals are generally very small and, in some samples, less than 1  $\mu\text{m}$  in size; thus, only the larger inclusions could be quantitatively analyzed.

### *Experimental Procedure*

The ore samples were cut into one-inch blocks, mounted in room temperature polymerizing epoxy resin, polished to less than 1  $\mu\text{m}$  relief with diamond paste, and coated with approximately 100 Å of carbon. In one sample, four single crystals were extracted from a vug, placed on a glass slide with epoxy, and polished flat and smooth.

An ARL-EMX-SM electron microprobe was used operating at 15 kV and 0.1  $\mu\text{A}$  reference current (approximately 1 nA sample current). Pure metals (> 99.9% purity) and reference minerals were used as standards. Background, dead time, and ZAF corrections were made. Table 1 shows the analysis for Ag and the assay values of the bulk ore. Table 2 shows total analyses of four tetrahedrite,  $(\text{Cu,Ag})_{12}\text{Sb}_4\text{S}_{13}$ , crystals that were found in a vug in Sunshine mine ore.

To analyze the silver content it was necessary to find a silver-rich area on the polished section. We did that by tuning a crystal spectrometer to the silver X-ray line, traversing around the sample until the ratemeter indicated high intensity, and then analyzing that area.

To see whether Ag was present in the galena matrix, very careful off-peak background measurements over a long period (100 s) were used to compare with the peak position. This

---

The author is at the Idaho Bureau of Mines and Geology, Moscow, ID 83843.

TABLE 1.--Microprobe analysis and assays of ore samples.

Sample Number	Microprobe Silver %	Assay Silver oz	Assay Lead %	Ratio Ag:Pb
LF2600-094	4.4	42.0	57	0.74
LF2600-102	11.0	60.0	40	1.50
LF2600-104	23.1	60.0	40	1.50
LF4450-090	17.9	55.0	48	1.14
LF4450-101E	22.4	55.0	43	1.30
LF4450-103FINE	12.2	53.0	56	0.95
LF4450-103COARSE	12.5	47.0	42	1.12
LF4450-105	19.0	40.6	34.5	1.18
LF4450-109	-0-	59.0	35.5	1.66
SM1450	-0-	2.55	5.10	0.50
SM4300-127	25.6	3.78	3.56	1.06
SM4500-127MB	24.0	4.21	4.58	0.92
SM5300-154GALENA	14.2			
SM5300-154TETRAHEDRITE	9.5	19.84	0.41	48.4
SM6500-113	21.5	3.19	4.72	0.67
SM7500-109W	24.0	2.70	5.96	0.45
SM7700-10MWW	-0-	1.95	6.00	0.32
SM7700-106	69.2*	1.38	2.25	0.61
G4000-94	19.6			
G4000-104	15.3	15.2		
G4300-164E	71.0*			
G4300-164EB	34.7	9.5	13.6	0.70
G4600-164	-0-	11.0	14.9	0.74
G4900-MB	-0-			
S3700-72	8.3			
S5200-13	-0-			
B2300-16-132	18.7	46.0	56.0	0.82
B2300-21-23	8.2	22.0	58.0	0.38
B2500-16-23	14.8			

\* Polybasite. LF--Lucky Friday mine; SM--Star Morning mine; G--Galena mine; S--Sunshine mine; B--Bunker Hill mine.

TABLE 2.--Microprobe analysis of tetrahedrite--Sunshine Mine.

Crystal	Cu	Sb	Ag	As	Fe	Zn	S
#1	32.7%	26.7%	8.9%	2.2%	4.5%	2.3%	23.7%
#2	34.6	26.8	6.5	2.4	4.7	2.4	23.9
#3	31.7	26.9	9.5	1.6	5.1	1.6	23.8
#4	34.0	26.8	8.2	1.7	4.7	2.5	23.7
Average	33.2	26.8	8.3	2.0	4.7	2.2	23.8

Formula Analysed  $(\text{Cu}_{9.4}, \text{Fe}_{1.5}, \text{Zn}_{0.6}, \text{Ag}_{1.4})(\text{Sb}_{3.9}, \text{As}_{0.5})\text{S}_{13}$

Idealized Formula<sup>2</sup>  $\text{Cu}_{12+x}\text{Sb}_{4+y}\text{S}_{13}$  where  $0 < x < 1.92$  and  $-0.02 < y < 0.27$

procedure was also done by means of a CAMECA probe at the Washington State University geology department in addition to the ARL instrument. The sensitivity on both instruments at long counting times is better than 0.1% for silver.

Silver-rich regions were examined by means of scanning x-ray photographs and backscatter electron imaging (Fig. 1).

### *Results*

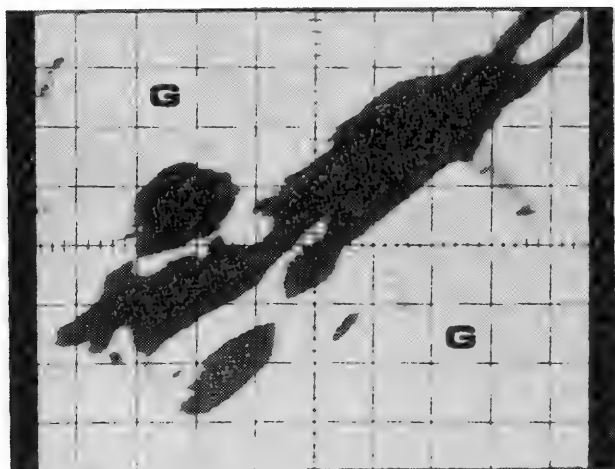
No silver could be detected in the galena matrix above a low detection limit of less than 0.1%. Hundreds of regions were examined on each sample. The silver was present interstitially as discrete minerals in the galena. The two minerals found were argentiferous tetrahedrite,  $(\text{Cu},\text{Ag})_{12}\text{Sb}_4\text{S}_{13}$ , and polybasite,  $\text{Ag}_{16}\text{Sb}_2\text{S}_{11}$ . In a few samples no silver could be found in the matrix or as discrete minerals. The particular section examined may have been devoid of silver minerals, or they may have been missed by the probe owing to the small size of some of these inclusions.

### *Conclusions*

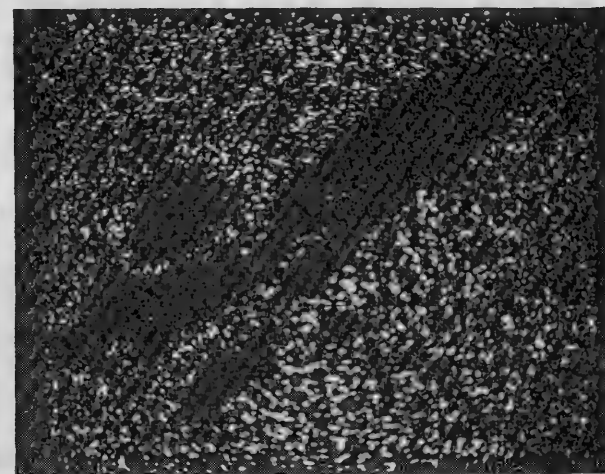
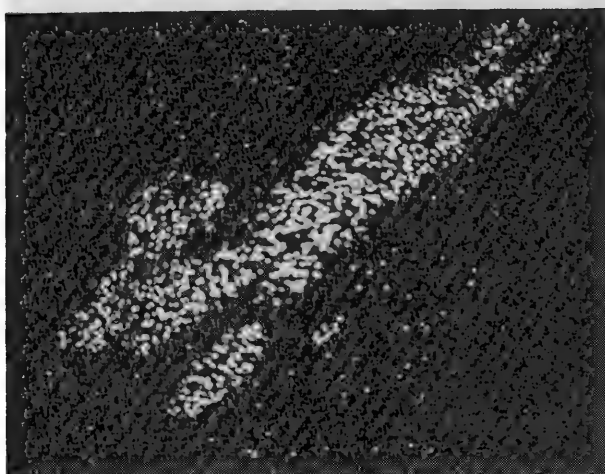
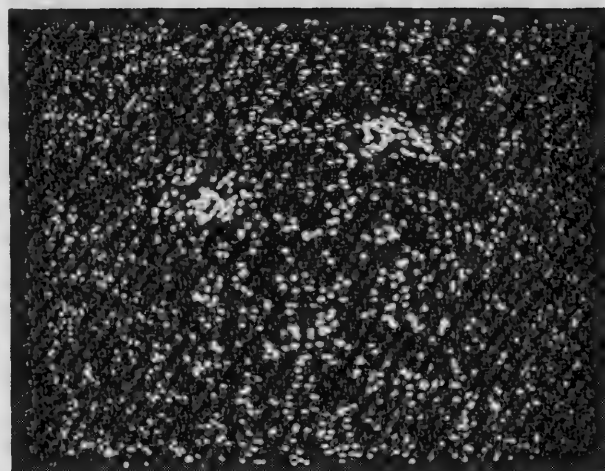
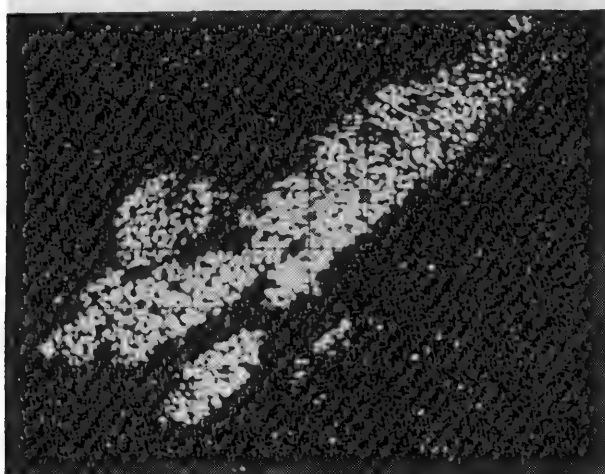
The assay results for silver and lead and their ratios are shown in Table 1. The ore vein assays have approximate ratios of 1:1 for Ag to Pb. We would expect to see at least 0.3% of Ag in the galena matrix. It could not be measured; however, most samples contained very fine inclusions of silver-rich minerals that would give spurious results if bulk analysis was used. Only microprobe methods could measure most of these inclusions.

### *References*

1. U. S. Bureau of Mines, *Minerals Yearbook 1980*, Vol. II, Washington, D. C.: U. S. Government Printing Office, 1982, 157-170.
2. B. J. Skinner et al., "Studies of the sulfosalts of copper: III. Phases and phase relations in the system Cu-Sb-S," *Economic Geology* 67: 924, 1972.



(a)



(b)

FIG. 1.--(a) Backscatter electron scan image of sample SM7700-106 and (b) corresponding x-ray scan images of elements Ag, Cu, Sb, and Pb; 1cm grid can be seen and corresponds to 10  $\mu$ m scan length. In BSE scan *G* is galena area and *Po* is polybasite (the dark region).

## STRUCTURE AND COMPOSITION OF COMPLEX PYRITE ORE FROM SOTIEL (HUELVA, SPAIN)

F. A. Calvo and J. M. Guilemany

Samples of the complex pyrite ore from Sotiel (Southwest Spain), which is claimed to belong to the largest complex pyrite reserves in the world, have been studied by optical microscopy (OM), scanning electron microscopy (SEM), and electron probe microanalyzer (EPMA). From the results<sup>1</sup> a magmatic origin is proposed and recommendations for the optimum benefit are made.

### Structure

A preliminary examination of polished surfaces of the ore by conventional optical microscopy showed three sulfides other than pyrite: *Sphalerite*, *galena*, and *chalcopyrite*, located in cavities (fissures and intercrystalline spaces). Pyrite mineralizes a host rock where the quartz crystals are cemented by carbonates, such as dolomite and siderite.

The pyrite crystals are clearly idiomorphic, whereas the other sulfides are allotriomorphically distributed between the pyrite crystals. *Bourmonite*, *boulangerite*, *pyrrhotite*, *stannite*, *tetrahedrite* and *zinckenite* have been identified, however in smaller proportions, in similar position. *Arsenopyrite*, which has been also found, exhibits a characteristic idiomorphic form.

Bulk chemical analysis<sup>2</sup> (3.82 wt.% Zn, 1.60 wt.% Pb, 0.61 wt.% Cu, 37 wt.% Fe, together with other metallic elements) shows that sphalerite is the main of the major mineral constituents, apart from pyrite. Galena occurs as anhedral grains of different sizes associated with *sphalerite*, *chalcopyrite*, and sulphosalts which are rich in Pb and Cu. Chalcopyrite is the least abundant of the four major sulfides identified in the Sotiel ore. It normally occurs as small crystals, precipitated in the sphalerite, but large ones are also found.

Ore samples were broken, after being cooled in liquid air, and covered with a gold film (200 Å) by sputtering. The fracture surfaces were observed by SEM both before and after etching. At low magnification (Fig. 1) aggregates of very different crystals of sulfides can already be seen in the as-broken condition; these minerals have a very small particle size, which enhance the difficulties of the metallurgical treatment of this ore.

At higher magnifications the following interesting details were observed;

1. The pyrite crystals are clearly idiomorphic, their sizes ranging from large ones, twinned or not (which, when broken, exhibit conchoidal fracture) to very small crystals of 4–5 µm).

2. The idiomorphic pyrite crystals are soaked on allotriomorphic sphalerite (Fig. 2) which replicates the surface details of the pyrite (Fig. 3).

3. There is practically no cohesion between the sphalerite and the pyrite crystals; both minerals can be easily separated (Figs. 3 and 4).

4. On the sphalerite surface (Figs. 3 and 4), small crystals of chalcopyrite can be seen; in some places those crystals were loosened during the fracture and the corresponding cavities were left behind. These crystals are polyhedral and have sizes ranging from 0.75 to 1 µm; this fact accounts for the difficulty of its "liberation" by ore grinding. Large aggregates of chalcopyrite crystals have been found at sphalerite grain boundaries and in the contact sphalerite-pyrite.

5. Galena appears on the fracture surface with its characteristic stepped cleavage (Fig. 6). In whatever way it happens to be in close contact with pyrite crystals, fracture details show that there is no cohesion between pyrite and galena.

6. The contact pyrite sphalerite was such that perfect replications of idiomorphic

---

Author Calvo is at the Departamento de Metalurgia, Facultad de Ciencias Químicas, Universidad Complutense, Madrid; author Guilemany, at the Universidad de Barcelona.



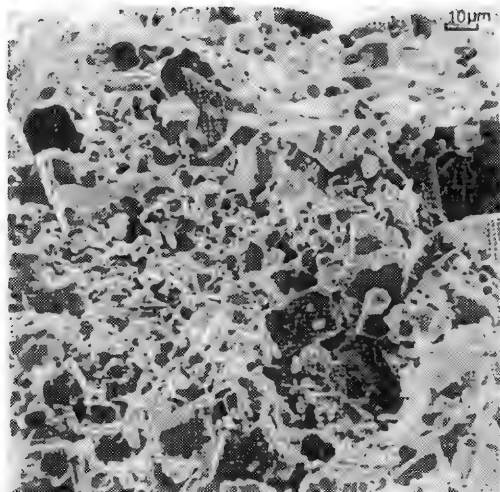


FIG. 1  
Fracture surface of Sotiel ore, showing varying sizes and morphologies of various constituents (phases).

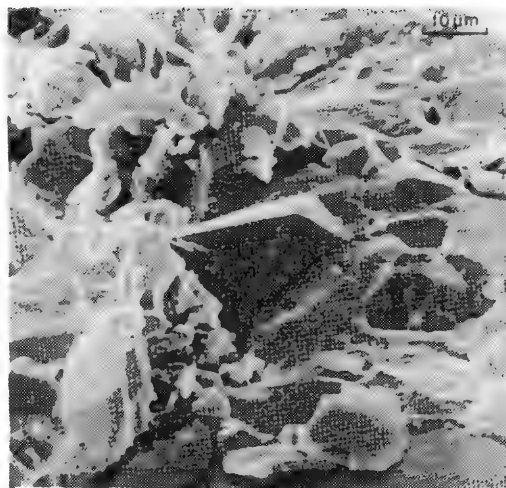


FIG. 2  
Idiomorphic pyrite crystals included in sphalerite.

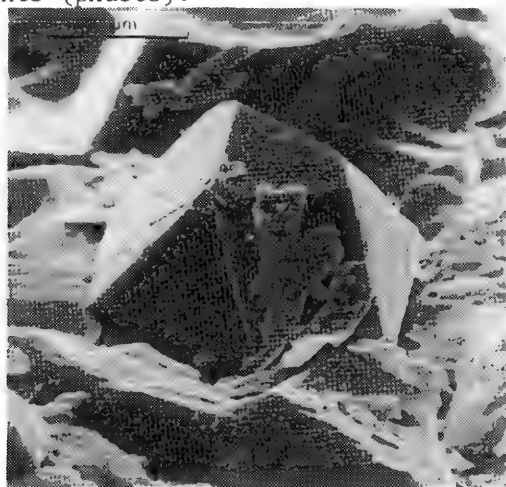


FIG. 3  
Sphalerite lying on pyrite crystals.

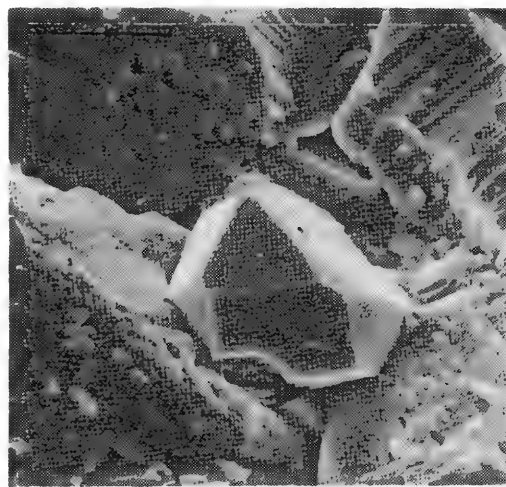


FIG. 4  
Lack of coherence between pyrite and sphalerite.

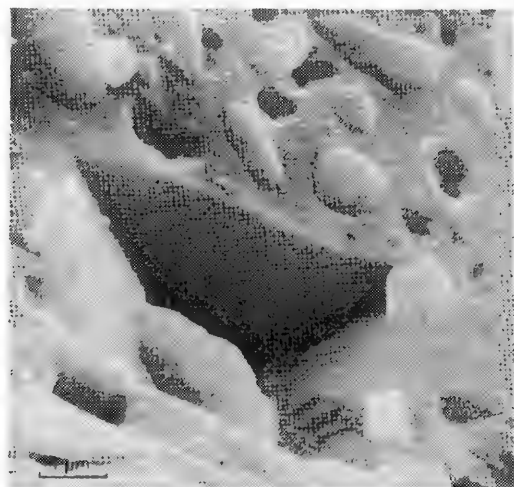


FIG. 5  
Small chalcopyrite crystals dispersed in sphalerite matrix; note rounded morphology and imprints in matrix.

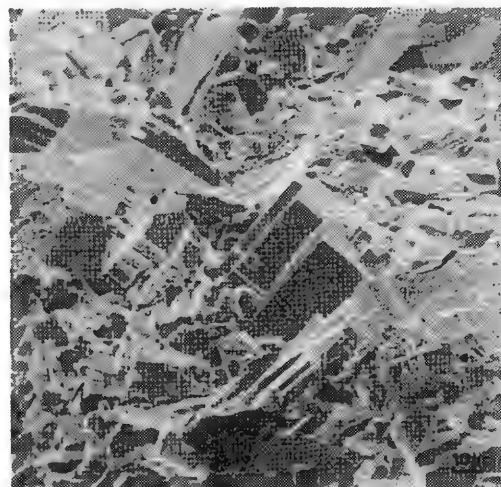


FIG. 6  
Galena crystals between pyrite crystals.

pyrite crystals can be seen on the allotriomorphic sphalerite (Fig. 7, imprints A, B, C, D, E, F, G, H, is a pyrite crystal). The small chalcopyrite crystals, already reported (Figs. 3-5), or their cavities, can be seen also reproduced in the sphalerite/pyrite boundary (Fig. 8). Galena crystals also left their "imprints" behind on the sphalerite surface fracture.

7. Monoclinic arsenopyrite crystals were also found (see a twinned form in Fig. 9). Peculiar morphologies for other allotriomorphic sulfides were also observed.

8. Fracture surfaces were etched for selected chemical dissolution of the constituents; in this way the pyritic "skeleton" of the complex ore was shown. In Fig. 10 pyrite crystals can be seen after surface fracture etching for 3 min using concentrated hydrochloric acid at 100°C. The sphalerite matrix being in a dissolution process, the small chalcopyrite crystals appeared, undissolved, on the surface of the remaining sphalerite. After a slightly longer attack (5 min, Fig. 11) the pyritic "skeleton" of the bulk complex ore can be seen, formed by pyrite crystals of different sizes. Some of them exhibit growth defects (cavities) which were filled up with sphalerite; others are "unfinished" because they were growing when the process ended.

The chemical composition of the major and minor constituents was established by qualitative and quantitative microanalysis EPMA, with conventional polished specimens covered with a fine carbon layer; Table 1 summarizes the nature of the minerals (mainly sulfides) that were properly identified in the Sotiel ore according to the composition. Some elements were detected in solid solution, as is recorded.

### Discussion

The structural facts that have been observed are:

- a. high compactness;
- b. lack of cohesion between the mineral constituents;
- c. imprints of the idiomorphic crystals on the allotriomorphic constituent;
- d. perfect replication even of the minute details of the "casted" crystal;
- e. complex and not quite stoichiometric chemical composition of the constituents; and
- f. solid solution of some elements in the identified minerals.

These facts lead us to propose a magmatic origin of this ore.

Supposing that, in the magma, a sulfidic molten phase--whose components were the *elements* detected in the ore--was segregated. On slow cooling, from the multicomponent and initially homogeneous system, the corresponding equilibrium phases would have precipitated, or solidified, according to their stability in the new conditions (lower temperature). The result would be the successive, or simultaneous, formation of the various phases (mineral compounds) that are found in the ore, whose composition, size, form, and distribution are the result of the thermodynamic conditions and kinetic requirements applied to that multicomponent system. Pyrite and arsenopyrite appear idiomorphic because they were nucleated and grew in a melt. Sphalerite, allotriomorphic, would have been the last molten phase to solidify.

Experiments are in progress to reproduce the magmatic state by mixing elements in the right proportions. The results are encouraging.

Because of the very fine grain size of some of the phases which contain metallic elements in solid solution, complete differential separation based on physical methods of concentration should be discarded. Instead, a global sulfide concentration by flotation, followed by a hydrometallurgical process, seems to be advisable.

### Conclusions

1. The microstructural facts discussed support the idea of a magmatic origin for the Sotiel ore. The actual constituents of the ore were formed on solidification of a molten magma.

2. Global flotation of the ore and hydrometallurgical treatment are suggested in view of the nature and size of the mineral constituents.

### References

1. F. A. Calvo and J. M. Guilemany, *Estructura y mineralogénesis del mineral complejo*

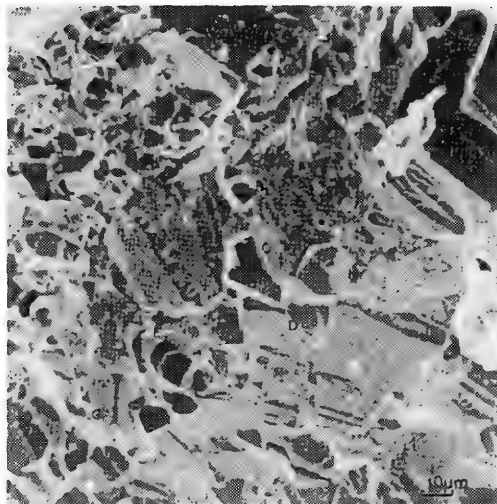


FIG. 7  
Imprints of pyrite crystals on sphalerite; a crystal (H) has been retained.

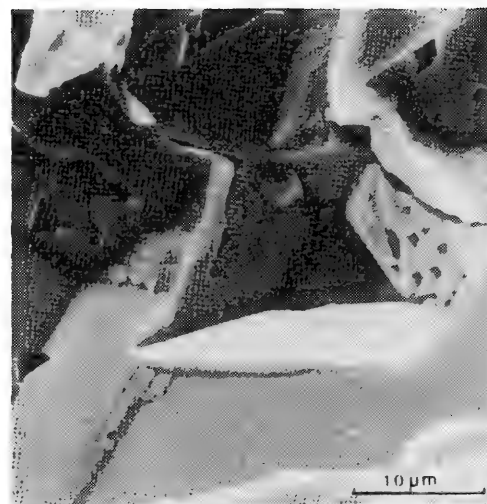


FIG. 8  
Large imprint on sphalerite of pyrite crystals; smaller imprints from chalcopyrite.

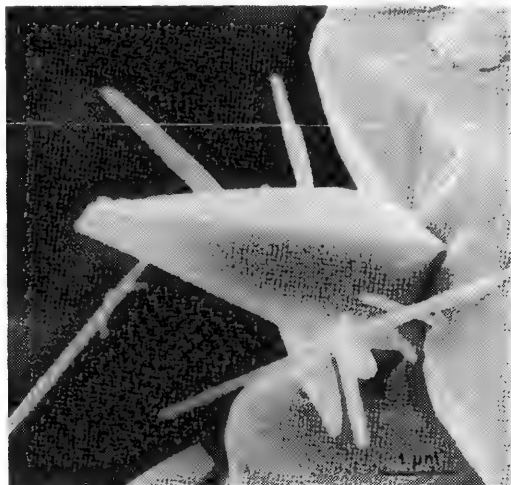


FIG. 9  
Twinned arsenopyrite crystal.

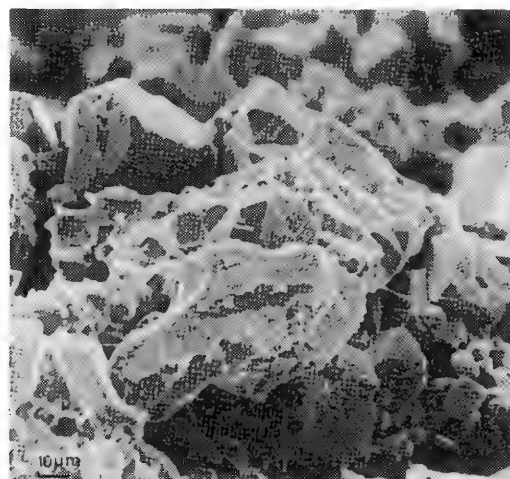


FIG. 10  
Sphalerite in process of being dissolved in concentrated hydrochloric acid (100°C, 3 min); pyrite and chalcopyrite crystals not affected.

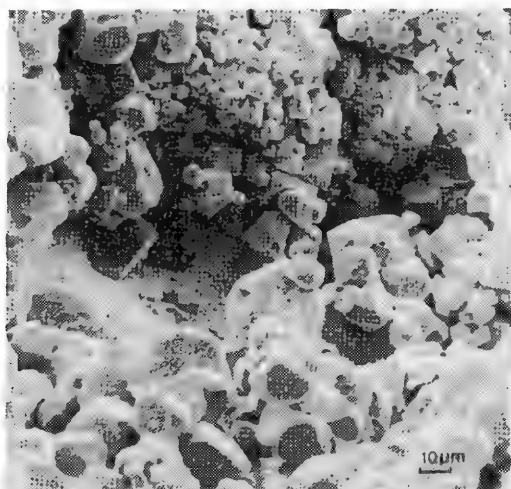


FIG. 11  
"Skeleton" of ore, observed after etching in concentrated hydrochloric acid (100°C, 5 min); note intracrystalline defects in idiomorphic pyrite crystals.

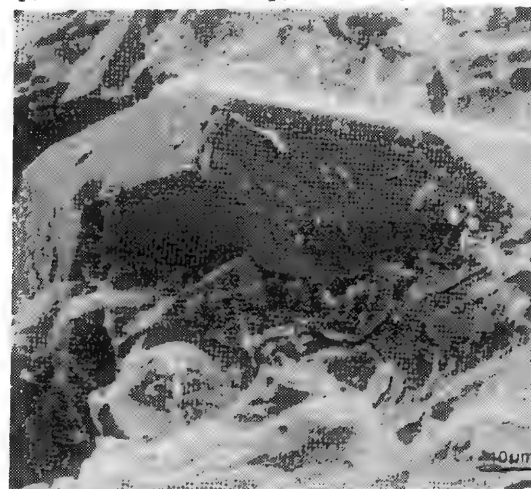


FIG. 12  
Idiomorphic pyrite crystal included in allotriomorphic sphalerite. Synthetic ore samples.

*sulfurado de Sotiel*, Madrid: Foundation of Instituto Nacional de Industria, 1974.

2. Minas de Almagrera, S. A., *Estudio de Viabilidad: Minería II*, Internal Report, 1977, 1-123.

TABLE 1.--Microanalysis EPMA: Chemical composition of various sulfides associated in Sotiel ore.

Element Minerals	Wt %	Fe	Zn	Pb	Cu	Sb	As	Sn	Mn	Co	Ag
Pyrite		44,7-45,5					0,6			0,08	
Sphalerite		9,5-11	55-56		0,5						
Galena		0,15-0,20	0,15-0,30	85,3-86	0,15-0,20		2,8		0,15-0,30 not always		
Chalcopyrite		32-34,5*			32-35,5						
Bournonite		0,09	0,5	40,6-41	15-15,5**	20-20,5	2,6				
Boulangerite				53,8	1,63	24,8	1,3		0,20 not always		
Arsenopyrite		34-36 31,1				2,25	45,2-46 45,5				
Pyrrhotine		58,8-59,2					0,1			0,1	
Stannite		12,6-14	2,8		29,5-30		2,1	22,5-23,1			
Tetrahedrite		***	***		36,8	28,3					***
Zinckenite		****	****	34,2	****	40,3	****				

\* Fe present in excess of stoichiometric composition

\*\* Cu present in excess of stoichiometric composition.

\*\*\* Fe % + Zn % + Ag % = 10 % in solid solution.

\*\*\*\* Between 0,4 and 1,65% in solid solution.

## 2 Quantitative Microbeam Analysis

### SIMULTANEOUS ELECTRON AND X-RAY SPECTROMETRY IN A SCANNING TRANSMISSION ELECTRON MICROSCOPE

L. E. Thomas

Energy-dispersive x-ray spectrometry (EDXS) and electron energy loss spectrometry (ELS) are both used in transmission and scanning transmission electron microscopes (TEM/STEMs) for elemental analyses of micro-areas. For microanalysis, the microscope is operated with a focused convergent electron probe--usually in the scanning transmission mode--first to image the specimen microstructure and then to set the probe on a selected specimen region of interest to excite characteristic electron energy losses and x rays. The STEM equipped with a field-emission electron source provides probes as small as 2 nm in diameter with ample current for ELS or EDXS of thin foil or particulate samples.<sup>1</sup> Moreover, by performing both EDXS and ELS in a field emission gun STEM one should be able to analyze thin foil regions as small as 5 nm in diameter for nearly all elements. To obtain 5 nm spatial resolution in analysis, however, the specimen must in general be less than 30-50 nm in thickness.

Although microanalysis of elements lighter than sodium is usually left to ELS, ultra-thin window (UTW) EDX detectors which are sensitive to elements as light as carbon have been adapted to TEM/STEMs.<sup>2</sup> The UTW detector uses a 0.15-0.3  $\mu\text{m}$  window of aluminum or aluminum-coated parylene ( $\text{C}_8\text{H}_8$ ) in place of the conventional 7  $\mu\text{m}$  thick beryllium window, and can detect about 10% of the carbon x rays or 40% of the oxygen x rays that hit the detector window.<sup>3</sup> Even with a UTW detector, however, there are advantages in performing both EDXS and ELS. Besides providing a combination of quantitative elemental, chemical, and specimen thickness information that is not available from either individual technique, EDXS and ELS can be performed simultaneously to assure that the specimen composition, thickness, and crystal orientation, and the electron probe conditions, are identical for both types of analysis. This paper describes simultaneous EDXS and ELS analysis with an electron spectrometer and a UTW x-ray detector on a 100 KV field-emission-gun STEM. Applications of this system used as examples include quantitative analyses of metal carbide and oxide phases.

#### *Equipment and Specimens*

The microscope used in this work is a Vacuum Generators model HB-501 STEM which is equipped with a cold field-emission electron source, double condenser lens, virtual objective aperture (VOA), and a  $\pm 40^\circ$  x-y tilting beryllium-tipped specimen cartridge. The VOA is a probe-forming aperture located near the electron source (as far from the specimen as possible) to minimize x-ray incidence at the specimen. For microanalysis operation, the VOA size determines the probe current, the double condenser lens inversely varies probe size and probe convergence, and a "selected area" aperture which is optically conjugate to the object plane of the objective lens acts as a splash aperture to reduce the flux of x rays and uncollimated electrons in the probe further. A Gatan model 607 double focusing, second-order corrected magnetic sector type electron spectrometer and a Kevex model 6 UTW detector are adapted to the STEM as shown in Fig. 1. The UTW detector has an active area of about 8  $\text{mm}^2$  and can be inserted to 22 mm from the specimen by means of a 0.2m bellows motion. For periodic bakeouts of the STEM, the UTW detector can be interchanged with minimal vacuum disturbance, via a double vacuum-valved airlock. A Tracor-Northern model 2000/4000 computer-based multichannel analyzer was used for simultaneous EDXS and ELS data acquisition and for analysis.

The specimens included hot-pressed  $\text{Cr}_3\text{C}_2$  obtained from CERAC Corp., yttria-stabilized cubic  $\text{ZrO}_2$  (CZ), and a standard of  $\text{TiC}_{0.94}$  which was obtained through the courtesy of Prof. A. H. Heuer at Case Western Reserve University. The  $\text{Cr}_3\text{C}_2$  and CZ specimens were sliced by

---

The author is at the Hanford Engineering Development Laboratory, Box 1970, Richland, WA 99352.



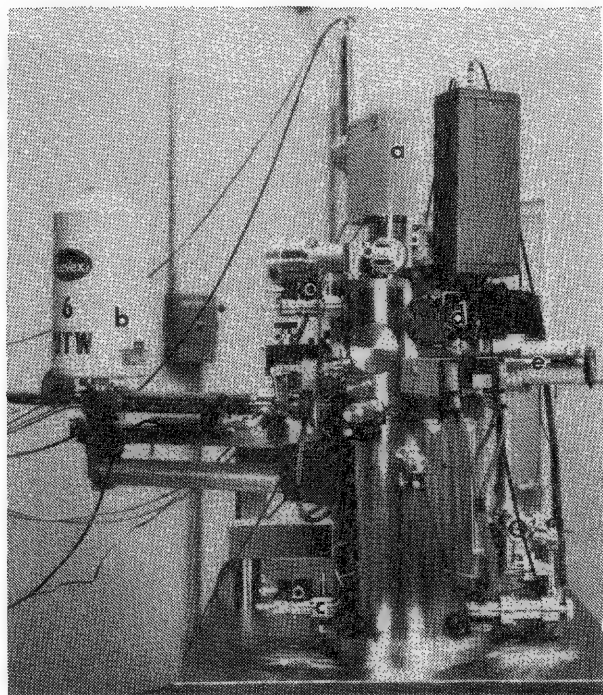


FIG. 1.--Electron-optical column of HB-501 STEM with (a) electron spectrometer, (b) ultrathin window Si(Li) detector, (c) virtual objective aperture, (d) diffraction viewing TV camera, and (e) specimen exchange.

and selected area aperture, and no objective aperture produces very low x-ray hole counts and allows no electrons to reach the x-ray detector. Also, the detector elevation angle of  $15^\circ$  at the closest detector approach to the specimen yields low x-ray backgrounds due to continuum x rays. Figure 2 shows a spectrum obtained from  $\text{TiC}_{0.94}$  with the specimen tilted  $20^\circ$  toward the UTW detector. A hole count taken with the same probe moved about 40 nm off the edge of the specimen (Fig. 2b) contains fewer than 10 counts over the entire 0.2-10keV spectrum. More often, the hole count rate was 1 cps over the entire spectrum.

The high-excitation objective lens also affects ELS operation since the lens postfield demagnifies the diffraction pattern by about 4.6 times at the lens excitation used in this work. There are no other postspecimen lenses in the microscope. With a choice of four entrance apertures in the electron spectrometer, the spectrometer entrance half-angles (referred to the specimen) could be varied from 12 to 30 mrad. For most work, an 18 mrad acceptance half-angle was used. The ELS slits were adjusted to maintain the spectrometer energy resolution at an arbitrarily chosen value of 1.5 eV, measured as the FWHM of the zero loss peak. By closing the slits further it was possible to obtain a resolution of about 0.35 eV.

#### *Simultaneous EDXS and ELS Data Acquisition*

Most simultaneous data acquisitions were performed for 100 s of live time by acquisition of the data into halves of a 2048 channel memory. With the TN 2000/4000 multichannel analyzer, EDXS data acquisition has to start before and end after ELS acquisition. For all but the thinnest specimen regions, the automatic correction for instrument deadtime in PHA acquisition extended the actual counting time enough to avoid any timing problem. The acquisition could be started by either manual or computer program control and ended automatically in the required sequence. Usually, the ELS data were acquired in two 50s scans of the spectrometer magnet, at 50 ms per data channel. The low energy loss part of the spectrum was counted with a 1MHz voltage-to-frequency converter and the high loss part by single electron counting, with automatic changeover between counting modes at a preset

low-speed diamond sawing, ultrasonically cut into 3mm-diameter disks, polished and dimple-ground with diamond paste, and ion micromilled to perforation at their centers. Vendor-independent total carbon analysis of the  $\text{Cr}_3\text{C}_2$  gave a carbon concentration of  $13.24 \pm 0.01$  wt.%, in good agreement with the value expected from stoichiometry.

#### *Choice of Operating Conditions*

Previous characterization of the HB-501 STEM<sup>1</sup> showed that the smallest probes with enough electron current (2-4 nA) for analysis of thin foils with the UTW detector were 2 nm in diameter at a convergence half-angle  $\alpha$  of 10 mrad. At larger convergence angles the probe size increases rapidly since it is then controlled by spherical aberration in the objective lens. If the highest spatial resolution is not needed, however, much larger probe currents can be obtained by an increase in the convergence. Probe currents as great as 16 nA were obtained with 5-6nm diameter probes with  $\alpha = 16$  mrad. Under these conditions, 40-50nm-thick specimen regions typically yielded total x-ray count rates of about 1000 cps. Probe diameters from 2 to 6 nm, and convergence angles from 10 to 16 mrad were used for most analyses in this work.

Operation of the HB-501 STEM with the high excitation objective lens, virtual objective

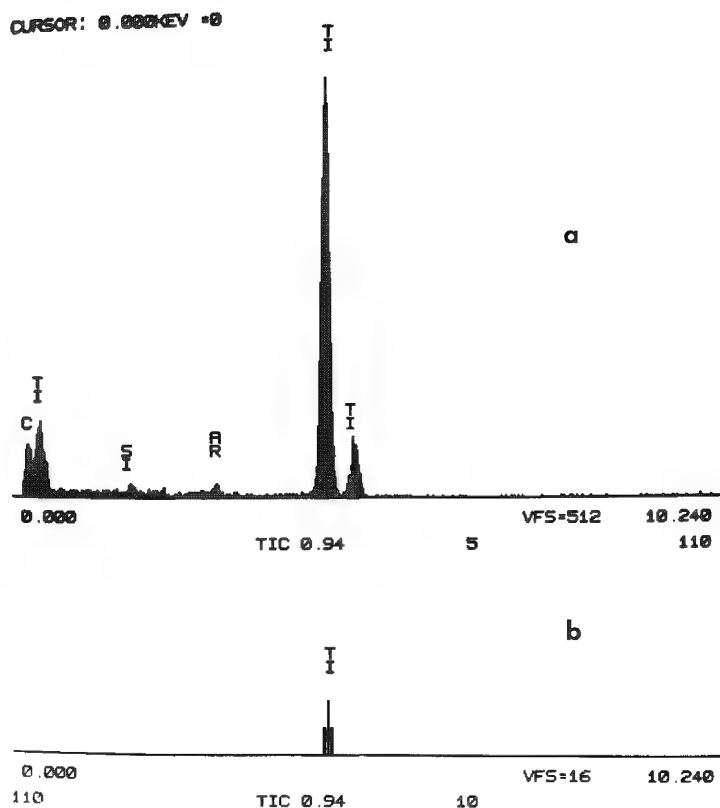


FIG. 2.--(a) X-ray spectrum from  $\text{TiC}_{0.94}$  standard, obtained with 2nm-diameter, 3nA electron probe. (b) Corresponding x-ray hole count taken with electron probe 4 nm from specimen edge.

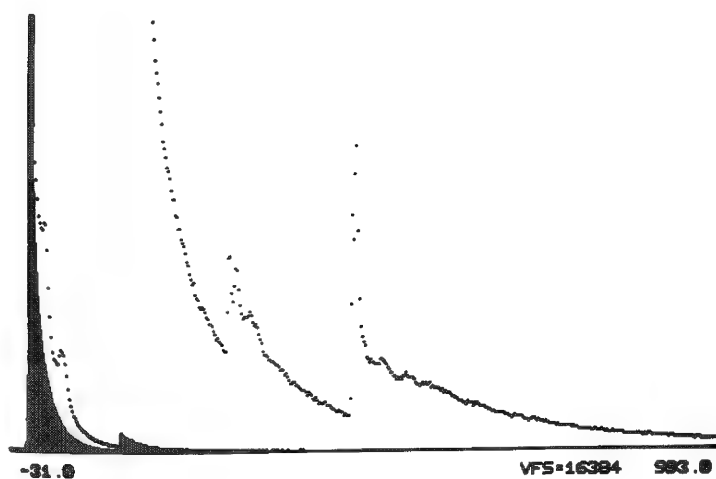


FIG. 3.--ELS spectrum acquired from low to high energy losses at 50 ms/channel from  $\text{TiC}_{0.94}$  (dotted curve). Solid spectrum shows background contribution due to scintillator or photomultiplier afterglow.

tamination on the specimen surfaces and the carbon in a metal carbide. Figure 4 shows several of these characteristic carbon edge structures. The diamond spectrum was obtained

data channel. The gain change between counting modes was a factor of 375.

Several instrumental problems were found in the course of the work. The UTW detector developed a pinholed window and, subsequently, a broad spurious peak which appeared at energies just below any major x-ray peak. Also, the analog-to-digital converter in the multichannel analyzer was found to be adding noise to the x-ray spectra. These problems were corrected. In the electron spectrometer, it was found that the NE 161 plastic scintillator/photo multiplier gives a pronounced afterglow as the spectrometer is scanned through the zero loss peak. The afterglow produced spurious counts mainly in the low loss region of the spectrum during 50 ms per channel data acquisition as shown by the specimen and hole count spectra in Fig. 3. With data acquired at higher scan rates, the afterglow swamped the low-loss region and also affected the high-loss region of the spectrum. Since this problem affects thickness measurements and absolute quantitation, which both use the low-loss region, initial efforts to analyze the data involved fitting and stripping normalized hole count spectra from the sample spectra. After the problem was recognized, the ELS data were acquired by scanning of the the spectrometer from high to low losses and by providing a delay between repeated scans. A further problem that affected ELS data analysis was caused by limited count rate throughput of the ELS/MCA equipment. In the single-electron counting mode, the response became nonlinear above 1.5 MHz. The nonlinear counting response appeared in spectra from relatively thick specimen regions as apparently anomalous gain changes at the changeover between analog and pulse counting modes. The ease with which artifacts in EDXS and ELS can pass unnoticed makes it important to characterize each analysis system thoroughly.

#### *Analysis of Metal Carbides*

One of the main contributions of ELS in the analysis of light elements is its ability to distinguish different types of chemical bonds. The K edge structures from various forms of carbon, for example, are highly distinctive,<sup>4</sup> and can be used to distinguish between hydrocarbon con-



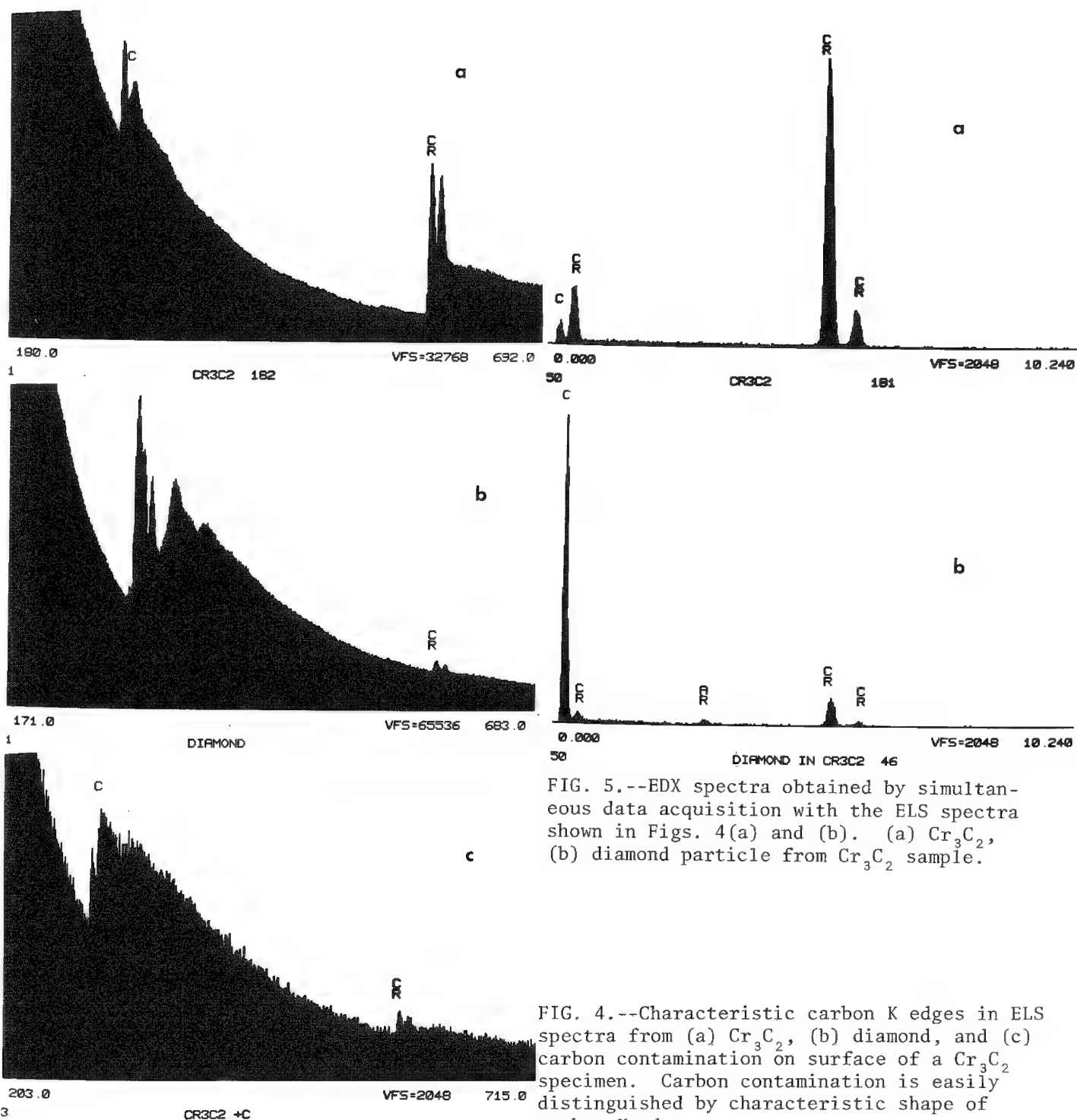


FIG. 5.--EDX spectra obtained by simultaneous data acquisition with the ELS spectra shown in Figs. 4(a) and (b). (a)  $\text{Cr}_3\text{C}_2$ , (b) diamond particle from  $\text{Cr}_3\text{C}_2$  sample.

FIG. 4.--Characteristic carbon K edges in ELS spectra from (a)  $\text{Cr}_3\text{C}_2$ , (b) diamond, and (c) carbon contamination on surface of a  $\text{Cr}_3\text{C}_2$  specimen. Carbon contamination is easily distinguished by characteristic shape of carbon K edge.

from the  $\text{Cr}_3\text{C}_2$  specimen, which had been polished using diamond paste. Amorphous carbon produced by vacuum evaporation as an anticharge coating or, as in Fig. 4(c), by hydrocarbon contamination under the electron probe during analysis, is characterized by a small, narrow peak at the abrupt edge onset and a broad single peak after the edge. The carbon K edges from metal carbides characteristically show two sharp peaks of equal height, but differ very little among MC,  $\text{M}_{23}\text{C}_6$ , and  $\text{Cr}_3\text{C}_2$  phases.

Although the UTW detector is much less sensitive to carbon x rays than it is for heavier elements, the x-ray spectra from  $\text{Cr}_3\text{C}_2$  and  $\text{TiC}_{0.94}$  shown in Figs. 2 and 5 exhibit car-

bon x-ray peaks that are large enough and sufficiently resolved from the Ti and Cr-L x-ray peaks to allow quantitative analysis. The x-ray spectra in Fig. 5 from  $\text{Cr}_3\text{C}_2$  and diamond were acquired simultaneously with the ELS spectra shown in Fig. 4. Without the corresponding ELS spectra, it would be difficult to ascertain that the small carbon x-ray peaks from the metal carbides are from the specimens rather than from surface contamination. Tests with the STEM showed that initially clean specimens not containing carbon often remained carbon-free for at least 1000 s under a stationary probe. However, contamination rates vary widely from specimen-to-specimen.

For quantitative analyses of carbide standards, EDXS and ELS spectra were collected from regions of different thickness, ranging from the thinnest that could be found in the ion-milled specimens to the thickest that yielded detectable carbon K edges in the ELS spectra. ELS spectra from areas about 50 nm in thickness were also taken with a range of probe convergence and spectrometer collection angles to compare the effects of different operating conditions. The specimen orientations were set by use of the microbeam diffraction patterns to avoid exciting any strong Bragg reflection. Relative specimen thicknesses were obtained from the ELS spectra from<sup>5</sup>

$$t/\lambda_p = \ln(I_t/I_0) \quad (1)$$

where  $t$  is the thickness,  $\lambda_p$  is the "plasmon" mean-free path,  $I_t$  is the total intensity in the low-loss spectrum, and  $I_0$  is the intensity of the zero loss peak. To avoid error in the measurement of  $I_t$  due to scintillator afterglow, a low-loss intensity  $I_1$  was found by stripping suitably scaled ELS hole count spectra from the specimen spectra;  $I_t$  was taken as the sum of  $I_1$  and  $I_0$ . This procedure was not needed for ELS spectra acquired by scanning of the spectrometer from high to low losses. Also, the thickness measurements were calibrated by measurements of absolute thicknesses from stereoscopic micrographs and convergent beam diffraction patterns that were taken from some of the same regions analyzed by EDXS and ELS. The ELS edge intensities were found by use of the Tracor Northern computer program ELS4 to model and strip the spectrum backgrounds under the edges. This program also calculated partial ionization cross sections for the K and L edges by use of Egerton's hydrogenic atom model programs SIGMAK and SIGMAL.<sup>6,7</sup> We analyzed the EDX spectra by modeling and stripping the backgrounds, and then directly integrating the x-ray peak intensities.

To illustrate the effects of specimen thickness on the carbide analyses, Fig. 6 shows corresponding EDXS and ELS spectra acquired simultaneously from  $\text{TiC}_{0.94}$  at relative thicknesses  $t/\lambda_p$  from 0.57 to 2.67. The ELS spectra in this example were acquired from high to low energy losses to eliminate scintillator afterglow contributions to the low-loss regions. A measurement of  $\lambda_p$  (85.2 nm) yielded absolute thicknesses of 48.5, 146, and 227 nm. At the largest thickness, nearly all electrons have suffered multiple inelastic scattering and the carbon edge is lost against the background of inelastically scattered electrons. At the intermediate thickness, the carbon edge is still visible, but the Ti-L edge clearly shows the effects of multiple scattering. It would be of interest to try to recover the single-scattering distributions by deconvolution of these spectra. The main effect of increasing specimen thickness on the EDX spectra is to decrease the carbon K and titanium L x-ray intensities relative to the titanium K intensity due to preferential self-absorption of the softer x rays. However, the carbon x-ray peak is still significant at thicknesses beyond those which yield a detectable carbon signal in ELS. Of course, at such thicknesses the electron probe is considerably broadened in the specimen due to the inelastic scattering.

In Figure 7, the measured carbon K/titanium K x-ray intensity ratios and the carbon/titanium atom ratios determined by ELS are plotted against relative specimen thickness. The dashed curve in the x-ray intensity ratio plot is the result of an x-ray self-absorption calculation for  $\text{TiC}_{0.94}$ , based on the mass-absorption coefficients tabulated by Henke and Ebisu.<sup>8</sup> For this calculation, the specimen density was taken as 4.93 g/cm<sup>3</sup>, and the x-ray pathlength in the specimen was 1.74 times the specimen thickness--based on the actual x-ray takeoff angle of 35°. If we assume uniform x-ray production in a thin foil specimen, the fraction of generated x rays which are emitted after self-absorption is

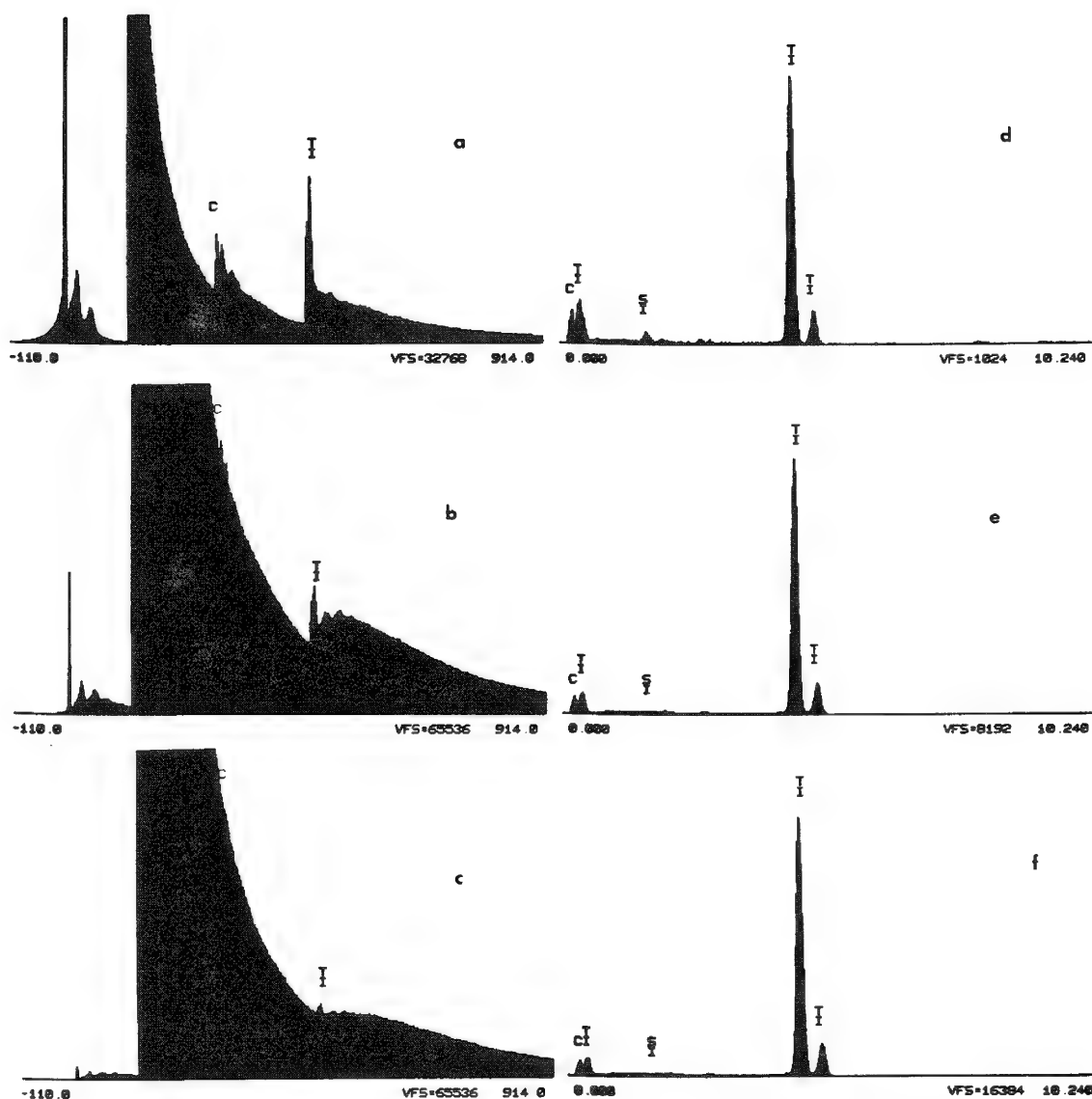
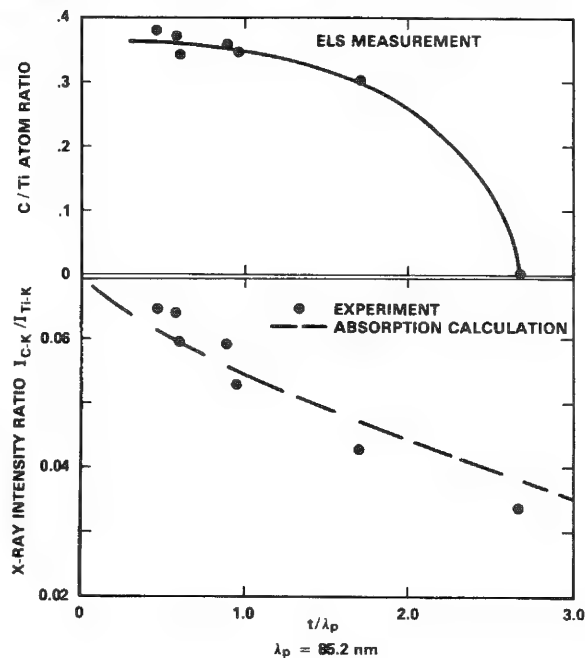


FIG. 6.--Simultaneously acquired EDX and ELS spectra from several thicknesses of  $\text{TiC}_{0.94}$ . Relative thicknesses were obtained by analysis of low-loss regions of spectra. (a) and (d)  $t/\lambda_p = 0.57$ , (b) and (e)  $t/\lambda_p = 1.71$ , (f)  $t/\lambda_p = 2.67$ . Plasmon mean free path for experiment was measured as 85.2 nm.

FIG. 7.--X-ray intensity ratios for carbon and titanium K x rays from  $\text{TiC}_{0.94}$  plotted against relative specimen thicknesses (lower figure). Dashed curve shows variation in x-ray intensity ratios calculated for self-absorption in the specimen. Upper curve shows effect of specimen thickness on carbon/titanium atom ratios determined from SIGMAKL analysis of ELS spectra.



$$f_x = \frac{1 - \exp[-(\mu/\rho)t^*]}{(\mu/\rho)t^*} \quad (2)$$

where  $\mu/\rho$  is the mass absorption coefficient for the x ray in the material of interest,  $\rho$  is the sample density, and  $t^*$  is the x-ray pathlength in the sample. The self-absorption calculations show reasonable agreement with the observed decrease in x-ray intensity ratios, and indicate that an absorption correction based on tabulated mass absorption coefficients will suffice for x-ray analysis of carbon in TiC. A similar result was obtained for  $\text{Cr}_3\text{C}_2$ .

The carbon/titanium atom ratios plotted in the upper part of Fig. 7 were obtained from ELS measurements of the integrated C-K and Ti-L edge intensities. The atom ratios for two elements A and B are

$$\frac{C_A}{C_B} = \frac{\sigma^B(\beta, \Delta) I^A(\beta, \Delta)}{\sigma^A(\beta, \Delta) I^B(\beta, \Delta)} \quad (3)$$

where the partial ionization cross sections  $\sigma$  and edge intensities  $I$  refer to the same energy integration range  $\Delta$  and spectrometer acceptance angle  $\beta$ . The partial ionization cross sections were calculated from the SIGMAK and SIGMAL programs. Although the ratios of C/Ti edge intensities (and the corresponding atom ratios plotted in Fig. 7) remained nearly constant up to thicknesses of  $t = 1.5\lambda_p$ , this result appears to be misleading. Examination of the background fitting and extrapolation to the ELS spectrum from the specimen region  $1.71\lambda_p$  in thickness, for example, showed that most of the integrated intensity measured in the carbon and titanium edges arose from plural scattering and thus was a thickness artifact.

The carbon/metal atom ratios obtained by ELS also differed considerably from the known atom ratios in standard materials. For a series of ten ELS measurements each on  $\text{Cr}_3\text{C}_2$  and  $\text{TiC}_{0.94}$  with a 16mrad probe convergence angle and a 18mrad acceptance angle, the C/Cr and C/Ti atom ratios were  $1/(3.1 \pm 0.4)$  and  $1/(2.7 \pm 0.3)$ , respectively. Table 1 gives the results of another series of ELS measurements which were performed to determine the effects of the probe convergence and spectrometer acceptance angles on the analyses. The C/Ti atom ratios obtained from the  $\text{TiC}_{0.94}$  standard varied from 1/2.2 to 1/4; the ratios decreased as the probe convergence decreased relative to the acceptance angles. Although the cross-section calculations for K-edges have been verified by comparison with experimentally measured values and are considered to be reliable, the calculated L-edge cross-sections used in the ELS analysis may be partly responsible for the apparent failure of the analysis. Thus, at present carbon analyses of metal carbides by either EDXS or ELS require the use of standards.

#### *Self-absorption of Soft X Rays*

Zaluzec<sup>9</sup> has expressed concern that strong absorption of x rays from the light elements in carbides, nitrides, and oxides will make quantitative analysis of these materials impractical for UTW detectors due to limitations on the useful specimen thickness. However, his argument is based on a pessimistic calculation of x-ray self-absorption. Table 2 compares specimen thicknesses for the Philibert-Tixier thin-film criterion, calculated from the Henke and Ebisu<sup>8</sup> x-ray mass absorption coefficients, with some of those published by Zaluzec.<sup>9</sup> The thin film criterion can be written

$$(\mu/\rho)_{ij}^i \rho t = 0.1 \quad (4)$$

With a 15° x-ray takeoff angle and 30° specimen tilt toward the UTW detector in the HB-501, the x-ray pathlength in the specimen is 1.4 times the thickness of the untilted specimen. Zaluzec's calculations are evidently for a different, although unstated, x-ray takeoff geometry and give much smaller limiting thickness for carbides and nitrides than the present calculations. In addition, the Philibert-Tixier criterion just gives the thickness from which 95% of the generated x rays are emitted. A less restrictive thin-film criterion could be used for carbide analyses where high sensitivity is not expected. Table 3 gives calculated values for self absorption of carbon x rays in  $\text{TiC}_{0.94}$  and oxygen x rays in  $\text{Zr(Y)O}_2$ . These calculations further demonstrate that x-ray self-absorption is not in general a severe limitation in light-element analysis with a UTW detector.

TABLE 1.--Effect of electron spectrometer parameters on C/Ti ratio analysis in Ti C<sub>0.94</sub> standard.

PROBE CONVERGENCE HALF ANGLE (m RAD)	SPECTROMETER ACCEPTANCE HALF ANGLE (m RAD)	C/TI ATOM RATIO
20	18.1	1/2.64
10	18.1	1/2.62
8	18.1	1/3.06
6	18.1	1/3.24
3	18.1	1/3.54
6	30.2	1/3.86
6	12.1	1/3.51

TABLE 2.--Calculated limiting specimen thickness for 95% x-ray emission (Philibert-Tixier criterion).

MATERIAL	DENSITY (g/cm <sup>3</sup> )	X-RAY	LIMITING THICKNESS (nm)	
			THIS WORK*	ZALUZEC
TiC	4.93	C-K	29.1	8.9
TiN	4.22	N-K	59.2	29.4
MgO	3.58	O-K	82.2	54.1
Cr <sub>3</sub> C <sub>2</sub>	6.68	C-K	18.8	-
Zr <sub>0.75</sub> Y <sub>0.25</sub> O <sub>1.88</sub>	5.95	O-K	13.8	-

TABLE 3.--X-ray emission after self-absorption.

PATH LENGTH IN SPECIMEN (nm)	FRACTION OF X-RAYS EMITTED			
	Ti C <sub>0.94</sub>		Zr <sub>0.75</sub> Y <sub>0.25</sub> O <sub>1.88</sub>	
	C-K	Ti-K	O-K	Zr-K
50	0.92	1.00	.84	1.00
100	0.85	1.00	.71	1.00
150	0.78	1.00	.61	1.00
200	0.72	1.00	.53	1.00
250	0.66	0.99	.46	1.00

Either ELS or EDXS with an ultrathin window Si(11) detector can be used for quantitative microanalysis of carbides and oxides (and nitrides) in a STEM. Both methods have their strengths and shortcomings; the preferred method depends in large measure on the material being analyzed. The best choice for the analyst is to use both methods. ELS and EDXS data can be collected simultaneously to insure that the analyses refer to the identical specimen region and electron probe conditions, and the capital cost of the alternative spectrometer is a small fraction of the total for an analytical TEM or STEM. The field emission gun STEM is the instrument of choice for highest spatial resolution in microanalysis since it provides a clean, ultra-high vacuum at the specimen and high-current electron probes as small as 2 nm in diameter.

## References

1. L. E. Thomas, "High spatial resolution in x-ray microanalysis," *Ultramicroscopy* 9. 1982, 311-318.
2. L. E. Thomas, "Microanalysis of light elements with an ultrathin window x-ray

## Zirconium Oxide Analysis

Zirconia is difficult to analyze by ELS because the broad, poorly defined zirconium M edge interferes with the light element K edges and with the similarly broad M edges from adjacent numbered elements such as yttrium and niobium. Further spectral interferences arise from the anticharge coating (usually vacuum-evaporated carbon) which is essential for ELS analysis of insulators. Figure 8 shows the characteristic "sleeping whale" shape of the Zr M edge in a background stripped ELS spectrum from yttria-stabilized cubic zirconia. The ELS method fails to resolve the overlapping Y and Zr M edges and shows the oxygen K edge on a large background caused by these edges. For this case, EDXS analysis appears more tractable. The simultaneously acquired x-ray spectrum shown in Fig. 8(b) from the CZ specimen demonstrates the sensitivity of the UTW detector for oxygen. In addition, the zirconium and yttrium K $\alpha$  peaks are well resolved near 15 keV and can be used to determine the concentration ratios for these elements. Using the x-ray k-ratio  $k_{Y/Zr}$  of 0.91 calculated from Zaluzec's tables,<sup>10</sup> we obtained measured intensities from 15 analyses of  $C_Y/C_{Zr} = 0.329 \pm 0.015$ . This result yields  $Zr_{0.75}Y_{0.25}O_{1.88}$  for stoichiometric CZ. In Fig. 9, the x-ray intensity ratio for O<sub>K</sub> and (Zr + Y)<sub>L</sub> is plotted against specimen thickness. The dashed curve shows the calculated effect of self-absorption on the x-ray intensity ratios, which agrees with the experimentally determined behavior. Thus, with a self-absorption correction for the oxygen x rays, the UTW detector allows quantitative analysis of oxygen in zirconia and similar materials which are difficult to analyze by ELS.

## Concluding remarks

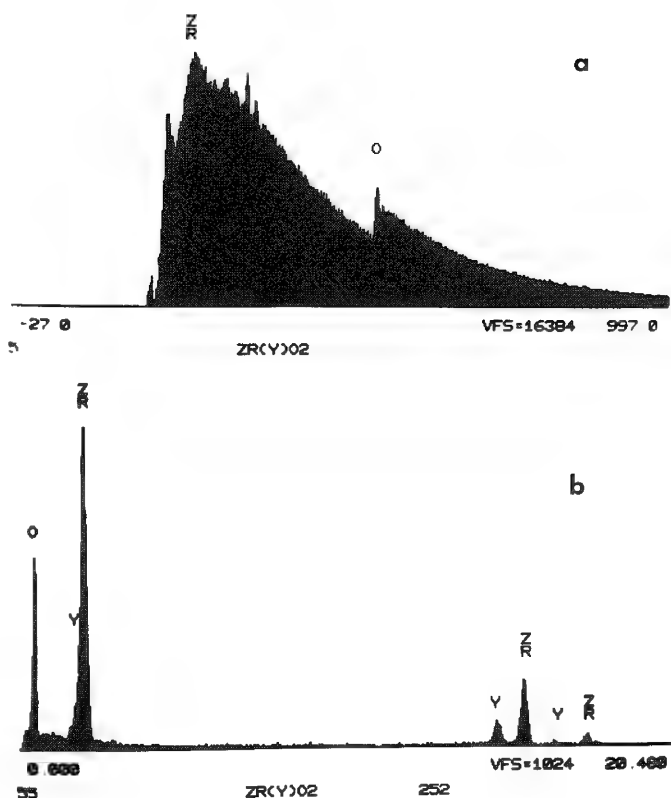


FIG. 8.--(a) Background-stripped Zr (Y) M-edges and oxygen K-edge in ELS spectrum from yttria-stabilized cubic zirconia. (b) Simultaneously acquired EDX spectrum showing well-resolved oxygen, zirconium, and yttrium K x-ray peaks.

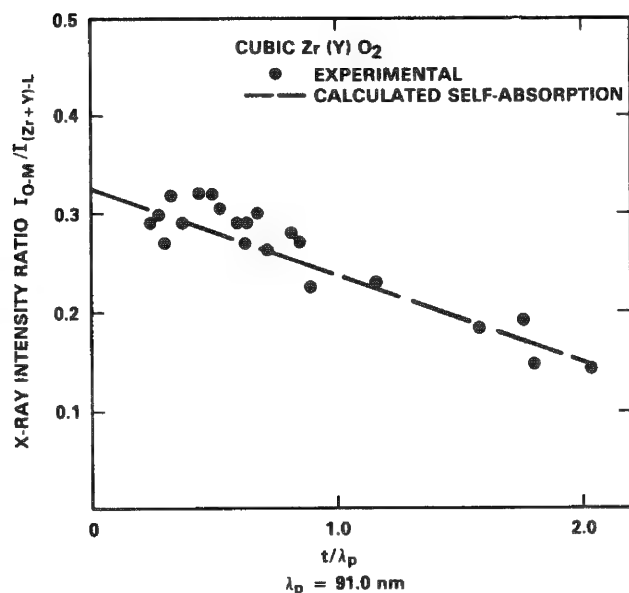


FIG. 9.--X-ray intensity ratios for oxygen K and zirconium plus yttrium L-x rays plotted against relative specimen thickness. Dashed curve shows thickness dependence calculated for x-ray self-absorption in specimen.

spectrometer," in G. W. Bailey, Ed., *Proceedings EMSA/1980*, Claitors Publishing, 1980, 90-93.

3. R. G. Musket, "Properties and applications of windowless Si(Li) detectors," in K. J. F. Heinrich et al., Eds., NBS Special Technical Publication 604, *Energy Dispersive X-ray Spectrometry*, 1981, 97-126.

4. R. F. Egerton and M. J. Whelan, "Electron energy loss spectra of diamond, graphite and amorphous carbon," *J. Electron Spectroscopy* 3: 232-236, 1974.

5. R. F. Egerton, "The range of validity of EELS microanalysis formulae," *Ultramicroscopy* 6: 297-300, 1981.

6. R. F. Egerton, "K shell ionization cross-sections for use in microanalysis," *Ultramicroscopy* 4: 169, 1979.

7. R. F. Egerton, "SIGMAL: A program for calculating L-shell ionization cross-sections," in G. W. Bailey, Ed., *Proceedings EMSA/1981*, Claitors Publishing, 1981, 198-199.

8. B. L. Henke and E. S. Ebsu, "Low-energy x-ray and electron absorption within solids," in C. L. Grant et al., Eds., *Advances in X-ray Physics* 17: 150-213, 1974.

9. N. J. Zaluzec, "Elemental microanalysis using analytical electron microscopy," in J. R. Holland, L. K. Mansur, and D. I. Potter, Eds., *Phase Stability During Irradiation*, AIME, 1981, 141-164.

10. N. J. Zaluzec, "Quantitative x-ray microanalysis: Instrumental considerations and applications to materials science," in J. J. Hren, J. I. Goldstein, and D. C. Joy, Eds., *Introduction to Analytical Electron Microscopy*, Plenum Press, 1979, 121-168.

## THIN-FILM ANALYSIS WITH A MONTE CARLO SIMULATION BASED ON THE MOTT CROSS SECTION

Kenji Murata, Serge Cvikevich and John D. Kuptsis

Monte Carlo calculations have been utilized for quantitative electron microprobe analysis by many authors. Although the method requires a relatively long CPU time on a large modern computer, it is useful for analyses of samples with unusual boundary conditions because the program can easily be modified to take them into account. Several workers have successfully performed quantitative electron microprobe analysis of thin films, which was based on the old Monte Carlo simulation model developed by Kyser and Murata.<sup>1</sup> However, in cases in which this model was applied to regimes at lower electron beam energy or to analysis of heavy elements, the results were less than satisfactory.

More recently, the old Monte Carlo simulation model was improved by the use of the Mott cross section for elastic electron scattering instead of the classical Rutherford scattering cross section.<sup>2</sup> The new model was tested by application to a limited number of elements (Al, Cu, and Au) that have been extensively studied and for which the best theoretical atomic potential values are available.

In this paper, we propose a method for extending the limited calculated Mott cross section data to other elements for which such data are not available by the use of interpolation and extrapolation when needed.

### *Calculation Procedure*

*Monte Carlo Simulation.* Recent experimental results obtained by Murata, Kotera, and Nagami have shown that the use of the Mott cross section for elastic scattering gives a better accuracy in the description of electron scattering in heavy elements and at low energies for all elements.<sup>2-4</sup> In this model the differential cross section is calculated by

$$\frac{d\sigma(\theta)}{d\Omega} = |f(\theta)|^2 + |g(\theta)|^2 \quad (1)$$

where  $f(\theta)$  and  $g(\theta)$  can be obtained from theoretical models of atomic potentials by calculation of the partial wave expansion of the relativistic wave equation of Dirac. For energy loss the modified Bethe equation<sup>5</sup> was used at low energies as follows, in the usual notation:

$$-\frac{dE}{dS} = \frac{2\pi e^4 n Z}{1.26\sqrt{JE}}, \quad E < 6.338J \quad (2)$$

The calculation of the Mott scattering cross section for all possible elements of interest from Eq. (1) is hindered by the lack of good theoretical atomic potential values for many of the elements. In addition, the calculation time and storage capacity required for such data for all elements and energies of interest would be prohibitive even on the large modern computing systems. For this reason, we propose to obtain the needed values of Mott

---

Author Murata's permanent address is University of Osaka Prefecture, Sakai, Osaka, Japan; author Cvikevich's is IBM East Fishkill, Hopewell Junction, NY 12533. Author Kuptsis is at the IBM Thomas J. Watson Research Center, Yorktown Heights, NY 10598, where this work was performed. The authors wish to acknowledge the support of D. F. Reilly, R. W. Bowers, J. N. Ramsey, and E. K. Brandis from IBM GTD, East Fishkill, N.Y.; and of V. Sadagopan and W. Reuter from the IBM Thomas J. Watson Research Center. The contribution of M. Kotera from the University of Osaka Prefecture, who helped with the calculation of Mott cross sections, is also gratefully acknowledged.



cross sections by interpolation and extrapolation based on somewhat better-known values for Mott cross sections available for a few elements such as Al, Cu, Ag, and Au. The Mott differential cross sections are provided at intervals of  $2^\circ$  in scattering angle and for a range of representative discrete energies. The specific differential cross-section data for specific energies and elements are obtained by interpolation and extrapolation, when applicable, from values available in the Mott cross-section database.

*The Mean Ionization Potential  $J$  and Ionization Cross Section  $Q(U)$ .* The mean ionization potential  $J$  in the modified Bethe equation (Eq. 2), is an important parameter that determines the electron penetration, as already pointed out by Myklebust et al.<sup>6</sup> The values most commonly used in quantitative electron microprobe analysis are those of Duncumb and Reed<sup>7</sup> (DR) and Berger and Seltzer<sup>8</sup> (BS). These values were obtained by empirical fitting to experimental data. The former values are given as numerical tables. The latter are described by

$$J = 9.76Z + 58.8Z^{-0.19} \quad (3)$$

Typical examples of  $J/Z$  values obtained from the above quoted sources are listed in Table 1. The effect of these differences is relatively small since it is reduced by the inverse square root dependence of the stopping power and  $J$ . However, this difference leads to a change in generated x-ray intensities for a pure Pt standard of about 10%. Since the x-ray intensity is calculated as a ratio of sample to standard intensity, the absolute value of the ionization cross section is not required for the present analysis. Some of the commonly used expressions for the ionization cross section are

$$(i) \quad \text{Worthington-Tomlin (WT)}^9 \\ Q_{WT}(U) = a_{WT} \ln[4U/\{1.65 + 2.35\exp(1 - U)\}]/U \quad (4)$$

$$(ii) \quad \text{Hutchins (modified Bethe equation, H)}^{10} \\ Q_H(U) = a_H \ln U/U^{0.7} \quad (5)$$

$$(iii) \quad \text{Gryzinski (G)}^{11} \\ Q_G(U) = a_g \{(U - 1)/(U + 1)\}^{3/2} [1 + (2/3)(1 - \frac{1}{2}U) \ln\{2.7 + (U - 1)^{1/2}\}]/U \quad (6)$$

$$(iv) \quad \text{Original Bethe equation (B)}^{12} \\ Q_B(U) = a_B \ln U/U \quad (7)$$

These equations are shown in a normalized form in Fig. 1. At sufficiently large values of the overvoltage  $U$ , the WT and H cross sections represent the lowest and highest values, respectively. In this investigation, we evaluated these two most widely differing expressions for the ionization cross section by comparing the simulated and experimentally obtained  $k$  ratios. In his recently published book Heinrich states that uncertainties in the value of the ionization cross section become significant for the x-ray generation in thin films and small particles.<sup>13</sup>

### Results and Discussion

The  $k$  ratios referred to in this paper are not the same as those used in conventional electron microprobe analysis. In our case, the  $k$  ratio is defined as the ratio of x-ray intensity emitted from an element in a thin film on a substrate to that generated by a semi-infinite pure or known composition standard. In Figs. 2 and 3 experimentally obtained  $k$  ratios from the work by Reuter et al.<sup>14</sup> for thin films of Pt on Si and Au substrates are plotted for a range of electron-beam energies. These results are compared with  $k$  ratios obtained from Monte Carlo simulations using different combinations of ionization cross sections  $Q(u)$  and mean ionization potentials  $J$ . Results from the old Monte Carlo simulation model, which used the Rutherford scattering cross sections, are also shown for comparison. The simulations using the new model were performed with three different combinations of the ionization cross section  $Q(u)$  and mean ionization potential  $J$  values. These combinations are shown in Figs. 2 and 3 as solid circles (Hutchins; Duncumb and Reed), open circles (Worthington and Tomlin; Duncumb and Reed), and cross marks (Worthington and Tomlin; Berger and Seltzer). The first combination of parameters yields the best agreement with experimental results. The simulated values deviate from experiment only in the low-keV region, where the  $k$  ratio approaches unity. The combination of parameters represented

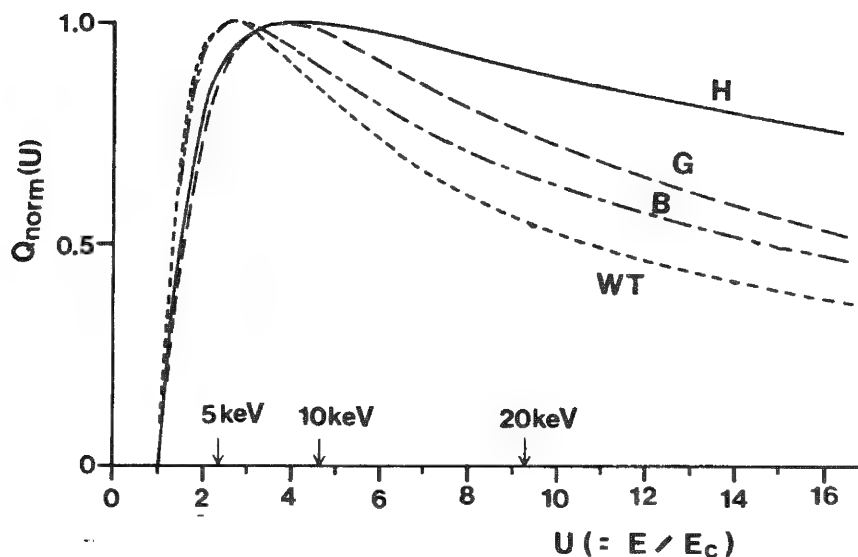


FIG. 1.--Normalized ionization cross sections as function of overvoltage  $U$ . H: Hutchins, G: Gryzinski, B: Bethe, WT: Worthington & Tomlin. Values of energy shown on horizontal axis are for Pt  $M\alpha$  ( $E_C = 2.15$  keV).

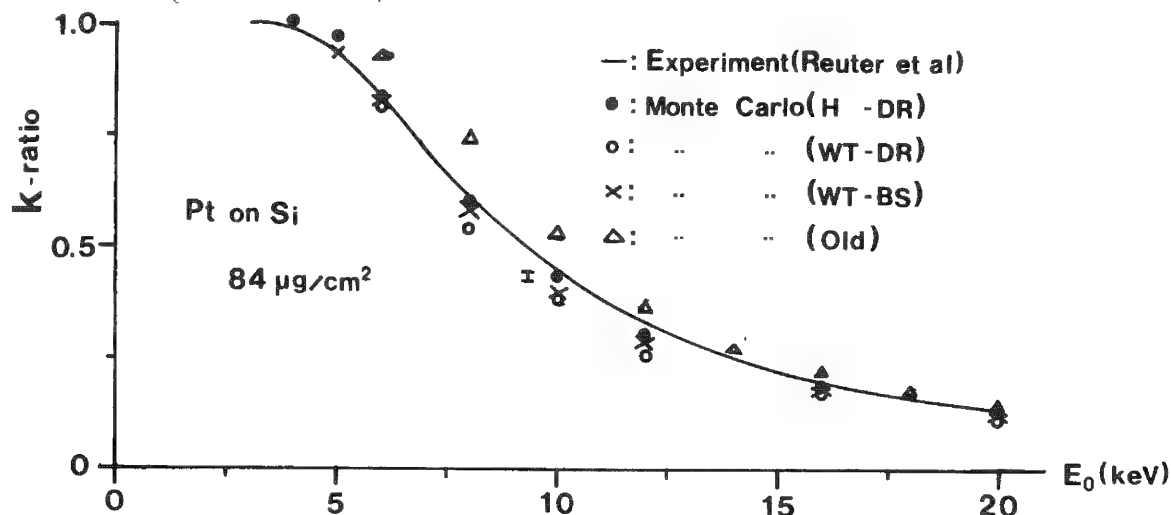


FIG. 2.--Variation of  $k$  ratio with electron impact energy for Pt thin film on Si substrate. Results of Monte Carlo simulations are compared with experimental results.

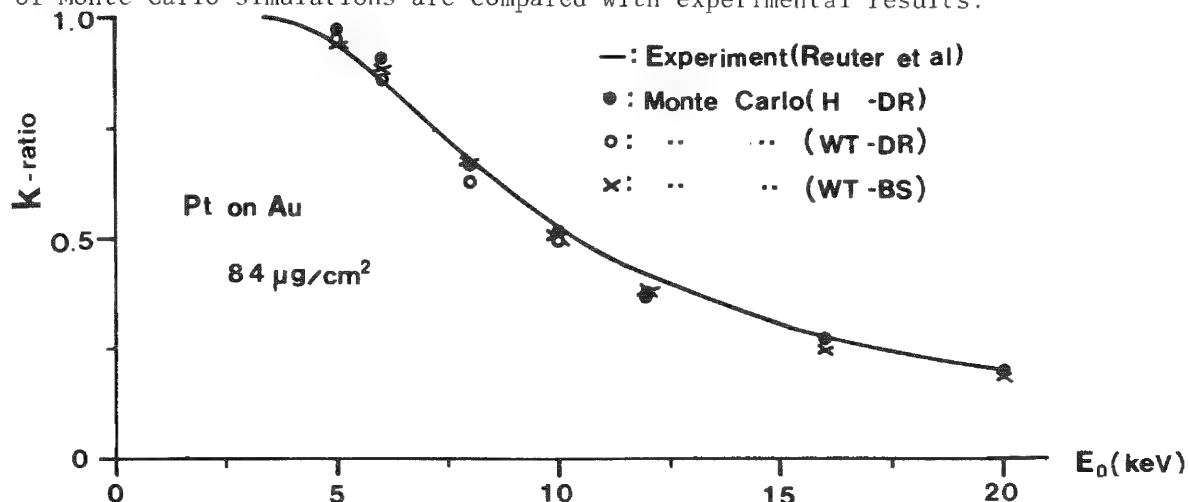


FIG. 3.--Variation of  $k$  ratio with electron impact energy for Pt thin film on Au substrate. Results of Monte Carlo simulations are compared with experimental results.

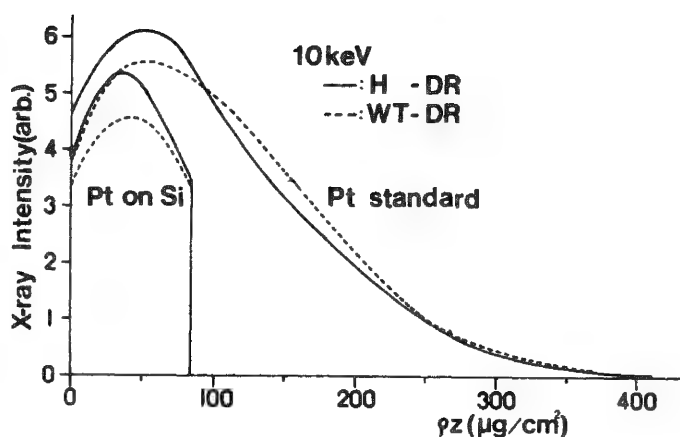


FIG. 4.--Effect of the ionization cross section on depth distribution of x-ray production in Pt standard and Pt film on Si substrate.

The ionization cross-section curves in Fig. 1 are shown in a normalized form and the actual difference between them is best expressed by the difference in gradient at any given overvoltage. This difference in gradient is most significant for energies below 20 keV. An example of the effect of the choice of an ionization cross section on the value of the  $\phi(\rho z)$  curve is shown in Fig. 4. The two  $\phi(\rho z)$  curves calculated for PtM $\alpha$  in a Pt standard target correspond to two different ionization cross-section values of H and WT and the same mean ionization potential  $J$  (from DR). These curves are normalized to yield the same total generated x-ray intensity value. One can see that the use of WT ionization cross section reduces the generated x-ray intensity near the surface, where the high-energy electrons are dominant. From the  $\phi(\rho z)$  curves for a thin Pt film on a silicon substrate, which are shown in the same figure, one can see that the x-ray intensity generated in the film is determined primarily by high-energy electrons for which the integrated ionization cross section is smaller than that corresponding to the full range of electron energies in the semi-infinite standard. As in the case of standard sample, the H ionization cross sections yields a higher x-ray intensity than that of WT. When the intensity ratio  $k$  is obtained from the x-ray intensity emitted from the film divided by the intensity emitted from the standard, the use of the WT ionization cross section results in a smaller  $k$  ratio than that which is obtained when the H ionization cross section is used. The small difference in x-ray absorption which results from the difference in shape of the  $\phi(\rho z)$  curves is considered to be negligible. In the extreme case of an isolated thin film, without the backscattering contribution from a substrate, one obtains the greatest possible difference in  $k$  ratios derived from the H and WT ionization cross sections. On the other hand, in the case of a Pt film on an Au substrate, which generates a large contribution of back-scattered electrons, this difference in  $k$  ratios is reduced (Fig. 3). In this case of a substrate material of a close atomic number the  $\phi(\rho z)$  curve for the film is similar to that of the standard over the mass-thickness range of the film. The ionization cross-section-dependent difference in the  $k$  ratios is reduced by a greater contribution of the lower-energy electrons, which is lost for the case of an unsupported film or a low-atomic-number substrate. A comparison of Figs. 2 and 3 confirms the validity of our arguments. The statistical fluctuation error, shown by the vertical bar in Fig. 2, was estimated from the output data at each 100 trajectories taken from a total of 1000 trajectories used in our simulations. This finding shows that the above comparison of simulated results is statistically significant. We have also compared simulated results based on the H-DR parameters with experimental results for Al and Mo films on Si and carbon substrates. A good agreement was obtained between simulated and experimental  $k$  ratios for these film-substrate combinations.

We next turn our attention to the influence of a particular choice of the mean ionization potential  $J$  on the simulated  $k$  ratios. As seen from Table 1 the  $J$  values due to Berger and Seltzer (BS) are 30% smaller than those given by Duncumb and Reed (DR) for

by WT-DR results in a maximum deviation from experiment of about 20%. The values of the ionization cross sections beyond the overvoltage value of  $u = 3.2$  deviate from each other and lead to substantial differences at higher overvoltages. The difference in cross sections is less important in the tail part of the electron penetration range for the relatively high initial electron energies.

If one considers electrons impinging on a standard (semi-infinite) sample, one can see from the ionization cross-section curves in Fig. 1 that at the higher electron energies the ionization probability increases with decreasing electron energy down to a value of overvoltage at which a maximum value is reached. For calculations of generated x-ray intensity, the WT cross section places more weight on lower-energy electrons than does the H cross section.

TABLE 1.--Mean ionization potentials divided by atomic number for Al, Cu, Pt, and Au. BS: Berger & Seltzer, DR: Duncumb & Reed.

	Al	Cu	Pt	Au
$J(BS)/Z$	12.54	10.83	10.09	10.09
$J(DR)/Z$	10.09	13.00	13.55	13.56

TABLE 2.--Comparison of ratios of x-ray intensity  $I_{DR}/I_{BS}$  and absorption  $F(x)_{DR}/F(x)_{BS}$  between DR and BS for Pt standard.

$E_0$ (keV)	20	16	12	10	8	6	5
Intensity ratio	1.05	1.07	1.12	1.09	1.13	1.14	1.06
$F(x)$ ratio	0.991	0.968	0.987	0.990	0.993	0.995	1.000

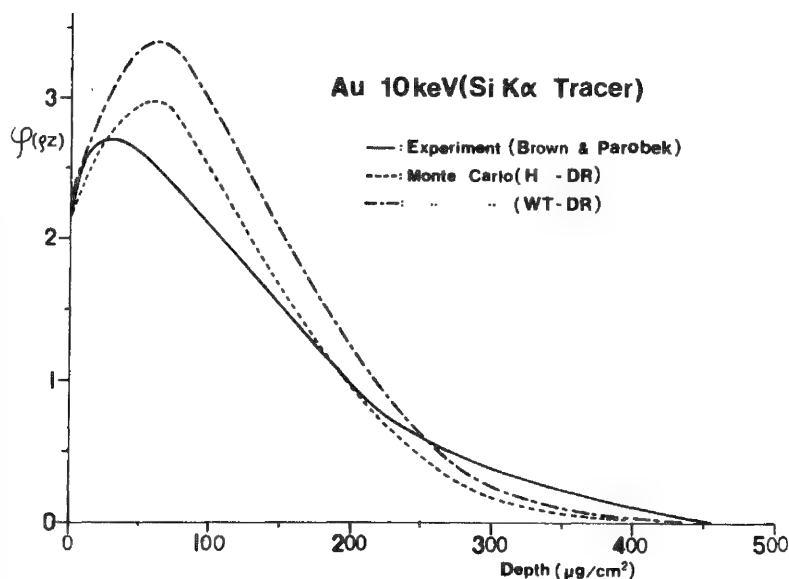


FIG. 5.-- $\phi(\rho z)$  curves for Au target obtained by Monte Carlo simulation are compared with experiment of Brown and Parobek.

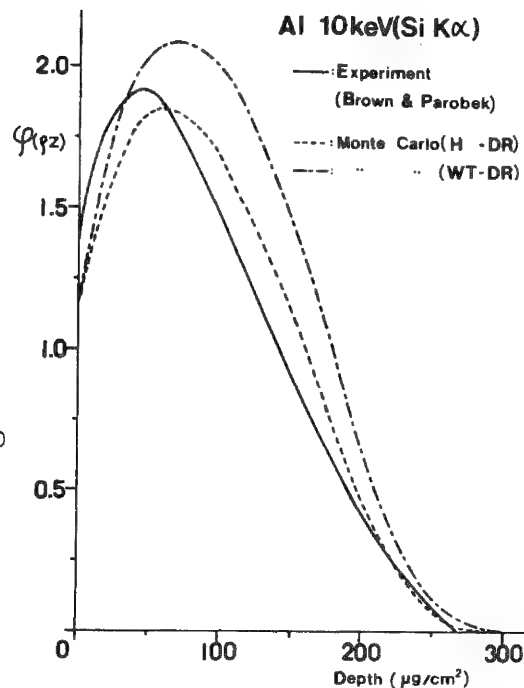


FIG. 6.-- $\phi(\rho z)$  curves for Al target obtained by Monte Carlo simulation are compared with experiment of Brown and Parobek.

heavy elements. The net effect is a reduction of the electron trajectory range and the ensuing x-ray production in a standard specimen when the  $J$  values of BS are used. The slight increase in generated x-ray intensity due to a decrease in the backscattering coefficient associated with a decrease in the average electron trajectory length, does not compensate for the x-ray intensity loss due to the above causes. Table 2 compares simulated x-ray intensities and  $F(x)$  values as ratios of these values when either the DR or BS values of  $J$  are used. These ratios are given for a range of initial electron energy values. Although the difference in the two  $F(x)$  values is small, the difference in intensity ratios appears to be significant and is expressed by a range of ratios from 1.05 to 1.14. From this comparison of values in Table 2 and Figs. 2 and 3, it can be seen that if the H ionization cross section is combined with the  $J$  values of BS, the resulting  $k$  ratios are higher than the experimental ones. Thus, it appears that if one were to use the mean ionization potential values of BS, a better choice of ionization cross section

would be the one proposed by Gryzinski (G).

An additional error introduced into any k ratio obtained by simulation is that due to uncertainty in the mass-absorption coefficient ( $\mu/\rho$ ). The published values of the PtMa self-absorption coefficient range from  $1192(\text{cm}^2/\text{g})^{15}$  down to  $1050(\text{cm}^2/\text{g})^{16}$ . The uncertainty in the  $F(\chi)$  value and thereby in the simulated x-ray intensity value will be 0.7, 1.7, 3.4, and 4.5% for initial electron energies of 6, 10, 16, and 20 keV, respectively.

As a final test of our Monte Carlo simulation model, we compared our simulated  $\phi(\rho z)$  curves for Au and Al standards at 10 keV with the experimental results on the same elements of Brown and Parobek<sup>17</sup> in Figs. 5 and 6. Brown and Parobek used a tracer technique (described in the above reference) in which the  $\text{SiK}\alpha$  radiation generated by a thin layer of Si embedded at various depths in matrices of Au and Al was measured. Our simulated results are normalized by the x-ray intensity emitted from an unsupported thin film, which corresponds to the procedure used in the measurements of Brown and Parobek. From the comparison of our simulations with their data, we can see that although the H-DR parameter combination yields a better agreement with experiment than does the WT-DR combination, neither combination of parameters can properly describe the experimentally obtained  $\phi(\rho z)$  curves near the peak region.

### Conclusion

We have proposed an extension of a Monte Carlo simulation model based on the use of Mott scattering cross sections to quantitative electron microprobe analysis of thin films on substrates. Although, for the energy range of interest in quantitative electron microprobe analysis, the Mott scattering cross sections are established only for a few elements, the Mott scattering cross-section data needed for the analysis of other elements can be obtained by interpolation and occasionally by extrapolation. Using the present model, we investigated the influence of the choice of ionization cross section and the mean ionization potential on the resulting k-ratio with various parameter combinations such as the ionization cross-section formulas of Hutchins or Worthington-Tomlin combined with mean ionization potential values of Duncumb and Reed or those proposed by Burger and Seltzer. At this writing, we are not prepared to recommend anything that could be considered as the best combination of ionization cross section and mean ionization potential parameters such as Hutchins-Duncumb and Reed or Gryzinski-Berger and Seltzer. More experimental data, including more experimentally measured  $\phi(\rho z)$  curves, will be needed to establish the optimal choice of parameters to be used in our simulation model.

### References

1. D. F. Kyser and K. Murata, *IBM J. Res. Develop.* 18: 352, 1974.
2. K. Murata, M. Kotera, and K. Nagami, *J. Appl. Phys.* 54: 1110, 1983.
3. M. Kotera, K. Murata, and K. Nagami, *J. Appl. Phys.* 52: 997, 1981.
4. M. Kotera, K. Murata, and K. Nagami, *J. Appl. Phys.* 52: 7403, 1981.
5. T. S. Rao-Sahib and D. B. Wittry, *J. Appl. Phys.* 45: 5060, 1974.
6. R. L. Myklebust, D. E. Newbury, and H. Yakowitz, K. F. J. Heinrich, D. E. Newbury, and H. Yakowitz, Eds., *Use of Monte Carlo Calculations in Electron Probe Microanalysis and Scanning Electron Microscopy*, NBS Special Publication 460, 1976, 105.
7. P. Duncumb and S. J. B. Reed, K. F. J. Heinrich, Ed., *Quantitative Electron Probe Microanalysis*, NBS Special Publication 298, 1968, 133.
8. M. J. Berger and S. M. Seltzer, Washington, D.C.: NAS/NRC 1133, 1964, 205.
9. C. R. Worthington and S. G. Tomlin, *Proc. Phys. Soc. A*-69: 401, 1956.
10. G. A. Hutchins, in P. F. Kane and G. B. Larrabee, Eds., *Characterization of Solid Surfaces*, New York: Plenum Press, 1974, 441.
11. M. Gryzinski, *Phys. Rev.* 138: A336, 1965.
12. H. Bethe, *Ann. Physik* 5: 325, 1930.
13. K. F. J. Heinrich, *Electron Beam X-ray Microanalysis*, New York: Van Nostrand Reinhold, 1981.
14. W. Reuter, J. D. Kuptsis, A. Lurio, and D. F. Kyser, *J. Phys.* D-11: 2633, 1978.
15. J. Leroux and T. P. Thinh, *Revised Tables of X-ray Mass Absorption Coefficients*, Corp. Scientifique Claisse Inc., 1977.
16. K. F. J. Heinrich, in T. D. McKinley, K. F. J. Heinrich, and D. B. Wittry, Eds., *The Electron Microprobe*, New York: Wiley, 1966, 296.
17. J. D. Brown and L. Parobek, *X-ray Spectrometry* 5: 36, 1976.

## THE DEPENDENCE OF BREMSSTRAHLUNG EMISSION ON $\bar{Z}$ IN COMPOUND SAMPLES

T. B. Vander Wood, J. G. Pearson, and P. R. Buseck

The bremsstrahlung radiation emitted by a thick flat specimen under high-energy electron bombardment is generally described by a relation similar to that proposed by Kramers:<sup>1</sup>

$$N_E dE = KZ[(E_0/E) - 1] dE \quad (1)$$

where  $N_E$  is the number of photons emitted with energy  $E$ ,  $Z$  is the atomic number of the specimen,  $E_0$  is the energy of incident electrons, and  $K$  is a constant. More recently Rao-Sahib and Wittry<sup>2</sup> have proposed that the dependence of  $N_E$  on  $Z$  is better described by  $N_E \propto Z^n$ , where  $n \cong 1.2$ . For samples composed of more than one element it is generally assumed that the average atomic number  $\bar{Z}$  can be substituted for  $Z$ , where

$$\bar{Z} = \sum_i C_i Z_i \quad (2)$$

and  $C_i$  is the weight fraction of element  $i$ . This expression has been shown to be true for several alloys and a few uranium compounds by Moreau and Calais<sup>3</sup> and Heinrich.<sup>4</sup> We present here measurements of the bremsstrahlung emissions of a series of pure-element, oxide, and sulfide samples. The results indicate that the production of bremsstrahlung radiation by a compound is not a simple function of  $\bar{Z}$ .

### Results

In order to minimize self-absorption effects, we measured the bremsstrahlung emission excited from a series of targets by a 200pA beam of 25keV electrons in the energy windows 15 to 16 keV, 16 to 17 keV, 17 to 18 keV, 18 to 19 keV, and 19 to 20 keV using a JEOL model JSM 35 scanning electron microscope and an energy-dispersive x-ray detector with a channel width of 40 eV. Since the detected x-ray intensity is a function not only of emission but of detection, we have normalized all x-ray counts to those detected from silicon under the same conditions. The data are summarized in Table 1 and Fig. 1. Each analysis consists of the average of at least five (for compounds) or three (for elements) measurements. Quoted errors are those calculated from  $2\sigma$  counting errors.

The  $Z$  dependence of bremsstrahlung radiation between 15 and 20 keV for the pure elements analyzed in this study satisfies  $N_E \propto Z$  as proposed by Kramers.<sup>1</sup> Linear correlation coefficients between  $Z$  and  $N_E$  determined for these elements are given in Table 2. In contrast, these data do not satisfy the relationship proposed by Rao-Sahib and Wittry.<sup>2</sup>

Bremsstrahlung emissions by the compounds in this study do not fall on the line predicted from Kramers' law based on the data from pure elements and Eq. (2) for  $\bar{Z}$ . Differences in the measured bremsstrahlung (normalized to Si) from that predicted on the basis of the pure elements and Kramers' law are given in Table 3. Measured radiation for each compound is lower than predicted by a constant fraction, independent of the energy of radiation. Furthermore, the iron oxides appear to form linear arrays with iron metal (e.g.,  $r = 1.000$  in the 15-16keV range); these arrays define a Kramers' law constant different from that for the pure elements, as shown by the different slope for the iron-iron oxide system. These relationships cannot persist to the pure oxygen end-member, since  $\bar{Z}$  extrapolates to a value  $< 0$  at  $\bar{Z} = 8$ .

Author Buseck is with the Departments of Geology and of Chemistry at Arizona State University, Tempe, AZ 85287; author Vander Wood (formerly also with the Chemistry department) is now with Walter C. McCrone Associates, 2820 South Michigan Avenue, Chicago, IL 60616; author Pearson is with the School of Pharmacy, University of Wisconsin, Madison, Wis. We should like to thank D. E. Newberry for valuable comments. Supported by NSF grant ATM-8022849.

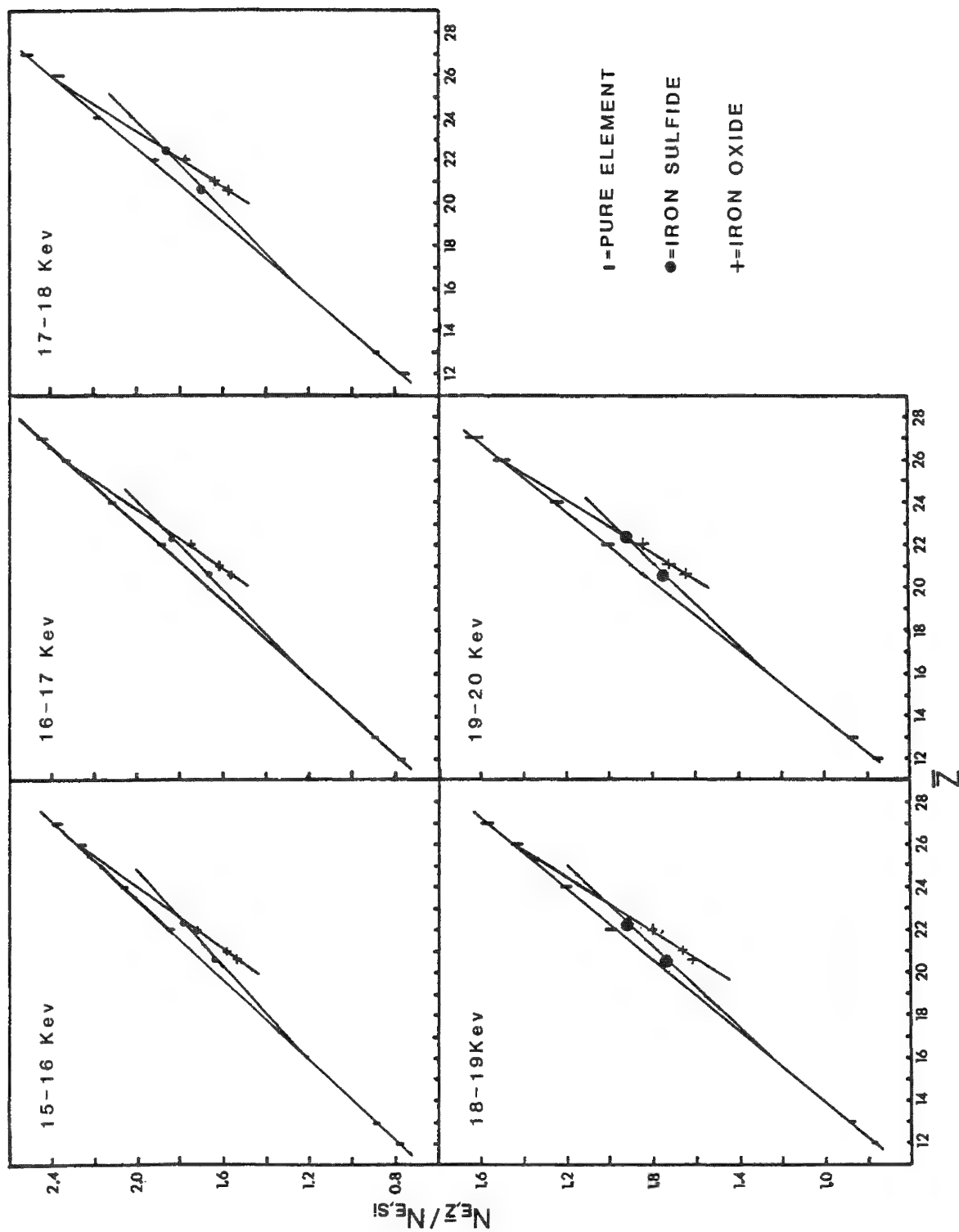


FIG. 1.--Normalized bremsstrahlung radiation vs  $\bar{Z}$ : energy of incident electrons is 25 keV,  $2\sigma$  errors are approximately the height of corresponding symbol.



TABLE 1.--The ratio of x-ray intensity for various samples produced by 25keV electrons and normalized to silicon. Errors are determined from 2 $\sigma$  counting statistics.

Element	$\bar{Z}$	$N_{E,Sample}/N_{E,Si}$				
		15-16 keV	16-17 keV	17-18 keV	18-19 keV	19-20 keV
Mg	12	0.778 $\pm$ .012	0.774 $\pm$ .012	0.763 $\pm$ .014	0.753 $\pm$ .015	0.753 $\pm$ .017
Al	13	0.890 $\pm$ .012	0.879 $\pm$ .013	0.887 $\pm$ .015	0.883 $\pm$ .017	0.863 $\pm$ .018
Ti	22	1.845 $\pm$ .019	1.886 $\pm$ .021	1.926 $\pm$ .025	1.964 $\pm$ .029	2.003 $\pm$ .034
Cr	24	2.063 $\pm$ .017	2.118 $\pm$ .019	2.185 $\pm$ .024	2.208 $\pm$ .027	2.247 $\pm$ .031
Fe	26	2.259 $\pm$ .023	2.327 $\pm$ .025	2.367 $\pm$ .029	2.428 $\pm$ .034	2.508 $\pm$ .040
Co	27	2.379 $\pm$ .026	2.444 $\pm$ .031	2.516 $\pm$ .035	2.569 $\pm$ .040	2.623 $\pm$ .046
FeO	22.07	1.726 $\pm$ .015	1.751 $\pm$ .017	1.770 $\pm$ .020	1.802 $\pm$ .022	1.860 $\pm$ .025
Fe <sub>3</sub> O <sub>4</sub>	21.02	1.589 $\pm$ .013	1.615 $\pm$ .014	1.648 $\pm$ .016	1.654 $\pm$ .020	1.714 $\pm$ .022
Fe <sub>2</sub> O <sub>3</sub>	20.59	1.539 $\pm$ .012	1.561 $\pm$ .014	1.586 $\pm$ .015	1.610 $\pm$ .017	1.650 $\pm$ .020
FeS <sub>2</sub>	20.65	1.638 $\pm$ .015	1.661 $\pm$ .016	1.702 $\pm$ .019	1.728 $\pm$ .021	1.731 $\pm$ .025
FeS	22.35	1.789 $\pm$ .015	1.838 $\pm$ .017	1.865 $\pm$ .019	1.919 $\pm$ .021	1.927 $\pm$ .025

TABLE 2.--Linear correlation coefficients  $Z_{\text{Pure element}}$  vs  $N_{E,\bar{Z}}/N_{E,Si}$ .

Energy Window	r
15-16 keV	1.000
16-17	1.000
17-18	0.999
18-19	0.999
19-20	0.999

TABLE 3.--Measured and predicted bremsstrahlung intensities for compounds:  $\Delta$  = Meas./Pred.; estimated 2 $\sigma$  error  $\pm$ 0.01.

Compound	15-16 keV			16-17 keV			17-18 keV			18-19 keV			19-20 keV		
	Meas.	Pred.	$\Delta$	Meas.	Pred.	$\Delta$	Meas.	Pred.	$\Delta$	Meas.	Pred.	$\Delta$	Meas.	Pred.	$\Delta$
FeO	1.72	1.84	.93	1.75	1.89	.93	1.77	1.91	.92	1.80	1.97	.91	1.86	1.99	.93
Fe <sub>3</sub> O <sub>4</sub>	1.59	1.74	.91	1.61	1.78	.91	1.65	1.81	.91	1.65	1.85	.89	1.71	1.86	.92
Fe <sub>2</sub> O <sub>3</sub>	1.54	1.69	.91	1.56	1.73	.90	1.59	1.76	.90	1.61	1.80	.89	1.65	1.81	.91
FeS <sub>2</sub>	1.64	1.70	.96	1.66	1.76	.94	1.70	1.78	.95	1.73	1.81	.95	1.73	1.81	.95
FeS	1.79	1.88	.95	1.84	1.93	.95	1.86	1.98	.94	1.92	2.01	.95	1.93	2.02	.95

Iron sulfide compounds may also form linear arrays with a pure end member, but in this case the pure element is sulfur (interpolated from the pure element line) rather than iron, and pure iron does not lie along the linear extrapolation. Nonlinear curves may be drawn that pass through both element end members and intermediate compounds.

#### Discussion

Clearly, Kramers' law is not an adequate description of the bremsstrahlung radiation emitted by a set of samples of mixed chemistry, although it appears to hold within a series of samples of related chemistries, e.g., pure elements, alloys, or a series of oxides or sulfides. Furthermore, the differences between bremsstrahlung emitted by the three series of samples appear to be functions of the chemistries of the samples and are not simply dependent on  $\bar{Z}$  and/or energy.

The reasons for these variations are not understood at present. Variations in self-absorption are not expected to be important at the high energies at which these measurements were taken, and there is no sign of absorption-related phenomena in the data. The data might be explained by bulk sample charging beneath the carbon conducting layer re-

sulting in deceleration of the incident electrons. Such an effect may give rise to an exaggerated decrease in the measured bremsstrahlung (compared to the predicted value) for a given compound at higher energies. The data in Table 3 indicate that if such an effect is present, it is at less than the 1% level. It is possible that the discrepancies between the measured and predicted intensities result from unknown chemical effects in the generation of bremsstrahlung radiation.

These observations are important for quantitative analyses of compounds by use of energy-dispersive systems and background modeling in order to remove background radiation from an acquired spectrum. Although these data were acquired at high energies, where there are few analytical peaks, the independence of the effect from energy shown in Table 3 indicates that it persists to lower energies, where background corrections are commonly made. These data indicate that backgrounds modeled on a given series of compounds or alloys may not be indiscriminately used in correcting for background emissions for a differing series of compounds.

### Conclusions

Bremsstrahlung emission between 15 and 20 keV of pure elements  $12 < Z < 27$  appear to obey the linear relationship between  $Z$  and  $N_E$  proposed by Kramers,<sup>1</sup> and are not consistent with the exponential relation proposed by Rao-Sahib and Wittry.<sup>2</sup> The bremsstrahlung emission by compounds is not a simple function of  $Z$ , but appears also to reflect a chemical effect, perhaps based on the electrical insulating properties of the material. Within a given series of compounds (e.g., FeO, Fe<sub>3</sub>O<sub>4</sub>, Fe<sub>2</sub>O<sub>3</sub>) Kramers' law may be obeyed, but it is not obeyed by a sample set incorporating different classes of compounds. This effect is important for attempts to model the background radiation in quantitative energy-dispersive x-ray analysis.

### References

1. H. A. Kramers, "On the theory of x-ray absorption and the continuous x-ray spectrum," *Phil. Mag.* 48: 836, 1923.
2. T. S. Rao-Sahib and D. B. Wittry, "X-ray continuum from thick elemental targets for 10-50 keV electrons," *J. Appl. Phys.* 45: 5060, 1974.
3. P. G. Moreau and D. Calais, "Détermination du numéro atomique moyen d'un binaire homogène ab (solution solide ou composé défini)," *J. Phys.* 25(Suppl.)6: 83, 1964.
4. K. F. J. Heinrich, *Electron Beam X-ray Microanalysis*, New York: Van Nostrand Reinhold, 1981.

$\phi(\rho z)$

R. H. Packwood, J. D. Brown, and Guy Remond

Whether the true form for the ionization distribution has finally been found and placed safely in the collection of microprobe formulas is a question still to be answered. However, there can be no doubt that much time and effort has been spent on the search and it seems to be a good time now to take stock of some of the proposed  $\phi(\rho z)$ 's.

The ionization distribution or  $\phi(\rho z)$  as it may be called for short is a measure of the depth distribution of x-ray production by an electron beam impinging on a target as a function of mass depth  $\rho z$  into the target. It can be measured experimentally by various techniques, the most common of which is the "tracer layer" or "sandwich" technique devised by Castaing and Descamps.<sup>1</sup> This technique records the x rays generated in a similar layer in space.  $\phi(\rho z)$  is a function of electron beam energy  $E_0$ , the critical excitation potential  $E_C$  of the x-ray line of interest, the angle of incidence of the electron beam on the target, and the target composition. The electron beam is considered to strike the target at right angles to its surface in the following account, although other angles could be considered. However, most microprobe analysis employs a normal-incidence angle, which is the easiest configuration to understand.

The importance of  $\phi(\rho z)$  in microprobe analysis lies in the need to calculate how many x rays are generated from the number that are observed. X-ray absorption reduces the observed intensity by a factor that increases exponentially with mass thickness  $\rho x$  along the direction of observation (Beer's law):

$$I = I_0 \exp\{-\mu\rho x\}$$

where  $I_0$  and  $I$  are the initial and observed intensities, respectively, and  $\mu$  is the mass absorption coefficient. The number of x rays  $I_A^{\text{unk}}$  generated for element A is assumed to be proportional to the weight fraction  $W_A$  of A in the unknown sample material. Hence the observed intensity ratio  $k_A$  for the unknown versus the intensity  $I_A$  from pure A is given by

$$k_A = \frac{I_A^{\text{unk}}}{I_A} = W_A \frac{\int_0^\infty \phi_A^{\text{unk}}(\rho z) \exp\{-\chi_A^{\text{unk}} \rho z\} d\rho z}{\int_0^\infty \phi_A(\rho z) \exp\{-\chi_A \rho z\} d\rho z} \quad (1)$$

where  $\chi = \mu \csc \theta$  and  $\theta$  is the x-ray take-off angle.

#### Review of $\phi(\rho z)$ Formulas

When Castaing<sup>2</sup> first addressed the problem of determining  $\phi(\rho z)$  experimentally he made measurements on a cylindrical target that allowed him to vary the x-ray take-off angle. The results led him to believe that  $\phi(\rho z)$  decreased with depth in a manner that was roughly exponential. Thus, he based his analysis on the work of Lenard,<sup>3</sup> who had measured the transmission of electrons through thin foils and found that the transmitted flux  $I_x$  at thickness  $\rho x$  was

$$I_x \cong I_0 \exp\{-\sigma\rho z\}$$

where  $I_0$  is the initial flux and  $\sigma$  is the Lenard coefficient. Hence  $\phi(\rho z) = \text{const.} \exp\{-\sigma\rho z\}$  (Fig. 1). It is probably true that most, if not all, microprobe correction programs still

Author Packwood is at Energy, Mines and Resources Canada, Ottawa; author Brown is in Engineering Science at the University of Western Ontario, London, Ont., Canada; and author Redmond is at the Bureau de Recherches Géologiques et Minières, Géochemie-Analyses, Orléans, France. The assistance of V. C. Chartrand in preparing the illustrations is acknowledged.

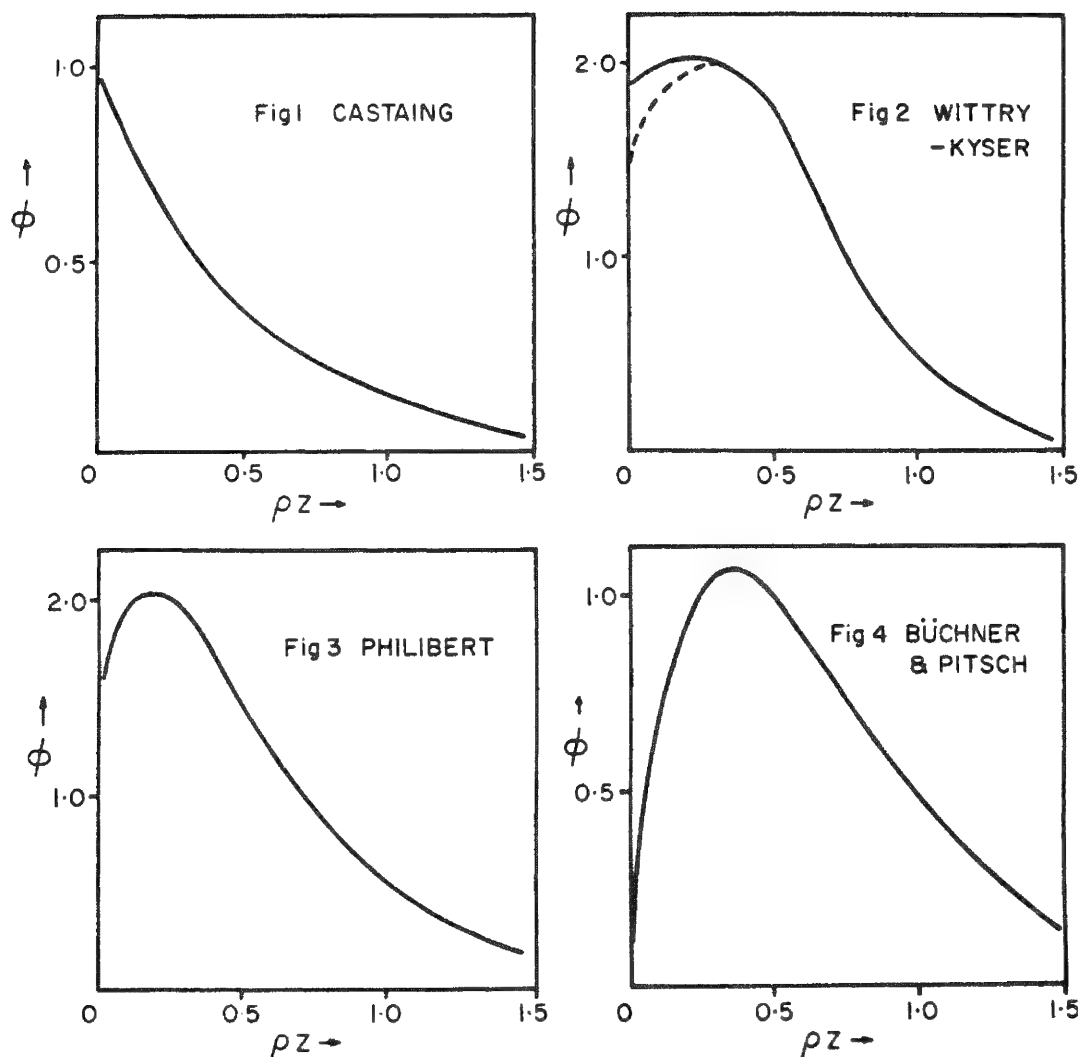


FIG. 1.--Castaing with Lenard's  $\sigma = 2000$ . FIG. 2.--Wittry with  $a = 2.21$ ,  $\rho z_0 = 0.224$  scaled to match Ref. 1. FIG. 3.--Philibert with  $\sigma = 2000$ ,  $h = 0.4$ ,  $R_0 = 1.5$  scaled to match Ref. 1. FIG. 4.--Büchner and Pitsch,  $a = 1.4$ ,  $n = 1.56$ ; note scale on vertical axis.

use this form of  $\phi(\rho z)$ , not in the absorption correction but in the fluorescence factor. In 1955 Castaing and Descamps<sup>1</sup> made the first systematic  $\phi(\rho z)$  measurements, only to discover that the generated intensity did not fall with depth but instead increased to a maximum at a value approximately 50% greater than the surface value  $\phi_0$ , and then decreased.

The value for  $\phi(\rho z)$  at the surface was not equal to 1 as might be expected but instead was around 1.5. This was the result of electrons backscattered out of the subsurface layers, which increased the total electron flux at the surface vis-à-vis the thin layer in space. The increase in  $\phi(\rho z)$  with depth was caused by the paths of the electrons diverging away from their initial direction perpendicular to the tracer layers buried in the target, which made these paths in each layer longer than in the isolated reference layer. The x-ray ionization cross section also changes with the overvoltage ratio  $U = E/E_C$ , and it may either increase or decrease the rate of x-ray production, depending on the variation of starting  $U$  with path length into the target.

In 1958 Wittry put forward the notion that the electron beam could only penetrate the target a short distance before becoming randomized. This situation was described by a Gaussian distribution with its center placed at the depth of maximum x-ray production  $\rho z_0$ ;

$$\phi(\rho z) = \text{const.} \exp\{-a_1(\rho z - \rho z_0)^2\} \quad (2)$$

as shown in Fig. 2. The factors used in this formula and its successor<sup>5</sup> require some prior

knowledge of the value of the  $\rho z_0$  parameter, which is possibly why it has not been used by many workers.

The next  $\phi(\rho z)$  curves put forward were those of Philibert<sup>6</sup> in 1963. First was the full formula, which assumed that  $\phi(\rho z)$  is given by a function of the form

$$\phi(\rho z) = \text{const.} \exp\{-\sigma \rho z\} (1 - q \exp\{-\sigma \rho z/h\}) \quad (3)$$

with  $q = (4 - \phi_0)/4$  and  $h = 1.2A/Z^2$  (Fig. 3). The second was an approximate formula where  $q = 1$ ; i.e.,  $\phi_0 = 0$ , which of course is incorrect. However, at that time  $\phi_0$  was not known for many elements and this approximation had little effect for the small-to-moderate absorption conditions for which it was proposed. In the light of subsequent events, such as the frequent misapplication of the formula, a lot of unnecessary criticism could have been avoided by setting  $\phi_0 = 1.5$  and adjusting  $h$  to  $h = 0.5A/Z^2$ . However, be that as it may, Philibert's approximate formula has enjoyed wide use and a very large measure of success by the subsequent modifications to the value of  $\sigma$  by Duncumb<sup>7</sup> and Heinrich.<sup>8</sup>

In 1966 Criss and Birks<sup>9</sup> proposed the expression

$$\phi(\rho z) = \sum_{i=1}^n a_i \exp\{-b_i \rho z\} \quad (4)$$

where the constants  $a_i$  and  $b_i$  are to be determined for the case in question. Although capable of representing  $\phi(\rho z)$  with great precision, the absence of measured  $\phi(\rho z)$  curves at that time handicapped this method. The example shown gave the coefficients to  $n = 5$  for copper at 29 keV.

Also shown in Fig. 2 is the modification of the shifted Gaussian suggested by Kyser<sup>5</sup> in 1971, namely, an exponential term that is subtracted from the near surface zone:

$$\phi(\rho z) = \text{const.} [\exp\{-a_1(\rho z - \rho z_0)^2\} - \text{const.} \exp\{-a_2 \rho z\}] \quad (5)$$

This form was so well established as far as Kyser was concerned that he used it as part of a method for determining absorption coefficients for soft x rays!

At about the same time Büchner and Pitsch<sup>10</sup> proposed a somewhat different form of  $\phi(\rho z)$ :

$$\phi(\rho z) = a n (\alpha \rho z)^{n-1} \exp\{-(\alpha \rho z)^n\} \quad n = \frac{205 - Z}{113}, \quad a = [\alpha / (E_0 - E_c)]^\beta \quad (6)$$

where  $\alpha = 34 - 0.7E_c + [36/(2.25 + E_c^2)]$  and  $\beta = 1.5 - (E_c/27)$ .

These factors were determined empirically from  $\phi(\rho z)$  curves measured by the wedge method.<sup>11</sup> Again,  $\phi_0 = 0$  is an obvious drawback to this form of  $\phi(\rho z)$ .

At this time, Reuter<sup>12</sup> proposed somewhat different parameters for Philibert's complete formula with a view to using it for the analysis of thin films on substrates. More recently, Love et al.<sup>13</sup> in 1977 extended this process to obtain better quantification--but still maintained the basic Philibert formula.

Almost as a protest against the increasing complexity of the suggested  $\phi(\rho z)$  formulas, Bishop<sup>14</sup> in 1975 advanced the idea of replacing them by a simple square-wave model for use in moderate-absorption conditions (Fig. 5):

$$\begin{aligned} \phi(\rho z) &\cong \phi_0 & \rho z &\leq 2\overline{\rho z} \\ \phi(\rho z) &= 0 & \rho z &> 2\overline{\rho z} \end{aligned} \quad (7)$$

This decisive application of Occam's razor yields surprisingly good results.

In 1976 Heinrich<sup>15</sup> suggested that  $\phi(\rho z)$  could be written as

$$\phi(\rho z) = \frac{\rho z}{a\gamma} \exp\{-\rho z/a\gamma\} \quad (8)$$

with  $\gamma = f(E_0^n, E_c^n)$  and  $a = f(\rho z, \rho z_0)$ . This form has the  $\phi_0 = 0$  problem that Heinrich resolved by moving the  $\phi$  axis to positive  $\rho z$ ; at the same time the  $\rho z$  axis is lifted to cut off the exponential tail in the  $\phi(\rho z)$  distribution at large  $\rho z$  values because that was known to be incorrect, too. The resulting  $\phi(\rho z)$  is much easier to draw than it is to write out (Fig. 6)! The mathematical form is shown in Heinrich's book on microprobe analysis.<sup>16</sup>

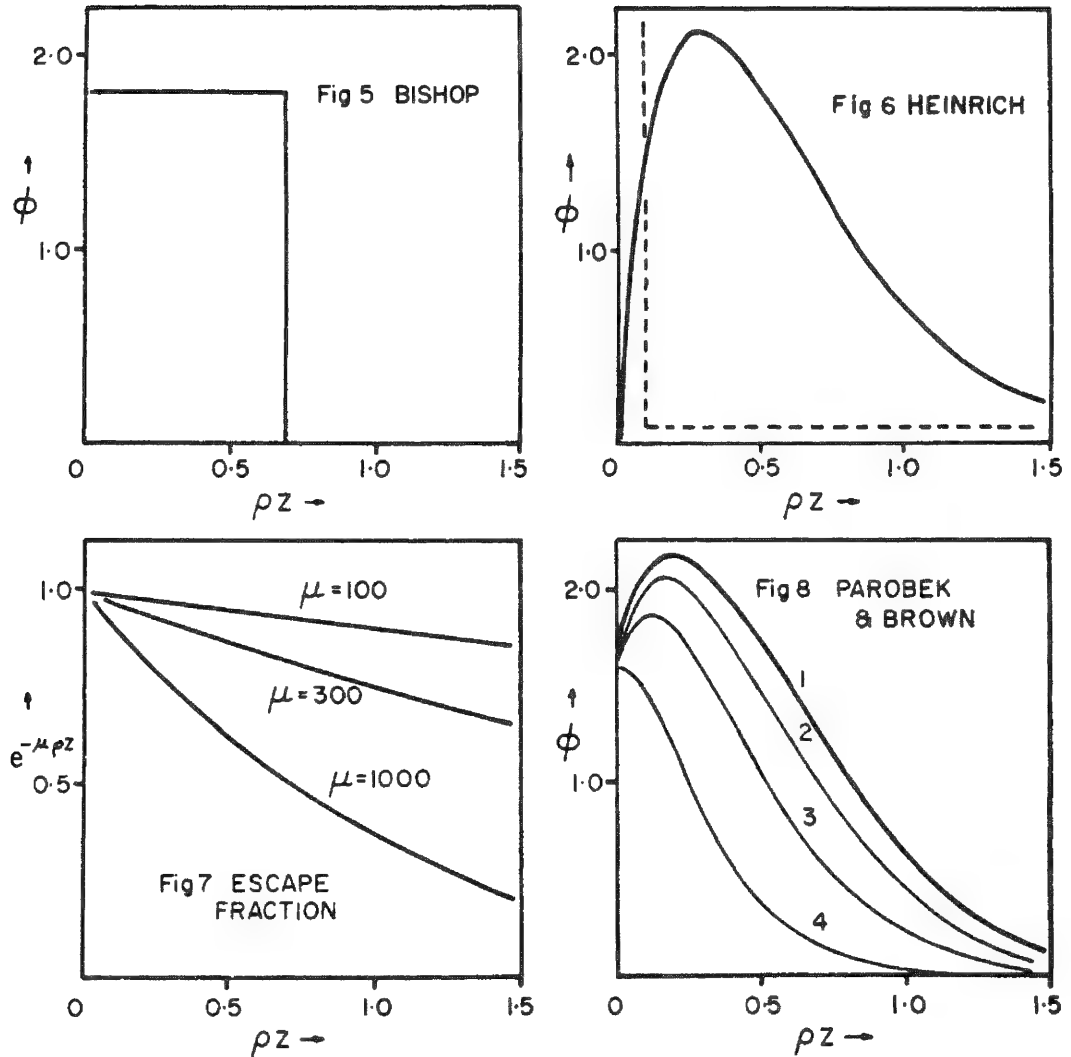


FIG. 5.--Bishop with  $\phi_0$  from Ref. 1,  $\rho z_0$  from Philibert formula.. FIG. 6.--Heinrich from  $\phi$  in Ref. 16 scaled to match Fig. 8. FIG. 7.--Fraction of x rays escaping as a function of depth and mass absorption coefficient. FIG. 8.--Curve 1, experimental and Gaussian fit to ZnKa in Cu at 30 kV; curves 2, 3, 4, "observed  $\phi(\rho z)$ " for  $\chi = 300, 900$ , and 3000, respectively.

While these various models were being developed, a number of workers were making measurements of  $\phi(\rho z)$  curves and so increasing the database on which to build more realistic analytical expressions for  $\phi(\rho z)$ . Among them, Parobek and Brown<sup>17</sup> in 1978, and later Brown and Robinson,<sup>18</sup> used their data to develop an empirical formula for  $\phi(\rho z)$  that could be used to interpolate accurately between the actual  $\phi(\rho z)$  measurements.

Most recently a theoretical form for  $\phi(\rho z)$  has been proposed by Packwood and Brown<sup>19,20</sup> based on the observation that essentially all published  $\phi(\rho z)$  curves can be plotted as  $\ln \phi(\rho z)$  versus  $(\rho z)^2$  to yield straight lines. Only a segment at the surface, the part that rises from  $\phi_0$  to peak intensity, follows another relationship. From this result it was deduced that

$$\phi(\rho z) = \gamma_0 \exp\{-(\alpha \rho z)^2\}(1 - q \exp\{-\beta \rho z\}) \quad (9)$$

The transient term has the same purpose as the transient in Philibert's formula--namely, to model the increasing path length per tracer layer as the electrons diverge from the direction of the incident beam;  $\alpha$  and  $\beta$  are parameters of the Gaussian and transient regions and  $q = (\gamma_0 - \phi_0)/\gamma_0$ , where  $\gamma_0$  is the peak value of the Gaussian at the sample surface.

The question arises, why can be so many apparently diverse equations used to perform this function in microprobe analysis? The answer is in several parts: the formulas have

not the same applications; some are intended for use only in certain well-specified circumstances, whereas others have more general application.

As is well known, correcting observed intensity to generated intensity can be done in two distinct ways. The first is the ZAF method, which treats the absorption correction via ratios of observed to generated intensities on a relative basis, leaving differences in total x-ray generation to an atomic-number correction term

$$k_A^{\text{unk}} = f(\chi)^{\text{unk}} = W_A \frac{\int_0^\infty \phi_A^{\text{unk}}(\rho z) \exp\{-\chi_A^{\text{unk}} \rho z\} d\rho z}{\int_0^\infty \phi_A^{\text{unk}}(\rho z) d\rho z} \quad (10)$$

A second such term is required for the standard. This method makes smaller demands on the accuracy of  $\phi(\rho z)$ . Figure 7 shows a plot of  $\exp\{-\mu \rho z\}$  for a selection of  $\mu$  values typical of those encountered in microprobe analysis:  $\mu = 100, 300, 1000$ . With such values for  $\mu$ , the integral in the numerator of Eq. (10) is simply the area under the  $\phi(\rho z)$  curve when multiplied by the appropriate  $\exp\{-\chi \rho z\}$  curve. The result is a distorted  $\phi(\rho z)$  (Fig. 8). The severity of the distortion depends on the magnitude of  $\chi$ . Evidently, the shape of  $\phi(\rho z)$  is not all that critical for  $\chi = 300$  or  $900$  and yet when  $\chi = 3000$  the details of the shape in the surface become important if the transformation of the true  $\phi(\rho z)$  is to be accurately imitated. This is best done by having the right shape, of course!

The second correction method for microprobe data, the " $\phi(\rho z)$  method," depends critically on the size and shape of the model  $\phi(\rho z)$  curves being accurate replicas of the true distributions. Should that be the case, then Eq. (1) can be evaluated and the electron-generated x-ray signal calculated in one step. Only the fluorescence correction has to be dealt with separately. Parobek and Brown,<sup>17</sup> Brown and Robinson,<sup>18</sup> and later Brown and Packwood<sup>21</sup> chose to use the  $\phi(\rho z)$  correction method with reasonable success.

We now comment on how to perform the Laplace transformations of the functions in Eqs. (1)-(9) and the level of complexity found in the mathematics.

Philibert's complete formula gives an absorption correction

$$f(\chi) = \frac{1 + h(1 - q)[1 + (\chi/\rho)]}{[1 - qh/(1 + h)][1 + (\chi/\sigma)][1 + h[1 + (\chi/\sigma)]]} \quad (11)$$

Setting  $q = 1$  gives the widely used approximate formula. The Gaussian  $\phi(\rho z)$ 's give integrals that involve  $\text{erf}(x)$  or  $\text{erfc}(x)$  terms that are a little unfamiliar, but present no real problem. Büchner and Pitsch<sup>22</sup> show that their  $\phi(\rho z)$  produces an integral that sums a series of gamma functions. In a subsequent paper, tables of correction factors are given in order to make the method easier to apply.

The Bishop method gives a particularly simple formula for  $f(\chi)$ :

$$f(\chi) = \frac{1 - \exp\{-2\chi\bar{\rho z}\}}{2\chi\bar{\rho z}} \quad \bar{\rho z} = \frac{2h + 1}{h} \frac{E_0^{1.65}}{4.5 \times 10^5} (1 - U^{-1.65}) \quad (12)$$

Setting  $h = 0$  in Eq. (11) gives Castaing's original  $\phi(\rho z)$  integral. The expressions used by Parobek, Brown, and Robinson cannot be integrated analytically; however, the equations can be readily handled by a numerical integration routine on a computer. On the other hand, the Packwood and Brown  $\phi(\rho z)$  can be integrated and yields (this is the correct formula when the Gaussian term is written  $\exp\{-\alpha^2 x^2\}$ ; the version in Ref. 18 was inadvertently given for  $\exp\{-\alpha x^2\}$ ):

$$\int_0^\infty \phi(\rho z) \exp\{-\chi \rho z\} d\rho z = \frac{\gamma_0}{\alpha} [\exp\{(\chi/2\alpha)^2\} \text{erfc}\{\chi/2\alpha\} - q \exp\{[(\beta + \chi)/2\alpha]^2\} \text{erfc}\{[(\beta + \chi)/2\alpha]\}] \quad (13)$$

Equation (13) is not the most comfortable of equations but the literature shows accurate approximation formulas for  $\text{erfc}(x)$ . Those by Hastings<sup>23</sup> involve an  $\exp(-x^2)$  which fortunately eliminates the  $\exp(x^2)$  in the integral, with the result that Eq. (13) becomes



$$\int_0^{\infty} \phi(\rho z) \exp\{-\chi \rho z\} d\rho z \approx \frac{\gamma_0}{\alpha} \left\{ A \left[ \frac{\chi}{2\alpha}, 5 \right] - qA \left[ \frac{\beta + \chi}{2\alpha}, 5 \right] \right\} \quad (14)$$

As shown in the Appendix,  $A(x, 5) = \sum_{i=1}^5 (a_i t^i)$  with  $t = (1 + px)^{-1}$ ;  $a_i$  and  $p$  are constants.

Examples of the application of these various  $\phi(\rho z)$  formulas are to be found in the literature cited.

### *Novel Applications of the Gaussian $\phi(\rho z)$ Formula*

Surface layers, deposits, coatings, or contamination are of considerable interest in experimental science, e.g., electronic devices, corrosion studies, trace element analyses, etc. It can be demonstrated that the Gaussian  $\phi(\rho z)$  approach lends itself to studying these phenomena if a small assumption is made. Suppose that the surface film is of thickness  $\delta$ ; thus, when it is very thin, the exact distribution is not crucial, and can be conveniently described as a Gaussian concentration distribution of magnitude  $A$  and form  $A \exp\{-(\rho z/\delta)^2\}$ . This term can be incorporated into Eq. (13) very simply because the multiplication of exponential terms is accomplished by addition of their exponents; so the new form can be obtained from the old by the simple expedient of replacing  $\alpha^2$  by  $(\alpha^2 + \delta^2)$ . It may appear a little arbitrary, but the procedure arose out of work of a very practical nature. Remond et al.,<sup>24</sup> when measuring trace quantities of Ag in chalcopyrite ( $\text{CuFeS}_2$ ) inclusions in an acanthite ( $\text{Ag}_2\text{S}$ ) matrix, discovered a strange phenomenon. During and after polishing, the chalcopyrite grains rapidly became colored either orange or yellow depending on their distance from the acanthite. The same grains showed Ag concentrations that varied with the electron beam energy as shown in Table 1. Suspicion of surface contamination was confirmed by Auger analysis combined with ion milling. Further work with optical reflectometry was also consistent with the general thickness and composition determined by electron spectroscopy; i.e.,  $150\text{\AA} \rightarrow 30\text{\AA}$  and  $80\% \rightarrow 30\%$  Ag for orange and yellow grains, respectively. These estimates for  $A$  and  $\delta$  gave rise to the predicted "false" compositions shown in Table 1. More details will be found in the proceedings of this year's SEM conference.<sup>25</sup>

It is not a new idea,<sup>26, 27</sup> but nevertheless it is still intriguing to consider the possibility of analyzing very thin surface films with the microprobe. A simple order-of-magnitude calculation based, for example, on monolayer of tungsten gives a signal equivalent to about 0.2% of that expected from the solid. A signal of that size hardly presents a challenge for any modern microprobe. It is tacitly assumed that the film is different from the substrate and that the substrate does not contain significant quantities of the elements in the film to be measured, otherwise data would have to be taken at different electron beam potentials and processed in a fashion analogous to that described in the previous paragraph. Corrosion inhibitors, at least, are generally different from the metal to be protected (phosphate, chromate, molybdate, tungstate, etc.). Table 2 shows some preliminary results for various inhibitors on a 1010 steel. The equivalent number of monolayers is also noted and must not be taken to indicate that nothing else is present, because obviously that would be untrue. A more detailed report of this work is to be published elsewhere.

It should be pointed out that the excellent work by Mitchell and Sewell<sup>27</sup> was on a low-angle, low-energy electron beam, soft x-ray spectrometer, high-vacuum apparatus they had

TABLE 1.--Intensity ratios for Ag from Ag-rich surface film on chalcopyrite grains.

keV	Orange coloured		Yellow coloured	
	Observed	Predicted (a)	Observed	Predicted (b)
8	3.69	3.92	0.61	0.60
15	1.09	1.08	0.18	0.16
30	0.45	0.43	0.075	0.13

TABLE 2.--X-ray intensities from corrosion inhibitor films on 1010 steel at 10 keV.

Inhibitor	Counts above background	
	per 120 seconds*	Equivalent mono-layers
Chromate	800 $\pm$ 30/(195,000)	~4
Molybdate	40 $\pm$ 25/(290,000)	~0.25
Tungstate	600 $\pm$ 60/(106,000)	~0.25

\*Standard intensity shown in parenthesis.

developed that could detect 0.01 of a monolayer of surface species, whereas an unmodified Camebax MICRO is being used in the current work.

### References

1. Raymond Castaing and Jacques Descamps, "Sur les bases physiques de l'analyse ponctuelle par spectrographie X," *J. Phys. Radium* 16: 304-317, 1955.
2. Raymond Castaing, "Application of electron probes to local chemical and crystallographic analysis," Publ. No. 55, Office National d'Etudes et de Recherches Aeronautique, Chatillon-sous-Bagneux (Seine), 1951.
3. P. Lenard, *Ann. Phys. Chem.* 56: 255, 1895, or *Quantitatives über Kathodenstrahlen*, Heidelberg, 1918.
4. D. B. Wittry, "Resolution of electron probe microanalyzers," *J. Appl. Phys.* 29: 1543-1548, 1958.
5. D. F. Kyser, "Experimental determination of mass absorption coefficients for soft x-rays," *6th Int. Conf. X-ray Optics and Microanal.* (ICXOM)/1971, 147-156.
6. Jean Philibert, "A method for calculating the absorption correction in electron-probe microanalysis," *3rd ICXOM/1963*, 379-392.
7. Peter Duncumb and P. K. Shields, "Effect of critical excitation potential on the absorption correction," in T. D. McKinley, K. F. J. Heinrich, and D. B. Wittry, Eds., *The Electron Microprobe*, New York: Wiley, 1966, 284-295.
8. K. F. J. Heinrich, "Common sources of error in electron probe microanalysis," in J. B. Newkirk, G. R. Mallett, and H. G. Pfeiffer, Eds., *Adv. X-ray Anal.* 11: 40-55, 1967.
9. J. W. Criss and L. S. Birks, "Intensity formulae for computer solution of multicomponent electron probe specimens," in T. D. McKinley, K. F. J. Heinrich, and D. B. Wittry, Eds., *The Electron Microprobe*, New York: Wiley, 1966, 217-236.
10. A. R. Büchner and Wolfgang Pitsch, "A new correction for absorption and for atomic number in quantitative microprobe analysis of metals," *Zeit. Metall.* 62: 392-400, 1971.
11. V. Schmitz et al., "An experimental method for determining the depth distribution of characteristic x-rays in electron microprobe specimens," *5th ICXOM/1968*, 104-113.
12. W. Reuter, "The ionization function and its application to the electron probe analysis of thin films," *6th ICXOM/1971*, 121-130.
13. G. Love et al., "Assessment of Philibert's absorption correction models in electron-probe microanalysis," *J. Phys. D-8*: 1686-1702, 1975.
14. H. E. Bishop, "The prospects for an improved absorption correction in electron probe microanalysis," *J. Phys. D-7*: 2009-2020, 1974.
15. K. F. J. Heinrich, "Analytic model for the depth distribution of direct X-ray generation in the target bombarded by electrons," *Microbeam Analysis--1976*, #26.
16. K. F. J. Heinrich, "Electron-beam X-ray Microanalysis," New York: Van Nostrand Reinhold, 1981, 295.
17. Len Parobek and J. D. Brown, "The atomic number and absorption corrections in electron microprobe analysis at low electron energies," *X-ray Spectrom.* 7: 26, 1978; 8: v, 1979.
18. J. D. Brown and W. H. Robinson, "Quantitative analysis by  $\phi(\rho z)$  curves," *Microbeam Analysis--1979*, 238-242.
19. R. H. Packwood and J. D. Brown, "A Gaussian expression to describe  $\phi(\rho z)$  curves for quantitative electron probe microanalysis," *X-ray Spectrom.* 10: 138-146, 1981.
20. R. H. Packwood and J. D. Brown, "Concerning x-ray production and quantitative analysis," *Microbeam Analysis--1980*, 45-48.
21. J. D. Brown and R. H. Packwood, "Quantitative electron probe microanalysis using gaussian  $\phi(\rho z)$  curves," *X-ray Spectrom.* 11: 187-193, 1982.
22. A. R. Büchner and Wolfgang Wepner, "Berechnung von Tafeln der Absorptions- und Ordnungszahlkorrektur für quantitative Analyse mit der Mikrosonde," *Archiv. Eisenhütten* 42: 565-573, 1971.
23. C. Hastings Jr., "Approximations for digital computers," Princeton, N.J.: Princeton University Press, 1955.
24. Guy Remond et al., "Bulk and surface silver diffusion related to tarnishing of sulphides," *SEM/1982*.
25. Guy Remond et al., "The effect of volume and surface diffusion of impurities on the detection limit in microprobe analysis," *SEM/1983* (in press).
26. G. H. Crockett and C. D. Davies, "Coating thickness measurement by electron probe microanalysis," *Brit. J. Appl. Phys.* 14: 813-816, 1963.

27. D. F. Mitchell and P. B. Sewell, "Quantitative determination of oxygen in thin oxide films on metals by electron excited x-ray emission," *Thin Solid Films* 23: 109, 1974.

28. R. H. Packwood and J. D. Brown, "A new theory for microprobe analysis," *Canadian Met. Quart.* 1983 (in press).

#### Appendix

$$\text{erf}(z) = 1 - (ax + bx^2 + cx^3 + dx^4 + ex^5) + \varepsilon(x) = 1 - A(x,5)$$

$$x = (1 + pz)^{-1}, p = 0.3275911$$

$$a = 0.254829592$$

$$b = -0.284496736$$

$$c = 1.421413741$$

$$d = -1.453152027$$

$$e = 1.061405429 \text{ and } \varepsilon(x) \leq 1.5 \cdot 10^{-7}$$

$$\text{erfc}(z) = 1 - \text{erf}(z)$$

## MEASUREMENTS OF $\phi_0$ --THE SURFACE IONIZATION COEFFICIENT FROM C-K $\alpha$ TO Cu-K $\alpha$

S. B. Hale and R. H. Packwood

$\phi_0$  is defined as the ratio of x rays generated by an electron beam in a thin layer in the surface of a target to x rays generated in an identical thin film isolated in space.

It is a good question to ask, "Why do we need to know  $\phi_0$ ?" because it is true that the most popular method for correcting microprobe data to date, the ZAF method with the simplified Philibert correction, has always assumed that  $\phi_0 = 0$ , even though theoretically  $\phi_0$  must have a minimum value of unity. In general, therefore,  $\phi_0$  has not been considered a major concern, at least not for the majority of microprobe users.

However, there always has been a need for  $\phi_0$  values, even in the ZAF method, because as absorption increases so does the importance of having an accurate representation of the x-ray production in the vicinity of the surface of the target.

Another situation demanding a knowledge of  $\phi_0$  is the analysis of surface films. Here, the intensity of excitation of the film is by definition equal to  $\phi_0$ .

More recently, concerted efforts by various authors<sup>1-3</sup> to develop the " $\phi(\rho z)$  method" as a strong alternative to the ZAF method has led to considerable interest in determining  $\phi_0$  for as large a set of conditions and atomic numbers  $Z$  as possible. For example, in the Gaussian descriptions<sup>3,4</sup> of  $\phi(\rho z)$ ,  $\phi_0$  is one of four parameters used to model the x-ray generation in the sample.

As a practical matter, we need to know  $\phi_0$  at electron beam voltages below 10 kV and critical excitation potentials  $E_c$  in the soft x-ray range, as well as the variation of  $\phi_0$  with the angle of incidence of the electron beam on the target.

With these considerations in mind, we find there are comparatively few  $\phi_0$  determinations<sup>5,6</sup> and none at very low critical excitation values. There are at least three theoretical formulas for  $\phi_0$ ,<sup>4,7,8</sup> none of them applicable to soft x rays or tilted targets.

Before one looks at these formulas it is worth examining the parameters that will affect the magnitude of  $\phi_0$ . We know the following.

a.  $\phi_0 > 1$ , which follows by inspection from the definition and the physical fact of backscattering of electrons from the substrate (how much greater than unity depends on these factors);

b. the fraction  $\eta$  of the electron flux that is backscattered and its distribution with respect to energy  $E$  and direction  $\alpha$ :

i. energy because the ionization cross section  $Q(u)$  is a strong function of  $E/E_c$ ,

ii. direction because the longer the path of an electron at a given depth the greater the chance of producing an x ray.

Measurements of the backscattered electron distribution<sup>9</sup> shows strong dependencies on both  $E$  and  $Z$ , which means that accurate theoretical predictions will be difficult to make and cumbersome to use. Therefore, it is most likely that a semi-empirical equation will suffice. The  $\phi_0$  formulas available at present are examples of such equations:

$$\phi_0 = 1 + 2.8\eta[1 - (0.9/U)] \quad \text{Reuter}$$

$$\phi_0 = 1 + \frac{\eta}{1 + \eta} [I(U_0) + G(U_0)\ln(1 + \eta)] \quad \text{Love, Scott and Cox}$$

$$\phi_0 = 1 + \pi\eta[Q(U_{0.5})/Q(U_0)] - \eta \quad \text{Packwood and Brown}$$

---

Author Hale is a masters student at The University of Western Ontario, London, Ont., Canada N6A 5B9, studying electron probe microanalysis; author Packwood is a research scientist at the Department of Energy, Mines and Resources, Ottawa, Canada. The assistance of V. E. Moore in taking measurements is gratefully acknowledged.

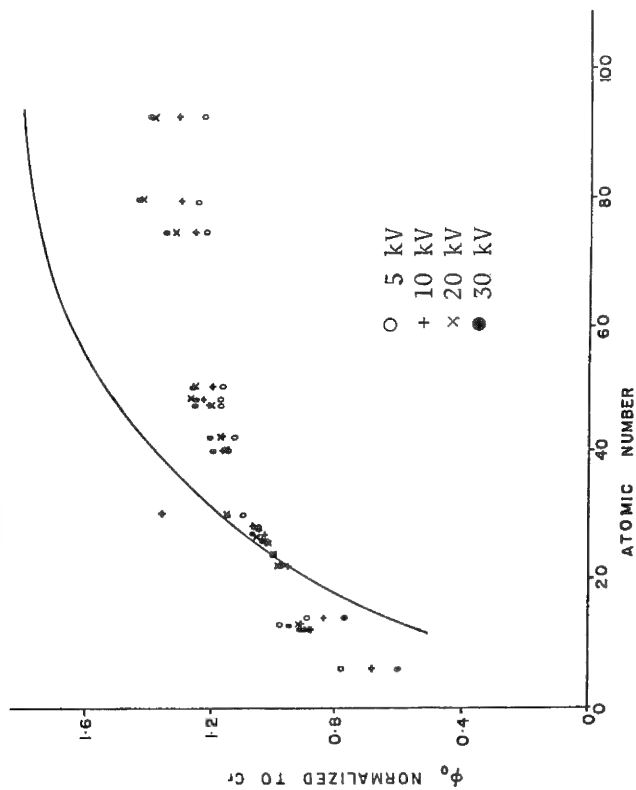


FIG. 1.-- $\phi_0$  measurements of Cu La x rays from copper-coated substrates normalized to Cr; solid line is Reuter's equation at 10 kV.

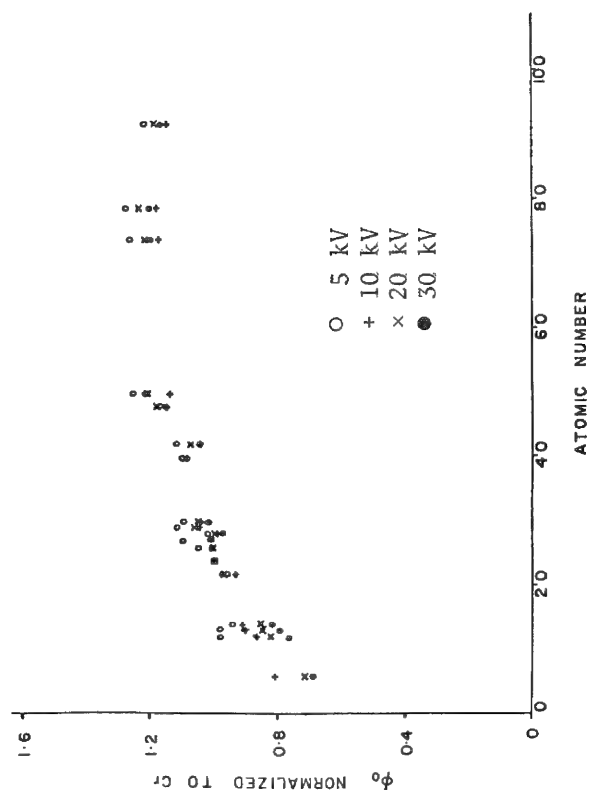


FIG. 3.-- $\phi_0$  measurements of Ag La x rays from silver-coated substrates normalized to Cr.

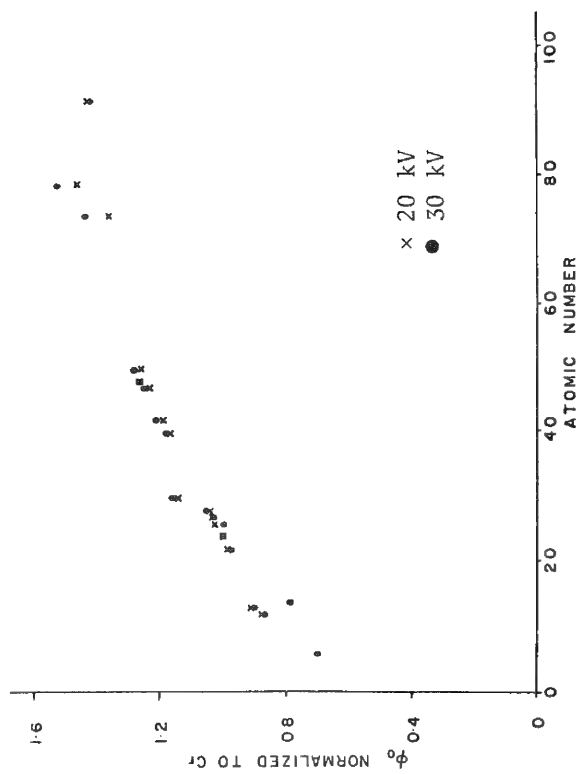


FIG. 2.-- $\phi_0$  measurements of Cu Ka x rays from copper-coated substrates normalized to Cr.

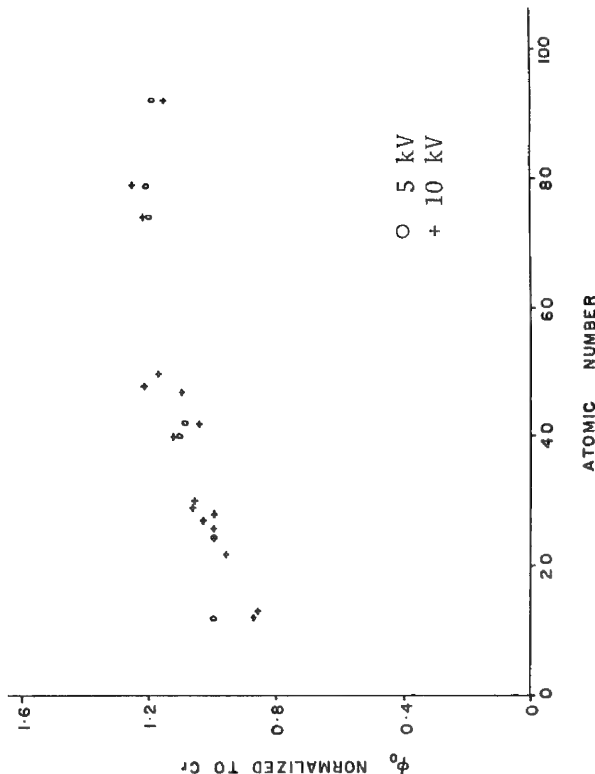


FIG. 4.-- $\phi_0$  measurements of C Ka x rays from carbon-coated substrates normalized to Cr.

where  $I(U_0)$  and  $G(U_0)$  are polynomials in  $U_0$ , are examples of such equations.

In order to see which, if any, of the above are suitable for soft x-ray work, and possibly adaptable to tilted targets, we made a series of experiments.

### Experimental Method

A microprobe standard sample holder containing 17 metals was used as the basic suite of elements. Those present were Mg, Al, Ti, Cr, Fe, Co, Ni, Cu, Zn, Zr, Mo, Ag, Cd, Sn, W, Au, and U, to which was added Si and BN in separate holders. Thin films of carbon, copper, and silver were evaporated onto one half of each polished standard.

The coated samples were tested in a CAMEBAX-MICRO electron probe at electron beam voltages of 5, 10, 20 and 30 kV, at normal electron incidence. Several regions were chosen and count times were such that several thousand counts were collected for each element. The backgrounds were recorded from the uncoated region of the samples.

For carbon, special care was taken to insure that contamination was not a problem. The electron probe vacuum was better than  $2 \times 10^{-6}$  torr. The special soft x-ray spectrometer, when operated with a reduced pressure of 150 mm Hg of P-25 in the proportional counter, is capable of reading 150 000 cps/100 nA from diamond.

Typical plots of  $\phi_0$  normalized to Cr are shown in Figs. 1 through 4. Figure 1 also shows the relationship between Reuter's equation for  $\phi_0$  and the experimental data. The data have not yet been corrected for fluorescence.

### Conclusions

In conclusion, the experimental evidence suggests that any semi-empirical equation for  $\phi_0$  will have an exponential format. Further investigation, however, is required to determine the final form of the equation.

### References

1. J. D. Brown and W. H. Robinson, "Quantitative analysis by  $\phi(\rho z)$  curves," *Microbeam Analysis--1979*, 238-240.
2. J. D. Brown, R. H. Packwood, and K. Milliken, "Quantitative electron probe microanalysis with Gaussian expression for  $\phi(\rho z)$  curves," *Microbeam Analysis--1981*, 174.
3. L. Parobek and J. D. Brown, "X-ray production as a function of depth for low energies," *X-ray Spec.* 5: 36-40, 1976.
4. R. H. Packwood and J. D. Brown, "A Gaussian expression to describe  $\phi(\rho z)$  curves for quantitative electron probe microanalysis," *X-ray Spec.* 10: 138-146, 1981.
5. V. E. Cosslett and R. N. Thomas, "Multiple scattering of 5-30 kV electrons in evaporated metal films: III. Backscattering and absorption," *Brit. J. Appl. Phys.* 16: 779-795, 1965.
6. H. J. Fitting, "The energy loss of transmitted and backscattered electrons," *J. Phys.* D-8: 1480-1486, 1975.
7. W. Reuter, "The ionization function and its application to the electron probe analysis of thin films," *Proc. 6th Intern. Conf. X-ray Optics and Microanalysis*, 121-130.
8. G. Love, M. G. C. Cox, and V. D. Scott, "Assessment of Philibert's absorption correction models in electron probe microanalysis," *J. Phys.* D-11: 1369-1372, 1978.
9. H. E. Bishop, "Some electron backscattering measurements for solid targets," in R. Castaing et al., Eds., *X-ray Optics and Microanalysis*, Paris: Hermann, 1966, 153-158.





### 3 Laser Microbeam Mass Analysis

#### MICROANALYSIS OF BULK SAMPLES BY LASER-INDUCED ION MASS ANALYSIS

C. A. Evans Jr., B. W. Griffiths, Trevor Dingle, M. J. Southan, and A. J. Ninham

Laser-induced ion mass analysis (LIMA) has only become a really practical microanalytical technique during the past decade. As with any relatively new analytical technique, its precise capabilities, advantages, and limitations will take some time to be established. In the context of metallurgy and materials science, there is an obvious comparison between LIMA and the well-established electron-probe microanalyzer; LIMA offers speed and ease of analysis, is not restricted to analysis for a few elements at a time, can detect and measure quantitatively all light elements (including hydrogen), can be used to analyze nonconducting samples, and offers a greater sensitivity to trace elements with the additional capability to distinguish isotopes and to provide chemical information by identifying molecular ions. In comparison with the less widely used nuclear microprobe, LIMA offers especially simplicity of operation and a much cheaper and less complex equipment. In comparison with ion-probe microanalysis and the related SIMS, LIMA again offers a faster analysis and also a much simpler mass spectrum, ease of handling a wide diversity of samples, and (for a bulk analysis technique) the positive advantage that LIMA is not especially surface sensitive in its present form and does not display the widely varying sensitivities to different elements that are a severe disadvantage of these secondary-ion techniques.

In this paper, we present the results obtained on a variety of bulk samples analyzed in LIMA-2A, a laser-induced ion mass-analyzer manufactured by Cambridge Mass Spectrometry Ltd. These results illustrate some advantages and limitations of LIMA compared to other microanalytical techniques.

#### *Instrumental*

An overall view of the instrument is shown in Fig. 1, with the main elements of the system indicated. This instrument has been fully described previously;<sup>1</sup> only a brief resumé is given here, with emphasis on particular design features. A short pulse from a Q-switched laser (Nd:YAG, frequency doubled to  $\lambda = 0.53 \mu\text{m}$ ) is focused onto the sample and evaporates and ionizes a small volume of material. Analysis is performed by time-of-flight mass spectrometry of ions extracted from the resulting microplasma.

Sample viewing is by an optical microscope. The instrument can be used in a transmission mode for thin samples but we shall concentrate here on the reflection mode of operation for analysis of bulk samples. The area for microanalysis is identified and defined by the focused spot of an auxiliary He-Ne laser. Optimum optical performance and ion extraction are both achieved in a direction normal to the sample surface by extraction of ions for analysis through a series of axial apertures in the reflecting (Cassegrain) optics. The t-o-f mass spectrometer uses a folded flight path incorporating an electrostatic reflecting element that compensates for the relatively large spread in the initial ion energies. Positive or negative ions are detected by a conventional electron multiplier and the resulting time spectrum typically up to 100  $\mu\text{s}$  is acquired by a fast transient recorder for immediate oscilloscope display and is transferred to a microcomputer for conversion to a mass spectrum, further data processing as required, and for output as a video display, hard copy, or in magnetic form for permanent storage.

The vacuum system is of a conventional bakable ultrahigh-vacuum construction. As LIMA

---

Author Evans is at Charles Evans & Associates, San Mateo, CA 94402; authors Griffiths and Dingle are at Cambridge Mass Spectrometry Ltd., Cambridge, England; and authors Southan and Ninham are at the Department of Metallurgy and Materials Science, University of Cambridge, England. They are grateful to J. H. Cleland and P. J. Burnett of the Department of Metallurgy and Materials Science at Cambridge University for their assistance on the LIMA studies on corroded stainless steel and for ion-implanted semiconductors, respectively.

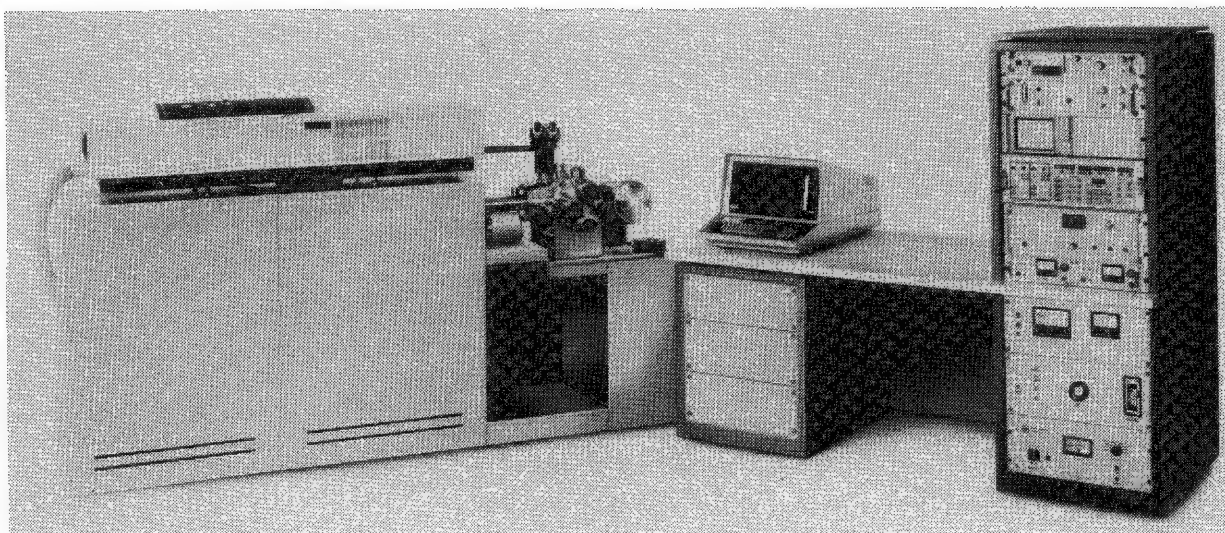


FIG. 1.--Overall view of LIMA 2A.

is not strictly a "surface" analysis technique, the u.h.v. capability may seem superfluous, however, although a vacuum environment in the  $10^{-7}$  torr region is generally adequate; for desorption work or in, say, the detection of hydrogen at low levels, a u.h.v. environment insures that unambiguous results are produced. In addition, a clean vacuum environment diminishes any potential problems due to spurious ion emission from contaminants on optical components. Finally, the u.h.v. capability allows surface analytical techniques such as SIMS or SAM to be combined with LIMA.

A high-stability precision specimen manipulator is used in LIMA 2A. Specimens can be positioned with an accuracy and reproducibility in the micrometer range. A sample carousel can accommodate eight specimens. The samples are initially put into a loading chamber (Fig. 1) which is isolated from the main analysis chamber and transferred under vacuum onto the carousel, a step that insures that the main analysis chamber is not let up to air during specimen exchange. Samples are loaded and ready for analysis within a matter of minutes. The loading chamber is pumped by a turbomolecular pump and the analysis chamber and flight tube by an ion pump.

### *Results*

The performance of LIMA can be summarized as follows. The minimum volume analyzed is limited by the diffraction-limited diameter of the focused laser beam (between 1 and 3  $\mu\text{m}$  in the present instrument) and by the depth of the laser induced crater, some tenths of a micron. These parameters depend on the beam power and specimen material. The beam power is continuously variable over a wide range and specimen materials can include not only metals and alloys, but semiconductors, glasses and ceramics, polymers, composites, coatings, and powders, as well as organic and biological specimens. Positive- and negative-ion spectra may be obtained with a mass-resolution of  $m/\Delta m$  in excess of 500. The relative sensitivity of the instrument to various elements requires further investigation but appears to lie within a range of one order of magnitude at most for all elements (and probably a good deal less once optimum operating conditions have been determined), and the detection limit for trace elements is in the ppm range.

LIMA has already demonstrated the ability to give valuable microanalytical information on a wide diversity of materials problems. Here are a few of the many examples that might be cited: quantitative analysis of 10 ppm of hydrogen in a titanium alloy, and measurement of the depth profile (at a depth resolution of about 1  $\mu\text{m}$ ) of less than 10 ppm of hydrogen in 20  $\mu\text{m}$ -thick oxide layers on uranium; measurement of the iron-boron ratio, and other elemental concentrations including unsuspected silicon, as a function of depth in sections through boronized layers on steel; measurement of the concentration of elements ion implanted into silicon and sapphire; characterization of oxide layers in corroded stainless steels; analysis of paint films, polymers, photographic materials, impurity

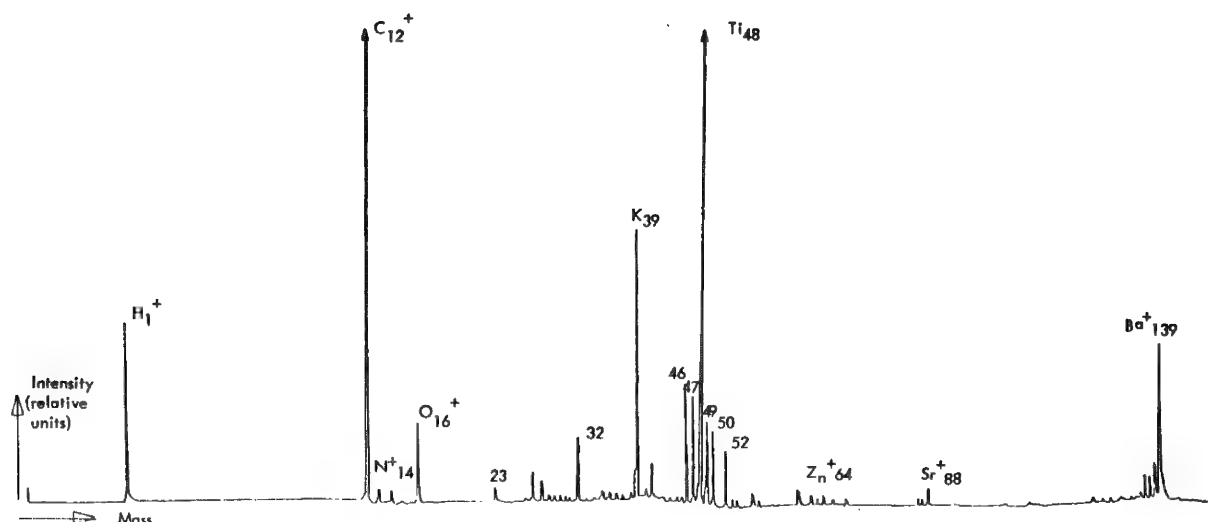


FIG. 2.--Positive ion LIMA spectrum from paint sample.

inclusions in pharmaceutical pills, and insoluble residues from soda-lime mines; the detection of trace levels of pollutions such as lead in human tissue--and a preliminary assessment of the quantitative accuracy of LIMA by analysis of a series of Pd-Ni alloy standards that gave compositions within 5% of the nominal values with analytical procedures, which could certainly be improved. Some of these applications are described in more detail to illustrate the advantages and limitations of the LIMA technique.

The measurement of the metallic constituents in paints (as an aid to forensic identification, quality control, and paint development) is a promising application area for LIMA. Various samples have shown that the spectra are in general much easier to interpret than those from the ion probe, because the organic constituents that are present in the ion-probe spectra can be eliminated in LIMA by choice of the laser power density to dissociate the organics into atomic ions of O, C, N, and H, which simplifies spectral interpretation. Second, the detection of trace elements such as barium or strontium appears easier in LIMA than in the ion probe. Similarly, compared to the electron probe, detection sensitivities appear to be better by at least an order of magnitude for most elements. Finally, there are no specimen-charging problems in LIMA and it has proved possible to obtain rapidly depth profiles of paints to the 30 $\mu$ m level and below. Figure 2 shows a typical spectrum obtained by LIMA on a paint.

However, measurements of the surface composition of nitrogen-ion implanted silicon illustrate some present limitations of the technique. Silicon implanted with the very high dose of  $8 \cdot 10^{17} \text{ N}_2^+/\text{cm}^2$  gave a nitrogen concentration of about 10% by LIMA analysis, with the concentration essentially constant across the sample surface. A similar sample implanted with  $4 \cdot 10^{17} \text{ N}_2^+/\text{cm}^2$  showed a correspondingly smaller average nitrogen concentration which varied considerably (by a factor of 5) across the sample area. It is not likely that the true nitrogen concentration varied to this extent; the heavy nitrogen dose had produced an amorphous surface layer in both samples, but the more heavily dosed sample had suffered significant surface roughening which was not evident by SEM examination of the more lightly dosed surface. It is likely that the interaction of the laser pulse was strong and uniform for the roughened surface but less regular, at the same power density, for the smooth silicon surface. These results confirm that it is necessary to establish with care the correct laser power density for reproducible and quantitative analysis, especially of weakly absorbing samples, but show that LIMA is capable of providing a quick, quantitative characterization of ion-implanted materials, not easily achieved by other methods, in cases where a suitable calibration is available.

Another project was concerned with the measurement of the composition of films on corroded stainless steel. During the course of corrosion of a stainless steel in a hostile environment, the state of the metal surface is continually changing; it is postulated that a relatively insoluble film grows on the surface competing with the corrosion reaction, the dissolution of metal to ions. Information on the growth kinetics and the composition of

this film at different stages would permit a better prediction of the corrosion behavior of stainless steels. The thickness of these films is such that the use of surface analysis techniques would be tedious.

A preliminary LIMA investigation of such a film has given most encouraging results. A 304L steel was held at a negative potential, in the active corrosion range, in 3.4 molar  $\text{H}_2\text{SO}_4$  for 20 hr at ambient temperature. LIMA analysis of the resulting film showed that the Cr/Fe ratio in the film is greater than in the bulk metal (0.45 and 0.27, respectively) and that the Cr/Fe ratio was surprisingly constant through the thickness and across the area of the film although subsequent SEM examination showed it to be very irregular in thickness and texture; on the assumption that a single laser pulse removed about  $0.5\mu\text{m}$  of material at the power density employed, it was deduced that the thickness of the film was markedly nonuniform and varied between 0 and  $10\mu\text{m}$ .

Finally, consider the characterization of boronized surface layers on a mild steel. Boronizing is increasingly being used for the production of hard and wear-resistant surfaces. The process is similar to carburizing, but the necessary heat treatments are shorter and at lower temperatures, and no final surface quench is required. Surface microhardness in excess of 1800 Vickers can be obtained in layer thicknesses up to 200-250 $\mu\text{m}$ .

Investigation of the composition of the boride layer and of any segregation ahead of its boundary, indicating perhaps which elements limit the growth rate, is a task ideally suited to laser-microprobe analysis. LIMA's particular advantages are the ease with which it can detect quantitatively elements of low atomic number such as boron (in contrast to conventional electron microprobes) and the speed with which concentration profiles can be examined. Previously, one has had to resort to techniques as complicated as  $\alpha$ -autoradiographic tracing<sup>2</sup> to search for boron (and even then only qualitatively) ahead of the main boride layer.

For materials such as mild steel, it is often stated that  $\text{FeB}$  is formed at the surface and  $\text{Fe}_2\text{B}$  below it.<sup>2,3</sup> LIMA investigations of sections through boronized mild steel have indicated that this may not be the case; boron concentrations have been observed near the

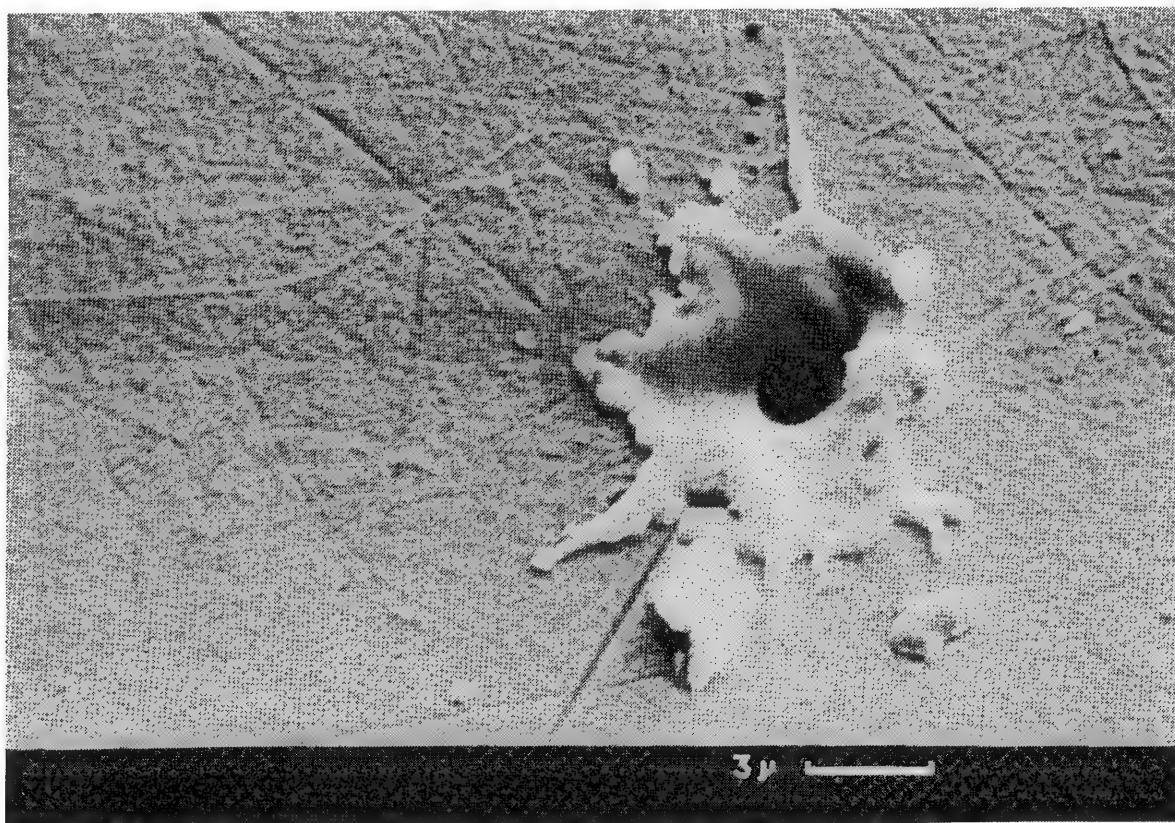


FIG. 3

surface that are smaller than those further from the surface. Ion-to-boron ratios approaching 2 (1.84) have been observed close to the specimen edge. Multiple laser shots into the same spot have shown a varying Fe/B ratio, which suggests an FeB/FeB<sub>2</sub> mixture. High silicon levels in the substrate very close to the boride layer have also been noted, in contrast to results reported elsewhere.<sup>2</sup> No carbon has been detected in the boride layer itself.

Figure 3 shows a scanning electron micrograph of a typical crater produced on this sample. The laser power density was relatively high to insure uniform ionization efficiency of the elements detected. Although the main crater produced in the metal is less than 2µm in diameter, an appreciable volume of material has exploded out and recondensed on the sample, which illustrates the care that must be taken in optimizing the laser power density for unambiguous elemental concentrations and spatial distributions.

### Conclusions

LIMA is rapidly establishing itself as a microanalytical technique that can yield useful results to many practical problems. The full potential of the technique has probably not yet been realized and requires more systematic work to establish a firm physical basis for quantitatively relating raw LIMA data (the mass spectrum) to the true composition of the sample under analysis.

### References

1. T. Dingle, B. W. Griffiths, J. C. Ruckman, and C. A. Evans, "The performance of a laser-induced ion mass-analyzer for bulk samples," *Microbeam Analysis--1982*, 365-368.
2. N. Bozkurt et al., "Autoradiographic study on boronized steel," *Materials Science Engineering* 57: 181-186, 1983.
3. S. C. Singhal, "A hard boride coating for ferrous materials," *Thin Solid Films* 45: 321-329, 1977.

## LASER MICROPROBE MASS ANALYSIS OF SINGLE CELLS AND CELL COMPONENTS

Buko Lindner and Ulrich Seydel

In our laboratory the laser microprobe mass analyzer LAMMA<sup>R</sup> 500 is mainly applied to single bacterial cell mass analysis with the aims of obtaining information on their physiological state and its alterations under the action of various external influences, of differentiating bacterial strains from their mass fingerprints, and of examining transport properties. Furthermore, the instrument serves as a so-called soft-ionization source for the mass spectrometric determination of molecular weight and chemical structure of isolated bacterial components, especially of lipids.

The application of the LAMMA instrument for pure mass spectrometric purposes aims at determining the optimal instrumental parameters and the detection limits for biomolecular substances. These findings should help to predict in special cases how promising the utilization of the LAMMA instrument would be for the tracing of a compound within the intact biological matrix with the lateral resolution offered by the instrument. In the present contribution we present some results that might demonstrate the applicability of the LAMMA technique in microbiology.

### *Experimental*

The LAMMA instrument (Leybold-Heraeus Co., Köln, F.R.G.) has been described in detail elsewhere.<sup>1</sup> Briefly, a high energy UV laser pulse is focused through the objective of a light microscope onto the sample to be analyzed and evaporates and partly ionizes it. Depending on sample conditions and on laser energy a lateral resolution below 1  $\mu\text{m}$  may be achieved. The produced positive and negative atomic and molecular (fragment) ions are registered alternately by means of a time-of-flight mass spectrometer at a mass resolution of approximately 800 and a sensitivity down to  $10^{-20}$  g (for sodium and potassium) from an analyzed mass of approximately  $10^{-13}$  g.

For single-cell analysis with LAMMA the bacteria are generally treated as follows: the cells are harvested from the appropriate growth medium and washed twice quickly--to avoid ion dislocation--in distilled water, and are brought onto Formvar-coated Cu-grids; excess fluid is drained off with tissue. In this way a widespread distribution of the bacteria is achieved, which permits the laser vaporization of a single cell at a time. For statistical purposes up to 400 single bacteria (for the establishment of distribution patterns) are analyzed from one preparation.

For mass spectrometric investigations of isolated cell components the substances analyzed are thoroughly mixed in a mortar with an appropriate amount (1:5 by weight) of various alkali salts (Na, K, Cs-chloride). This admixture favors the formation of quasimolecular peaks with high relative intensity by alkali attachment.<sup>2</sup>

### *Results and Discussion*

In Fig. 1 the mass spectra of two single *Escherichia coli* K12 cells are shown which were prepared in the above way. However, the right spectrum was obtained from a cell treated with the drug HN32, a nitrofurantoin derivative, which was added to the culture at approximately five-fold the minimal inhibitory concentration (m.i.c.) 2 hr before harvesting. Among other differences the marked alterations in the various cation contents (Na, Mg, K, Ca) can be clearly recognized. The unlabeled mass peaks are most likely of organic origin. Increasing the laser power density and/or the input sensitivity of the LAMMA 500 yields increasing numbers and intensities of mass peaks which at the present time cannot be as-

---

The authors are at Research Institute Borstel, Biophysics Division, D-2061 Borstel, Federal Republic of Germany.



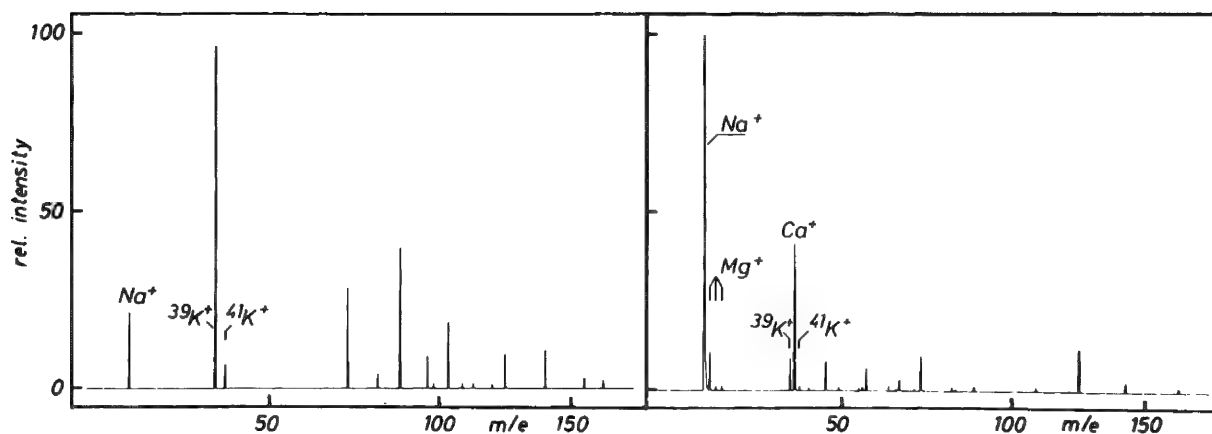


FIG. 1.--LAMMA-spectra of two single *Escherichia coli* K12 cells from an untreated control (left) and from a treated culture (right) 2 hr after application of nitrofurantoin derivative HN32.

signed to definite cell components but are the basis for a differentiation (taxonomy) of various bacterial strains from their mass fingerprints.<sup>3</sup> Very recently we have developed a computer program for the automatic classification. This procedure has already enabled us to differentiate among three samples of the same strain which were treated with three different chemotherapeutics, and between resistant and nonresistant strains on the basis of less than 100 single-cell analyses (to be published).

In a kinetic study in which the time dependence of the Na,K ratio after chemical treatment was compared with results from more established microbiological techniques it could be demonstrated that the intracellular Na,K ratio is a sensitive indicator of the physiological state of a cell.<sup>4</sup> Under the influence of a drug the transport properties of the cell membrane (among other factors the active transport or the passive diffusion of Na and K or even both) may be altered and sometimes lead to dramatic shifts in their intracellular concentrations. To study this effect with LAMMA we have, in a first step, grown *E. coli* cells in a medium containing Na and K (ratio 1:2) and then transferred the cells into a similar medium where the potassium was replaced by rubidium (which should be a satisfactory substitute for potassium<sup>5</sup>). Cultures were kept at two different temperatures (0°C, 37°C). Controls were kept in the original medium at the same temperatures. At different times samples were prepared from all cultures for LAMMA analysis. In Fig. 2 the averaged LAMMA spectra from 100 single cells in each case for the conditions 0°C, 0.5 hr and 37°C, 0.5 hr, respectively, are given. Obviously, at 0°C the influx of Rb and the efflux of K are lower than at 37°C. This result may be explained by the reduced permeability of the membrane at 0°C due to a decrease in its fluidity and by the cessation of the active pump. Use of stable isotopes of the elements under study rather than only "similar" elements will probably allow more reliable investigation of mechanisms of membrane active effects.

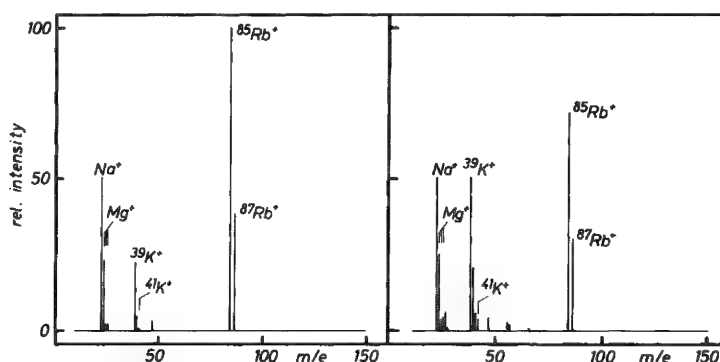


FIG. 2.--Averaged LAMMA-spectra from 100 single cells in each case grown in Na- and K-containing medium, then transferred into Na- and Rb-containing medium and kept at 37°C (left) and 0°C (right), respectively.



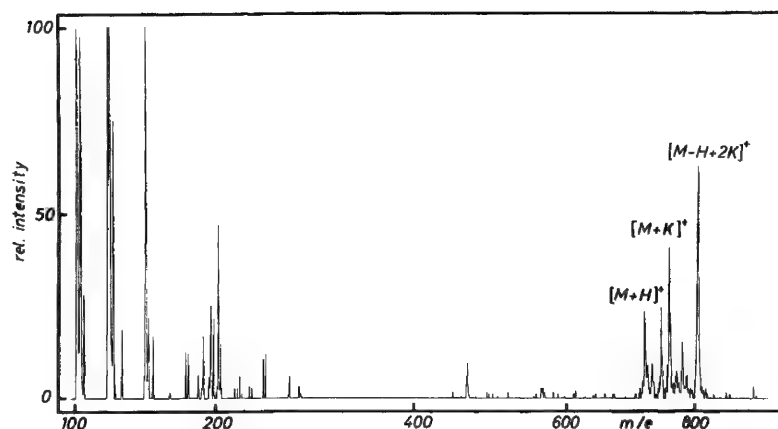


FIG. 3.--LAMMA-spectrum of dipalmitoylphosphatidylcholine + KCl.

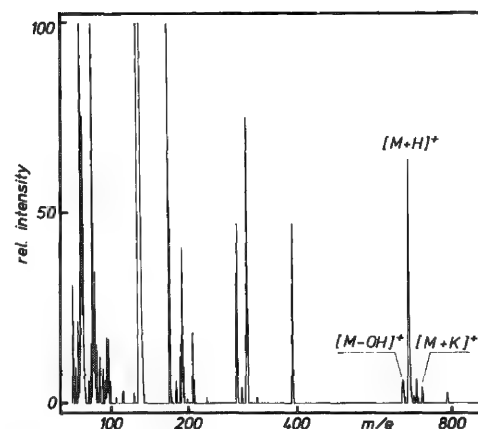


FIG. 4.--LAMMA-spectrum of an ornithin lipid isolated from *Rhodimicrobium vaniellii*.

The ability of the LAMMA technique for organic mass spectrometry is demonstrated for two cell wall components in Figs. 3 and 4, which show the LAMMA spectra of dipalmitoylphosphatidylcholine (DPPC) and an ornithin lipid isolated from *Rhodimicrobium vaniellii* by O. Holst (Max Planck Institute, Freiburg, F.R.G.), respectively. Both spectra show simple, easily interpretable patterns. Positive results from more complex bioorganic substances of high molecular weight ( $m/e \leq 2000$ ) have been published elsewhere.<sup>6</sup> However, these results do not necessarily mean that pure isolates can be successfully traced in a biological matrix in general, except in some advantageous cases (high accumulation, low interaction of the compound with the matrix). These conditions are met, for example, in the detection of phytoalexin glyceollin in thin sections of infected soybean cotyledons on the cellular level.<sup>7</sup>

#### References

1. R. Kaufmann et al., "Recent advances of laser microprobe mass analysis (LAMMA) as applied to biological and technical specimens," *Microbeam Analysis--1979*, 63-72.
2. H. J. Heinen, "On ion formation in laser desorption mass spectrometry with LAMMA," *Int. J. Mass Spectrom. Ion Phys.* 38: 309-322, 1981.
3. Ulrich Seydel and H. J. Heinen, "First results on fingerprinting of single mycobacterial cells with LAMMA," in A. Frigerio and M. McCamish, Eds., *Recent Developments in Mass Spectrometry in Biochemistry and Medicine*, Amsterdam: Elsevier Scientific Publishing Co., 1980, vol. 6, pp. 489-496.
4. Buko Lindner and Ulrich Seydel, "Mass spectrometric analysis of drug-induced changes in  $\text{Na}^+$  and  $\text{K}^+$  contents of single bacterial cells," *J. Gen. Microbiol.* 129: 51-55, 1983.
5. Tilly Bakker-Grunwald and Michael Sinensky, " $^{86}\text{Rb}^+$  fluxes in Chinese hamster ovary cells as a function of membrane cholesterol content," *BBA* 558: 296-306, 1979.
6. Ulrich Seydel and Buko Lindner, "Mass spectrometry of organic compounds ( $\approx 2000$  amu) and tracing of organic molecules in plant tissue with LAMMA," in A. Benninghoven, Ed., *Ion Formation From Organic Solids* (Springer-Series on Chemical Physics), New York: Springer Verlag (in press).
7. Peter Moesta et al., "Detection of glyceollin on the cellular level in infected soybean by laser microprobe mass analysis," *Z. Naturforsch.* 37c: 748-751, 1982.

## 4 Computer-assisted Microbeam Analysis

### REPRODUCIBILITY CONSIDERATIONS IN AN AUTOMATED MICROPROBE

W. F. Chambers

Ever since the advent of automated electron microprobes, instrument manufacturers have worked diligently to improve the reproducibility and stability of their products. With current technology, it is possible to obtain mechanical reproducibilities of about  $1\text{ }\mu\text{m}$  in the stage and  $0.00001$  to  $0.00002 \sin \theta$  in the spectrometers. Coupled with beam regulation systems which are capable of stabilities in the parts-per-million-per-hour range, these reproducibilities have resulted in instruments that should be capable of very reproducible results.

Sandia-TASK, an electron microprobe software automation system designed jointly at Sandia National Laboratories and Rockwell Rocky Flats, was intended to take advantage of such instrument stabilities. Among other things, Sandia-TASK utilizes reference tables of elemental information that normalize standard count rates to beam currents. We had hoped that by incorporating the beam current normalization we would be able to utilize a given "element" table over extended periods of time without recalibration. That was not possible at first. Some factors we found to be responsible for drift and/or irreproducibilities are enumerated below along with solutions where we have found them.

1. *Beam Current Drift.* This effect is noticed only immediately following the cleaning of the electron column. It is caused by a gradual buildup of contamination on the apertures of the sampling system for the beam-regulation device. This contamination buildup has the effect of altering the backscattering characteristics of the apertures and thus the percentage of the beam current sampled. It is a problem even in well-shielded systems. To compensate for this drift effect one must periodically quantify the beam current with a remotely insertable Faraday cup. Over a period of a few days the backscattering characteristics asymptotically approach their final values and the quantification period can be increased from about once per hour to about once per day.

2. *Temperature Drift.* Spectrometer temperature variations change the peak position for an x-ray line by about  $-0.00005 \sin \theta/^\circ\text{C}$ . This effect became particularly evident during an extended run when the building air-conditioning system failed: a rise of about  $5^\circ\text{C}$  resulted in analytical totals nearer 85% than 100%. The remedy was to install a temperature sensor on the case of one of the spectrometers, to read the spectrometer temperature whenever any spectrometer is accessed, to store calibrated values at an arbitrary spectrometer temperature ( $25^\circ\text{C}$ ), and to add a thermal-expansion offset into the spectrometer position. Since this was done, room temperature changes of as much as  $10^\circ\text{C}$  have produced no data loss.

3. *Sample Focusing.* Since the human eye normally is a part of the light-optics system of the microprobe, two operators may focus a sample slightly differently. This causes the peak position for each x-ray line to change in order to compensate for the corresponding change in the focal point for the x-ray optics. The change is not large enough to cause a degradation in the count rate and is immaterial so long as the same person performs the focusing of all standards to be used and of the unknown analysis points. However, the discrepancy can invalidate a calibration table prepared by one operator for use by another. We have overcome this difficulty by replacing the binocular microscope head with an industrial-grade color television camera, which has also resulted in several ancillary improvements. Not only is the focus position repeatable from operator to operator, the system has also provided an easy method of recording analysis areas and has provided a means for several people to view the sample simultaneously. In order to attain

---

The author is at Sandia National Laboratories, Albuquerque, NM 87185. Supported by U. S. Department of Energy under Contract DE-AC04-76DP00789.

sufficient illumination levels for proper use of the television camera we replaced the standard tungsten illuminator with a quartz-iodine illuminator connected to the microprobe via a fiber-optic system. This modification also provides illumination of the sample at the proper color temperature for the television system. Although we have kept our binocular head and were careful to design the optics system to the television camera so as to permit the exchange of the two systems by loosening one screw, we have found no instances where we wanted to return to the binocular viewing system.

*Counting Gas Variations.* We have found that commercially available P-10 counting gas varies enough from tank to tank to require re-adjustment of the amplifier gains whenever a tank is changed. To our surprise, we have not been able to correlate any count-rate changes with either atmospheric pressure changes or room temperature changes, as one might expect from Avogadro's law. Other than varying the amplifier gains, the only special care required of the counting gas seems to be to follow the common-sense rules of not permitting a gas tank to run completely empty and purging the supply line after a new tank has been installed, so that detector contamination is avoided as much as possible.

*Crystal Degradation.* As the crystals are bombarded with x rays they gradually degrade. Fortunately, this is a long-term, slow process. However, it does provide one of the limits to how long a particular reference table can be used without updating even if extreme care is maintained.

By paying attention to details such as those described above, we have been able to operate our microprobes reliably through long, unattended analysis sets and have in fact operated in quantitative-analysis mode for periods of up to two weeks without recalibration. During these periods, the integrity of the data is verified by analysis of a multiple-element secondary standard on a daily basis. As instrumentation improves and as additional sources of irreproducibility are identified and eliminated, we expect to be able to extend the periods between calibration even farther and to make the use of the microprobe system more productive and less tedious.

## A SELF-EDUCATING CLASSIFICATION SCHEME FOR PARTICLE AND PHASE IDENTIFICATION

J. C. Russ and T. M. Hare

We have previously described<sup>1-3</sup> methods to characterize heterogeneous samples such as poly-phase ceramics, dispersed raw material powders, metals, geological specimens, and particulates such as pollutants collected on filter papers. The simplest technique analyzes many points "at random," but problems arise when a single analysis point (actually covering a volume of about  $1 \mu\text{m}^3$ ) overlaps more than one grain. We have found that selection of grain or particle centers by use of the backscattered electron image,<sup>4</sup> and control of beam position,<sup>5</sup> improves the quality of the results, which are scatterplots in N-dimensions (the number of elements) of the total counts (characteristic plus background) collected in a few seconds with the beam on the point. The data are normalized to compensate for beam drift; each element's counts are divided by the total counts, which takes into account the presence of unexpected elements of high relative background intensities (as from organic particles) and makes the axes of the plots simple to interpret, since the range from 0 to 1 corresponds (very approximately) to elemental concentration. The plots are projected on 2-dimensional (2-element) planes; clusters of points identify phases or classes of particles. The number of points in each cluster gives the relative abundance of the phase, and the location, shape, and size of the cluster reflects the average composition (and variations in composition, shape of particles, surface roughness, and so forth). Much of our previous work has dealt with techniques to locate these clusters.

### *Iterative Classification*

Figure 1 shows a non-normalized 1000-point plot of intensities for two elements measured from a single-phase material. A rectangular counting window placed at the distribution's center with dimensions of  $\pm 2$  s.d. (standard deviations) will include more than 90% of the points. If the window is placed off center on the distribution, the mean values of the points will lie toward the center of the cluster. The initial placement shown by the axes, at a position 3 s.d. away from the true centroid, produces a mean X,Y location of the points which is then used to reposition the window (the second marker), and the operation is repeated. After five iterations the location found is within 1% of the true centroid position and does not move further.

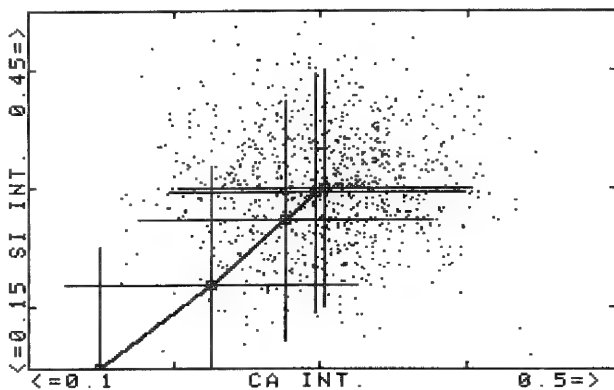


FIG. 1.--Motion of iterative window on 2-dimensional intensity distribution, with fixed window size.

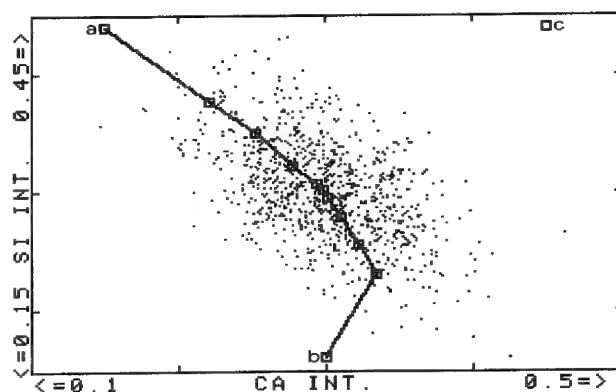


FIG. 2.--Normalized intensity plot projected into 2-D plane, with iteration paths for three starting positions: (a) and (b) reach same final point, but (c) never approaches cluster.

The authors are with the School of Engineering, North Carolina State University, Box 5995, Raleigh, NC 27650.

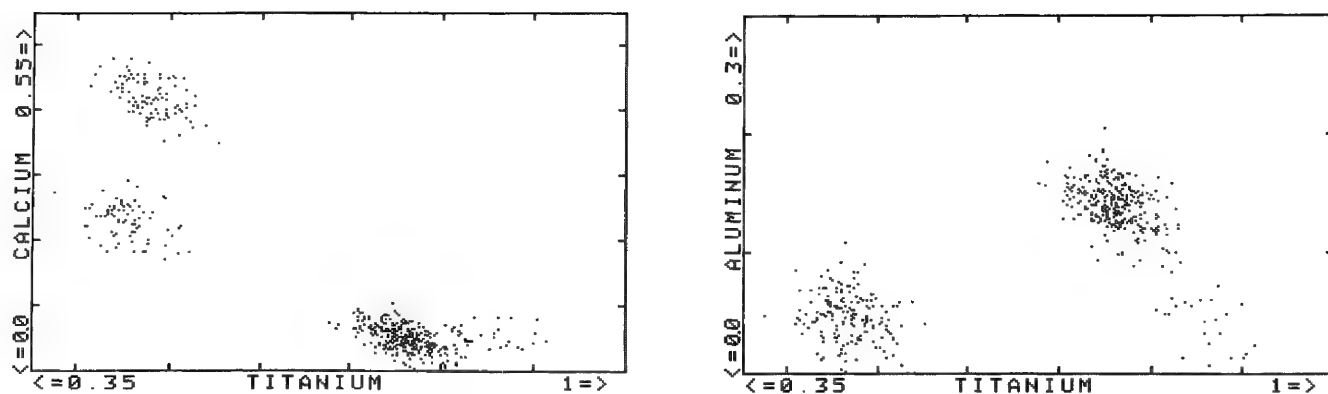


FIG. 3.--2-D views of 4-element scatter plot of elements in SYNROC (see also Table 1).

A more difficult case is shown in Fig. 2. Here the same data are presented in normalized form, which skews the distribution. The plots show the motion of windows approaching the center from different initial locations, each 3 s.d. out. Two of them reach exactly the same final point at the centroid of the cluster, but one never finds the actual cluster. Any point within  $\pm 2$  s.d. converges to the true center in 4 or fewer iterations. In practice we also allow the window size to vary with location. The s.d. of the points within the window is not the actual standard deviation of the cluster, even in the case when the window finally reaches the centroid, because the window cuts off outlying points. A search window size 2-3 times the computed s.d. in each dimension produces reliable iteration and excludes a minimal number of points.

#### *Multiphase Samples*

For more complex specimens, such as the SYNROC on which we have previously reported, there are clusters for each phase. This is a fine-grained ceramic with three major phases produced by sintering oxides of five elements (Ca, Ti, Al, Zr, and Ba, the last not analyzed owing to overlap by the larger Ti peak). Changes in proportions of oxide raw materials, preparation of powders, the sintering process, or the admixture of radioactive waste material can produce additional phases which we wish to identify. Figure 3 shows several views of the 4-dimensional distribution of points from material in which, besides the principal phases, there is an additional 5% of rutile (excess  $\text{TiO}_2$ ). Table 1 summarizes the four phases. Note that the normalized intensities for elements absent in a particular phase are not zero because of background counts in the ED spectrum.

A grid search of the multidimensional plot, comparing the number of points in each grid cell of size 0.1 to its neighbors, finds three local maxima. Iteration from these starting points quickly converges (3 iterations) to the centroids of the clusters for the three major phases. However, the process misses the rutile (a small cluster of 25 points in this 500-point example), because it is too close to the major hollandite cluster. A finer grid search will locate the rutile, but requires more points for adequate statistics. For the three major phases, the iteration procedure is very robust; any point near a cluster will find the same centroid location in not more than 5 iterations.

Because SYNROC is a very fine-grained material, the point clusters are rarely so well defined. Figure 4 shows the point plots for analyses in which the grain size is not large compared to the analyzed volume, and about 75% of all analyses overlaps to some extent onto

TABLE 1.--Normalized intensities for phases in Figs. 3-6.

Phase	Ti	Ca	Zr	Al	Abundance (%)
Hollandite	$0.76 \pm 0.04$	$0.05 \pm 0.02$	$0.05 \pm 0.02$	$0.14 \pm 0.03$	60
Perovskite	$0.48 \pm 0.03$	$0.42 \pm 0.04$	$0.05 \pm 0.02$	$0.05 \pm 0.02$	20
Zirconolite	$0.46 \pm 0.04$	$0.23 \pm 0.03$	$0.27 \pm 0.04$	$0.05 \pm 0.04$	15
Rutile	$0.85 \pm 0.04$	$0.05 \pm 0.04$	$0.05 \pm 0.04$	$0.05 \pm 0.04$	5

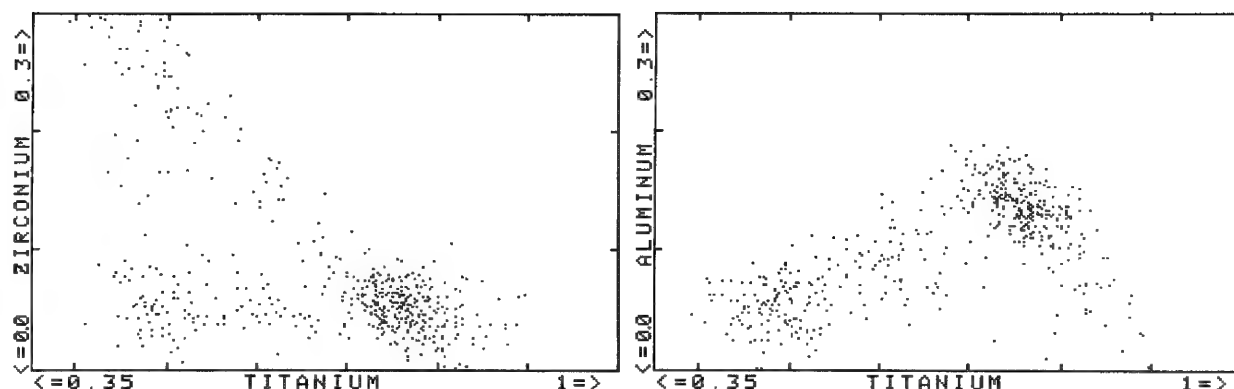


FIG. 4.--Point plots for fine-grained material in which 75% of points analyzed overlap another grain.

a neighboring grain, which may be a different phase. The broadening of the clusters frustrates attempts to find them automatically by a simple grid search for maxima, and then the iterative moving window.

#### *Neighbor-distance Filtering*

Location of clusters is significantly improved by use of a filtering method in which points are discarded if their second nearest neighbor distance (in an N-dimensional vector sense) exceeds an arbitrary cutoff level.<sup>6</sup> Figure 5 shows what happens when a cutoff value of 0.0175 is applied to the data of Fig. 3. The remaining clusters are small and very apparent, with the rutile well resolved from the hollandite. Figure 6 shows the application

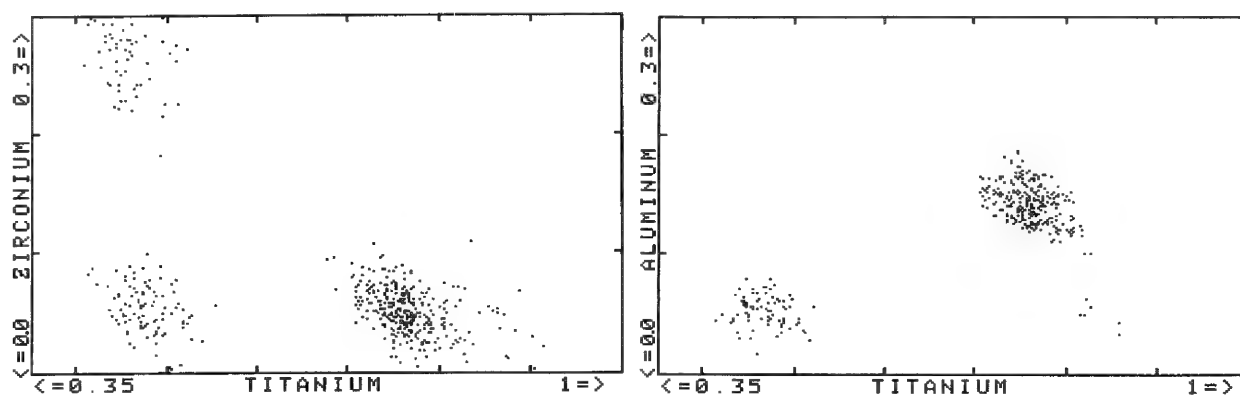


FIG. 5.--Second nearest neighbor filtering (distance = 0.0175) applied to data of Fig. 3.

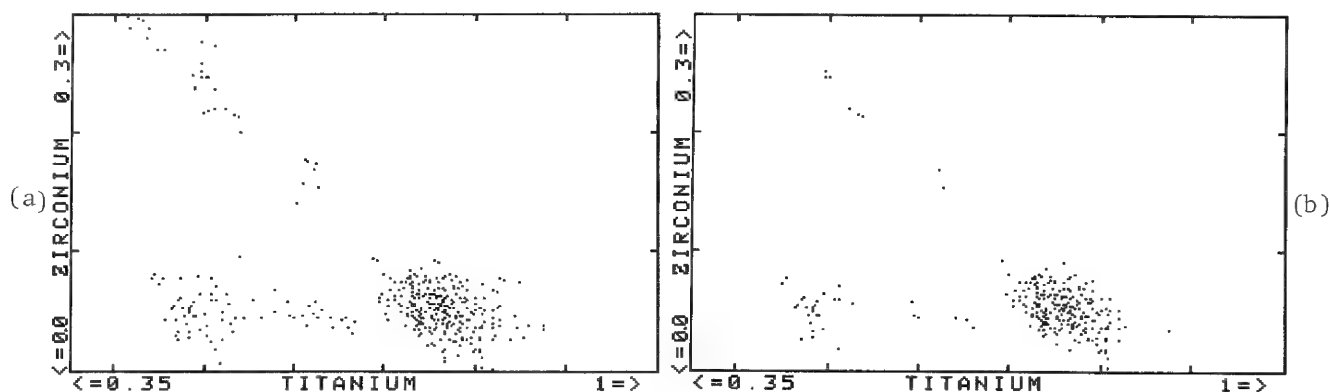


FIG. 6.--Second nearest neighbor filtering applied to data of Fig. 4: (a) threshold distance = 0.025, (b) threshold distance = 0.0175.

of the filter to Fig. 4, with different filter settings. The rutile cluster is again separated from the hollandite, although with very few points remaining. One may use these small clusters to find all the phases, using a grid search and iterative moving window.

The principal difficulty with neighbor-distance filtering is the time required to carry out the operation (typically hours compared to minutes for the grid search). Adjustment of the filter threshold remains a human operation; we have found no universal way to calculate an ideal value. Although it is a powerful method for examining these plots, the long time required to apply the filter and the need for human judgment make it less attractive than a grid search and iterative window. Indeed, the use of bins or grids and a smoothing operation (N-dimensional convolution) will always be faster than any neighbor search method, and is mathematically equivalent.<sup>7</sup> We plan further evolution of grid search methods in which the size varies automatically with the number of points in each large grid, to find small clusters.

#### *Particle Classification Strategy*

The method described assumes that all analysis data have been recorded for subsequent plotting and analysis. A different strategy may be adopted to classify particulates as analyzed. An initial class is established for each expected composition beforehand, either by intelligent guesswork, running a quantitative program in reverse, or by analyzing a few "representative" particles of each. The initial class ranges are used as in traditional sorting schemes, to identify particles as measured. Each set of coordinates in N-dimensions is also saved until the classes are periodically recomputed as for the iterative window search described above: all points lying in the class are used to determine a new class location and size, and iteration proceeds until it does not change by more than 1%.

These new classes are then used for further sorting, until the next recomputation takes place. The number of analyses between recalculations should increase each time, reflecting the statistical nature of the process; in practice it is easier, because of limited storage in the system, to do so at regular intervals (e.g., each 100 analyses). Unclassified points can be (a) assigned to the class to which they are nearest<sup>8</sup>; (b) stored on disk in case a later recalculation of the classes might gather them in; (c) saved for a search for unexpected composition classes as described above; or (d) ignored (as most traditional methods do).

Since diskette storage is cheap and not too slow, (c) is best for dealing with systems in which a large (>10%) number of the analyses produce unknown classifications. However, this method, like all statistical searches for clusters, will not readily find minor phases or rare particle compositions. For routine use, option (a) is most appropriate, since it gives the operator an immediate answer on every analysis, either as a confirmed (inside a class) or suggested (nearest class) identification.

#### *References*

1. J. C. Russ, "Quantitative analysis of multiphase sample," *Microbeam Analysis--1979*, 259-264.
2. J. C. Russ and T. M. Hare, "Characterization of heterogeneous polycrystalline materials," *Microbeam Analysis--1981*, 186-189.
3. T. M. Hare, D. Batchellor, and J. C. Russ, "Multipoint x-ray analysis by use of the backscattered electron signal as a guide," *Microbeam Analysis--1982*, 491-494.
4. T. M. Hare, J. C. Russ, and J. C. Russ, "Image measuring algorithms for a small computer," *ibid.*, 509-516.
5. E. M. Gregory, T. M. Hare, and J. C. Russ, "Controlling a Scanning Electron Microscope with a Dedicated Microcomputer," *ibid.*, 499-503.
6. H. Schwartz and H. E. Exner, "The characterization of the arrangement of feature centroids in planes and volumes," *J. Microscopy* 129(pt.2): 155, 169, 1983.
7. T. R. Edwards, "Two-dimensional convolute integers for analytical instrumentation," *Anal. Chem.* 54: 1519-1524, 1982.
8. J. C. Russ, T. M. Hare, and F. U. Luehrs, "A novel and efficient alloy sorting algorithm," *Proc. Denver X-ray Conf.*, 1980, 130-131.

## POSTPROCESSING OF X-RAY MAPS

Albert Sicignano and William Friday

The use of microprobes and SEMs with x-ray spectrometers attached to them for the characterization of materials has become common practice in many industrial and research laboratories throughout the world. The technique of using electron excited x-ray analysis with these instruments is a powerful method of rapidly investigating the elemental composition of a particular sample. The three modes of x-ray analysis possible are point, line scan, and map. In the point mode, the composition of a fixed point or the averaged composition of a selected area is determined. Use of the line scan and map modes provides additional information about the elemental spatial distribution of the sample.

In more than a decade of providing hundreds of analyses to sample originators with a wide range of technical backgrounds, we have repeatedly encountered the problem of effective and efficient transfer of elemental spatial information back to the sample originator. Our goal was to provide a user-friendly environment to both the analyst and the end user of such spatial/composition data. (At times that may be the same person.) The environment includes: the entire process of analyzing the sample; collecting the data; and any necessary final processing of the data, particularly the ease of transferring this newly gained information from analyst to end user.

The easiest way to convey x-ray information is to put it in a user recognizable format. To achieve this objective, our format utilizes the following:

1. Correct aspect ratio for the x-ray map (match SEM micrograph).
2. Gray scales that correspond to the relative concentration 4, 6, or 10 levels (dot matrix printer).
3. Colors and color overlays to distinguish elements (4-color ribbon).
4. Computer storage of x-ray maps for off-line processing (frees SEM and x-ray system).
5. Printed copies of the selected x-ray maps and line scans (done unattended).

In the system we have developed at Philips Laboratories for the handling of x-ray maps and line scans, the environment was made user friendly with the aid of a microcomputer and dot matrix color printer, up to 4 elements out of 16 can be selected to be simultaneously overlaid with separate colors, gray levels, and thresholds.

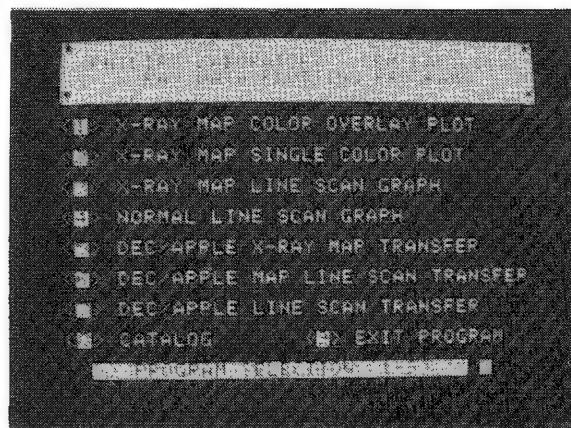


FIG. 1.--Apple crt display of "user-friendly" main menu.

The authors are at Philips Laboratories, Briarcliff Manor, NY 10510.



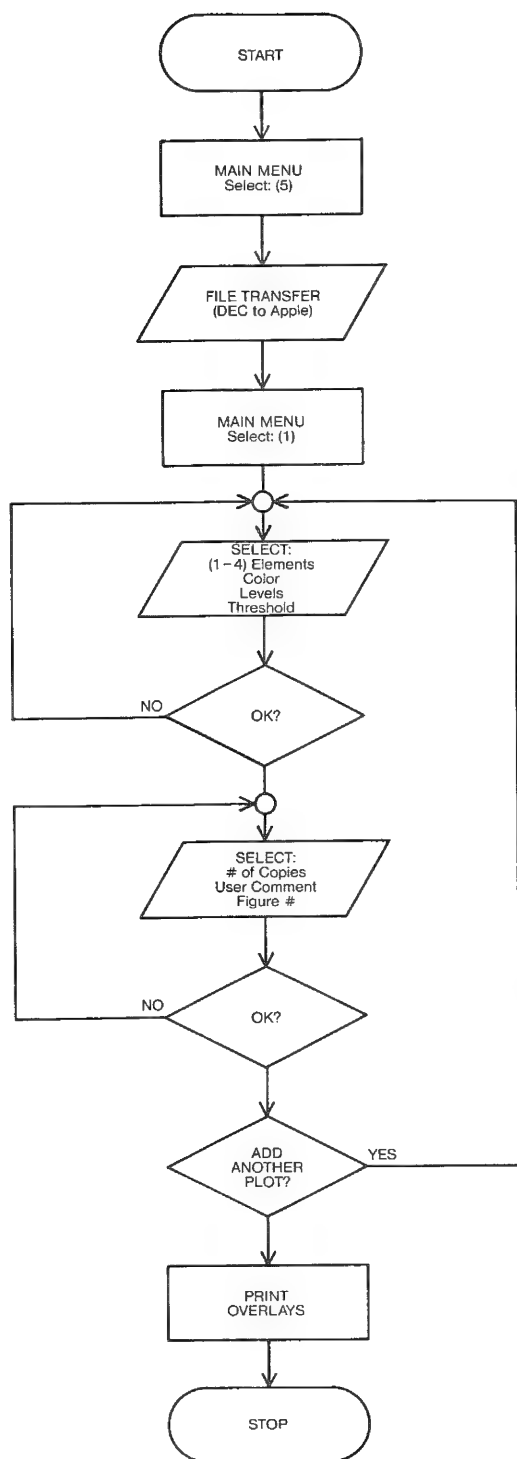


FIG. 2.--Flow-path diagram for processing of x-ray color maps, from data transfer to unattended hard-copy printing.

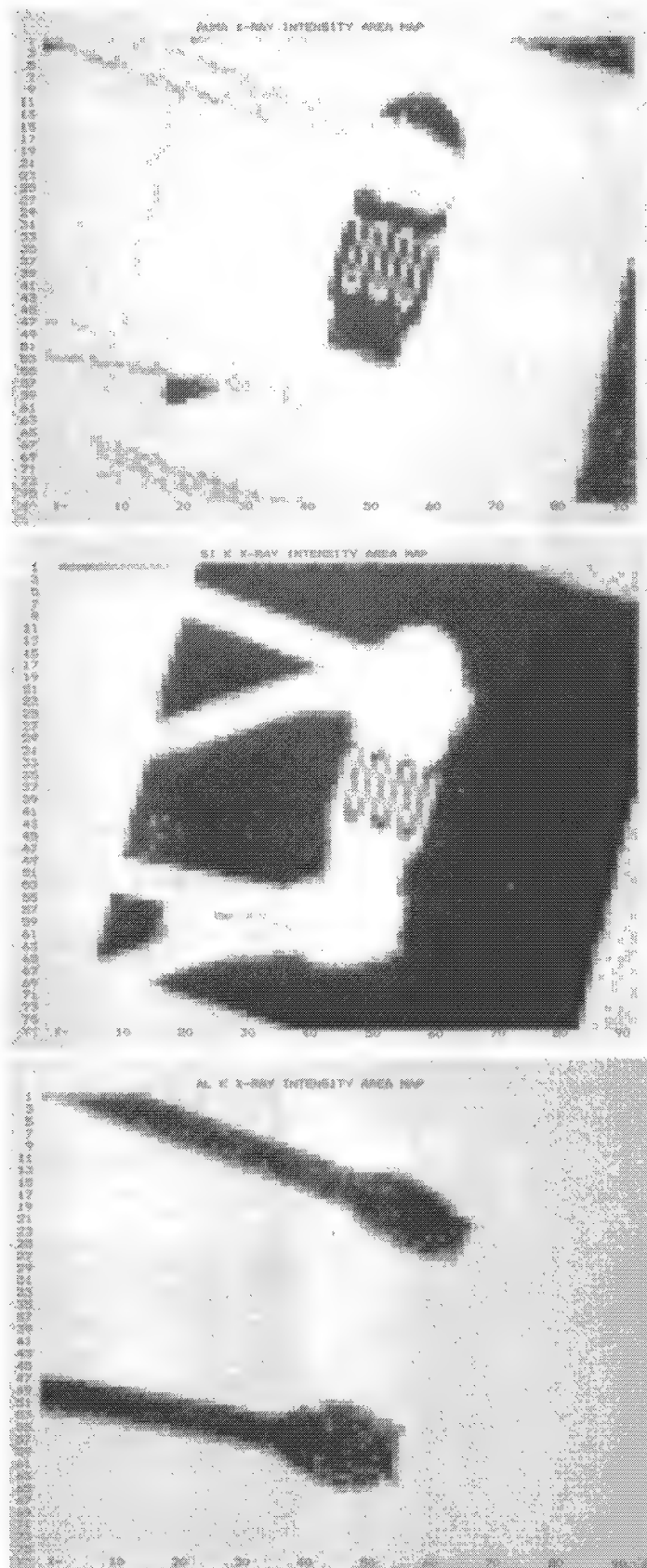


FIG. 3.--Example of a set of processed x-ray maps from diode with Au, Si, and Al displayed, at 10 gray levels and 0 threshold. In final version maps are assigned color and overlaid.

## Microbeam Analysis of Metals, Ceramics, and Glass

### GRAIN BOUNDARY CAVITATION AND WELD UNDERBEAD CRACKING IN DOP-26 IRIDIUM ALLOY

W. Clanton Mosley Jr.



FIG. 1.--Welded DOP-26 iridium alloy capsule.

Plutonium-238 oxide fuel pellets for the General Purpose Heat Source Radioisotopic Thermoelectric Generators to be used on the NASA Galileo Mission to Jupiter and the International Solar Polar Mission are produced and encapsulated in DOP-26 iridium alloy (Fig. 1) at the Savannah River Plant. DOP-26 iridium alloy was developed at the Oak Ridge National Laboratory (ORNL) and contains nominally 0.3 wt.% tungsten, 60 ppm thorium, and 50 ppm aluminum.<sup>1</sup> Underbead cracks occasionally occur in the girth weld on the iridium alloy cladding in the area where the gas tungsten arc is quenched.<sup>2</sup> Various electron-beam techniques have been used to determine the cause of cracking.

#### *Experimental*

Specimens from  $^{238}\text{PuO}_2$ -fueled capsules were examined with a contained SEM (Cambridge Stereoscan 600) at the Savannah River Laboratory (SRL). Studies of grain surface structure and elemental distributions were performed on specimens from unfueled capsules by means of SEM/EDX (AMR 900/KeveX 5000A), EMPA (ARL SEMQ), and SAM (Perkin-Elmer 545 at SRL and Perkin-Elmer 590 at ORNL). The following observations were made.

1. Cracks occurred beneath the quench along grain boundaries in alloy (both welded and unwelded) affected by heat from quenching (Fig. 2). Some cracks extended into the columnar-grain region of the quench (Fig. 3). Cracking in welds away from quench areas was not significant.
2. Grain surfaces in cracks exhibited ridge networks extending over many grains (Fig. 4). Ridge network patterns on mating grain surfaces were mirror images of each other (Fig. 5). Mating depressions between ridges constituted grain-boundary cavities a few tenths of a micrometer thick and up to 10  $\mu\text{m}$  across. Cavities had smooth, almost mirror-like surfaces. Fracturing of uncracked weld-quench areas generally revealed small ridge networks covering only a portion of a grain facet. Some small ridge networks were located near the centers of grain facets where it is apparent that mating grains had not separated during welding. Ridge networks were not present on grain surfaces in welded alloy away from quench areas.
3. Two other types of cavities have been detected in DOP-26 iridium alloy. Elongated cavities consisting of mating depressions a few tenths of a micrometer deep, a few micrometers wide and several tens of micrometers long were detected along grain edges (often along with small ridge network cavities) on grain surfaces in weld-quench areas, but not in welded alloy away from quench areas. Submicrometer pores were detected in grain boundaries and within grains of welded alloy, but not in unwelded alloy.
4. Thorium-bearing deposits in the form of particles, stringers, and patches (some with eutectic structure) have been detected on grain boundaries of welded DOP-26 iridium alloy. Small cavities were located in areas without thorium-bearing deposits (Fig. 6) with only iridium and tungsten at concentrations corresponding to bulk alloy being detected by SEM/EDX and EMPA in ridges and cavity surfaces. Thorium-bearing particles were

The author is with the E. I. du Pont de Nemours and Co., Savannah River Laboratory, Aiken, SC 29808. Supported by U. S. Department of Energy under Contract DE-AC09-76SR00001. The author thanks W. R. Kanne Jr., J. D. Scarbrough, E. F. Sturcken, and C. L. White for technical assistance.

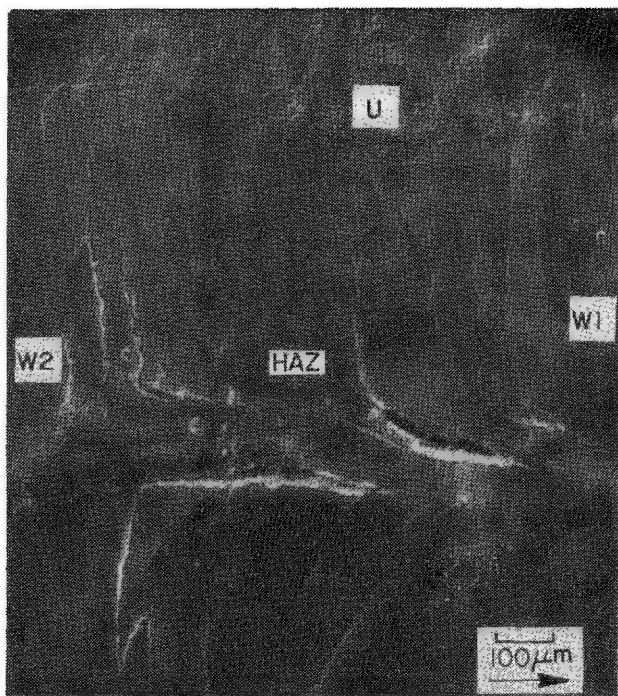


FIG. 2.--Weld-quench cracks on capsule inner surface.

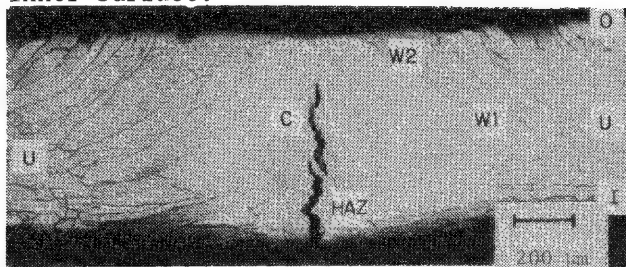


FIG. 3.--Section across quench shows crack. forming mechanisms that weaken grain boundaries as possible causes of cracking. Gas porosity and high-temperature creep are two such mechanisms.

Gas trapped or formed in the alloy could migrate to grain boundaries and form cavities in areas affected by heat from quenching. Pores within grains of welded alloy are indications of a source of gas in DOP-26 iridium alloy. Pores, grain-edge cavities, and ridge networks could form as increasing quantities of gas are released to grain boundaries. Formation of ridge networks near the center of grain facets indicates a pressurization process. Ridge spacing indicates a greater cavity depth near the centers of ridge networks as expected for gas porosity. The smooth surfaces of cavities are a general characteristic of gas porosity. The SAM results suggest the pressurizing gas contains carbon and, possibly, calcium but not oxygen. Hydrogen and helium, two gases used in DOP-26 iridium alloy processing that are not detectable by Auger electron spectroscopy, could also be involved in cavity formation.

detected on surfaces of extended ridge networks. Cavities and thorium-bearing patches were found to respond differently to heat treatment. Heating a weld-quench region at 1500°C for 1 hr had no effect on grain boundary cavities but caused thorium-bearing patches to coalesce into micron-size particles and stringers. Heating at 2000°C for a few minutes apparently healed grain boundary cavities.

5. SAM analyses showed that ridge network surfaces contained carbon and calcium that were not present on uncavitated grain surfaces (Table 1). Ridge network surfaces also had thorium concentrations higher than those detected on grain surfaces in thorium-doped iridium alloys.<sup>3</sup>

### Conclusions

Since the ridge networks that characterize weld-quench cracks in DOP-26 iridium alloy have been shown to constitute grain-boundary cavities, it is natural to consider cavity-

### LEGEND

I – Inner Surface	
O – Outer Surface	HAZ – Heat-Affected Zone in W1
U – Unwelded Alloy	C – Columnar Grains
W1 – Welded Once	← – Weld Direction
W2 – Welded Twice	

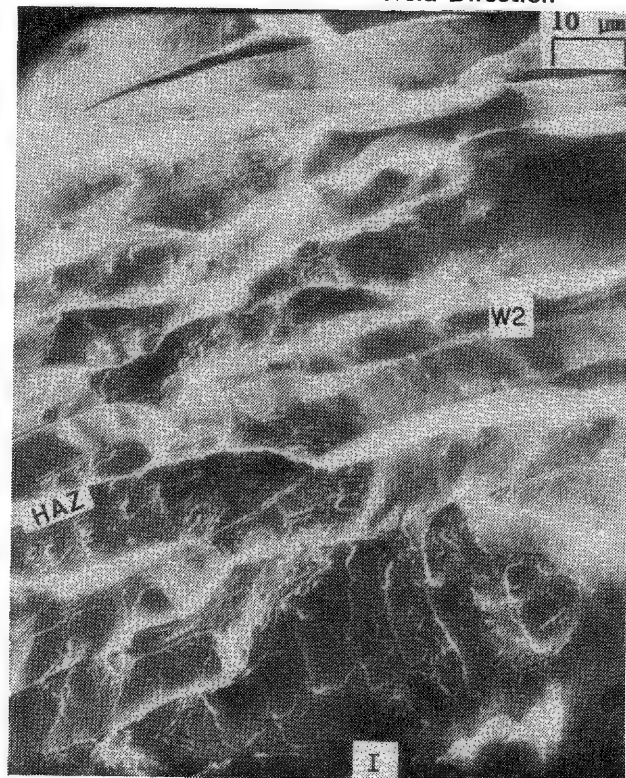


FIG. 4.--Extended ridge networks on grain boundaries in crack.



Creep is normally regarded as a very slow process, but at temperatures near the melting point, intergranular cracking due to creep can occur rapidly.<sup>4</sup> Two types of grain-boundary cavities are formed by high-temperature creep. Cavities on grain faces (called r-type cavities), which form at temperatures very close to the melting point and at low stresses, often lead to cracking failures. Ridge networks in DOP-26 iridium alloy could be r-type cavities. Cavities at grain-boundary triple lines (called w-type cavities),

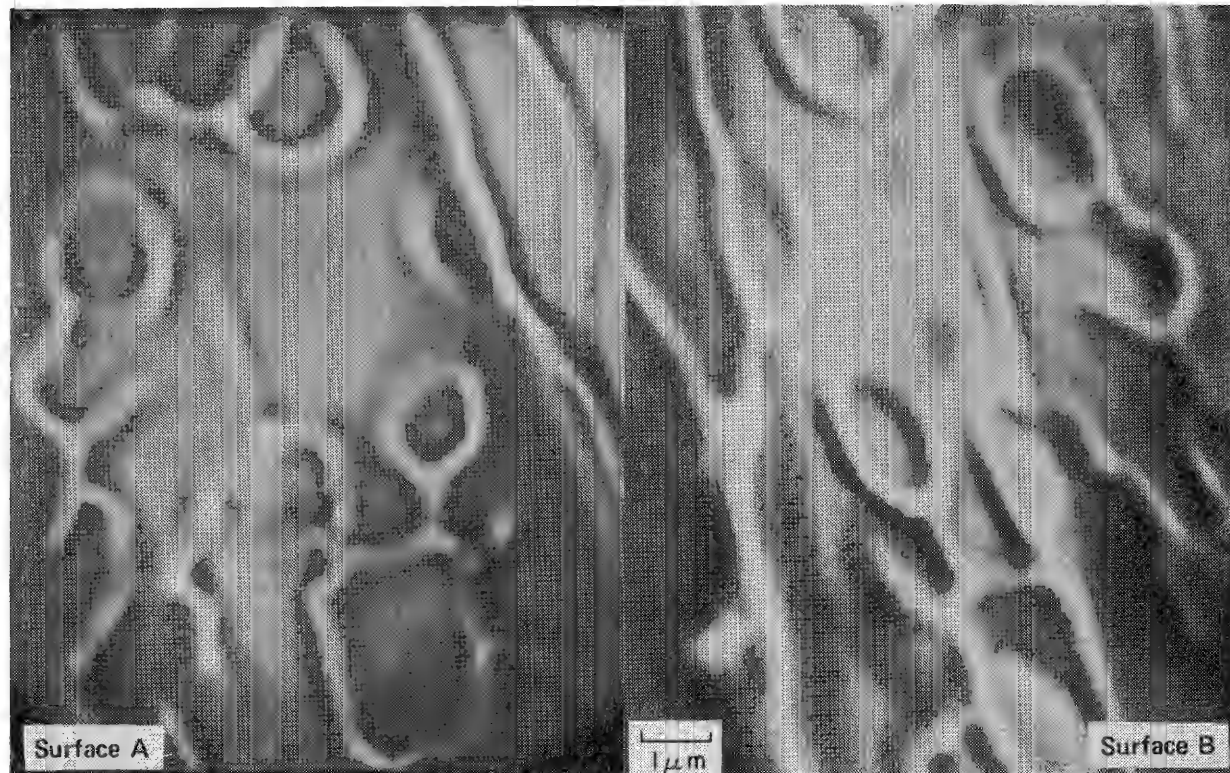


FIG. 5.--Mating grain surfaces in weld-quench crack exhibit mirror-image ridge patterns. Depressions between ridges constitute grain-boundary cavities. Submicrometer particles in surface contain thorium.

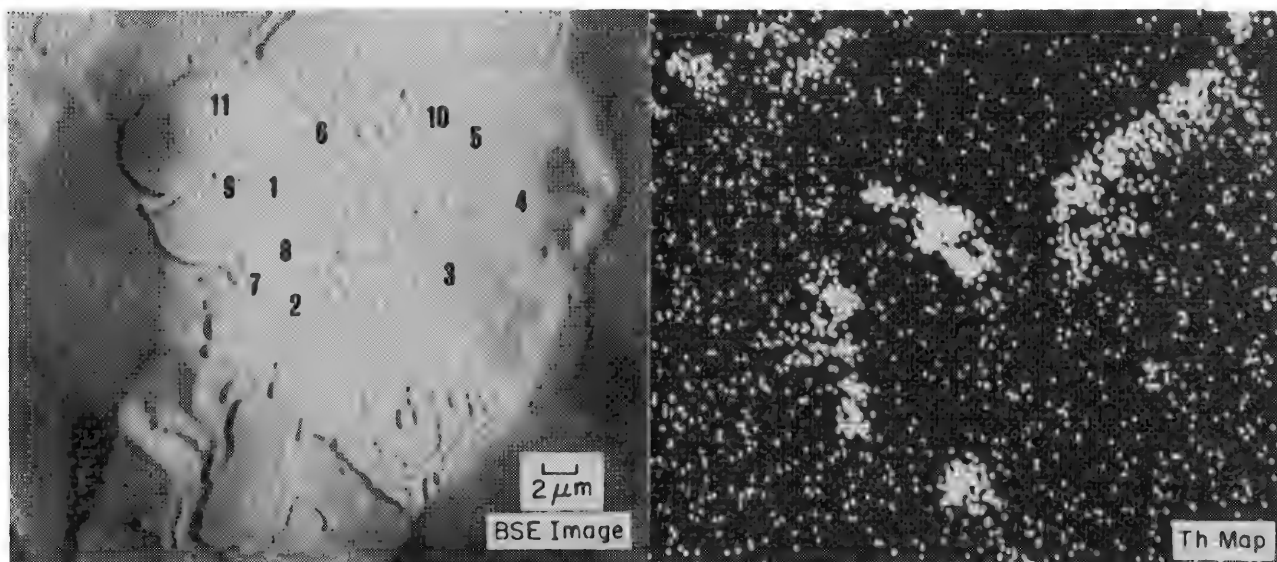


FIG. 6.--BSE image and corresponding thorium map showing thorium deposits outside small ridge network. Point analyses detected thorium (up to 5.9 wt.%) at locations 1, 3, 5, and 9 outside ridge network. Thorium concentrations at locations within ridge network were below detection limit ( $\sim 0.1$  wt.%).

TABLE 1.--SAM results for a small ridge network.

Analysis Point No.	As Fractured	Auger Peak Intensity Ratios*			Estimated			
		Th (67 eV)	C (272 eV)	Ca (291 eV)	Atom Fractions			
		Ir (54 eV)	Ir (229 eV)	Ir (229 eV)	Ir	Th	C	Ca
1	Ridge	0.36	0.35	0.45	0.66	0.24	0.07	0.03
2	Points	0.45	0.43	<0.1	0.68	0.28	0.09	0.00
3	Between Ridges	0.42	0.43	<0.1	0.64	0.27	0.09	0.00
4	Grain Boundary	0.15	<0.2	<0.1	0.88	0.12	0.00	0.00
5	Outside	0.22	<0.2	<0.1	0.83	0.17	0.00	0.00
6	Ridge Network	0.26	<0.2	<0.1	0.81	0.19	0.00	0.00
Same Points After Sputtering 5 minutes								
1	Ridge	<0.02	0.80†	<0.1	0.79	0.00	0.21†	0.00
2	Points	<0.02	0.72†	<0.1	0.81	0.00	0.19†	0.00
3	Between Ridges	<0.02	0.82†	<0.1	0.79	0.00	0.21†	0.00
4	Grain Boundary	<0.02	0.86†	<0.1	0.79	0.00	0.21†	0.00
5	Outside	0.02	0.70†	<0.1	0.81	0.02	0.17†	0.00
6	Ridge Network	0.07	0.61†	<0.1	0.80	0.05	0.15†	0.00

\*Peaks reported as < were not detected.

†Carbon probably introduced by sputtering.

that form at lower temperature and higher stress levels, produce small cracks. Grain-edge cavities in DOP-26 iridium alloy could be w-type cavities.

Grain-boundary liquation is usually not considered as a mechanism that produces grain-boundary cavities. The structural and compositional differences between ridge networks and thorium-bearing grain boundary deposits suggest that weld-quench cracking in DOP-26 iridium alloy may not be caused by the liquation mechanism that produces weld-metal cracking in iridium alloys containing more than 100 ppm thorium.<sup>5</sup>

#### References

1. H. Inouye, "Platinum group alloy containers for radioisotopic heat sources," *Platinum Metal Review* 3: 100-107, 1979.
2. W. R. Kanne Jr., "Welding iridium heat source capsules for space missions," *Welding J.* (to be published).
3. C. L. White, R. E. Clausen, and Lee Heatherly, "The effect of trace element additions on the grain-boundary compositions of Ir + 0.3 Pct W alloys," *Metallurgical Trans. A10A*: 683-691, 1979.
4. D. McLean, *Mechanical Properties of Metals*, New York: Wiley, 1962.
5. S. A. David and C. T. Liu, "Weldability and hot cracking in thorium-doped iridium alloys," *Metal Technology* 7: 102-106, 1980.

## ELECTRON METALLOGRAPHY OF 316 SS AS RELATED TO UNUSUAL CREEP BEHAVIOR (STRAIN BURST)

D. L. Davidson

Optical and backscattered electron metallography have been used to investigate the microstructure of a specimen of 316 stainless steel. This cast microstructure has exhibited discontinuous strains in creep, known as "strain bursts." By using atomic number and channeling contrast, together with selected area electron channeling patterns, one may delineate metallurgical factors that help to explain how "strain bursts" might occur.

Several investigators have found that discontinuous changes in strain occur during the creep and cyclic testing of certain metals. The various reports of these discontinuous strains--the phenomenon is called "strain bursts," or strain "jumps"--trace the history of observation back to one of the original investigators of creep mechanisms, E. N. Andrade, who apparently discovered or at least first reported the phenomenon in 1910.<sup>1</sup> Strain bursts have been observed in polycrystalline and single crystal copper,<sup>2</sup> Al-4% Mg,<sup>3</sup> 304<sup>4</sup> and 316 stainless steels,<sup>4,5</sup> several nickel-based alloys,<sup>6</sup> Alloy 800,<sup>7</sup> and Fe-Al alloys.<sup>8</sup> The metallurgical condition of these different materials is varied, or at least it seems so: both wrought and cast alloys exhibit strain bursts, as do weld structures, and both single and polycrystals. The experimental conditions, particularly temperature, also have been different for the different materials and investigators; this aspect of the strain burst phenomenon has been reviewed recently by Sikka and David.<sup>5</sup>

Various mechanisms have been suggested to account for strain bursts, but they all have in common the development of a dislocation structure which becomes unstable, or a metallurgical structure which becomes unstable, and allows dislocations to move long distances. Klueh<sup>7</sup> believes that dislocation pile-ups result from short-range ordering in Ni-Cr alloys; Sikka and David attribute strain bursts to the formation of strong and weak regions in their cast, dendritic structure. Strong and weak regions are formed, they postulate, by the precipitation of Mo<sub>2</sub>C particles in the molybdenum rich dendrites. Monteiro et al.<sup>4</sup> conclude that a phenomenon similar to the propagation of a Luders band is responsible for strain bursts; Klueh and King have suggested the same thing.

This paper reports the metallographic investigation of one untested 316 stainless-steel specimen machined from material from which many of the specimens exhibited strain bursts when tested in creep. The specimen was No. 48 of the series tested by Sikka and David at Oak Ridge National Laboratory, who have described the composition of the material, the conditions under which it was tested, the location of the specimen within the cast ingot, and other information.<sup>5</sup> Specimen No. 48 was taken from the same relative position in the ingot as Specimen No. 28, which exhibited two strain bursts while being tested in creep at 866°K at a stress of 241 MPa.

### *Technique and Results*

Specimen No. 48 was examined by optical metallography and by the backscattered electron metallographic techniques of atomic number contrast, electron channeling contrast, and selected area electron channeling patterns (SACP). Backscattered electrons were collected by a 4-section silicon p-n junction collector, approximately 2 cm<sup>2</sup>, positioned directly beneath the objective lens, and with no specimen tilt. SACP were made using an after-lens deflection coil arrangement and with a rocking angle of about 10°, at 30 keV.<sup>9</sup> The specimen was cut diametrically by diamond saw and then electropolished in methanol, 25% nitric acid at -20°C. Etching for light optical examination was with the same ferric chloride solution used by Sikka and David. This solution attacks the molybdenum-rich dendritic

---

The author is with the Department of Materials Sciences, Southwest Research Institute, San Antonio, TX 78284. Continued support by the Office of Basic Sciences, Department of Energy, is acknowledged.

regions of this cast structure.

Emphasis was placed on comparative optical and electron metallography of the same regions in order to have the maximum comparative benefit with other work on this material. Thus, Fig. 1 shows relatively low-magnification views of a portion of the specimen obtained by backscattered electrons and optical metallography. The grain boundary in the upper portion of Fig. 1(a) is visible due to electron channeling contrast, with the contrast arising from the crystallographic misorientation between adjacent grains. This grain boundary is shown in its approximate location on Fig. 1(b) by the dashed black line. A faint groove along the grain boundary may be seen between the black dashes. The dendritic structure so evident by light microscopy is only faintly seen in the backscattered image. Here, the contrast is due to the difference in atomic number of the matrix and the dendrites. The atomic number difference is about one half. This effect is better illustrated by Fig. 2, which is a detail of Fig. 1 at higher magnification. The optical micrographs give the appearance of the dendrites having sharp boundaries, so that the idealized concentration profile might appear as a square wave. Conversely, the backscattered electron micrograph indicates that the molybdenum concentration profile is much more sinusoidal in

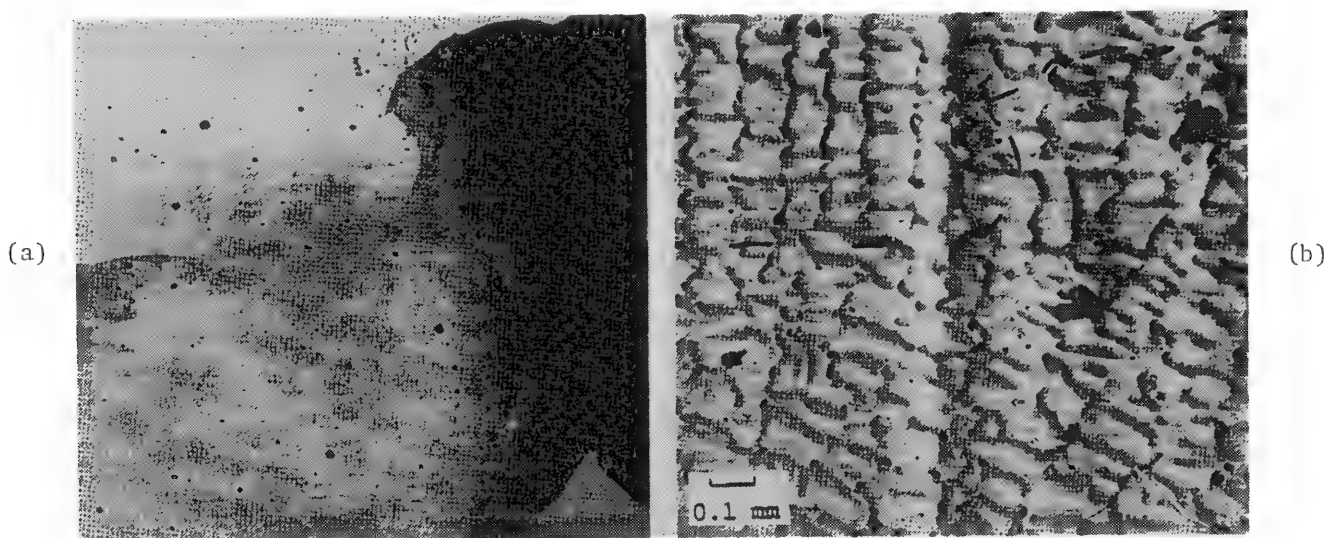


FIG. 1.--(a) Backscattered image and (b) light optical image (Nomarski) of same region showing dendritic and grain boundary structure.

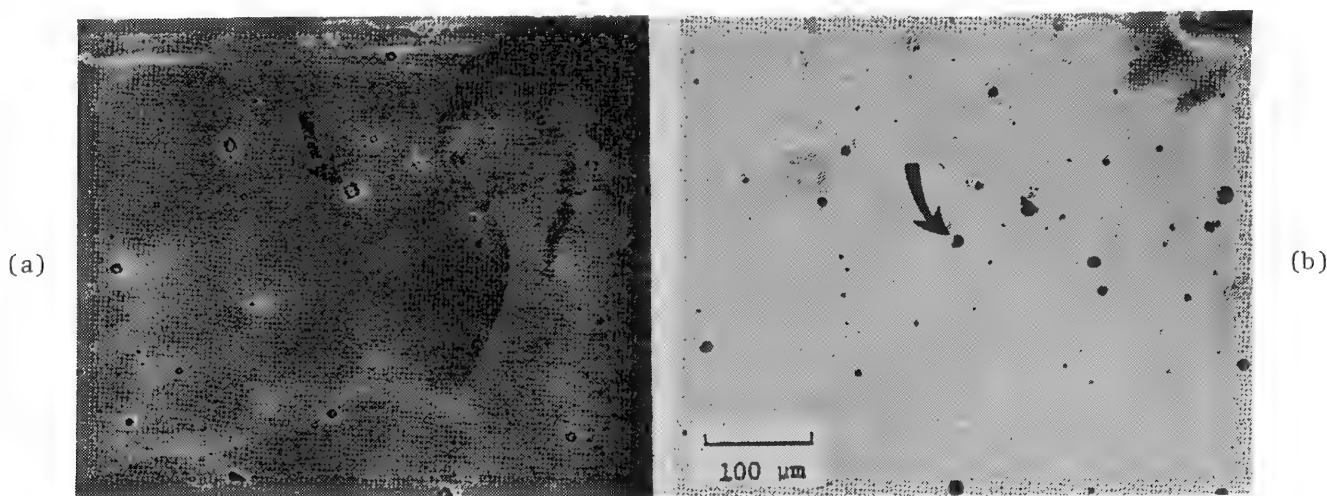


FIG. 2.--(a) Backscattered image and (b) light optical image of same region showing dendritic and grain boundary structure.



gradient, so that the dendrites lack sharply defined concentration boundaries. Note that the regions of higher molybdenum concentration are lighter gray because of the increased backscattered yield of this region of slightly higher atomic number. In fact, concentration profiles by microprobe analysis (Fig. 8 of Sikka and David) indicate much the same results as the backscattered electron micrograph.

A low-magnification channeling micrograph, which reveals at least 10 grains, is shown in Fig. 3, together with the SACP from the grains numbered. The scale is such that 90% of the 6.4mm specimen area is being viewed in this micrograph. Thus, there are approximately 10 grains constituting the specimen cross-sectional area, with grains 1, 2, 3, and 6 covering about 90% of the area of the micrograph. The crystallographic and relative spatial orientations of 6 of the largest grains are shown in Fig. 4. Note that all of the grain orientations lie along a broad band between the (001) and ( $\bar{1}22$ ), except for grain 5. The maximum angular misorientation between normals is  $28^\circ$  between grains 1 and 6. Grains 1 and 3 lie within  $3^\circ$  of the (111) and cover approximately 40% of the cross-sectional area of the specimen.

### Discussion

The results of this metallographic examination would indicate that the material being tested which exhibits strain bursts is not polycrystalline in the sense of being an aggregate of randomly oriented crystallites whose maximum dimension is small as compared to the

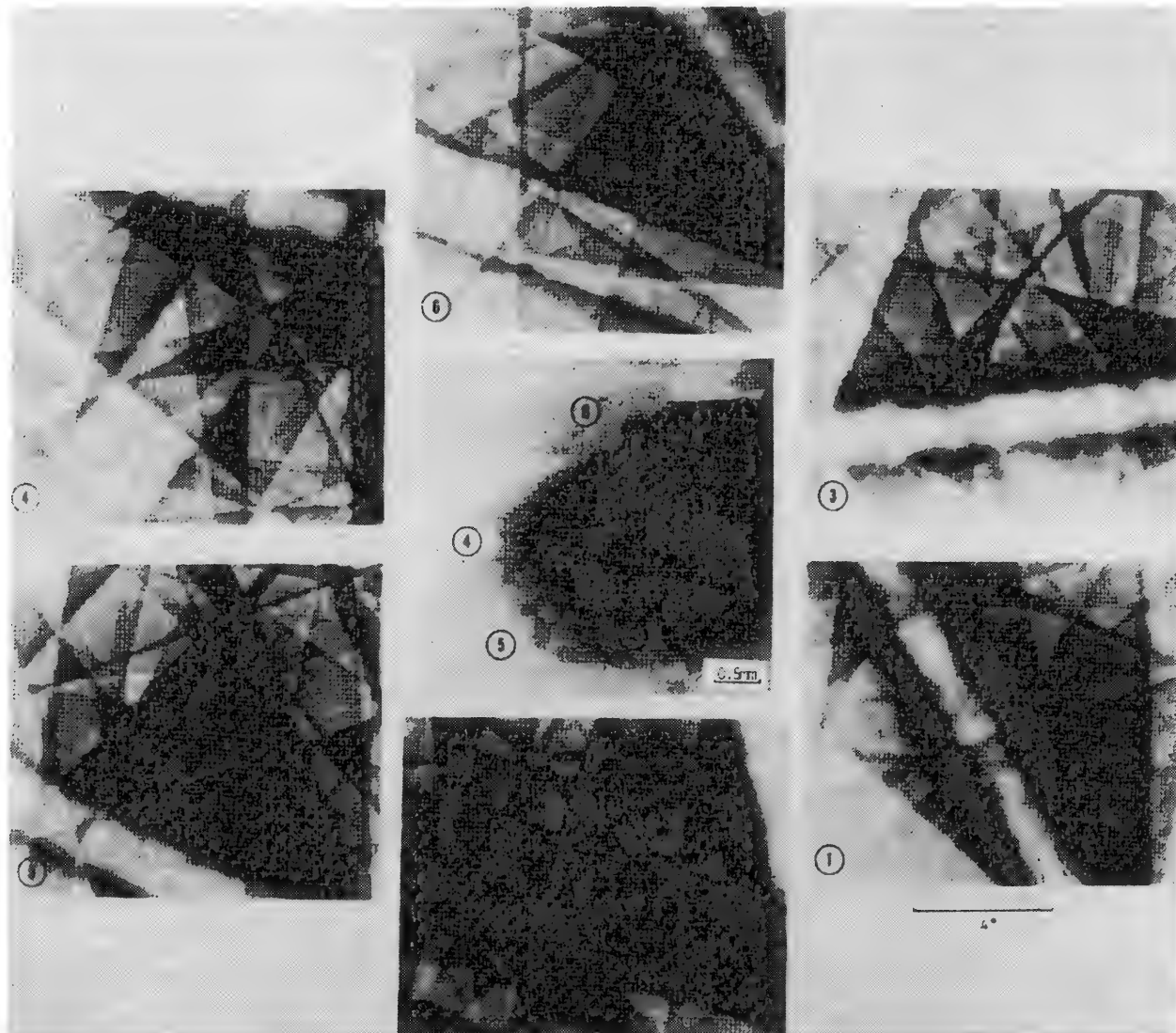


FIG. 3.--Backscattered micrograph of 90% of cross-sectional area of specimen showing very large grains. Selected area electron channeling patterns of numbered grains are also shown.



size of the solid of which they are a part. Conversely, this specimen is a quasi-single crystal, more correctly described as a few crystallites separated by relatively low-angle boundaries. Within each crystallite, there is a slight sinusoidal-type concentration modulation caused by the dendritic structure. Thus, it is easy to understand how dislocations might initiate at a grain boundary, the specimen surface, or some other discontinuity and glide long distances--nearly the diameter of the specimen--without encountering a barrier. The initial barrier might even be a dislocation pile-up caused by strain aging or short range order or something else. Whatever the barrier, slip would then be initiated by thermal activation and the dislocations could glide long distances before meeting another barrier. The SACP of Fig. 3 have very sharp lines and higher-order lines, which indicate the dislocation density of the as-cast material was  $\sim 10^4$ - $10^6$   $\text{cm}^{-2}$ . With such large grain size and low dislocation density, unstable deformation behavior in this material is not surprising, and it is not necessary to hypothesize, in this material, any unusual or complex mechanisms to describe the strain-burst events.

### References

1. E. N. deC. Andrade, *Proc. Royal Soc.* A84:1, 1910.
2. F. Lorenzo and C. Laird, *Mat. Sci. and Engng.* 52: 187-194, 1982.
3. J. L. Kirk, D. K. Matlock, G. R. Edwards, and W. L. Bradley, *Met. Trans.* 8A: 2030-2032, 1977.
4. S. N. Monteiro, T. L. deSilveira, and I. LeMay, *Scripta Metall.* 15: 957-960, 1981.
5. V. K. Sikka and S. A. David, *Met. Trans.* 12A: 883-892, 1981.
6. R. L. Klueh and J. F. King, *Scripta Metall.* 13: 205-209, 1979.
7. R. L. Klueh, *Mat. Sci. and Engng.* 54: 65-80, 1982.
8. A. Lawley, J. A. Coll, and R. W. Cahn, *AIME Trans.* 218: 166-173, 1960.
9. D. L. Davidson, *J. Phys. E* 9: 341-343, 1976.

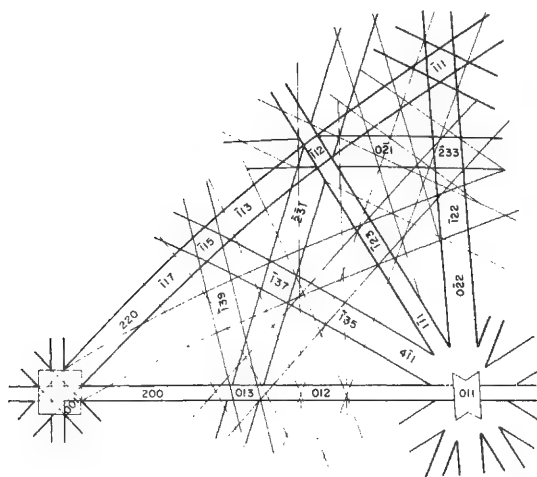
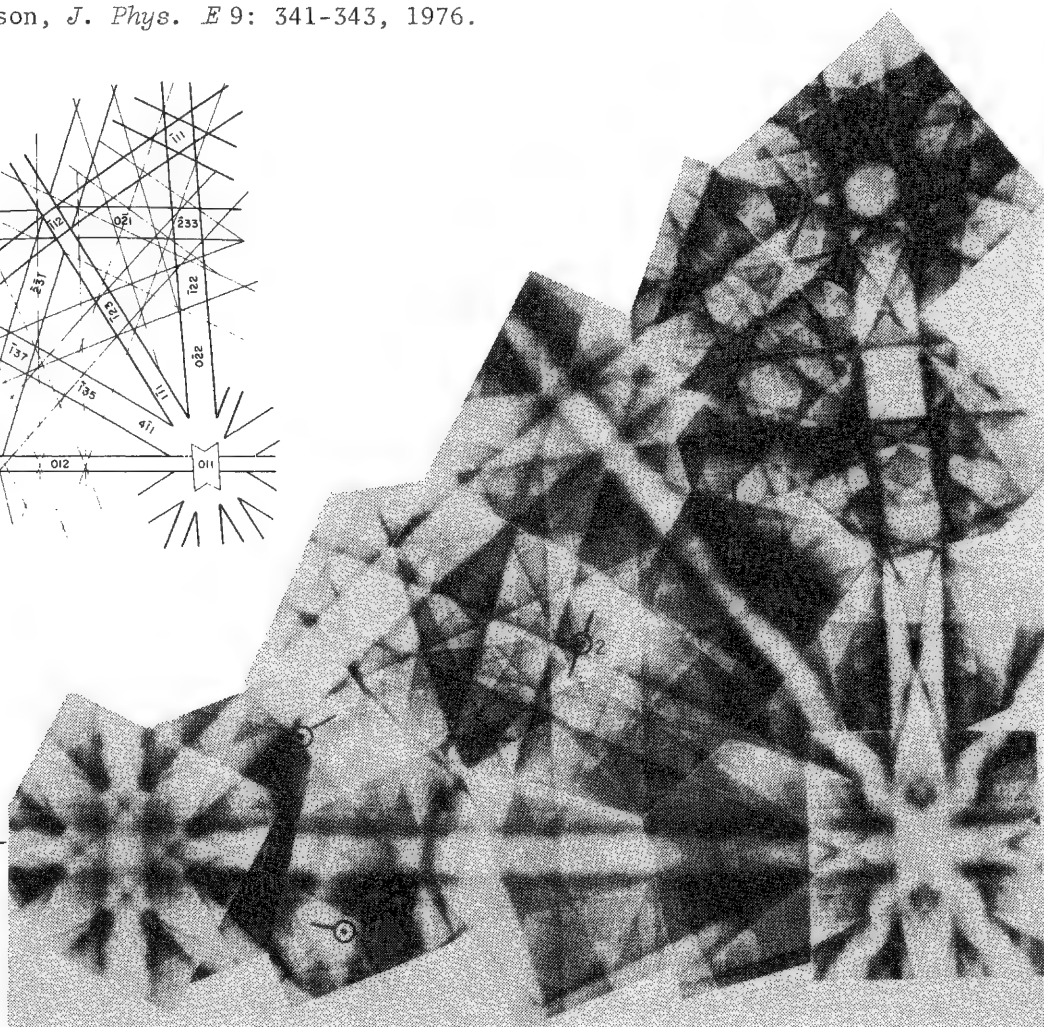


FIG. 4.--Face-centered cubic channeling map and crystallographic key (copper, 30 keV) showing location and relative orientation of SACP in Fig. 3.



## MICROPROSPECTING FOR PRECIOUS METALS WITH AN AUTOMATED ELECTRON MICROPROBE

M. D. McConnell, R. B. Bolon, and W. T. Grubb

Precious minerals occurring in micron-size particles but dispersed in other phases so that their overall average concentration is 1 ppm or less have been successfully located with automated electron microprobe procedures. Although initially developed to locate gold in discarded mine tailings, this technique has also been used to find micron-size silicon grains in aluminum oxide and arsenic grains in heavy mineral concentrates.

The ability to find small micron-size grains at the parts per million level in a matrix of solid material or fine powder becomes important not only when one is looking for low-level impurities, but also for valuable minerals in low concentration. The advantage in finding these particles in place is that the phase or phases they are associated with can also be identified. This information can be valuable in optimizing extraction processes.

### *Method*

The procedure combines specimen stage stepping and electron beam scanning or rastering to examine large areas of polished specimens. To get a feeling for the size of the area that must be scanned to find one particle, we considered the problem of finding 1  $\mu\text{m}$  gold particles at a level of 0.1 ppm. A 1  $\mu\text{m}$  particle of gold weighs  $2 \times 10^{-11}$  g in tailings with an average density of 2.8 g/cm<sup>3</sup>. Therefore 1 cm<sup>3</sup> would contain 14 000 1  $\mu\text{m}$  particles of gold. Based on an average analysis depth of 1  $\mu\text{m}$ , that corresponds to 1.4 particles per square centimeter of sample surface. A 50  $\mu\text{m}$  raster was selected as a compromise between too large an area to permit detection of a particle within it and too small so as to extend the analysis time beyond acceptable limits. The crystal spectrometers were used because of their superior wavelength resolution and count rate capability relative to energy-dispersive systems. The x-ray intensity on the pure gold standard at 25 kV and a beam current of 250 nA is 35 000 counts per 5 s. The fractional area of a 2  $\mu\text{m}$ -diameter particle in a 50  $\times$  50  $\mu\text{m}$  raster is  $1.6 \times 10^{-3}$ . Therefore the signal expected from this particle in 5 s would be approximately  $56 \pm 20$  counts. In order to cover 1 cm<sup>2</sup> sample surface, it was determined that 40 000 areas would have to be scanned for a total data collection time of 56 hr. Any increase in data collection time to improve sensitivity would go beyond the constraints of machine stability and availability. However, some improvement in sensitivity was obtained by tuning two spectrometers to the Au M $\alpha$  line and summing the values.

A computer-controlled Cameca model MBX microprobe was used to search the sample at 50  $\times$  50  $\mu\text{m}$  fields with a dwell time of 5 s. Two crystal spectrometers were tuned to the gold M $\alpha$  line at 5.84 Å. A flextran program was written to step the stage, measure intensities, and store coordinates of values which are twice the average background. Initial experiments revealed a minor zirconium line at 5.83 Å that overlapped the gold line, and many zirconium-rich particles were being counted. Thus a third spectrometer was tuned to a major zirconium line and these hits were automatically rejected. The microprobe was set up to operate overnight, and the following day hits were relocated and a detailed analysis of the particles and their surrounding mineral phases was accomplished by use of the energy-dispersive detector and the scanning capabilities.

### *Sample Preparation*

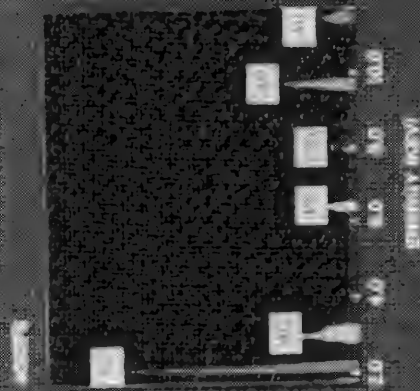
Since the samples used in this study were powders about 100-200 mesh in size, it was necessary to press and mount the samples for microprobe examination. The powders were

The authors are with General Electric Corporate Research and Development, K-1, GE R&D Center, Schenectady, NY 12303.

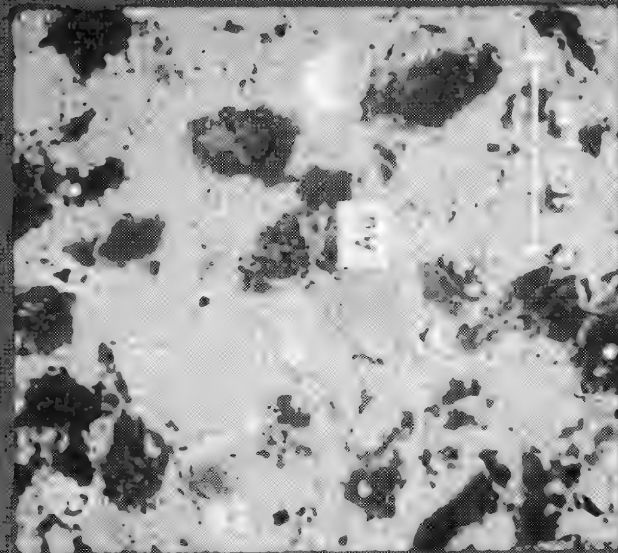
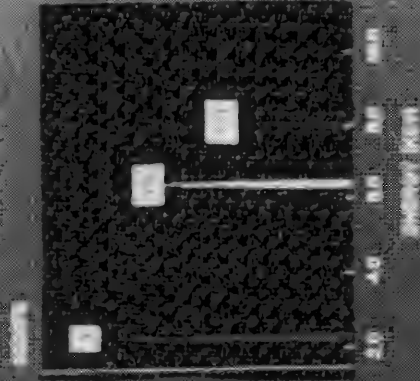
**Results from  
Raster Step Scan**

**One Gold Particle  
Found for Ten  
Thousand Areas  
Scanned — 15 Hours**

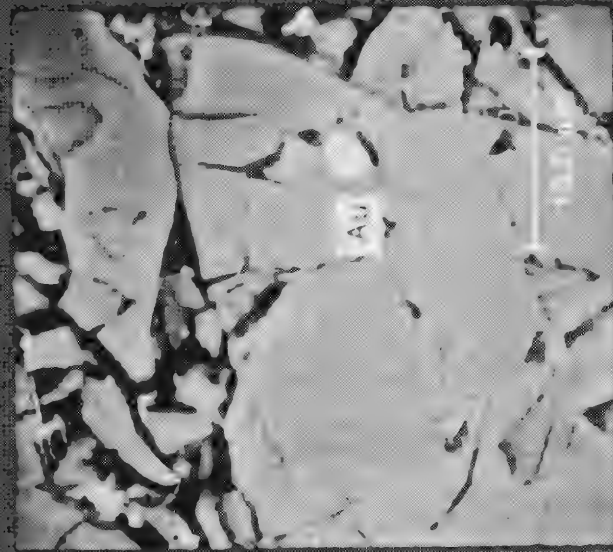
40.00 HOURS  
IN CHARGE TIME



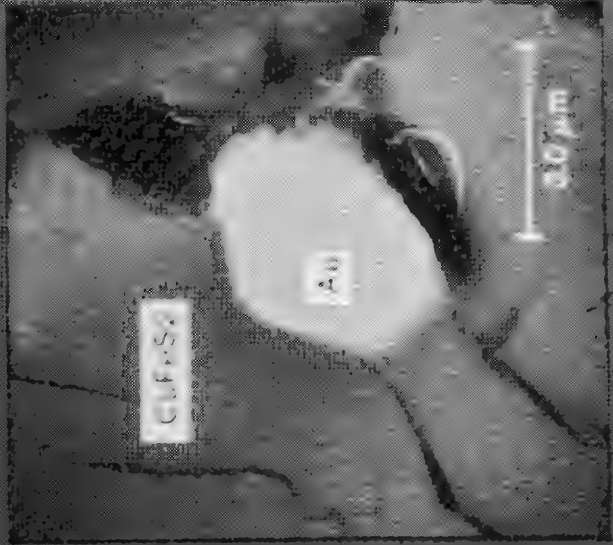
CHARGE RATE



PROCESSED ORE 6PPM Au  
25 KV X200



PROCESSED ORE 6PPM Au  
25KV X2,00K



PROCESSED ORE 6PPM Au  
25KV X10,0K

pressed at 25 tons into half-inch disks. The disks were mounted in epoxy resin and carefully polished through a series of abrasives ending with 0.3 $\mu$ m aluminum oxide. Experimentally it was found that heavy mineral concentrates could be prepared in this manner in the as-received condition. However, tailings and ground ore rock were not coherent enough to withstand the polishing procedure. In these cases, the powders were first coated with copper by an electroless deposition procedure<sup>3</sup> and then pressed, mounted, and polished. The copper not only acted as a binder, but also provided electrical and thermal conductivity. Samples were lightly coated with carbon to improve conductivity.

### *Results and Discussion*

The first sample analyzed was a copper concentrate with 6 ppm Au. After 15 hr of microprobe time, during an overnight run, one gold particle 3 $\mu$ m in diameter was located within a chalcopyrite grain. Plate 1 is a series of micrographs of this particle and the surrounding matrix. The lower left micrograph typifies the problem. The gold particle at 200 $\times$  is just visible to the left of the white label. High-atomic-number elements show up as bright areas in a low-z matrix; however, this feature is not always sufficient for a successful search. Note that the actual gold particle is not visually distinguishable on that basis. Other investigators<sup>1,2</sup> used this method of searching by scanning polished sections in the backscattered electron mode looking for bright areas. All bright areas had to be examined to determine their noble-metal content. This procedure is very time consuming and tedious. The method described herewith leaves the microprobe unattended until several hits have been located on the sample. Subsequently a second gold particle about 2.5  $\mu$ m in diameter was found embedded in an aluminum silicate mineral.

A final tailings sample composed mostly of aluminum silicates and containing 0.1 ppm of gold was prepared metallographically and searched. After scanning 26 000 areas, one 5 $\mu$ m gold particle was discovered. A copper halo surrounded this gold particle, which suggests that it was a free particle that received copper plating during preparation. Energy-dispersive analysis revealed little if any silver in this particle. At the close of this study a total of 13 Au particles were identified and characterized.

In a similar study, heavy mineral concentrates were searched for the presence and association of arsenic, thought to be present at the 1000ppm level. Two arsenic phases were located in a 10 000 raster analysis. Another project successfully located 1 $\mu$ m silica particles in alumina powder. Future work is planned to locate specific impurities in coal ashes.

### *References*

1. H. D. Freeman, J. N. Hartley, and O. J. Wick, "Scanning electron microscopic and microprobe analysis of refractory gold ores and process implications of the analysis," *Process Mineralogy, Extractive*, Chicago, 1981.
2. R. W. G. Wyckoff and F. D. Davidson, "A use of the scanning electron microprobe in mining exploration," *Norelco Reporter* 29 (No. 2), July 1982.
3. A typical electroless Cu deposition procedure is described by E. B. Saubestre et al. in U. S. Patent 3 460 952.

## DETERMINATION OF XENON IN IRRADIATED NUCLEAR FUEL BY MEANS OF A SHIELDED ELECTRON MICROPROBE

E. D. Jenson

A technique for the determination of fission product xenon in irradiated nuclear fuels is presented. Xenon concentrations under 0.5% in a  $\text{UO}_2/\text{PuO}_2$  matrix are routinely determined using this technique. Due to the radioactivity of the samples, a shielded microprobe, MAC 450, is used. Results on experimental breeder reactor fuel show that the retained xenon is almost entirely contained in the unrestructured fuel area, i.e., the outer 1/4 of the pin radius.

The distribution of xenon in irradiated nuclear fuel has important thermal and nucleonic consequences. Thermally, the presence of xenon gas bubbles decreases the fuel conductivity relative to unirradiated fuel and can thus limit the effective power delivered by a reactor. Also, the gas bubbles lead to fuel swelling,<sup>1</sup> which is highly undesirable. From the nucleonic standpoint, the high affinity of  $^{135}\text{Xe}$  for neutrons has been known to depress the nuclear flux so severely that reactor criticality could not be achieved.<sup>2,3</sup> Clearly, the influence of xenon on fuel performance is such that we should be well informed on its behavior during reactor operation. Therefore, we need good analytical techniques to determine xenon in irradiated fuel.

Much of the early work on fission gases in nuclear fuel was carried out by use of transmission electron microscopy (TEM),<sup>1</sup> to study the distributions, size, and morphology of the xenon/krypton bubbles. More recent work has been with scanning electron microscopy, laser fusion techniques,<sup>4</sup> and high-temperature fusion with gas chromatographic detection.<sup>5</sup> The present contribution addresses a technique of determining relative xenon concentration by means of a shielded electron microprobe.

The determination of xenon by microprobe is done by driving a spectrometer over the  $\text{Xe L}\alpha$  x-ray peak (3.016 Å) from about 8 x units above to 8 x units below the peak maximum. The wavelength-dispersive spectrometer is driven over the peak in 0.5 x units steps, counting for 10 s at each position. The data are then smoothed and the minimum on each side of the peak is located. The count rates at the minima are averaged and used as backgrounds. The sum of all count data (minus background) between the minima is taken as the peak area. An approximate concentration is obtained by comparison to the corresponding peak area of barium in the mineral benitoite. Since long runs (4-8 hr) are typical, the matrix element uranium is used as an internal standard to correct for beam current drifts during the analysis. The concentrations of xenon found are usually a few tenths of a percent, rarely as much as 1%. Normally a sample current of 1  $\mu\text{A}$  at 25 kV is used.

It is frequently difficult to tune the microprobe to elements at this concentration range due to the low counting rate. The above technique eliminates that problem by covering a range including the peak. Also, backgrounds across a section of irradiated nuclear fuel change due to the uneven distributions of fission products, and therefore beta/gamma activity, across the pin. These effects are also corrected for since backgrounds are taken at every analysis position.

Xenon standards for electron microprobe work are nonexistent. The compound  $\text{Na}_4\text{XeO}_6$  has been used to determine the wavelength of the xenon x-ray lines,<sup>6</sup> but is unstable under electron-beam bombardment and therefore is not usable. Xenon implanted in fuel is probably an acceptable alternative, but we have not tried that approach. Our work has been more concerned with relative xenon concentrations than absolute values. On a relative basis, the xenon standard has been approximated by a barium standard. The sample current is reduced from 1  $\mu\text{A}$  on fuel to a few tenths of a microamp on benitoite to avoid damaging the mineral surface. Use of Ba in this way allows direct comparison between xenon concentra-

---

The author is with the Hanford Engineering Development Laboratory, Richland, WA 99352.



tions in different fuel samples. Since relative values of concentrations are all that is needed, we apply no ZAF (atomic number, absorption, fluorescence) corrections to the data. Also, the xenon distribution is inhomogeneous and the ZAF corrections would be difficult to apply rigorously.

Interference with the xenon determination arises from either the  $\text{UO}_2/\text{PuO}_2$  matrix or the other fission products generated along with xenon. A uranium fourth-order  $\text{L}\beta$  line is almost superimposed on the xenon line.<sup>7</sup> However, it is easy to discriminate against that line by the pulse-height analyzer. A potentially more serious problem is from the first-order tellurium  $\text{L}\beta$  line, at 7 x units lower wavelength. However, the concentration of tellurium is only about 20% of that of xenon (after a reasonable time is allowed for radioactive decay) and its x-ray intensity, from elemental tellurium, is less than 10% of the intensity of the xenon  $\text{L}\alpha$  line used for analysis. Therefore, the extent of tellurium interference should be small. Another fission product, antimony, has a first-order  $\text{L}\beta$  peak 5 x units from xenon and could create some problems. However, the concentration of antimony is only about 1% of that of xenon. Also, the line intensity is only about 15% that of xenon. Hence, we expect no problems from this source. Other interferences exist from other fission products, but they are from multiple-order lines and can easily be discriminated against by use of the pulse-height analyzer.

A comparison of xenon concentrations determined by microprobe analysis and by some other independent method is highly desirable. The best comparison would be between two fuel samples from the same pin at adjacent positions. This procedure would assure the same neutron exposure and temperature history for both samples. Such a comparison has never been made. However, a comparison has been attempted between sibling pins--with the same fuel composition, pin structure, and (if possible) irradiation history--on which xenon has been determined gas chromatographically (after fusion) on one sample and by microprobe on the other.

The gas chromatographic technique measures the total amount of xenon present in a sample; the microprobe technique measures the concentration of xenon in a very small area. Hence the microprobe data must be integrated across the entire surface of the pin. The results have been variable, ranging from excellent agreement to poor. One of the problems is having a true sibling pin following irradiation and thus a valid comparator. Accumulated dose, operating temperature, and power are usually different and lead to different microstructure of the fuel. Changes in the fuel microstructure can lead to significant differences in retained fission gas. For example, changes in microstructural properties such as open or closed porosity lead to changes in the amount of fission gas retained. Closed porosity effectively traps xenon bubbles within the fuel; open porosity allows gas to move readily to cracks or the surface and escape. Such differences in fuel structure make comparison between fuel pins very difficult.

The effect of localized heating by the impinging electron beam could be significant. Sufficiently high temperature could increase the mobility of the xenon enough to allow it to diffuse through the fuel matrix and escape. Experiments to look for this effect have shown that the xenon concentration remains constant for at least 30-40 min. However, since a measurement takes 8-10 min, an initial rapid loss of xenon would not be detected.

In prototype breeder reactor type fuels, almost all the xenon is found in the outer 1/4 of the fuel radius, i.e., the unrestructured region. Some xenon may still be detected in the thermally hotter central region of the fuel in pins operated at lower power levels. However, in high-power fuel pins, xenon is usually undetectable in the central region of the fuel. Figure 1 shows the relative xenon concentration from 3 fuel pins irradiated to about the same burnup, but at power levels differing by about a factor of 2.

## References

1. D. R. Olander, *Fundamental Aspects of Nuclear Reactor Fuel Elements*, Springfield, Va.: DOE, 1976.
2. J. F. Hogerton, *The Atomic Energy Handbook*, New York: Reinhold.
3. Stephane Groueff, *Manhattan Project*, Boston: Little, Brown, 1967.
4. D. G. Graczyk, G. Dandyopadhyay, S. M. Gehl, J. P. Hughes, and H. T. Goodspeed, *A Laser Microsampling Method for Determination of Retained Fission Gas In Irradiated Nuclear Fuel*, ANL-79-86.
5. D. L. Baldwin, *New Instrument Method for Determining Noble Fission Gas Retained in Irradiated Oxide Fuels*, HEDL-Misc-7004.

6. W. F. Zelezny, G. W. Gibson, and M. J. Graber, *A Microprobe Study of the Retention of the Fission Gas Xenon in Irradiated Uranium Fuels Dispersed in Aluminum Clad Nuclear Reactor Fuel Plates*, CONF-690910.

7. E. W. White and G. G. Johnson Jr., *X-Ray Emission and Absorption Edge Wavelengths and Interchange Settings for L. F. Geared Curved Crystal Spectrometer*, Earth and Mineral Sciences Experiment Station Special Publication 1-70, University Park, Pa.: Pennsylvania State University.

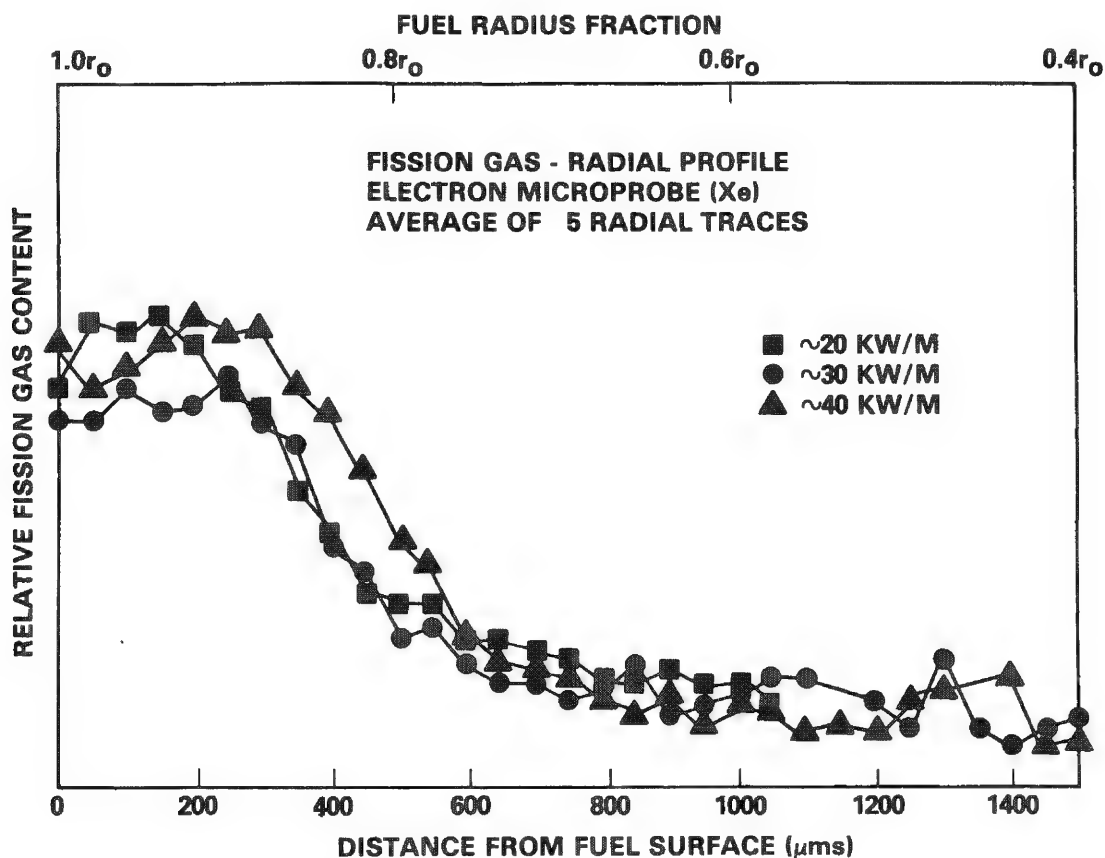


FIG. 1.--Relative radial profiles of retained (intragranular) fission gas at axial midplane from three fuel pins irradiated to about 50 kWd/kg at about 20, 30, and 40 kW/m.

## 6

# Scanning Electron Microscopy

### MEASURING THE FIELD FROM A MAGNETIC RECORDING HEAD IN THE SCANNING ELECTRON MICROSCOPE

O. C. Wells, P. J. Coane, and C. F. Aliotta

In optical photography, the schlieren image can show the shock wave from a bullet or from the model of a supersonic airplane in a wind tunnel.<sup>1</sup> A similar effect can be achieved in the SEM by rocking the beam about a point in the plane of a knife edge, contrast aperture, or reference mesh<sup>2,3</sup> by means of the selected-area electron channeling pattern (SA-ECP) scanning mode.<sup>4</sup> This procedure makes it possible to modify the field-plotting techniques of Thornley and Hutchison<sup>5</sup> (the TH method) and of Rau and Spivak,<sup>6</sup> so that the image now shows the contours of equal beam deflection directly (although at present over a smaller area), rather than in a derived manner. As is so often the case, the TH method can now be used together with the new ideas to give a more powerful combined approach.

#### Scanning Modes

In the TH method, the sample is mounted at a glancing angle in the SEM so that the electron beam must pass through the fringing field to reach a reference mesh located below (Fig. 1a). In the image, the reference mesh occupies half the space; the recording head is seen edge-on in the foreground (Fig. 2). If there is a fringing field above the specimen, the beam is deflected through an angle

$$\theta_{\text{def}} = 17BL/\sqrt{E_0} \text{ degrees} \quad (1)$$

where  $E_0$  is the electron beam energy in eV and  $BL$  is the deflecting field-times-distance integral (FDI) in gauss-cm. The displacement  $D$  in the reference plane caused by this deflection is then

$$D = S \sin \theta_{\text{def}} \quad (2)$$

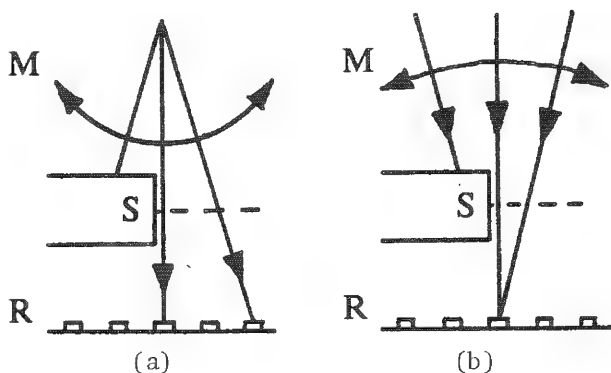


FIG. 1.--(a) Topographic scanning mode as used by Thornley and Hutchison.<sup>5</sup> (b) SA-ECP scanning mode as used in schlieren method.<sup>2,3</sup> (M = scanning mode, S = specimen, R = reference mesh)

where  $S$  is the distance between the specimen and the reference plane. In the present work, where  $S = 0.45$  cm and  $E_0 = 10$  keV, Eq. (2) reduces to:

$$D = 0.0027BL \quad (3)$$

where  $D$  is in cm and  $BL$  in gauss-cm. If the beam is scanned in the manner shown in Fig. 1(a), this displacement distorts the image of the mesh. The FDI can be expressed as either  $(FDI)_{\rightarrow}$ ,  $(FDI)_{\uparrow}$  or  $(FDI)_0$  depending on whether it is a component of the field in the direction of the arrow or the total field that is being integrated in the FDI. The direction of the arrow (whether  $\rightarrow$  or  $\uparrow$ ) also shows the direction of the mesh bar that is displaced sideways in the image by that component of

The authors are at IBM Thomas J. Watson Research Center, PO Box 218, Yorktown Heights, NY 10598. They wish to thank B. P. Piggan for providing the samples and for helpful discussions, and J. J. Bucchignano, D. P. Kern, J. L. Speidell, R. G. Viswanathan, and H. R. Voelker for fabricating the reference meshes.



the field.

In the schlieren method in the SEM, the beam is rocked about a point in the reference plane using the SA-ECP scanning mode (Fig. 1b). The following argument can be used to show that the two sets of mesh bars are now distorted in the image to lie along the contours of equal  $(FDI)_{\rightarrow}$  and  $(FDI)_{\uparrow}$  in the specimen plane. Consider first the mesh bars  $\rightarrow$  that are parallel to the surface of the specimen. If there is no field, the beam lands in the center of a mesh bar throughout the entire scanning motion, to give a uniform gray level in the recorded secondary-electron image. At points that lie along a certain contour in the specimen plane, the  $(FDI)_{\rightarrow}$  have the precise value needed to deflect the beam onto the edge of the adjoining mesh bar, whose edge therefore appears in the recorded image to lie along that contour in the specimen plane. In other words, the edges of the mesh bars will appear to lie along the contours of equal FDI because the point of arrival of the beam in the reference plane is determined (to first order) *only* by the FDI along the electron path, and *not* by the position of the scanning beam.

### Nomenclature

The word *schlieren* is derived from the German noun *Schlieren*, meaning *shadow*. The Foucault test for telescope mirrors also involves the use of a knife edge and is mathematically very similar. The present application, which shows a *shadow* of the magnetic field (such as in Fig. 4a) resembles the schlieren method for showing shock waves in air more closely than it resembles the testing of mirrors for geometrical accuracy.<sup>1</sup> The word *schlieren* was used by Marton and Lachenbruch<sup>7</sup> to describe images of the fringing field from a magnetized wire in the transmission electron microscope, which is entirely appropriate. (It is not clear why the word *Foucault* later replaced the word *schlieren* in that situation.) For the purpose of describing this image contrast in the SEM, it would seem that the word *schlieren* is also appropriate.

Marton and Lachenbruch<sup>7</sup> drew a clear distinction between two methods for studying magnetic fields in the TEM. The first was the schlieren method, which is the reciprocal of the schlieren method as described here.<sup>2</sup> The other involved "deformed shadows of a thin obstruction" and gave images that were essentially the same as are given by the TH method. A problem with the nomenclature then arises if the knife edge in the schlieren method is replaced by a mesh, because *in both cases* the image (whether obtained by the TH method as in Fig. 2b or by the schlieren method as in Fig. 4b) can then be regarded *either* as a spatially undistorted image of the specimen plane *or* as a distorted image of the mesh.

The critical distinction between these two methods is whether the mesh lines appear to be lined up along the FDI contours or not. In this paper, the word "schlieren" has been extended to refer to images in which the mesh bars *are* lined up along the contours of constant FDI. This extension can be justified by regarding Fig. 4(b) as a superposition of schlieren images where each side of each mesh bar corresponds to a knife edge.

### Experimental

Two types of reference mesh were used. The first consists of parallel lines in two directions at right angles (Fig. 2). The periodicity is 10  $\mu\text{m}$ ; the line width is 2.66  $\mu\text{m}$ . This shows the contours of equal deflection about lines that were parallel  $\rightarrow$  and perpendicular  $\uparrow$  to the surface of the head. The second consists of concentric circles with a difference of 2.5  $\mu\text{m}$  in the radius from one circle to the next (Fig. 5a). This was used to show the lines of *total* beam deflection. In both cases, the meshes were formed by electron beam lithography from a 4000Å gold film on a silicon wafer. The reference mesh could be centered in the SEM independently of the motions of the sample.

Figures 2-4 show some results obtained with an experimental ferrite recording head and the rectilinear reference mesh. The SEM was a Stereoscan S-250 (Cambridge Instrument Co.). The head had been mounted during manufacture at the center of an approximately flat, circular "flying assembly" of diameter 0.72 cm. It was carbon coated to prevent charging and mounted with the gap parallel to the beam at an adjustable glancing angle of between zero and  $\sim 2^\circ$ . The surface of the head and of the flying assembly can therefore be seen (if at all) with considerable foreshortening. Owing to the rocking motion, the magnification in the plane of the head is less than the magnification of the foreground detail on the closer edge of the head assembly.

Figure 2 shows the TH method. Here, Fig. 2(a) was obtained with the head switched off;

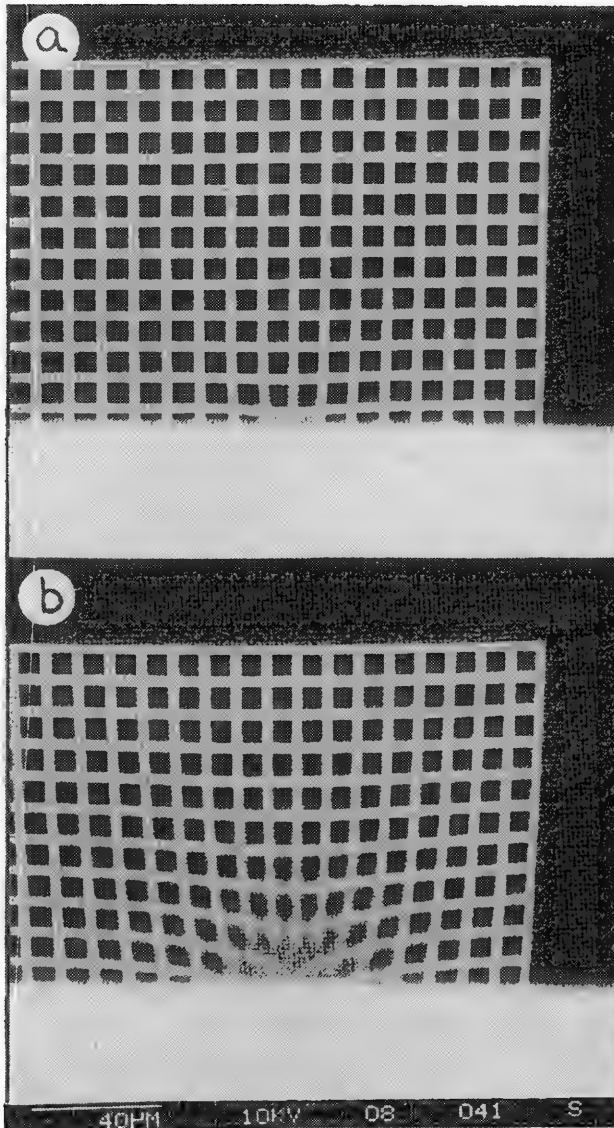


FIG. 2--Study of an experimental ferrite magnetic recording head by the TH method:<sup>5</sup> (a) with no current; (b) with 10 mA dc excitation ( $E_0 = 10$  keV, periodicity of mesh =  $10 \mu\text{m}$ .)

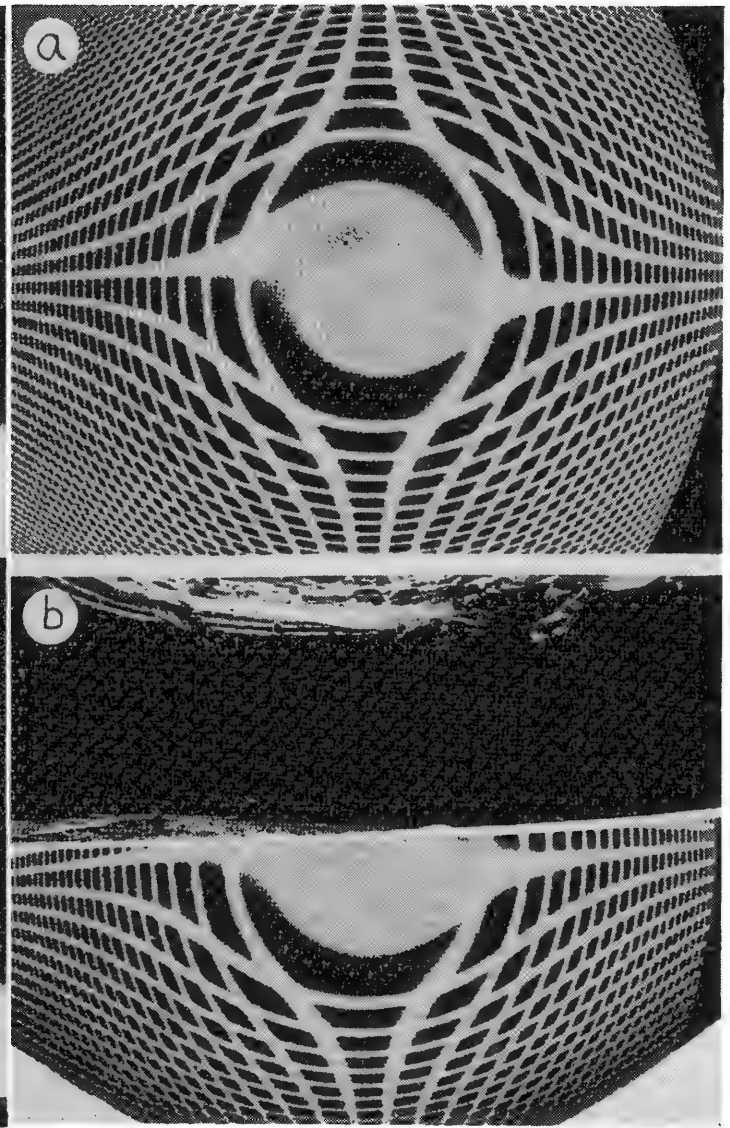


FIG. 3--Setting up for schlieren method: (a) SA-ECP image of reference mesh at lowest available magnification (note central uniform area); (b) with head moved to center of field.

Fig. (2b) shows the effect of 10 ma dc. Three effects can be seen. First, the entire mesh shifts downwards by 1.0 mesh spacings ( $= 10 \mu\text{m}$ ), as is shown by the displacement of the top right corner of the mesh. This uniform shift is the result of a uniform "background"  $(\text{FDI})_{\rightarrow}$  of 0.1 gauss-cm produced by this particular head. Second, there is a localized distortion in Fig. 2(b) caused by the field from the gap. Third, there is a small (but nevertheless quite visible) distortion of 0.15 mesh spacings close to the gap even when the head is switched off, which is caused by the remanent magnetization (equivalent to an  $(\text{FDI})_{\rightarrow}$  of 0.03 gauss-cm) of the head. (In this image, as with Figs. 4 and 5 below, the position of the gap is several microns into the bright region where the beam strikes the head.)

The procedure for obtaining a schlieren image is as follows. First an SA-ECP image of the reference mesh is obtained at lowest possible magnification (Fig. 3a). The central uniform area represents the angular range of scan over which the rocking beam is incident onto a mesh bar. In the outer parts of the image, the spherical aberration in the final

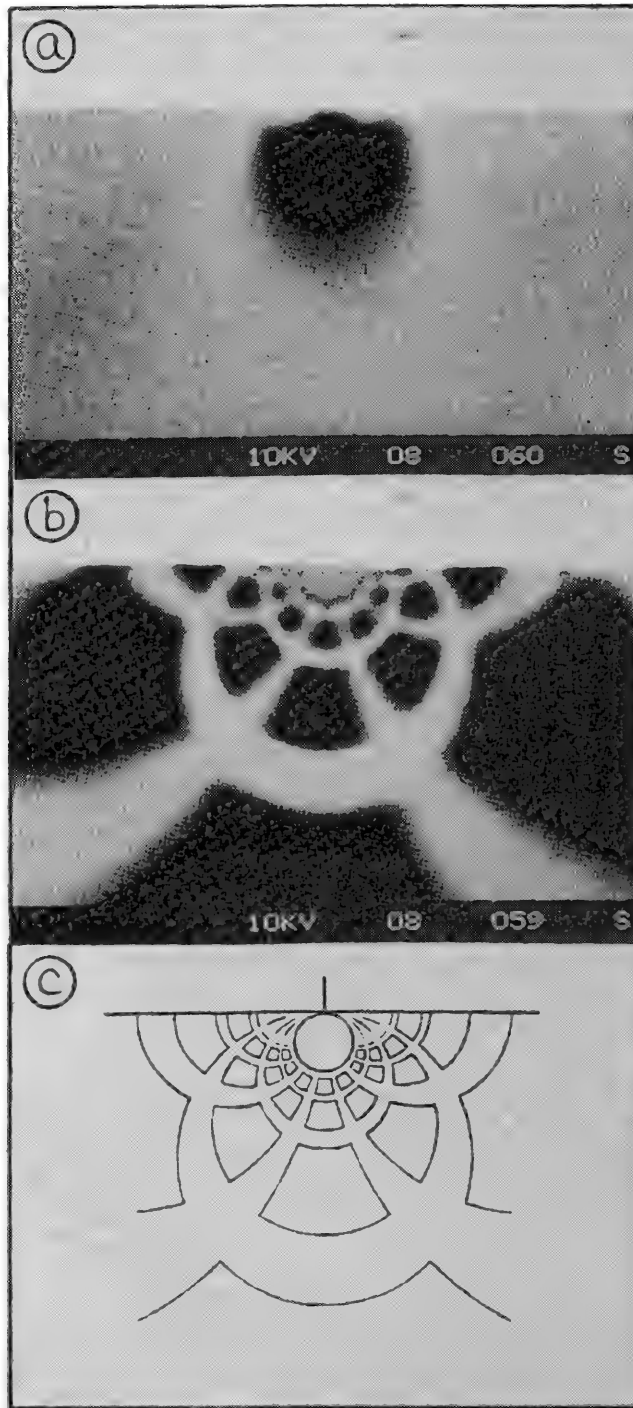


FIG. 4.--After increasing magnification in Fig. 3: (a) schlieren image with no current (showing x component of remnant field); (b) with 10 mA dc excitation; (c) circles drawn according to model proposed in text. ( $E_0 = 10$  keV; horizontal field of view in plane of field measures  $45\text{ }\mu\text{m}$  from left to right.)

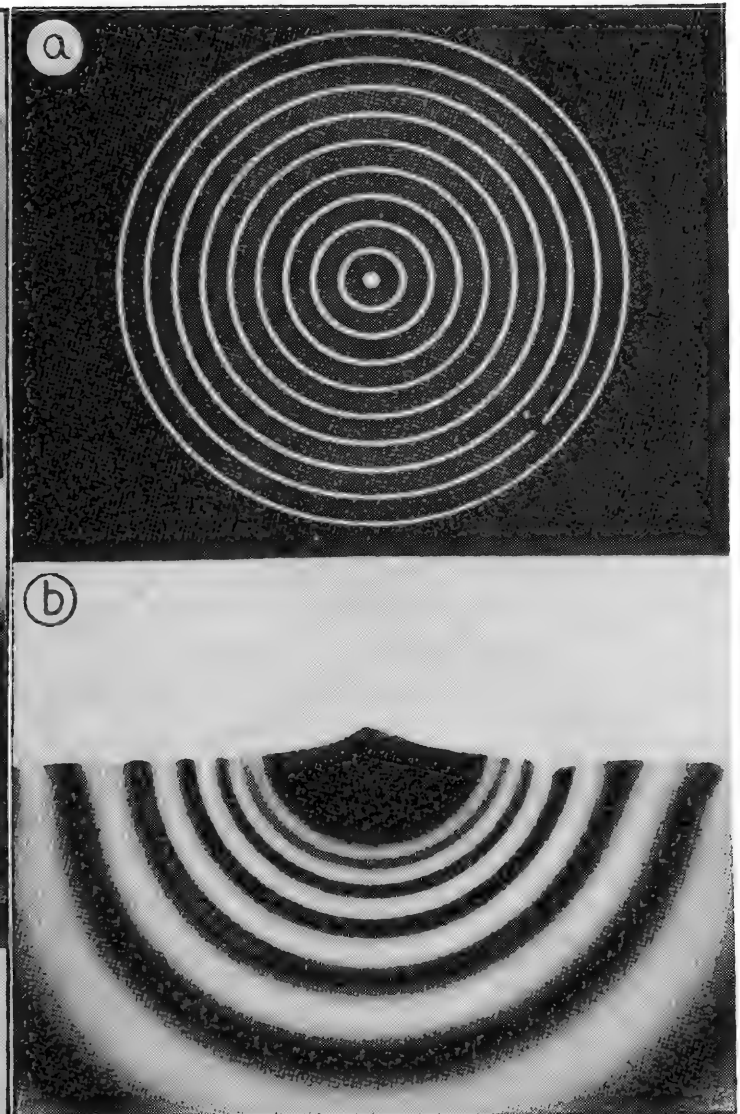


FIG. 5.--Plotting contours of *total*  $(FDI)_0$  rather than  $(FDI)_\rightarrow$  or  $(FDI)_\uparrow$ : (a) reference target consists of concentric rings that must be accurately centered on SEM axis (diameter of outer circle =  $45\text{ }\mu\text{m}$ ); (b) in schlieren image, innermost circle corresponds to outermost circle in target.

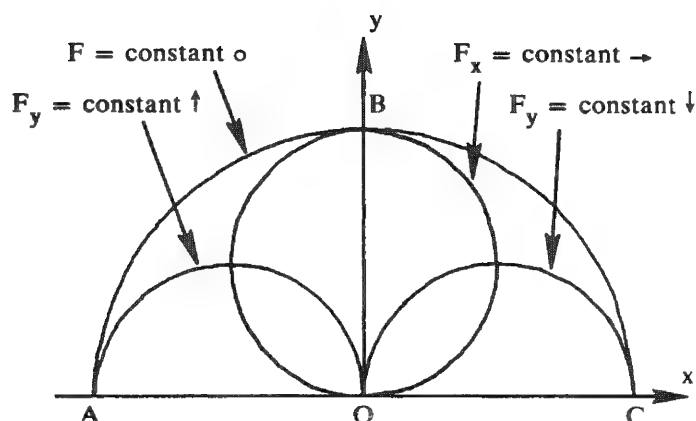


FIG. 6.--Lines of constant  $F$ , constant  $F_x$ , and constant  $F_y$  drawn according to two-dimensional potential distribution given by Eq. (4).

ic scanning mode. (The micrographs are shown here as they appear on the screen of the SEM.)

The small dark area in Fig. 4(a) shows the  $x$  component of the remanent flux when the head is switched off. The edge of this area corresponds to a deflection of half of the width of the mesh bar, or a  $(FDI)_\rightarrow$  of 0.5 gauss-cm. If the head is energized, the mesh bars are distorted to lie along the contours of equal  $(FDI)_\uparrow$  or  $(FDI)_\rightarrow$  about axes parallel to the directions of the mesh bars (Fig. 4b). The interval in  $(FDI)_\uparrow$  or  $(FDI)_\rightarrow$  between the successive mesh bars in Fig. 4(b) is calculated to be 0.37 gauss-cm from Eq. (3).

The easiest way to obtain an absolute calibration for the curved mesh bars in Fig. 4(b) is to rock the beam about a bar that is--for example--the fifth from the edge of the reference target. The curved bars in the center of Fig. 4b then disappear (as is the case in Fig. 4c). The calibration of the innermost bar is then given by the deflection to the edge of the reference mesh. A mesh with coded bars is being prepared to facilitate calibration of the image.

Another way to identify the bars is from the model for an unsaturated head with a vanishingly small gap described below. The circles in Fig. 4(c) are drawn according to this model on the assumption that the rocking point is at the center of the fifth bar from the edge of the reference mesh. (A better angular fit with the radial bars would be obtained if the rocking point was assumed to be 1  $\mu\text{m}$  along the bar from the center point.)

The procedure with the ring target is similar. An SEM image of this target is shown in Fig. 5(a). This image must be accurately centered below the specimen plane in the SEM; the SA-ECP scanning mode is used in the same way as before. The schlieren image that represents the contours of  $total (FDI)_o$  is shown in Fig. 5(b). Here, the *inner* ring in the schlieren image represents the *outer* circle in the target. Since the radius of the outer circle in Fig. 5(a) is 22.5  $\mu\text{m}$ , the  $(FDI)_o$  of the inner circle in Fig. 5(b) must be 0.833 gauss-cm from Eq. 3. The difference in  $(FDI)_o$  between successive circles in Fig. 5(b) is calculated to be 0.093 gauss-cm. (According to the model that is described below, these contours should be circles centered on the gap.)

### Discussion

This work has demonstrated the possibility of plotting the FDI derived from either a component of the field or from the total field by the schlieren method with either a rectilinear or a circular target. The main experimental requirement is to center the mesh accurately below the specimen on the axis of the SEM. (In this work, an additional  $x$ - $y$  mechanism was used.) With a gold-on-silicon mesh, the signal is obtained from the usual secondary-electron detector. An idea that suggests itself would be to use a solid-state detector with a gold pattern on the surface. Another idea would be to increase progressively the width and spacing of the bars (or circles) in a given direction, so that the high-field regions in the center of Figs. 4(b) or 5(b) can be more clearly resolved.

SEM lens spoils the rocking motion to give a distorted image of the mesh. The reference mesh must be shifted and the final lens must be adjusted until the central uniform area is as large as possible. (This central uniform region, which in Fig. 3 measures  $\sim 300 \mu\text{m}$  in diameter in the plane of the fringing field, is the region over which the schlieren method will work.) The preceding lens must be adjusted so that the bars are sharp. The recording head is then moved forward until it bisects the central uniform region (Fig. 3b).

If the magnification is increased, the uniform central region in the SA-ECP image of the mesh expands to fill the entire lower half of the image. The image obtained with this scanning mode is inverted on the screen of the SEM in comparison with the more usual topograph-

Coded bars would facilitate the calibration of the image.

A simplified two-dimensional model for an unsaturated recording head with a vanishingly small gap is as follows. Suppose that the fringing field above the gap is approximated by the two-dimensional scalar potential distribution

$$\phi = \phi_0 \tan^{-1} (y/x) \quad (4)$$

where  $x$  and  $y$  are shown in Fig. 6. This distribution has the following properties. First, the field line corresponding to a constant field  $F$  is the semicircle ABC of radius  $R$ , where

$$F = 2\phi_0/\pi R \quad (5)$$

At the highest point B of this semicircle, the  $x$  component of the field  $F_x$  is also equal to  $F$ . It can be shown that the contour of constant  $F_x$  is a circle drawn on OB as a diameter. Likewise, the contours of constant  $F_y$  (positive and negative) are semicircles drawn on AO and OC as diameter. This model predicts that the contours of constant  $F_x$  should be families of circles that are tangent to the surface of the head at the gap and whose diameters are inversely proportional to the distance by which the beam is deflected in the reference plane. Specifically, the center lines of the first three mesh bars should appear as circles with diameters in the ratio of (1/1) : (1/2) : (1/3) : . . . that are tangent to the surface of the head at the gap. (The outer circle in Fig. 4b can therefore be identified as the first mesh bar.) The contours of constant  $F_y$  should be similar families of circles, but tangent to the *normal* to the surface of the head at the gap (Fig. 4c).

In the schlieren image that was described earlier,<sup>2</sup> the lower edge of the sample was used as a knife edge, which avoids the need for a centering mechanism for the reference mesh. Although easier to set up, this configuration is harder to calibrate. Also, it only shows a single contour for the field component parallel to the surface.

Preliminary experiments have indicated that this method will show the field from magnetized particles. The method might be also useful for investigating the deflection and/or scattering of electrons from the edges of SEM beam-defining apertures.

The size of the area in the specimen plane over which the field can be plotted is smaller with the schlieren method than with the TH method, because the final lens in the SEM is designed to give the best possible resolution under the usual operating conditions and has a high spherical aberration coefficient when weakly excited for the SA-ECP scanning mode. The schlieren method would work better if dynamic focus could be applied to the final lens in order to increase the angle over which the beam rocks accurately about a point (or if the bore and spacing of the polepieces in the final lens could be increased in order to reduce the spherical aberration coefficient in the weakly excited condition.)

Insofar as magnetic contrast is concerned, it is to be expected that the detection limit with all of these methods (and with a diffraction-limited SEM) will be related to the fluxon unit.<sup>8,9</sup>

## References

1. See, for example, E. B. Brown, *Modern Optics*, New York: Reinhold, 1965, 448-478.
2. O. C. Wells and M. Brunner, "Schlieren method as applied to magnetic recording heads in the scanning electron microscope," *Appl. Phys. Lett.* 42: 114-116, 1983.
3. O. C. Wells, "Method for measuring the field from a magnetic recording head in the scanning electron microscope," *J. Microscopy* 130: RP1-2, 1983.
4. C. G. van Essen, E. M. Schulson, and R. H. Donaghy, "Electron channelling patterns from small (10 $\mu$ m) selected areas in the scanning electron microscope," *Nature* 225: 847-848, 1970; "The generation and identification of SEM channelling patterns from 10 $\mu$ m selected areas," *J. Materials Science* 6: 213-217, 1971.
5. R. F. M. Thornley and J. D. Hutchison, "Magnetic field measurements in the scanning electron microscope," *Appl. Phys. Lett.* 13: 249-250, 1968; *IEEE Trans. MAG-5*: 271-275, 1969.
6. E. I. Rau and G. V. Spivak, "Scanning electron microscopy of two-dimensional magnetic stray fields," *Scanning* 3: 27-34, 1980.
7. L. Marton and S. H. Lachenbruch, "Electron optical mapping of electromagnetic fields," *J. Appl. Phys.* 20: 1171-1182, 1949.
8. D. Wohlleben, "On the detection of magnetic microstructures with charged particles," *Phys. Lett.* 22: 564-566, 1966.
9. J.-P. Lazzari and R. H. Wade, "Electron probe measurements of field distributions near magnetic recording heads," *IEEE Trans. MAG-7*: 700-704, 1971.



## THERMAL-WAVE IMAGING IN A SCANNING ELECTRON MICROSCOPE

Allan Rosencwaig

High-resolution thermal-wave imaging of surface and subsurface thermal features can be performed in a scanning electron microscope. Applications include the detection of subsurface mechanical defects, such as microcracks and delaminations; the imaging of dopants or variations in crystal structures; and the evaluation of bonding integrity.

Thermal-wave imaging is a new technique by which microscopic thermal features on or beneath the surface of a sample can be detected and imaged.<sup>1,2</sup> Thermal features are those regions of an otherwise homogeneous material that exhibit variations, relative to their surroundings, in either the density, the specific heat, or (most important) the thermal conductivity of the sample. Variations in these thermal parameters can arise from changes in basic material composition, from the presence of mechanical defects such as microcracks, voids, and delaminations; from changes in crystalline order or structure; and even from the presence of small concentrations of foreign ions or lattice defects in an otherwise perfect crystal.

In thermal-wave electron microscopy<sup>1-4</sup> the electron beam of a scanning electron microscope is blanked in the 100kHz-10MHz range. The periodic surface heating that results from the absorption of the electron beam generates thermal waves that propagate from the initially heated region. These diffusive thermal waves are critically damped and propagate only one to two wavelengths before their intensity becomes negligibly small. Nevertheless, within their propagation range, the thermal waves scatter and reflect from thermal features much like conventional propagating waves do from optical or acoustic features. Imaging of the thermal features thus requires the detection of the scattered and reflected thermal waves. This process takes place in a Therma-Wave, Inc.,<sup>5</sup> thermal-wave microscope by detection of the effect of these thermal waves on the thermoacoustic signals generated in the bulk of the sample. The thermoacoustic signals are detected in turn with a suitable piezoelectric transducer in acoustic contact with the sample. The magnitude and phase of the thermoacoustic signals are directly affected by the presence of scattered and reflected thermal waves.<sup>6</sup> Thus, by measuring the magnitude and/or phase of the thermoacoustic signal as a function of electron-beam position on the surface of the sample, an image is generated that depicts the various thermal-wave scattering and reflection events that occur at each point on the sample.

### *Subsurface Defects*

Subsurface mechanical defects such as voids, cracks, and delaminations represent substantial thermal features and are thus readily detected with a thermal-wave microscope.<sup>3,4,7</sup> One illustration of this application is shown in Fig. 1. Figure 1(a) is the electron backscatter image of a GaAs device, where the only visible defects are two seemingly insignificant chip-outs at the edge of the device, one along the right-hand edge and the other along the bottom. However, the thermal-wave image (Fig. 1b) shows that the small chip-out along the right-hand side is a much larger subsurface delamination that extends into the lower gate of the device, where it results in a "loop-like" subsurface flaw. The small chip-out along the bottom is also seen to be the origin of a long subsurface crack. Therefore, where optical and electron images show only two insignificant defects, the thermal-wave image shows the presence of serious subsurface defects.

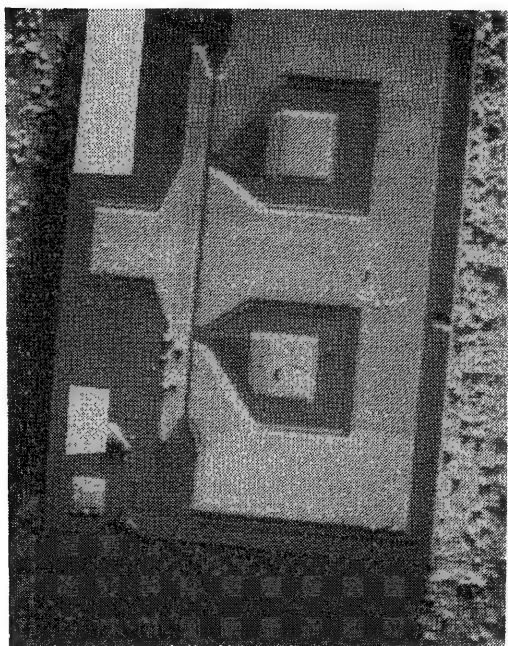
### *Crystalline Variations*

When a crystal lattice is highly ordered, minor changes in lattice structure can produce measurable changes in the local thermal conductivity of the material and thus can be

---

The author is with Therma-Wave, Inc., Fremont, CA 94539.

(a)



(b)

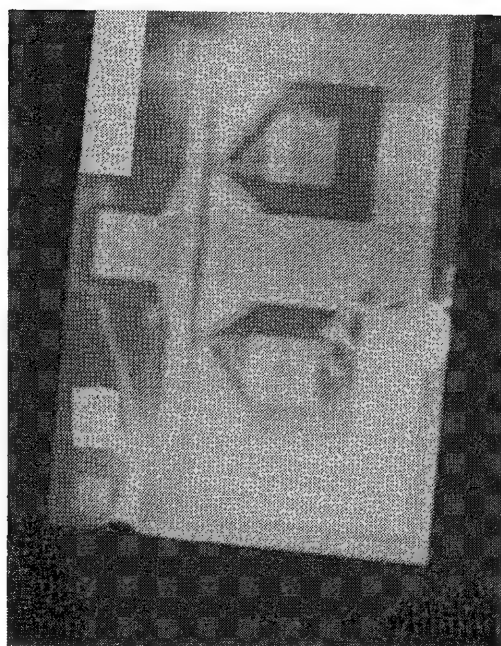
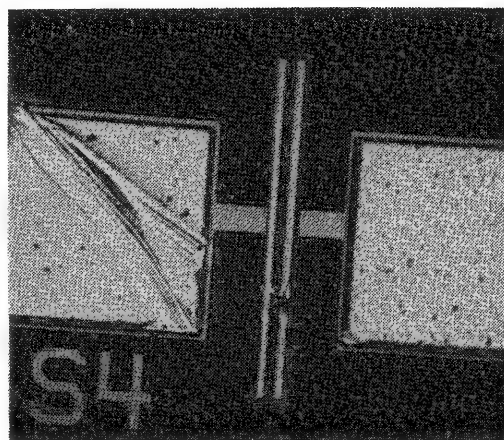


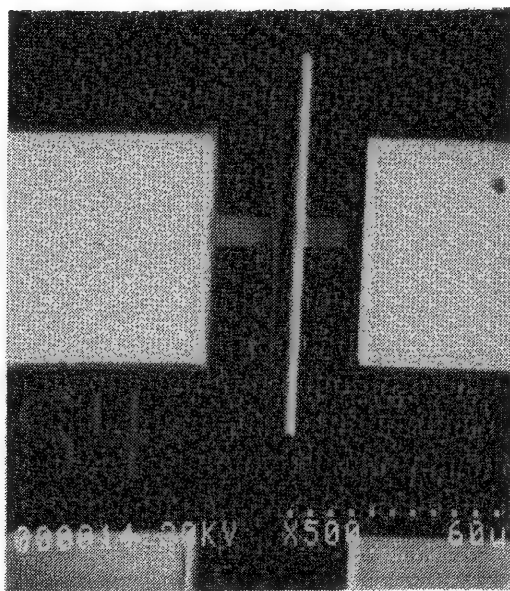
FIG. 1.--Examples of subsurface defects in a GaAs device. Electron micrograph (a) shows only two small edge chip-outs, one along right-hand side, other at bottom. Thermal-wave image (b) shows more serious defects: chip-out along right-hand side is seen as substantial subsurface delamination extending into lower gate region where a "loop-like" defect is visible; chip-out at bottom is origin of long subsurface microcrack running up into device. (Mag. 220 $\times$ .)

FIG. 2.--Images of GaAs test transistor. (a) Optical and (b) backscattered electron micrographs show visible features of gate region; (c) thermal-wave image at 982 kHz shows in addition Si-doped regions of GaAs, demonstrating extent of lateral dopant diffusion. (Mag. 500 $\times$ .)

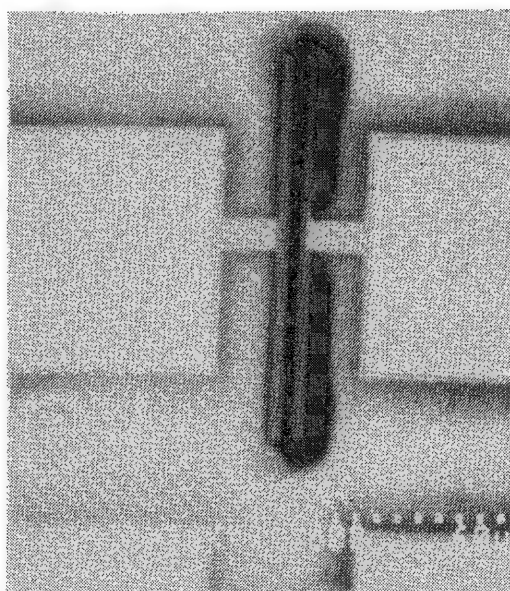
(a)



(b)



(c)



imaged with a thermal-wave microscope.<sup>3,8</sup> This capability is illustrated in Fig. 2, which shows a GaAs device. The optical and electron micrographs image the visible features of the gate structure in the device. The thermal-wave image shows, in addition, the Si-doped regions of the GaAs, since these regions have thermal conductivity different from that of the undoped regions. Such images permit a rapid and nondestructive analysis of the effects of lateral diffusion of dopants in semiconducting crystals.

The imaging of crystalline variations can also be useful in metallography,<sup>2,3</sup> since different metallic phases or grains can be readily imaged with no special sample preparation. In Fig. 3 the columnar grains that have formed in a weld region of an aluminum alloy are visible in the thermal-wave image. Another example is shown in Fig. 4. The electron micrographs of the Al-Zn alloy show only surface topographical features. The thermal-wave micrographs, however, clearly show both the grain structure and, at high magnification, the presence of Fe or Sn precipitates. Other studies with metals have indicated applications in studies of mechanical deformation<sup>9</sup> and grain boundaries.<sup>2</sup>

### *Bonding Integrity*

Microscopic details in a thermal-wave image are due to reflection and scattering of

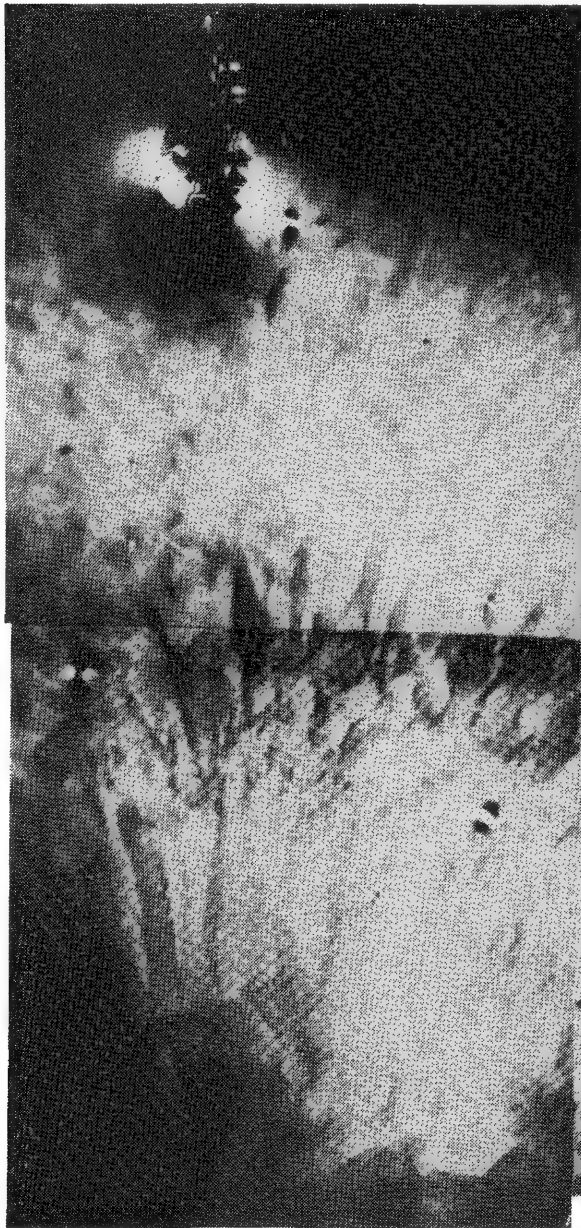
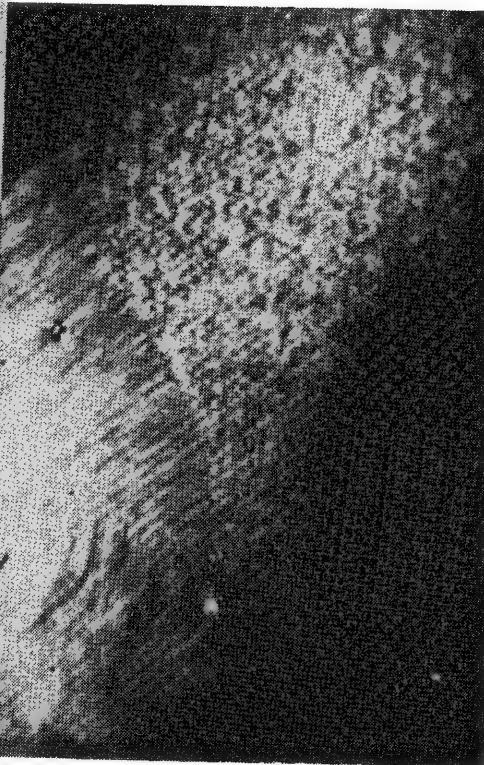
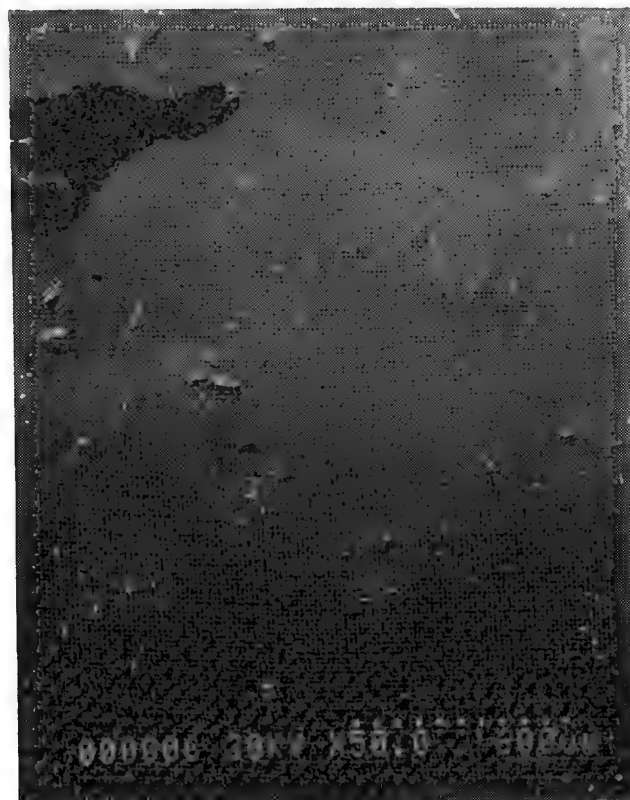
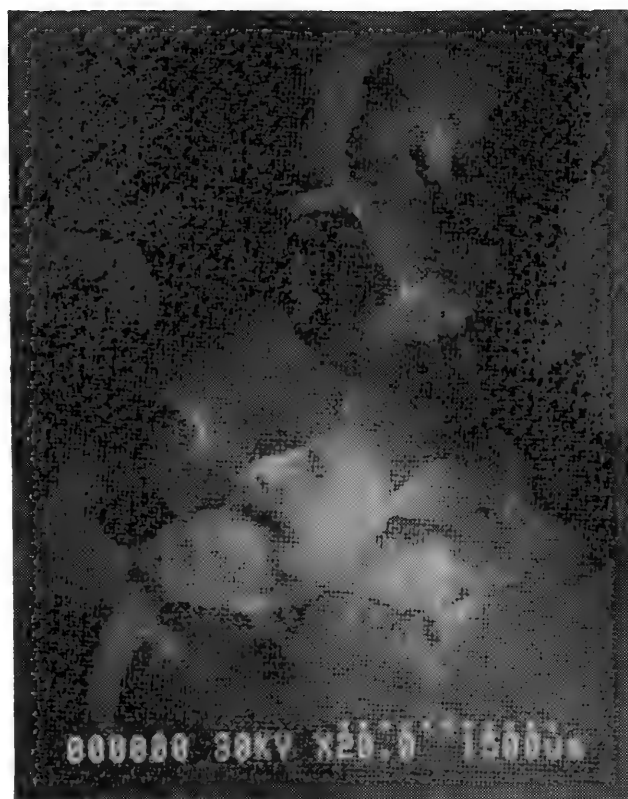
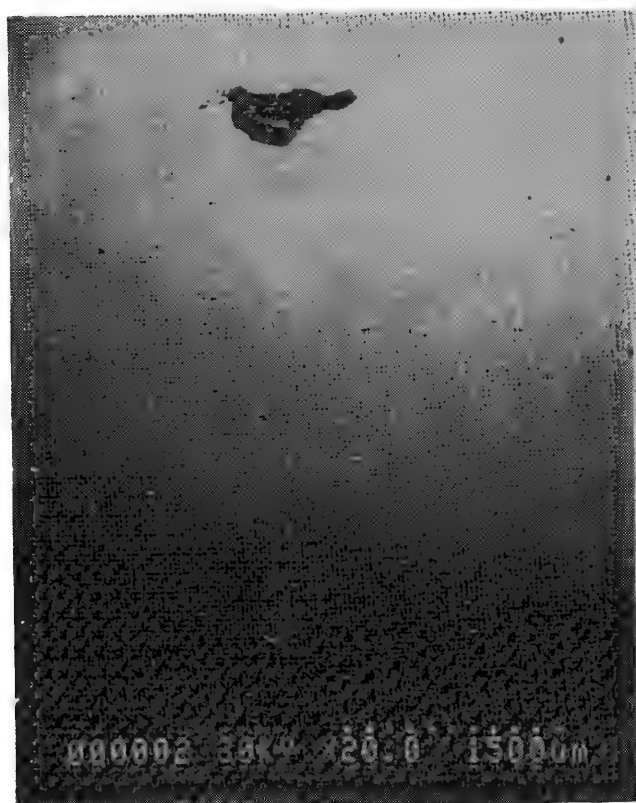


FIG. 3.--Thermal-wave image of weld region in aluminum alloy. Columnar grains in this region are clearly visible. (Mag. 30 $\times$ .)







(a)

(b)

FIG. 4.--(a) Electron and (b) thermal-wave micrographs at 20 $\times$  and 50 $\times$  of Al-Zn alloy. Thermal-wave micrographs show Al-Zn grains and (in 50 $\times$  image) presence of Fe or Sn precipitates.

thermal waves from surface and subsurface thermal features. In addition, thermal-wave images often exhibit large bright and dark areas which represent the acoustic modes of the sample.<sup>10</sup> The incident electron beam is very effective in exciting the plate modes of vibrations in thin samples such as IC chips and wafers. Thus, at certain resonant frequencies, vibration patterns are set up in the sample characterized by regularly spaced nodes and antinodes. When the electron beam is at a plate node on the sample surface there is no enhancement of the thermoacoustic signal. However, at the antinodes there is considerable enhancement, 180° out of phase between a positive and negative antinode. Thus the plate mode vibration pattern is seen as a pattern of bright and dark regions in the thermal-wave image, corresponding to the positive and negative antinode regions on the sample surface. If the sample is a wire, then the thermal-wave image displays the radial acoustic modes in the wire.

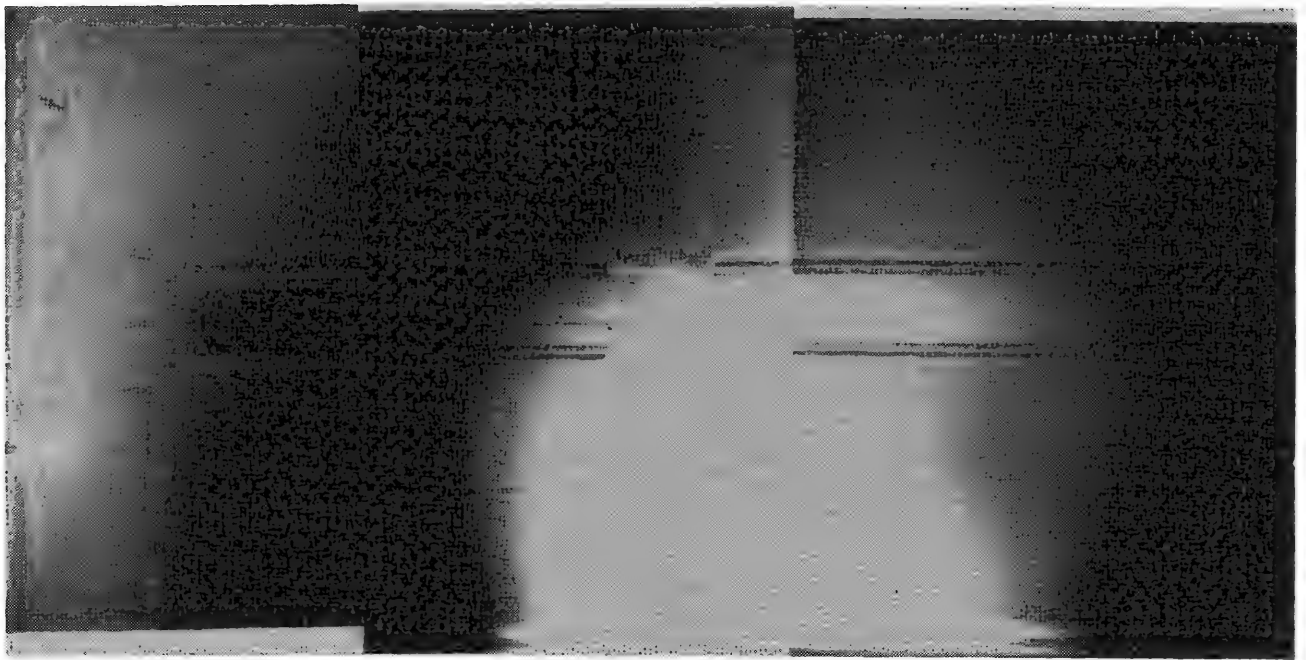
Because of their short wavelength (generally below 20  $\mu\text{m}$ ), thermal waves are unable to penetrate through an IC die to probe the bonding between the die and its support structure. However, IC dies are thin plates and thus exhibit plate mode vibration patterns in their thermal-wave images. The intensity of these vibrations is a sensitive function of the thickness of the sample, decreasing as the thickness increases. The same effect occurs when a thin sample is bonded to a thicker substrate. The combination of the two structures now constitutes a much thicker sample and the vibration intensities decrease. How strong this effect is depends on the integrity and uniformity of the bond between the die and its supporting structure. The plate mode patterns seen in the thermal-wave image can thus be used for comparative evaluation of die attach.

Figure 5 shows the thermal-wave images of two large silicon IC dies mounted in large ceramic DIP packages. The die in Fig. 5(a) is known to have a "poor" die-attach; that in Fig. 5(b) is a "good" die-attach. In agreement with that, the die in Fig. 5(a) shows a strong plate mode pattern indicative of a "thin plate" sample; that is, of a die that is poorly attached. On the other hand, the die in Fig. 5(b) shows little evidence of a plate mode pattern, indicating a "thick-plate" sample; that is, a die firmly and uniformly bonded to its support structure.

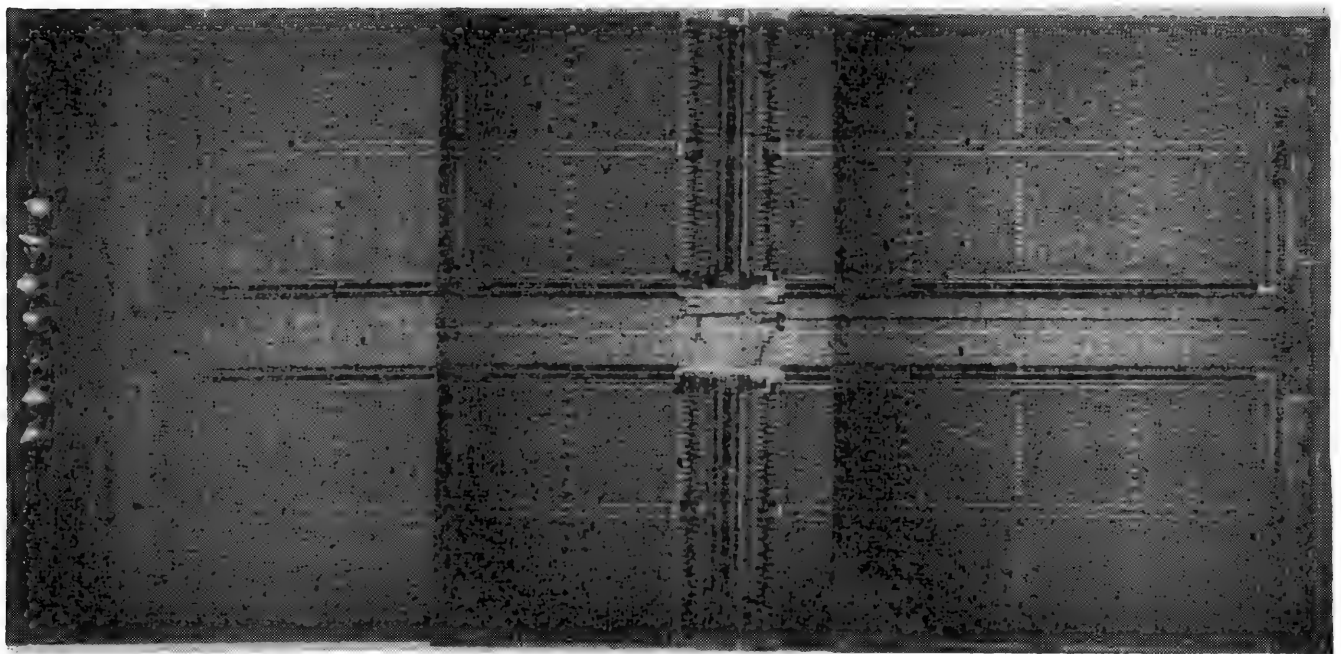
Although still in its formative stage, thermal-wave imaging has already demonstrated several interesting and useful applications for a variety of material studies. As an add-on system to a scanning electron microscope, it can provide the electron microscopist with another valuable analytical tool.

## References

1. E. Brandis and A. Rosencwaig, "Thermal-wave microscopy with electron beams," *Appl. Phys. Lett.* 37: 98-100, 1980.
2. G. S. Cargill, "Electron-acoustic microscopy," *Physics Today* (10): 27-32, October 1981.
3. A. Rosencwaig, "Thermal-wave imaging," *Science* 218: 223-228, 1982.
4. A. Rosencwaig, "Thermal-wave microscopy," *Solid State Technology*, 91-97, March 1982.
5. Therma-Wave, Inc., 47734 Westinghouse Drive, Fremont, CA 94539.
6. J. Opsal and A. Rosencwaig, "Thermal-wave depth profiling: Theory," *J. Appl. Phys.* 53: 4240-4246, 1982.
7. A. Rosencwaig, "Thermal-wave imaging and microscopy," in E. A. Ash, Ed., *Scanned Image Microscopy*; London: Academic Press, 1980, 291-317.
8. A. Rosencwaig and R. M. White, "Imaging of dopant regions in silicon with thermal-wave electron microscopy," *Appl. Phys. Lett.* 38: 165-167, 1981.
9. G. S. Cargill, "Electron-acoustic microscopy of polycrystalline metals and alloys," *EMSA-1981*, 390-391.
10. G. S. Cargill, "Ultrasonic imaging in scanning electron microscopy," *Nature* 286: 691-693, 1980.



(a)



(b)

FIG. 5.--Examples of bonding integrity study: (a) thermal-wave image of large IC die in DIP package with poor die-attach and exhibiting strong plate mode pattern; (b) same type of device but with good die-attach exhibiting no plate mode pattern. (Mag. 40 $\times$ .)

## CRYSTAL LATTICE STUDIES USING ELECTRON CHANNELING PATTERNS

D. C. Joy and R. C. Farrow

Electron channeling patterns (ECP) permit crystallographic studies to be made of bulk samples in the scanning electron microscope (SEM) in the same way as diffraction patterns allow the examination of electron transparent crystals in the transmission electron microscope (TEM). The electron channeling contrast is a weak (typically 5%) modulation in the backscattered signal which occurs as the angle of incidence between the beam and the lattice planes is varied through deviations of the order of a Bragg angle. When optimum electron-optical conditions are set up patterns can be obtained at visual recording rates from areas as small as a few microns in diameter. The choice of these conditions and the required operating procedures have been discussed in detail elsewhere.<sup>1</sup>

An ECP can be characterized in two different ways. First, by its geometry, which is determined by the crystallographic constants of the sample (i.e., the lattice type, lattice spacings, and crystal orientation) and by the energy of the incident beam; provided that these parameters remain unchanged the geometric representation of the ECP is invariant. Second, the pattern can be specified in terms of its "quality," where the parameters of concern are the angular resolution ("linewidth") and contrast, as defined in Fig. 1. It has been known from the earliest observations on ECPs that pattern quality is not consistent, but varies greatly with the physical state of the crystal.<sup>2</sup> The purpose of this review is to identify the origin of changes in pattern quality, to outline a method of quantifying these changes, and to illustrate, by means of applications, the kind of data that is available.

### *Theory*

The mathematical descriptions of channeling contrast formation in imperfect crystals, accurately predict the effects on a pattern to be expected as the lattice is perturbed.<sup>3,4</sup> However, the calculations involved are complex, and for the purposes of explaining experimental observations a simple qualitative argument can be applied. The channeling contrast depends on the angle between the incident beam and the lattice planes. For a perfectly collimated incident beam the linewidth  $d\theta$ , as defined in Fig. 1 has a value:

$$d\theta = 2/(S_g \cdot g) \quad (1)$$

where  $S_g$  is the extinction distance for the lattice reflection  $g$ , and  $g_{hk1} = 1/d_{hk1}$ .<sup>5</sup> Small deviations (i.e., less than the Bragg angle) in the incident angle caused by such effects as the bending of lattice planes around a dislocation, or resulting from finite beam convergence, lead to an increase in the linewidth such that the total width  $\Delta$  becomes

$$\Delta^2 = d\theta^2 + dw^2 \quad (2)$$

where  $dw$  is the deviation. Thus, for example, deforming a material increases the number of dislocations and so leads to an increased average angular offset in the lattice and a rise in the linewidth.

However, deviations of the beam through angles greater than a Bragg angle may cause it to de-channel. In this condition only those fractions of the beam correctly oriented produce ECP contrast, so that the result of large-angle deviations is to reduce the contrast  $dI$  of the detail in the pattern without causing significant line broadening. For example, a thin amorphous layer scatters the incident beam through angles of the order of tens of

---

The authors are with Bell Laboratories, Murray Hill, NJ 07974.

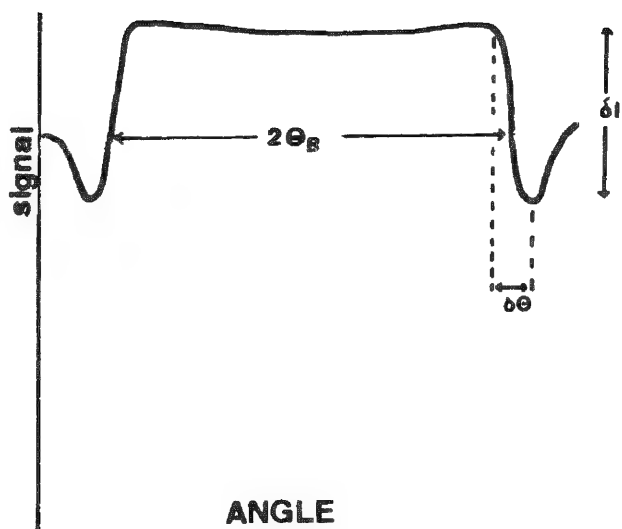


FIG. 1.--Definitions of linewidth and line contrast in ECP.

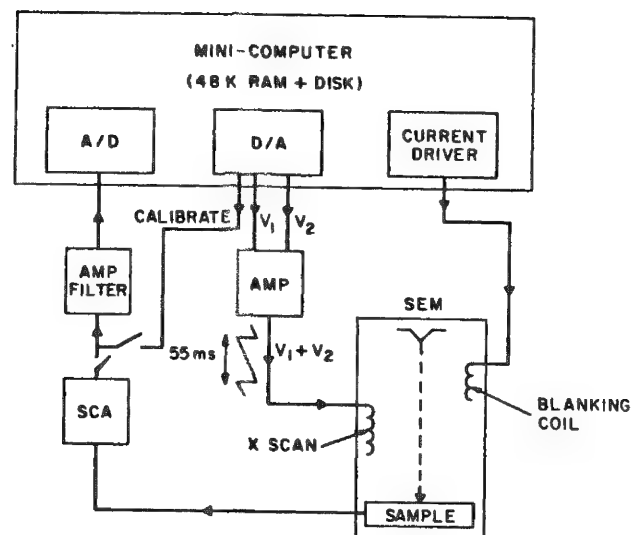


FIG. 2.--Schematic layout of computer-based system for ECP measurement.

milliradians and thus leads to a loss of intensity in this way. If the linewidth and intensity can be measured simultaneously, then both types of effect can be observed, and various types of damage to the lattice can be distinguished. Only in a few special cases does both the line width and contrast change at the same time. An example, arising from the so-called "critical voltage effect," is discussed later.

#### Experimental Method

Linewidths and contrast values are most reliably obtained from line profiles that have been directly digitized and stored in a computer memory. This approach allows the data to be acquired quickly, which minimizes problems caused by contamination and permits multiple line scans to be added to enhance the poor signal-to-noise ratio of the signal. Figure 2 shows the schematic of a suitable system.<sup>6</sup> The APPLE microcomputer generates a 512-step ramp to drive the line scan, by summing the outputs of two eight-bit digital-to-analog converters (DACs). The signal from the backscattered detector is digitized by a twelve-bit analog-to-digital converter (ADC), and the incoming signal is stored in memory. Up to 255 line scans, each lasting 55 ms, can be acquired and summed to enhance the signal-to-noise ratio. After the data are collected a sequence of subroutines identifies channeling line features and measures their width and contrast. Under normal conditions an angular precision of about 0.1 milliradians is attainable, and line contrast can be determined to better than 1 part in 100.

#### Examples of Use

*Ion Implantation Studies.* Samples of [100] silicon wafers, ion implanted with moderate doses (less than about  $3 \cdot 10^{16}/\text{cm}^2$ ) of As and then laser-beam annealed, were examined as described above. At a fixed incident energy it was found that the width of the [220]-type lines in the pattern increased with the ion dose, and decreased after laser annealing, although no change in the contrast of these lines was observed. From the analysis discussed above it can be therefore deduced that these levels of irradiation are sufficient to generate static disorder (e.g., point and line defects) in the lattice, but not sufficient to destroy the crystallinity of the structure. Additional information can be obtained by a study of the linewidth as a function of accelerating energy at a fixed ion dose. A comparison of the line width in unimplanted and implanted areas (Fig. 3) indicates that while both fall (as expected from Eq. 1, since  $S$  increases with keV), the difference between them also falls steadily. This finding can be attributed to the finite depth of the implant region and the depth of information of the channeling contrast. The implant region is known, from TEM studies, to be about 500 Å thick. At low beam energies (10 keV) all the channeling contrast is coming from within this region, and a large broadening is



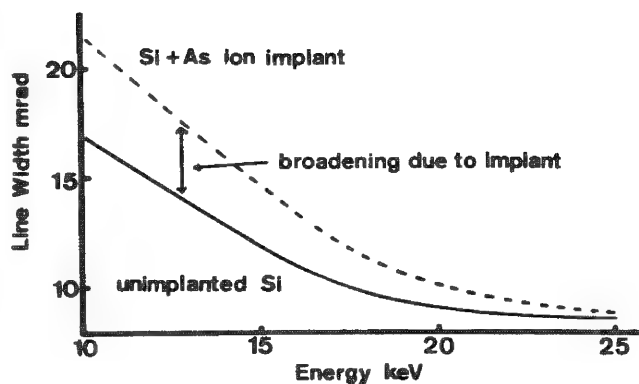


FIG. 3.--Angular width of [220] line, as function of incident energy, in arsenic implanted, and unimplanted, silicon.

nal matrix. However, at very high laser doses line broadening is seen to occur again, as visible in the 25keV data, which suggests that at high powers the laser beam itself causes damage, and that this damage is initially localized at some depth beneath the surface, where the energy absorption is high.

*Surface Films.* A second example is that of oxide films formed on [100] silicon. In this case it was observed that the channeling pattern showed a significant fall in contrast over the oxide region, and that the contrast relative to the same line on clean material fell rapidly with accelerating voltage (Fig. 5), although no change in width was noted. This result is consistent with the effects expected from the dechanneling produced by scattering in an amorphous layer. We may gain an idea of the sensitivity of this technique by noting the sharp fall in contrast for even a 200Å film, and the error bars on the data. At 10 keV this would suggest that a layer as thin as 10 to 15 Å could be detected in this way, a result that compares favorably with that of conventional surface techniques. This sensitivity comes in part from the limited information depth of the channeling contrast, which can be estimated by extrapolating the data in Fig. 5 to zero contrast. The intercepts indicate that contrast comes from only about 200 Å at 5 keV and 500 Å at 15 keV. Consequently even shallow amorphous layers can have a significant effect on the ECP. Plots of the contrast variation with beam energy have slopes that vary substantially with the mean atomic number of the amorphous layer. This result may make it possible to both measure the thickness of an unknown film and estimate its probable composition.

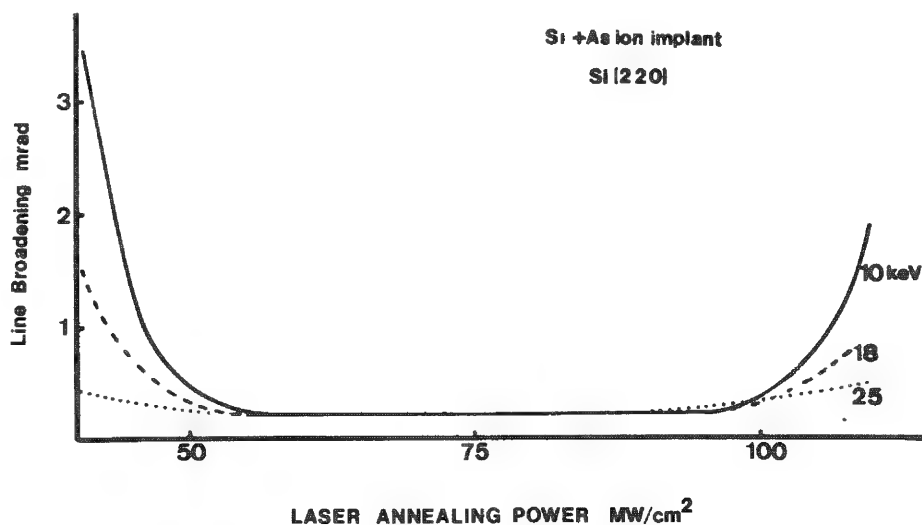


FIG. 4.--Measured broadening of [220] line in implanted silicon as function of laser annealing power for three accelerating voltages.

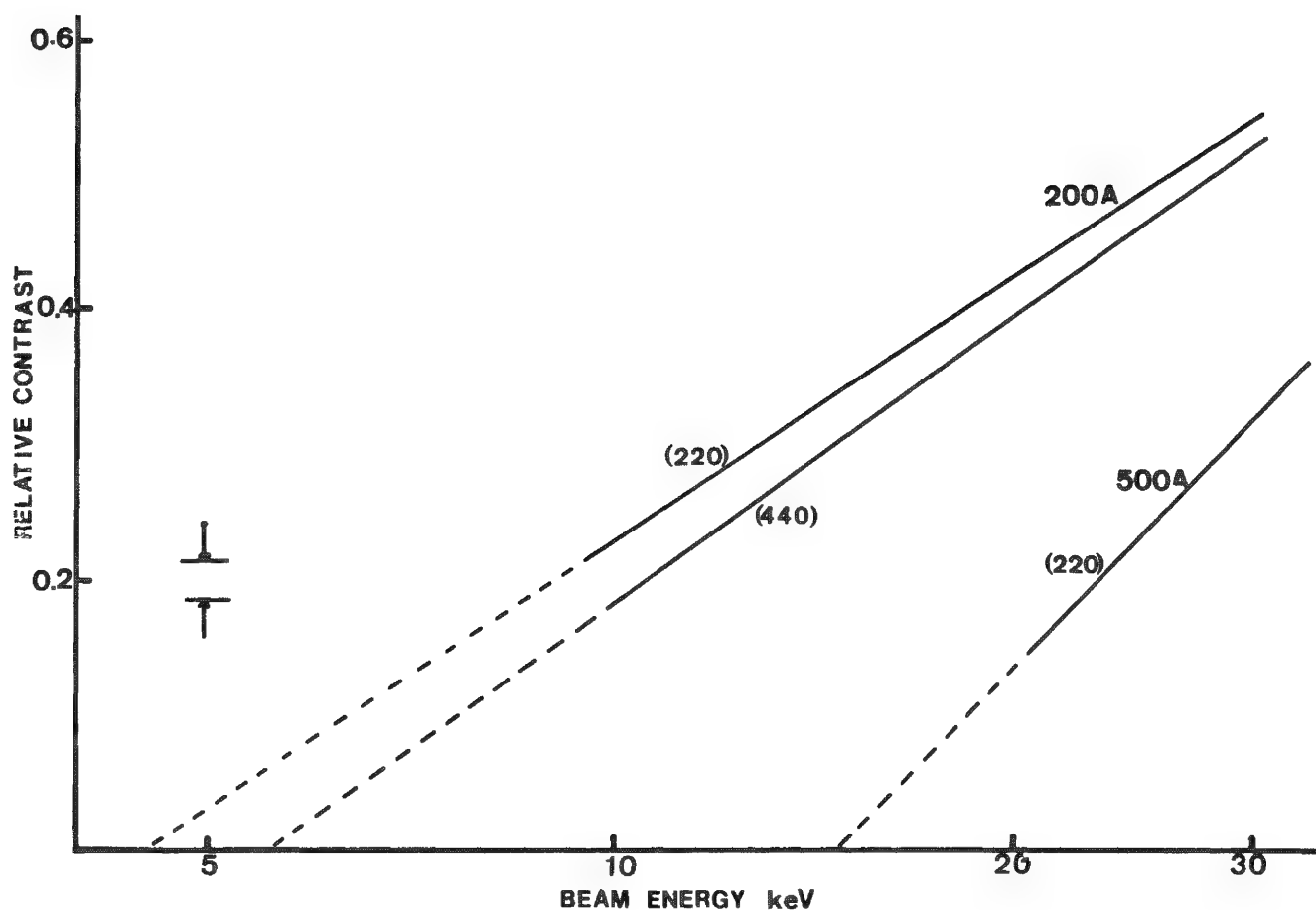


FIG. 5.--Variation of line contrast from oxide-covered silicon with beam voltage.

*Critical Voltage Studies.* The [220] line in tungsten is usually of low visibility since its width is a significant fraction of the Bragg angle. However, during a systematic study of the tungsten ECP it was observed that the [220] line became much easier to see at low accelerating voltage (below 15 keV).<sup>7</sup> A measurement of the width of this line as a function of energy (Fig. 6) showed that it went through a pronounced minimum at 10.50 keV. At the same time the contrast of the line reversed relative to other lines in the pattern. As shown by Eq. (1), the linewidth would be expected to rise as the energy falls. A minimum in the linewidth must therefore result from some other effect. The explanation is the so-called "critical voltage effect," which arises from an accidental degeneracy between two Bloch waves at some energy. When this effect occurs  $S_g$  becomes very large and leads, for a TEM Kikuchi pattern, to the disappearance of the line associated with the reflection  $g$ . The effect on an ECP is to produce an anomalously narrow line for this reflection, as can be seen from Eq. (1), and as was observed here. It has been shown that the reversal in line contrast is also consistent with this explanation.<sup>8</sup> Although the critical voltage effect is essentially a relativistic interaction, this observation confirms predictions that the critical voltage for some heavy materials may be as low as a few keV. The accurate measurement of a critical voltage, made possible by the technique described here, is important because it permits the refinement of theoretical lattice potential values.

#### Conclusion

The state of a crystal lattice can be monitored by observation of the contrast and angular width of lines in the ECP. If these parameters can be measured accurately, detailed quantitative information about the properties of the crystal can be obtained.

## References

1. D. C. Joy et al., "Electron channeling patterns," *J. Appl. Phys.* 53: R81-122, 1982.
2. D. G. Coates, "Generation of orientation patterns in SEM," *Phys. Stat. Solidi* 27: K11-K13, 1968.
3. J. P. Spencer et al., "Dynamical theory of contrast of perfect and imperfect crystals," *Phil. Mag.* 26: 193-213, 1972.
4. R. Sandstrom et al., "Energy Dependence of electron channeling patterns," *J. Phys. (D)* 7: 1030-1046, 1974.
5. E. M. Shulson, "Interpretation of widths of SEM ECPs," *Phys. Stat. Solidi* B46: 95-101, 1971.
6. R. C. Farrow and D. C. Joy, "A new method for ECP measurements," *SEM/1981 I*, 397-403.
7. R. C. Farrow and D. C. Joy, "Critical voltage effects in ECP," *Phys. Rev. Lett.* 44: 1590-1593, 1980.
8. S. M. Payne, "Critical voltage effects in backscattered ECP," in J. Venables, Ed., *Proc. EMAG-81*, London: Institute of Physics, 1981, 293-296.

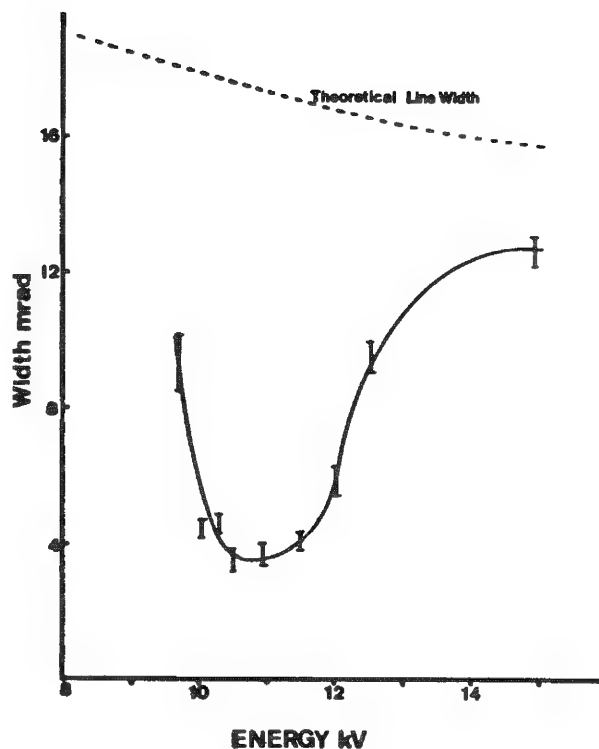


FIG. 6.--Width variation of [220] line in tungsten as function of beam energy, and corresponding theoretical linewidth.



## THE VISIBILITY OF ASBESTOS FIBERS IN THE SCANNING ELECTRON MICROSCOPE

John Small, Dale Newbury, and Robert Myklebust

The analysis of asbestos mineral fibers in environmental samples requires the careful determination of fiber loading on filter media.<sup>1</sup> Well-established techniques exist for the transfer of asbestos fibers from such filter media to thin carbon films and subsequent counting in the transmission electron microscope (TEM).<sup>2,3</sup> However, due to the cost of TEM instrumentation and the time required for sample preparation, there has been considerable interest in the development of techniques for direct examination of the filter in the scanning electron microscope (SEM). In this work, we have considered the problem of fiber visibility under SEM imaging conditions in a fiber search/counting procedure.

### *Procedures*

The asbestos mineral chrysotile is typically found in environmental samples as long fibers composed of one or more fibrils. Individual fibrils have a diameter of approximately 40 nm and a length which can extend to several micrometers. In order to estimate the visibility of single fibrils and fiber bundles in an SEM image, we have used a three-stage procedure: (1) calculation of the contrast of the asbestos fiber compared to the filter background, (2) calculation of the threshold beam current necessary to observe that contrast, and (3) calculation of the smallest beam size which could contain the required threshold current. By comparing the size of the beam given by step (3) with the fiber diameter, one can estimate the visibility of the fiber.

*Calculation of Fiber Contrast.* The signals generated from an electron beam impinging on a carbon-coated asbestos fiber placed on a carbon-coated filter substrate were calculated as follows: (a)  $\eta_F$ , backscattering from the fiber, was calculated by Monte Carlo electron trajectory simulation;<sup>4</sup> (b)  $\eta_{SS}$ , backscattering from the substrate, was set equal to that for bulk carbon with a correction for scattering in the overlying fiber; (c)  $\delta_F$ , secondary electron emission from the fiber, was calculated by partitioning the total secondary electron coefficient  $\delta_T$  into its primary-electron-excited and backscattered-electron-excited components,  $\delta_p$  and  $\delta_{BS}$ ,<sup>5</sup> and since the beam enters the fiber with minimal backscattering,  $\delta_F$  was taken to be equal to  $\delta_p$ ; (d)  $\delta_{SS}$ , secondary electron emission from the substrate: the fiber effectively covers the entrance point of the beam into the substrate, and hence  $\delta_{SS}$  was set equal to  $\delta_{BS}$  for a bulk carbon target. Detection of these backscattered and secondary electron signals was calculated for an Everhart-Thornley detector.<sup>5</sup> The efficiency for secondary detection was assumed to be  $\epsilon_{SE} = 0.5$ . The efficiency for collection of backscattered electrons was assumed to be  $\epsilon_{BS} = 0.25$ , including contributions from direct detection as well as indirect collection from the chamber walls. The signal from the fiber is thus

$$S_F = [\eta_F + (1 - \eta_F)\eta_{SS}]\epsilon_{BS} + [\delta_F + (1 - \eta_F)\eta_{SS}\delta_{SS}]\epsilon_{SE} \quad (1)$$

The signal from the substrate is given by:

$$S_{SS} = \eta_{SS}\epsilon_{BS} + \delta_{SS}\epsilon_{SE} \quad (2)$$

The contrast  $C$  is calculated as:

$$C = (S_{\max} - S_{\min})/S_{\max} = (S_F - S_{SS})/S_F \quad (3)$$

The authors are at the Center for Analytical Chemistry, National Bureau of Standards, Washington, DC 20234.

TABLE 1.--Calculations of asbestos fiber contrast and visibility.

Fiber diameter	Contrast	Threshold Current	Beam Diameter	Visibility
(nm)		(nA)	(nm)	
40	0.013	540	1050	No
80	0.025	147	550	No
120	0.031	95	440	No
160	0.039	60	350	No
200	0.049	38	280	?
240	0.061	25	220	Yes

Values of the contrast calculated for fibers of various widths are listed in Table 1.

*Calculation of the Threshold Current.* The threshold equation relates the contrast of the fiber against the background to the minimum (threshold) beam current  $i_{th}$  required to form an image.<sup>5</sup> For a 512-line scan, the threshold current is given by

$$i_{th} \geq 1.1E - 12/(\epsilon C^2 t_f) \quad (A) \quad (4)$$

where  $\epsilon$  is the overall collection efficiency per incident electron and  $t_f$  is the frame time. We calculated the overall collection efficiency to be 0.12 by scaling the backscatter and secondary coefficients by the individual signal collection efficiencies. In order to survey a filter at an adequate pace to cover a sufficient area and to reduce operator fatigue, a rapid frame time of 0.1 s or less is desirable. However, from Eq. (4), the threshold current increases with the reciprocal of the frame time. As a compromise, a frame time of 0.5 s was assumed for the calculations. The threshold current necessary to image fibers of various diameters at this frame speed is listed in Table 1.

*Calculation of Beam Diameter.* The threshold current can be related to the beam size  $d$  by the brightness equation:

$$\beta = 4i/\pi^2 d^2 \alpha^2 \quad (5)$$

where  $\beta$  is the source brightness (taken as  $5 \times 10^4$  A/cm<sup>2</sup> ster for a conventional tungsten hairpin at 20 keV), and  $\alpha$  is the beam divergence ( $\alpha = 2 \times 10^{-2}$  for a 400- $\mu$ m-diameter aperture at 1 cm working distance). The minimum beam diameter that can contain the threshold current is listed in Table 1 for each fiber diameter. The final visibility has been determined on the basis that the beam size must be of the same size as the fiber diameter or smaller. Note that due to the low level of the contrast of the fibers, proper image processing such as black level suppression would have to be applied to ensure sufficient image contrast on the final display.

### Results and Discussion

Examination of Table 1 reveals that asbestos fibers below approximately 200 nm in diameter will not be visible in a scanning image made under the conditions specified for searching large areas of a filter sample. Only for fibers 240 nm in diameter and above is the threshold visibility condition substantially exceeded, which should insure adequate image quality. The minimum fiber size for visibility can be reduced by use of more efficient detectors and higher brightness electron sources. For practical conditions such improvements might decrease the minimum fiber diameter that would be visible by a factor of two. However, since the statistical assumptions used in deriving the threshold equation are based on an average observer, working with objects near the visibility threshold will produce counting results that are erratic and subject to great uncertainty. Since environmental asbestos samples are likely to contain fibers of small diameter, it therefore does

seem prudent to employ an SEM counting procedure for characterization of such samples.

This analysis is also being extended to other types of sample preparation, including coating of the fibers and substrates with a heavy metal such as gold to increase the secondary-electron coefficient for increased contrast; to other types of detectors, such as large solid angle backscatter detectors; and to other types of asbestos minerals.

#### References

1. A. V. Samudra, C. F. Harwood, and J. D. Stockham, *Electron Microscope Measurement of Airborne Asbestos Concentrations: A Provisional Methodology Manual*, Environmental Protection Agency, EPA-600/2-77-178, revised 1978.
2. P. M. Cook and D. R. Marklund, "Sample preparation for quantitative electron microscope analysis of asbestos fiber concentrations in air," in J. Small and E. Steel, Eds., *Asbestos Standards: Materials and Analytical Methods*, Washington, D.C.: National Bureau of Standards, Special Publication 619, 1982, 53.
3. E. J. Chatfield, "Analytical procedures and standardization for asbestos fiber counting in air, water, and solid samples," *ibid.*, 91.
4. H. Yakowitz, D. E. Newbury, and R. L. Myklebust, "Approaches to particulate analysis in the SEM with the aid of a Monte Carlo program," *SEM/1975 I*, 93.
5. J. I. Goldstein, D. E. Newbury, P. Echlin, D. C. Joy, C. Fiori, and E. Lifshin, *Scanning Electron Microscopy and X-ray Microanalysis*, New York: Plenum, 1981, 172-175.

## A DIODE ARRAY SPECTROGRAPH AND ASSOCIATED OPTICS FOR CATHODOLUMINESCENCE MEASUREMENTS IN A SCANNING ELECTRON MICROSCOPE

Dianna Jones and D. O. Landon

We describe a diode array spectrograph and an optical system for efficiently coupling to a commercial SEM. Cathodoluminescence measurements can be made in the 200-900nm range. Some experimental results obtained with the instrumentation are presented.

Cathodoluminescence (CL) is a technique of studying the emission of light through excitation by electrons. The technique is of particular interest in the scanning electron microscope (SEM) and has attained increasing importance as a spatially resolving measurement method for evaluating local material parameters in luminescent semiconductor materials.<sup>1,2</sup> CL measurements are also useful in the investigation of biological,<sup>3</sup> geological, and metallurgical samples.<sup>4</sup>

Several SEMs offer some form of CL accessory. Typically, light is collected from the sampled point with a refractive or reflective microscope objective and then passed through a narrow band filter, or sometimes a monochromator to a photomultiplier detector.<sup>5</sup>

Still, the CL mode of analysis is not yet in wide use by SEM users. In a review paper on CL, Holt and Datta<sup>1</sup> point out the need for improved CL detection systems. The use of parallel detection in the CL mode allows one to measure the CL spectrum as a function of a variable. This and other advantages of parallel optical detection techniques, where the entire spectrum is recorded simultaneously, are well known, but only Lohmert et al.<sup>6</sup> have described the use of such a system on an SEM.

The optical coupling of the light from a CL experiment in an SEM requires some experimentation. It appeared to us that it would be advantageous to collect the light from the small emitting source--of the order of 1-2  $\mu\text{m}$ --with a microscope objective having a relatively large NA, 0.6 to 0.9 if possible. Then the magnified image of the source (typically 20 $\times$ ) is placed on the entrance end of an ultraviolet transmitting fiber-optics bundle. A relatively short bundle transmits well from 180 nm to beyond 2  $\mu\text{m}$ . The exit end of the fiber bundle becomes the entrance slit of a compact spectrograph with a relative aperture (f number) adequate to accept the entire cone of light emerging from the fiber bundle. It is even possible to use single fibers in this way.

As described, the optical system is quite efficient. The optical transmittance of a good microscope objective is above 90%. The fiber optics transmit typically 50%, and a spectrograph with high efficiency grating transmits 60%. The composite transmittance-- $0.9 \times 0.5 \times 0.6 = 0.27$  insures that ample light falls on the intensified diode array detector.

Interfacing such a CL detection apparatus to various commercial SEMs is feasible. We have obtained CL spectra of aluminum oxide, hafnium oxide, some composite samples, and some rare earths with the apparatus described attached to a JEOL JSM35 microscope.

### References

1. D. B. Holt and S. Datta, "The cathodoluminescent mode as an analytical technique: Its development and prospects," *SEM/1980* I, 259-278.
2. C. B. Norris and C. E. Barnes, "Cathodoluminescence studies of anomalous ion implantation defect introduction in lightly and heavily doped liquid phase epitaxial GaAs: Sn," *J. Appl. Phys.* 51: 5764-5772, 1980.
3. W. Brocker and G. Pfefferkorn, "Applications of the cathodoluminescence method in biology," *SEM/1979* II, 125-132.
4. K. P. Gumz and J. M. Walsh, "Cathodoluminescence image analysis technique for

The authors are at Tracor Northern, Inc., 2551 West Beltline Highway, Middleton, WI 53562.

oxide inclusion classification of nickel-base superalloys," *Microbeam Analysis--1981*, 258-260.

5. L. Carlson and C. G. van Essen, "An efficient apparatus for studying cathodoluminescence in the scanning electron microscope," *J. Physics* E-7: 98-100, 1974.

6. K. Lohnert, M. Hastenrath, and E. Kubalek, "Spatially resolved cathodoluminescence studies of GaP LEDs in the scanning electron microscope using optical multichannel analysis," *SEM/1979 I*, 229-235.

## 7

# Analytical Electron Microscopy/Electron Energy Loss Spectroscopy

### DETECTION LIMITS AND ERROR ANALYSIS IN ENERGY-LOSS SPECTROMETRY

Peter Rez

The calculation of detection limits is fundamental to energy-loss spectrometry and a reliable estimate of error is important for quantitative analysis. To calculate both error and detection limit one needs a statistical analysis, and such an analysis can also be used to investigate the relative merits of various background-subtraction schemes for energy-loss imaging.

Detection limits have been discussed before by Isaacson and Johnson.<sup>1</sup> Their analysis shows that the minimum mass fraction (which is always the quantity of interest in energy loss due to the large background) decreases as the square root of the current density and collection time. However, it is not easy to apply their analysis to observed spectra. It is often useful to be able to determine the proportion of an element that is detectable compared with a major constituent. This quantity can be easily related to the minimum mass fraction if the concentration of the major constituent in the sample is known. If the unknown edge appears at position B with  $N_B$  counts in a window starting at B, then  $\alpha\sqrt{N_B}$  counts of the unknown element implies detection, where  $\alpha$  is related to the confidence level ( $\alpha$  is usually taken as 3, which implies a confidence level of 99% for the normal distribution). If there are  $N_C$  counts in a window after an edge after background subtraction (note that there is no requirement that the windows be the same) the detectable fraction relative to the major constituent element is

$$\frac{\alpha\sqrt{N_B}}{N_C} \cdot \frac{\sigma_C}{\sigma_B} \quad (1)$$

where  $\sigma_C$  is the appropriate partial cross section for the window after the major constituent edge and  $\sigma_B$  is the relevant partial cross section for the element of interest. This analysis takes no account of the errors in fitting the background (see Egerton<sup>2</sup>) which of course raise the detectable limit depending on how the background fitting region is chosen. It might then be more appropriate to use the formula given as Eq. (3) below.

The errors in quantitative energy loss analysis have already been discussed by Egerton,<sup>2</sup> Zaluzec,<sup>3</sup> and Statham.<sup>4</sup> There are two sources of error; one from the counting error in the region of interest, the other from background fitting. The background fitting error is composed of two parts. The most difficult to calculate is the systematic error in the model of the background. The power law  $AE^{-r}$  is based on empirical observation and although it can be justified on theoretical grounds (Leapman et al.<sup>5</sup>), it is only valid over a limited range. One test that can be applied is to compare the theoretical shape of an edge a long way from threshold to the power-law fit. Preliminary work on Carbon K for various collection angles suggest that for a fitting region of 50 eV starting 450 eV above threshold the error in the shape of 150 eV from the start of the background region is less than 2%. The error in background fitting due to statistical fluctuations have been given by Egerton,<sup>2</sup> Zaluzec,<sup>3</sup> and Statham.<sup>4</sup> The formulas quoted are all different. An exact error analysis gives the fractional error in the background fit as

$$\left(\frac{\Delta B}{B}\right)^2 = \frac{F^2(E^2Y + N^2Z) + (S^2Y + E^2Z)}{(E^2 - NS)^2} \quad (2)$$

---

The author is at VG Microscopes, Charlwoods Road, East Grinstead, Sussex, England, RH19 2JQ. Supported by the National Science Foundation (Contract DMR 80-23462). The aid of Drs. O. L. Krivanek and C. Colliex in bringing this problem to our attention is gratefully acknowledged.

$$Y = \sum_i (1/y_i), \quad Z = \sum_i (\ln E_i)^2 / y_i, \quad E = \sum_i \ln E_i, \quad S = \sum_i (\ln E_i)^2, \quad F = \sum_j \ln E_j$$

The sum over  $i$  is a sum over background channels with counts  $y_i$  and energy  $E_i$ . The sum over  $j$  is a sum over the channels in the region after the edge to which the background has been extended. This formula can be approximated by

$$\left(\frac{\Delta B}{B}\right)^2 = (\ln E_B)^2 \frac{288N^3}{Y_B} \left(\frac{E_B}{\Delta E}\right)^4 \frac{(\ln E_A)^2 + (\ln E_B)^2}{N^4(N^2 - 1)^2} \quad (3)$$

where  $E_B$  is a typical energy in the background,  $E_A$  is a typical energy after the edge,  $Y_B$  is a typical number of background counts in a channel of width  $\Delta E$ , and  $N$  is the number of background channels.

For energy-loss imaging it might not be necessary to do a power-law fit. Ottensmeyer<sup>6</sup> does a simple subtraction of background before an edge from the signal after the edge. Rez and Ahn<sup>7</sup> fit a straight line to two points before the edge and extrapolate it to a point after the edge. These simpler procedures can be justified when the difference between their background estimate and the power-law fit (assumed to be correct in this discussion) is less than any statistical error. For a simple background subtraction the error is  $Br\Delta E/E_B$ , where  $r$  is the exponent,  $\Delta E$  is the energy difference between the energy after the edge and the background energy, and  $E_B$  is the background energy. The error in the background is of order  $3\sqrt{B}$  (3 confidence limit). As  $r$  is about 3-4 and typical values of  $\Delta E$  and  $E_B$  are 30 and 300 eV, respectively, this means that if there are fewer than 100 counts in the background the procedure would be justifiable. Note that the background is overestimated and the minimum detectable number of counts of the element in question is also given by  $Br\Delta E/E_B$ . What this corresponds to in quantitative analysis can only be inferred from the spectrum in comparison with other edges. The difference between a straight-line fit and a power law is

$$B \frac{r(r+1)}{2} \left(\frac{E_2 - E_1}{E_1}\right) \left(\frac{E_3 - E_1}{E_1}\right)$$

where  $E_1$  and  $E_2$  are energies before the edge and  $E_3$  is after the edge. The error in the background fit is approximately  $1.4[\sqrt{E_1^2 + E_3^2}/(E_2 - E_1)]\sqrt{B}$ . Typical values for  $(E_2 - E_1)$  and  $(E_3 - E_1)$  are 30 eV and 60 eV so the estimated relative difference is of the order of 0.1, which is the same as the estimated counting error for about 10 000 counts. This procedure overestimates the amount of the element present.

When there are few counts it is not worth doing sophisticated fits to the data. If anything, attempts to fit function to noisy data will make background estimates worse.

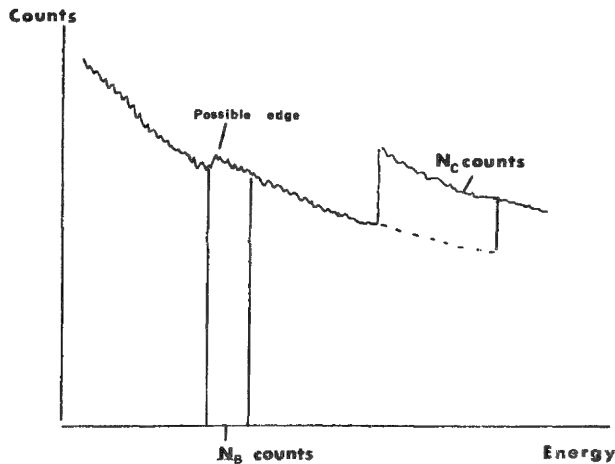


FIG. 1.--Spectrum illustrating features for detection limit calculation.

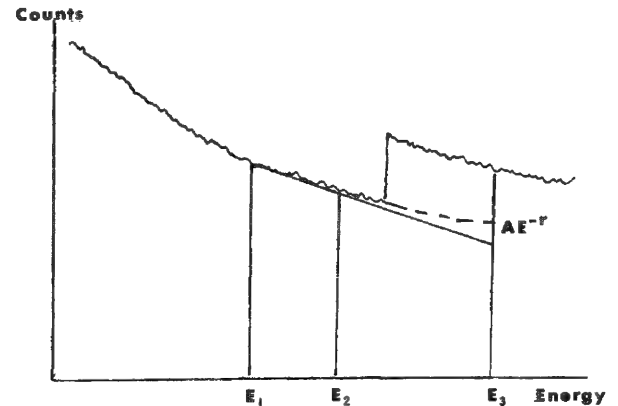


FIG. 2.--Spectrum illustrating straight-line background fit.



## References

1. M. Isaacson and D. Johnson, *Ultramicroscopy* 1: 33, 1975.
2. R. F. Egerton, *Proc. 40th EMSA*, 1982, 488.
3. N. J. Zaluzec, *Microbeam Analysis--1981*, 329.
4. P. J. Statham, *Microbeam Analysis--1982*, 1.
5. R. D. Leapman, P. Rez, and D. F. Mayers, *J. Chem. Phys.* 72: 1232, 1980.
6. F. P. Ottensmeyer and J. W. Andrew, *J. Ultrastru. Res.* 72: 336, 1980.
7. P. Rez and C. Ahn, *Ultramicroscopy* 8: 361, 1982.

## STATISTICS OF EDGE AREAS IN QUANTITATIVE EELS IMAGING: SIGNAL-TO-NOISE RATIO AND MINIMUM DETECTABLE SIGNAL

Thierry Pun and J. R. Ellis

### *Quantitative EELS Imaging*

Electron energy loss spectrometry (EELS) is now a widely used technique in quantitative microanalysis, especially for the estimation of light elements.<sup>1</sup> The computerized acquisition and processing of those EELS spectra gives the possibility of creating images representing elemental compositions of a sample.<sup>2</sup> The intrinsic accuracy of the digital processing of EELS spectra may however mask the fact that these recorded and computed values are statistical in essence. Attention must therefore be paid in the evaluation of their characteristic properties, such as probability density functions (pdf), moments (mean, variance, etc.), and confidence domains.<sup>3-5</sup>

The EELS image is obtained by subtraction, at each pixel, of the noncharacteristic background contribution (background area in the energy range of interest, denoted BA) from the spectrum area (total area, TA). This operation provides the edge area (EA) value above a given core edge energy. Over a limited range of energy losses  $E_i$  ( $i = 1 \dots n$ ), the background can usually be approximated by an inverse-power law,  $c_i = \alpha E_i^{-r}$ , where  $c_i$  is the number of recorded counts and  $\alpha$  and  $r$  are constants that may vary from pixel to pixel. A background BA is computed above the core edge, then extrapolated and subtracted from the measured TA, which yields the edge area EA.

### *Least-squares Estimation*

The two parameters  $\alpha$  and  $r$  are usually determined by the use of a least-squares estimation procedure (LSE) in order to fit the data to the background model law

$$y_i = a + b(x_i - \bar{x}), \quad i = 1 \dots n \text{ (LSE region)} \quad (1)$$

where  $y_i = \ln c_i$ ,  $x_i = \ln E_i$ ,  $\bar{x} = (1/n) \sum x_i = \ln \sqrt[n]{E_1 E_2 \dots E_n}$ ,  $a = \ln \alpha + b \bar{x}$ , and  $b = -r$ . (2)

The value  $n$  is the number of energy channels in the LSE region. The reason for using  $\bar{x}$  is that the parameters  $a$  and  $b$  obtained in that way are statistically independent.

If one assumes independence among the  $y_i$ , the least-square estimators  $A$  and  $B$  of  $a$  and  $b$  are obtained by minimization of  $\sum [w_i \{y_i - [A + B(x_i - \bar{x})]\}^2]$ . They are<sup>6</sup>

$$A = \bar{y} = (\sum w_i y_i) / (\sum w_i) \quad (3)$$

$$B = \frac{\sum w_i y_i (x_i - \bar{x})}{\sum w_i (x_i - \bar{x})^2} \quad (4)$$

where the  $w_i$  are weights proportional to the inverse of the variance of the  $y_i$ . These weights are often ignored; i.e., the hypothesis of homogeneous variances (homoscedasticity) is assumed. Due to the Poisson statistics of the  $c_i$ , this hypothesis is not true; nonuse of the weights yields estimates for  $a$  and  $b$  that have nonminimum variances. However, the variation in the LSE region of  $y_i = \ln c_i$  is normally relatively small. Consequently the

---

The authors are at the Division of Research Services, Biomedical Engineering and Instrumentation Branch, National Institutes of Health, Bethesda, MD 20205. They thank Dr. R. D. Leapman for many valuable discussions related to this work, as well as all the collaborators of the EBIMF laboratory at NIH for their support.

following results are obtained if one assumes homoscedasticity ( $w_i = 1$  in Eqs. 3 and 4). The developments would remain essentially the same without this hypothesis.

Using Eqs. (3) and (4), one can estimate the variances of the parameters  $a$  and  $b$ . However, the knowledge of the statistics of the  $c_i$  gives the possibility of deriving the probability distribution functions of these parameters. Having the pdf of a variable, rather than only its moments, provides a more complete understanding of its behavior. In particular, this information gives a handle on statistical properties such as confidence limits.

In what follows a distinction will be made between random (measured or estimated) variables and their "true" values. The former will be written in upper-case letters, the latter in lower-case letters. Denoting then by  $C_i$  the random variable (measured) associated with  $c_i$ , one has for the pdf of  $C_i$

$$p(C_i) = \frac{e^{-c_i}(c_i)^{C_i}}{(C_i)!} \quad (\text{Poisson pdf, parameter } c_i) \quad (5)$$

It is assumed that  $C_i$  is large enough to have its Poissonian distribution approximated by a normal distribution of mean  $c_i$  and variance  $c_i$ :

$$p(C_i) = \frac{1}{\sqrt{2\pi c_i}} \exp\left[-\frac{(C_i - c_i)^2}{2c_i}\right] \quad (6)$$

Furthermore, the normalized variable  $s_i = (C_i - c_i)/\sqrt{c_i}$  will be used. Its pdf is then

$$p(s_i) = \frac{1}{\sqrt{2\pi}} \exp(-s_i^2/2) \quad (7)$$

with  $Y_i$  as the random variable associated with  $y_i$ :

$$Y_i - y_i = \ln C_i - \ln c_i = \ln[1 + (s_i/\sqrt{c_i})] \quad (8)$$

With  $C_i$  taken as an estimate for  $c_i$ , and using the fact that  $s_i/\sqrt{C_i}$  is small,

$$Y_i - y_i = s_i/\sqrt{C_i} \quad (9)$$

From Eq. (3), the deviation between the random (estimated) variable  $A$  and its "true" unknown value  $a$  is

$$\Delta A = A - a = (1/n) \sum_{i=1}^n (Y_i - y_i) = (1/n) \sum_{i=1}^n (s_i/\sqrt{C_i}) \quad (10)$$

Like the  $c_i$ , the  $s_i$  are mutually independent. Therefore,

$$p(\Delta A) = \frac{1}{\sigma_a \sqrt{2\pi}} \exp(-\Delta A^2/2\sigma_a^2) \quad (11)$$

where

$$\sigma_a^2 = (1/n^2) \sum_{i=1}^n (1/C_i) \quad (12)$$

and similarly

$$p(\Delta B) = \frac{1}{\sigma_b \sqrt{2\pi}} \exp(-\Delta B^2/2\sigma_b^2) \quad (13)$$

where

$$\sigma_b^2 = \left[ \frac{1}{\sum_{i=1}^n (x_i - \bar{x})^2} \right]^2 \sum_{i=1}^n \frac{(x_i - \bar{x})^2}{C_i} \quad (14)$$

This shows that A and B are normally distributed about a and b, with variances  $\sigma_a^2$  and  $\sigma_b^2$ . Conversely, a confidence level in the estimation of a and b can be given: they are included between  $(A - h\sigma_a, A + h\sigma_a)$  or  $(B - h\sigma_b, B + h\sigma_b)$  with a confidence  $1 - 2\text{erfc}(h)$ . For example,  $r (= -b)$  is between  $(-B - 3\sigma_b, -B + 3\sigma_b)$  with a confidence level of 99.73%. Equations (12) and (14) show that, in order to decrease the variances of the estimated parameters, the numbers of counts  $C_i$ , the number n of channels, and their width may be increased.

#### Probability Density Function of the Background Area

The background area (random variable BA, "true" value  $ba$ ) is the area of the extrapolated background in the edge region above the core edge energy (integration region):

$$ba = \sum_{j=1}^m e^{a_j} e^{b(x_j' - \bar{x})}, \quad j = 1 \dots m \quad (\text{edge region}) \quad (15)$$

The value m is the number of acquisition channels in the integration region. The prime denotes energies and counts values in the integration region. Use of a Taylor expansion for BA(A,B) about  $ba$  yields

$$\Delta BA = BA - ba = (BA\Delta A + \mu\Delta B) + (\frac{1}{2}BA\Delta A^2 + \frac{1}{2}\nu\Delta B^2 + \mu\Delta A\Delta B) \quad (16)$$

where

$$\begin{aligned} (\partial BA / \partial A) &= (\partial^2 BA / \partial A^2) = BA, & (\partial BA / \partial B) &= (\partial^2 BA / \partial A \partial B) = \sum_{j=1}^m e^{a_j} (x_j' - \bar{x}) e^{B(x_j' - \bar{x})} = \mu \\ (\partial^2 BA / \partial B^2) &= \sum_{j=1}^m e^{a_j} (x_j' - \bar{x})^2 e^{B(x_j' - \bar{x})} = \nu \end{aligned} \quad (17)$$

As mentioned above, the deviations  $\Delta A$  and  $\Delta B$  are statistically independent; therefore, the joint pdf  $p(\Delta A, \Delta B)$  is equal to  $p(\Delta A)p(\Delta B)$ . The variance of the deviation  $BA - ba$  is then

$$\begin{aligned} \text{var}(\Delta BA) &= \int_{-\infty}^{+\infty} \int_{-\infty}^{+\infty} (\Delta BA)^2 p(\Delta A) p(\Delta B) d(\Delta A) d(\Delta B) \\ &= (BA^2 \sigma_a^2 + \mu^2 \sigma_b^2) + [3/4 BA^2 \sigma_a^4 + 3/4 \nu^2 \sigma_b^4 + (\frac{1}{2} BA \nu + \mu^2) \sigma_a^2 \sigma_b^2] \end{aligned} \quad (18)$$

Many numerical simulations have confirmed that the development of Eq. (18) converges rapidly. For a number of counts in the background area BA greater than a few dozen, the second-order terms in Eq. (16) may be neglected. The approximation for  $\Delta BA$  is therefore linear, and its pdf can easily be evaluated. From Eq. (16),

$$\Delta BA = BA\Delta A + \mu\Delta B \quad (19)$$

and consequently

$$p(BA - ba) = p(\Delta BA) = \frac{1}{\sigma_{ba} \sqrt{2\pi}} \exp \left[ -\frac{\Delta BA^2}{2\sigma_{ba}^2} \right] \quad (20)$$

$$\text{with } \sigma_{ba}^2 = BA^2 \sigma_a^2 + \mu^2 \sigma_b^2 \quad (21)$$

The distribution of BA about  $ba$  is therefore normal, with mean  $ba$  and variance  $\sigma_{ba}^2$ . As mentioned for  $\Delta A$  and  $\Delta B$ , confidence levels can be given for the estimation of  $ba$ . From Eqs. (17) and (21) it appears that in order to decrease the variance of the background area, the distance between the LSE and edge regions has to be decreased.

#### Probability Function of the Edge Area

As described in the first section, the area of interest for the image formation is the edge area EA obtained as follows:

$$EA = TA - BA = \sum_{j=1}^m C_j' - \sum_{j=1}^m e^{a_j} e^{B(x_j' - \bar{x})} \quad (22)$$

Each  $C_{j'}$  follows a Poissonian distribution of parameter  $c_{j'}$ . Assuming independence among the  $c_{j'}$ , TA still has a Poissonian distribution of parameter  $\Sigma c_{j'} = ta$ . Making use again of the Gaussian approximation to the Poisson law, and of the fact that TA (measured random variable) is an estimate for ta ("true" value), one obtains the probability density function of TA

$$p(TA) = \frac{1}{\sqrt{2\pi}TA} \exp\left[-\frac{(TA - ta)^2}{2TA}\right] \quad (23)$$

From Eqs. (20)-(23), it follows that

$$p(EA) = \frac{1}{\sigma_{ea}\sqrt{2\pi}} \exp\left[-\frac{[EA - (ta - ba)]^2}{2\sigma_{ea}^2}\right] \quad (24)$$

with

$$\sigma_{ea}^2 = TA + \sigma_{ba}^2 = TA + BA^2\sigma_a^2 + \mu^2\sigma_b^2 \quad (25)$$

This result not only provides the estimate of the variance of each picture element of the EELS image, it also gives the confidence level with which each of them is known. That is of importance for any further processing to be done with this image, such as its separation into its constitutive parts or identification of its features.

#### *Signal-to-noise Ratio, Relative Edge Concentration, and Minimum Detectable Signal*

The signal-to-noise ratio of the edge area (that is, of each pixel of the EELS image, is defined as<sup>5</sup>

$$snr = EA/\sigma_{ea} \quad (26)$$

Defining the "relative edge concentration" (signal-to-background ratio) by

$$K = EA/BA \quad (27)$$

one can express the signal-to-noise ratio as

$$snr = \frac{EA}{\sigma_{ea}} = \frac{TA - BA}{\sqrt{TA + BA^2\sigma_a^2 + \mu^2\sigma_b^2}} = \frac{K*BA}{\sqrt{(1 + K)BA + BA^2\sigma_a^2 + \mu^2\sigma_b^2}} \quad (28)$$

This expression shows that one can increase the signal-to-noise ratio by acting independently on the LSE region or on the edge-region parameters. To decrease the variance of A and B, and therefore the variance  $\sigma_{ba}^2$ , (1) more counts have to be recorded in the LSE region, and (2) the number of channels and their width have to be increased. As a fixed number n of LSE channels is often used, their width should be increased as far as Eq. (1) remains valid.

As also shown in Ref. 5, Eq. (28) yields an optimum number m of integration channels assuming a constant channel width. However, this value m is usually predetermined. Therefore, to decrease the variance  $\sigma_{ea}^2$ , (3) the width of the channels in the edge region has to be small, and (4) the integration and LSE regions must be as close as possible. The condition (3) implies in fact a high number of counts to be recorded near the core edge energy.

Figure 1 presents the improvement of the snr provided when the LSE region width is increased (i.e., for a predetermined number of channels, when their width is increased). This figure is obtained for a spectrum with 10 000 counts at a core edge energy of 500 eV. For other numbers of counts, it can easily be shown that the snr is proportional to their square root.

Figure 2 illustrates point (3) in the above enumeration. Compared to Fig. 1, the degradation of snr is, however, relatively limited when the integration region width increases. That points out the critical importance of the choice of the LSE region.

It is also interesting to know the minimum number of counts, for a given concentration, that have to be collected to provide an exploitable EELS image. By "exploitable" one means a picture from which it is possible to extract some relevant information (either by direct observation or by image processing). Such a number of counts would be the one providing a sort of "minimum detectable signal." Its knowledge is of importance, because it may permit

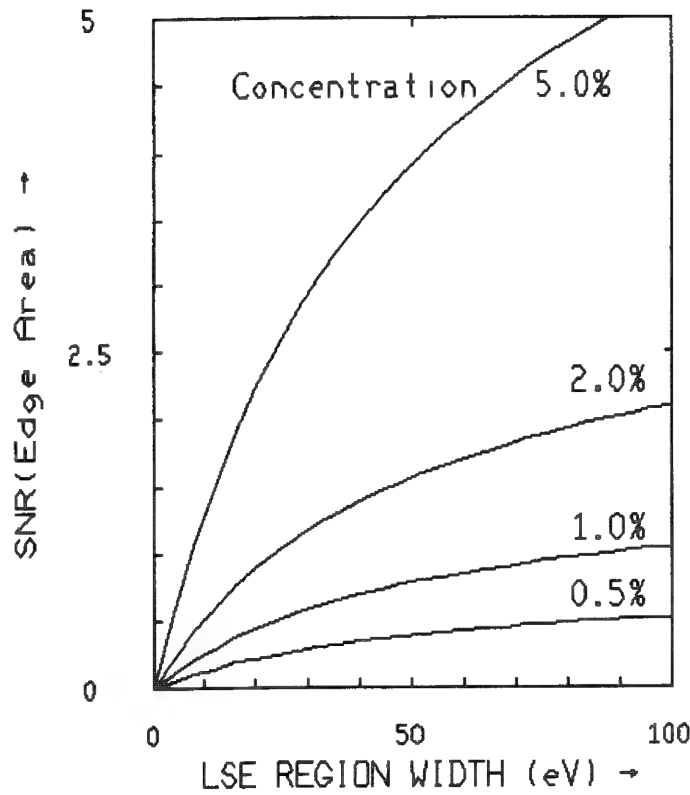


FIG. 1.--Signal-to-noise ratio (from Eq. 28) vs LSE region width (fixed number of channels) for various values of relative edge concentration: 10 000 counts at 500 eV (core edge energy),  $r = 4$ , LSE region below 490 eV (5 channels), integration region between 500 and 540 eV (5 channels).

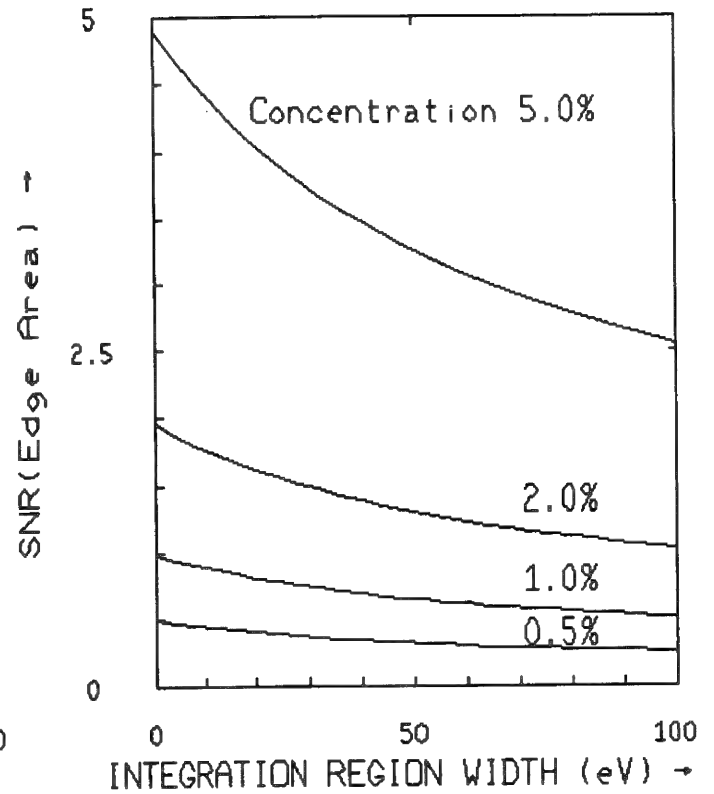


FIG. 2.--Signal-to-noise ratio vs integration region width (fixed number of channels) for various values of relative edge concentration: 10 000 counts at 500 eV (core edge energy),  $r = 4$ , LSE region between 450 and 490 eV (5 channels), integration region above 500 eV (5 channels).

optimization of acquisition time, thereby for example limiting radiation damage to the sample.

Some simulations have led to the rough conclusion that an snr at each pixel of 0.5-1 is necessary to enable one to discern the element of interest from the statistical noise in the image (by direct observation). This value probably should be of the same order of magnitude for processing the image. Figure 3 presents, as a function of relative edge concentration, the number of counts (at core edge energy) necessary to reach this limit. These values are obtained by use of Eqs. (12), (14), and (28). This curve is highly nonlinear (note the logarithmic scale) and shows that for small concentrations the required number of counts increases dramatically as concentration decreases.

An approximate pdf can also be derived for the relative edge concentration  $K = EA/BA = (TA/BA) - 1$ . This expression can be expanded into a Taylor series. As for the expression of Eq. (16) for the background area value, it appears that for BA values greater than a few dozen counts, this Taylor series can be linearized:

$$K(\text{estimated}) - k(\text{true}) = \Delta K = (1/BA)\Delta TA - (TA/BA^2)\Delta BA \quad (29)$$

and from Eqs. (20), (21), and (23),

$$p(\Delta K) = \frac{1}{\sigma_K \sqrt{2\pi}} \exp(-\Delta K^2 / 2\sigma_K^2) \quad (30)$$

$$\text{where } \sigma_K^2 = (1 + K)/BA + (1 + K)^2 \sigma_{ba}^2 / BA^2 \quad (31)$$

If the relative edge concentration were defined by  $K' = q*EA/BA = q*K$ , where  $q (>0)$  is

a proportionality factor, the pdf of  $K'$  would become

$$p(\Delta K') = (1/q)p(\Delta K) \big|_{\Delta K = \Delta K'/q} \quad (32)$$

$$\text{where } \sigma_{K'}^2 = q^2 \sigma_K^2 \quad (33)$$

As before, it is possible to have confidence levels in the estimation of  $K$ .

Figure 4 presents the standard deviation of the relative edge concentration  $K$  as a function of this concentration, for various numbers of counts at core edge energy. It can easily be shown that  $\sigma_K^2$  is proportional to the inverse of this number of counts. In order to obtain a high degree of confidence in the estimation of the concentration, it appears that the number of counts has to be higher than required for a correct assessment of the edge area. For example, the numbers of counts used for curves 2 and 3 of Fig. 4 are those giving  $\text{snr} = 1$  for a relative edge concentration of 0.1% (2 062 200 counts) and 1% (20 640 counts), respectively. These count values yield a ratio  $K/\sigma_K \approx 1$  for  $K = 0.1\%$  (curve 3) and  $1\%$  (curve 2), respectively. This ratio is clearly insufficient to provide a high degree of confidence in the estimation of the concentration, at least when each value is examined separately. When working with an image of relative concentration values, it might be possible to make use of several estimates in the same neighborhood to increase the minimum detectable concentration.

### Conclusion

By taking into account the statistical properties of the counting processes, approximate probability density functions have been derived for each parameter and result of interest.

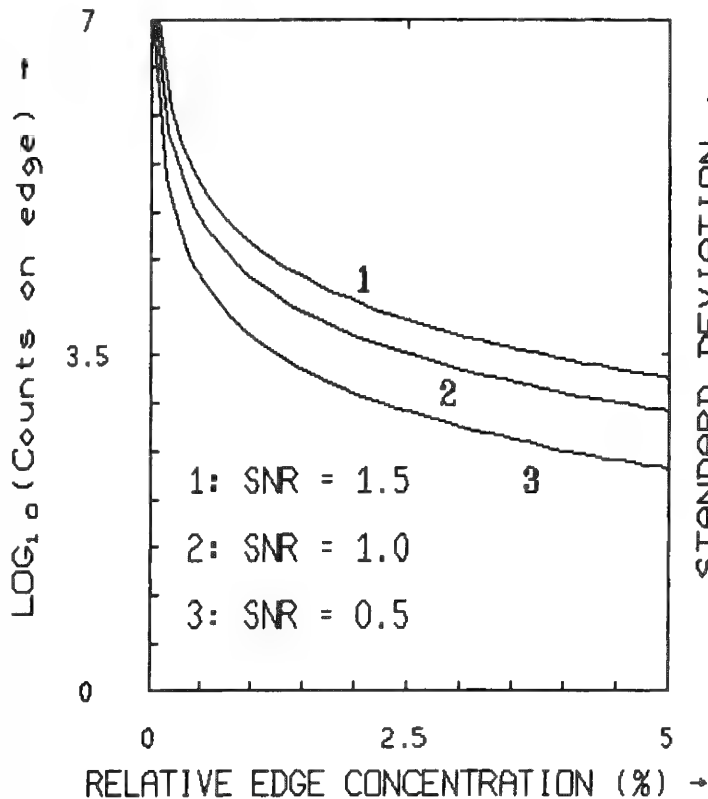


FIG. 3.--Decimal logarithm of total number of counts at core edge necessary to reach given signal-to-noise ratio  $\text{snr}$  vs relative edge concentration: core edge energy 500 eV,  $r = 4$ , LSE region between 450 and 490 eV (5 channels), integration region between 500 and 540 eV (5 channels).

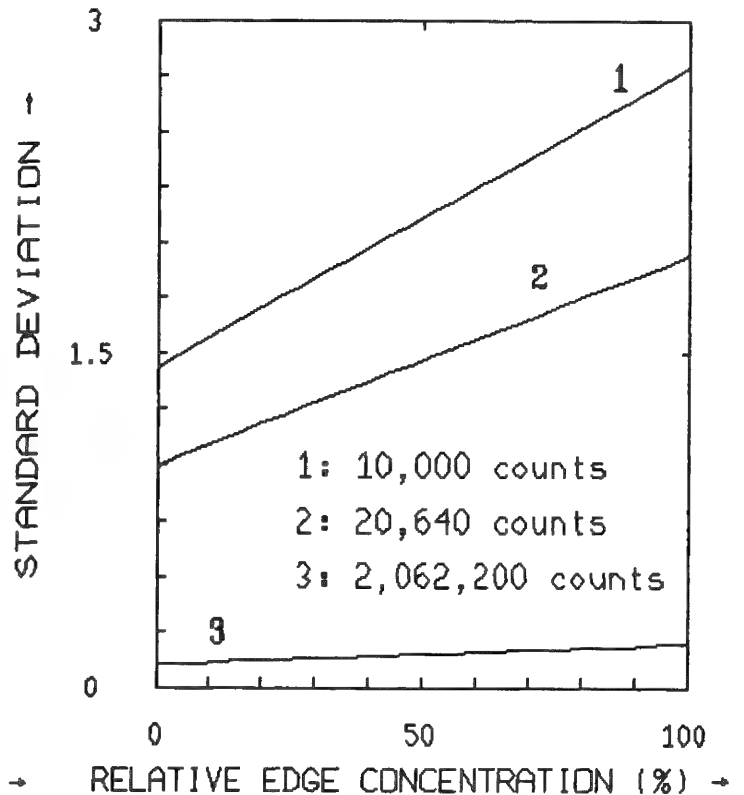


FIG. 4.--Standard deviation  $\sigma_K$  of relative edge concentration  $K$  as function of this concentration (%) for various numbers of counts at core edge energy of 500 eV;  $r = 4$ , LSE region between 450 and 490 eV (5 channels), integration region between 500 and 540 eV.



In addition to a quantitative estimate of the variances of these parameters, the pdf's give us an assessment of the confidence levels related to these estimates. Signal-to-noise ratios as a function of the acquisition parameters have been given, pointing out the importance of the choice of the LSE region. The notion of minimum detectable signal has been presented, and minimum numbers of counts required to reach this detectability level have been derived.

#### References

1. V. E. Cosslett, "Electron energy loss spectrometry," *Proc. 8th Intern. Cong. X-ray Optics and Microanalysis*, Boston, 1982, 8-12.
2. R. D. Leapman et al., "Combined elemental and structural imaging in a computer controlled analytical electron microscope," *Proc. EMSA 1983*, 10.
3. M. Ancey, F. Bastenaire, and R. Tixier, "Application of statistical methods to electron probe microanalysis," *Proc. 8th Intern. Cong. X-ray Optics and Microanalysis*, Boston, 1982, 49-56.
4. C. E. Fiori, C. R. Swyt, and J. R. Ellis, "The theoretical characteristic to continuum ratio in energy dispersive analysis in the analytical electron microscope," *Microbeam Analysis--1982*, 57-71.
5. R. F. Egerton, "A revised expression for signal/noise ratio in EELS," *Ultramicroscopy* 9: 387-390, 1982.
6. A. Hald, *Statistical Theory with Engineering Applications*, New York: Wiley, 1965.

## ELECTRON ENERGY LOSS IMAGING IN THE STEM: SYSTEMATIC AND STATISTICAL ERRORS

R. D. Leapman and C. R. Swyt

Electron energy loss imaging may now be carried out in a variety of ways both in the CTEM and the STEM. In the CTEM energy-filtered images are recorded in parallel with a Castaign-Henry spectrometer, a magnetic energy-filter, or a magnetic sector spectrometer.<sup>1-4</sup> Images are recorded below and above a characteristic core edge so that the difference between them provides an elemental map of the sample. In STEM the electron probe is raster-scanned across the sample and part of the spectrum is collected at each pixel in the image, normally with the use of a magnetic sector spectrometer.<sup>5,6</sup> This type of system makes it possible to collect single-electron counts at a number of channels around one or more core edges. Certain advantages are offered by each instrument. In particular, the STEM allows a precise quantitative analysis of the EELS images since the data may be acquired and processed digitally by means of a computer.<sup>7-13</sup> We are often interested in measuring rather small signals superimposed on a large background. Typically the signal to background ratio is comparable to the atomic ratio of the element to be detected. Low concentrations are therefore only detectable when there are many counts in the spectrum so the statistical errors are minimized. In this paper we discuss some of the ways in which the data can be analyzed to reduce the systematic and statistical errors when the background is subtracted from the spectrum above an edge.

### *Two-Parameter Fit for the Background*

Both experiment and theory verify that the smoothly varying background intensity in the energy loss spectrum often satisfies an inverse power law  $I = AE^r$  over a limited range of energy loss  $E$ , where  $r$  is typically -3 or -4.<sup>14,15</sup> In general if we do not know  $r$  exactly we should fit both of the parameters  $A$  and  $r$  using at least two channels below the edge.<sup>16</sup> When several channels are collected the fit is normally achieved by a least-squares procedure. The statistical error in the fitted background, extrapolated into the core edge region, has been estimated previously.<sup>17,18</sup> It depends on the size of the fitting and edge windows in the spectrum and their energy separation as well as the number of counts that are measured. Figure 1 defines the relevant quantities for one edge.

If  $T$  is the total number of counts in the edge window and  $B_2$  is the number of counts in the fitted background in the same energy window, the estimated core signal is

$$S = T - B_2 \quad (1)$$

the standard deviation of the characteristic signal  $\sigma_S$  can be obtained from

$$\sigma_S^2 = \sigma_T^2 + \sigma_{B_2}^2 = T + \sigma_{B_2}^2 \quad (2)$$

It is found that the statistical error in  $B_2$  is always larger than  $\sqrt{B_2}$ . It has been written by Egerton in the form

$$\sigma_{B_2}^2 = hB_2 \quad (3)$$

where  $h$  varies typically between 5 and 20.

The error (i.e.,  $h$ ) can be reduced by an increase in the width of the fitting region and

---

The authors are with the Biomedical Engineering and Instrumentation Branch, DRS, National Institutes of Health, Bethesda, MD 20205. They wish to thank T. Pun, J. R. Ellis, and K. E. Gorlen for helpful discussions.

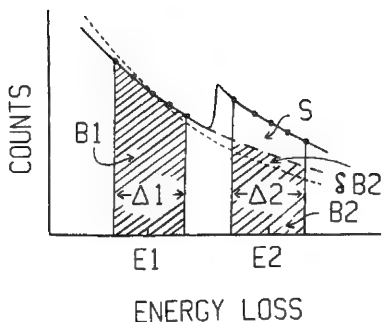


FIG. 1.--Pre-edge fitting window 1 and postedge integration window 2 each containing 5 channels.  $B$  is total number of counts in fitted background,  $E$  is center energy of window,  $\Delta$  is its width.  $\delta B_2$  is error in total counts in fitted background for post-edge window due to error in  $r$  (small dash curve).

a decrease in the width of the post-edge region. In practice the fitting region cannot be extended beyond a certain limit because the inverse-power law breaks down, due for example to the occurrence of another edge. The energy interval between the edge and the post-edge region should be larger than both the edge width and the energy drift of the spectrometer during acquisition of the image.

#### One-parameter Fit for the Background

If the parameter  $r$  is constant ( $r = R$ ) over the entire image, we may fit only the parameter  $A$  for the background. In this case the statistical error due to the background fit is significantly reduced. The greater error, due to  $r$ , in the two-parameter fit can be visualized by "pivoting" the curve through the center of the fitting region: the effect of pivoting is amplified in the edge region. If only the parameter  $A$  is fitted there is no pivoting and the error depends only on the counts in the fitting region. The standard deviation is then given by

$$\sigma_{B_2} = B_2 / \sqrt{B_1} \quad (4)$$

or

$$\sigma_S^2 = T + (B_2^2 / B_1) \quad (5)$$

We note that the success of the energy-filtered imaging carried out in the CTEM normally depends on the validity of the one-parameter fit since the background shape is assumed constant over the entire image.<sup>1-4</sup> The pre-edge image is scaled (sometimes arbitrarily) to match the true background for the post-edge image and is then subtracted to yield the elemental distribution. This circumstance partly explains why the elemental maps obtained in the CTEM appear to have better statistics than maps obtained in the STEM with a two-parameter fit. The high beam dose available in the CTEM over a wide area of the sample with high spatial resolution is also an important factor here.

#### Factors Influencing the Core Edge Intensity and the Background

1. *Elemental Concentration.* The core edge intensity is proportional (in the limit of thin samples) to the number of atoms of the element per unit area of the sample, i.e., to density  $\rho$ , the thickness  $t$ , and the weight concentration of the element  $c_x$ . The constant of proportionality includes the incident probe current, the counting time, the cross section for the core excitation in the energy window, and the collection angle selected.

$$S_x \propto \rho t c_x \quad (6)$$

It is the quantity  $c_x$  or  $\rho t c_x$  that we wish to display in the elemental image.

2. *Elastic Scattering.* As the sample thickness increases, there is an increasing probability that electrons which have undergone a core excitation will also be elastically scattered outside the collection aperture. If elastic scattering is represented by an average cross section per atom  $\sigma_e$ , then the fraction of electrons lost at the objective aperture is approximately

$$f_e = \exp(-\rho t N_0 \sigma_e / A) \quad (7)$$

where  $N_0$  is Avogadro's number and  $A$  is the mean atomic weight. By dividing two core edge images to yield a ratio map, we can eliminate the elastic-scattering effect. It is also possible to divide by the zero-loss image to yield a corrected elemental distribution. Contrast in a background-subtracted core image without a correction for  $f_e$  may be dominated

by elastic scattering, since the mean free path  $\lambda_e = A/(\rho N_0 \sigma_e)$  is typically only about 1000 Å at 100 keV beam energy for light elements and decreases rapidly for heavier elements.

3. *Plural Inelastic Scattering.* As the sample thickness increases there is also an increasing probability for plural inelastic scattering involving one or more valence excitations as well as a core loss. If the total inelastic scattering cross section is  $\sigma_i$ , the fraction of electrons scattered outside a narrow energy window is given approximately by

$$f_i = \exp(-\rho t N_0 \sigma_i / A) \quad (8)$$

This effect on the image could be reduced by an increase in the integration window, but the statistical errors are then increased. Alternatively a ratio of two images recorded with the same integration window serves to remove this inelastic scattering effect, as in the case of elastic scattering.

So far we have assumed that the shape of the background remains unchanged when the sample thickness changes. In fact plural inelastic scattering can cause subtle changes in background shape. It is therefore important to estimate how the power-law fit is altered and in particular to estimate the magnitude of fluctuations in  $r$  that give rise to systematic errors in the background if a one-parameter fit is assumed. An estimate for the change in background shape as a function of thickness can be made as follows. We take as the single-scattering distribution a measured spectrum obtained with good statistics from a very thin sample. We choose a 100Å carbon film and a 200keV beam energy. From this spectrum we generate the plural scattering spectrum for different values of  $t/\lambda_i$ , where  $\lambda_i = A/(\rho N_0 \sigma_i)$  is the total inelastic mean free path. For carbon  $\lambda_i$  is about 600Å at 100 keV beam energy. The change in the exponent  $r$  is then measured for different fitting windows. For energy losses up to about 200 eV, the entire spectrum is computed by means of a Fourier transform to convert the Poisson distribution into an exponential of the transformed single-scattering spectrum. For higher energy losses, where the background originates mainly from the tails of core edges, an exact power law with exponent  $r = -3$  is assumed for the single scattering spectrum and the spectrum at finite thickness is generated by convolution with the already determined low loss spectrum. A fuller discussion of these procedures has been given previously.<sup>19-21</sup>

Figure 2 shows the fitted value of  $r$  as a function of  $t/\lambda_i$  for an energy window 15 or 30 eV wide at various energy losses in pure carbon. At high energy losses  $r$  is quite constant over a wide range of thickness but at energies close to the carbon K edge (285 eV) there are large variations in  $r$  due to changes in spectral shape from the superposition of a 25eV plasmon above the edge threshold. This result indicates that a one-parameter fit

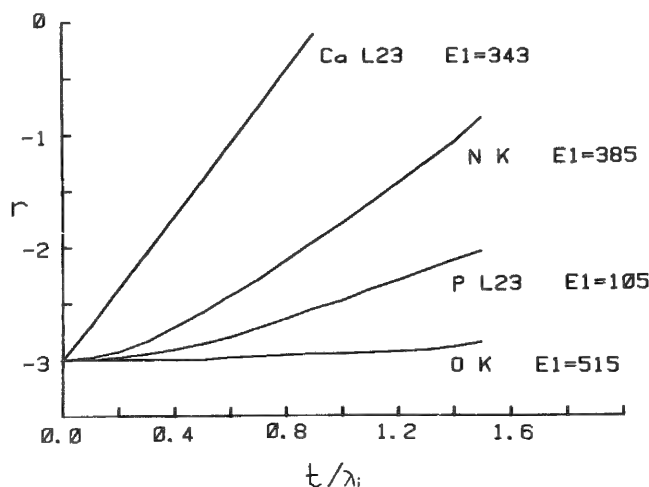


FIG. 2.--Fitted parameter  $r$  as function of  $t/\lambda_i$  for pure carbon obtained from computer-generated spectra. Values are shown for energy losses  $E_1$  (in eV) just below four different core edges. For Ca  $\Delta_1 = 15$  eV and for N, P, and O  $\Delta_1 = 30$  eV.

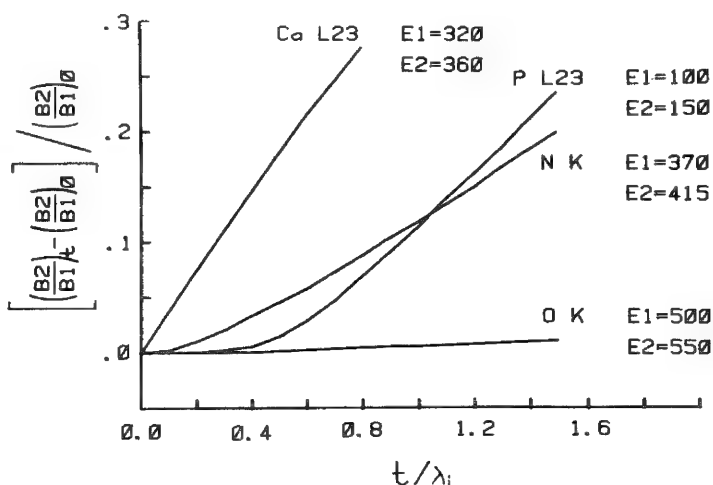


FIG. 3.--Relative variation of  $B_2/B_1$  as a function of  $t/\lambda_i$  for Ca  $L_{23}$ , P  $L_{23}$ , N  $K$ , and O  $K$  edges in carbon.  $E_1$  and  $E_2$  are indicated in eV. Energy windows  $\Delta_1$  and  $\Delta_2$  were chosen to be narrow. Measurements were made on computer-generated spectra.

for the background is normally not adequate for detection of calcium ( $L_{23}$  edge is about 350 eV) in the presence of carbon when there are mass thickness variations. Significant changes in  $r$  are evident for edges in the 100-200eV range, suggesting that a one-parameter fit may also be inadequate for detection of phosphorus ( $L_{23}$  edge  $\cong$  135 eV) or sulfur ( $L_{23}$  edge  $\cong$  165 eV). Since  $r$  decreases with increasing thickness in this range, a region of the sample with slightly higher mass thickness would tend to give a brighter intensity in the elemental map, a potentially misleading result. For a given systematic error,  $\delta r = r - R$ , in the one-parameter fit, we can also estimate the systematic error in the background  $\delta B$ , which is given approximately by

$$\frac{\delta(B_2/B_1)}{(B_2/B_1)} = \left( \frac{E_2}{E_1} \right) \delta r - 1 \quad (9)$$

where  $E_1$  and  $E_2$  are the centers of the pre-edge fitting window and the post-edge integration window, respectively (Fig. 1). Figure 3 shows the fractional change in the background ratio  $B_2/B_1$  as a function of  $(t/\lambda_i)$  for narrow energy windows at  $E_1$  and  $E_2$ . The curves were obtained by measurements on the generated spectra. When  $\delta B_2$  is comparable with the size of the characteristic signal it is clear that the one-parameter fit is not valid. The largest changes in  $B_2/B_1$  occur for energies closest to the carbon K edge, for example in the neighborhood of the calcium  $L_{23}$  edge; there is less effect near the nitrogen K edge. At the oxygen K edge very little effect is predicted even for a large thickness range. At low energy losses significant changes in  $B_1/B_2$  also occur, for example at the phosphorus  $L_{23}$  edge.

#### *Correction Procedures for Imaging and Comments*

From the preceding discussion we can outline certain procedures for acquiring and processing the data in STEM energy loss imaging.

1. Since we do not in general know how  $r$  varies across the image, prior to recording the data, we should first carry out a two-parameter fit at each pixel to obtain  $A$  and  $r$  which should be stored. The computed background should then be subtracted from the window above the threshold to give the core edge signal,  $S$ . This procedure can be carried out while the computer is acquiring the image.<sup>9,10,12,13</sup>

2. We should choose as wide a fitting window as possible in relation to the edge integration window. This choice minimizes the standard deviation in the extrapolated background.

3. If the expected systematic error  $\delta B_2$  due to mass thickness variations is less than the statistical error  $\sigma_{B_2}$  in the two-parameter fit then a one-parameter fit should be attempted to reduce  $\sigma_{B_2}$ . We can test the validity of assuming a constant value for  $r$  by examining the  $r$  image for any structure. Alternatively, we can use curves such as those of Figs. 2 and 3 to estimate the relative size of  $\delta B_2$ .

4. When a one-parameter fit is considered to be valid a corrected image  $S'$  can be derived from the previously determined signal  $S$  (by use of the values of  $A$  and  $r$  stored at each pixel) and an expression similar to Eq. (9). The mean value  $\bar{r}$  over the whole image can be used to estimate the true value of the parameter  $r$ . The fluctuations of  $r$  from pixel to pixel are then given by  $\delta r = r - \bar{r}$ . The detection limits in the corrected image are expected to be lower than those in the two-parameter fitted image by a factor of between typically 2 and 5, depending on the choice of energy windows.

5. Finally, we must normalize the effects of elastic scattering and inelastic scattering by dividing one core edge image by another core edge image or by the zero loss image. This step is more important when a major species is being imaged since small variations in concentration may be of interest. If a minor species is being imaged, detection of the element may be the most important consideration and small variations in its concentration may only be of secondary interest.

#### *References*

1. F. P. Ottensmeyer and J. W. Andrews, "High resolution microanalysis of biological specimens by electron energy loss spectroscopy and by electron spectroscopic imaging," *J. Ultrastruct. Res.* 72: 336, 1980.

2. B. Jouffrey, Y. Kihn, J. P. Perez, J. Sevely, and G. Zanchi, "On chemical analysis of thin films by electron energy loss spectroscopy," in J. M. Sturgess, Ed., *Electron Microscopy*, Micro. Soc. Canada 3: 292, 1978.
3. M. P. Rust and D. Krahll, "On line recording and processing of CTEM images," *Ultramicroscopy* 8: 287, 1982.
4. H. Shuman and A. P. Somlyo, "Energy filtered transmission electron microscopy of ferritin," *Proc. Natl. Acad. Sci. USA* 79: 106, 1982.
5. J. Hainfeld and M. Isaacson, "Use of electron energy loss spectroscopy for studying membrane architecture: a preliminary report," *Ultramicroscopy* 3: 87, 1978.
6. D. C. Joy and D. M. Maher, "A practical electron energy loss spectrometer," in C. P. Lechene and R. R. Warner, Eds., *Microbeam Analysis in Biology*, New York: Academic Press, 1977, 87.
7. J. M. Butler, F. Watari, and A. Higgs, "Simultaneous collection and processing of energy-filtered STEM images using a fast digital data acquisition system," *Ultramicroscopy* 8: 327, 1982.
8. P. Rez and C. Ahn, "Computer control for x-ray and energy loss line profiles and images," *Ultramicroscopy* 8: 341, 1982.
9. C. E. Fiori, K. E. Gorlen and C. C. Gibson, "Comments on the computerization of an analytical electron microscope," *Proc. 39th EMSA Meeting*, 1981, 246.
10. K. E. Gorlen, L. K. Barden, J. S. Del Priore, A. K. Kochhar, C. E. Fiori, C. C. Gibson, and R. D. Leapman, "A data acquisition system for an analytical electron microscope," *Proc. Digital Equipment Corporation User Society (USA) Fall Meeting* 9 (No. 2), 1982.
11. P. E. Batson and G. Trafas, "The IBM computer-STEM system," *Ultramicroscopy* 8: 293, 1982.
12. C. Jeanguillaume, M. Tencé, P. Trebbia, and C. Colliex, "EELS chemical mapping of low Z elements in biological sections," *SEM/1983* (in press).
13. R. D. Leapman, C. E. Fiori, K. E. Gorlen, C. C. Gibson, and C. R. Swyt, "Combined elemental and structural imaging in a computer controlled analytical electron microscope," *Proc. 41st EMSA Meeting*, 1983 (in press).
14. R. F. Egerton, "Inelastic scattering of 80 keV electrons in amorphous carbon," *Phil. Mag.* 31: 199, 1975.
15. R. D. Leapman, P. Rez, and D. F. Mayers, "K, L and M shell generalized oscillator strengths and ionization cross sections for fast electron collisions," *J. Chem. Phys.* 72: 1232, 1980.
16. C. Jeanguillaume, P. Trebbia, and C. Colliex, "About the use of electron energy loss spectroscopy for chemical mapping of thin films with high spatial resolution," *Ultramicroscopy* 3: 273, 1978.
17. R. F. Egerton, "A revised expression for the signal/noise ratio in EELS," *Ultramicroscopy* 9: 387, 1982.
18. T. Pun and J. R. Ellis, "Statistics of edge areas in quantitative EEL imaging: signal to noise ratio and minimum detectable signal," *Microbeam Analysis--1983*, 156.
19. D. W. Johnson and J. C. Spence, "Determination of the single scattering distribution for plural scattering data," *J. Phys. D7*: 771, 1974.
20. R. D. Leapman and C. R. Swyt, "Electron energy loss spectroscopy under conditions of plural scattering," *Analytical Electron Microscopy--1981*, San Francisco: San Francisco Press, 1981, 164.
21. C. R. Swyt and R. D. Leapman, "Plural scattering in electron energy loss spectroscopy (EELS) microanalysis," *SEM/1982 I*, 73.

## OBSERVATIONS ON THE DETERMINATION OF $\phi(\rho z)$ CURVES FOR THIN FILMS IN THE ANALYTICAL ELECTRON MICROSCOPE

D. E. Newbury, R. L. Myklebust, A. D. Romig Jr., and K. W. Bieg

A description of the depth distribution of x-ray production under electron bombardment, designated  $\phi(\rho z)$ , where  $\rho z$  is the mass thickness, is important for the development of accurate methods of quantitative analysis in analytical electron microscopy (AEM).<sup>1</sup> The measurement of  $\phi(\rho z)$  curves for solid specimens is a well-established experimental procedure in electron probe analysis,<sup>2</sup> and recently attempts to measure the  $\phi(\rho z)$  function for thin foils in the AEM have been reported.<sup>3</sup> These AEM measurements utilized a simplification of the traditional method of  $\phi(\rho z)$  determination. In this paper, we demonstrate that the  $\phi(\rho z)$  curve determined by this simplified method is in substantial error in cases in which significant scattering occurs within the foil because of the use of (1) high atomic number targets or (2) highly tilted specimens.

In solid specimens, the  $\phi(\rho z)$  function is measured by placing a thin layer of tracer at a known depth in a bulk matrix of similar atomic number to that of the tracer. The intensity measured from the tracer in the composite specimen is normalized by the intensity measured from the free-standing tracer layer. In the work of Stenton et al. on thin foils,<sup>3</sup> the tracer layer was placed at the bottom of matrix foils of various thicknesses to measure  $\phi(\rho z)$ . The value of the x-ray intensity ratio (tracer in matrix/tracer) was assumed to represent the value of  $\phi(\rho z)$  at the equivalent mass thickness in a foil of thickness equal to the largest value of  $\rho z$  utilized in the experiment. That is, the incremental measurements were used to construct a grand curve which represented  $\phi(\rho z)$  for a foil of total thickness 380 nm. These authors recognized that this simplified sample configuration, which eliminated matrix material below the tracer layer, was a compromise since it did not account for scattering in the foil below the tracer. They limited their experiments to normal beam incidence and foils of low to intermediate atomic number, where scattering is minimized. The resulting  $\phi(\rho z)$  curves showed a monotonic increase with depth.

The scattering situation is sharply altered if the specimen is tilted relative to the beam. Although electron scattering is strongly peaked in the forward direction, in a tilted foil small-angle multiple scattering causes a significant flux of electrons back through the foil that cannot be ignored in constructing an accurate  $\phi(\rho z)$  curve. In the present study, a combination of experiments and Monte Carlo calculations have been used to construct  $\phi(\rho z)$  curves from tilted samples of high atomic number.

### *Experimental and Calculational Procedures*

Composite heavy element foils were fabricated by sputtering of hafnium and gold onto 20nm-thick carbon foil. Thicknesses were determined by quartz oscillator, gravimetry and ellipsometry. The uncertainty in the foil thickness was 15% at a thickness of 20 nm and 5% at a thickness of 300 nm. On a base foil of hafnium (20 nm thick), a series of gold foils was deposited to thickness of 11, 50, 100, 150, 200, 230, and 300 nm. The production of hafnium  $L\alpha$  x rays was measured at a beam energy of 100 keV and a specimen tilt of 45° (take-off angle 49°). Approximately 15 000 counts (FWHM) were accumulated in the Hf  $L\alpha$  peak, and six spectra were measured at different locations in each sample to check for local variation in the sample thickness. The measured intensities from the hafnium and hafnium-gold specimens were used to calculate the ratio

---

Authors Newbury and Myklebust are with the Center for Analytical Chemistry of the National Measurement Laboratory, National Bureau of Standards, Washington, DC 20234; authors Romig and Bieg are with Sandia National Laboratory, Albuquerque, NM 87185.



$$\phi(\rho z_{\max}) = [\text{Hf(in Hf-Au)}/\text{Hf}(20 \text{ nm})]$$

No absorption correction was applied because of the high energy of the x rays measured (7.8 keV) and the small mass thickness. The maximum absorption correction for the thickest film was estimated to be less than 5%.

Monte Carlo calculations were carried out with a simulation specifically designed for thin foils and high beam energies.<sup>4</sup> For each  $\phi(\rho z)$  curve, 100 000 trajectories were calculated. In the construction of the histogram, each depth increment received contributions from at least 90% of the trajectories calculated, so that the statistical uncertainty associated with each point on the curve is approximately  $\sigma = 0.3\%$  (relative).

### Results and Discussion

Figure 1 presents the results of  $\phi(\rho z)$  curves for gold calculated by Monte Carlo simulation for foils 50, 100, 150, 200, 250, and 300 nm thick, with the results in each box of the histogram normalized to the intensity of x rays calculated for a gold foil 10 nm thick. Also plotted in Fig. 1 are the experimental results obtained from the Au-Hf composite foils. The thickness value plotted represents the midpoint of the hafnium tracer layer.

If the tracer material is placed on the bottom of the matrix foil, each experimental measurement represents the last box in the  $\phi(\rho z)$  histogram for a foil of that total thickness. Thus, each experimental measurement can only be compared with a single point on the Monte Carlo curve calculated for that thickness. Considering the uncertainty in the determination of the thickness of the composite foils, good correspondence is obtained between the experiment and the calculations.

Using the Monte Carlo calculations, one may compare the actual  $\phi(\rho z)$  curve for a foil of a given thickness with the apparent  $\phi(\rho z)$  curve that would be constructed by application of the method of Stenton et al.<sup>4</sup> We can obtain the apparent  $\phi(\rho z)$  curve from the calculated Monte Carlo curves in Fig. 1 by drawing a curve through the final  $\phi(\rho z)$  value for each thickness. When that is done for a total thickness of 300 nm, the apparent  $\phi(\rho z)$  curve is seen to differ greatly from the actual curve. The actual  $\phi(\rho z)$  curve rises to a higher peak value (1.53 vs 1.21) and has a more negative slope than the apparent curve. If we consider foils of lesser thickness, substantial differences between the apparent and actual  $\phi(\rho z)$  curves are still noted, even for foils as thin as 50 nm. Thus, the monotonically increasing  $\phi(\rho z)$  curves observed at normal incidence by Stenton et al.<sup>3</sup> should not be considered applicable to tilted foils.

These calculations and experiments demonstrate that if an accurate  $\phi(\rho z)$  curve is to

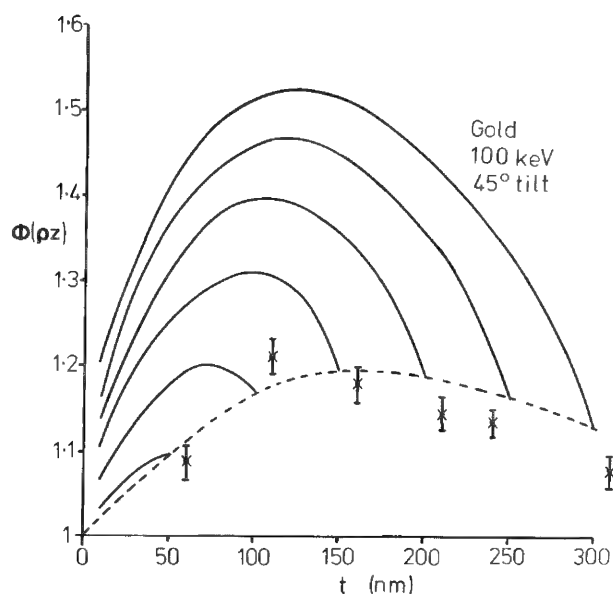


FIG. 1.--X-ray generation depth distribution functions  $\phi(\rho z)$  for gold tilted  $45^\circ$ , beam energy 100 keV. Solid lines give results of Monte Carlo electron trajectory calculations; 100 000 trajectories were calculated for each thickness. Dashed line gives apparent depth distribution constructed from succession of Monte Carlo calculations of binary foils with tracer foil on bottom. Experimental points are derived from binary gold-hafnium (tracer) foils.

be measured, then the simple binary target of Stenton et al.<sup>3</sup> fails for all but the cases of minimal scattering. Considering the experimental difficulties and uncertainties in constructing composite foils of matrix-tracer-matrix form, it is probably more reasonable to utilize the Monte Carlo procedure to calculate  $\phi(\rho z)$  curves as they are needed. From Fig. 1, it can be seen that the  $\phi(\rho z)$  curve depends markedly on thickness. In view of the realistic limitations to the application of the Monte Carlo simulation for all possible cases, it would thus be useful to develop a generalized analytic  $\phi(\rho z)$  expression, which would incorporate the parameters of atomic number, thickness, tilt, and beam energy, from a limited collection of curves calculated by Monte Carlo simulation.

#### References

1. J. I. Goldstein, "Principles of thin film x-ray microanalysis," in J. J. Hren, J. I. Goldstein, and D. C. Joy, Eds., *Introduction to Analytical Electron Microscopy*, New York: Plenum, 1979, 83-120.
2. J. I. Goldstein, D. E. Newbury, P. Echlin, D. C. Joy, C. E. Fiori, and E. Lifshin, *Scanning Electron Microscopy and X-ray Microanalysis*, New York: Plenum, 1981.
3. N. Stenton, M. R. Notis, J. I. Goldstein, and D. B. Williams, "Determination of  $\phi(\rho t)$  curves for thin foil microanalysis," in *Quantitative Microanalysis with High Spatial Resolution*, London: The Metals Society, Book 277, 1981, 35-40.
4. D. E. Newbury and R. L. Myklebust, "A Monte Carlo electron trajectory simulation for analytical electron microscopy," in R. H. Geiss, Ed., *Analytical Electron Microscopy--1981*, San Francisco: San Francisco Press, 1981, 91-98.

## AEM/STEM ANALYSIS OF VAPOR DEPOSITED MULTILAYER LASER TARGETS

K. A. Johnson, K. P. Staudhammer, G. A. Reeves, and L. R. Vesser

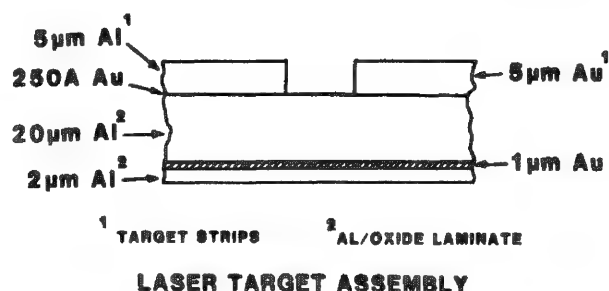


FIG. 1.--Schematic of vapor deposited laser target.

Large pulsed lasers have been used for shock studies, particularly for equation-of-state measurements, for several years.<sup>1-3</sup> One experimental problem has been accurate measurement of absolute density of the target foils. The foils examined here were made and measured for that purpose.<sup>4</sup> The layout of the targets and supporting substrate is shown in Fig. 1.

S(TEM) examinations were made to augment the other types of measurements of absolute density. We examined the structure of the 5μm-thick layers of aluminum and gold on aluminum laminate gold substrate to establish film integrity, to characterize the micro-

structure, and to estimate the surface roughness of this multilayer material. The TEM samples proved to be somewhat difficult to prepare due to the multilayers within the material, particularly the amorphous nonconducting aluminum oxide ( $\text{Al}_x\text{O}_y$ ).

It is important to know the uniformity of the target layers as well as the roughness of the surfaces. The aluminum in the substrate was made homogeneous by the introduction of a small amount of oxygen (in pulses) to break up the growth of grain structure during the evaporation process.<sup>5</sup> We did not add oxygen to the target layers since the requirements dictate a pure metal. The target layers required a homogeneous, uniform structure as close to theoretical density as possible. For the hardened substrate aluminum, there was additional interest in the uniformity and structure because this material is finding a wide variety of applications in physics experiments which require very thin, self-supporting aluminum foils.

The targets were made by physical vapor deposition of the materials onto glass slides. To insure adherence of the interfaces between deposition layers, the entire deposition cycle was carried out without any air being admitted into the vacuum chamber, except for the oxygen used to smooth and strengthen the aluminum in the substrate.

Disks 3 mm in diameter were prepared by mechanical punching and then electropolished in a twin jet electropolisher. The 5μm target layers were prepared by selective coating to prevent removal of that layer and then thinning from the substrate side.

The difficulty of electrothinning materials of various electrochemical properties generally poses a problem, but the anticipated difficulty due to this electrochemical difference between the gold target and substrate did not arise. The solution used in this investigation was 7:1, perchloric/acetic acid, electropolished at 5 V and -8°C. Electron microscopy examinations were done in a Phillips 400 AEM and a 200B JEOL to characterize these films. The techniques included CTM, (S)TEM, secondary and backscatter images, and energy-dispersive spectrometry (EDS).

The strengthening and smoothing of the aluminum substrate is caused by a thin uniform aluminum oxide layer at uniform intervals. A secondary electron image micrograph (Fig. 2) illustrates this layering. An interesting feature of the target aluminum/ $\text{Al}_x\text{O}_y$  substrate is the formation of discrete periodic  $\text{Al}_x\text{O}_y$  layers. We note the stepwise etching of this material in Fig. 2, and that the  $\text{Al}_x\text{O}_y$  layer cracks and spalls as the etching progresses. This cracking indicates that a differential stress exists between the aluminum and  $\text{Al}_x\text{O}_y$  layers. A typical microstructure of the etched substrate surface is shown in Fig. 3.

The authors are at the Los Alamos National Laboratory, Los Alamos, NM 87545.

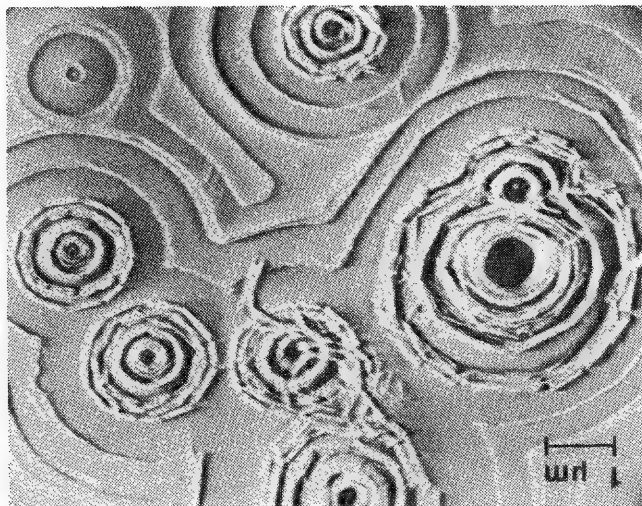


FIG. 2.--Secondary electron image of thinned aluminum/ $\text{Al}_x\text{O}_y$  surface.

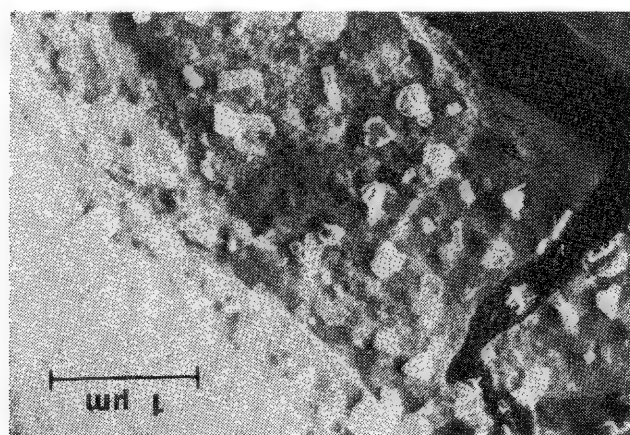


FIG. 3.--STEM dark-field image of thinned aluminum/ $\text{Al}_x\text{O}_y$  thin layers.

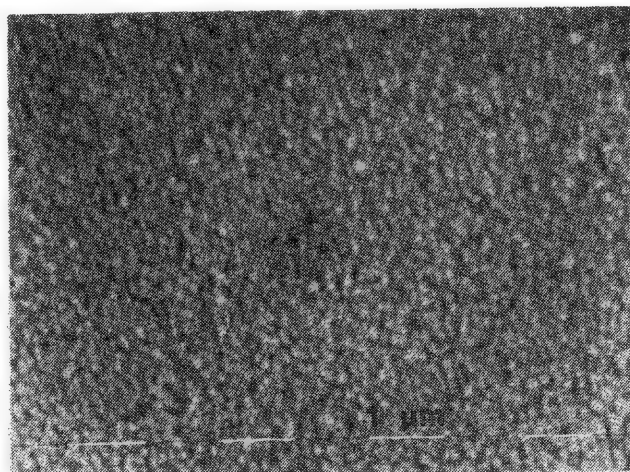


FIG. 4.--Secondary electron image of gold target surface.

The stepped layers are caused by the inhibiting action of the oxide layers in the electropolishing technique.

Backscatter and topological contrast on both target strips was very poor (no sharp edges); we can assume the roughness height is somewhat smaller than the detectable periodicity of surface roughness. The surface of the gold and aluminum were examined by both secondary electron and backscatter electron imaging to estimate the surface roughness. Figure 4 is a secondary electron micrograph of the gold surface near the edge of the gold strip; the contrast was very poor and only the suggestion of a surface topography could be detected. The periodicity is approximately  $0.15\text{ }\mu\text{m}$ . Consequently, our estimate based on the periodicity is that the surface roughness was less than half that. No significant contrast could be achieved on the aluminum surface except at the edge, where there were larger grains (Fig. 5). What we see on the aluminum target layer is not roughness but orientation effects of the grains (i.e., channeling). The assumption based on this lack of evidence is that the aluminum surface with even poorer contrast is smoother than the gold. A light additional gold coating on the aluminum surface did not reveal any detectable surface structure.

Using standard TEM, examinations were made of both the gold and aluminum target foils. The grain size of both is the same size as that of the aluminum on the  $\text{Al}_x\text{O}_y$  substrate ( $0.13\text{ }\mu\text{m}$ ). Note that the gold grain size is approximately the same as the periodicity of the gold surface roughness. In both cases the composition was verified by EDS. Typical TEM of the target layers are shown in Fig. 6 (Al) and 7 (Au). Note the gold in Fig. 7 is twinned.

TEM of the  $\text{Al}_x\text{O}_y$  was also done to characterize its structure. It is uniform, continuous, and amorphous, as shown in Fig. 8 along with its associated selected area diffraction pattern. All the  $\text{Al}_x\text{O}_y$  layers observed were of this character. The  $\text{Al}_x\text{O}_y$  layers thickness is approximately  $50\text{ }\text{\AA}$  and the associated aluminum layer thickness is approximately  $250\text{ }\text{\AA}$ ; these thicknesses were estimated from the deposition rates.

Characterizing laser target thin films was accomplished via multiple and mixed imaging modes in (S)TEM, EDS, and AEM. By these techniques the estimate of surface roughness was bracketed to be less than 1% of the  $5\text{ }\mu\text{m}$  target thickness, which was sufficient to satisfy the needs for the laser physics experiment.

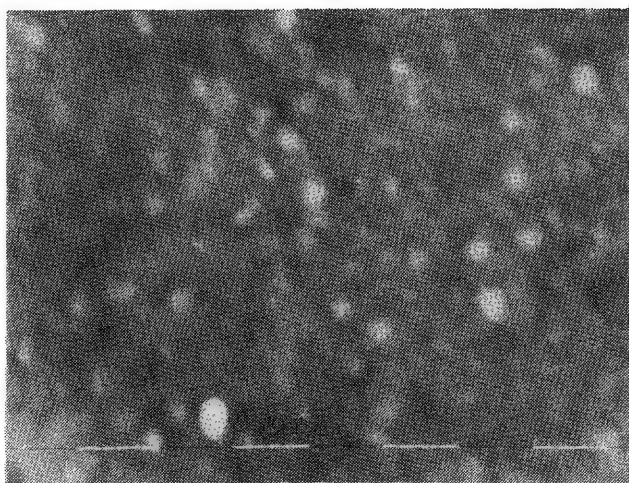


FIG. 5.--Secondary electron image of larger grained edge of aluminum step surface.

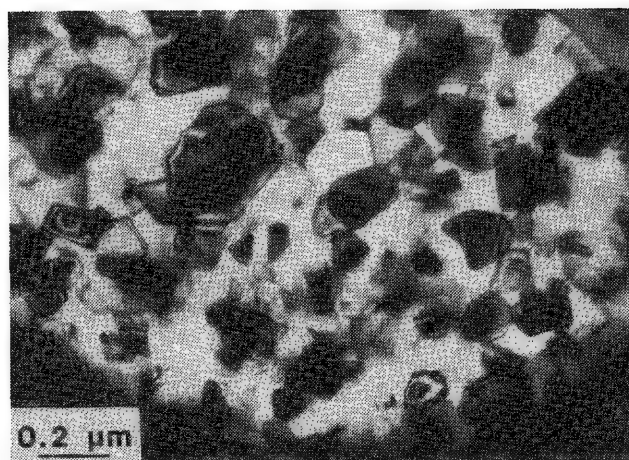


FIG. 6.--CTEM of thinned aluminum target step.

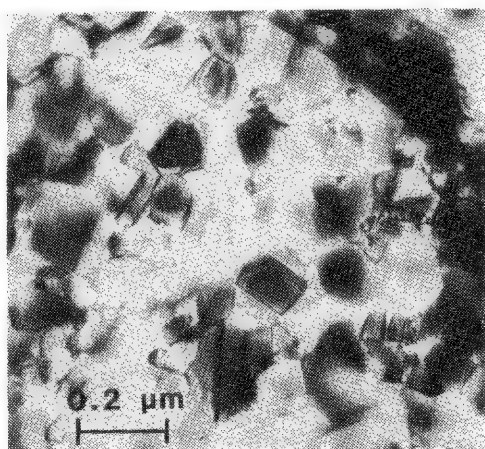


FIG. 7.--CTEM of thinned gold target step.

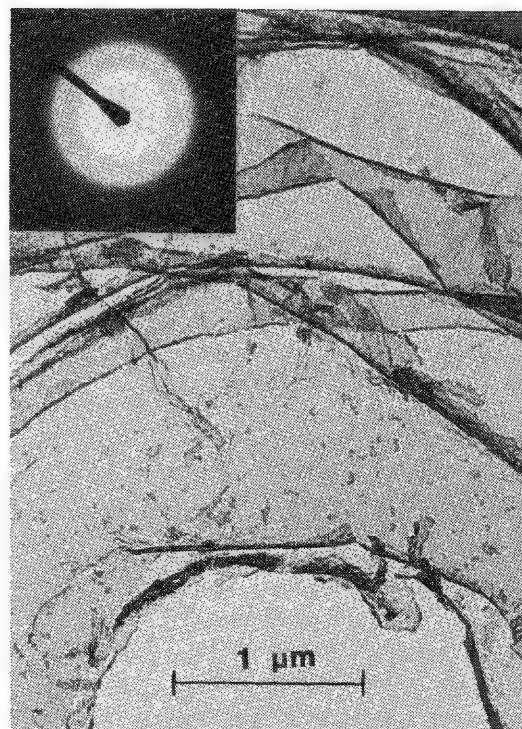


FIG. 8.-- $\text{Al}_x\text{O}_y$  continuous layer and associated selected area diffraction pattern.

#### References

1. L. R. Veaser and J. C. Solem, *Phys. Rev. Lett.* 40: 1391, 1978.
2. R. J. Trainor, J. W. Shaner, J. M. Auerback, and N. C. Holmes, *Phys. Rev. Lett.* 42: 1154, 1979.
3. L. W. Veaser, J. C. Solem, and A. J. Lieber, *Appl. Phys. Lett.* 35: 761, 1979.
4. L. R. Veaser, C. J. Maggiore, and G. A. Reeves, "Density measurements for thick-film laser targets" (submitted to *Nucl. Instrum. Methods*).
5. R. W. Springer and D. S. Catlett, *Thin Solid Films* 54: 197, 1978.



# THE Si(Li) DETECTOR-SPECIMEN ANGLES IN AN AEM

R. L. Myklebust

For quantitative energy-dispersive analysis in an AEM, the position of the detector with respect to the specimen and electron beam must be known. The angle of the detector with respect to the electron beam is generally a fixed instrumental parameter that is known

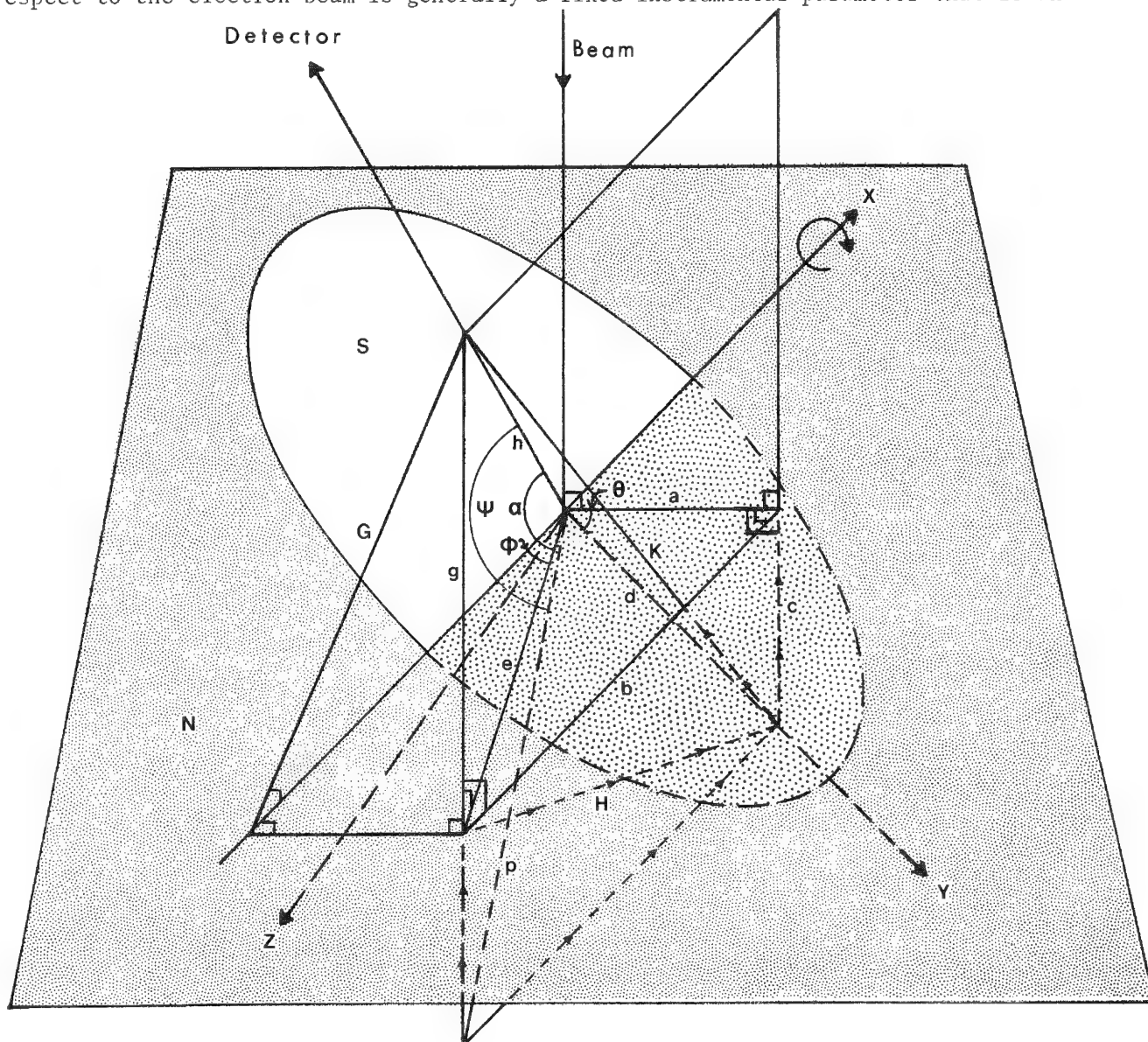


FIG. 1.--Detector-specimen geometry: plane N is normal to electron beam, x and y axes lie in plane of specimen S, dashed lines with arrows all lie in same plane with b, g, and k and this plane is normal to plane N and parallel to x axis; plane containing G and g is normal to plane N and normal to x axis.

The author is at the Center for Analytical Chemistry, National Bureau of Standards, Washington, DC 20234.

for each system. The specimen tilt axis is also an easily obtained parameter for each microscope and the aximuthal angle of the detector with respect to the specimen tilt axis can be specified. The angle between the detector and the specimen surface (usually called the take-off angle) can be easily determined if the specimen is tilted toward the detector (aximuthal angle =  $90^\circ$ , detector axis at right angles to the tilt axis).<sup>1</sup> However, in many instruments that is not the case and calculating the take-off angle is more complicated. In the following discussion, the angular relations between the detector and the axes of the specimen together with the take-off angle are derived.

The x, y, and z axes are defined relative to the specimen. The z axis is normal to the surface of the specimen with its positive direction into the specimen. The x and y axes lie in the surface, plane S, of the specimen with the x axis as the tilt axis. All parameters are defined relative to the plane N normal to the electron beam that contains the x axis (tilt axis). The detector elevation angle  $\alpha$  is the detector-to-plane N angle, and the detector aximuthal angle  $\phi$  is the angle between the projection of the detector on the plane N and the x axis which lies in the plane N. The tilt angle  $\theta$  is the angle between the y axis and the plane N. Figure 1 shows all the planes and angles involved in the derivation.

The first step is to determine the angles the detector makes with the three axes of the specimen. These are the angles required when one makes x-ray emission calculations from Monte Carlo electron trajectory simulations. The second step is to determine the x-ray take-off angle for this case.

Assign a value of unity to the length of the projection of the y axis on the plane N normal to the beam ("a" in the drawing). The plane b,c,H,g is normal to the projection of the y axis on the plane a,b,e. Then:

$$\begin{aligned}d &= 1/\cos \theta \\e &= 1/\sin \phi \\b &= \cos \phi/\sin \phi \\c &= \sin \theta/\cos \theta\end{aligned}$$

and

$$\begin{aligned}h &= 1/[\cos \alpha \sin \phi] \\g &= \sin \alpha/[\cos \alpha \sin \phi]\end{aligned}$$

$$K^2 = (c + g)^2 + b^2$$

It is now possible to solve for the angle  $\tau$  between the detector and the y axis:

$$\cos \tau = (h^2 + d^2 - K^2)/2hd$$

Substituting the above values for h, d, and K, and simplifying, we obtain

$$\cos \tau = \cos \alpha \cos \theta \sin \phi - \sin \alpha \sin \theta$$

To solve for the angle  $\beta$  of the detector with the x-axis,

$$\cos \beta = b/h$$

Substituting the above values for h and b, and simplifying gives

$$\cos \beta = \cos \alpha \cos \phi$$

The angle  $\gamma$  of the detector with the z axis is then

$$\cos \gamma = \text{SQRT}[\sin^2 \tau - \cos^2 \beta]$$

The angles of the detector with respect to the three axes of the specimen have thus been defined.

The only remaining step is to determine the x-ray take-off angle  $\psi$ . For that we must determine one additional segment:



$$p = \text{SQRT}(e^2 + c^2)$$

Then the take-off angle is given by

$$\cos \psi = [p^2 + h^2 - (g + c)^2]/2ph$$

Substituting the above values for p, h, g, and c, and simplifying, we obtain

$$\cos \psi = [\cos \alpha \cos \theta - \sin \alpha \sin \theta \sin \phi]/\text{SQRT}[\cos^2 \theta + \sin^2 \theta \sin^2 \phi]$$

This is only a take-off angle and does not account for any differences in the distribution of the x rays within the specimen when the electron beam is not normal to the specimen surface. A treatment of the nonuniformity of x-ray production in tilted foils has been considered by Newbury et al.<sup>2</sup>

#### References

1. J. I. Goldstein, D. E. Newbury, P. Echlin, D. C. Joy, C. Fiori, and E. Lifshin, *Scanning Electron Microscopy and X-ray Microanalysis* New York: Plenum, 1981, 337-338.
2. D. E. Newbury, R. L. Myklebust, A.D. Romig, and K. W. Bieg, "Observations on the determination of ( $\rho z$ ) curves for thin films in the analytical electron microscope," *Microbeam Analysis--1983*, 168.

## Microbeam Analysis of Particles

### DEVELOPMENT OF A MINIATURE SCANNING ELECTRON MICROSCOPE FOR IN-FLIGHT ANALYSIS OF COMET DUST

J. M. Conley, J. G. Bradley, C. E. Giffin, A. D. Tomassian, and A. L. Albee

The SEMPA (Scanning Electron Microscope and Particle Analyzer) electron miniprobe is a miniaturized electrostatically focused electron microscope and energy dispersive x-ray analyzer for in-flight analysis of comet dust particles. The instrument was designed to be flown on board a comet rendezvous spacecraft. Other potential mission applications are asteroid rendezvous and planetary lander missions.

Hart et al. described the instrument and discussed the design considerations.<sup>1</sup> The goal of the development effort is to achieve a reliable, light-weight, low-power instrument capable of imaging and elemental analysis of particles in the size range of 0.25  $\mu\text{m}$  and larger.<sup>2</sup> An electrostatic lens design best meets the requirement for light weight and low power. The SEMPA flight electron optical column design parameters are summarized in Table 1.

#### *Flight Instrument Concept*

Figure 1 is a drawing of a conceptual flight instrument. The electron-optical column and imaging detector have thus far been breadboarded. The high-voltage power supply, vacuum pump, and photomultiplier now in use are commercial laboratory devices. A room-temperature x-ray detector assembly is now being designed. A manual sample stage is being used in the development of the column. Construction of the automated flight sample stage awaits the definition of a flight project.

TABLE 1.--Summary of SEMPA flight instrument design parameters.

Power	28 watts
Mass	
Sensor (includes sensor electronics)	13.0 kg
Bus electronics	1.9 kg
Detector cooler	2.0 kg
Total	16.9 kg
Dimensions	
Sensor	60 x 20 x 18 cm
Sensor electronics	10 x 8 x 4 cm
Bus electronics	18 x 42 x 6.3 cm
Beam voltage	15 kV
Beam current	10-10A
Field size	200 x 200 $\mu\text{m}$
Imaging resolution:	
Tungsten cathode	400 nm
LaB <sub>6</sub> cathode	40 nm
X-ray energy range	0.2 to 10 keV
X-ray energy resolution	~150 eV
Electrostatic lens focal lengths	
Condenser	0.36 cm
Objective	1.77 cm
Scanning and stigmation	magnetic

The electron source is at present a 0.1mm tungsten hair-pin cathode, which will be replaced with a LaB<sub>6</sub> cathode for the flight application. Electrostatic condenser and objective lenses are utilized to minimize power and weight. A beam centration detector and beam alignment coils minimize the centering requirement for the Wehnelt cathode, to ease the tolerances for a mechanism for automatic replacement of the Wehnelt/cathode assembly in flight. Two sets of coils for double deflection scanning of

The authors are at the Jet Propulsion Laboratory, California Institute of Technology, Pasadena, CA 91109; A. D. Tomassian is currently at Perkin-Elmer Corp., Pomona, Calif. The authors express their thanks to other members of the original SEMPA proposal team, especially Donald Brownlee, Anthony Finnerty, and Raymond Hart. Charles Kurzwil designed the magnetic shield and Robert Frazer the stage. James Hill of JPL has done much of the machining, assembly, electronics, and vacuum system development. The research was carried out at JPL under NASA Contract NAS 7-100.

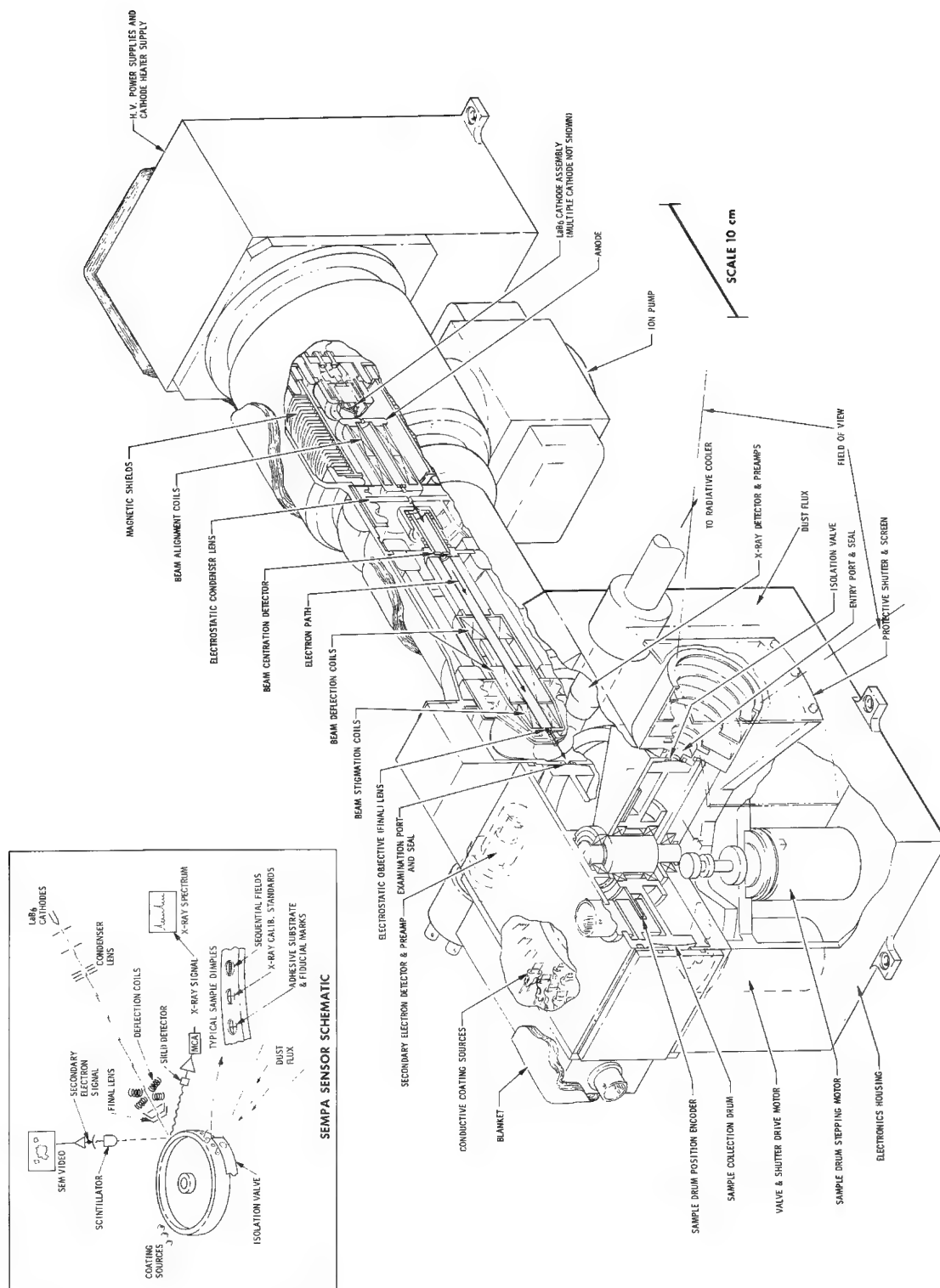


FIG. 1.--View of conceptual SEMPA flight instrument.

the beam are followed by stigmation coils and the objective lens. The x-ray detector indicated on the drawing is Si(Li). The heat pipe marked "to radiative cooler" cools the detector to 140° K to attain an energy resolution of 150 eV. The conventional secondary-electron detector for imaging has an accelerating potential of 10 kV on the scintillator. The column high-voltage power supply and the ion pump for differential pumping of the cathode region are shown at the cathode end of the column. Additional details of the instrument are presented in Ref. 1.

The somewhat detailed drawing of the planned flight sample stage, shown in Fig. 1, is clarified by the inset schematic drawing. The sample drum is fitted with 64 dimples, 14 of which are used as calibration sites. The remaining 50 are coated with an adhesive material<sup>3</sup> which is exposed to dust being carried from the comet head at a velocity of about 10-100 m/sec. Models<sup>2</sup> for the pressure in the region of the spacecraft (~40 km from the comet nucleus at closest approach) indicate a pressure of about  $10^{-5}$  Torr. Based on dust-flux estimates from other instruments aboard the spacecraft the isolation valve is opened for up to several hours to allow deposition of approximately 300 particles on a single sample site of  $200 \times 200 \mu\text{m}$ . The valve is then closed and the sample drum is rotated 120° to allow coating of the sample by carbon evaporated from the filaments shown in the drawings. A further 120° rotation places the dimple in the beam for imaging and elemental analysis of the dust particles.

For the current laboratory tests commercial electronics supply signals to the breadboard and process the imaging data.

### *Breadboard Performance*

The breadboard column has exceeded the imaging performance expected when used with a tungsten cathode. This result was achieved only after careful attention to magnetic-field reduction. The Type 321 stainless steel lenses initially used in construction of the instrument were found to possess enough remnant magnetism following operation of the beam alignment and scanning coils to prevent transmission of the electron beam. The beam is very easily deflected within the lenses where the electron velocity is quite low. After replacement of the lenses and most other stainless steel components near the optical axis with titanium elements, no further beam-transmission problems occurred.

The initial imaging performance of the column was limited by the magnetic fields of the laboratory power line and the geomagnetic field. The lowest 60Hz laboratory background observed was approximately  $7 \times 10^{-8}$  Tesla (0.7 milligauss), corresponding experimentally to a beam deflection of  $0.4 \mu\text{m}$  at the target. The  $2 \times 10^{-5}$  T horizontal component of the geomagnetic field resulted in a beam deflection of the order of  $300 \mu\text{m}$ . A two-layer Hipernom magnetic shield, which attenuates the dc field by a factor of 100 and the ac field by 10, was fabricated. Figure 2 is a photograph of the column installed in the shield. A smaller integral shield would be suitable but would hinder access to the breadboard adjustments.

The measured spatial resolution in the center of the field of view is about  $0.3 \mu\text{m}$ , somewhat better than anticipated for a tungsten filament. This is consistent with a  $40 \mu\text{m}$  effective source diameter and the design demagnification of 125 in the optical column.

The maximum field size at a 15keV beam energy and 15mm working distance is  $\sim 600 \times 600 \mu\text{m}$ . The internal voltage-divider arrangement originally installed for objective focusing was replaced with an external supply to achieve a fully focused beam.

Figures 3 and 4 illustrate the present imaging capabilities of the system. Figure 3 is a secondary electron image of a metal grid. The rectangular holes are about  $39 \mu\text{m}$  square. Figure 4 is a backscattered electron image of the same target.

The electron-optical column has proven to be rugged as well as easy to align. The objective lens and aperture ( $200 \mu\text{m}$ ) positions are fixed in the vacuum housing. The condenser lens and aperture ( $600 \mu\text{m}$ ) are radially adjustable by about  $\pm 0.3 \text{ mm}$  in the column by means of external screws. There is one additional aperture  $400 \mu\text{m}$  diameter just below the condenser. One can routinely achieve optical alignment by clamping the condenser at an approximately center location in the housing and adjusting the cathode assembly radially to obtain maximum beam current to the sample. It has not proved necessary to adjust the condenser position further. Once aligned, the system does not need realignment except after disassembly. Laboratory tests indicate that adjustment of the centration field can compensate for deviations of the Wehnelt cathode centering of about  $125 \mu\text{m}$  from the optical axis.

The electron detector for low-energy and backscatter imaging is a scintillator-photo-

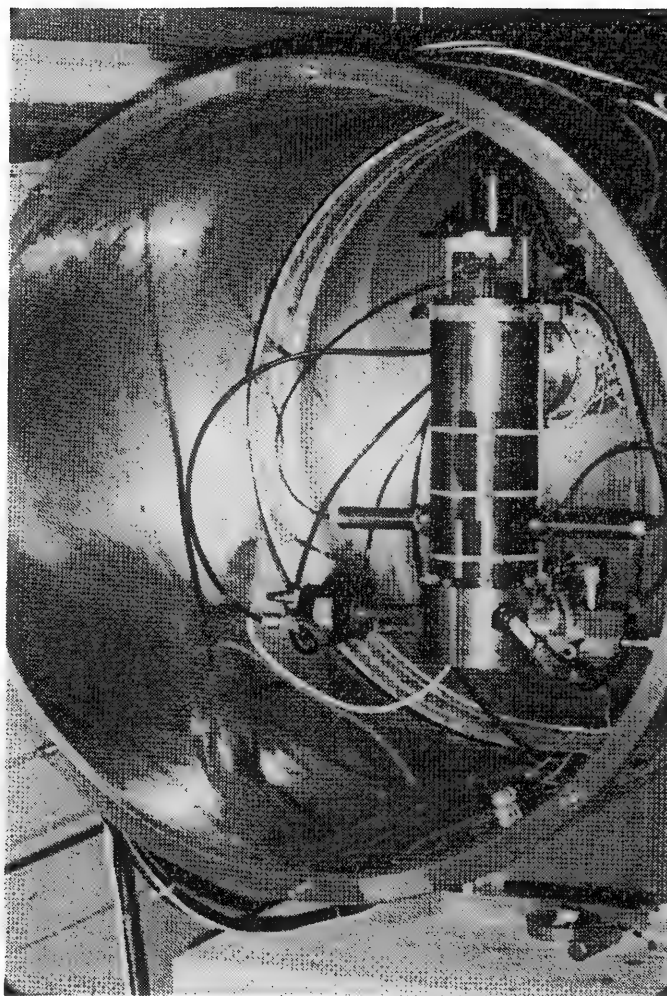


FIG. 2--SEMPA breadboard column mounted in magnetic shield.

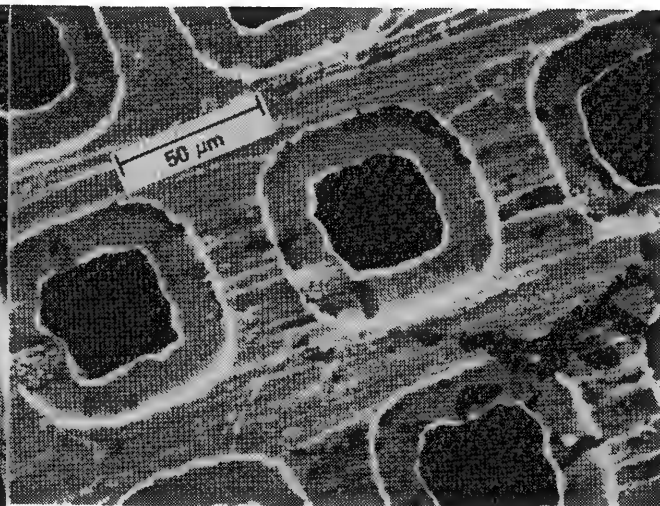


FIG. 3--SEMPA secondary-electron image.

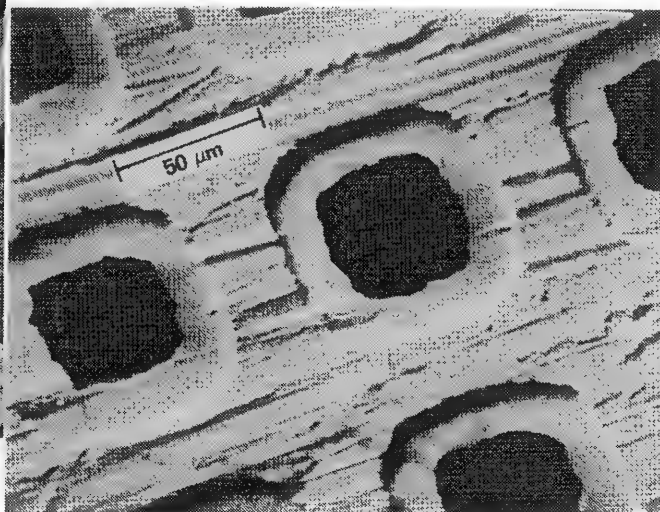


FIG. 4--SEMPA backscattered electron image.

multiplier system. A +10kV bias is applied to the 13 mm-diameter scintillator for low-energy secondary electron imaging. The photomultiplier is coupled to a polycarbonate light pipe and Eu:CaF<sub>2</sub> scintillator. For backscattered imaging the 10kV bias is turned off.

#### *Spacecraft Environment*

Current models project an ambient gas pressure of  $10^{-5}$  Torr at closest approach to the comet by a rendezvous spacecraft.<sup>2</sup> Residual gas emanating from the spacecraft would result in a lower but significant pressure contribution. Therefore, differential pumping of the cathode region will be necessary to achieve the  $10^{-8}$  Torr required for long life of a LaB<sub>6</sub> cathode.

The dc magnetic moment of typical spacecraft (e.g., Voyager) has been of the order of 1000 pole-cm,<sup>5</sup> corresponding to a field of about  $2 \times 10^{-7}$  T at a distance of 1 m. A small amount of shielding will reduce this field to a negligible level at the instrument. At the spacecraft power supply frequency of 2400 Hz, the Voyager field was below the monitoring magnetometer noise level of  $10^{-10}$  T. Although it is expected that SEMPA could be flown without shielding, a light-weight two-layer magnetic shield will allow freedom in placement of the instrument aboard the spacecraft.

## Future Efforts

The original goal of this development was to fly the instrument on the International Comet Mission, which was scheduled for a 1985 launch. That mission was cancelled due to budgetary constraints, but it now appears that a mission of reduced scope will be initiated in 1987 with a launch in about 1990. The immediate goal of the effort is to complete a demonstration of flight readiness prior to the 1987 project definition. Toward this end the tasks described below are now being pursued.

A joint effort with Drs. A. Dabrowski and G. Huth of the University of Southern California will culminate in the installation of a room-temperature  $\text{HgI}_2$  detector in the breadboard column. The USC team has demonstrated 175eV resolution at 5.9 keV and 145eV resolution at 1.5 keV with  $\text{HgI}_2$  x-ray detectors operating at room temperature.<sup>4</sup> Although a cooled FET pre-amp might still be required, its temperature requirement of about 200° K could be accomplished with a Peltier cooler rather than the large and costly radiative cooler necessary for the 140° K requirement of the Si(Li) detector. In addition, fabrication of a low-noise room-temperature preamplifier may be possible with new semiconductor technology (e.g., gallium arsenide).

Two options are under consideration for the solution of the question of cathode reliability. The first, reported in Ref. 1, is to provide redundant cathodes and to accept a lifetime of the order of 300 hr with moderate reliability ( $\sim 10^{-2}$  probability of early failure per element). However,  $\text{LaB}_6$  emitters are now commercially guaranteed for 1000 hr at  $10^{-8}$  Torr, and so the second option under consideration is to qualify a nonredundant  $\text{LaB}_6$  design by demonstrating long life (1000 hr) and very low probability of early failure ( $10^{-6}$ ). Such an effort is similar to the qualification of pyrotechnic devices for spacecraft, a difficult task which must be weighed against that of developing redundant cathodes.

In addition to the above tasks the breadboard column will be used to quantify a number of design parameters that would be difficult to address without an operating instrument. For example, it will be possible to determine parameters such as power supply and dimensional tolerances, sensitivity of the beam to drive signals and ambient fields, and imaging detector signal-to-noise ratio, all of which will be required to begin design of the flight instrument. A complete parameteric analysis will be done. We also plan to implement automation features such as digital beam control to allow scientists to begin development of the algorithms to be used in sequencing the flight instrument.

As the column is used in the tasks described above, continuing tests will demonstrate the long-term stability and the high vacuum required for long cathode life. An existing  $\text{LaB}_6$  cathode design will be sought to prove vibration qualification as well as ultimate resolution, lifetime, and reliability.

The plan summarized above has been developed in detail in order to resolve any questions of technology readiness prior to the definition of a flight opportunity for the SEMPA instrument.

## References

1. R. K. Hart, A. L. Albee, A. A. Finnerty, and R. Frazer, "A mini scanning electron microscope and particle analyzer for space applications," *SEM/1981 I*, 16-104.
2. R. L. Newburn, Jr., "Models of P/Tempel 2," Jet Propulsion Laboratory Publ. 76-60, 1979.
3. S. K. Anderson and B. C. Clark, "Comet dust collection techniques," Final Report, Contract JPL 977180, Martin Marietta Corp., Box 179, Denver, CO 80201, Rep. MCR-81-574, 1981.
4. W. E. Drummond, L. Ames, A. Dabrowski, and J. Iwanczyk, "Mercuric iodide and lithium drifted silicon detector comparison for energy dispersive x-ray detection," *Pittsburgh Conf. Anal. Chem. and Appl. Spectroscopy*, Atlantic City, N. J., 1983.
5. J. Bastow, Jet Propulsion Laboratory, private communication.

## ENERGY-DISPERSIVE X-RAY ANALYSES OF INDIVIDUAL PARTICLES FROM TWO SECONDARY IRON FOUNDRIES

J. E. Post and P. R. Buseck

Quantitative microprobe and scanning electron microscope (SEM) analyses of individual particles are important for determining chemical speciation in atmospheric aerosols; possibly of even greater significance are their application for characterization of emissions from specific point sources of aerosol particles. These techniques can provide information that is normally not obtainable from conventional bulk analytical methods, e.g. elemental associations, particle morphologies and surface coatings, and detailed distribution of elements according to particle size. In the ideal situation, it is possible to characterize or "fingerprint" the particle emissions from a source sufficiently so that they can be recognized in ambient aerosol samples. We present here, as an example, the results of our study of the emissions from the secondary iron foundries in Phoenix, Ariz.

In a recent study of individual particles from the Phoenix aerosol, we determined that although natural crustal material and S compounds comprise the bulk of the samples, about 10% of the particles originated from anthropogenic sources in the Phoenix area.<sup>1,2</sup> Of special interest are particles enriched in Fe, Zn, Cr, and Pb that are emitted from two secondary iron foundries south of Phoenix. Foundry particles were observed in each of the Phoenix aerosol samples examined, but were most abundant in samples collected in south Phoenix, where they accounted for 20-30% of the nonsulfate anthropogenic particles. Armstrong<sup>3</sup> and Armstrong and Buseck<sup>3,4</sup> studied the emissions from the two foundries, but because they used an electron microprobe lacking secondary-electron imaging capabilities, they were able to analyze only particles larger than about 1  $\mu\text{m}$  in diameter. In the present study, we used an analytical scanning electron microscope with attached energy-dispersive x-ray analyzer to image and analyze particles as small as 0.1  $\mu\text{m}$  in diameter.

The goals of this study were threefold: (1) to characterize the particle emissions from the foundries, (2) to link particle types to the specific steps in the foundry processes that produce them, and (3) to establish criteria for distinguishing between emissions from the two foundries.

### *Foundry Processes*

The two foundries are less than 3 km apart, and for the purpose of this discussion, are designated foundry "A" and foundry "B" (consistent with the designation used by Armstrong<sup>3</sup>). The operations at the two foundries are similar; scrap iron and steel is melted, adjusted to a desired composition, and cast into the final products.

In general, foundry A uses only high-quality scrap iron and steel, consisting largely of old automobiles and train wheels. The iron and steel are separated from nonmetal impurities (e.g., plastic, paint, cloth, rubber, electrical components, galvanized metal, nonferrous alloys, glass, etc.), either by hand or with magnets. At foundry B, the average composition of the scrap metal is less consistent than at foundry A, and might include a variety of items, such as old machinery, automobiles, metal used in buildings, or almost any other form of scrap iron and steel. Attempts are made to separate out most obvious nonmetal components; however, in general, the raw metal used by foundry B contains a higher fraction of impurities than at foundry A.

The shredded scrap metal is loaded into furnaces fueled by natural gas (foundry A) or electric arcs (foundries A and B) and heated to about 1650°C. Depending on the composition of the melt, Cr and Mn (foundry A) or "ferromanganese" and "silica Mn" (foundry B) are

---

Author Post is at Harvard University (Department of Geological Sciences), Cambridge, MA 02138; author Buseck is at Arizona State University (Departments of Chemistry and Geology), Tempe, AZ 85287. Supported by grant ATM-8022849 from the Atmospheric Sciences Division of the National Science Foundation.



added to produce the desired type of steel. A deoxidizer is added to the molten steel near the end of the melting process. The deoxidizer used by foundry A is Al, although occasionally a Ca compound, "hypercal," is substituted; foundry B uses CaO as a deoxidizer. At both foundries, the molten metal is poured into silica sand molds.

### Experimental

Particles for analysis were collected downwind of foundry B on two successive evenings in March 1980, and downwind of foundry A on two successive evenings in August 1980. Both sets of samples were collected from about 9 to 10 P.M. The samplers were placed approximately 800 m northwest of foundry B and 200 m east of foundry A, and in all cases were within the respective foundry plumes for at least half of the total sampling time. The samples were collected onto stack sequences of 0.4, 3, and 12  $\mu$ m Nuclepore filters by Anderson pumps with flow rates of about 15 l/min.

The foundry particles were analyzed by a JEOL JSM35 scanning electron microscope with attached PGT energy dispersive x-ray analyzer. The analytical procedures used are described in detail by Post and Buseck.<sup>2</sup> All analyses were corrected by means of the particle analysis programs of Aden<sup>5</sup> and Aden and Buseck.<sup>6,7</sup>

### Results and Discussion

**Particle Compositions.** The most abundant particle types emitted by the foundries, as observed in this study and by Armstrong,<sup>3</sup> are oxides of Fe and Zn, usually containing various amounts of Si, Cr, Pb, Cl, Ca, Na, Ni, Mg, Cu, Al, and Mn. The assumption that the metals occur as oxides is based on the fact that the particles form at high temperatures in an oxidizing environment. The majority of particles from foundry A are primarily Fe oxide, although in some particles Si, Zn, or Mn is the most abundant element. The average composition for 15 metal oxide particles from foundry A is given in Table 1. The magnitudes of the standard deviations indicate considerable variation in composition among particles.

Most particles emitted by foundry B are mixed Zn and Fe oxides, although Pb and Cl are abundant in many particles. The average composition for 24 particles emitted by foundry B (Table 1) is significantly different from that of foundry A particles. Particles from

TABLE 1.--Mean compositions\* of metal oxide particles from samples of secondary iron foundry emissions, as determined in this study and by Armstrong.<sup>3</sup>

	Foundry A				Foundry B			
	This Study+		Armstrong (1977)		This Study+		Armstrong (1977)	
Fe	54.0	(14.7)	34.0	(12.6)	25.4	(13.6)	16.1	(20.0)
Zn	1.8	(2.5)	21.5	(16.3)	20.3	(9.3)	46.7	(26.7)
Pb	Trace		2.6	(3.2)	12.6	(10.5)	0.3	(1.1)
Mn	1.8	(2.0)	2.6	(3.1)	5.1	(5.6)	0.8	(1.3)
Cl	0.3	(0.4)	0.5	(2.5)	3.6	(4.5)	4.5	(11.7)
Si	6.0	(7.0)	7.5	(3.9)	2.3	(1.7)	2.3	(4.3)
Mo	Trace		-		-		-	
Cr	0.9	(0.8)	0.7	(1.6)	Trace		Trace	
Ni	Trace		0.2	(0.4)	-		-	
Ca	0.5	(0.5)	0.1	(0.4)	0.7	(0.7)	3.2	(6.0)
Mg	0.2	(0.3)	0.1	(0.2)	2.5	(2.4)	0.2	(0.4)
Al	0.4	(0.5)	0.1	(0.2)	0.5	(0.7)	1.4	(5.3)
Cu	0.2	(0.3)	0.1	(0.2)	0.4	(0.6)	Trace	
K	0.1	(0.1)	0.1	(0.2)	0.9	(0.9)	0.1	(0.4)
O <sup>++</sup>	32.3	(3.9)	29.9	(3.3)	25.3	(5.1)	23.8	(7.7)

\*Values given in elemental weight percent, standard deviations in parentheses.

+Quantitative analyses of the individual particles are listed in Post (1)

++Determined by cation stoichiometry

foundry A, on the average, contain more Fe and Si, but less Zn, Cl, Mn, and Pb than those from foundry B. Also, particle emissions from foundry A usually contain small amounts (< 3%) of Mo, Ni, and Cr, all of which are rare in particles from foundry B.

Although the compositions of the particles from the foundries as determined in this study are in general similar to those reported by Armstrong,<sup>3</sup> there are some obvious differences (Table 1). For example, the present study shows significantly higher concentrations of Pb and Mn particles from foundry B and lower amounts of these elements in emissions from foundry A than reported by Armstrong.<sup>3</sup> Also, the current study found less Zn and more Fe in particles from both foundries than did Armstrong.<sup>3</sup> The original study did not report finding Mo in emissions from foundry A, although it is a common minor component in particles in the recent samples.

In addition to the particles on which quantitative analyses were performed, several hundred particles from both foundries were analyzed quantitatively by Post.<sup>1</sup> They show that the compositions listed in Table 1 are, in general, representative of the emissions from foundries A and B.

*Specific Sources of Foundry Particles.* The sources of most of the elements in the foundry particulate emissions are the scrap metal, chemicals added to the melt, or the casting molds. The use by foundry A of generally high-grade steel with a minimal amount of nonferrous impurities is consistent with particle emissions from this foundry that are enriched in Fe, with relatively low concentrations of other elements. Minor elements, such as Mo and Ni, and some of the Mn and Cr, probably originate in the scrap steel; most of the Mn, Al, Ca, and Cr result from materials added to the molten metal, either to adjust the melt composition or as deoxidizers. The Si may originate either from impurities in the scrap metal (e.g., glass), the "silica Mn" sometimes added to the melt, or from the silica sand molds. The remaining elements are mainly from the great variety of impurities in the scrap metal. Because most of the noniron and nonsteel materials are separated before melting, the particles emitted by foundry A usually have relatively low concentrations of these "impurity" elements. On the other hand, elements such as Zn, Pb, Cl, Ca, K, As, and Mg are more abundant in particles from foundry B; especially common are Zn, Pb, and Cl. The greater average concentration of Mn in particles from foundry B, compared to foundry A, arises because the only chemicals used to adjust the melt composition at foundry B are "ferromanganese" and "silica Mn," whereas foundry A uses about equal amounts of Mn and Cr. That also explains why Cr is rarely observed in foundry B.

Obviously, the nature of the foundry particulate emissions depends strongly on the scrap-metal composition, which probably accounts for most of the differences between the present study and the earlier work by Armstrong.<sup>3</sup> Apparently, the scrap metal used by foundry A now contains less nonferrous impurities than in 1971. It is also likely that the compositions of the foundry particles differ somewhat from day to day and week to week. According to foundry officials, however, attempts are made to maintain the average scrap metal composition as constant as possible; thus, variations in particle emissions should be minimized, at least over the short term. Other factors that affect the compositions of particle emissions are changes in foundry processes and chemicals added to the melt.

*Particle Morphologies, Surface Coatings, and Sizes.* Most of the particles emitted by the two foundries are rounded, but those from foundry A are more often spherical; Figs. 1 and 2 show SEM photographs of particles from foundries A and B. Many of the particles have smaller particles or coatings adhering to their surfaces (Fig. 1). Commonly the surface coatings are filamentous and show no peaks in EDS spectra; they are presumably carbonaceous. In other cases, small metal oxide spheres, or particles showing only S in EDS spectra, are attached to the surfaces of metal oxide spheres. TEM examination of some foundry fly-ash spheres reveals an abundance of surface coatings, some of which appear to be euhedral crystals. Detailed TEM, STEM, and EDS-SEM studies of surface coatings on fly ash from Cu smelters have revealed an abundance of various surface coatings, many of which are relatively volatile compounds.<sup>8,9</sup> A detailed study of surface coatings on foundry particulate emissions would be of great interest.

SEM examination of particles from foundry B show that many are less homogeneous in appearance than particles from foundry A (Fig. 2). EDS analyses of particles from foundry B reveal that many consist of two or more phases. For example, Fig. 2 shows a particle that consists of a Zn-rich phase and Fe-rich phases. Several of the metal-oxide particles have attached grains containing Pb and Cl. EDS analyses indicate that most of these Pb-rich

crystals are  $\text{PbCl}_2$ , but in some cases are depleted in Cl, suggested a mixed chloride and oxide (or carbonate) of Pb. Also, crystals of mixed Pb, K, and Fe chlorides are associated with the Fe or Zn oxide particles. Not all the Pb-rich particles from foundry B show obvious crystals or coatings of  $\text{PbCl}_2$ ; presumably in these cases the Pb is homogeneously mixed with the other oxides in the particles.

In addition to the Fe, Zn oxides, particles of  $\text{ZnCl}_2$ ,  $\text{PbCl}_2$ , PbO [or  $\text{PbCO}_3$ , Pb,  $\text{Pb(OH)}_2$ ], and As oxide were observed in samples collected near foundry B. It appears, then, that the volatile elements exist as chlorides or oxides, and that they can occur either as individual particles, as surface coatings on the mixed metal oxide particles, or in apparently homogeneously mixed oxide particles.

The particles from foundry B range in diameter from about 0.2 to 2  $\mu\text{m}$ , with the majority smaller than 1  $\mu\text{m}$ ; by comparison, foundry A particles range from about 0.5 to 5  $\mu\text{m}$ , and most are between 0.8 and 3  $\mu\text{m}$  in diameter. A greater abundance of submicron particles from foundry B, compared to foundry A, was also observed by Armstrong,<sup>3</sup> in part perhaps because samples were collected in both studies at a greater distance from foundry B than from foundry A.

*Na- and Ca-rich Particle Emissions.* In addition to the metal oxide spheres, the samples collected near foundry A also contain a large number of particles showing Na, Ca, Cl, Mg, Si, S, or K in EDS spectra. These particles are typically rounded or are euhedral crystals, or a combination. The rounded particles generally are composed of Ca, Cl, S, Si, Mg, and K and are probably a mixture of chlorides and sulfates, although quantitative analyses suggest that some elements might exist as oxides or carbonates. The euhedral crystals are of two types: NaCl, and those that show only Na in EDS spectra (presumably  $\text{Na}_2\text{CO}_3$ ).

The abundance of Ca- and (especially) Na-rich particles in the samples from foundry A was at first somewhat surprising. The Cl and S probably originate from impurities in the scrap metal, and the source of the Ca is likely the "hypercal" deoxidizer; but the source of the Na was not obvious. Conversations with representatives of foundry A were helpful in pinpointing the Na source. For many types of castings, cores were placed into molds to help shape the final casting. Until recently the foundry made all cores by forming and

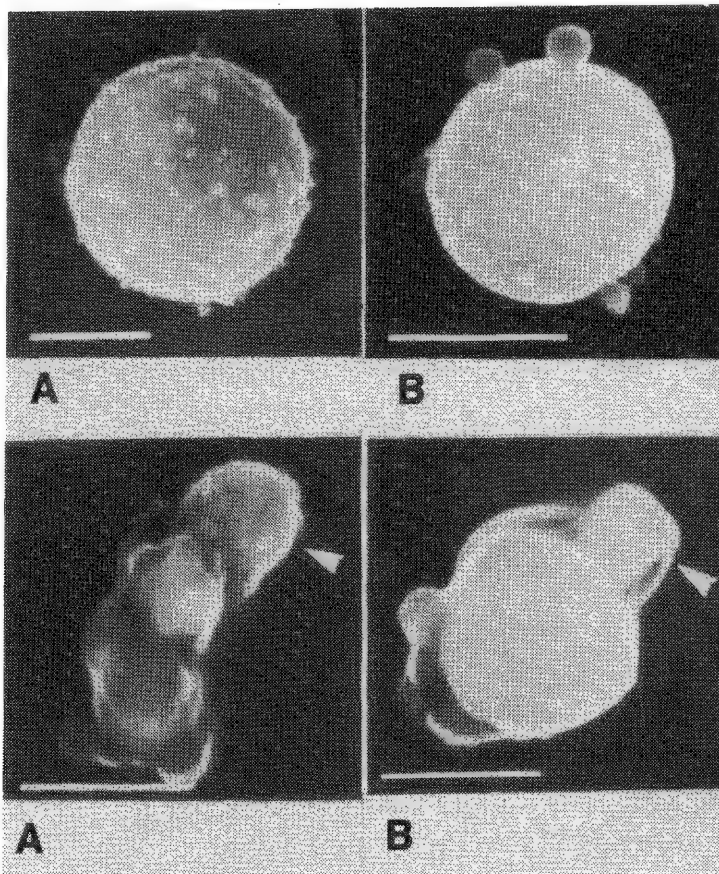


FIG. 1.--SEM images of metal oxide particles collected downwind of foundry A. Scale bars represent 1  $\mu\text{m}$ . Both particles are predominantly Fe oxide, although particle A contains about 1% Cr. (A) Fe (Cr); (B) Fe; smaller particles on surface show only FE.

FIG. 2.--SEM images of particles collected downwind of foundry B. Scale bars represent 1  $\mu\text{m}$ . (A) Agglomerate of three metal oxide particles. All three particles contain Fe, Zn, Mn, Pb, Cl and Si, with minor Cu, K, and Ca; particle indicated by arrow has Zn > Fe; other two particles have Fe > Zn. (B) Fe and Zn oxide particle (minor Mn, Cl, and Si) with attached crystal containing Pb and Cl (arrow).

baking a mixture of sand and linseed oil. Since 1979 a new method of making cores has also been used. Sand and Na silicate solution are mixed and blown into a core box, and the mixture is purged with  $\text{CO}_2$ . The resulting reaction produces a solid core consisting of  $\text{SiO}_2$  and  $\text{Na}_2\text{CO}_3$ . When the molten metal is added to the mold and core,  $\text{Na}_2\text{CO}_3$  is vaporized and emitted into the air, where it crystallizes as individual particles or on the surfaces of other particles. The  $\text{Na}_2\text{CO}_3$  can also react with  $\text{Cl}_2$  or  $\text{HCl}$  to form  $\text{NaCl}$ .

### Summary

We have used individual particle analysis methods to characterize emissions from two secondary iron foundries. Despite the similarity in the processes of the plants, we have been able to recognize chemical differences in their particle emissions and relate those differences to specific stages in the foundry processes. Armstrong<sup>3</sup> proposed criteria, based on composition, for distinguishing between particles emitted by foundries A and B. For example, he found that particles originating from foundry A generally had more Fe than Zn and more than 3% Si, and commonly contained Cr. The particles from foundry B, on the other hand, usually had less Fe than Zn and less than 3% Si, and rarely contained Cr. For the most part, our results are consistent with Armstrong's criteria. We find Fe to be slightly more abundant than Zn in particles from foundry B. Also, we suggest that particles containing Mo or high concentrations of Na are probably from foundry A and those containing more than trace amounts of Pb and Cl are from foundry B. In addition to compositional criteria, size and morphology can be used to distinguish between emissions from the two foundries. Particles from foundry A are usually individual spheres and larger than  $1.5\text{ }\mu\text{m}$ , whereas those from foundry B are rounded, but irregularly shaped, and commonly occur as agglomerates. The foundry B particles are usually smaller than  $1\text{ }\mu\text{m}$  in diameter.

Using the criteria listed above, we have identified foundry particles in samples collected at several locations in the Phoenix area. In most cases, it has been possible to pinpoint the foundry from which the particle probably originated. It is our belief that these results underscore the importance of applying individual-particle analysis methods to source characterization.

### References

1. J. E. Post, *Characterization of Particles in the Phoenix Aerosol, and Structure Refinements of Hollandite Minerals*, Ph.D. Thesis, Arizona State University, 1981.
2. J. E. Post and P. R. Buseck, "Characterization of individual particles in the Phoenix urban aerosol, using electron beam instruments," submitted to *Environ. Sci. Technol.*
3. J. T. Armstrong, *Quantitative Electron Microprobe Analysis of Airborne Particulate Material*, Ph.D. Thesis, Arizona State University, 1978.
4. J. T. Armstrong and P. R. Buseck, "Applications in air pollution research of quantitative analysis of individual microparticles with electron beam instruments," in P. A. Russel and A. E. Hutchings, Eds., *Electron Microscopy and X-ray Applications to Environmental and Occupational Health Analysis*, Ann Arbor, Mich.: Ann Arbor Press, 1978, 211-228.
5. G. D. Aden, *Quantitative Energy Dispersive Analysis of Small Particles*, Ph.D. Thesis, Arizona State University, 1981.
6. G. D. Aden and P. R. Buseck, "A minicomputer procedure for quantitative EDS analyses of small particles," *Microbeam Analysis--1983*, 195.
7. G. D. Aden and P. R. Buseck, "Rapid quantitative analysis of individual particles by energy-dispersive spectrometry," *Microbeam Analysis--1979*, 254-258.
8. J. P. Bradley, *Anthropogenic Airborne Microparticles: Compositions, Structures, and Surface Reactions*, Ph.D. Thesis, Arizona State University, 1981.
9. P. R. Buseck and J. P. Bradley, "Electron beam studies of individual natural and anthropogenic microparticles: Compositions, structures and surface reactions," in D. R. Schryer, Ed., *Heterogeneous Atmospheric Chemistry*, *Amer. Geophys. Union Geophysical Monograph*, 1982, 26: 57-76.

## MICROANALYSES OF INTERSPERSED INTERPLANETARY DUST PARTICLES

J. P. Bradley and D. E. Brownlee

One of the more challenging aspects of microbeam analyses is that of individual particle characterization. Particulate phenomena are becoming increasingly important in several areas of materials research, including atmospheric chemistry and physics,<sup>1</sup> heterogeneous catalysis,<sup>2</sup> and extraterrestrial materials characterization.<sup>3</sup> Individual particles can range from clusters of molecules a few tens of Ångströms in diameter up to those of 100  $\mu\text{m}$  ( $10^6$  Å). Often the analytical information required can only be determined at the single particle level, and therefore it is necessary to utilize instrumentation that offers a microprobe capability.

We have developed specialized procedures for collection, preparation, and analyses of individual interplanetary dust particles (IDPs). Individual IDPs are retrieved from the stratosphere (at 18-20 km) by impaction onto silicone oil-coated plates mounted on NASA U-2 aircraft. Silicone oil provides a highly viscous medium to cushion and entrap the impacting particles. Thirty tons of IDPs fall into the atmosphere daily but their spatial density is still so low that a typical U-2 flight results in collection of only one particle ( $>10$   $\mu\text{m}$ ) per hour of flight time.

Once the collection plates are returned to the laboratory, IDPs are located as dark specks (typically 5-25  $\mu\text{m}$  in diameter) embedded in silicone oil. Some particles are fragile aggregates of grains and can disintegrate into thousands of submicron fragments on impact. These particles appear on the collection surface as dense populations of debris covering an impact area up to 300  $\mu\text{m}$  in diameter.

### *Particle Preparation*

Among the important prerequisites for the analysis of these particles are (a) cleaning them of the silicone oil used for collection and (b) dispersal and mounting of the particles on appropriate TEM substrates (Fig. 1), which often requires cleaning, crushing, and mounting fragments from a single 5 $\mu\text{m}$  particle onto the center square of a 200 mesh grid. Because the particles are small it is crucial that their components be localized on the TEM grid and that contaminants at the 0.1 $\mu\text{m}$  level be kept at an absolute minimum. The crushing is carried out between polished glass surfaces; for some particles that is done dry and in other cases a viscous medium is used so that shear forces can gently disaggregate the particle. Workers in the field have used a variety of methods to mount dispersed particles onto a small area of a TEM grid. The most straightforward approach is to use a tungsten needle to scrape fragments off the glass crushing substrate, and directly transfer them to a thin-film ( $<100\text{\AA}$ ) carbon substrate for TEM analyses. This procedure requires delicate technique so as not to rupture the carbon film. In addition, it is not efficient for moving submicron grains because of the difficulties of lifting small particles from the crushing surface and then having them jump from the transfer needle to the carbon film. Another successful mounting procedure (used by the Walker group at Washington University in St. Louis) involves evaporating a carbon film directly over the crushed particle, floating the film onto water, and then mounting the film on a grid. This technique works well but has the disadvantage that the sample comes into contact with water, which can produce artifacts as well as degradation of water-soluble phases.

Another mounting procedure that has been used with success is a modified replica technique in which fragments from the crushing substrate are pulled up with a replica plastic, which is then carbon coated and placed onto a TEM grid. The plastic is then removed by use of either the Jaffee wick method or a vapor reflux unit. With care, this

---

The authors are at the Department of Astronomy, University of Washington, Seattle, WA 98195.



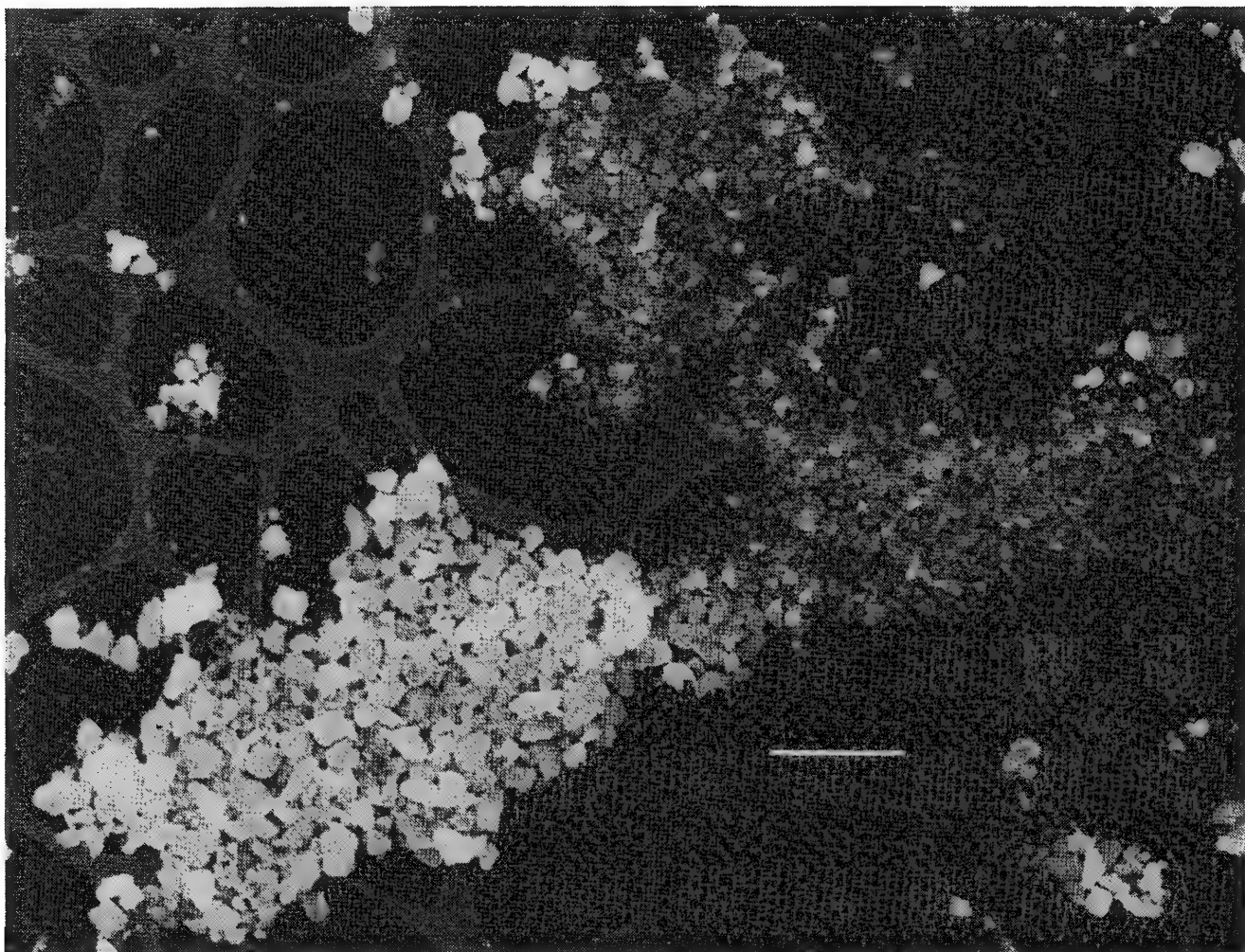


FIG. 1.--Scanning electron micrograph of interplanetary dust particle that has been dispersed as large number of fragments onto TEM grid. The substrate consists of holey-carbon mesh on which a thin ( $<100\text{\AA}$ ) continuous carbon film is supported. Particle fragments have been transferred directly onto this thin carbon film. Scale bar =  $2.5\text{ }\mu\text{m}$ .

method can be used to mount grains exactly in the center of a specific grid square but the technique has the serious drawback that removal of the replica plastic is often incomplete.

It is also possible to mount fragments on holey-carbon films by direct transfer of fragments in an oil droplet. The sample (usually smaller than  $10\text{ }\mu\text{m}$ ) is crushed between glass surfaces, with a tiny amount of silicone oil (viscosity 500 000 centistokes) used to help provide shear for efficient dispersal of submicron grains. The oil is then scraped up with a  $10\text{ }\mu\text{m}$  (tip) tapered glass needle and transferred to a holey-carbon grid resting on a porous glass frit saturated with hexane. When the needle just touches the hexane film the particles transfer to the film. To minimize sample loss it is crucial to use films with very small holes. The oil is efficiently removed from the samples.

A final and very promising sample mounting method we have used involves the use of a solid organic material, which can be sublimed after the transfer. The crushed particle is picked up with a small ( $200\text{ }\mu\text{m}$ ) piece of the organic solid and then with a small needle the solid is placed on the appropriate region of the TEM grid. Upon heating, the substance sublimates and the particles are left nicely dispersed on a localized region of the grid.

#### *Particle Analysis*

There is a range of electron-beam methods for particle analysis, including scanning electron microscopy (SEM), conventional transmission electron microscopy (CTEM), and

scanning transmission electron microscopy (STEM). For SEM studies IDPs are mounted either whole or as crushed particles onto Nuclepore substrates. In this configuration SEM enables determination of particle morphology (by secondary electron imaging) and particle composition (by x-ray energy-dispersive spectrometry). Until recently few attempts have been made to perform quantitative chemical analyses of particles, largely because of the difficulties involved in correcting observed x-ray intensities for the effects of particle geometry. However, correction procedures have since been developed that permit quantitative chemical analyses of single particles as small as 0.1  $\mu\text{m}$  in diameter.<sup>4</sup>

Despite the obvious application that CTEM has for single-particle characterization, very few studies have exploited this capability in the past. We have found that CTEM offers an extremely powerful capability for acquisition of structural information about IDPs. CTEM methods that we employ include high-resolution lattice fringe imaging, bright field/dark field imaging, and electron diffraction. One of the major advantages of CTEM is that it can offer structural information from grains as small as 100 Å in diameter.

Perhaps the most versatile electron optical configuration for individual particle studies is that provided by STEM, since it offers the user multipurpose capability that is ideally suited to single particle analyses. For example, the fine probe-forming ability of the STEM configuration provides a means of acquiring chemical information from regions less than 100 Å in diameter. Such instruments can also be equipped with both energy-loss and x-ray spectrometers, which enable determination of both light ( $Z \leq 11$ ) and heavy ( $Z \geq 11$ ) elements within a particle. Thus, the STEM configuration is ideally suited for individual particle studies since structure, morphology, and compositional data (for both light and heavy elements) are all available from a single instrument.

Electron-beam studies (with SEM, CTEM, and STEM) of IDPs are providing fundamental information about their morphological, structural, and chemical characteristics. These studies have shown that IDPs consist of extremely complex aggregates of several crystalline phases, together with lesser amounts of amorphous carbon. Often the mean grain size is less than 500 Å. Crystalline phases that we have so far identified include olivine, pyroxenes, sulfides, carbides, alloys, and others.

In a recently completed study we characterized very unusual pyroxene crystals.<sup>3</sup> These grains are ubiquitous but volumetrically minor constituents of a type of IDP we call CP (chondritic porous). Morphological features of these crystals, together with microstructural defects (axial screw dislocations), strongly suggest that they were formed by direct gas-to-solid condensation. These observations are important since they establish a possible link between IDPs and early solar system processes.

In addition to refractory mineral phases like olivine and pyroxenes, we also observe low-temperature phases within IDPs. For example, tetragonal FeS grains occur in some samples, as well as isolated grains of epsilon FeNi carbide. Tetragonal FeS has an upper thermal stability between 130 and 250°C,<sup>5</sup> and epsilon FeNi carbide undergoes an irreversible phase transition at 380-400°C.<sup>6</sup> All IDPs sustain a brief thermal pulse during atmospheric entry. The amplitude of this pulse depends on (a) entry velocity, (b) angle of entry, (c) particle density, and (d) particle size. Thus, identification of low-temperature phases, such as tetragonal FeS and epsilon FeNi carbide, may provide an indication of the degree to which the host particle was heated during atmospheric entry.

Perhaps the most elusive phase found within IDPs is carbon. In most particles carbon resides interstitially, and can sometimes be seen as amorphous coatings on mineral grains. In this configuration and structural state carbon is exceedingly difficult to characterize by electron-beam methods. Furthermore, carbonaceous material is a significant contaminant during particle collection, preparation, and analysis. Despite these problems we are developing an understanding of the extreme importance of carbonaceous phases within IDPs. In addition to amorphous rims on mineral grains we have observed: (1) discrete particles of amorphous carbon, (2) carburized FeNi grains, and (3) carbon filaments with embedded catalyst ( $\text{Fe}_3\text{O}_4$ ) particles. All these phases are characteristic of material formed by catalytic deposition from carbon-containing gases (e.g., carbon monoxide and hydrocarbons).<sup>8</sup> They are also byproducts of the Fischer-Tropsch synthesis, a reaction that is believed to have played an important role in the evolution of carbonaceous chondrites.<sup>9</sup> Our observations indicate that heterogeneous catalysis has played an important role in the formation of some IDPs, and they may provide a means of establishing a link between IDPs and early solar system processes.



## References

1. J. P. Lodge Jr., A. P. Waggoner, D. R. Klodt, and C. N. Crain, "Non-health effects of airborne particulate matter," *Atmos. Environ.* 14: 392-397, 1980.
2. A. Howie, L. D. Marks, and S. J. Pennycook, "New imaging methods for catalyst particles," *Ultramicroscopy* 8: 163-174, 1982.
3. J. P. Bradley, D. E. Brownlee, and D. R. Veblen, "Pyroxene whiskers and platelets in interplanetary dust: Evidence of vapour phase growth," *Nature* 301: 473-477, 1983.
4. J. T. Armstrong, "New ZAF and  $\alpha$ -factor correction procedures for the quantitative analysis of individual microparticles," *Microbeam Analysis--1982*, 175-180.
5. A. H. Clark, "Some comments on the composition and stability relations in mackinawite," *N. Jb. Miner. Mh.* 10: 300-304, 1966.
6. S. Nagakura, "Study of metallic carbides by electron diffraction Part III. Iron carbides," *J. Phys. Soc. Japan* 14: 186-195, 1959.
7. P. Fraundorf, "Interplanetary dust in the transmission electron microscope: Diverse materials from the early solar system," *Geochim. Cosmochim. Acta* 45: 915-943, 1981.
8. R. T. K. Baker and P. S. Harris, "Formation of filamentous carbon," *Chem. Phys. Carbon* 14: 83-165, 1978.
9. M. S. Lancet and E. Anders, "Carbon isotope fractionation in the Fischer-Tropsch synthesis and in meteorites," *Science* 170: 980-982, 1970.

## INDIVIDUAL PARTICLE MICROANALYSIS OF EXOTIC COMPONENTS IN CARBONACEOUS CHONDRITE METEORITES: A TOOL FOR UNRAVELING THE PETROGENETIC HISTORY OF THE EARLY SOLAR SYSTEM

J. T. Armstrong and G. J. Wasserburg

A combination of SEM examination, point analysis, and quantitative broad-beam particle analysis with the electron microprobe has been employed to determine the purity, homogeneity, and bulk elemental composition of individual micrograins of exotic components dissected and removed from fine-grained inclusions in carbonaceous chondrite meteorites. Isotopic analyses by means of direct-loading thermal-ionization mass spectrometry were performed on the suitable grains found by electron beam analysis. The combination of individual-particle x-ray analysis and isotopic analysis with the mass spectrometer provides important information regarding isotopic anomalies due to the decay of short-lived radionuclides thought to be present during the initial formation of the solar system--information that could not be obtained simply by isotopic analyses of bulk aggregates of crystals.

Carbonaceous chondrite meteorites contain rare small inclusions composed of refractory phases rich in calcium and aluminum. These Ca-, Al-rich inclusions (CAI) are thought to contain some of the earliest material condensed from the solar nebula, mineral phases that have remained essentially unaltered since the formation of the solar system.<sup>1</sup> A variety of isotopic anomalies have been observed in these inclusions, including excesses of isotopes thought to be produced by the decay of short-lived and now extinct radionuclides present in the early solar nebula.<sup>2</sup> Determination of such anomalies requires very precise and accurate isotopic measurements of separated pure phases. The complexity of the isotopic variations observed within CAI often requires that such isotopic measurements be made on individual crystals or portions of individual crystals.<sup>3</sup>

Among the most important of the isotopic anomalies observed in Al-rich, Mg-poor phases from CAI is an excess of  $^{26}\text{Mg}$  thought to be due to the decay of  $^{26}\text{Al}$  present in the inclusion at the time of formation.<sup>4</sup> Techniques have been developed to permit Mg isotopic analysis of individual 10-100 $\mu\text{m}$  particles with thermal ionization mass spectrometry by direct loading of individual crystals on a thermal ionization filament.<sup>5</sup> These techniques have been applied to the determination of  $^{26}\text{Mg}$  excesses in individual mineral grains from CAI as well as individual cosmic dust grains.<sup>5-6</sup> The direct loading technique has also been used to determine Pb and Ca isotopic systematics of individual mineral grains from meteorites<sup>5,7</sup> and Rb-Sr isotopic systematics for lunar, meteorite, and tektite micrograin samples.<sup>8</sup>

Individual particle analysis by electron-beam instruments can play an essential role in the successful application of the direct loading technique to determination of isotopic systematics. Electron-beam instruments can provide important information regarding the homogeneity, degree of purity, and bulk elemental composition of the micrograins used for isotopic analysis. Initial experiments involving direct loading mass spectrometry were limited by an inability to perform quantitative elemental analysis of the individual grains.<sup>5</sup> The development of accurate quantitative analysis procedures for individual unpolished microparticles with the electron microprobe provides a ready means to determine the elemental compositions of such samples. This paper presents an example of the application of individual-particle quantitative analysis with use of the electron microprobe and SEM to characterize mineral grains from the "Blue Angel," an important CAI from the Murchison carbonaceous chondrite, that were used in direct loading mass spectrometry experiments for determination of Mg isotopic systematics.

---

The authors are at the Charles Arms Laboratory, Division of Geological and Planetary Sciences, California Institute of Technology, Pasadena, CA 91125. Supported by the National Aeronautics and Space Administration through Grant NGL 05-002-188. Division Contribution Number 3900(440).

### Sampling and Analysis

The Murchison Blue Angel is a relatively large CAI (approximately 1.5 mm in diameter) found in the Murchison carbonaceous chondrite. The detailed petrography and mineral chemistry of this inclusion have been previously described and a model for its petrogenesis has been proposed.<sup>9</sup> A major component of the Blue Angel is hibonite (nominally  $\text{CaAl}_{12}\text{O}_{19}$ ), which is a mineral thought to be one of the first phases to have condensed from the cooling solar nebula.<sup>10</sup> The possible condensation-related origin of hibonite coupled with the high Al and low Mg abundances typically found in the mineral makes it an especially likely phase to have excesses of  $^{26}\text{Mg}$  formed from the decay of  $^{26}\text{Al}$ . Individual unaltered hibonite grains in the Blue Angel range from less than 5  $\mu\text{m}$  to approximately 60  $\mu\text{m}$  in diameter. Intergrown with the hibonite are a variety of other phases including spinel ( $\text{MgAl}_2\text{O}_4$ ) and Mg-rich silicates which have a normal Mg isotopic composition. Determination of  $^{26}\text{Mg}$  excesses in hibonite requires good separation of hibonite from the isotopically normal Mg-rich phases.

The Murchison Blue Angel inclusion is composed of very friable and powdery portions. Great care was required to isolate and prepare the hibonite particle samples. All sample handling and dissection was done with stainless steel and tungsten microtools under microscopic observation with clean-room conditions. An unpolished fragment of the Blue Angel which contained a sizable portion of the inclusion's hibonite-rich core (Fig. 1) was removed, carbon coated, examined with the SEM, and then mounted in epoxy and micropolished with diamond polishing materials. The section was then reexamined with the optical microscope and SEM and analyzed with the electron microprobe. Selected regions of the polished section were then removed, portions were crushed, and individual hibonite particles were extracted. These particles were examined with the optical microscope to determine whether they appeared to be homogeneous and free of inclusions. Appropriate hibonite particles were then attached to a pyrolytic graphite planchet with microdrops of a citrate/sucrose solution and the planchet was carbon coated for analysis.

The isolated hibonite particles were examined with the SEM and qualitative EDS point analyses were performed at high magnifications to determine whether the individual grains were relatively free of contamination by other phases. Grains found to be composed of reasonably pure hibonite (e.g., Fig. 2) were then analyzed with the electron microprobe. WDS analyses were performed at various points over the surface of each particle by means of a finely focused static electron beam in order to determine the sample's homogeneity. Replicate point analyses were performed with the particle rotated to different orientations with respect to the spectrometers.

The relative x-ray intensities measured on unpolished grains in focused-beam experiments are obviously affected by sample geometry and orientation in addition to composi-

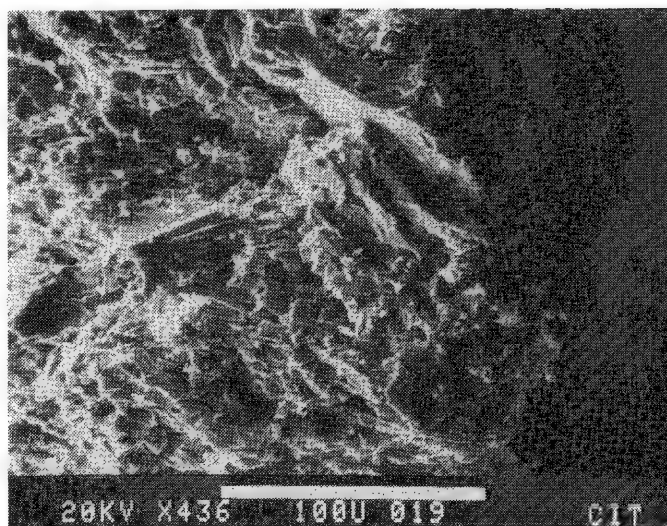


FIG. 1.--SEM image of fragment of Blue Angel interior. Dominant phase is hibonite. Scale bar is 100  $\mu\text{m}$ .

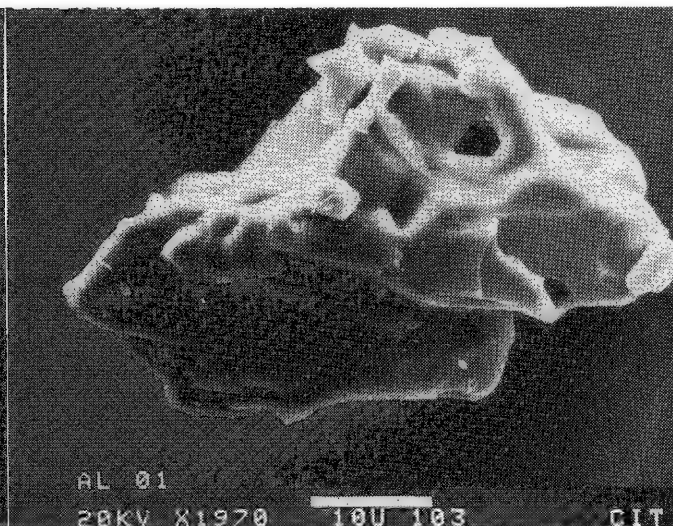


FIG. 2.--SEM image of typical individual hibonite grain extracted from interior of Blue Angel. Composition of grain is given in Table 1, analysis 3. Scale bar is 10  $\mu\text{m}$ .

tional variation. To a first approximation, one can determine the effect of particle geometry on the relative x-ray intensities in a focused-beam experiment by calculating the change in relative x-ray intensities produced by varying the spectrometer take-off angle. Such a calculation is shown in Fig. 3 for a typical hibonite composition. As can be seen in the figure, the relative intensities of dissimilar elements, such as Ca/Al, vary substantially with sample orientation and cannot be used in a focused-beam experiment to determine homogeneity. However, the relative intensities of pairs of elements with similar atomic numbers (and thus similar mass absorption and atomic number corrections) are relatively insensitive to sample orientation. As shown in Fig. 3, Mg/Al and Ti/Ca vary by less than 10% relative for take-off angles ranging from 20 to 90°. These were the element pairs whose intensities were used to test the sample homogeneity in these experiments.

Those hibonite grains determined to be homogeneous were quantitatively analyzed with the electron microprobe by use of a rastered beam covering the entire individual particle surfaces. The particle correction procedures of Armstrong and Buseck were employed.<sup>11-13</sup> Replicate analyses of each particle were performed with at least two different orientations to the crystal spectrometer. The corrected replicate analyses agreed to better than 5% relative. Typical hibonite particle analyses thus obtained are given in Table 1, along with typical hibonite analyses performed on a polished section of the inclusion. As can be seen in the table, there is an excellent agreement between the particle and polished section analyses. The particle analyses show the high degree of stoichiometry observed in hibonites from this inclusion, corresponding closely to the ideal formula  $\text{Ca}(\text{Al}, \text{V}, \text{Cr}, \text{Fe}, \text{Mg} = \text{Ti}, \text{Si})_{12}\text{O}_{19}$ . The somewhat higher levels of Fe and Si observed in the hibonite particles are possibly due to slight contamination by Fe-rich silicates from the meteorite's matrix. Al/Mg atomic ratios for the analyzed hibonite particles ranged from 24 to 36 with a typical

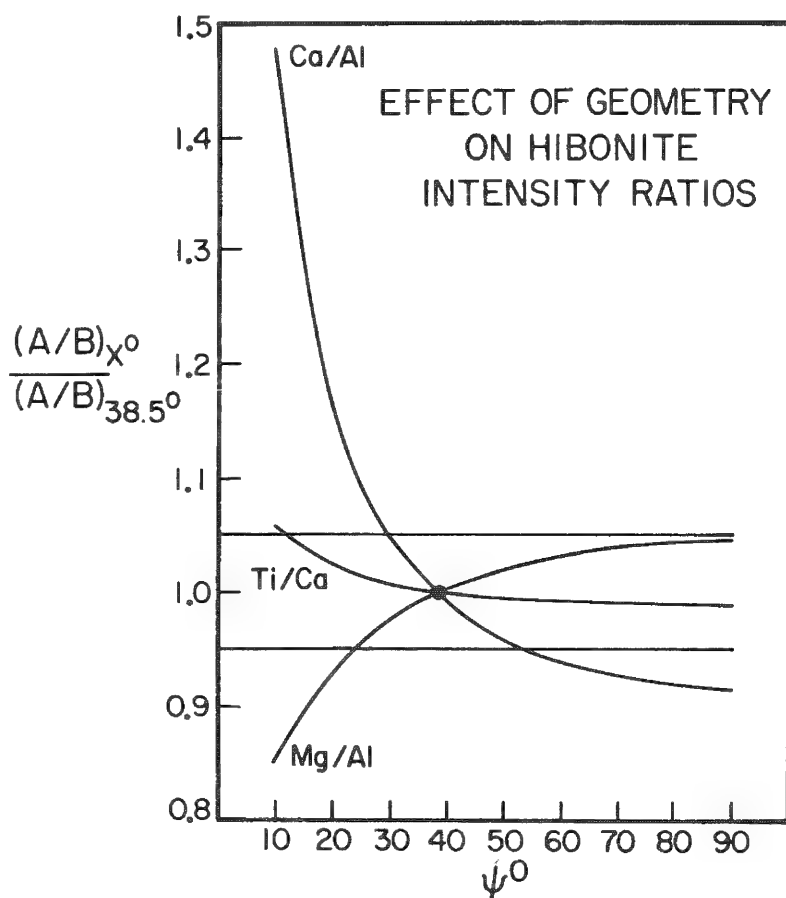


FIG. 3.--Effect of spectrometer take-off angle on relative intensities of element pairs in hibonite at 15 keV.

TABLE 1.--Composition of hibonites from the interior of the Murchison Blue Angel (atomic proportions).<sup>a</sup>

	1 <sup>b</sup>	2	3	4
Ca	1.02	0.99	1.03	1.00
Al	11.16	11.00	10.95	11.00
V	0.10	0.09	0.08	0.05
Cr	0.005	0.01	---	0.009
Fe	0.001	---	0.008	0.01
Mg	0.34	0.43	0.44	0.43
Ti	0.35	0.45	0.45	0.43
Si	0.02	0.02	0.04	0.07
O	19.00	19.01	19.00	19.03

<sup>a</sup>Atomic proportions are normalized to 13 total cations.

<sup>b</sup>Analyses: 1 is the average of 120 analyses of hibonite grains from polished sections of the interior of the Blue Angel; 2 is typical high Mg and Ti containing hibonite from a polished section of the interior; 3 and 4 are typical analyses for unpolished hibonite particles extracted from the interior, particle 3 is shown in Fig. 2.

value of 27, corresponding to the same distribution observed for polished samples of hibonites from the interior of the Blue Angel.

Several of the quantitatively analyzed hibonite grains were individually direct-loaded onto filaments and isotopically analyzed with the mass spectrometer. The combination of the Mg isotopic analyses determined with the mass spectrometer and the Al/Mg elemental ratios determined with the electron microprobe was used to determine that excesses of  $^{26}\text{Mg}$  found in the grains were correlated to the Al/Mg and thus most probably due to decay of live  $^{26}\text{Al}$  present at the time of formation of the inclusion. The details of the isotopic analyses are presented elsewhere.<sup>14</sup>

### Summary

The proper interpretation of isotopic measurements of a wide variety of terrestrial, meteoritic, and lunar samples requires detailed petrologic information regarding the individual samples analyzed. In certain applications, combined electron microprobe and ion microprobe analysis of polished sections can provide the necessary petrologic and isotopic information (e.g., Ref. 3). Many applications, however, require isotopic measurements of higher precision than can be readily performed with the ion microprobe, and thermal-ionization mass spectrometry is the isotopic analytical technique of choice. For these applications, the ability to perform quantitative elemental analyses of individual particles and portions of particles can provide essential complementary information and should be routinely employed.

### References

1. L. Grossman, "Refractory inclusions in the Allende meteorite," *Ann. Rev. Earth Planet. Sci.* 8: 559-608, 1980.
2. G. J. Wasserburg and D. A. Papanastassiou, "Some short-lived nuclides in the early solar system: A connection with the placental ISM," in C. A. Barnes, D. D. Clayton and D. N. Schramm, Eds., *Essays in Nuclear Astrophysics*, London: Cambridge University Press, 1982, 77-140.
3. J. T. Armstrong and G. J. Wasserburg, "Mg isotopic systematics in the Allende inclusion WA: PANURGE takes a second look," *Lunar and Planetary Science XIV*, Houston: The Lunar and Planetary Science Institute, 1983, 11-12.
4. T. Lee, D. A. Papanastassiou, and G. J. Wasserburg, " $^{26}\text{Al}$  in the early solar system: Fossil or fuel?" *Astrophys. J. (Letters)* 211: 107-110, 1977.
5. T. Lee, D. A. Papanastassiou, and G. J. Wasserburg, "Mg and Ca isotopic study of individual microscopic crystals from the Allende meteorite by the direct loading technique," *Geochim. Cosmochim. Acta* 41: 1473-1485, 1977.
6. T. M. Esat et al., "Mg isotopic composition of interplanetary dust particles," *Science* 206: 190-197, 1979.
7. F. Tera and G. J. Wasserburg, "Precise isotopic analysis of Pb in picomole and subpicomole quantities," *Anal. Chem.* 47: 2214-2220, 1975.
8. D. A. Papanastassiou and G. J. Wasserburg, "Microchrons: The  $^{87}\text{Rb}$ - $^{87}\text{Sr}$  dating of microscopic samples," *Proc. Lunar Planet. Sci.*, New York: Pergamon Press, 1981, 12B: 1027-1038.
9. J. T. Armstrong et al., "The Blue Angel: I. The mineralogy and petrogenesis of a hibonite inclusion from the Murchison meteorite," *Geochim. Cosmochim. Acta* 46: 575-595, 1982.
10. L. Grossman and S. P. Clark, "High-temperature condensates in chondrites and the environment in which they formed," *Geochim. Cosmochim. Acta* 37: 635-649, 1973.
11. J. T. Armstrong and P. R. Buseck, "Quantitative chemical analyses of individual microparticles using the electron microprobe: Theoretical," *Anal. Chem.* 47: 2178-2192, 1975.
12. J. T. Armstrong, "Methods of quantitative analysis of individual microparticles with the electron beam instruments," *SEM/1978 I*, 455-467.\*
13. J. T. Armstrong, "New ZAF and  $\alpha$ -factor correction procedures for the quantitative analysis of individual microparticles," *Microbeam Analysis--1982*, 175-180.
14. D. A. Papanastassiou and G. J. Wasserburg, "Evidence of  $^{26}\text{Mg}$  excess in hibonite from Murchison," *Meteoritics* 15: 348-349, 1980.

## A MINICOMPUTER PROCEDURE FOR QUANTITATIVE EDS ANALYSES OF SMALL PARTICLES

G. D. Aden and P. R. Buseck

Quantitative analysis of small unpolished particles is important for many applications, yet few computer programs are available to perform the necessary data reduction. A new procedure is presented here for performing rapid quantitative analyses of unpolished particles in an electron-beam instrument equipped with an energy-dispersive spectrometer (EDS). Data are presented that demonstrate unpolished particles, ranging in diameter from 0.1 up to 20  $\mu\text{m}$ , can be quantitatively analyzed with an accuracy of 5-10% relative, based on thick polished simple oxide standards. This correction has been incorporated in a minicomputer program FRMRUN.

### *Previous Work*

The irregular nature of small particles (0.1-20  $\mu\text{m}$  in diameter) makes quantitative analysis difficult because standard ZAF corrections, which require a well-defined geometry, cannot be directly applied. In addition, for electron accelerating voltages under 30 kV, particles in this size range are not small enough to be treated as true thin films and the interelement corrections cannot be ignored.

An extensive review of the problems of the quantitative analysis of unpolished particles is available.<sup>1</sup> Several methods for quantitative data reduction of particle samples have been proposed. Early approaches to particle data reduction utilized a model that assumes particles can be treated as thin films.<sup>2,3</sup> However, the thin-film model is limited to the analysis of particles with thicknesses much less than 1  $\mu\text{m}$ .

A more rigorous set of particle corrections involves the detailed calculation and numerical integration of the particle shape effects on the absorption and fluorescence corrections.<sup>4</sup> This correction procedure has been shown to give excellent results for particles larger than 1  $\mu\text{m}$ , but the calculations are extensive and require considerable computer power. Monte Carlo calculations have also been used to simulate particle size and shape effects,<sup>5,6</sup> but once again the lengthy computations involved limit their general use.

Another form of particle correction has been presented that uses the x-ray peak-to-background ratio (P/B) to determine particle correction effects.<sup>6-8</sup> This correction is simple to apply, but it requires that the particles be suspended so as to minimize the contribution to the background from the substrate, a limitation that can be severe for many particle-analysis applications. In addition, the P/B method gives erroneous results when the thickness of the particle is smaller than the electron range in the sample (about 1  $\mu\text{m}$  in a silicate matrix).

A modification of the thin-film approximation of Philibert and Tixier<sup>2</sup> has been suggested for quantitative data reduction of particles that are too thick (semithin film) to be correctly considered thin films.<sup>9</sup> This method uses the thin-film atomic number correction factor (P-factor) in conjunction with a particle size/electron range correction in an attempt to model semithin film behavior. Using this modified P-factor equation, we have observed some improvements in the reduction of particle data compared to a pure thin film correction, but the form of the equation used to modify the P-factors (see below) does not appear to model correctly the atomic number effect for semithin films.<sup>10</sup> Even though there are problems associated with the initial application of the modified P-factor correction, the approach does provide a correction procedure for the intermediate case between thin and thick particles and it is a similar approach that is described in this work.

---

Author Aden is a senior staff scientist at Princeton Gamma-Tech, 1200 State Rd., Princeton, NJ 08540; author Buseck is a professor at Arizona State University (Chemistry and Geology), Tempe, AZ 84287. Supported in part by funds from the National Science Foundation under grant ATM-8022849.

### Algorithms

Several authors have pointed out that some type of modified ZAF correction must be performed on the data from the electron beam analyses of particles if reasonable results are to be obtained. These corrections must apply to particles that are thicker than the electron range (which have one set of correction requirements) and particles that are thinner than the electron range (with a completely different set of correction requirements) and all particle thicknesses in between. In the version of the modified P-factor approach<sup>9</sup> the following equations were used for atomic number and absorption corrections. For a particle of estimated thickness  $z$  and a calculated electron range  $z_r$ , the atomic number correction  $P'$  for the particle follows the form of

$$P' = [(1 - P)z/z_r] + P \quad (1)$$

The absorption correction  $f'(x)$  for particles is the Yakowitz-Newbury thin film equation<sup>11</sup>

$$f'(x) = 1 + (z/z_r)[f(x) - 1] \quad (2)$$

The absorption correction equation for the semithin film case yields intuitively reasonable results because the  $f(x)$  is calculated as an influence factor and is usually near unity (which is required by the form of this equation). The form of the modified atomic number correction is not adequate because the  $P$  factor calculated from the Philibert-Tixier equation is not an influence factor and is never near unity. Therefore, the  $P'$  value that is calculated is nearly always too large in the semithin particle. There is a problem with the form of Eq. (1), but the idea of providing a correction between the two boundary conditions of the thick and thin atomic number correction seems sound, and a new form of the equation for the semithin case has been implemented.

To alleviate the problems associated with using specific  $P$  factors, we developed a new atomic number correction factor  $F'(s)$  based on a linear equation of thick and thin influence factors for the atomic number correction. The atomic number correction factors for all elements in a sample are calculated as if the entire sample were a thin section  $Z(\text{thin})$ , and a second set of factors are calculated as if the sample were a thick flat specimen  $Z(\text{thick})$ . A linear equation of the two correction factors is then applied to the sample based on the thickness to electron range ratio:

$$F'(s) = (z/z_r)Z(\text{thick}) + [1 - (z/z_r)]Z(\text{thin}) \quad (3)$$

In the case of pyrite,

$$Z(\text{thick}) = f_{s(S)}/f_{s(Fe)} = 0.886 \quad (4)$$

$$Z(\text{thin}) = P(S)/P(Fe) = 1.61 \quad (5)$$

and for the pyrite semithin case where  $z/z_r = 0.1$  then,

$$F'(s) = (0.1 * 0.886) + (0.9 * 1.6) = 1.53 \quad (6)$$

Equation (3) meets the boundary conditions for the particles, as does Eq. (1), but it also gives reasonable values in the semithin case. Although there is no theoretical justification for a linear correction between the thick and thin atomic number corrections, tests between this model and a numerically integrated model show that the deviations resulting from nonlinearities are usually less than 10% relative.<sup>10</sup>

The specific electron range equation that is used in the FRMRUN program is that presented by Philibert and Tixier and includes the calculation of the logarithmic integral.<sup>2</sup> This equation requires a calculation of the sample density for particle samples. Since



most of the samples that are analyzed in our laboratory are oxides, a table of density for oxides of the elements is included in the program. Use of this table tends to underestimate the densities for metals and sulfides by about 25%, and additional tables for density should be added as needed.

The absorption correction that is employed in FRMRUN is that of Yakowitz-Newbury (Eq. 2) and is implemented as described in Ref. 9. The Philibert absorption term  $f(x)$  is used throughout.<sup>12</sup> The fluorescence correction that is used is modeled after the absorption correction, with  $f(x)$  replaced by the fluorescence influence correction from FRAME  $f_f$ .<sup>13</sup> This approximation is empirical and is used without a specific test of its accuracy. The fluorescence effects should decrease faster than the absorption effects and therefore tend to be overcorrected by this equation for small particles. However, for most of the samples that we analyzed, fluorescence was a second-order effect and did not play a major role in any of the corrections.

### *Background and Peak Fitting*

The calculation of the bremsstrahlung for a particle on a substrate is not trivial. In general, theoretical programs for background modeling tend to overestimate the absorption effects for particles and usually do not produce a calculated model that fits the spectrum very well. Digital filtering techniques can be used to remove the background and avoid this limitation, but the most popular model (top-hat digital filter<sup>14</sup>) always produces systematic errors in the region of the background under the overlaps of the Mg, Al, and Si peaks. Since the majority of the samples that we analyze are silicates, the digital filter technique is not acceptable.

The procedure that is used in FRMRUN involves the calculation of a theoretical background for the particle on the initial assumption that it is infinitely thick. A stored spectrum of carbon, collected at a specific beam current that has been processed to remove self-absorption effects, is used as a model of detector efficiency and dead layer thicknesses. Absorption effects in the regions of interest are then calculated for the sample with the Philibert absorption correction.<sup>12</sup> This calculated background spectrum is then used in linear combination with the substrate spectrum and the calculated background is fit to the particle spectrum by the TWIST procedure.<sup>15</sup>

The linear combination of the two spectra is used because part of the background is produced by the substrate and part by the particle. The contribution of each background spectrum that is used is determined by the concentration summations of the elements found in the particle compared to standards collected at the same beam current. For example, a silicate particle that is 0.5  $\mu\text{m}$  in diameter may have an unnormalized summation of 17% when compared to the standards; thus 17% of the calculated background for the spectrum would be added to 83% of background for the substrate and the resulting background fit to the sample at three background points. This type of background calculation is rapid and produced a good fit for all samples tested from small particle (down to 0.1  $\mu\text{m}$  in diameter) to thick flat samples.<sup>10</sup>

Peak fitting is performed by a simplified least-squares method. Stored standard spectra for each element are stripped of background and overlapping peaks. The window integrals of the elements of interest are measured at the FWHM of the peak, back corrected for ZAF effects, and stored in a matrix (A) of  $m$  standards by  $m$  "pure element" window integrals. For stable detector systems, where the peaks shift less than a few electron-volts from day to day and the overlapping elements to be deconvoluted do not overlap above the FWHM level of the peaks, the following linear equations may be used. The peaks in the sample of interest can be treated as linear combinations of pure element intensities scaled by the ZAF  $k$ -values; thus, for a matrix of the window integrals (B) from  $m$  elements of interest in the sample,

$$(A) \cdot (k) = (B) \quad (7)$$

where  $(k)$ , the matrix of  $k$ -values for the sample, is the quantity that is desired. By inverting the matrix (A) we can obtain the matrix  $(k)$  by matrix multiplication;

$$(k) = (B) \cdot (A)^{-1} \quad (8)$$

Although the inversion of the matrix is slow, the calculation needs to be done only once for any given set of standards. The matrix multiplication on the other hand is rapid (a few seconds for a  $10 \times 10$  matrix) and yields k-values for the sample that have been deconvoluted and stripped of other spurious peaks or tails that are normally present in EDS spectra (such as incomplete charge collection and escape or sum peaks). Particles made from a wide variety of standard materials were then analyzed to test these new correction procedures.

### *Experimental*

The FRMRUN program was developed in BASIC on the PGT 1000 system; a complete listing with manual is given in Ref. 10 and is available from the authors. Data were collected on a JEOL JSM-35C scanning electron microscope and an EDS detector with a fixed  $35^\circ$  take-off angle. Homogeneous mineral samples from the ASU electron microprobe collection were prepared according to procedures described in Ref. 16. Albite, pyrite, titanite, rhodonite, orthoclase, olivine, and anorthite were used. All standards were characterized prior to crushing by wet chemistry or by electron probe analysis against other well-characterized standards and each standard met the Goldstein criterion for homogeneity.<sup>17</sup>

The particle samples were analyzed against simple oxide standards, or as simple a standard as was possible. The standards used in all cases were: Na from albite, Mg from synthetic MgO, Al from corundum, Si from quartz, S from sphalerite, K from orthoclase, Ca from anorthite, Ti from rutile, Mn from synthetic MnO, and Fe from synthetic  $\text{Fe}_2\text{O}_3$ . The standards data that were used for the analyses presented here were collected three months prior to performing these particle analyses. A thick flat standard of Kakanui hornblende was analyzed against these standards daily to see if the spectrometer had drifted. Typically, standards data were only collected every 6 months.

Particles with diameters ranging from 0.1 up to 20  $\mu\text{m}$  were analyzed at 15 kV according to the optimizing procedures developed by Armstrong<sup>18</sup> and then processed by FRMRUN. Particle thicknesses were estimated from the measured particle diameters. A relative error histogram of the results of 395 data points from 150 particles is shown in Fig. 1. Only measured elements with concentrations above 5% were included in the histogram. The data show that analyses for 65% of the elements in the particles have relative errors of less than  $\pm 3.5\%$  and 95% of the data points fall within  $\pm 7.5\%$  relative to the true values for the minerals as determined by wet chemistry.

A sample output from FRMRUN is shown in Table 1 for the analyses of two particle types, albite and pyrite. The calculated density  $\rho$  for the sample is printed together with the measured k-value, a normalized k-value (uncorrected), the normalized ZAF correction for the particle if it is treated as a thick flat sample, the normalized correction for the particle if it is treated as a true thin film, and finally the normalized calculation based on Eq. (3), called the mix calculation. The atomic proportions on which stoichiometry may be based are also presented in the particle correction output.

The range of the results between the thick and the thin limiting cases give the analyst a feeling for the amount of variation that can occur if the particle thickness is not estimated correctly. The values from the mix calculation are the only ones that should be used; the other values are just printed for information or for other calculations.

The results of the analyses of nearly five hundred particles are presented in Table 2 and are grouped so that the errors in the calculations for the small particles ( $< 1 \mu\text{m}$ ) can be evaluated separately from particles larger than 1  $\mu\text{m}$ . All particles were analyzed for eleven elements, but concentrations below 0.1% are not printed. The programs, written in BASIC, required 3.5 min for the completion of an analysis of the eleven elements.

### *Conclusions*

A simple method for the rapid quantitative analysis of small particles has been presented. The method includes a new form of the equation for a semithin atomic number correction and describes a method for calculating the background for thin particles mounted on a substrate. In most cases the analyses are within 10% relative of the correct values, and in all cases the precision of the analyses is better than 10%. The small particle analyses all show larger precision errors than the large particles, which can be attributed to counting statistics and errors in the thickness measurements. In all cases the numbers presented are significantly better than the numbers obtained from normalized

TABLE 1.--Typical analysis printout for two particles, pyrite and albite, by the FRMRUN minicomputer routine.

<b>Pyrite</b>						
275	Thickness	0.4 $\mu$ m				
E $\theta$ = 15 keV		Psi = 35 $^{\circ}$	Estimated Rho = 4.0			
Element	k-value	norm k	thick <sup>a</sup> wt%	thin <sup>b</sup> wt%	particle <sup>c</sup> wt%	atomic prop
S	0.0372	45.96	46.41	58.39	54.45	49.98
Fe	0.0437	54.04	53.59	41.61	45.55	24.00
sum <sup>e</sup>			8.77			
<b>Albite</b>						
290	Thickness	0.5 $\mu$ m				
E $\theta$ = 15 keV		Psi = 35 $^{\circ}$	Estimated Rho = 2.6			
Element	k-value	norm k	thick <sup>a</sup> wt%	thin <sup>b</sup> wt%	particle <sup>c</sup> wt%	atomic prop
Na	0.0052	7.62	9.70	8.43	8.71	2.98
Al	0.0066	9.74	9.54	10.05	9.94	2.90
Si	0.0225	33.35	32.20	32.55	32.48	9.08
O <sup>d</sup>	---	49.30	48.55	48.96	48.87	24.00
sum <sup>e</sup>			9.22			

- a - Normalized FRAME ZAF correction  
b - Philibert and Tixier P-factor correction (normalized)  
c - This work (normalized)  
d - calculated by stoichiometry  
e - Summation relative to a thick polished sample at the same operating conditions

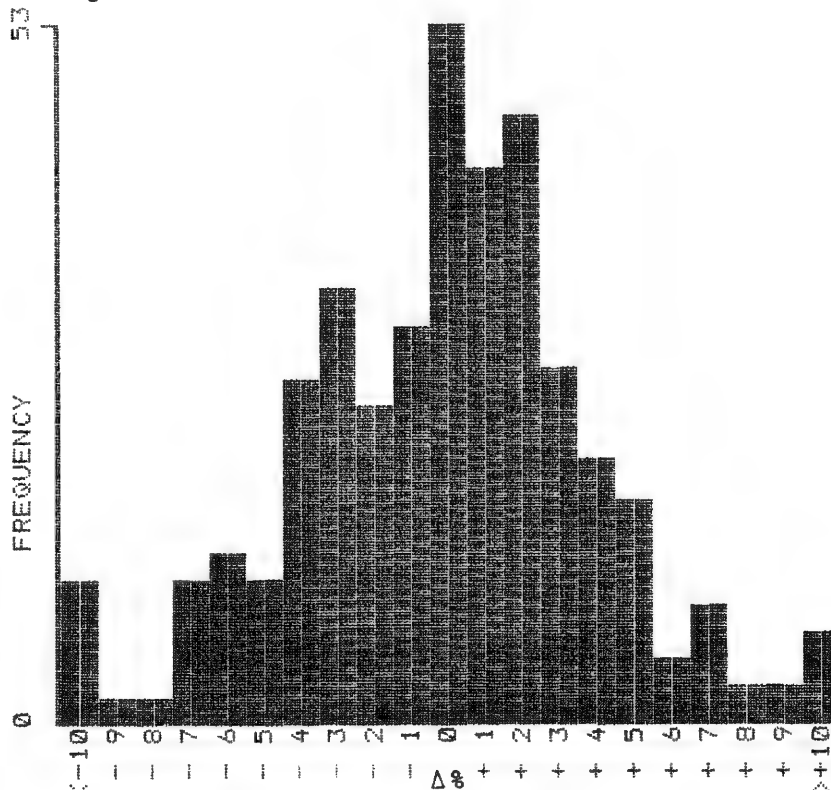


FIG. 1.--Error histogram of relative error for 395 points from 150 particles for particle samples ranging from 0.1 to 20  $\mu$ m in diameter. Absolute numbers are printed above each histogram block. Only 18 points fall outside  $\pm 9\%$  relative error.

TABLE 2.--Quantitative analyses of particles.

**Rhodonite**  
number of particles = 49  
average calculated density = 4.0 true = 3.7 (rel.err.=8.1%)

Particle thickness: $\leq 1\mu\text{m}$ $> 1\mu\text{m}$ Average					
WDS					
Element	True wt%	wt% ( $\sigma$ )	$\Delta\%$	wt% ( $\sigma$ )	$\Delta\%$
Si	21.9	22.3 (.69)	+1.6	21.3 (.42)	-2.7
Ca	2.90	3.01 (.35)	+3.8	2.95 (.13)	+1.7
Mn	27.5	27.0 (.43)	-1.9	28.4 (.62)	+3.3
Fe	10.1	10.4 (.78)	+2.8	10.7 (.50)	+5.5
Oa	37.0	37.4 (.45)	+1.0	36.7 (.34)	-7.8

**Anorthite**  
number of particles = 44  
average calculated density = 2.9 true = 2.7 (rel.err.=7.4%)

Particle thickness: $\leq 1\mu\text{m}$ $> 1\mu\text{m}$ Average					
WDS					
Element	True wt%	wt% ( $\sigma$ )	$\Delta\%$	wt% ( $\sigma$ )	$\Delta\%$
Na	2.53	2.47 (.54)	-2.4	2.66 (.24)	+5.1
Al	16.1	16.4 (.34)	+2.1	16.0 (.13)	-68
Si	24.0	24.3 (.38)	+1.1	24.5 (.15)	+2.1
Ca	9.59	9.43 (.21)	-1.7	9.49 (.25)	-1.0
Fe	0.40	0.33 (.26)	-18	0.33 (.15)	-18
Oa	46.6	47.1 (.15)	+9.7	47.0 (.09)	+7.9

**Olivine**  
number of particles = 51  
average calculated density = 3.5 true = 3.3 (rel.err.=6.1%)

Particle thickness: $\leq 1\mu\text{m}$ $> 1\mu\text{m}$ Average					
WDS					
Element	True wt%	wt% ( $\sigma$ )	$\Delta\%$	wt% ( $\sigma$ )	$\Delta\%$
Mg	26.5	27.5 (.70)	+3.8	27.0 (.17)	+2.0
Si	18.1	18.2 (.22)	+3.9	18.2 (.23)	+50
Fe	13.3	12.2 (1.2)	-8.3	12.7 (.56)	-4.7
Oa	41.9	42.3 (.32)	+8.6	42.1 (.19)	+5.3

a - Oxygen calculated by stoichiometry

**Albite**  
number of particles = 58  
average calculated density = 2.6 true = 2.6 (rel.err.=0%)

Particle thickness: $\leq 1\mu\text{m}$ $> 1\mu\text{m}$ Average					
WDS					
Element	True wt%	wt% ( $\sigma$ )	$\Delta\%$	wt% ( $\sigma$ )	$\Delta\%$
Na	8.68	9.20 (1.0)	+5.6	8.77 (.44)	+1.0
Al	10.3	10.4 (.32)	+3.9	10.0 (.16)	-3.1
Si	32.1	31.9 (.70)	-7.8	32.4 (.25)	+7.8
Oa	48.8	48.7 (.36)	-1.8	48.8 (.16)	+0.8

**Orthoclase**  
number of particles = 41  
average calculated density = 2.6 true = 2.6 (rel.err.=0%)

Particle thickness: $\leq 1\mu\text{m}$ $> 1\mu\text{m}$ Average					
WDS					
Element	True wt%	wt% ( $\sigma$ )	$\Delta\%$	wt% ( $\sigma$ )	$\Delta\%$
Na	0.85	0.45 (.37)	-47	0.70 (.22)	-18
Al	9.83	10.2 (.10)	+3.4	9.80 (.10)	-31
Si	30.4	31.2 (.41)	+2.8	31.2 (.27)	+2.6
K	12.4	11.2 (.58)	-10	11.5 (.45)	-7.3
Oa	46.2	47.1 (.25)	+1.9	46.9 (.23)	+1.4

**Titanite**  
number of particles = 47  
average calculated density = 3.2 true = 3.5 (rel.err.=8.6%)

Particle thickness: $\leq 1\mu\text{m}$ $> 1\mu\text{m}$ Average					
WDS					
Element	True wt%	wt% ( $\sigma$ )	$\Delta\%$	wt% ( $\sigma$ )	$\Delta\%$
Si	14.4	14.7 (.49)	+2.2	14.3 (.28)	-97
Ca	20.6	19.5 (.35)	-5.5	19.4 (.39)	-5.9
Ti	23.9	24.5 (.71)	+2.7	25.1 (.53)	+4.9
Oa	40.7	41.1 (.17)	+9.1	40.9 (.16)	+4.9

a - Oxygen calculated by stoichiometry

**Pyrite**  
number of particles = 73  
average calculated density = 3.9 true = 4.9 (rel.err.=20%)

Particle thickness: $\leq 1\mu\text{m}$ $> 1\mu\text{m}$ Average					
WDS					
Element	True wt%	wt% ( $\sigma$ )	$\Delta\%$	wt% ( $\sigma$ )	$\Delta\%$
S	53.5	54.6 (1.2)	+2.2	52.6 (.77)	-1.6
Fe	46.6	45.7 (1.4)	-1.8	47.4 (.77)	+1.9

a - Oxygen calculated by stoichiometry

FRAME values or normalized k-values. It is evident from these data that the particle corrections that were used yield acceptable analyses for all particles tested. Considering the accuracy, ease of use, and speed, the FRMRW program provides a good method for routine particle analyses.

#### References

1. J. T. Armstrong, Ph.D. Thesis, Arizona State University, Tempe, 1978.
2. J. Philibert and R. Tixier, "Electron penetration and the atomic number correction in electron-probe microanalysis," *Brit. J. Appl. Phys.* 1: 685-694, 1968.
3. J. C. Russ, "Microanalysis of thin sections, coatings and rough surfaces," *SEM/1973* I, 114-119.
4. J. T. Armstrong and P. R. Buseck, "Quantitative chemical analysis of individual microparticles using the electron microprobe: Theoretical," *Anal. Chem.* 47: 2178-2192, 1975.
5. R. L. Myklebust, D. E. Newbury, and H. Yakowitz, "NBS Monte Carlo electron trajectory calculation program," in K. F. J. Heinrich, D. E. Newbury, and H. Yakowitz, Eds., *Use of Monte Carlo Calculations in Electron Probe Microanalysis and Scanning Electron Microscopy*, Washington, D.C.: NBS Special Publication 460, 105-125.
6. J. A. Small, K. F. J. Heinrich, D. E. Newbury, and R. L. Myklebust, "Progress in the development of the peak-to-background method for the quantitative analysis of single particles with the electron probe," *SEM/1979* II, 807-816.
7. J. A. Small, D. E. Newbury, and R. L. Myklebust, "Analysis of particles and rough samples by FRAME-P, a ZAF method incorporating peak-to-background measurements," *Microbeam Analysis--1979*, 243-246.
8. P. J. Statham and J. B. Pauley, "A new method for particle x-ray microanalysis based on peak-to-background measurements," *SEM/1978* I, 469-478.
9. N. C. Barbi, M. A. Giles, and D. P. Skinner, "Estimating elemental concentrations in small particles using x-ray analysis in the electron microscope," *SEM/1978* I, 193-199.
10. G. D. Aden, *Quantitative Energy Dispersive Analysis of Small Particles*, Ph.D. dissertation, Arizona State University, Tempe, 1981.
11. H. Yakowitz and D. E. Newbury, "A simple analytical method for thin film analysis with massive pure element standards," *SEM/1976* I, 151-162.
12. J. Philibert, "A method for calculating the absorption correction in electron-probe microanalysis," in H. H. Pattee, V. E. Cosslett, and A. Engstrom, Eds., *X-ray Optics and Microanalysis*, New York: Academic Press, 1963, 379-392.
13. R. L. Myklebust, K. F. J. Heinrich, and H. Yakowitz, *FRAME: An On-line Correction Procedure for Quantitative Electron Probe Microanalysis*, Washington, D.C.: NBS Tech. Note 796, 1973.
14. F. H. Schamber, "A new technique for deconvolution of complex x-ray spectra," *Proc. 8th Nat'l. Conf. Electron Probe Analysis*, 1973, 85-91.
15. G. D. Aden and P. R. Buseck, "Rapid quantitative analysis of individual particles by energy dispersive spectrometry," *Microbeam Analysis--1979*, 254-258.
16. G. D. Aden and P. R. Buseck, "Collection and preparation of particulate solids for quantitative electron-beam analysis," *SEM/1983* (in press).
17. J. I. Goldstein, "Statistics of x-ray analysis," *Proc. 11th Ann. MAS Conf.*, 1976, T1A-T1H.
18. J. T. Armstrong, "Methods of quantitative analysis of individual microparticles with electron beam instruments," *SEM/1978* I, 455-467.

## LIMITS TO QUANTITATION IN PARTICLE ANALYSIS: SOME EMPIRICAL DETERMINATIONS

A. M. Isaacs

It has been undertaken to evaluate empirically the limits to quantitation in the x-ray energy-dispersive analysis of particles. The limits investigated here are with respect principally to particle size and secondarily to elemental concentration. Raw concentration data were obtained on unpolished particulate standard olivines under carefully controlled conditions in scanning mode in a JEOL 100CX. These data were reduced by the program DUST2, developed at Johnson Space Center as a FORTRAN version of the Armstrong ZAF particle correction procedure. Errors for individual particle analyses were determined and then evaluated as a function of grain size for each element in each standard material. Results indicate that very reliable analyses may be obtained over a range of particle sizes. The results also suggest that, in general, concentration level more critically constrains analytical accuracy for single particles than does particle size.

### *Previous Investigation*

The error associated with particle analysis by electron beam techniques has been widely discussed.<sup>1-10</sup> The several particle analysis procedures currently in use have been evaluated for accuracy to varying degrees.<sup>1</sup> The study most directly applicable to this work is that of Aden who, using a reduction scheme different from ours and employing simple oxide standards, included a section directed specifically at analytical error as a function of particle size.<sup>2</sup> Aden examined the error in analyses for Na, Al, and Si in albite and Fe in pyrite from many variously sized particles. However, only a few of the particles examined had sizes in the range of interest here, from a few tenths of a micrometer to a couple of micrometers. Aden also presents tabulated results on particles of these and five other minerals indicating the average analytical error for several dozen grains of each, divided into two groups, greater or smaller than 1.0  $\mu\text{m}$  in diameter.<sup>2</sup> His data indicate that slightly better overall analyses may be obtained on the larger particles. However, his plots for albite and pyrite show a strong degradation in analytical quality for particles smaller than about 1  $\mu\text{m}$  in diameter, but the data are poorly constrained in that size range.

### *Technique*

We intend to examine the limits of quantitation attainable in individual microparticle analysis using rapid and generally applicable techniques and data-reduction routines. Of particular interest is the probable breakdown in analytical quality for particles with diameters smaller than the electron range (about 1-2  $\mu\text{m}$  for 20 kV in most geological materials) and greater than the thin-film condition (100-200 nm). Elemental x-ray intensities were obtained on standard particles with PGT energy-dispersive detectors and System IV analyzers on each of two JEOL instruments, a JSM-35CF and a JEM-100CX, under carefully controlled conditions at 20 kV. To date, only the data from the 100CX have been fully reduced; it is results from those analyses that are presented here.

The standards used for this portion of the study are three forsteritic olivines, which serve as standard materials in this facility. Olivines require fairly large atomic number and absorption corrections for accurate analysis, but are free of peak overlaps. Olivine is therefore generally considered an excellent standard with which to test the Z and A

---

The author, who is in the Planetary and Earth Sciences Department, MC C23, Lockheed at Johnson Space Center, Houston, TX 77058, is grateful to J. T. Armstrong and G. D. Aden for discussions and suggestions. The program DUST2 was adapted to FORTRAN by D. H. Anderson of JSC. Supported in part by grant RTOP 152-02-40-26 from the NASA Planetary Materials Program to D. S. McKay at JSC.

TABLE 1.--Analyses of standard olivines used as dispersed particulate "unknowns" and thick, polished standards.

	Marjahlatti	San Carlos	Forsterite (syn.)
SiO <sub>2</sub>	40.30	40.51	42.70
TiO <sub>2</sub>	---	0.02	---
Cr <sub>2</sub> O <sub>3</sub>	0.08	0.04	---
FeO	11.39	9.38	---
MnO	0.29	0.16	---
MgO	47.45	48.74	57.30
CaO	---	0.07	---
NiO	---	0.46	---
TOTAL	99.51	99.38	100.00

portions of the corrections. The compositions chosen, given in Table 1, are intended as an initial test of the procedures, and have now been expanded by the inclusion of other minerals.

Particles of each standard, mostly smaller than 10  $\mu$ m in diameter, were dispersed on holey carbon films supported by Be grids and coated with a thin layer of carbon. A polished microstandard of each material was also prepared, similarly to microprobe standards, but as part of a planchette compatible with the 100CX. Thus, for each material of known composition, x-ray data could be obtained from thick, polished mounts and also from unpolished particles dispersed on carbon films. This last aspect of sample preparation varies from many previous studies in that the thin carbon substrate used here produces a negligible bremsstrahlung contribution to the spectrum relative to that generated by the solid carbon substrates more commonly used. This feature is of particular importance in obtaining a high peak-to-background ratio on submicrometer particles where the generated flux of characteristic x rays is small.

Several instrumental conditions should be noted here. First, the 100CX instrument employed has a horizontal detector which requires that the sample stage be tilted to achieve a line of sight between the sample and the detector colimator. Second, the detector axis is 45° from the stage tilt axis, not the 90° common in many SEMs. Both these factors complicate the determination of an appropriate x-ray take-off angle.<sup>11,12</sup> An optimized take-off angle must thus be used, whereas in an instrument with a horizontal sample and a fixed, high take-off angle detector, the physically measured value is most valid. The input take-off angle is held constant throughout each set of calculations, but it is apparent that as particle size and shape vary, with electron range held constant (constant accelerating potential), the effective take-off angle may vary.<sup>1</sup> Since the absorption correction depends on the average take-off angle, the resulting analysis is affected. This aspect has been effectively tested by Aden who has shown that analyses from intensity data reduced by use of an extreme range of take-off angles vary generally by no more than 10%.<sup>2</sup> These relative errors were determined with a different correction program, but his results appear to be consistent with our own. Therefore, any empirically derived optimum take-off angle can be only a best-fit value if data are to be reduced for a variety of particle shapes and sizes.

Beam current was standardized in the 100CX by the use of a Faraday cup modification to the end of the backscattered electron detector immediately above the sample plane. To minimize incident current and take-off angle variations among the particulate samples and the polished standards, all intensity measurements were collected with the sample at the focused, eucentric position, an easily reproducible condition. Accelerating potential was determined by measurement of the Duane-Hunt bremsstrahlung limit. Detector and sample geometry and spectral collection conditions were standardized and reproduced for each data set. Particle data were collected with a rastered beam, and mean particle diameter was measured in the plane containing the incident beam and the detector axis. Finally, our 100CX instrument has been modified and found to be spectrally clean through incorporation of the column and sample environment alterations suggested by Allard and Blake.<sup>13</sup>



Raw elemental peak intensities were obtained from x-ray spectra on particles following a simple linear-fit background subtraction. Two 100s count spectra were collected on each particle and treated as separate analyses, rather than being averaged. Particles up to several micrometers in diameter of each of the three materials were analyzed, particularly in the size range of 0.5-1.5  $\mu\text{m}$ . The standard intensities were obtained under conditions identical to those for the particles, except that multiple spectra were averaged.

### *Data Reduction*

The program employed for data reduction is an in-house modification of Armstrong's ARMST1 program for the quantitative x-ray analysis of individual microparticles.<sup>3,14</sup> The program uses theoretically derived equations to correct for atomic number, absorption, and fluorescence effects in rough particles of an input mean size and approximate shape.<sup>15</sup> ARMST1 uses essentially the FRAME C correction procedure<sup>16,17</sup> modified by particle geometry, with a recent upgrade in the expression for x-ray production depth in the sample.<sup>4</sup> Our version, DUST2, is an RSX FORTRAN translation of ARMST1 from the original HP BASIC. DUST2 is also user-interactive, in that almost all variables in the reduction process may be modified in real time. A typical analysis with four elements and four iterations for convergence requires about 15 s for processing on our PDP 11/45. The necessary CPU time is therefore negligible compared to the analysis time involved. This program is available from the author upon request.

### *Results*

Results of the particle analyses are given on the plots of elemental relative error versus particle size which follow. For all of these plots, the polished Marjahlati olivine served as the analytical standard. Initially, a subset of the particle data was reduced by use of each of the five particle shape subroutines (Models) in DUST2, so as to determine empirically which of the geometries best approximated the mean particle shape over the range of sizes of these olivines. This test with a known particle composition for the best-fit model is probably a necessary precursor to the analysis of an unknown when one is using a geometry-approximating correction. Once the best model is determined, the full data set may be reduced.

Previous tests of this process have shown that most mineral fragments are best reduced by one particular model. For these cleavage-free olivine particles, however, geometry Model 4 (for particles with rounded tops and straight sides) and Model 5 (for particles with rounded tops and curved sides) gave analytical results of very nearly the same quality; both were better fits than the other models. Figure 1 is an example of the former case and Fig. 2 gives the latter. A comparison of these two plots shows that Model 5 data are shifted to slightly more negative values, but do not show a significantly greater spread of error than those of Model 4. Because this close similarity is consistently encountered, only results based on Model 4 will be given in the figures which follow.

It was anticipated that the errors for submicrometer particles would show a strong departure from the trend of errors for larger particles, and therefore a greater sample was obtained for 0.5-1.5  $\mu\text{m}$  particles. However, Figs. 1 and 2 show that although a decrease in analytical quality is evident in submicrometer particles, it is at worst a doubling of the relatively small error (about  $\pm 3\%$  maximum) for larger particles. For both of these data sets, about 76% of the analyses have errors less than  $\pm 2\%$  relative and about 95% have errors less than  $\pm 4\%$  relative, which is very good for particle analysis and is probably due to the high Mg concentration and the standard composition being identical to those of the particles, following the method of Armstrong.<sup>3</sup> The magnitude of the error is similar to that of Aden,<sup>2</sup> who gives a mean relative error of +3.8% for submicrometer particles and +2.0% for larger particles of a forsteritic olivine.

The results for Si and Fe analyses on the same set of particles are given in Figs. 3 and 4, respectively, which show trends not evident in the previous plots. Figure 3 indicates (a) that the analytical error for Si increases substantially for submicrometer particles, and (b) that the correction procedure produces results that are systematically high and yield a predominance of positive relative errors. For Fig. 3, 71% of the errors are within  $\pm 2\%$  relative and 95% are within  $\pm 4\%$  relative of the true value. Figure 4 again shows a clear systematic error to positive relative values. With only 25% of the analyses showing errors within  $\pm 2\%$  of the true value and 47% within  $\pm 4\%$ , this is a marked

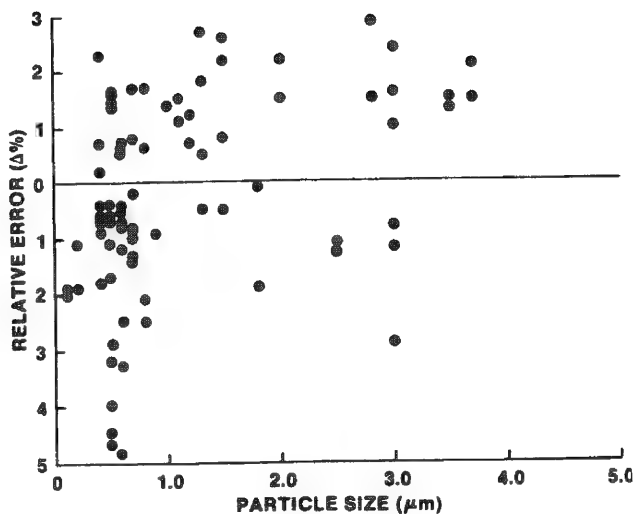


FIG. 1.--Analytical error for Mg in individual particles of Marjahlatti olivine vs size, Particle Model 4. (Marjahlatti olivine was used as standard material for these and following data.)

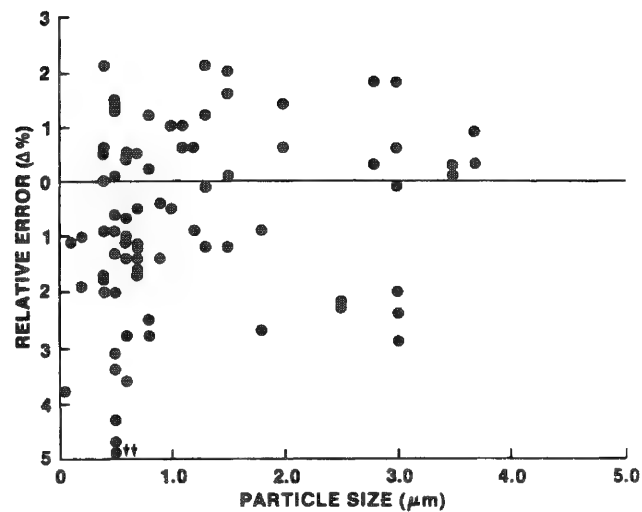


FIG. 2.--Analytical error for Mg in individual particles of Marjahlatti olivine vs size, Particle Model 5. (Arrows on this and following figures indicate data points just off figure.)

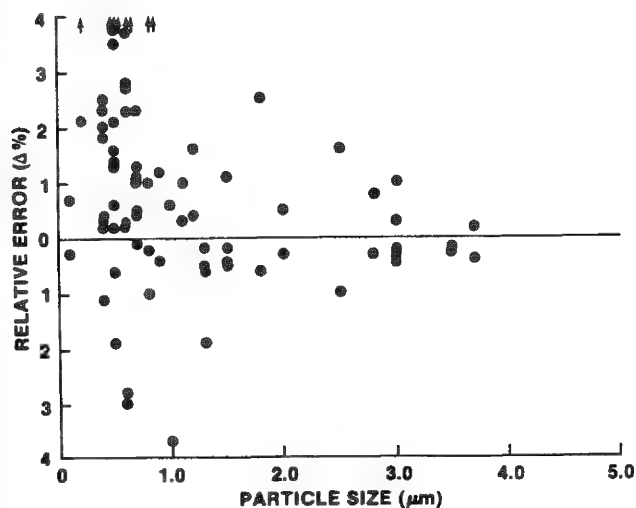


FIG. 3.--Analytical error for Si in individual particles of Marjahlatti olivine vs size.

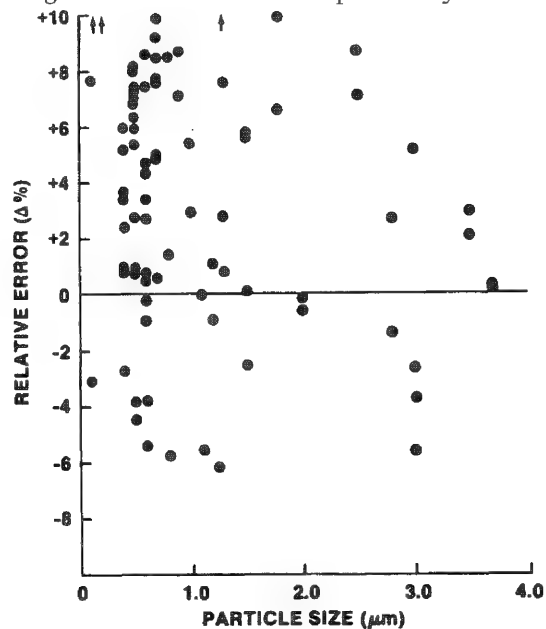


FIG. 4.--Analytical error for Fe in individual particles of Marjahlatti olivine vs size.

decrease in analytical quality, most likely due to the much poorer counting statistics on Fe in low concentration at 20 kV than for the other elements, combined with the systematic error. However, there is no obvious decrease in the error spread at the larger diameters based on the measured sample. Again, these relative errors are consistent with the data of Aden,<sup>2</sup> who found mean errors for Fe in olivine of -8.3% relative for submicrometer particles and -4.7% relative for larger particles.

Figures 5, 6, and 7 are analyses for Mg, Si, and Fe, respectively, on particles of San Carlos olivine, and show trends similar to those observed in the previous plots, which suggests that the types of errors observed are not specific to one material but are inherent in the procedures. Figure 5 shows no significant systematic error for Mg analyses, Fig. 6 shows generally positive relative errors for Si, and Fig. 7 has a strongly defined trend to positive errors. For the San Carlos data the sample is not large enough to define a change in the error as a function of size for particles larger than 2  $\mu\text{m}$ , although there is no significant variation among the smaller particles. Generally the errors at the  $\pm 4\%$  level are similar to those in the previous data set, with inclusion of 100% of the sample for Mg, 91% for Si, and 37% for Fe.

Figures 8 and 9 of the errors for forsterite analyses have equal but opposite trends with respect to each other. The errors for both Mg and Si increase for smaller particles, with the Mg analyses increasingly below the correct value and the Si data tending to higher values. At the  $\pm 4\%$  relative level, 96% of the Mg analyses and 79% of the Si analyses are included.

### *Conclusions*

The preceding data indicate that the techniques employed can routinely produce reasonable analyses on micrometer and smaller particles, particularly for elements present in concentrations greater than about 10%. There are several probable sources of error in these analyses, including systematic errors in the correction procedures, the take-off angle problem associated with particulate analysis, inaccurate background subtraction, counting statistic problems inherent in the EDS analysis of small particles, and other causes.

As to systematic correction errors, it has been established that DUST2 is identical to FRAME C and nearly equivalent to Bence-Albee data reduction for bulk samples. However, this result does not test for systematic errors in the particle geometry portion of the program. This work is also the first application of Armstrong's corrections directed specifically at submicrometer particles.<sup>18</sup> The most likely cause for the systematic errors observed is in the correction procedures, although this interpretation should be evaluated in greater detail.

The inaccuracy of the take-off angle used in data correction is unavoidable in analyzing particles, as that quantity is largely unknown, and variable as a function of particle size.<sup>1</sup> However, its effect is probably limited, as previously discussed. The geometry of the 100CX used to obtain these data is certainly not ideal; the data set collected in the SEM should show improvements, if only because of its conventional sample-detector arrangement.

Probably a major contribution to error is inaccurate background subtraction, which is critical for particle analysis.<sup>2</sup> This feature is also being improved with future data sets. Poor background subtraction is especially likely to introduce greater error for data from smaller particles with their lower peak-to-background ratios. The root cause of this effect is that as particle volume decreases, the mass of material generating characteristic x-rays decreases, a relationship that becomes a particular problem when EDS is used as the quantitative technique because of the low intensity of spectral lines.<sup>19</sup> Poor counting precision because of low characteristic x-ray intensity from the particle should tend to increase the scatter in relative errors at smaller diameters, an effect observed especially in Fig. 3. More, typically though, the spread of error does not appear to vary greatly as a function inverse to particle size (as in Fig. 4), which suggests that the level of concentration of an element of interest in a particle more critically controls the attainable accuracy than does particle size. Since relative error increases with decreasing elemental concentration, accuracies should be enhanced for minor elements in particles by increases in count rates and counting times, averaging of particle analyses if of identical composition, etc. Finally, the use of increasingly

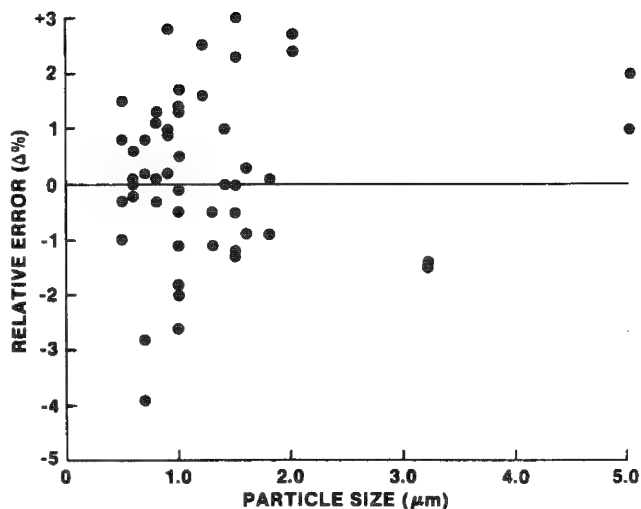


FIG. 5.--Analytical error for Mg in individual particles of San Carlos olivine vs size.

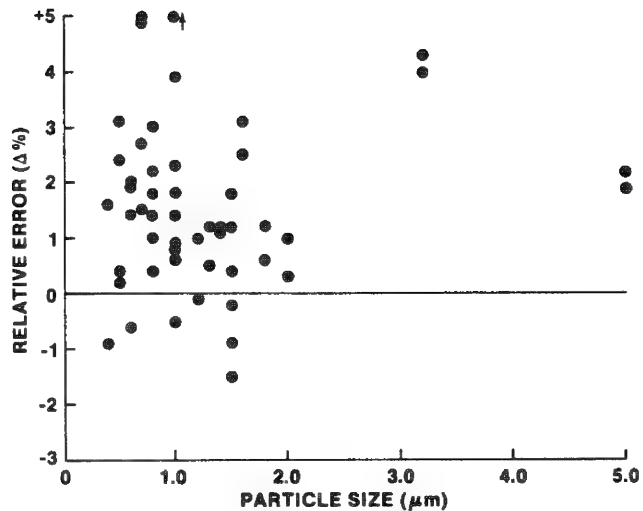


FIG. 6.--Analytical error for Si in individual particles of San Carlos olivine vs size.

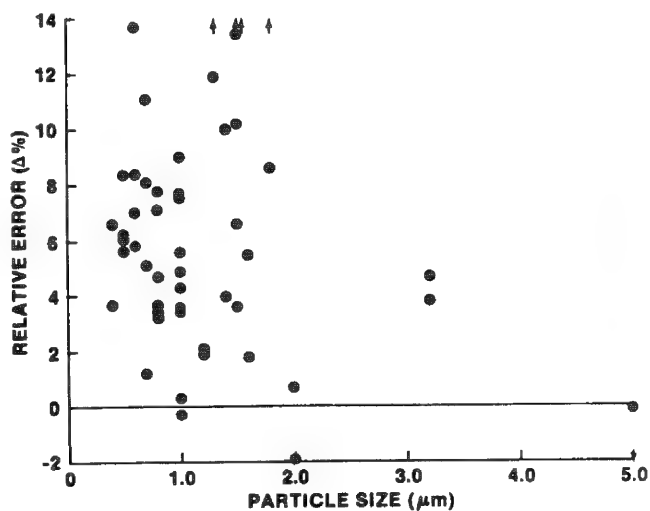


FIG. 7.--Analytical error for Fe in individual particles of San Carlos olivine vs size.

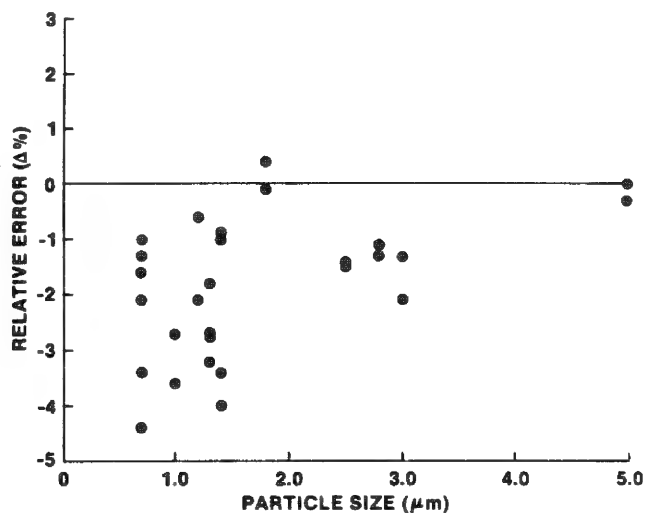


FIG. 8.--Analytical error for Mg in individual particles of forsterite vs size.

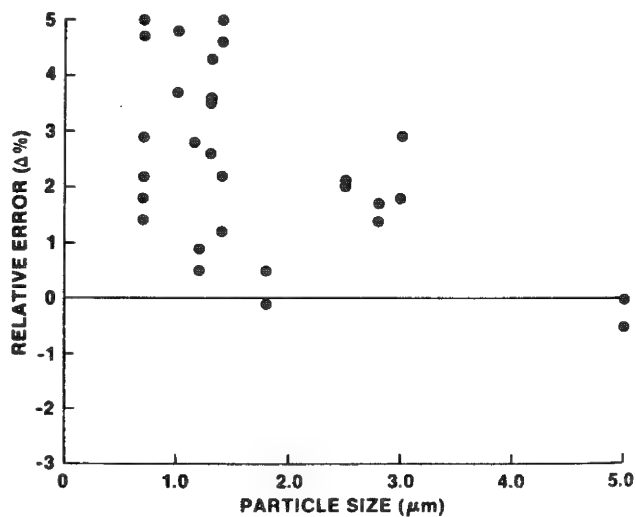


FIG. 9.--Analytical error for Si in individual particles of forsterite vs size.

dissimilar standards is likely to decrease the attainable accuracy in particle analysis by more strenuously testing the correction procedures. This effect is also currently being evaluated.

#### References

1. J. A. Small, "Quantitative particle analysis in electron beam instruments," *SEM/1981 I*, 447-461.
2. G. D. Aden, *Quantitative Energy Dispersive Analysis of Small Particles*, Ph.D. dissertation, Arizona State University, Tempe, 1981.
3. J. T. Armstrong, "Methods of quantitative analysis of individual microparticles with electron beam instruments," *SEM/1978 I*, 455-467.
4. J. T. Armstrong, "New ZAF and  $\alpha$ -factor correction procedures for the quantitative analysis of individual microparticles," *Microbeam Analysis--1982*, 175-180.
5. R. L. Myklebust and D. E. Newbury, "The use and abuse of a quantitative analysis procedure for energy-dispersive x-ray microanalysis," *Microbeam Analysis--1979*, 231-237.
6. R. L. Myklebust, J. A. Small, and D. E. Newbury, "Errors observed in the analysis of particle mixtures by overscanning," *SEM/1981 I*, 477-481.
7. J. T. Armstrong and P. R. Buseck, "Application of individual particle quantitative analysis in the determination of ambient and source aerosol heterogeneity," *Microbeam Analysis--1980*, 213-215.
8. J. T. Armstrong, "Rapid quantitative analysis of individual microparticles using the  $\alpha$ -factor approach," *Microbeam Analysis--1980*, 193-198.
9. P. J. Statham and J. B. Pawley, "A new method for particle x-ray micro-analysis based on peak to background measurements," *SEM/1978 I*, 469-478.
10. J. A. Small, D. E. Newbury, and R. C. Myklebust, "Analysis of particles and rough samples by FRAME P: A ZAF method incorporating peak-to-background measurements," *Microbeam Analysis--1979*, 243-246.
11. N. C. Barbi, *Electron Probe Microanalysis Using Energy Dispersive X-ray Spectroscopy*, Princeton Gamma-Tech, Princeton, N.J., 1980.
12. D. E. Newbury, R. L. Myklebust, K. F. J. Heinrich, and J. A. Small, "Monte Carlo electron trajectory simulation: An aid for particle analysis," in *Characterization of Particles*, Washington, D.C.: NBS Special Publication 533, 1980, 39-62.
13. L. F. Allard and D. F. Blake, "The practice of modifying an analytical electron microscope to produce clean x-ray spectra," *Microbeam Analysis--1982*, 8-20.
14. J. T. Armstrong, *Quantitative Electron Microprobe Analysis of Airborne Particulate Material*, Ph.D. dissertation, Arizona State University, Tempe, 1977.
15. J. T. Armstrong and P. R. Buseck, "Quantitative chemical analysis of individual microparticles using the electron microprobe: Theoretical," *Anal. Chem.* 47: 2178-2192, 1975.
16. R. L. Myklebust, C. E. Fiori, and K. F. J. Heinrich, "FRAME C: A compact procedure for quantitative energy-dispersive electron probe x-ray analysis," *Microbeam Analysis--1977*, 96.
17. R. L. Myklebust, C. E. Fiori, and K. F. J. Heinrich, *FRAME C: A Compact Procedure for Quantitative Energy-Dispersive Electron Probe X-ray Analysis*, Washington, D.C.: NBS Technical Note 1106, 1979.
18. J. T. Armstrong, personal communication, 1983.
19. D. R. Beaman and L. F. Solosky, "Accuracy of quantitative electron probe micro-analysis with energy dispersive spectrometers," *Anal. Chem.* 44: 1598-1610, 1972.

## FABRICATION OF METALS AND METAL ALLOYS AS PARTICLE STANDARDS

J. A. Small, J. A. Norris, and R. L. McKenzie

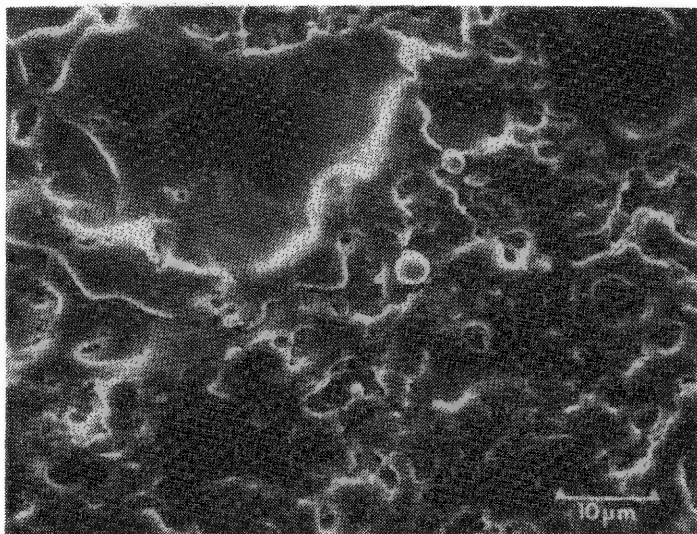


FIG. 1.--Micrograph of spark interaction zone on analyte material.

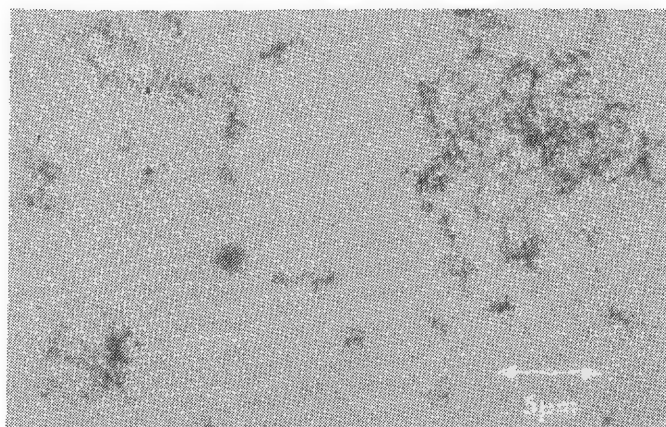


FIG. 2.--Micrograph of type one particles.

molten analyte material expelled from the bulk sample. The particles are spherical in shape, range in size from 100 nm to about 5 μm, and are polycrystalline.

The particles are removed from the spark region in an Ar stream. They are prepared for analysis directly on thin films supported by transmission electron microscope grids. The collection is made with an NBS-designed electrostatic/thermal precipitator. In addition, the sampler can be equipped with a backup filter for additional particle collection.

To test the utility of this approach for fabrication of standards, we are testing

For the past several years the micro-analysis group at the National Bureau of Standards has maintained a program for the development of microanalytical standards.<sup>1</sup> The primary materials used for these standards are multielement glasses made from high-purity metal oxides and halides. In an effort to extend the use of these standards to individual particle analysis, the glasses have been formed into fibers, irregular particles, and spheres.<sup>2-4</sup> The fibers are extracted from a melt by a high-speed rotating drum and are limited to diameters generally greater than 5 μm. The irregular particles are made by grinding of the bulk glass in a carbide mortar and pestle and the spheres are formed by heating of the ground shards.

Recently, in studying the mechanism of analyte excitation in spectrochemical analysis, it was noticed that the spark of the emission spectrometer very efficiently produced particles in the 5nm-10μm range. This process may be suitable for the production of particle standards, since it produces a large number of pure metal or metal alloy particles with a broad size range. Since the particles can be produced in large numbers, they can be used as particle standards for both micro and bulk analytical techniques.

The spark interaction area on the analyte, shown in Fig. 1, produces two basic types of particles. Particles of the first type are probably formed from condensed vapor and are 5-10 nm in diameter (Fig. 2). These particles usually form large aggregates and are crystalline. Particles of the second type, an example of which are shown in Fig. 3, are probably formed from

The authors are at the Center for Analytical Chemistry, National Bureau of Standards, Washington, DC 20234.

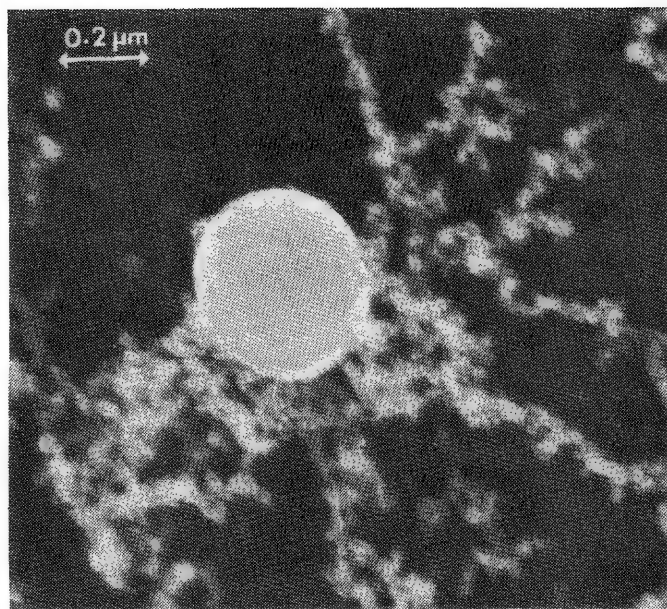


FIG. 3.--Micrograph of type two particles.

particles formed from binary alloys of known composition. The homogeneity and final composition of the particles will be compared to the composition of the starting materials.

#### References

1. C. E. Fiori et al., "An overview of the glass standards program for microanalysis at the National Bureau of Standards," *Microbeam Analysis--1976*, 27.
2. J. A. Small et al., "The production and characterization of glass fibers and spheres for microanalysis," *SEM/1978 I*, 445-454.
- J. A. Small et al., "Procedure for the quantitative analysis of single particles with the electron probe," in *Characterization of Particles*, NBS SP-553, Washington, D.C.: Government Printing Office, 1980, 29-38.
4. R. A. Velapoldi et al., "Inorganic ion-doped glass fibers as microspectra fluorimetric standards," *J. Microscopy* 103: 293, 1974.



## Microbeam Analysis in Biological Science

### PEAKLESS CONTINUUM: INACCURACIES IN BIOLOGICAL QUANTIFICATION BY MEANS OF THE ANALYTICAL MICROSCOPE

R. R. Warner, M. C. Myers, and D. A. Taylor

The Hall technique for quantitative analysis of thin biological samples requires accurate measurement of continuum x rays originating from the sample. Since the EDS detector collects continuum from a number of additional (nonsample) sources, these sources must be identified and either eliminated or their contribution quantified. We report a previously unappreciated source of extraneous radiation, the peakless continuum, which can be a major problem for biological quantitation in analytical electron microscopes. This continuum varies in magnitude across the available area of a specimen grid. We are developing a procedure to minimize the effects of this extraneous continuum on analytical measurements and report initial attempts to identify and eliminate the source of this problem.

#### *The Hall Technique*

The Hall continuum-normalization method<sup>1,2</sup> is the technique most frequently used for quantitative analysis of thin biological samples. In spite of its popularity, proven accuracy<sup>3,4</sup> and potential simplicity,<sup>4</sup> it remains a difficult and demanding technique to use correctly. The unwary user can easily obtain results that are inaccurate but give no indication of underlying analytical problems. In the Hall continuum-normalization method, element concentrations  $C$  are obtained from element x-ray intensities  $I$  by use of the equation<sup>2</sup>

$$C_{sp} = \frac{(I/I_w)_{sp} (Z^2/A)_{sp}}{(I/I_w)_{st} (Z^2/A)_{st}} C_{st}$$

In this equation, subscripts  $sp$  and  $st$  refer to the specimen and standard, respectively,  $I_w$  is the continuum x-ray intensity (bremsstrahlung) from the sample integrated over a given energy range, and  $Z^2/A$  is the mass fraction average (for all elements within the analyzed volume) for the ratio of atomic number squared over atomic weight.

Most difficulties with the Hall technique occur in obtaining accurate measurements of  $I_w$ .  $I_w$  represents the continuum that originates from the sample only, whereas the continuum measured by the EDS detector may originate not only from the sample but from additional (extraneous) sources as well. The sources of extraneous continuum must be identified and either eliminated or their contributions subtracted. Identified sources of extraneous continuum for which there are established correction procedures are the underlying support film,<sup>4</sup> contamination at the point of analysis,<sup>3,5</sup> and electrons scattered by the sample which generate x-rays from surrounding metallic surfaces (e.g., grid bars).<sup>2,3</sup> It is easy to detect this last component of extraneous continuum by the presence of the associated extraneous element peak in the spectrum. We refer to this component as the "peak-associated" continuum.

We believe there are sources of extraneous continuum in an analytical electron microscope in addition to those mentioned above. These other sources contribute in a major way to the continuum recorded by EDS detectors. We show that additional extraneous sources can severely limit the accuracy of biological quantitative measurements.

#### *Peakless Continuum*

In a quantitative analysis for sulfur in sections of human hair,<sup>6</sup> we observed consistent structure-associated differences in sulfur concentration in a single

---

The authors are at Procter and Gamble Co., Box 39175, Cincinnati, OH 45247.

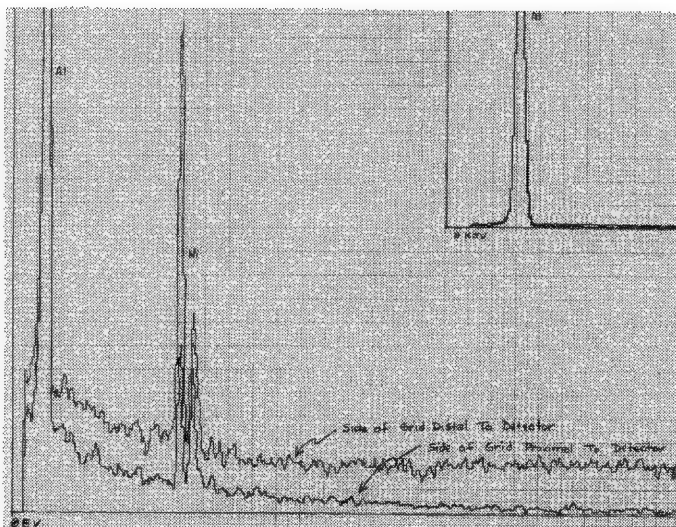


FIG. 1--Spectra from 0.75 m Al foil mounted on nickel grid and analyzed at a position proximal (lower trace) and distal (upper trace) to detector along long axis of slot grid.

hair section but a large variation in concentration among different sections. Initially we attributed the scatter in these numbers to biological variation. However, we discovered an alternate explanation for this variability when we successfully reduced our peak-associated extraneous continuum by switching from conventional EM mesh grids to slot grids (in which bulk metal is further removed from the sample). With slot grids we noticed that the continuum intensity was a strong function of the section location within the slot. The peak-associated extraneous continuum was not responsible for this pattern; removal of extraneous peaks and their associated continuum by established correction procedures<sup>2,3</sup> had little effect on the observed variation in the continuum. We have defined this non-peak-associated extraneous radiation as "peakless continuum."

We investigated the pattern of this peakless continuum using Formvar films or thin foils (aluminum or silver) mounted on a nickel slot grid (1 × 2 mm). The grid was positioned for analysis with the long axis of the slot aligned in the direction of the detector (projected in the horizontal plane). Aluminum and silver foils were obtained from Reactor Experiments, San Carlos, Calif. Analysis was at 100 kV with a high-angle detector; the continuum was integrated over the energy ranges of 4 to 7 keV and 10 to 20 keV.

In our instrument the variation in continuum intensity occurred in the direction parallel to the (projected) detector axis; variation was not observed perpendicular to the detector axis. The magnitude of the continuum variation was a function of the electron scattering properties of the foil. The variation in continuum intensity was greatest with the silver foil and not detectable with a Formvar film. The silver  $K\alpha$  peak/continuum ratio ( $I/I_w$ ) on a homogeneous silver foil (0.15  $\mu$ m) varied from 13 at the analysis position most proximal to the detector to 2 at the most distal position. Similar results with an aluminum foil are shown in Fig. 1, which shows that the aluminum  $K\alpha$  peak intensity was approximately the same in the two locations, but the continuum, corrected for extraneous peak-associated contributions (not shown), varied by a factor of 4. This observation explains our results on hair. Since hair sections are small with respect to the available slot grid area, consistent results were obtained on any one section, but variability was observed among different sections depending on their position on the grid.

In addition to making measurements on our instrument, we tested several other analytical microscopes (having a variety of detector geometries) for peakless continuum. The peakless continuum was most apparent in instruments having high-angle detectors (Fig. 2). The spectra in Fig. 2 were obtained from the same sample (a 0.15  $\mu$ m silver foil) at approximately the same analysis position and under similar analytical conditions. The upper spectrum was obtained with a high-angle detector and the lower spectrum with a horizontal detector. The lower spectrum is similar in shape to that which would be predicted from theoretical models,<sup>7</sup> whereas the upper spectrum shows an abnormally elevated continuum in the high-energy region.

Although horizontal EDS detectors appear to have fewer problems with extraneous background than the high-angle detectors, it would be incorrect to conclude that horizontal detectors have no problems. We have noticed significant changes in the shape of the continuum measured from opposite sides of a homogeneous foil using a horizontal detector. These changes suggest a difference in absorption or a difference in the target(s) seen by the detector at the two sites.

#### *Sources of the Peakless Continuum*

We believe at least two sources contribute to the peakless continuum: hard x rays and

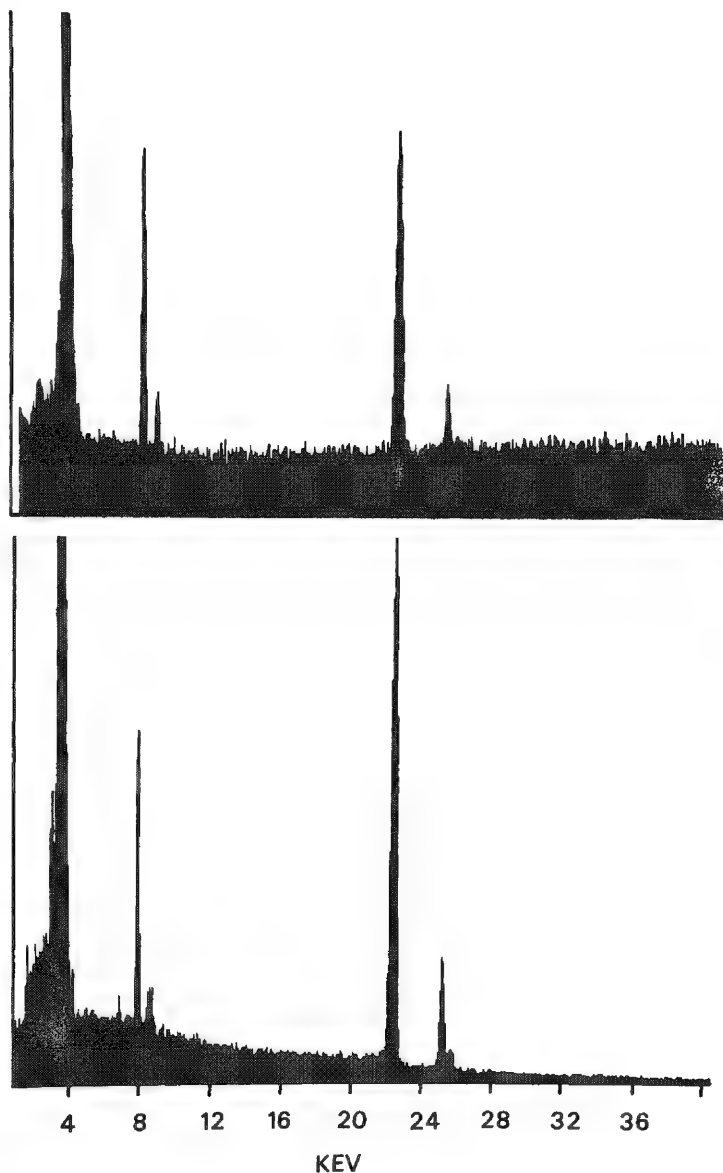


FIG. 2.--Spectra from a 0.15 $\mu$ m Ag foil mounted on nickel grid and analyzed at 100 kV in two different analytical microscopes. Analysis was on distal edge of foil in both cases. Upper spectrum obtained with high-angle detector; lower spectrum obtained with detector with low take-off angle.

the sample and standard will be similar and will have equivalent electron scattering properties. In addition, the spatial juxtaposition of sample and standard will minimize the effect of the inhomogeneous distribution of the peakless continuum across the slot grid.

### *Summary*

We have demonstrated the existence of extraneous continuum that is distributed inhomogeneously across the available area of a slot grid and is not associated with an element peak. This peakless continuum exists in most of the analytical microscopes we evaluated and can compromise the accuracy of quantitative measurements by the Hall technique. The problem most likely arises from a number of sources but can be eliminated or minimized by improved detector shielding, improved objective polepiece and anticontamination device design, and the use of appropriate procedures for sample analysis.

backscattered electrons. Hard x rays can pass through the detector window or snout and produce continuum either directly or by Compton scattering.<sup>8</sup> This effect may be greater for high-angle detectors that are more exposed to column-generated hard radiation. However, based on the shape of our continuum, we believe that it is backscattered electrons that generate the bulk of the peakless continuum present in our instrument. Backscattered electrons from the specimen area or from the lower objective pole piece can be swept toward the detector, particularly a high-angle detector, by the magnetic field of the objective lens. These electrons can directly enter the detector or can generate continuum x rays by interacting with low-Z elements (carbon and beryllium) typically used by instrument manufacturers to reduce system peaks.

### *Solution to the Peakless Continuum Problem*

The ideal solution to the peakless continuum problem is to identify and eliminate the source(s) of extraneous radiation. This has proven to be a nontrivial task. We have improved our detector shielding<sup>8</sup> and are modifying (with the manufacturer's help) our anticontamination device and the lower objective lens pole piece. It may not be possible to eliminate peakless continuum completely; consequently, we are developing a software approach that we believe will minimize the problem.<sup>9</sup> The Hall procedure is a ratio technique that by nature is very forgiving of additive errors. If errors in the continuum measurement are similar in the sample and standard, they will tend to cancel. If appropriate external standards are applied to (and sectioned with) the sample, the mass thickness of

## References

1. T. Hall, "The microprobe assay of chemical elements," in: G. Oster, Ed., *Physical Techniques in Biological Research*, New York: Academic Press, 1971, 157-275.
2. T. A. Hall, "Problems of the continuum-normalization method for the quantitative analysis of sections of soft tissue," in: C. Lechene and R. R. Warner, Eds., *Microbeam Analysis in Biology*, New York: Academic Press, 1979, 185-208.
3. H. Shuman, A. V. Somlyo, and A. P. Somlyo, "Quantitative electron probe micro-analysis of biological thin sections: Methods and Validity," *Ultramicroscopy* 1: 317-339, 1976.
4. B. L. Gupta, M. J. Berridge, T. A. Hall, and R. B. Moreton, "Electron microprobe and ion-selective microelectrode studies of fluid secretion in the salivary glands of *Calliphora*," *J. Exp. Biol.* 72: 261-284, 1978.
5. J. J. Hren, "Barriers to AEM: Contamination and etching," in: J. J. Hren, J. I. Goldstein, and D. C. Joy, Eds., *Introduction to Analytical Electron Microscopy*, New York: Plenum Press, 1979, 481-505.
6. M. C. Myers, J. Van, and R. R. Warner, "Ultrastructural distribution of sulfur in human hair," in: *Microbeam Analysis--1981*, 210-212.
7. C. E. Fiori, R. L. Myklebust, K. F. J. Heinrich, and H. Yakowitz, "Prediction of continuum intensity in energy-dispersive x-ray microanalysis," *Anal. Chem.* 48: 172-176, 1976.
8. C. E. Fiori and D. E. Newbury, "Operation of energy-dispersive x-ray spectrometers in the analytical electron microscope," in: *Analytical Electron Microscopy--1981*, San Francisco: San Francisco Press, 1981, 17-24.
9. R. R. Warner and J. C. Wirfel, "A comprehensive computer program for the quantitative analysis of thin biological sections," *Microbeam Analysis--1983*, 231.

## BREMSSTRAHLUNG PRODUCTION IN THIN SPECIMENS AND THE CONTINUUM NORMALIZATION METHOD OF QUANTITATION

W. A. P. Nicholson and J. N. Chapman

Most schemes for the reduction of x-ray spectral data to give elemental concentrations in thin specimens are based on the fact that the characteristic line intensity is proportional to the number of atoms of the element in the volume of the sample excited by the beam. Evidently variations in the characteristic intensity can reflect changes in both the specimen thickness and density, i.e., mass-thickness variations as well as changes in composition. The continuum normalization (C-N) or Hall method<sup>5-8</sup> seeks to eliminate the effect of mass-thickness variations by use of the intensity of some region of the bremsstrahlung, since this parameter depends on the total number of atoms excited by the beam, i.e., the total mass-thickness. Thus, the ratio of the characteristic to bremsstrahlung intensities is approximately independent of mass-thickness and proportional to the atomic fraction of the element. For microanalysis of thin specimens the mass fraction is a more usual measure of the elemental concentration; it can be defined as

$$F_x = \frac{\text{mass per unit area of element } x \text{ in beam}}{\text{total mass per unit area in beam}} = \frac{M_x}{M_t} \quad (1)$$

The characteristic count  $P_x$  is proportional to  $M_x$ :

$$P_x = K_x M_x \quad (2)$$

where  $K_x$  is a constant. In his development, Hall<sup>5</sup> uses Kramer's 1923 theory of bremsstrahlung production, which predicts that the bremsstrahlung intensity will be proportional to  $\sum_r N_r Z_r^2$  (providing the energy band of the bremsstrahlung is not close to the electron energy), where  $N_r$  is the number of atoms/unit area and  $Z_r$  is the atomic number of element  $r$  in the sample, and the sum is taken over all  $r$  elements in the sample.  $\sum_r N_r Z_r^2$  can be written in terms of  $M_t$ :

$$\sum_r N_r Z_r^2 = N_0 M_t \sum (F_r Z_r^2 / A_r) \quad (3)$$

where  $N_0$  is Avagadro's number,  $A_r$  is the atomic weight, and  $F_r$  is the mass fraction of element  $r$ , so that the bremsstrahlung count can be written

$$B = K_t M_t \sum (F_r Z_r^2 / A_r) \quad (4)$$

and  $P_x/B$  is hence proportional to  $F_x$ . If we divide Eq. (2) by Eq. (4),

$$F_x = \frac{M_x}{M_t} = \frac{K_t P_x}{K_x B} \sum (F_r Z_r^2 / A_r) \quad (5)$$

The constant  $K_t/K_x$  can be eliminated by measuring the peak to bremsstrahlung ratio for  $x$  on a standard  $(P_x/B)_{st}$ , so that:

$$F_x = \frac{(P_x/B)_{sp} [\sum_r (F_r Z_r^2 / A_r)]_{sp}}{(P_x/B)_{st} [\sum_r (F_r Z_r^2 / A_r)]_{st}} F_s \quad (6)$$

The authors are at the Department of Natural Philosophy, University of Glasgow, Scotland, G12 8QQ.

where  $F_s$  is the concentration of the element  $x$  in the standard and the external suffices of the sums, sp and st, refer to the specimen and the standard, respectively. The equation may be rearranged to eliminate the quantities  $F_x$  in the specimen which are unknown, provided characteristic lines of all the elements in the sample are detectable. In biological samples that is not usually the case as the matrix contains carbon, oxygen, nitrogen, and hydrogen. However, if an assumption is made about their relative proportions, then the  $(F_x)_{sp}$  can still be eliminated.<sup>5</sup> Evidently if the mean value of  $Z^2/A$  is the same for the specimen and the standard as is often the case when organic standards are used, Eq. (6) can be much simplified:

$$F_x/F_x = [P_x/B]_{sp}/[(P_x/B)_{st}] \quad (7)$$

The inaccuracies that may arise in quantitative analyses of biological specimens by the C-N method fall into three groups: (1) limitations in the basic theory, (2) difficulty in extracting the peak and bremsstrahlung intensities due to the specimen from the recorded spectrum, and (3) limitations imposed by changes in mass of specimen under the beam. The last effect can be due to contamination increasing the total mass under the beam, radiation damage decreasing the specimen mass, and inadvertent changes in the state of hydration during analyses of frozen hydrated specimens. These topics will not be considered further here, but the interested reader is referred to recent reviews.<sup>6-8,14</sup> We shall consider the help basic x-ray theory can give in estimating the likely magnitude of the errors in areas 1 and 2.

#### *Bremsstrahlung Production in Thin Specimens*

We have investigated a number of theories of bremsstrahlung production to find a formula, suitable for evaluating in a minicomputer, which would accurately predict x-ray production in thin specimens.<sup>2</sup> The definition of "thin" implies that the average energy lost by the electrons as they pass through the specimen must be small compared to their incident energy. Comparison with experimental spectra showed that a modified form of the Bethe-Heitler theory (MBH) predicts the bremsstrahlung shape well (better than 5%), and predicts the absolute magnitude with an average error of about 10% for the ranges investigated; viz., electron energies 40 to 100 keV, photon energies 3 to 16 keV, and atomic numbers 6 to 79.

Figure 1 shows how the reduced cross section for bremsstrahlung production  $\sigma''$  varies theoretically and experimentally with x-ray energy for aluminum. We obtained  $\sigma''$  by multiplying the true cross section by  $h\nu T_0/Z^2$ , where  $h\nu$  is the photon energy and  $T_0$  that of the incident electron. From Kramer's theory  $\sigma''$  would be constant, but as Fig. 1 shows MBH predicts that it decreases with increasing  $h\nu$  and  $T_0$ . The experimental data show that this prediction is borne out in practice. The spectra were recorded from a 60nm-thick aluminum foil in a JEOL JEM 100C transmission electron microscope with the specimen tilted at 20° toward the x-ray detector and the detector axis normal to the electron beam (90° geometry). Before experimental values of  $\sigma''$  were calculated extraneous contributions were removed from the recorded spectra in the way described in the remainder of this paper. Aluminum was selected as the example here because its atomic number (13) is in the range normally found in biological specimens, since  $\bar{Z} \approx 6$  for soft tissue and  $\approx 15$  for fully mineralized tissues.

Figure 2 shows the bremsstrahlung data presented in a different form-- $\sigma''$  as a function of atomic number for several electron energies and x-ray energies. It can be seen that the  $Z^2$  dependence assumed in the C-N quantitation is most closely followed at higher electron and photon energies. To evaluate the magnitude of errors that could occur in practice, we have taken as an example (possibly a worst case) the analysis of low concentrations of calcium in an organic matrix ( $\bar{Z} \approx 6$ ) for which enamel (mainly hydroxyapatite,  $\bar{Z} \approx 15$ ) is used as a calcium standard. We have calculated the ratio of the bremsstrahlung intensities  $(B)_{sp}/(B)_{st}$ , predicted by MBH and Kramer's law for photon energies similar to those which have been used in practice for C-N, i.e., 1.5 keV,<sup>13</sup> 5 keV,<sup>10</sup> 15 keV,<sup>9,11</sup> 20 keV.<sup>9</sup> The amount by which the calcium concentration is in error due to Kramer's theory in C-N is shown in Table 1. Providing the bremsstrahlung radiation is not monitored at low photon energies nor at energies too close to the incident electron energy, the  $Z^2$  assumption leads to modest errors. Hall and Werba<sup>9</sup> and Krefting et al.<sup>10</sup> examined the

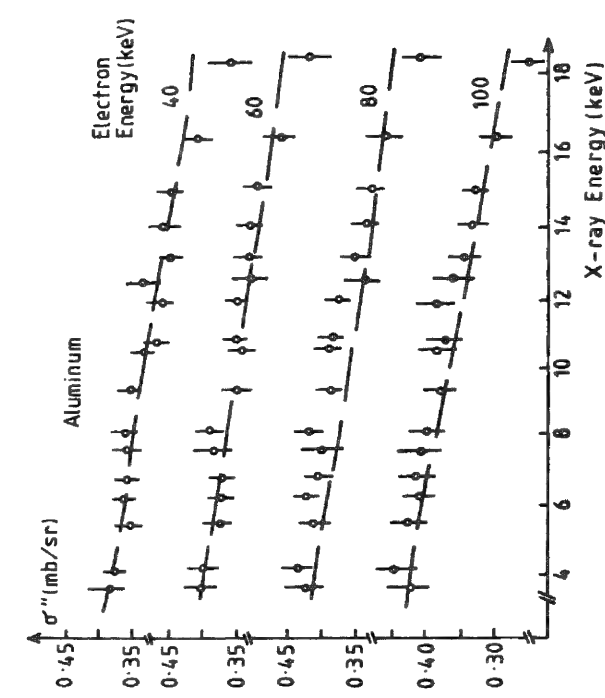


FIG. 1--Reduced cross section for aluminum as function of x-ray energy; dashed lines show values predicted by modified Bethe-Heitler theory.

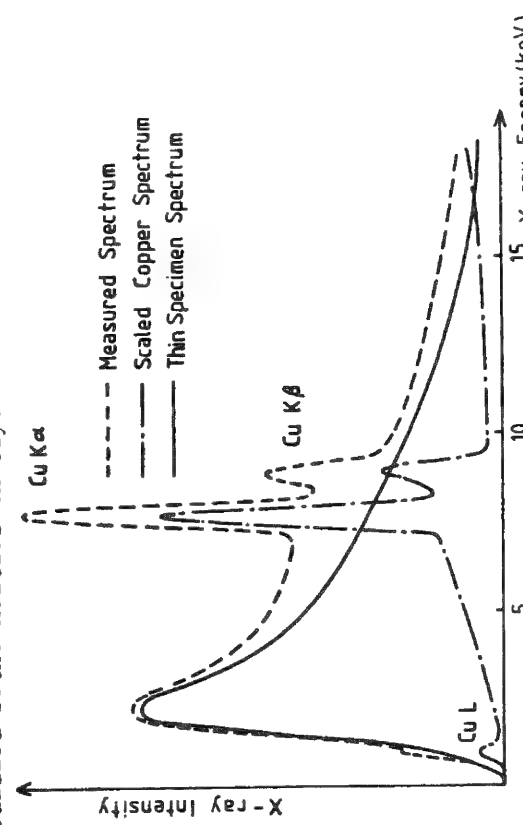


FIG. 3.--Scheme for obtaining thin-specimen spectrum by removal of instrumental spectrum. X-ray lines of copper down by a factor of ca 18 relative to copper background.

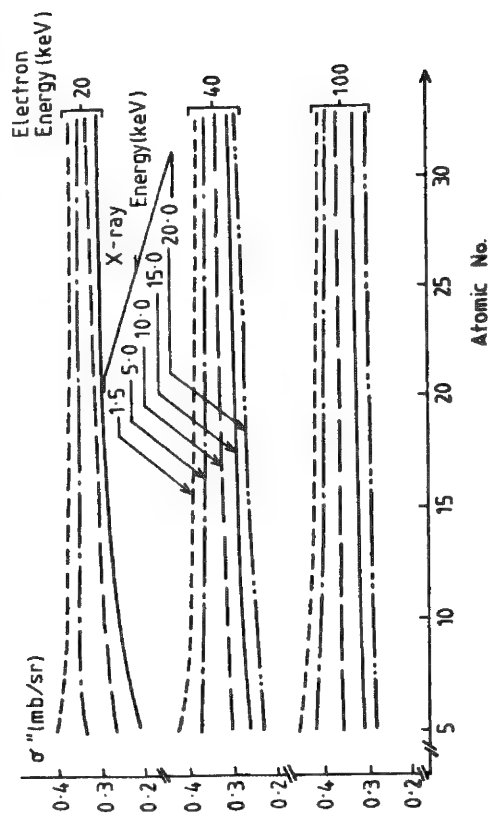


FIG. 2.--Reduced cross section as function of atomic number.

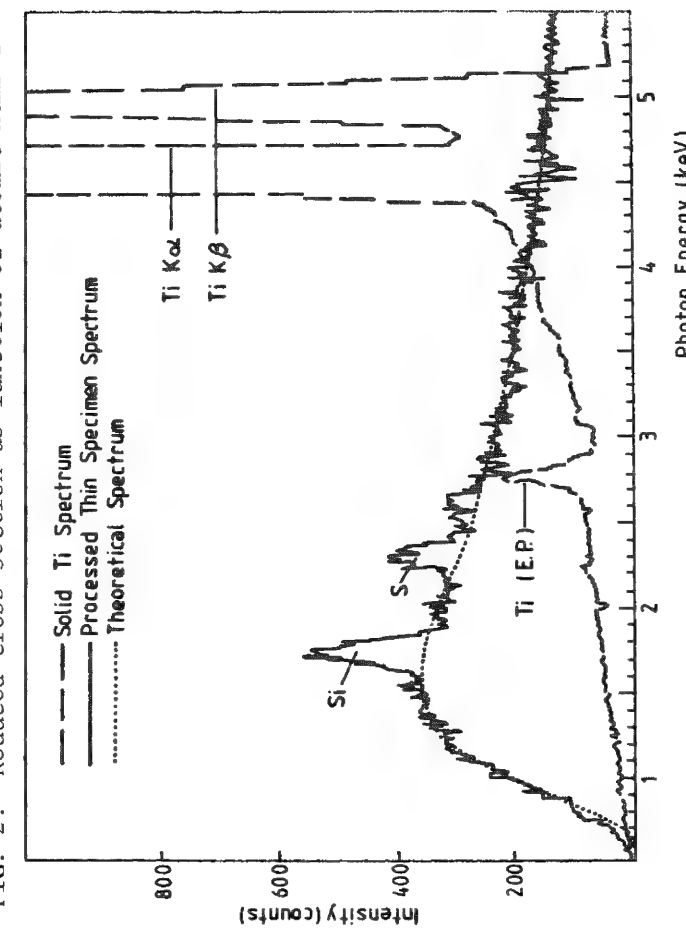


FIG. 4.--Fitting of (theoretical spectrum)  $\times$  (detector efficiency) to experimental thin spectrum. Scaled titanium spectrum shown  $2\times$ .



TABLE 1.--Error % in calculated elemental concentration for specimen  $\bar{Z} = 6$  using standard  $\bar{Z} = 15$  assuming  $Z^2$  proportionality for bremsstrahlung production.

Photon Energy (keV)	Electron Energy (keV)				
	20	40	60	80	100
1.5	4.7	6.1	6.6	6.7	7.0
5.0	-2.6	1.1	2.6	3.2	3.9
10.0	-10.8	-3.1	-0.9	-0.3	1.1
15.0	-22.0	-6.3	-3.0	-1.3	-0.3
20.0	xx	-10.6	-5.1	-2.8	-1.7

intensity from the support film is about half that due to the specimen, since their densities and mean atomic numbers are similar. However, support foils are generally very uniform in thickness and so by averaging measurements from several different areas of foil, one can keep the error in this subtraction close to that due to counting statistics.

Methods of minimizing the instrumental contribution to the measured x-ray spectrum have been discussed extensively in the literature.<sup>3,7,12</sup> The essential features are (1) to insure by careful collimation that the incident electron beam is 'clean,' i.e., that there are insignificant numbers of electrons and x-rays peripheral to the main beam incident on the specimen; and (2) that the mass of solid materials both above and below the specimen (onto which electrons will be forward- or backscattered) which the x-ray detector can "see" is cut down to the minimum mechanically feasible and that these materials are of a low atomic number to reduce x-ray production.<sup>12</sup> The principle of estimating the instrumental contribution to the measured spectrum requires the solid components to have a characteristic line which is detectable by the x-ray detector used for measuring the bremsstrahlung intensity, usually a Si(Li) detector. The procedure is to record a spectrum from the pure solid material under constant instrumental conditions, i.e., accelerating voltage and specimen-detector geometry. This solid spectrum is then scaled to the height of its characteristic line in the specimen spectrum and subtracted (Fig. 3). In practice we are usually only interested in the bremsstrahlung intensity integrated over a particular window, so that the solid correction can be made as a single scaling factor. The value of (B)foil should be corrected for the instrumental contribution in the same way.

Usually the largest source of the instrumental bremsstrahlung is the specimen grid. By use of beryllium or carbon-coated nylon grids this source may be minimized and then ignored. However, it is much better to use a support of relatively low atomic number (e.g., aluminum, titanium, copper) for which the corrections can be calculated. The choice of metal is, of course, determined by consideration of what overlaps may occur with expected characteristic lines from the specimen. For example, aluminum would not be used if sodium, magnesium, or aluminum peaks were expected from the specimen.<sup>1</sup>

The assumption made in the correction procedure is that the solid bremsstrahlung shape is the same in the two cases; that is unlikely, since the pure solid spectrum will be recorded with mono-energetic electrons and the angle between the beam and the solid surface and the x-ray take-off angle will both be well defined. The stray instrumental contribution to the specimen spectrum will be generated by electrons often multiply scattered through a range of angles and with a range of energies, so that the intensity and shape

$Z^2$  dependence experimentally over the range  $\bar{Z} = 5$  to  $\bar{Z} = 35$  and within their experimental errors their conclusions agree with ours.

#### Bremsstrahlung Corrections

Evidently, in the calculation of the ratio of peak to bremsstrahlung, the bremsstrahlung intensity used must be that originating from the specimen alone; i.e., the bremsstrahlung contribution from any foil supporting the specimen and from solid materials in the microscope surrounding the specimen must be evaluated and subtracted, so that in general

$$(B)_{\text{specimen}} = (B)_{\text{measured}} - (B)_{\text{foil}} - (B)_{\text{solids}}$$

Some error is involved in measuring the foil contribution, since these measurements must be made on regions of the foil surrounding the specimen. For a typical specimen of 100 nm of soft tissue supported on a 50nm organic film, the bremsstrahlung

of the bremsstrahlung when normalized to the characteristic line will only be to a first approximation the same as the pure solid spectrum. In unfavorable geometries, where a substantial fraction of the stray spectrum generated is transmitted to the detector through the specimen mount, absorption can severely affect the stray spectrum.<sup>6,12</sup> A simple method for demonstrating the success (or otherwise) of the solid correction procedure is to determine how well the resulting corrected spectrum represents a thin specimen; that is, by examining how well the experimental spectrum fits to that predicted by MBH when an appropriate scaling factor is applied.

Curves for the reduced cross sections of all elements in the energy ranges of interest are of a form similar to those in Fig. 1 and it is possible to fit them with a quadratic equation to an accuracy of about 1.5%.<sup>4</sup> The three coefficients are different for different atomic numbers, electron energies, and geometries (i.e., the angle between the incident electrons and the emergent x-rays); however, the latter two are generally fixed for an experiment so that it is simple to calculate the bremsstrahlung spectrum for a particular specimen if the mean atomic number of the matrix is known. In soft tissue samples this is the case and since the spectrum *shape* is only a weak function of atomic number it is only necessary to calculate the specimen bremsstrahlung once for all spectra recorded in an experiment. MBH predicts a continuous rise in intensity with decreasing photon energy, but in practice absorption in the x-ray detector window modifies the shape below about 3 keV. By examination of spectra with no characteristic lines in the low-photon-energy range, the x-ray detector efficiency can be calculated and used to modify the shape predicted by MBH to give the theoretical background. Figure 4 shows the close fit obtained to a Formvar spectrum corrected for the contribution due to the titanium specimen mount despite the large discontinuity in the solid spectrum at the titanium absorption edge.

Because of the approximations in the solid subtraction procedure, it will be most successful when the solid correction is small. It is useful to estimate the magnitude of the error introduced into the C-N quantitation if the solid contribution is completely ignored. We normally measure the bremsstrahlung in an energy band centered at 12 keV and 5 keV wide. In the microscopes in our laboratory (VG HB5 STEM and JEOL JEM 100C) the proportion of the bremsstrahlung originating from the instrument is generally less than 10%, although it can be considerably higher if it is necessary to use fine mesh grids (e.g., 400 lpi) or measure close to the metal of the specimen support. Quantitative data showing the advantage of analyzing some distance from solid material, best achieved by use of single-hole mounts is given by Nicholson et al.<sup>12</sup> From Eq. (6) it can be seen that if the proportion of the instrumental bremsstrahlung is the same in both specimen and standard, the result will be unaffected by the solid correction. However, in practice that is not always the case. If we choose again the example of a soft tissue matrix for the specimen and a mineral standard is used, we have observed values of 12% solid contribution for the standard and up to 25% for the soft tissue, which would lead to errors of up to 12% in the calculated elemental concentrations.

### Conclusions

An examination of the theory of bremsstrahlung production in thin films shows that provided the mass of specimen and standard are not altered by contamination or radiation damage, there are advantages to be obtained by use of standards of similar composition and mass thickness to the specimen, since the errors due to the  $Z^2$  assumption in the C-N quantitation will be eliminated and the instrumental contribution to the bremsstrahlung will be similar. In well-designed analytical electron microscopes, where the instrumental contributions are minimized and can be quantified, large differences in mean atomic number and mass thickness of specimen and standard do not pose any problems and mineral standards offer the advantages of good counting statistics and stability in the beam.

### References

1. B. F. Boyce et al., "Quantitation and localization of aluminum in human cancellous bone in renal osteodystrophy," *SEM/1981 III*, 329-337.
2. J. N. Chapman et al., "X-ray production in thin films by electrons with energies between 40 and 100 keV: I. Bremsstrahlung cross-sections," *X-ray Spectrometry*, 1983 (in press).
3. J. I. Goldstein and D. B. Williams, "Spurious x-rays in the scanning transmission

electron microscope," *SEM/1977 I*, 282, 427-434.

4. C. C. Gray et al., "X-ray production in thin films by electrons with energies between 40 and 100 keV: II. Characteristic cross sections and the overall x-ray spectrum," *X-Ray Spectrometry*, 1983 (in press).

5. T. A. Hall, "Microprobe assay of chemical elements," in G. Oster, Ed., *Physical Techniques in Biological Research*, New York: Academic Press, 1971, 157-275.

6. T. A. Hall, "Problems of the continuum normalization method for quantitative analysis of sections of soft tissue," in C. Lechene and R. R. Warner, Eds., *Microbeam Analysis in Biology*, New York: Academic Press, 1979, 185-208.

7. T. A. Hall and B. L. Gupta, "EDS quantitation and applications to biology," in J. J. Hren, J. I. Goldstein, and D. C. Joy, Eds. *Introduction to Analytical Electron Microscopy*, New York: Plenum Press, 1979, 169-197.

8. T. A. Hall and B. L. Gupta, "Quantification for the x-ray microanalysis of cryosections," *J. Microsc.* 126: 333-345, 1981.

9. T. A. Hall and P. Werba, "Quantitative microprobe analysis of thin specimens: Continuum method," *Proc. 25th Anniversary of EMAG*, London, Inst. Physics, 1971, 146-149.

10. E. R. Krefting et al., "Quantitative EPMA of biological tissue using mixtures of salts as standards," *SEM/1981 II*, 369-376, 368.

11. W. A. P. Nicholson and D. W. Dempster, "Aspects of microprobe analysis in mineralizing tissues," *SEM/1980 II*, 517-534.

12. W. A. P. Nicholson et al., "Optimizing thin film x-ray spectra for quantitative analysis," *J. Microscopy* 125: 25-40, 1982.

13. H. Shuman et al., "Quantitative electron probe microanalysis of biological thin sections: Methods and validity," *Ultramicrosc.* 1: 317-339, 1976.

14. K. Zierold, "X-ray microanalysis of frozen hydrated specimens," *SEM/1983* (in press).

## IMPROVED METHODS FOR X-RAY MICROANALYSIS OF CARDIAC MUSCLE

J. McD. Tormey

Microprobe analysis has enormous potential as a tool for the study of the physiology of cardiac muscle. The contractility of cardiac muscle is controlled by the distribution of electrolytes in various subcellular compartments, but information about this distribution has been obtained by indirect means. Direct quantitation of intact, adult, mammalian heart is now needed, and microprobe analysis is the only technique that appears capable of meeting this need.

A major goal of our work has been to develop the ability to analyze electrolytes in cardiac muscle to the point where meaningful physiological experiments are feasible. This point has now been reached, but it has required the implementation of diverse improvements in our techniques.

The samples are freeze-dried cryosections of the order of 100 nm thick. The analysis of such samples is "simply" the end result of a series of difficult techniques. Each of these techniques has had in the past a significant degree of unreliability. Successful application of microprobe analysis to the study of diffusible electrolytes in ultrathin frozen sections has been limited to a few laboratories, in large measure because the unreliabilities of the component techniques tend to propagate in such a way that readily reproducible results have been more the exception than the rule.

The goal of this paper is to show how the reproducibility of our techniques has been increased at each of several steps. The steps to be discussed are (1) freezing in defined physiological states, (2) cryoultramicrotomy, (3) freeze-drying, and (4) energy dispersive x-ray spectrometry of low levels of Ca in the presence of interference from high levels of K. The last step will receive the greatest emphasis here, because it is the issue of broadest concern to the field of microbeam analysis.

### *Freezing in Defined Physiological States*

The requirements of good freezing put limitations on the type of cardiac muscle preparation that is practical for microprobe studies. For this reason, papillary muscles have been the preparation of choice in our laboratory, as well as in other laboratories<sup>1,2</sup> carrying out microprobe analysis of cardiac muscle. These muscles are cylindrical outgrowths of the ventricular wall that have physiological properties virtually identical to the rest of the ventricle and that have diameters of the order of 500  $\mu\text{m}$ .

Papillary muscles are more of a challenge to freeze well than are other muscles with diameters in this range. This is because they are covered by a layer of connective tissue that is at least several microns thick and can be considerably thicker (see Fig. 1). We have previously found that frog extensor digiti IV muscles that were frozen in vigorously stirred liquid propane ( $-175^{\circ}\text{C}$ ) showed zones within 1-2  $\mu\text{m}$  perpendicular to the muscle surface that were completely free of ice crystal damage, beyond which the structure rapidly became progressively distorted. Adequate immersion freezing of papillary muscle would be thus extremely difficult.

We have therefore developed techniques that utilize the ultrarapid freezing methods of Heuser and Reese,<sup>3</sup> in which tissues are rapidly plunged onto a liquid helium cooled copper block. Considerable effort was required to adjust the parameters of the freezing apparatus so that samples do not bounce off of the copper block while freezing. The freezing of papillary muscle is now reproducible, with good ultrastructural preservation

---

The author is at the Department of Physiology, Center for Health Sciences, UCLA, Los Angeles, CA 90024. The collaboration of JoAnn Hill and Lyle G. Walsh is gratefully acknowledged. Supported in part by grants from the American Heart Association Greater Los Angeles Affiliate and the Muscular Dystrophy Association.

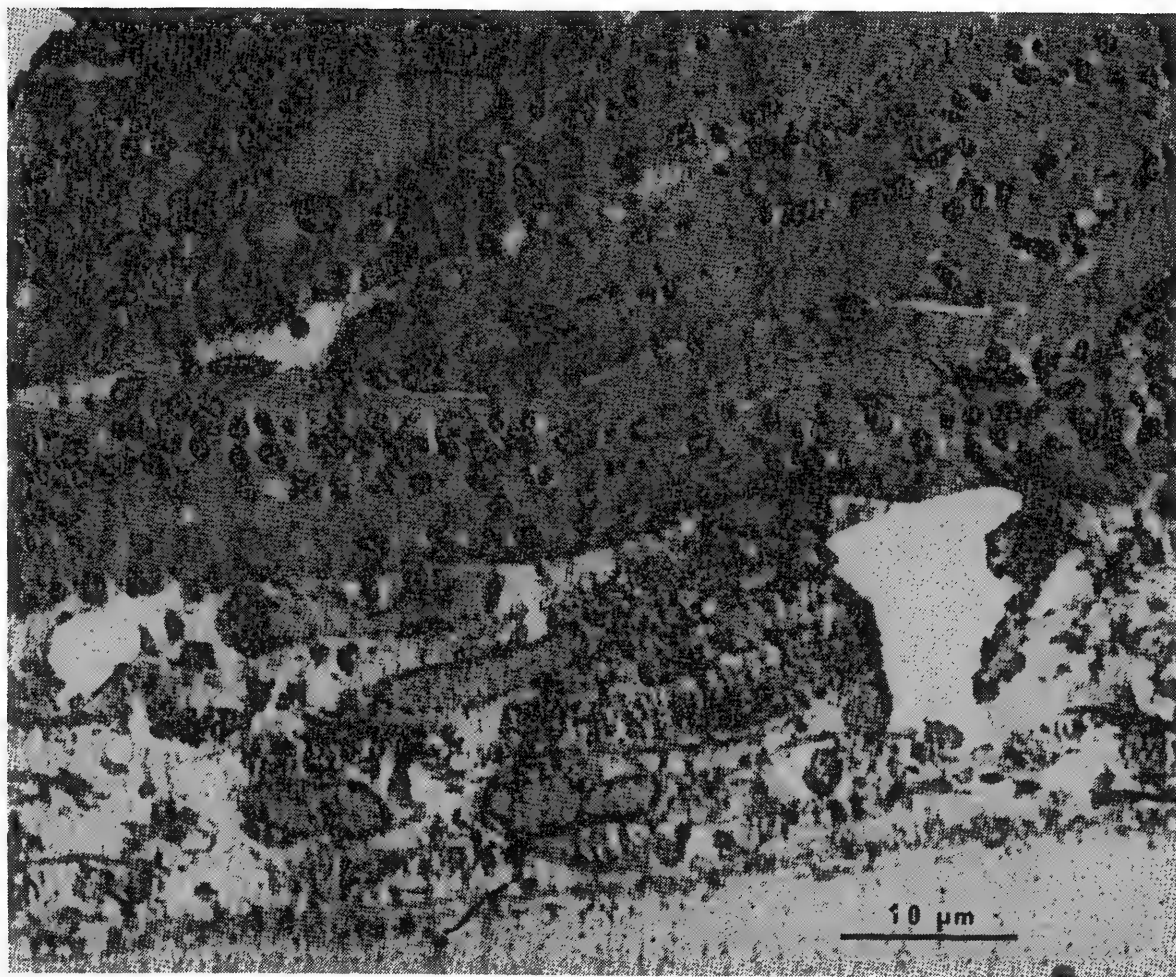


FIG. 1.--STEM micrograph of freeze-dried frozen section of papillary muscle from rabbit heart. Contrast is due entirely to local differences in dry mass. This sizable field includes three distinct regions. Low-density, slightly grainy region at bottom is comparatively thick (ca 8 $\mu$ m) layer of adhering solution that contains 5% dextran. Endocardium and unusually thick (ca 20 $\mu$ m) layer of connective tissue make up balance of lower half of picture. Upper half contains portions of at least three muscle fibers. Although some ice crystal damage can be seen on close examination, freezing of these cells is remarkably good considering how far they are from freezing surface. Mitochondria are extremely dense structures that stand out in sharp contrast to rest of each myocardial cell. Remaining intracellular structures demonstrate relatively low contrast. Nevertheless, two nuclei are distinctly visible. There are signs of "chatter" in places, yet distinct sarcomeric structure is apparent at several spots, and more is not seen because of slightly oblique cellular orientation. There are also several profiles suggestive of transverse tubules.

that gets past the connective tissue layer and includes several muscle fibers without significant damage.

At the time of freezing the papillary muscle needs to be in a defined physiological state. As compared with skeletal muscle preparations, extraordinary care must be taken to avoid hypoxia or deformation of the muscle at any point during its handling. The muscle must be allowed an adequate recovery period and be demonstrated to possess normal contractile properties.

Our procedure includes holding the muscle at rest length while it is removed from the ventricular wall and attached to a plastic ring which holds it during physiological experimentation and freezing. The ring with muscle attached is mounted in a temperature-controlled superfusion bath, where the muscle is electrically stimulated, its tension development is measured, and perfusion solutions are manipulated. After the physiological

status of the preparation has been ascertained, the muscle ring is transferred to a freezing head and is propelled against the liquid helium cooled block. Freezing is completed within 15 s of removal from the bath, during which time the muscle remains warm and moist and does not contract.

### *Cryoultramicrotomy*

Cryoultramicrotomy of sections ca 100 nm thick range from tissues frozen in their native state has been a major rate limiting step in many laboratories' progress. In retrospect, this situation may be explained by the relative crudeness of the equipment available until very recently. Though good quality sections were produced and analyzed, they were usually obtained in small numbers and at high price of time and effort.

We have successfully rebuilt our cryoultramicrotomy equipment so that it has much better mechanical and thermal stability for routine work. The new device, which is attached to a Sorvall MT-2 ultramicrotome, is an extensively reworked version of an early prototype design by Dr. Herbert Hagler for the Du Pont Sorvall MT-5000. (We are deeply indebted to Dr. Hagler and the Dallas group for sharing their experience with us.) As lineal descendant of a series of design modifications on the LKB Cryokit in several laboratories,<sup>4-6</sup> it places a liquid nitrogen reservoir directly in the cryochamber, and uses it both to provide a cold, dry ambient atmosphere and to cool individually thermostated knife and specimen holders. The unique improvements have been large increases in mechanical stability and thermal isolation that allow the system to cut reproducible thin sections for up to 10 hr without difficulty.

The time and effort involved in cryosectioning have accordingly been reduced by one to two orders of magnitude. Sections are now normally cut at -120°C. There is relatively little thermal interaction with the rest of the microtome, whose original cutting arm and knife stage remain stable at ca 15°C. Sequential serial sections 150 nm thick have been cut unattended for 2 hr, and flat gold sections up to 2 × 0.3 mm are obtained routinely. It is now common for us to prepare a dozen grids full of usable sections from two blocks in about 4 hr.

We have also devised a special vise chuck for muscle that has been frozen flat against a cold metal block. A papillary muscle that has been frozen in this way to a thickness of ca 300 μm is removed from its freezing stub, cleaved along its longitudinal axis, and further trimmed into several pieces. One of them can then readily be mounted between the jaws of the chuck and oriented for longitudinal sectioning.

Sections are individually transferred to 50 or 100 mesh folding Cu grids and are sandwiched between carbon-coated Formvar films. In spite of some loss in spatial resolution and a modest increase in background x-ray counts, this mounting procedure insures a subsequent yield of flat, stable sections after freeze-drying.

### *Freeze-Drying*

With the advent of the new cryoultramicrotome in our laboratory, it was found that the previously satisfactory freeze-drying equipment now yielded specimens that appeared melted by both morphological and x-ray analytical criteria. It became clear that substantial freeze-drying had been occurring in microtome cryostat we had used previously, which was cooled to -95°C by a flow of cold nitrogen gas from an external dewar.<sup>7</sup> Attempts at freeze-drying within the new cryomicrotome, where specimens were maintained between -95°C and -75°C for up to 2 hr, also proved unsatisfactory. We have therefore experimented with several prototype freeze-dryers, which has culminated in a design that has been giving reproducible morphological and analytical results for many months.<sup>8</sup>

The basic component of the new device is a container which holds 20 grids and fits readily into the cryomicrotome next to the knife. After it is loaded, it is sealed and transferred at near liquid nitrogen temperature into a long vertical tube, which is surrounded by liquid nitrogen and can be evacuated below 10<sup>-6</sup> Torr. The grid container has a built in temperature sensor and heater, and when the container is placed in the vertical tube, they are connected to an outside controller by an umbilical rod that also serves to hold the container away from the cold walls. Once the container is completely in place, the grids are uncovered by removal of a lid, and the vertical tube is evacuated to begin the drying run.

Since relatively little is known about optimal freeze-drying parameters for real tis-



sues, especially when they are sections covered by support films, a drying schedule was chosen whereby the grid container is warmed rapidly to  $-100^{\circ}\text{C}$  and then slowly at the rate of  $2.5^{\circ}/\text{hr}$  to  $-50^{\circ}\text{C}$ . Thereafter the grid container is brought rapidly to room temperature, covered, and transferred to a dry box. The drying run is controlled by a digital ramp generator designed specifically for this apparatus.

#### *Energy-dispersive Spectrometry of Calcium*

Calcium is the most important of all the elements in cardiac muscle, because its concentration is the primary determinant of muscle contraction. However, its measurement is an extraordinary challenge to the accuracy and precision of x-ray microanalysis. Its overall intracellular concentration is approximately 2 mmoles/kg dry mass. Precise measurement of such a low mass fraction (ca 1 part per 10 000) requires a relatively large number of counts in the gross calcium integral. Quantitation is further complicated by the simultaneous presence of potassium at concentrations of ca 500 mmoles/kg dry mass. The accurate deconvolution of the calcium  $K\alpha$  peak at 3.69 keV from a nearly two orders of magnitude larger potassium  $K\beta$  peak at 3.59 keV is therefore required. Although the deconvolution methods now available<sup>9-11</sup> can readily separate two overlapping peaks with centroids this close, the disproportion in the peaks' sizes causes small errors in deconvolution to have a large effect on estimated calcium values.

Table 1 illustrates an especially bad experience analyzing calcium in cardiac muscle. The data are calcium concentrations in mmoles/kg dry mass  $\pm$  standard error of mean (number of measurements). They were obtained with a JEOL 100CX analytical electron microscope operated at 100kV acceleration voltage in the STEM mode. The specimens were freeze-dried cryosections that had been prepared several days previously. Separate specimen grids were examined on three successive days (A, B, C). The cell data were obtained with rasters at ca 5000 $\times$  magnification; the cytosol data were obtained from extended regions of the cell that were free of mitochondria with rasters of ca 15 000 $\times$ ; the mitochondria data were obtained with rasters at ca 50 000 $\times$ . The energy-dispersive x-ray spectra were deconvoluted by means of a Tracor Northern 880 system with its standard software for linear least-squares fitting of filtered reference spectra to filtered sample spectra. Concentrations were estimated by Hall's peak-to-continuum approach to quantitation.<sup>12</sup>

Naive interpretation of Table 1 leads to absurd conclusions. For instance no significant calcium was measured in the cells, in spite of the fact that a substantial concentration was measured in the cytosol, which comprises 60% of the cell volume. Also, the difference between cell calcium concentrations measured on days A and C was statistically highly significant, as was the difference between cytosol concentrations on these two days.

These discrepancies were not attributable to x-ray counting statistics, inaccurate corrections for spurious continuum radiation, changes in sample mass during analysis, or sample deterioration with time. Therefore, we investigated the spectral deconvolution itself.

TABLE 1.--Day-to-day differences in calcium concentration measured from sections of heart muscle that were prepared at same time.

	Day			Pooled
	1	2	3	
Cell	-3.0 $\pm 1.8$ (8)	0.3 $\pm 0.9$ (9)	2.5 $\pm 1.4$ (6)	-0.3 $\pm 0.9$ (23)
Cytosol	1.3 $\pm 2.1$ (8)	3.5 $\pm 2.1$ (8)	9.6 $\pm 4.7$ (6)	4.4 $\pm 1.7$ (22)
Mitochondrion	1.2 $\pm 1.0$ (8)	0.1 $\pm 0.8$ (8)	0.7 $\pm 0.6$ (6)	0.7 $\pm 0.5$ (22)



Spectral deconvolution by the linear least-squares fitting approach assumes that reference and sample spectra have essentially the same peak positions and peak shapes. Small variations that are not important when isolated peaks are fitted can become significant when closely overlapping peaks are fitted. Attention was therefore focused on constancy of peak position and shape in our microprobe system. They turned out to be surprisingly inconstant.

Figure 2 demonstrates the effect of a change in STEM raster size on peak shape. (These and all subsequent data were obtained at 100kV acceleration voltage.) Dropping the magnification from 5000 $\times$  to 2000 $\times$  caused a pronounced broadening of peak "skirts" on both the high- and low-energy sides of the peak centroids. The resulting peaks were decidedly non-Gaussian in shape, and the calcium region was affected. Not obvious in the figure is the fact that skirt broadening was accompanied by reductions of potassium and sulfur peak widths (full widths at half maximum, FWHM) of 5 and 12 eV, respectively.

Peak position was also a strong function of raster size, when the detector was fully advanced into the column. (Detector was in standard horizontal configuration and was advanced until the front of the detector cryostat was 12 mm from the electron optical axis.) When the detector was retracted by 28 mm, however, no effect of raster size on

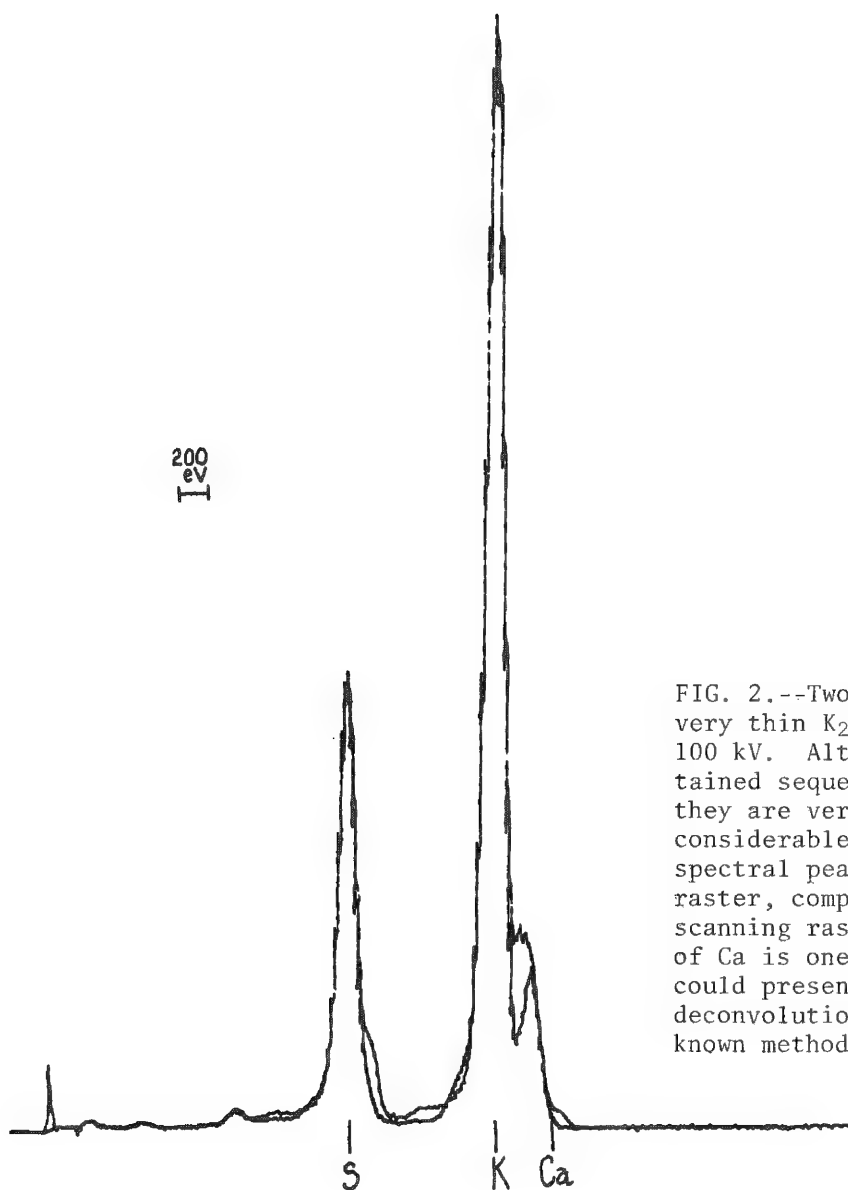


FIG. 2.--Two superimposed x-ray spectra from very thin  $K_2SO_4$  crystal that was analyzed at 100 kV. Although the two spectra were obtained sequentially from the same region, they are very poorly superimposed. There is considerable broadening of the "skirts" of spectral peaks obtained with a 2000 $\times$  scanning raster, compared to results with a 5000 $\times$  scanning raster. Critical region in vicinity of Ca is one of those obviously affected and could present serious problem for accurate deconvolution of K and Ca spectra by any known method.

centroid position was observed. Such effects, as well as those in Fig. 2, appear to be caused by electromagnetic interference between the scan coils and the x-ray detector. Thus they belong to the same category of energy dispersive spectrometry artifacts that can produce dramatic false peaks whose position is a function of raster size.<sup>13</sup>

Table 2 presents an experiment that shows the effect of a change in magnification on measured calcium as well as on potassium peak parameters. The sample was a freeze-dried frozen section of a calcium-free standard consisting of an aqueous solution that contained 450 mmolal potassium bromide and 25% w/w dextran. Any calcium measured in such a sample is an error of the deconvolution procedure, and can be shown in this case to be caused by discrepancies in potassium peak parameters between reference and sample spectra. The calcium error is expressed in units of mmoles Ca/mole K, since the magnitude of an error due to a potassium peak shift may be expected to be directly proportional to the size of that potassium peak. The calcium error was statistically insignificant at 150 000 $\times$  magnification. However, at 10 000 $\times$  the potassium peak centroid had shifted 1.0 eV, the potassium peak width (FWHM) had increased by 2.2 eV, and the calcium error had become significant. Two error values are given: 1.2 mmoles Ca/mole K was obtained after the shift in potassium peak position was measured in each spectrum and each was recalibrated so that the potassium shift was zero before deconvolution (a calcium value that therefore represents the error due to potassium peak broadening alone); 3.3 mmoles Ca/mole K was the value measured before this recalibration.

Since the effects of peak position and peak resolution (FWHM) on calcium error can be separated, we further explored the effects of spontaneous variations of FWHM on calcium error. Figure 3 shows that there is a rectilinear relationship between these two parameters. The measured linear regression coefficients can therefore be used for correcting calcium measurements for errors caused by variations in peak resolution, *provided* microanalysis is carried out within the constraints to be listed below.

Shuman et al.<sup>10</sup> have also discussed the effect of shifts in potassium calibration on the accuracy of calcium measurements. Using computer-generated Gaussian peaks and the same software for spectral deconvolution as we, they explored the effects of miscalibration in the range of  $\pm 5$  eV. They found rectilinear relationships between calcium error on the one hand and both the position and the resolution of the potassium peak on the other. They also suggested that such relationships could be used as a basis for correcting calcium data. The slopes of their relationships were, however considerably different from those we have observed.

In addition to scan coil induced effects, there were also variations in peak position and resolution due to instrumental drift. Close inspection of our spectra over a period of months led us to recognize such drift to be highly unpredictable. Shifts in potassium centroid position of up to  $\pm 2$  eV per day were observed. Sometimes these changes were progressive and at other times nearly instantaneous; sometimes calibration stayed within 1 eV for days. We also observed erratic cycles during which potassium FWHM changed by  $\pm 5$  eV over a period of days. The exact causes of these effects remain unclear. They could partially result from aging electronics and uncontrollable changes in ambient

TABLE 2.--Effect of change in magnification on position and resolution of potassium peak and on measurement of apparent calcium. Peak position is deviation from expected centroid energy in eV. Peak resolution is FWHM in eV. Ca error is mmoles calcium per mole potassium. Standard errors of means are presented.

Magnification	N	Peak Position	Peak Resolution	Ca Error
150,000 X	6	0.1 $\pm$ 0.1	128.3 $\pm$ 0.2	-0.3 $\pm$ 0.6
10,000 X	6	1.1 $\pm$ 0.1	130.5 $\pm$ 0.2	1.2 $\pm$ 0.3
				3.3*

\* See text.

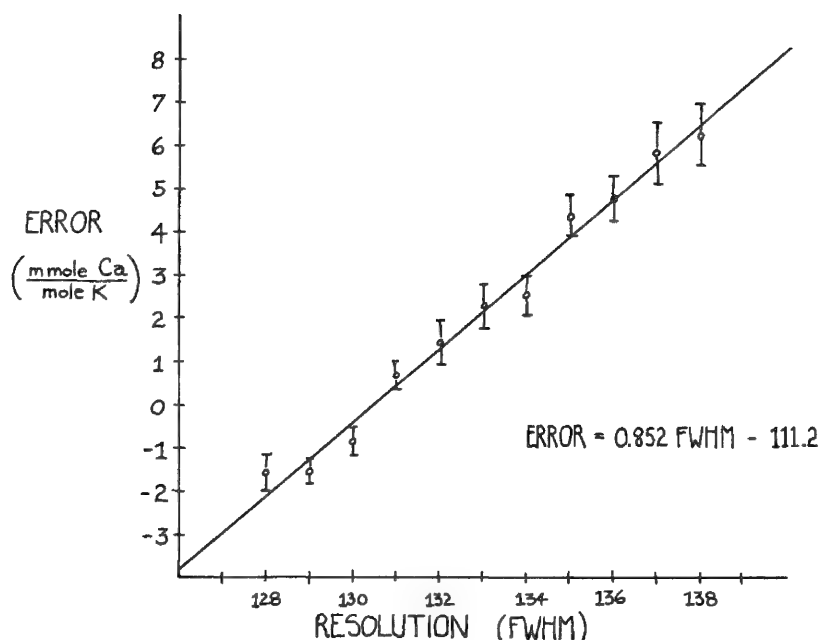


FIG. 3.--Regression line demonstrating linear relationship between variations in measured potassium peak width (resolution in FWHM) and resulting error in calcium measurement. This result provides parameters for correcting errors in low-level calcium measurements that would otherwise result from potassium peak fluctuations.

the measured calcium concentrations on a spectrum by spectrum basis.

As a result of such precautions, the precision of calcium analyses of standards has improved to the point where the observed standard deviations are close to those expected from counting statistics alone. Accuracy is also good; a series of measurements on a standard including 450 mmolal potassium and 3.0 mmolal calcium yielded a mean calcium value that was off by 0.1 mmolal. We are also observing remarkably little variance in calcium concentrations in control cardiac muscles, other than that which is attributable to counting statistics.

### Conclusion

The state of the art of biological microprobe analysis is rapidly advancing as a result of multiple refinements of technique. Our personal experience with improvements in four areas has been presented here. With the implementation of such refinements, accuracy, reproducibility, and throughput are increasing to the point where use of microprobe x-ray analysis to perform physiological experiments is becoming more practical than ever before.

### References

1. H. K. Hagler, K. P. Burton, C. A. Grieco, L. E. Lopez, and L. M. Buja, "Techniques for cryosectioning and x-ray microanalysis in the study of normal and injured myocardium," *SEM/1980 II*, 493.
2. M. F. Wendt-Gallitelli, H. Wolburg, M. Schwegler, and W. Schlote, "Electron probe x-ray microanalysis of unstained myocardial sarcoplasmic reticulum in situ and fragmented," *Experientia* 35: 1591, 1979.
3. J. E. Heuser, T. S. Reese, M. J. Dennis, Y. Jan, L. Jan, and L. Evans, "Synaptic vesicle exocytosis captured by quick freezing and correlated with quantal transmitter release," *J. Cell Biol.* 81: 275, 1979.
4. A. V. Somlyo and J. Silcox, "Cryoultramicrotomy for electron probe analysis," in C. P. Lechene and R. R. Warner, Eds., *Microbeam Analysis in Biology*, New York: Academic Press, 1979, 536.

temperature. On the other hand, they appear unrelated to such well-known effects as microphonics originating in ice ground loops or at the bottom of the detector dewar.

Once recognized, the effects described here can be coped with. We now observe all the following precautions: (1) Detector position is never varied for analytical measurements. (2) X-ray spectra are obtained at slow raster speeds, which greatly reduces scan coil induced changes in calibration and resolution. (3) Spectra are never obtained at magnifications below 5000, which further reduces scan coil effects. (4) The energy calibration of each spectrum is measured, and the spectrum is recalibrated before deconvolution, so that its major peaks fall within 1 eV of expectation and its potassium peak falls within 0.1 eV. (5) Potassium peak width (FWHM) is measured, and its value is used in conjunction with the data from Fig. 3 to correct

5. L. Seveus, "Cryoultramicrotomy as a preparation method for x-ray microanalysis," *SEM/1980* IV, 161.
6. H. K. Hagler, L. Lopez, J. S. Flores, R. J. Lundswick, and L. M. Buja, "Standards for quantitative energy dispersive x-ray microanalysis of biological cryosections. Validation and application to studies of myocardium," *J. Microscopy* (in press).
7. A. K. Christensen, "Frozen thin sections of fresh tissue for electron microscopy, with a description of pancreas and liver," *J. Cell Biol.* 51: 772, 1971.
8. J. McD. Tormey and L. G. Walsh, "Freeze-drying cryosections for x-ray microanalysis: An improved method," submitted for publication.
9. F. H. Schamber, "A modification of the linear least-squares fitting method which provides continuum suppression," in T. G. Dzubay, Ed., *X-ray Fluorescence Analysis of Environmental Samples*, Ann Arbor: Ann Arbor Science, 1977, 241.
10. H. Shuman, A. V. Somlyo, and A. P. Somlyo, "Quantitative electron probe microanalysis of biological thin sections: Methods and validity," *Ultramicroscopy* 1: 317, 1976.
11. K. F. J. Heinrich, D. E. Newbury, and R. L. Myklebust, Eds., *Energy Dispersive X-ray Spectrometry*, Washington, D. C. National Bureau of Standards Special Publication 604, 1981.
12. T. A. Hall, "The microprobe assay of chemical elements," in G. Oster, Ed., *Physical Techniques in Biological Research*, New York: Academic Press, 2d ed., 1971, 1A, 157.
13. C. E. Fiori, D. E. Newbury, and R. L. Myklebust, "Artifacts encountered in energy dispersive x-ray spectrometry in the analytical electron microscope," in Ref. 11, 365.

## INTRACELLULAR HYDRATION MEASUREMENT WITH FREEZE-DRIED, PLASTIC-EMBEDDED BIOLOGICAL SOFT TISSUE

F. Duane Ingram and Mary Jo Ingram

When an element not commonly associated with biological material is complexed into the plastic used for embedding freeze-dried tissue, the characteristic x-ray intensity for that element will be reduced in regions of the plastic block containing tissue. A direct relationship will exist between signal intensity and dilution of the embedding plastic by tissue solids, provided tissue water has been faithfully replaced by embedding medium.

Br has been selected as the element for estimating tissue water in this manner. The embedding medium is tagged with Br by incorporating 40 mg/kg dibromacetophenone into EPON 826 monomer. Tissue collection, freeze-drying, and osmium vapor fixation are performed in standard fashion,<sup>1</sup> with initial drying at a temperature near -80°C and completion of drying at +50°C. Final drying at the higher temperature is recommended to remove "bound" water more completely. It is essential that all water be removed for this preparation. Because the "bound" water is not expected to contribute to the osmotic state of the cell, measurements of cellular water that include the "bound" fraction must be corrected by some hitherto unknown factor when they are to be used in studies of cellular function. In the present work, electron microprobe estimations of cell water were compared with conventional techniques which involved drying tissue for two days at 105°C, so that it was appropriate to remove all cellular water before electron probe microanalysis. Drying was not attempted at 105°C with the freeze-dried tissue, as that temperature is beyond the recommended operating range for our freeze-dry apparatus.

Albumin standards, with different concentrations of tissue solids, that range from 10.7% to 37.7% by weight, were used to calibrate a wavelength-dispersive spectrometer with a 50nA, 10keV electron beam. The ratio of Br La counting rate on embedded albumin to counting rate on pure EPON was plotted against tissue water fraction to obtain a calibration curve. A straight line fitted to the data had a slope of  $1.027 \pm 0.069$  with intercept  $0.057 \pm 0.047$  and regression coefficient of 0.991. An independent evaluation of the set of standards is realized by examining the sulfur data that had been obtained simultaneously with data collection for the Br signal calibration. Tissue solids plotted against S K $\alpha$  signal, in counts/s, obtained with the wavelength-dispersive spectrometer and PET diffraction crystal had a slope of  $405.6 \pm 11.9$  with intercept  $3.2 \pm 2.9$  and regression coefficient of 0.9979. This result indicates an acceptable set of standards of varying tissue solids. The continuum from 4.2 to 7.2 keV in the Si(Li) energy detector spectrum was calibrated to provide a number representing background at each location that data were collected on the albumin standards.<sup>2</sup>

This method for measuring cellular water was evaluated by comparison of electron microprobe estimations of tissue water with conventional measurements of tissue water. Samples of gastrocnemius from each of four different sets of anesthetized rats were collected with a cold clamp for electron-probe microanalysis. The other gastrocnemius in each rat was excised for conventional wet chemical analysis. Excellent agreement was found between the two sets of measurements (Table 1).

The electron microprobe estimates of tissue water averaged approximately 3% higher than those obtained with conventional techniques on companion tissue. This difference represents a systematic error within the limits of uncertainty of calibration. Differences between electron microprobe measurement and conventional measurement of cellular water can result from (1) inaccurate knowledge of the amount of water remaining in the prepared albumin standards, (2) removal of a different fraction of tissue water with

---

The authors are at the USDA/ARS Children's Nutrition Research Center, Department of Pediatrics, Baylor College of Medicine, Texas Children's Hospital, Houston, TX 77030.

TABLE 1

	(n)	Wet Chemistry Water Fraction	Electron Probe Microanalysis Estimated Water Fraction	Difference
Set 1	(4)	$0.718 \pm 0.008$	$0.749 \pm 0.014$	0.031
Set 2	(5)	$0.733 \pm 0.010$	$0.759 \pm 0.039$	0.026
Set 3	(6)	$0.767 \pm 0.007$	$0.784 \pm 0.020$	0.017
Set 4	(4)	$0.783 \pm 0.008$	$0.811 \pm 0.019$	0.028

conventional methods where tissue is held at 105°C in an oven from that removed with the freeze-dry apparatus where final tissue drying is done at +50°C in a vacuum, and (3) systematic errors in the measurements and assumptions required for conventional determination of cellular water. The excellent agreement in tissue water measurement between these two diverse methods of cellular water determination either supports the contention that the various sources of error are of little consequence, or that fortuitously, errors cancel.

The primary assumptions made with this technique are: (1) embedding plastic faithfully replaces tissue water; (2) all tissue water is removed by freeze-drying; (3) the reduction of Br x-ray signal results primarily from dilution of plastic by tissue solids and not from counting losses from matrix effects; and (4) distortions, such as shrinkage, that accompany tissue preparation, are accurately reflected in fabricated albumin standards, and are the same from one type of tissue to another.

#### References

1. F. D. Ingram and M. J. Ingram, "Freeze-dried, plastic-embedded tissue preparation: A review," *SEM/1980* IV, 147-160.
2. F. D. Ingram and M. J. Ingram, "Wavelength dispersive spectrometer background estimation with Si(Li) energy detector," *Proc. 40th Ann. EMSA Meeting*, 1982, 384-387.

## A COMPREHENSIVE COMPUTER PROGRAM FOR THE QUANTITATIVE ANALYSIS OF THIN BIOLOGICAL SECTIONS

R. R. Warner and J. C. Wirfel

A multifunctional computer program called Hydra has been developed for the quantitative analysis of thin biological sections. This program monitors the loss or gain of mass and elements during data acquisition. Peak and background intensities are obtained from the acquired spectrum by a filtering and deconvolution routine. Element concentrations are calculated using two major biological quantitative techniques. With this program, potential problems of these quantitative techniques can be minimized.

Of the available quantitative procedures for microprobe analysis of biological tissue, the procedures of Hall<sup>1,2</sup> and Rick and coworkers<sup>3,4</sup> are widely used and have proven accuracy.<sup>5,6</sup> They are not without problems. The Hall technique requires accurate measurement of sample mass (continuum); problems of mass loss<sup>7</sup> or gain<sup>5</sup> and problems of extraneous continuum, whether peak-associated<sup>2,5</sup> or peakless,<sup>8</sup> can compromise an analysis unless adequately addressed. Similarly, the technique of Rick requires application of an external standard to the tissue that could compromise some samples or create difficulties during cryosectioning. In addition, the Rick procedure is based on several critical assumptions: (1) that the analyzed regions of the cryosectioned sample and attached standard are uniformly thick, and (2) that possible element loss or gain, or possible tissue shrinkage during freeze-drying, is identical in the standard and sample.

We have developed a generally applicable sample-analysis procedure that offers a number of advantages for the quantitative microprobe analysis of thin biological sections. The analytical portion of this sample-analysis procedure is incorporated in the Fortran computer program Hydra. This program utilizes both the Hall and Rick techniques and specifically addresses their inherent potential problems. The analysis procedure directs the acquisition of raw spectral data, monitors element and mass loss or gain, extracts peak and background intensities by use of a filtering and deconvolution routine, applies the various correction procedures, requests the appropriate standards, and calculates concentrations. The program incorporates a data storage and retrieval system.

The program Hydra is designed to minimize problems of peakless continuum described elsewhere in this volume.<sup>8</sup> As such, an external standard adherent to the sample (similar to that required by the Rick technique) is necessary. Procedures for application of an external standard that would be appropriate for any sample type are being developed at Procter & Gamble and will be published elsewhere.

Previously it has proven advantageous to compare directly results obtained with the Rick and Hall techniques.<sup>9</sup> Since there is little in common between these two data-reduction procedures, obtaining equivalent answers strongly supports their validity, whereas obtaining very different answers invites closer scrutiny. Our quantitative procedure Hydra utilizes both the Hall and Rick techniques to provide a direct comparison of results.

Continuum and element peak intensities are obtained by use of the spectrum filtering and deconvolution routines of the Sequential Simplex program by Fiori et al.<sup>10</sup> With this procedure, the exact energy of an element peak is one of the fitting parameters, which eliminates the dependence on an extremely accurate energy calibration common to other filtering routines.<sup>5</sup>

Since element and mass loss or gain can affect the accuracy of results obtained with the Hall and Rick techniques, the count rate for the continuum and each analyzed element should be monitored during the analysis. Following our previous technique,<sup>11</sup> the count rates are monitored automatically during data acquisition and the results are graphically plotted for visual interpretation.

For the Hall technique, extraneous peak-associated continuum is eliminated following

---

Author R. R. Warner is at Procter & Gamble Co., Cincinnati, Ohio; author J. C. Wirfel is at Cameca Instruments Inc., San Diego, California.



established procedures.<sup>2,5</sup> The film (substrate) continuum is also subtracted. Since it is not possible to correct for extraneous peakless continuum, this effect is minimized by use of external standards applied prior to or following quench freezing.

Other features of the program are the incorporation of a simple data storage and retrieval system, a calculation of sample and standard mass thicknesses, and an option to analyze or recalculate element concentrations using isolated standards and the element ratio technique.<sup>12</sup> The program Hydra was written for a DEC RSX operating system and a Kevex 7000 system.

### References

1. T. Hall, "The microprobe assay of chemical elements," in G. Oster, Ed., *Physical Techniques in Biological Research*, 2nd Edition, New York: Academic Press, 1971, 157-275.
2. T. A. Hall, "Problems of the continuum-normalization method for the quantitative analysis of sections of soft tissue," in C. Lechene and R. R. Warner, Eds., *Microbeam Analysis in Biology*, New York: Academic Press, 1979, 185-208.
3. R. Bauer and R. Rick, "Computer analysis of x-ray spectra (EDS) from thin biological specimens," *X-Ray Spectrometry* 7: 63-69, 1978.
4. A. Dorge, R. Rick, K. Gehring, and K. Thureau, "Preparation of freeze-dried cryosections for quantitative x-ray microanalysis of electrolytes in biological soft tissues," *Pflügers Arch.* 373: 85-97, 1978.
5. H. Shuman, A. V. Somlyo, and A. P. Somlyo, "Quantitative electron probe microanalysis of biological thin sections: Methods and validity," *Ultramicroscopy* 1: 317-339, 1976.
6. M. M. Civan, T. A. Hall, and B. L. Gupta, "Microprobe study of toad urinary bladder in absence of serosal K<sup>+</sup>," *J. Memb. Biol.* 55: 187-202, 1980.
7. T. A. Hall and B. L. Gupta, "Measurement of mass loss in biological specimens under an electron microbeam," in Hall, Echlin, and Kaufmann, Eds., *Microprobe Analysis as Applied to Cells and Tissues*, New York: Academic Press, 147-158, 1974.
8. R. R. Warner, M. C. Myers, and D. A. Taylor, "Peakless continuum: Inaccuracies in biological quantification by the analytical microscope," *Microbeam Analysis--1983*, 211.
9. J. A. T. Dow, B. L. Gupta, and T. A. Hall, "Microprobe analysis of Na, K, Cl, P, S, Ca, Mg and H<sub>2</sub>O in frozen-hydrated sections of anterior caeca of the locust, *Schistocerca gregaria*," *J. Insect Physiol.* 27: 629-639, 1981.
10. C. E. Fiori, R. L. Myklebust, and K. Gorlen. Sequential Simplex: A procedure for resolving spectral interference in energy dispersive x-ray spectrometry," in K. F. J. Heinrich, D. E. Newbury, and R. L. Myklebust, Eds., *Energy Dispersive X-ray Spectrometry*, Washington, D. C.: NBS Special Publication 604, 1981, 233-272.
11. M. C. Myers, J. Van, and R. R. Warner, "Ultrastructural distribution of sulfur in human hair," *Microbeam Analysis--1981*, 210-212.
12. T. A. Hall and B. L. Gupta, "EDS quantitation and application to biology," in J. J. Hren, J. I. Goldstein, and D. C. Joy, Eds., *Introduction to Analytical Electron Microscopy*, New York: Plenum Press, 1979, 169-197.

## IMAGING LYMPHOCYTE MAGNESIUM

G. R. Hook, C. E. Fiori, and R. J. Elin

Blood contains approximately 1% of the total body magnesium. Plasma and erythrocyte magnesium concentrations do not provide accurate information about total body magnesium status but peripheral blood mononuclear cell magnesium concentration may correlate with total body magnesium.<sup>1</sup> However, magnesium variation among individual mononuclear cells has not been well characterized. We present here a direct method for determining the magnesium variation among individual whole lymphocytes by x-ray microprobe elemental imaging. Magnesium was imaged in Burkitt lymphoma cells by use of a new sample preparation procedure and a computer-controlled microprobe with wavelength-dispersive spectrometers. This method minimizes continuum x rays, corrects a mass thickness artifact, and produces net magnesium maps.

The computer-controlled acquisition, storage, and display system is more flexible than a conventional x-ray dot map system because the intensity of each pixel within the image is proportional to the local amount of analyte. Using this system, one can correct for the effect of mass thickness variation on the continuum generation process by subtracting the continuum image from the magnesium-plus-continuum image pixel by pixel and making a net magnesium distribution map. Since a measure of both characteristic and continuum x rays at each pixel is available, these digitized images also permit the quantitation of magnesium in cells. We present continuum-corrected digital x-ray images of a biological sample and believe the overall method has general applicability to a variety of elements studied in many biological problems.

### *Instrumentation*

To make elemental digital maps requires a stable electron beam and stage and appropriate computer hardware and software. Our analytical system consists of a Cameca microprobe equipped with wavelength-dispersive x-ray spectrometers (WDS), Tracor Northern energy-dispersive x-ray detector and multichannel analyzer, secondary-electron (SEM) and scanning transmission electron (STEM) detectors linked via a Digital Equipment Corp. (DEC) LSI 11-23 satellite processor to a dedicated PDP 11/60 computer with dual 67M byte disk drives and a DeAnza color graphics display (4 planes of  $512 \times 512 \times 8$  bits).<sup>2,3</sup> The software for acquisition, storage, display, and processing the images has been described previously.<sup>4</sup>

### *Sample Preparation*

EW36 Burkitt lymphoma cells from cell culture were chosen because they provide a more homogeneous population than lymphocytes obtained from peripheral blood and cell-separation procedures are avoided. Cells were grown in RPMI 1640 (M. A. Bioproducts) with glutamine, 20% fetal calf serum, and 0.5% penicillin and streptomycin medium at 37°C for 4 days, harvested and washed four times in  $\text{NH}_4\text{NO}_3$  buffer (310 mosmole, pH 7.4) by centrifugation at 400 g for 10 min per wash.  $\text{NH}_4\text{NO}_3$  buffer is a compromise between controlling osmotic cell lysis and minimizing salt formation when the buffer dried. Salt crystal formation was a problem because the crystals can cover the cells and thus make it difficult to identify cells and contribute characteristic and continuum x rays. The  $\text{NH}_4\text{NO}_3$  is a volatile salt that is easily etched away with the electron beam to allow clear imaging of

---

Authors Hook and Elin are with the Clinical Pathology Department and author Fiori is with the Division of Research Services, National Institutes of Health, Bethesda, MD 20205. They thank Jeanette Hosseini for sample preparation assistance, Ian Magrath for the EW36 Burkitt lymphoma cell line, Keith Gorlen and James Ellis for computer imaging assistance, Carter Gibson for electronics assistance, and Richard Leapman and Carol Swyt for discussions.

cells and has a low average atomic number, which contributes a minimum amount of continuum x rays. After washing, the cells were concentrated (2 million cells/ml), loaded into a glass capillary tube, spray deposited on the sample support with a freon-propelled aerosol (E. Fullam), air dried, and carbon coated. Aerosol application of cells minimizes the amount of buffer deposited and insures against differential adsorption of the sample on the support.<sup>5</sup>

The sample support is a large-area film, thin enough to generate a low-continuum x-ray signal and allow transmission light-optical and electron-optical observation, yet strong enough to withstand sample handling and high electron beam currents. The support consists of a Teflon ring (14 mm OD, 12 mm ID, 2 mm high) over which a thin (0.3 $\mu$ m) formvar film is stretched; there are no support bars. We make the film by dipping a glass slide into a 2% formvar-ethylene dichloride solution, rapidly removing the slide from the solution, drying the film, and floating it on water. The face of the ring is painted with the formvar solution and allowed to dry before the painted surface is placed on the floating film. The ring and film is picked up from above with formvar-coated parafilm and excessive water is blown away. After the cells are applied, the film is reinforced by evaporative carbon coating of both sides of the film. This step produces a sample support that contributes very little continuum x rays, transmits light and electrons for imaging, has a large, unobstructed area (120 mm<sup>2</sup>), yet is able to withstand 10<sup>-6</sup> A electron beam currents. The ring is placed in a hole through a carbon-coated brass shuttle and the shuttle is transferred onto the standard Cameca STEM stage.

### *Imaging*

Operationally, image collection requires manually selecting and setting the beam current, focus, signal collectors, and area of interest, and entering the computer program. In the program, the operator is presented with a menu from which the option to collect an image is selected. The program requests a label for the image to be stored, the size of the pixel array to be collected (up to 1024  $\times$  1024) and the dwell time for each pixel (1  $\mu$ s to 1000 s). The computer methodically steps the beam over the sample for the number of pixels selected, dwells at each pixel for the prescribed amount of time, collects the signal at each pixel, and stores each of the selected signals on magnetic disk. The pixel array size and the image collection time are determined by many factors, including the elemental content of the sample, the efficiency of signal generation and collection, the electron beam current, the desired spatial resolution and statistical precision, and the number of samples to be investigated. The SEM and STEM images are efficiently produced and collected compared to x-ray production and WDS x-ray collection, so SEM and STEM images are made with a low beam current, large array size, and a short image collection time (less than 1 min), whereas WDS x-ray images require a high beam current, a smaller array size, and a long image collection time (30 min or more).

Multiple signals can be collected during one scan, but because of the large difference in beam currents used in structural and elemental images, the structural images and the x-ray images are collected separately. Also, the WDS x-ray peak-plus-continuum and continuum images are collected in two sequential scans of the sample. The WDS x-ray peak-plus-continuum image is detected by tuning of the WDS to the K $\alpha$  x ray for magnesium and the continuum image is acquired on the same area with the same beam current, array, time, spectrometer, and crystal as the peak-plus-continuum but with the spectrometer tuned off the peak.

Having collected the images, the operator enters the menu and selects to display the images. An image is loaded into one of three color planes (red, green, or blue) in the DeAnza color graphics system and shown on a color monitor. This scheme permits observation of three different images at one time, so direct comparisons among images can be made. The images can be placed side by side or coregistered.

After images are loaded, the menu is again entered and the image process software is selected. The relevant processing programs include brightness and contrast, increase magnification, scroll, arithmetic manipulations (addition, subtraction, multiplication and division), and smoothing of images. These programs were used to subtract the continuum image from the peak-plus-continuum image. After contrast and scaling adjustments of images have been made, the monitor is photographed. (In this paper the images are shown in black and white.)

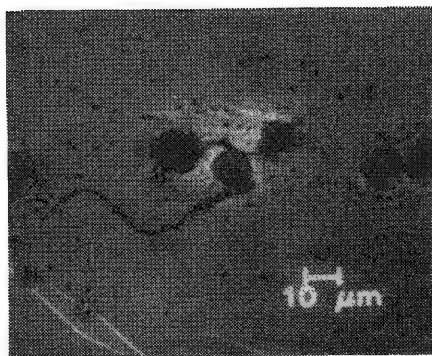


FIG. 1.--Digital bright-field STEM micrograph showing lymphocytes are clearly imaged.

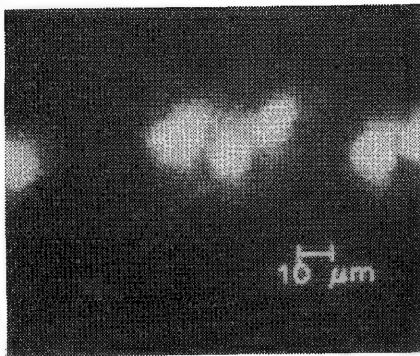


FIG. 2.--Digital WDS magnesium-plus-continuum x-ray image of same field as Fig. 1.

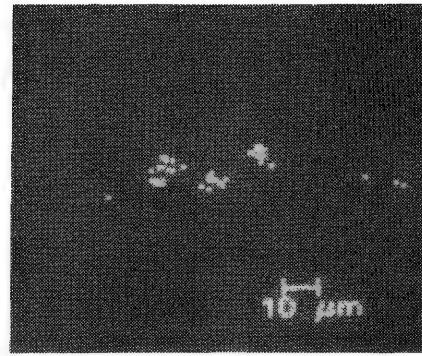


FIG. 3.--Digital WDS continuum x-ray image of same field.

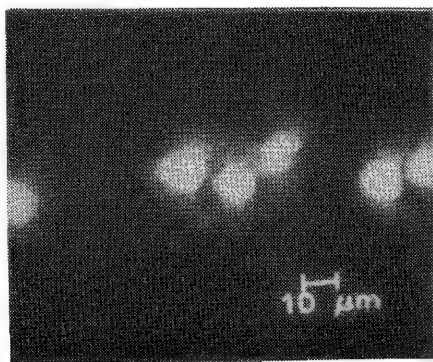


FIG. 4.--Net magnesium image obtained by subtraction of continuum image of Fig. 3 from magnesium peak-plus-continuum image of Fig. 2. Average magnesium content of these cells is 150 fg/cell as determined by atomic absorption.

### Results

Figure 1 is a STEM micrograph of Burkitt lymphoma cells prior to elemental imaging, which shows that cells can be clearly imaged in the microprobe by this procedure. These images were obtained with a 15keV,  $10^{-8}$ A beam (Faraday cup measurement) and are  $256 \times 256$  pixel arrays with a dwell time of 60  $\mu$ s per pixel or a total acquisition time of 6 s. Figure 2 is a WDS x-ray peak map of magnesium plus continuum from this region, which shows the x-ray signal localized in the cells and very little signal from the surrounding salt and film. This image was obtained using a 15keV,  $0.5 \times 10^{-6}$ A beam and is a  $128 \times 128$  pixel array with a dwell time of 1 s per pixel or a total acquisition time of 4 hr. Figure 3 shows the very-low-continuum x-ray image obtained from a second scan of the same area under the same operating conditions as Fig. 2, except the spectrometer is tuned off the peak. Figure 4 is the image that results from subtraction of the continuum image of Fig. 3, from the peak plus continuum image, Figure 2. This image shows that the net magnesium distribution is localized in the cells.

### Discussion

We have demonstrated a new method that produces net magnesium images of Burkitt lymphoma cells. This method consists of using a  $\text{NH}_4\text{NO}_3$  buffer, spraying the cells on large-area, thin-film supports to minimize continuum x-ray signal, and digitally acquiring and storing both characteristic and continuum x-ray images to correct an artifact due to mass thickness. However, this method needs further research in four areas. First, although 70% of the cells remains intact after washing,  $\text{NH}_4\text{NO}_3$  buffer may selectively lyse cells and correlative studies with atomic absorption are planned. Second, air drying may redistribute magnesium within the cells and comparisons are needed with freeze-dried and frozen hydrated procedures. Third, although the magnesium signal is stable at the electron dose rate used, studies are being conducted to compare high-current WDS images with low-current x-ray images collected with the more efficient energy-dispersive x-ray spectrometer. Fourth, quantitative cellular magnesium studies comparing the integrated intensity over

all pixels that define a given lymphocyte with a similarly integrated pixel value obtained from net magnesium images of standard glass spheres with a known magnesium concentration, size, and low average atomic number,<sup>6</sup> are being conducted.

### References

1. M. Ryan and M. Ryan, "Lymphocyte electrolyte alteration during magnesium deficiency in the rat," *IR J. Med. Sci.* 148: 108-109, 1979.
2. C. E. Fiori et al., "Comments on the computerization of an analytical electron microscope," *Proc. 40th Ann. EMSA Meeting*, 1982
3. R. D. Leapman et al., "Combined elemental and structural imaging in a computer-controlled analytical electron microscope," *Proc. 41st Ann. EMSA Meeting*, 1983.
4. K. E. Gorlen et al., "A data acquisition system for an analytical electron microscope," *Proc. DECUS*, 1982.
5. C. P. Lechene et al., "Electron probe microanalysis of chemical elemental content of single human red cells," *J. Cell. Physiol.* 90: 117-126, 1977.
6. C. E. Fiori and D. H. Blackburn, "Low Z glass standards for biological x-ray microanalysis," *J. Microscopy* 127: 223-226, 1982.

## VALIDATION OF QUANTITATIVE ENERGY-DISPERSIVE ELECTRON-PROBE X-RAY MICROANALYSIS OF ELECTROLYTES IN THIN CRYOSECTIONS OF ERYTHROCYTES

I. L. Cameron, K. E. Hunter, and N. K. R. Smith

Biological materials consist of extracellular and intracellular compartments containing diffusible ions which are in some cases maintained at vastly different concentrations. For example, in both man and mouse the erythrocytes suspended in the blood plasma are known to have dramatic intracellular-to-extracellular concentration gradients with the concentration of  $K^+$  within the erythrocyte about 10 times that in the blood plasma, whereas the concentration of  $Na^+$  is about 10 times lower and the concentration of  $Cl^-$  is also somewhat lower.<sup>1,2</sup> To prevent the possible diffusion of such ions along their concentration gradients during preparation for microprobe analysis, the biological specimens are usually rapidly frozen and thin frozen sections of the specimen are cut and freeze-dried at low temperatures.

Pure populations of mammalian erythrocytes, which are known to have a homogeneous intracellular structure and whose ionic composition is already accurately known by wet chemical analysis, provide us with an excellent biological test system for validating the accuracy of specimen preparation and instrumental microprobe procedures.<sup>3-5</sup>

In a series of studies with freeze-dried sections of erythrocytes used as such a test system, Tormey obtained anomalously high intraerythrocyte concentrations of  $Na$  and  $Cl$ , but accurate concentrations of  $K$ .<sup>3-5</sup> The excesses for  $Na$  and  $Cl$  were proportional to the concentration of each of these electrolytes in the extracellular environment. The source of the excess  $Na$  and  $Cl$  error was eventually traced to the scattering of electrons within the section; i.e., focusing of electrons on an intracellular area of a sectioned erythrocyte would result in enough lateral electron scatter to generate x rays from the extracellular environment, which is ten times higher in  $Na$  concentration. Being aware of this problem of doing microprobe analysis in the intraerythrocyte compartment immediately adjacent to the extracellular compartment with a high  $Na$  concentration, we decided that such a problem might be clarified and might also be circumvented in large measure by the centrifugal packing of the erythrocytes in such a way that the extracellular environment was almost eliminated. Thus, comparative analysis was done on packed and on unpacked erythrocytes to assess the extent of the electron scattering problem.

In addition, we were interested in an assessment of what temperatures are needed to prevent diffusion along the known intracellular-extracellular ion gradients during our specimen-preparation procedures. In this regard, packed and unpacked erythrocytes were prepared identically except that the cryosectioning and cryosorption were done at  $-40^\circ C$  in one case and at  $-100^\circ C$  in the other, which should allow us to assess the extent of any electron-scatter or ion-diffusion problem due to preparative temperature, as well as of possible interactions between these two variables.

Our overall objective in this study was to validate our electron-probe x-ray microanalysis methods by obtaining quantitative agreement with the known and accepted wet chemical measurements on erythrocytes.

### *Experimental Procedures*

To collect blood for determination of water content, mice were decapitated and the blood was collected in heparinized beakers. To obtain enough blood it was often necessary to pool blood from several mice. A tracer amount of  $^3H$  inulin, which served as an extracellular space marker, was added to a volume of blood. Aliquots of whole blood were trans-

---

The authors are at the Department of Anatomy, The University of Texas Health Science Center at San Antonio, San Antonio, TX 78284. Supported by National Science Foundation grant PCM 81084 to I. L. Cameron.

ferred into pre-washed and pre-weighed polyethylene microfuge tubes as described previously.<sup>6</sup> The cells were immediately agitated for 5 s at room temperature (24°C) to insure uniform distribution of the <sup>3</sup>H inulin and were centrifuged for 3-4 min in a microfuge at 1200×g. The residual plasma buffy coat was aspirated off from the packed erythrocytes; the weight of the remaining erythrocyte pellet was then determined. The tubes were placed in an oven at 80°C for 24-48 hr. The tubes were removed from the oven and placed in a vacuum dessicator to cool, and the dry erythrocyte weight was determined. This procedure was repeated until a constant weight was obtained. To determine extracellular space, heparinized cylindrical hematocrit tubes with a precise inside diameter of 1.15 mm were filled with whole blood and one end of the tube was sealed. The tube was then centrifuged for 3-4 min at 1200×g. A segment of the hematocrit tube containing packed erythrocytes or plasma was then broken off after score marks had been made with a diamond pencil. The volume of packed erythrocytes or of plasma was calculated from measurements of lengths of the tube filled with plasma and from the known inside diameter of the tube. The segments of the hematocrit tube with either packed erythrocytes or plasma were placed into scintillation vials containing 0.5 ml of ethanol. The vials were agitated until the contents of the hematocrit tubes were dispersed; then a 1:2 v/v mixture of Triton X: toluene (which also contained 0.4 g PPO and 0.01 g POPOP per liter of solution) was added to the vial as a scintillation cocktail. The samples were counted in a scintillation spectrometer.

For electron probe x-ray microanalysis a small drop of unpacked or of centrifugally packed erythrocytes from a single mouse was placed on a brass pin. The specimens were frozen by immersion in liquid propane cooled in a liquid nitrogen bath and were then transferred to and stored in liquid nitrogen until the time of sectioning. Sectioning was done on the LKB Ultratome V equipped with a modified cryokit and cooled to a temperature of -40°C or -100°C for both specimen and knife. A dry glass knife with a 40° angle and a sectioning speed of 0.5 mm/s was used for cutting. Ultrathin sections were obtained by advancing 0.1 µm on the microfeed. The 0.1µm-thick sections were positioned on a film of formvar (0.25% in dioxane) spanning a 1.5mm hole in a 3mm carbon grid. To minimize curling or movement of the sections, a carbon-coated formvar film on an aluminum ring was placed over the sections. The sandwiched specimen was dried within the LKB chamber at -40°C or at -100°C in a custom-made cryosorption apparatus by evacuation with a rotary pump for 2 hr. The sections were warmed to room temperature, vented with dry nitrogen gas, and stored in a desiccator. At the time of analysis the aluminum ring was removed, leaving a flat section sandwiched between two layers of formvar film. The sections were examined in a JEOL JSM35 scanning electron microscope under the following conditions: STEM mode, accelerating voltage 25 kV, specimen current 0.20 nA, raster size 0.27 µm<sup>2</sup>, analysis time 100 s, takeoff angle 40°, and specimen-to-detector distance 15 mm. Analysis was done by a Si(Li) x-ray detector and Tracor Northern NS-880 x-ray analysis system.

Our quantification technique is based on the Hall mass fraction method.<sup>7,8</sup> Continuum counts, due to the formvar, were measured and were subtracted prior to the calculation of elemental peak-to-continuum values, which were converted to content by a series of cryo-sectioned standards with known amounts of dried salts added to a 20% bovine serum albumin solution.

Analysis of variance statistics was used throughout. Where a significant F value was obtained, a Student-Newman-Keul's multiple range test was used to determine significant differences between the means of each treatment procedure.

## Results

An analysis of increasing force of gravity on the packed erythrocyte volume (hematocrit) was done to determine whether the erythrocytes could be further packed by an increase in the g force or whether hemolysis had occurred during the handling procedure. The packed erythrocyte volume (hematocrit) remained constant when subjected to g force of 1000×g or greater for 3-4 min (Fig. 1). Also, the layer of plasma immediately above the packed erythrocytes was clear and remained so for several hrs. At 1000×g and greater g force, the hematocrit was 46%. Thus, the g force used in the water-content studies was adequate to obtain maximal erythrocyte packing without hemolysis. Our results also indicate that g forces of up to 9300×g did not cause further cell packing or hemolysis.

Scanning transmission electron micrographs of cryosectioned and cryosorbed specimens used in this study exhibit a granularity within erythrocytes (Fig. 2), which is



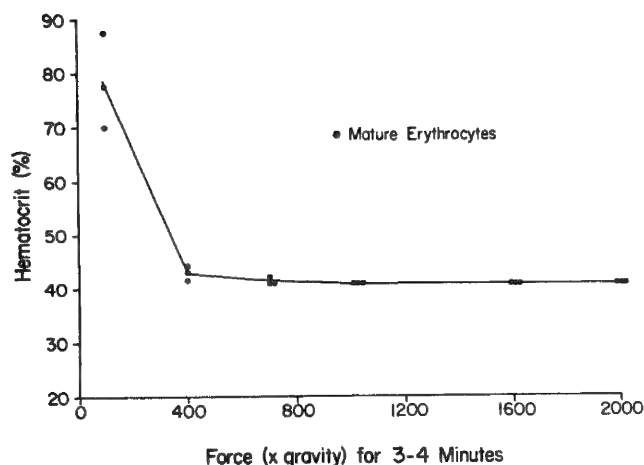


FIG. 1.--Centrifugal force (X gravity for 3-4 min) on packed erythrocyte volume (hematocrit) from heparinized blood of adult mice. No significant changes in hematocrit occurred above 1000xg.

other three preparative conditions. Although their mean values vary from 35 to 120 mM/kg dry weight, the variance is such that no other significant differences ( $p < 0.01$ ) were found between the other three preparative conditions. Likewise, for Cl, the unpacked erythrocytes processed at  $-40^{\circ}\text{C}$  had significantly higher Cl concentration values ( $p < 0.001$ ) than the other three conditions and no other significant differences ( $p < 0.01$ ) were found between the other three preparative conditions.

The mM/kg dry-weight data obtained on packed erythrocytes which were processed at  $-100^{\circ}\text{C}$  were converted to mM/kg water by use of the measured water content value given in a footnote to Table 2, which shows comparison of the mouse intraerythrocyte concentration of Na, Cl, and K as determined by electron-probe x-ray microanalysis and by wet chemical analysis. The microprobe data were subsequently corrected for the Na trapped in the extracellular space according to the formula: extracellular (trapped) Na = 140 mM sodium in the plasma  $\times$  3.6% extracellular (trapped) space  $\div$  100.

It seems reasonable to make a correction for the extracellular Na value, as the  $^3\text{H}$ -inulin measurements indicate that such an extracellular Na space does exist in the packed erythrocytes. Such a space could not be discerned or avoided during the microprobe of the packed erythrocytes. When the extracellular trapped-Na value is subtracted the intraerythrocyte, Na concentration falls within the range of Na concentration values reported by Benos.<sup>2</sup> Similar corrections for extracellular Cl and K were made but are of much smaller magnitude (Table 2). For K, the extracellular concentration is lower, so that trapped K value is added rather than subtracted to make the correction.

### Discussion and Conclusions

The data obtained in the present study indicate that the processing of erythrocytes suspended in blood plasma at a temperature of  $-40^{\circ}\text{C}$  leads to spuriously high erythrocyte Na and Cl concentration values. The most reasonable explanation for this finding is that Na and Cl have diffused from their higher concentration in the extracellular environment into the erythrocyte. Because of the small size of the erythrocytes, the area rastered for analysis is seldom if ever positioned more than 1  $\mu\text{m}$  from the extracellular space. Because the unpacked erythrocytes that were processed at  $-100^{\circ}\text{C}$  showed significantly less Na, we may conclude that the temperature difference is primarily responsible for the observed Na and Cl differences. Experiments are under way to determine whether the distances of Na and Cl diffusion in larger tissue cells are great enough to preclude use of  $-40^{\circ}\text{C}$  for the preparation of thin biological sections for microprobe analysis.

The observation that intracellular K did not show a significant diffusion along its

taken as evidence of ice crystal formation during specimen preparation. Almost no extracellular space can be seen in the packed erythrocytes and the edge of the individual erythrocytes is difficult to discern. Extracellular space and individual erythrocytes are clearly seen in the unpacked erythrocyte sample. The micrograph of the liver section is at the same magnification as the erythrocyte preparations and shows clearly the relatively small size of the erythrocytes and the surprisingly good morphological detail obtained with the cryopreparative procedure.

The results of the microprobe analysis are summarized in Table 1. A statistical analysis of variance of the data for each of the three elements was run. Highly significant F values were found for Na and Cl. As mentioned, a Student-Newman-Keul's multiple-range comparison test determines which of the four preparative conditions differ significantly from one another. For Na, the unpacked erythrocytes processed at  $-40^{\circ}\text{C}$  had significantly higher Na concentration values ( $p < 0.001$ ) than in the

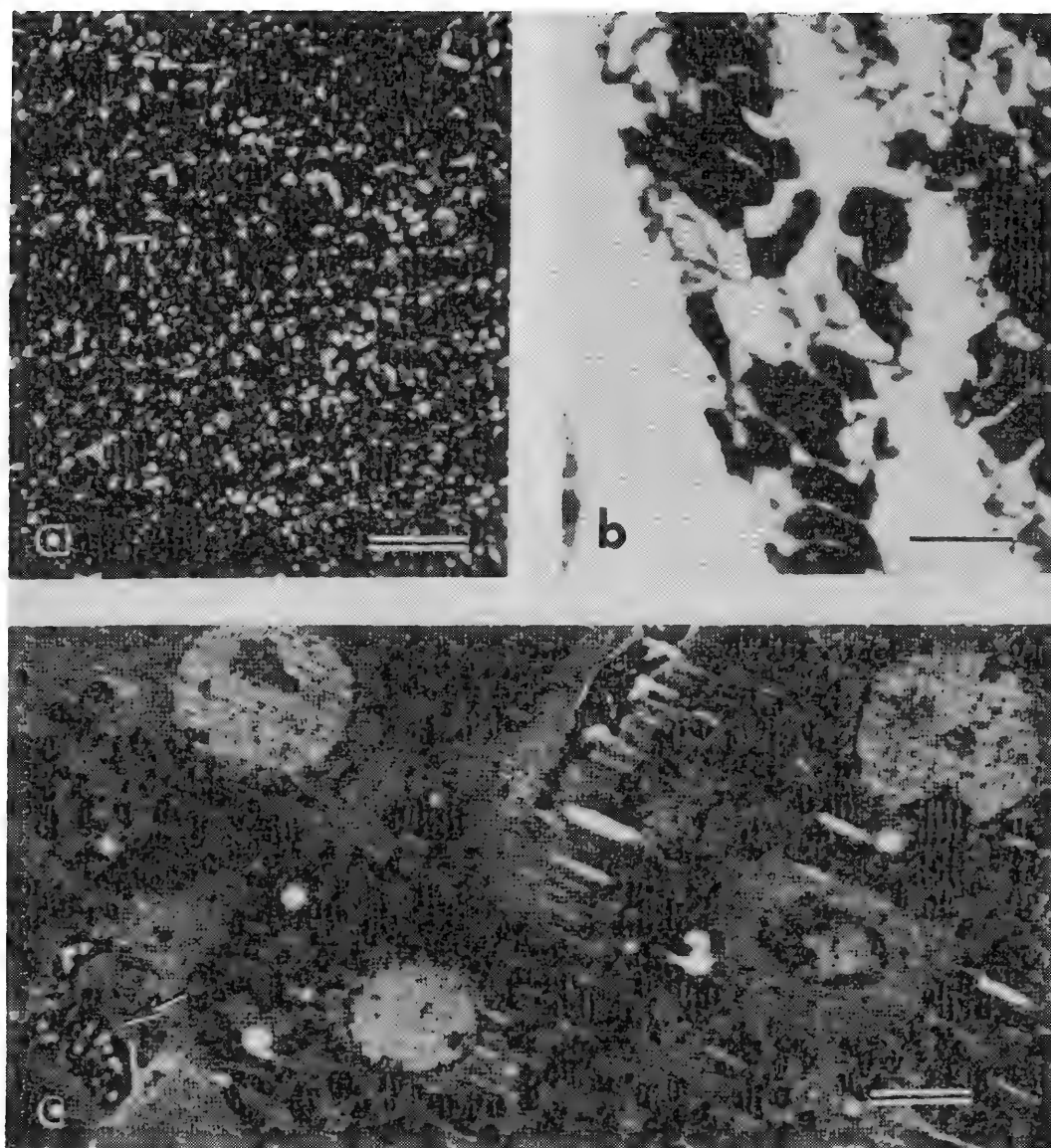


FIG. 2.--STEM micrographs of mouse erythrocytes packed at 9300 $\times$ g (upper left), erythrocytes in plasma (upper right), and liver (lower). Arrow in lower picture points to an erythrocyte. Ice crystals within erythrocytes are visible in all three micrographs. Scale bar = 5  $\mu$ m. All specimens were processed at  $-100^{\circ}\text{C}$ .

concentration gradient in the unpacked erythrocytes processed at  $-40^{\circ}\text{C}$  deserves comment. One possible explanation for the failure of K to diffuse from the erythrocyte is that a significant fraction of the intraerythrocyte K is not free to diffuse. Evidence for this possibility has been provided by x-ray absorption edge fine-structure studies of K in the erythrocytes from frogs. These studies show that an appreciable portion of the intraerythrocyte K is influenced by molecules other than water and is different from free K in solution.<sup>9</sup> On the other hand recent NMR reports on human erythrocytes indicate that most but not all of the intraerythrocyte Na is in a free ionic state.<sup>10</sup>

That no significant difference was found between the intraerythrocyte Na concentration values of packed and unpacked erythrocytes processed at  $-100^{\circ}\text{C}$  (Table 1) might be used to suggest that the scattering of electrons within the 0.1 $\mu$ m-thick cryosections is not a significant factor in our studies. However, because the mean erythrocyte Na concentration values are so variant we are somewhat reluctant to draw this as a firm conclusion until further studies with larger sample sizes have been made.

TABLE 1.--X-ray microanalysis data on intracellular concentration of Na, Cl, and K freeze-dried cryosections of erythrocytes estimated under different packing and processing temperature conditions (concentration in mM/kg dry weight, means  $\pm$  S.E.M.); ten erythrocytes were analyzed in each condition.

Conditions	Na	Cl	K
1. Packed -100°C	35 $\pm$ 10	173 $\pm$ 15	244 $\pm$ 15
2. Packed -40°C	64 $\pm$ 5	207 $\pm$ 3	302 $\pm$ 5
3. Unpacked -100°C	120 $\pm$ 11	208 $\pm$ 18	288 $\pm$ 12
4. Unpacked -40°C	393 $\pm$ 36	557 $\pm$ 37	242 $\pm$ 10

TABLE 2.--Comparison of the mouse intraerythrocyte concentration of Na, Cl, and K as determined by wet chemical analysis and by electron probe x-ray microanalysis (mM/kg H<sub>2</sub>O).

Technique	Na	Cl	K
Extraction and chemical analysis*	8 - 15	93 - 108	133 - 166
Microprobe analysis			
(uncorrected for extracellular space)	20 $\pm$ 6	101 $\pm$ 9	142 $\pm$ 9
(corrected for extracellular space)**	15	97.4	142.2

\*Range of values is from six different mouse strains as reported by Benos (2). The determinations were made on extracted dried pellets of erythrocytes using atomic absorption spectrophotometry for Na and K and using coulometric titration for Cl. Water content and extracellular spaces were measured and used in the calibrated concentration values.

\*\*These data were obtained on packed erythrocytes which were cryosectioned and cryosorbed at -100°C. The measured water content of the erythrocytes was 63.2  $\pm$  1.9 percent (n=3 determinations) while the mean extracellular (<sup>3</sup>H inulin) space ranged from 2.0 to 5.1 percent and averaged 3.6 percent. The concentration of extracellular Na, K and Cl used in the extracellular space correction were Na=140mM, K=6mM and Cl=120mM.

From the present study we do feel safe in concluding that we have developed and validated a procedure for the accurate quantification of intracellular electrolytes using energy-dispersive electron-probe x-ray microanalysis in thin cryosections of mouse erythrocytes.

#### References

1. J. Funder and J. O. Wieth, "Potassium, sodium, and water in normal human red blood cells," *Scand. J. Clin. & Lab. Investigation* 18: 167-180, 1966.
2. D. J. Benos, "Intracellular analysis of sodium, potassium, and chloride in mouse erythrocytes," *J. Cell. Physiol.* 105: 185-187, 1980.
3. J. M. Tormey, "Validation of methods for quantitative x-ray analysis of electrolytes using frozen sections of erythrocytes," *SEM/1978 II*, 259-266.
4. J. M. Tormey and R. M. Platz, "Instrumental factors affecting the accuracy of microprobe quantitation of electrolyte concentrations in frozen sections," *Microbeam Analysis--1979*, 77-79.
5. J. Tormey, "Preparation and use of erythrocyte sections as methodology for validating procedures for x-ray microanalysis of electrolytes," in Thomas Hutchinson and Andrew Somlyo, Eds., *Microprobe Analysis of Biological Systems*, New York: Academic Press, 1981, 172-195.
6. I. L. Cameron et al., "Changes in water proton relaxation time during erythrocyte maturation," *J. Cell Physiol.* (in press).
7. T. A. Hall, "The microprobe assay of chemical elements," in G. Oster, Ed., *Physical Techniques in Biological Research*, New York: Academic Press, 1971, 157-159.
8. T. A. Hall et al., "The use of thin specimens for x-ray microanalysis in biology," *J. Microsc.* 99: 177-182, 1973.
9. H. Huang, "X-ray absorption edge fine structure of potassium ions in various environments: Application to frog blood cells," *Science* 204: 191-193, 1979.
10. R. K. Gupta et al., "Direct observation of the state of  $^{23}\text{Na}^+$  ions in intact cells and tissues by noninvasive NMR spectroscopy: Intracellular  $\text{Na}^+$  ions in human normal and leukemic lymphocytes," in Alton Boynton et al., Eds., *Ions, Cell Proliferation, and Cancer*, New York: Academic Press, 1982, 1-12.

## ANALYTICAL PROCEDURES FOR BULK FROZEN-HYDRATED BIOLOGICAL TISSUES

Patrick Echlin, T. L. Hayes, and M. McKoon

The main advantage of using solid frozen samples for elemental x-ray microanalysis is the ease with which they may be prepared and maintained in the frozen-hydrated state. Within the limits imposed by the reduced spatial resolution of the method, the morphological identification of the tissue components is comparatively easy. These advantages are offset by the limited spatial resolution and the difficulty in obtaining quantitative analytical data from rough surfaces of solid samples. A consequence of these limitations is that the analysis of frozen-hydrated samples should generally be restricted to studies at the tissue and cellular level.

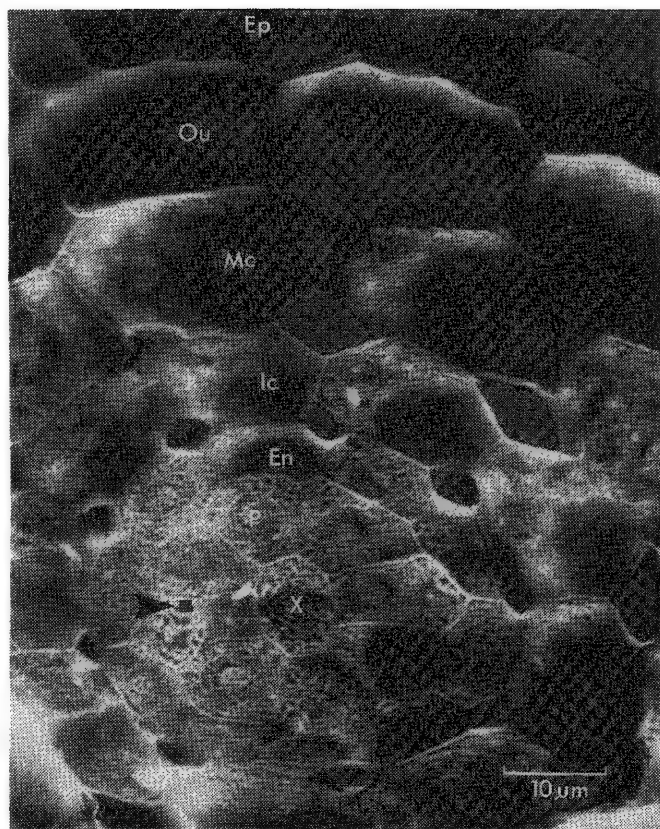
Bearing in mind these limitations, we have carried out an analysis for several elements in the developing root tips of *Lemna minor* L (Duckweed). A detailed description of the specimen preparation techniques, instrumentation, and x-ray analytical procedures are given in a recent paper.<sup>1</sup> In brief, fresh root tips of *Lemna minor* L, briefly encapsulated in a polymeric cryoprotectant, are quench frozen in melting nitrogen at ca. 70°K and transferred to the pre-cooled cold stage of an AMray Biochamber, a high-vacuum chamber attached to the column of an SEM via an air lock which allows frozen specimens to be fractured, etched, and coated at low temperature (100°K) and high vacuum 1-10  $\mu$ Pa) before being transferred via a second air lock to the pre-cooled cold stage of an AMray 1000A SEM. The analysis was carried out by means of a Kevex energy-dispersive detector by use of the peak-to-background ratio method.

These procedures allow us to obtain flat fracture faces (Fig. 1) in which we have been able to measure the relative concentrations of various elements at the various stages of differentiation in the root tissue. Table 1 shows the values for potassium and phosphorus in the xylem at various points along the long axis of the root tip. We are attempting to devise analytical procedures to enable us to convert these relative concentrations to absolute concentrations. Any attempt at quantitation must take into consideration a number of factors relating both to the specimen and the instrumentation.

TABLE 1. Peak/background ratios for  $K^+$  and P in *Lemna minor* root tip xylem.

Distance in $\mu$ m from root tip	70	85	95	150	200	225	400	1500	2500	5000
Potassium	1.26	0.24	0.43	0.74	0.37	0.41	0.70	1.04	1.78	2.21
Phosphorus	0.73	0.14	0.17	0.32	0.16	0.30	0.33	0.55	0.50	0.34

Author Echlin is at the Botany School, Downing Street, Cambridge, England CB2 3EA; authors Hayes and McKoon are at the Donner Laboratory, University of California, Berkeley, CA 94720. One of us (P.E.) is indebted to the Director of the Donner Laboratory at Berkeley for allowing him to carry out the x-ray analytical work associated with this study. Supported in part by U. S. Department of Energy.



### Spatial Resolution

Because the electron beam diffuses randomly in the frozen hydrated sample, there is still some discussion concerning the size and shape of the interactive volume. Using the most pessimistic range equations,<sup>3,4</sup> the x-ray spatial resolution for sodium is ca 4.0 μm lateral and 8.0 μm in depth at 15-17 kV.

A recent study by Marshall<sup>4</sup> has shown that these figures are probably an overestimate, since the micro volume from which x rays are emitted is smaller than the limits of electron penetration. On the basis of the  $\phi(\rho z)$  curves provided by Marshall we have calculated that 90% of the sodium x rays come from a microvolume 3.5 μm wide and 4.0 μm deep. Because sodium is the lightest element we have analyzed, these are the most pessimistic figures and the values for K<sup>+</sup> and P will be even smaller. We are confident that the analytical micro volume will be confined to the individual cell being analyzed. Figure 2 gives a diagrammatic representation of the two methods of calculating x-ray spatial resolution.

### Peak-to-background Ratio Method

This analytical program has been found to be more efficient and accurate than the more commonly used ZAF technique, which was designed for analyzing bulk samples of higher density. The rationale behind the development and use of the P/B procedure is that since the characteristic and background x rays of the same energy are generated within the same depth distribution, they are subject to the same compositional related absorption secondary fluorescence and atomic number effects. These assumptions are particularly valid for frozen-hydrated samples, which in *Lemna* contain 80-90% water and can for all intents be considered homogeneous specimens. Another advantage of the P/B ratio method is that the ratio of peak area to background immediately below the peak is more or less independent

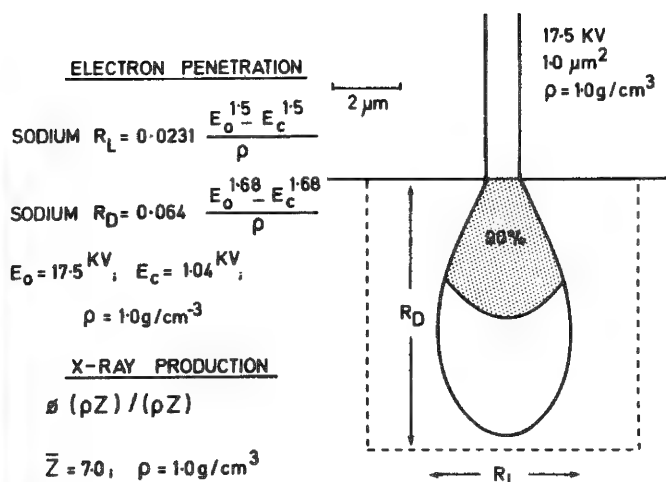


FIG. 2.--Two methods of calculating micro-volume in x-ray microanalysis.

FIG. 1.--Frozen-hydrated fracture face across root of *Lemna minor* L taken approximately 250 μm from root-tip. Surface has been lightly etched to reveal some of the subcellular contents. Carbon coated and photographed at 100 K and 15 keV. Small square (arrowed) shows size of raster used during x-ray microanalysis, slightly larger than average size of ice crystallites to insure representative analysis. In addition to the large air spaces, X = xylem; P = phloem; En = endodermis; Ic, Mc, and Oc = inner, middle, and outer cortex; Ep = epidermis.

of the sample geometry.

### *Sample Geometry*

Although the P/B ratio method is relatively insensitive to small changes in surface geometry, we have found that uneven fracture faces give unreliable x-ray data because of preferential masking and absorption. Because it is relatively easy to obtain smooth fracture faces, whose appearance may be readily checked by means of stereo pair photographs, we do not consider that small variations (i.e.,  $\pm 0.5 \mu\text{m}$ ) in the sample geometry contributes a significant error to the analytical procedures.

### *Degree of Hydration*

The analysis must be carried out in the fully hydrated state or where a surface layer has been etched to a depth of no more than  $0.2 \mu\text{m}$ . Lai and Hayes were able to show that there is a ten fold increase in the P/B ratio of a given element as one proceeds from the fully hydrated to the fully dried state.<sup>5</sup> In addition, the size of the interactive micro-volume shows a similar dramatic increase as one proceeds from the fully hydrated to the fully dried state. Thus the previously quoted figures of  $4 \times 8 \mu\text{m}$  for frozen-hydrated material rises to  $10 \times 22 \mu\text{m}$  if the same sample is simply frozen dried.

### *Standards*

Following a suggestion by Whitecross et al.,<sup>6</sup> we have made standards incorporating graphite. In addition we have used a small amount of a cryoprotectant, hydroxyethyl starch to insure a microcrystalline ice crystal formation and a consequent homogeneity of dispersion within the matrix. The standards have been prepared as follows. Aqueous solutions of Analar Reagent grade potassium phosphate ( $\text{KH}_2\text{PO}_4$ ) were made up in double distilled water at a range of concentration between 1000 and 10 mM. For each of the concentrations, 4 g of the salt solution were added to 1 g of hydroxyethyl starch (MW 450 000) that had been previously dialyzed against distilled water and then frozen dried. The hydroxyethyl starch dissolved in the salt solution by heating to  $300^\circ\text{K}$ . Once the polymer had dissolved, 2.5 g of Spec pure (TM) graphite powder grade 1 (Johnson Matthey Chemical Ltd.) were added to each sample and the whole thoroughly mixed. This procedure yields a series of  $\text{KH}_2\text{PO}_4$  concentrations of 615, 308, 154, 77, 39, 19, 10, and 5 mM containing 15.4% hydroxyethyl starch and 38.5% graphite. Independent analysis of the distilled water, graphite, and hydroxyethyl starch using atomic absorption spectroscopy and flame photometry failed to show any significant levels of potassium or phosphorus. Small droplets of each of the slurry standards were mounted on carbon specimen holders and frozen by plunging into melting nitrogen at ca  $70^\circ\text{K}$ . The frozen standards were transferred to the Biochamber where they were fractured and subsequently analyzed at  $100^\circ\text{K}$  by means of a 3nA beam current and 17.5kV accelerating voltage in the fully hydrated unetched, fully hydrated but surface etched, and frozen dried state.

The presence of graphite eliminated any charging problems; there was a significant change in the peak-to-background ratios of both potassium and phosphorus between the frozen dried and frozen hydrated state. The presence of the cryoprotectant and the graphite appears to promote the production of very small ice crystals as well as giving smooth fracture faces with optimized thermal and electrical properties.

We have been using these standards to study the following phenomena.

1. Conversion of the relative elemental concentrations measured in tissues to absolute values.
2. Measurement of the relative changes in peak-to-background ratio of various elements in relation to changes in accelerating voltage and beam current. An earlier study<sup>7</sup> has shown that there were only small variations in the  $\text{K}^+$  P/B ratio normalized to phosphorus with changes in accelerating voltage in the range 10-20 keV. We are now determining whether changes in the individual elements are on a sufficiently regular pattern that we can apply corrections to analytical data obtained at different accelerating voltages and beam current.
3. Measurement of the relative changes in P/B ratio for elements in the frozen-hydrated and frozen-dried state where the water concentration is known. In this way it should be possible to measure the water content of tissues by measurement of the P/B ratios



of elements in the frozen-dried and frozen-hydrated states.

### References

1. P. Echlin, C. E. Lai, and T. L. Hayes, "Low temperature x-ray microanalysis of the differentiating vacular tissue on root tips of *Lemna minor* L," *J. Micros.* 126: 285-306, 1982.
2. C. A. Anderson and M. F. Hasler, "Extension of electron microprobe techniques to biochemistry by the use of long wavelength x-rays," in R. Castaing, P. Deschamps, and J. Philibert, Eds., *Proc. 4th Intern. Cong. X-ray Optics and Microanalysis*, Paris: Hermann, 1966, 310.
3. S. J. B. Read, *Electron Microprobe Analysis*, London: Cambridge University Press, 1975, 211-217.
4. A. T. Marshall, "The application of  $\phi(\rho z)$  curves to the quantitative analysis of frozen biological material," *SEM/1982 I*, 243-260.
5. P. Echlin, C. Lai, and T. L. Hayes, "The distribution and relative concentration of potassium in the root tips of *Lemna minor* L analyzed by low temperature x-ray microanalysis," *SEM/1981 I*, 489.
6. C. Lai and T. L. Hayes, "Calibration of SEM frozen hydrated analysis using standard salt solutions and peak to background measurements," *Proc. 38th Ann. EMSA Meeting*, 1980, 800.
7. M. I. Whitecross, G. D. Price, and J. S. Preston, "Use of colloidal graphite in frozen hydrated standard solutions for x-ray microanalysis," *J. Micros.* 128: RP 3, 1982.

## QUANTITATIVE ELECTRON ENERGY LOSS SPECTROSCOPY OF LOW CONCENTRATIONS OF CALCIUM IN CARBON CONTAINING MATRICES

H. Shuman, P. Kruit, and A. P. Somlyo

The signal collected, for a given beam current, is far greater in electron energy loss spectra than in x-ray spectra.<sup>1-4</sup> However, it does not directly follow that for the measurement of *low concentrations* of elements electron energy loss spectroscopy (EELS) is a more sensitive technique than electron probe microanalysis (EPMA); the large signal collected with EELS is superimposed on a very large background originating from the low-loss part (collective excitations) of the spectrum and the high-energy tail of signals originating from inner shell excitations with absorption edges below those of the element of interest. The low-loss background can be fitted reasonably well to a power law  $AE^{-r}$  (where  $E$  is the energy loss),<sup>5</sup> and background subtraction can be performed with this technique. Quantitation of relatively high concentrations of elements is feasible with a precision of approximately 15-20%.<sup>6</sup> However, this background-fitting method does not solve the problem of overlapping EELS signals, particularly when the concentration of the element of interest is much lower than that of another element with which its signal overlaps. An important problem of this type is one commonly encountered in biology, involving the quantitation of low concentrations of calcium in cells. Carbon is the largest component of biological matrices, and the most suitable EELS signal for the quantitation of calcium,<sup>7</sup> the  $L_{2,3}$  edge at 350 eV, is overlapped by the carbon K-edge signal beginning at 284 eV.

The efficiency of EELS is greatly increased by the use of parallel detection techniques;<sup>1,7-10</sup> we have used a phosphor coupled silicon intensified video camera for this purpose.<sup>8</sup> Parallel collection also overcomes variations in the spectrum introduced by the relatively large fluctuations in the field emission gun current, but has the disadvantage of nonuniform gain due to channel-to-channel variations in the parallel detection system. In this communication we shall illustrate methods being developed for the quantitation of low concentrations of calcium in a carbon matrix with a parallel detection system corrected for nonuniform gain. Furthermore, because the Ca  $L_{2,3}$  edges are sharp (white lines), one can also reduce the background and correct gain variations by collecting the second difference of the EELS spectra.

Figure 1(a) shows part of an EELS spectrum obtained from a thin film standard of 30 mmol/kg Ca EGTA dissolved in polyvinylpyrrolidone (PVP) (~0.1 wt.%). The spectrum was obtained in 80 s with a magnetic-sector spectrometer below the projector chamber of a Philips EM400 equipped with a field-emission gun. The Ca signal, expected to be at 350 eV, cannot be distinguished from the gain variation-caused fluctuations in the carbon spectrum. The two methods for obtaining the calcium signal and some illustrations of its application to biological specimens follow.

### *The Second Difference Method*

Taking the second difference of the signal with respect to the energy enhances the sharp features like white lines and thresholds, as compared to the smooth but large and sloping background. It can be shown that a feature with half width of  $E_1$  eV compared to a feature of similar form but half width  $E_2$  eV is enhanced by a factor  $(E_2/E_1)^2$ . Moreover the method can reduce the effect of the gain variation. A measured parallel recorded spectrum is given by

$$X(n) = G(n)N(n) \quad (1)$$

The authors are at the Pennsylvania Muscle Institute and the Departments of Physiology and Pathology of the University of Pennsylvania School of Medicine, Philadelphia, PA 19104. Supported by HL15835 to the Pennsylvania Muscle Institute.

where  $n$  = channel number,  $G(n)$  = gain, and  $N(E_n)$  = number of electrons arriving in channel  $n$ . The numerical second difference is then

$$\delta^2 X = G(n-1)N(E_{n-1}) - 2G(n)N(E_n) + G(n+1)N(E_{n+1}) \quad (2)$$

If, however, we measure three spectra at different decelerating voltages and take the second difference between these three spectra,

$$SD(n) = G(n)N(E_n - \Delta E) - 2G(n)N(E_n) + G(n)N(E_n + \Delta E) = G(n)\delta^2 N \quad (3)$$

the effect of the gain variations is reduced with the same factor as the background. Figure 1(b) shows the second difference from the data of the spectrum of Fig. 1(a). The Ca  $L_{2,3}$  white lines are now clearly visible in this (nominally) 30mmol Ca/kg dry wt. specimen. One can quantitate the calcium concentration by fitting this spectrum to a standard spectrum obtained from material containing a higher Ca concentration. The standard contained 240 mmol/kg Ca, as measured by EPMA. Figure 1(c) shows the result of the fitting procedure. The regions of the spectrum containing the carbon, calcium, and nitrogen edges are each fitted separately to the standard plus a second-order polynomial. We then compare the relative height of the calcium peaks to the relative height of the carbon peaks. According to this fit, the concentration was 29 mmol/kg, with a statistical error of 2 mmol/kg. To check the consistency of the method, we have done some experiments on thin-film standards containing different concentrations of calcium and plotted the measured concentration against the nominal concentration (Fig. 2). The spread in the data is 2-3 times larger than we would expect from statistical errors, which leads to the conclusion that there is room left for improvement.

#### *The Gain Correction Method*

Although not to be expected over a long period, one can assume the gain in each channel to be constant during a short time. This feature enables the calculation of the gain directly from two EELS spectra, measured at different decelerating voltages:

$$\begin{aligned} X_1(n) &= G(n)N(E_n) \\ X_2(n) &= G(n)N(E_n + \Delta E) \end{aligned} \quad (4)$$

The shift of the second spectrum on the energy axis can be chosen in such a way that  $E$  corresponds to a one-channel shift

$$N(E_n + \Delta E) = N(E_{n+1}) \quad (6)$$

Substituting Eq. (6) in Eq. (5) and combination with Eq. (4) yields the equation:

$$\frac{G(n+1)}{G(n)} = \frac{X_1(n+1)}{X_2(n)} \quad (7)$$

from which the gain in each individual channel can be expressed relative to the gain in channel 1:

$$G(m) = G(1) \frac{\prod_{n=2}^m X_1(n)}{\prod_{n=1}^{m-1} X_2(n)} \quad (8)$$

Now the real signal  $N(E_n)$  can be retrieved easily.

An assumption is, of course, that  $N(E)$  in both measurements  $X_1$  and  $X_2$  was equal. If that is not the case (for instance, because of primary beam fluctuations), a correction is necessary. The result of this method, applied to the data of Fig. 1(a), is shown in Fig. 3(a). The spectrum is very much smoother, but even in this spectrum the Ca peaks are not directly visible. In principle, it is now possible to deconvolute the spectrum to an

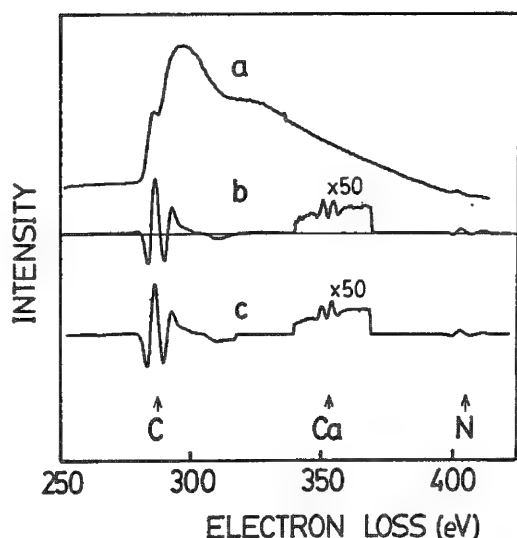


FIG. 1.--(a) EEL spectrum of PVP shows fluctuations caused by channel-to-channel gain variations of parallel detection; (b) second difference according to Eq. (3); (c) fit to standard spectrum.

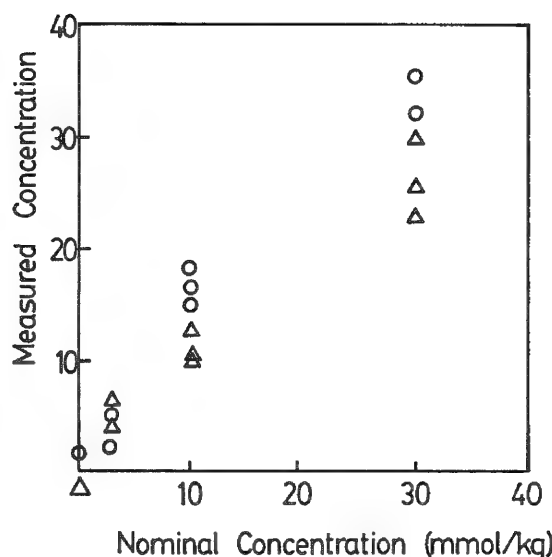


FIG. 2.--Measured concentrations of calcium in PVP, as obtained from fits of second difference spectrum to spectrum calibrated by x-ray microanalysis. Points arranged by same symbol are measured at same spot on sample.

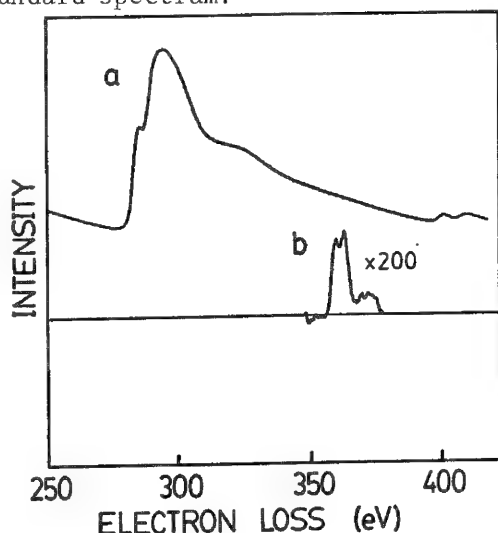


FIG. 3.--(a) Same spectrum as shown in Fig. 1(a), after correction for gain variations; (b) enlarged part of spectrum (a) after subtraction of similar spectrum, containing no calcium, plus straight line.

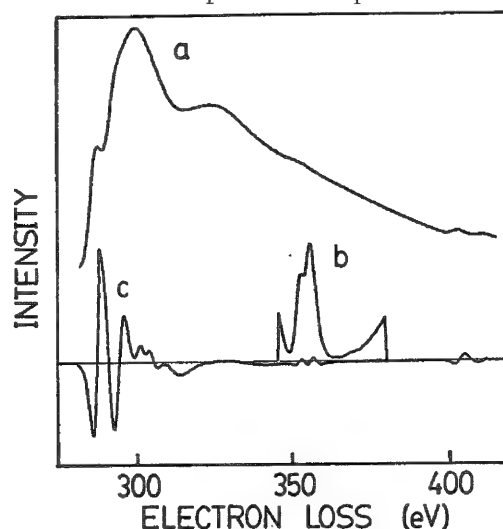


FIG. 4.--(a) EEL spectrum of terminal cisternae of frog muscle; (b) after subtraction of straight line, showing Ca  $L_{2,3}$  white lines; (c) second difference spectrum.

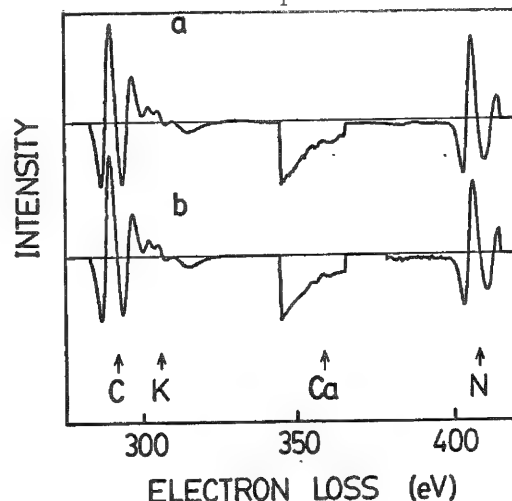


FIG. 5.--(a) Second difference of EEL spectrum of I-band of frog muscle cytoplasm; (b) fit to second difference of spectrum (a).

equivalent zero-thickness spectrum<sup>11</sup> and find the relative contributions of the different elements by fitting to library or computed pure element spectra. We are in the process of testing these procedures. As a preliminary result, we show in Fig. 3(b) the difference between the spectrum of Fig. 3(a) and a similar spectrum containing no calcium plus a straight line. It shows that the height of the Ca  $L_{2,3}$  lines is only 0.0035 of the background.

### Biological Applications

In most biological systems, calcium occurs either sequestered in organelles at high concentrations or distributed throughout the cytoplasm at relatively low concentrations. The best-studied example of this type of intracellular calcium distribution is in resting striated muscle, in which most of the intracellular calcium is localized in the terminal cisternae (TC) of the sarcoplasmic reticulum (SR).<sup>12-15</sup> In resting skeletal muscle the concentration of Ca is approximately 120 mmol/kg dry wt. in the TC<sup>14,15</sup> and about 3 mmol/kg dry wt. in the I-band (thin filaments). The precision of the EPMA measurements of the low concentrations of Ca in the presence of high concentrations (about 500 mmol/kg dry wt.) K in normal muscle is somewhat reduced due to the overlap between the potassium  $K\beta$  and calcium  $K\alpha$  x-ray peaks. In the A-band (myosin filament) region of frog skeletal muscle Ca is not detected with EPMA when this region is exposed to free  $Ca^{2+}$  concentrations comparable to in vivo resting levels.<sup>17</sup> EELS spectra were obtained from TC, I-band, and A-band regions in the same cryosections (~100-150 nm thick when wet) of rapidly frozen, relaxed semitendinosus muscles.<sup>14</sup> Second difference EELS spectra were collected in 45 s by focusing an approximately 1 nA probe on individual TC. The EELS spectrum of TC displayed in Fig. 4(a) is summed from 10 different TC and thus represents a total collection time of approximately 450 s. In Fig. 4(b) a straight line is subtracted to show the high signal to noise obtainable with this method. STEM imaging with real time processing has been demonstrated for high Ca concentrations.<sup>16</sup> We anticipate that with parallel collection imaging is also possible for these low concentrations, with measurement times less than 1 s per pixel.

A summed EELS second difference spectrum from the I-bands of the same muscle fibers is shown in Fig. 5, together with the best fit to the spectrum of the high calcium containing TC. We made corrections for minor shifts in the absolute energy values of the edges (due to stray fields, instrumental instabilities, etc.) by performing a cross correlation between the standard and unknown spectra, and shifting the standard by the appropriate amount. The Ca/N and Ca/C ratios for the I- and A-bands relative to the TC are

	$(Ca/N)/(Ca/N)_{TC}$	$(Ca/C)/(Ca/C)_{TC}$
I-band	$0.0134 \pm 0.0006$	$0.019 \pm 0.001$
A-band	$0.003 \pm 0.0005$	$0.006 \pm 0.001$

The errors given are the statistical errors; the real error is larger since the reduced  $\chi^2$  value of the fit was  $\chi^2 = 4.5$ . The A-band measurement is too close to the limits of quantitative precision to draw any reliable conclusions about the absolute concentration present in this region. Obtaining the Ca concentration relative to that of nitrogen has the distinct advantage of eliminating the contribution of carbon supporting film to the carbon K-edge loss in EELS. However, the rate and final extent of nitrogen loss due to radiation damage, known to occur in model compounds,<sup>18,19</sup> has not been determined in proteins. Therefore, the effects of radiation damage on nitrogen loss from protein and from standards (e.g., PVP) will have to be determined. The deconvolution of plural scattering<sup>11,20</sup> will also be desirable for eliminating thickness-dependent effects on the concentrations measured. Even in the cryosections used for these studies in which spectra were obtained from the TC and regions of the I- and A-bands that were adjacent (and therefore presumably cut to equal thickness), the mass thickness of the TC and A-band are still higher than that of the I-band, due to a relatively higher degree of hydration (lower protein content) of the latter. Plural scattering removes the loss edge electrons from the edge region and transfers them into a higher loss, broadened domain. This action results in an underestimate of the Ca signal, although normalization to the nitrogen or carbon edges reduces the error in the calculated concentrations. However, given these

precautions, EELS promises to be a sensitive and reliable means of quantitating calcium in biological material.

### References

1. M. S. Isaacson and D. E. Johnson, "The microanalysis of light elements using transmitted energy loss electrons," *Ultramicroscopy* 1: 33-52, 1975.
2. J. J. Hren, J. I. Goldstein, and D. C. Joy, Eds., *Introduction to Analytical Electron Microscopy*, New York: Plenum Press, 1979.
3. C. Colliex, "Electron energy loss spectroscopy in the electron microscope," *Advances in Optical and Electron Microscopy* (in press).
4. A. P. Somlyo and H. Shuman, "Electron probe and electron energy loss analysis in biology," *Ultramicroscopy* 8: 219-234, 1982.
5. R. F. Egerton, "A revised expression for signal/noise ratio in EELS," *Ultramicroscopy* 9: 387-390, 1982.
6. D. Maher and D. Joy, "Quantitative elemental analysis using electron energy loss spectroscopy," in T. E. Hutchinson and A. P. Somlyo, Eds., *Microprobe Analysis of Biological Systems*, New York: Academic Press, 1981, 325-350.
7. H. Shuman, A. V. Somlyo, and A. P. Somlyo, "Electron energy loss analysis and its biological applications with special reference to muscle," *Microbeam Analysis--1980*, 275-279.
8. H. Shuman, "Parallel recording of electron energy loss spectra," *Ultramicroscopy* 6: 163-168, 1981.
9. D. E. Johnson et al., "A photodiode, parallel detection system for energy loss spectrometry," *Proc. 39th Ann. Mtg. EMSA*, 1981, 370-371.
10. R. F. Egerton, "Design of a parallel-detection system for EELS," *ibid.*, 368-369.
11. R. D. Leapman and C. R. Swyt, "A practical method for removing plural scattering from core edges in EELS," *ibid.*, 636.
12. A. V. Somlyo, H. Shuman, and A. P. Somlyo, "Elemental distribution in striated muscle and effects of hypertrophy," *J. Cell Biol.* 74: 828-857, 1977.
13. A. V. Somlyo, H. Shuman, and A. P. Somlyo, "The composition of the sarcoplasmic reticulum *in situ*: Electron probe x-ray microanalysis of cryosections," *Nature* 268: 556-558, 1977.
14. A. V. Somlyo et al., "Calcium release and ionic changes in the sarcoplasmic reticulum of tetanized muscle: An electron probe study," *J. Cell Biol.* 90: 577-594, 1981.
15. H. Gonzalez-Serratos et al., "The composition of vacuoles and sarcoplasmic reticulum in fatigued muscle: Electron probe analysis," *Proc. Natl. Acad. Sci. USA* 75: 1329-1333, 1978.
16. C. Fiori, Private communication.
17. T. Kitazawa, H. Shuman, and A. P. Somlyo, "Calcium and magnesium binding to thin and thick filaments in skinned muscle fibers: Electron probe analysis," *J. Muscle Res. Cell Motil.* 3: 437-454, 1982.
18. R. F. Egerton, "Chemical measurement of radiation damage in organic samples at and below room temperature," *Ultramicroscopy* 5: 521-523, 1980.
19. R. F. Egerton, "Organic mass loss at 100 K and 300 K," *J. Microsc.* 126(Part 1): 95-100, 1982.
20. D. C. Joy, "Processing electron energy loss spectra," *Microbeam Analysis--1982*, 98-106.

## PHOTOELECTRON MICROSCOPY OF BIOLOGICAL SURFACES

O. Hayes Griffith

When a surface is illuminated by light of sufficiently short wavelength, electrons are ejected from the surface. Most students encounter the photoelectric effect in freshman physics and chemistry textbooks in the form of Einstein's photoelectric equation  $KE_m = h\nu - \phi$ , which stresses the relationship between the maximum kinetic energy  $KE_m$  of the photoelectron, the energy of the photon  $h\nu$ , and the work function  $\phi$  of the surface. This equation has played an important role in the development of the quantum theory, explaining the observed dependence of electron energy on radiation frequency. Less widely appreciated is that valuable information can be gained from observing *where* the photoelectrons leave the surface. To gather this information one must accelerate the photoelectrons as they emerge from the surface and image them with an electron optics system in an instrument called the photoelectron microscope (PEM or photoemission electron microscope). The first low-power emission microscopes, including photoelectron microscopes, pre-date transmission electron microscopy (TEM) and scanning electron microscopy (SEM), but until recently PEM has remained an obscure and relatively unknown technique. Nevertheless the physics is reasonably well understood<sup>1</sup> and in the 1970s the successful imaging of organic and biological specimens has broadened the interest in photoelectron microscopy.<sup>2</sup> Furthermore, the advent of modern ultrahigh-vacuum techniques, image intensifiers, and related technology has made this technique more practical and worthy of serious consideration in a wide range of surface studies.<sup>3</sup>

### *Comparison of PEM and SEM*

A comparison of PEM and SEM is shown schematically in Fig. 1. In PEM a large area of the specimen is irradiated with UV light and the photoelectrons are *simultaneously* collected from the entire area contributing to the image. In SEM an electron gun scans the specimen and the image is collected from a small spot point by point. In both techniques electrons are produced at various depths in the specimen. The electron escape depth  $D_p$  in PEM is extremely short, which means that this technique has a very high depth resolution. The depth resolution in SEM is good, but less than that in PEM.<sup>4</sup> In both techniques the emitted electron beams carry sharply defined information from surface details along with information from below the surface which is more diffuse, but PEM and SEM image this information differently. In PEM the sharply defined detail is imaged separately and superimposed on any diffuse information. In SEM, secondary electrons are emitted from within the escape depth  $D_{SE}$  under the probe and also the surrounding bloom area. Some of these secondary electrons are generated by backscattered electrons from greater depths. All these secondary electrons are collected in the SEM to give a larger depth of information, and hence poorer depth resolution.<sup>5</sup>

Another difference between PEM and SEM is that PEM excites the valence electrons whereas SEM probes most electronic states, in particular the core electrons. This is a direct consequence of the input energy. The UV excitation lamp in PEM is normally only 4-6 eV, barely above the threshold of photoemission, whereas the scanning beam of electrons in SEM has energies greater by three or four orders of magnitude. Material contrast in PEM arises from differences in the valence electron structures much in the same way as in fluorescence microscopy. Two molecules with similar elemental analyses can have very different photoelec-

---

The author is at the Institute of Molecular Biology, University of Oregon, Eugene, OR 97403. He wishes to thank Dr. Karen Nadakavukaren for her continued involvement in the cell biological aspects of this program and D. L. Habliston for expert technical assistance. Also acknowledged are useful discussions with Drs. G. B. Birrell, W. A. Houle, and Patricia Jost. This work was supported by PHS grant CA11695 from the National Cancer Inst.



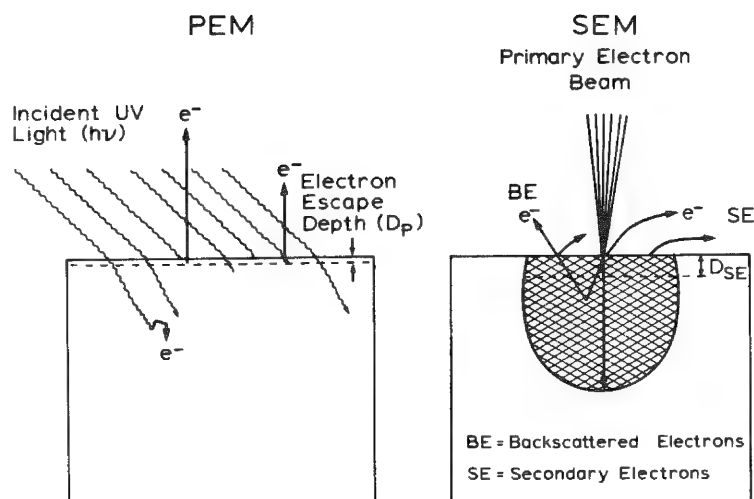


FIG. 1.--Comparison of PEM and SEM physical processes: in PEM there is no electron gun and UV light provides energy to photoeject electrons; in SEM specimen is scanned with tightly focused electron beam.

vapor lamps is reflected off the anode mirror onto the specimen surface, a geometry originally suggested by Engel to maximize the solid angle of illumination.<sup>7</sup> The specimen is maintained at high negative potential so that the emitted photoelectrons are quickly accelerated to 30-40 kV before entering the TEM-like electron optics system. In our instrument the objective, intermediate, and projector lenses are electrostatic unipotential lenses because this design is readily incorporated into an ultrahigh vacuum system, but magnetic lenses can also be used. The electrons are imaged on an aluminized phosphor screen fiber-optically coupled to a TV-image intensifier for viewing and focusing. An internal camera provides the permanent micrographs. The current resolution of PEM is of the order of 100 Å and the design limit of the present instrument is approximately 40 Å.

tron quantum yields. For example,  $\pi$ -conjugated hydrocarbons are much more photoemissive than saturated hydrocarbons.<sup>6</sup> This difference would be difficult to detect by SEM but on the other hand SEM and related microbeam techniques equipped with the appropriate detectors excel at elemental analyses, a property of the core electrons. Thus, in many respects PEM and SEM are complementary techniques and provide different information about biological surfaces.

### Instrumentation

Figure 2(a) shows a simplified diagram of a photoelectron microscope and Fig. 2(b) is an enlargement of the area around the specimen. Light from UV short-arc metal

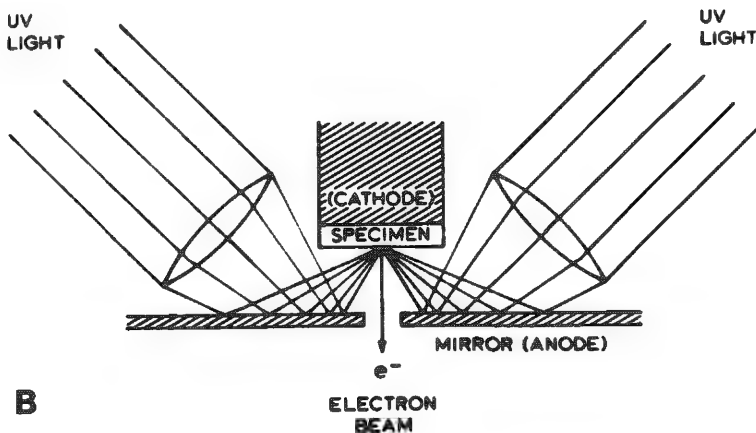
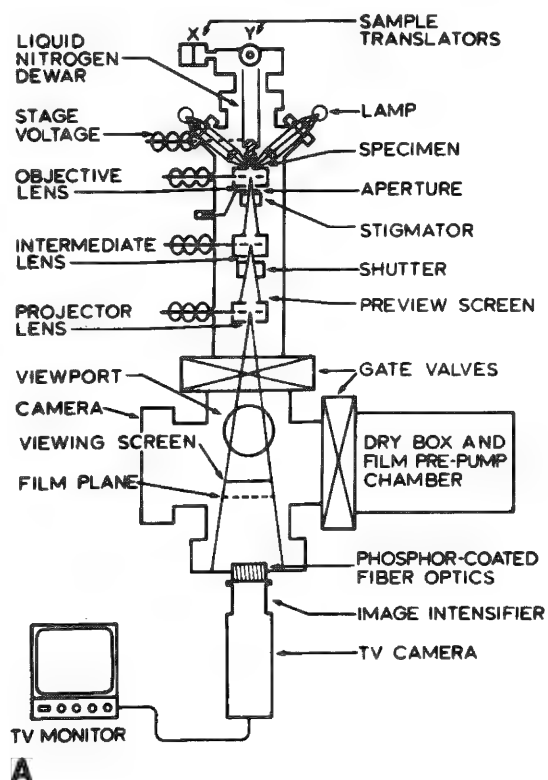


FIG. 2.--(a) Photoelectron microscope and (b) UV optics that focus light on specimen. Not shown: cathode cup that surrounds specimen (except for central 3mm-diameter aperture to allow UV light in and electrons out). This PEM is a stainless-steel, ultrahigh-vacuum instrument with copper seals and bellows in place of dynamic O-rings.



FIG. 3.--PEM micrograph of uncoated normal rat fibroblast cells (Rat-1 cell line) grown on serum-coated conductive (tin oxide coated) glass disks. Cells were fixed in a 2.5% glutaraldehyde (0.25 mM HEPES buffered saline), dehydrated through graded series of ethanol in water followed by 1:1 ethanol:amyl acetate and 100% amyl acetate, and dried in stream of warm air. Aperture, 50  $\mu$ m; exposure time, 40 s.

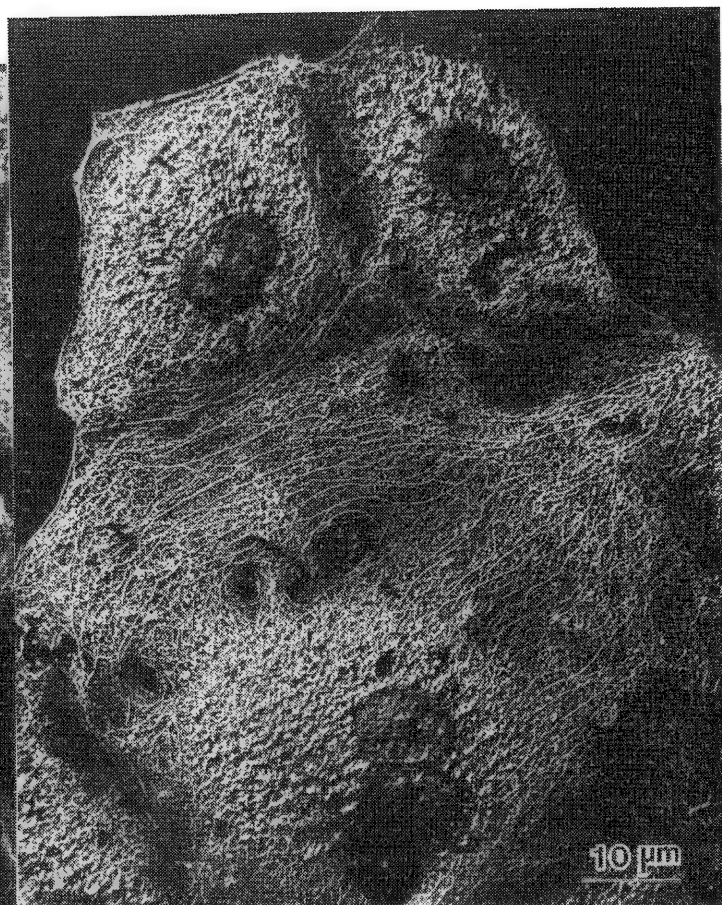


FIG. 4.--PEM micrograph of uncoated epithelial cells (PtK2 cell line) grown on tin oxide coated glass disk coated with serum and prepared for immunofluorescent visualization of keratin.<sup>8</sup> Cells were fixed and permeabilized in -20°C methanol, rinsed with distilled water and phosphate buffered saline, and treated with rabbit anti-keratin antibody followed by rhodamine-conjugated goat anti-rabbit IgG. Before insertion into PEM, specimen was fixed in 2.5% glutaraldehyde (0.1 M Na cacodylate, 0.1 M sucrose, pH 7.4) and dehydrated as for Fig. 3. Aperture, 50  $\mu$ m; exposure time, 40 s.

### *Results and Discussion*

A representative image obtained with the photoelectron microscope is shown in Fig. 3. This photoelectron micrograph is of a culture of cells that has been grown to near confluency on the substrate. Requirements of the substrate are that it must be flat and conductive, and preferably nonreflective. In this case the substrate is a round glass microscope coverslip (5mm diameter) which has been coated with tin oxide to make it conductive. The cultured cells are sufficiently conductive without any special treatment or metal coating. Easily recognized in Fig. 3 is the characteristic spindle shape of the fibroblast cells, the nuclei, nucleoli, elements of the cytoskeleton (e.g., stress fibers) and the cell membrane particularly near the cell peripheries.

Figure 4 is a photoelectron micrograph of PtK2 cells grown on the same substrate but in this case treated for the immunofluorescent visualization of keratin, an intermediate filament occurring in epithelial cells. Figure 4 illustrates the characteristic cobblestone appearance of a group of these cells growing together, each with a single nucleus and one nucleolus. The cytoskeletal elements are made more prominent in this preparation

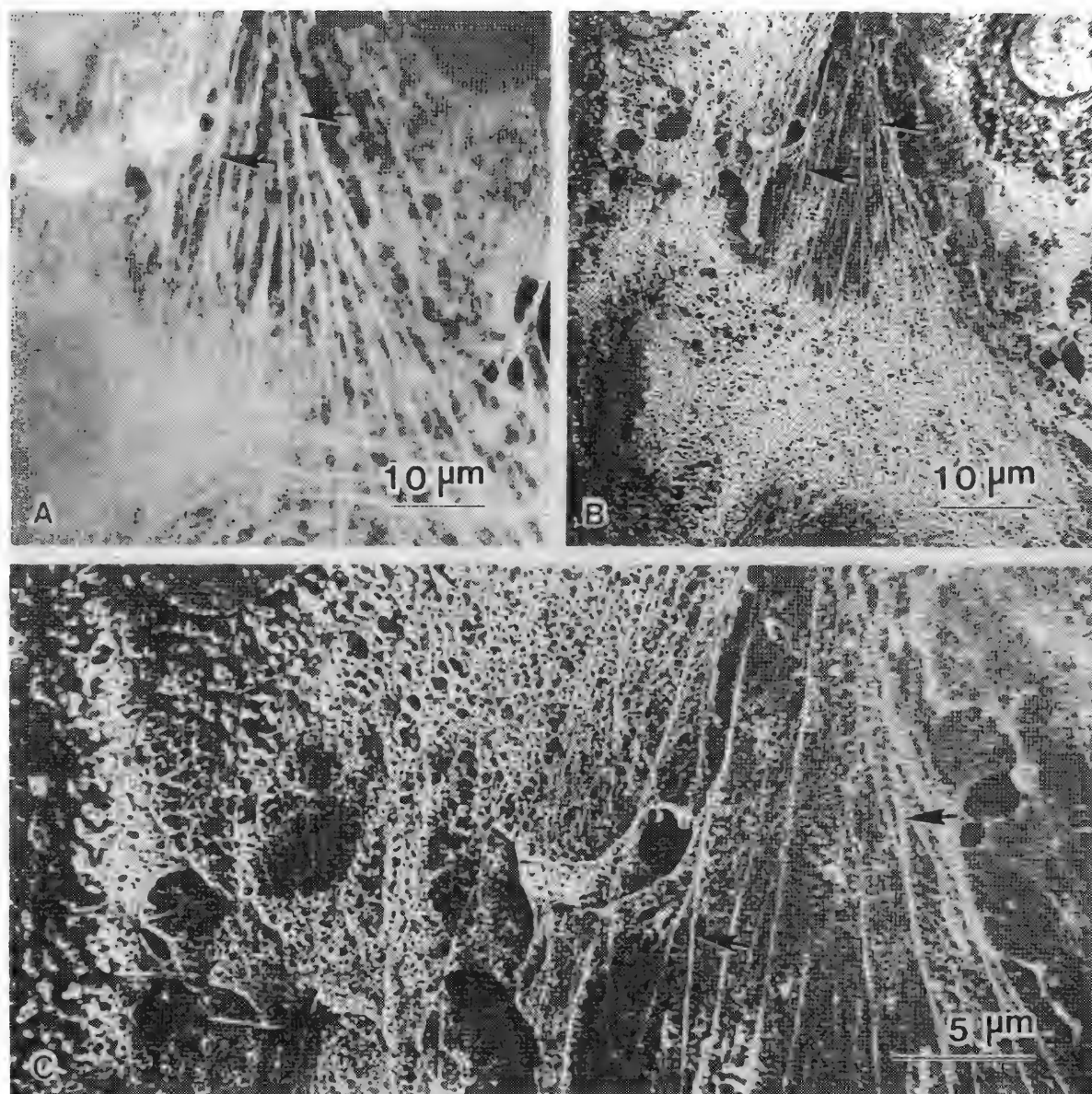


FIG. 5.--(a) Fluorescence micrograph and (b) photoelectron micrograph of identical rat fibroblast cells (Rat-1 cell line) at comparable magnifications; (c) enlargement of an area of (b). Cells were prepared for immunofluorescent visualization of actin and then fixed in 3.7% formaldehyde in PBS, permeabilized with  $-20^{\circ}\text{C}$  acetone, treated with mouse monoclonal anti-actin antibody followed by rhodamine-conjugated goat anti-mouse mixed Ig's.<sup>8</sup> After fluorescence microscopy cells were fixed in 2.5% glutaraldehyde and dehydrated for PEM, as for Figs. 3 and 4. Aperture, 50  $\mu\text{m}$ ; exposure time, 10 s.

by the permeabilization procedure which disrupts the membrane and allows the antibodies to reach and bind to the cytoskeleton. The photoelectron microscope does not detect the rhodamine dye in the low concentrations and after the long UV exposure times used here. Instead, the cytoskeletal elements are made visible by topographic contrast. The low kinetic energies of the electrons and the presence of the high electric field across the specimen in PEM have the important consequence that very small variations in surface height markedly influence the electron trajectories, so that PEM is especially sensitive to topography. This topographic contrast is an advantage in detecting fine details such as cytoskeletal elements in biological structures and can be a limitation when large variations in topography are encountered.

Nadakavukaren et al.<sup>8</sup> established recently that it is possible to perform both fluo-

rescence and photoelectron microscopy on the same cells and to identify by this procedure some of the cytoskeletal structures that can often be seen in photoelectron micrographs of whole cells. The most commonly encountered structures are the actin-containing cytoskeletal elements, since nearly all eukaryotic cells are rich in this protein, and some cell lines, such as the rat fibroblast and PtK2 epithelial cells, have well-developed stress fibers. Figure 5 shows (a) a fluorescence micrograph and (b) and (c) photoelectron micrographs of the same area of a rat fibroblast specimen. Arrows mark some of the many stress fibers that can be located in both types of micrographs. Comparisons such as this one build confidence that the photoelectron micrographs provide a faithful image of the biological structures, and that they can be readily interpreted and used in conjunction with the more established microscopic techniques. This comparison also demonstrates that the photoelectron micrographs, as predicted, contain much higher resolution detail than the corresponding fluorescence micrographs. One among many of the promising areas of application of PEM involves the development and use of photoelectron markers in conjunction with monoclonal antibodies to extend the immunofluorescence microscopy experiments to high resolution. The ultimate goal is to map cell surfaces at single protein resolution.

### References

1. R. A. Schwarzer, "Emission electron microscopy--A review; Part I: Basic concepts and applications in physics," *Microsc. Acta* 84: 51-86, 1981.
2. O. H. Griffith, G. H. Lesch, G. F. Rempfer, G. B. Birrell, C. A. Burke, D. W. Schlosser, M. H. Mallon, G. B. Lee, R. G. Stafford, P. C. Jost, and T. B. Marriott, "Photoelectron microscopy: A new approach to mapping organic and biological surfaces," *Proc. Natl. Acad. Sci. USA* 69: 561-565, 1972.
3. O. H. Griffith, G. F. Rempfer, and G. H. Lesch, "A high vacuum photoelectron microscope for the study of biological specimens," *SEM/1981* II, 123-130.
4. G. Pfefferkorn, L. Weber, K. Schur, and H. R. Oswald, "Comparison of photoemission electron microscopy and scanning electron microscopy," *SEM/1976* I, 129-142.
5. W. A. Houle, W. Engel, F. Willig, G. F. Rempfer, and O. H. Griffith, "Depth of information in photoelectron microscopy," *Ultramicroscopy* 7: 371-380, 1982.
6. W. A. Houle, H. M. Brown, and O. H. Griffith, "Photoelectric properties and detection of the aromatic carcinogens benzo(a)pyrene and dimethylbenzanthracene," *Proc. Natl. Acad. Sci. USA* 76: 4180-4184, 1979.
7. W. Engel, *Entwicklung eines Emissionsmikroskops hoher Auflösung mit photoelektrischer, kinetischer und thermischer Elektronenauslösung*, dissertation, Freie Universität Berlin, 1968.
8. K. K. Nadakavukaren, L. B. Chen, D. L. Habliston, and O. H. Griffith, "Photoelectron microscopy and immunofluorescence microscopy of cytoskeletal elements in the same cells," *Proc. Natl. Acad. Sci. USA* (in press), 1983.



## MICROBEAM ANALYSIS OF RESTING RAT PAROTID GLAND

K. T. Izutsu, D. E. Johnson, E. S. Wang, Arnold Tamarin, W. Y. Ensign, and M. K. Goddard

The application of microbeam analysis to salivary gland freeze-dried sections promises to yield important findings about salivary gland function in normal and pathological situations. Recent publications using insect<sup>1</sup> and rat<sup>2</sup> salivary glands demonstrate the potential value of the method. We used microbeam analysis to measure elemental concentrations in cytoplasm and secretory granules in rat parotid glands. The elemental concentrations in these two cellular compartments differed significantly, and the measured concentrations depended on the experimental format. Procedures requiring significant time before tissue sampling was completed generally resulted in higher intracellular sodium levels than procedures that allowed immediate sampling.

### *Experimental*

Male, Sprague-Dawley rats weighing approximately 300 g were manually restrained and anesthetized with nembutal (i.p.). Rats were then either intubated after the trachea was exposed by a ventral approach, or not. One of the parotid glands was exposed, and small pieces of gland approximately 1 mm in the longest dimension were dissected and laid over stainless-steel chucks. Care was taken to keep the dissected area away from the apex of the chuck in order not to sample injured cells. The chucks were rapidly plunged into stirred Freon 22 kept at  $-156^{\circ}\text{C}$  in a liquid-nitrogen bath. Samples were stored under liquid nitrogen until sectioned. In some instances, 30 min was allowed to transpire between exposure of the gland and the first sampling.

A Sorvall MT2-B cryoultramicrotome and glass knife were used to prepare sections. The cold-bowl temperature was maintained at  $-100^{\circ}\text{C}$ . Dry-cut sections were transferred to copper double grids precoated with formvar and carbon and freeze-dried in an Edwards high-vacuum evaporator. Freeze-dried sections were examined in the electron microscope (JEOL-100C) in both TEM and STEM modes. All spectra were collected by means of STEM. Energy-dispersive x-ray spectra from various cellular structures were recorded, stored, and analyzed by the super ML routine designed by Shuman et al.<sup>3</sup> The resulting concentrations were stored and analyzed by SPSS routines on a CDC Cyber 170-750 computer.

Salivary gland acinar cells along with secretory granules and nuclei were readily discernible in the freeze-dried sections (Fig. 1). However, the microbeam analysis results depended on how the animals were handled prior to gland sampling. Animals subjected to tracheal intubation had higher cytoplasmic Na concentrations than nonintubated animals ( $447.1 \pm 46.1$  mM/kg dry mass vs  $92.7 \pm 23.6$  mM/kg). Similarly, if there was an appreciable period (about 30 min) between exposure of gland and sampling, Na levels were again elevated. These results indicate care must be used when tissues are handled in preparation for freezing.

The results of microbeam analysis of freeze-dried sections from rapidly frozen gland samples are given in Table 1. All elemental concentrations except S, Cl, and Ca were significantly lower in secretory granules (SG) than in cytoplasm. S and Ca levels were significantly higher in SGs. Cl levels were not significantly different.

### *Conclusions*

Microbeam analysis appears to yield useful information about subcellular elemental concentrations in freeze-dried sections prepared from salivary glands.

Authors Izutsu and Ensign are in Oral Biology/Oral Medicine, author Tamarin is in Oral Biology and Biological Structure, and authors Johnson, Wang, and Goddard are in Bioengineering, in the Schools of Dentistry and Medicine, University of Washington, Seattle, WA 98195. NIH support is acknowledged.

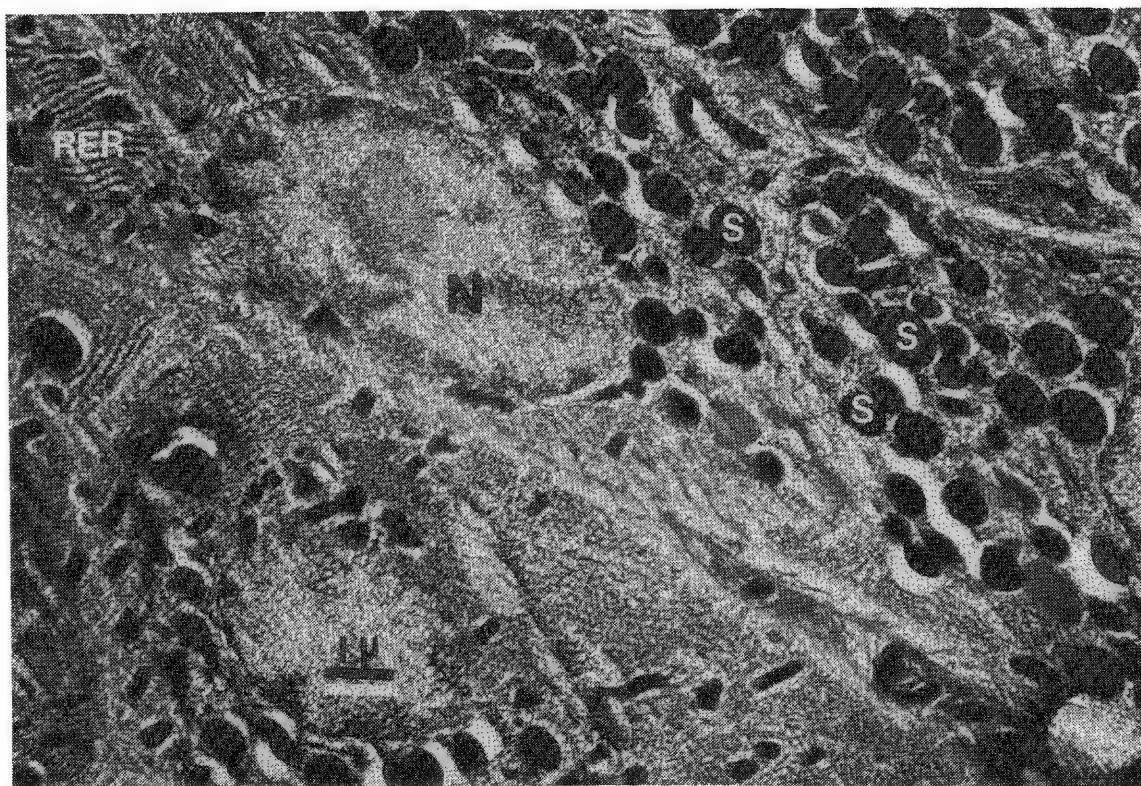


FIG. 1.--Electron micrograph of freeze-dried cryosection prepared from rat parotid gland. Acinar cells are readily discernible as are intracellular secretory granules (S), nuclei (N), and rough endoplasmic reticulum (RER).

TABLE 1.--Elemental analysis of rat parotid gland organelles.(in mM/kg dry mass).

Organelle	Na	Mg	P	S	Cl	K	Ca
1. Cytoplasm							
$\bar{x}$	92.72	57.36	677.40	101.75	182.33	561.35	29.20
SEM	23.62	4.72	48.81	9.80	23.46	41.20	4.71
n	28 spectra from 5 rats						
2. Secretory Granule							
$\bar{x}$	29.43	29.91	211.75	184.19	151.52	247.85	86.99
SEM	5.11	2.13	15.63	6.01	8.11	16.37	4.81
n	34 spectra from 5 rats						
P (t)	.014	.000	.000	.000	ns	.000	.000
(t-test between 1 and 2)							

### References

1. B. L. Gupta et al., "Electron microprobe and ion-selective microelectrode studies of fluid secretion in the salivary glands of *Calliphora*," *J. Exp. Biol.* 72: 261-284, 1978.
2. G. M. Roomans et al., "The reserpinized rat in the study of cystic fibrosis: X-ray microanalysis of submandibular gland and pancreas," *Ultrastructural Pathology* 3: 285-293, 1982.
3. H. A. Shuman et al., "Quantitative electron probe microanalysis of biological thin sections: Methods and validity," *Ultramicroscopy* 1: 317-339, 1976.

## CALCIUM LOCALIZATION IN MAMMALIAN SKELETAL MUSCLE

M. K. Goddard

It is commonly believed that the release and uptake of calcium from the terminal cisternae (TC) of the sarcoplasmic reticulum (SR) is a major component of excitation-contraction coupling of skeletal muscle.<sup>1</sup> Isolating SR produces abnormalities in SR membrane transport properties which are not representative of the *in vivo* state. The smallness of the SR has inhibited direct introduction of indicators of vesicular cation concentration. In studies of amphibian skeletal muscle whose TC are five times as large as mammalian TC, Winegrad inferred from his autoradiographic studies that the terminal cisternae is the major calcium storage site for the cell,<sup>2</sup> whereas Somlyo went on to show that the magnitude of the Ca released by the terminal cisternae is sufficient to saturate the calcium binding proteins in amphibian skeletal muscle.<sup>3</sup> The purpose of our study is to determine if the above conclusions are applicable to mammalian skeletal muscle.

### Procedures

Soleus muscles from anesthetized Sprague-Dawley 200g female rats were dissected intact, and incubated in oxygenated room-temperature Ringer's during removal of connective tissue from the exterior of the muscle. After coupling to a Kistler-Morse DSC-6 force transducer, the muscle was allowed to incubate for 1 hr in the above solution, or one in which 50 mM NaCl had been replaced by 50 mM NaCoEDTA (Cobaltic EDTA is nontoxic).<sup>4</sup> One hour is far more than enough time to allow CoEDTA to diffuse into T-tubules, and serves to allow distinguishing viable cells with high  $K^+/Cl^-$  ratios from damaged cells with low ratios. After incubation, the muscle was frozen via plunging into propane slush ( $T = -182^\circ C$ ) while still coupled to the force transducer. Thin sections (1000-2000 Å) obtained by means of a Sorval MT2-B ultramicrotome were placed on a copper 100-mesh carbon-coated formvar grids, freeze-dried, and analyzed by a JEOL 100C interfaced with a Kevex 7000 EDS x-ray microanalysis system. The quantification routine used is the super ML package described by Shuman,<sup>5</sup> which employs the basic Hall continuum theory. Calibrations (W values) were obtained by the use of albumin and binary salts.<sup>5</sup>

### Results and Discussion

Figure 1 shows a conventional micrograph of a freeze-dried rat soleus muscle section obtained by the above procedure. The low degree of freeze damage, along with careful pre-freezing tissue handling, have allowed the M and Z lines, the A-I band, and mitochondria to be all clearly visible. However, owing to the size of the terminal cisternae (approximate diameter 1500 Å)<sup>6</sup> and the T-tubule (diameter 200 Å)<sup>6</sup> coupled with the inherent low contrast of freeze-dried sections, the triadic region normally is not visible.

To identify more accurately the triadic region, NaCoEDTA was incorporated into the perfusate. It is an ideal extracellular marker for x-ray microanalysis owing to its non-toxicity (the affinity constant for CoEDTA is  $10^{35} M^{-1}$ ), and the isolated peak location of Co in the spectrum at 6.93 keV. Figure 2 shows the extracellular nature of the CoEDTA molecule in analysis performed on sections from depolarized rat soleus muscle incubated in 100 mM NaCoEDTA-Ringer's solution and frozen in Freon 22. The spectrum clearly shows that CoEDTA enters the T-tubule, but not the cell.

Preliminary analysis of relaxed soleus muscle's triadic region, A-band, and mitochondria indicate that the preparation does not damage the tissue and that calcium levels in terminal cisternae are high compared to all other intracellular locations. In healthy cells ( $K/Cl$  ratio ~6), a calcium concentration of  $16 \pm 6$  mmoles/kg dry weight (mean  $\pm$  SD,

---

The author is a graduate student at the Center for Bioengineering, University of Washington, Seattle, WA 98195. NIH Grant NL23 684 support is acknowledged.



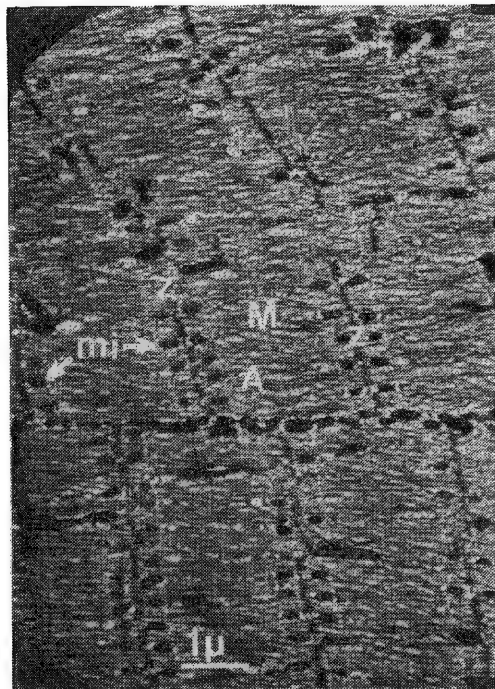


FIG. 1.--Freeze-dried rat soleus muscle: Z = Z line, M = M line, A = A band, Mi = mitochondria

## CO LOCALIZATION

PR= S 315SEC 0 INT  
V=512 H=10KEV 1:30 AQ=10KEV 10

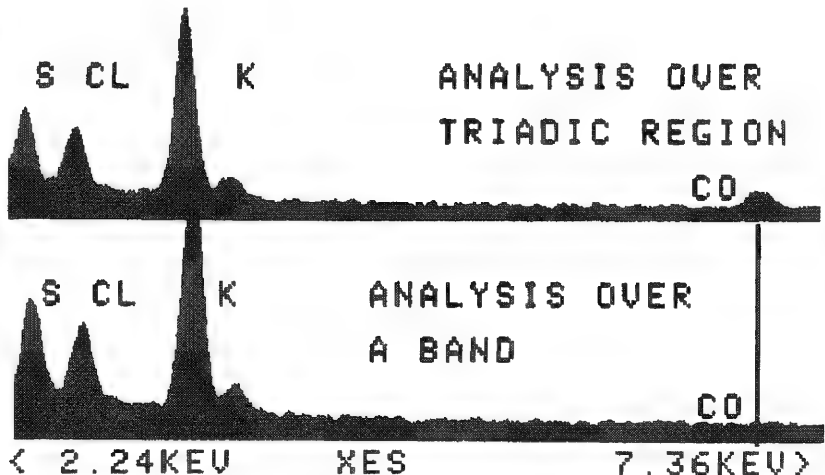


FIG. 2.--Cobalt localization in T-tubule.

N = 6) was found in the triadic region, and negligible amounts ( $\leq 2.0$  mmoles/kg dry wt.) were located in the A-band. Since the scan area used ( $0.1 \mu^2$ ) is approximately three times the area that conventional stereological analysis assigns to the terminal cisternae of one triad,<sup>6</sup> we calculate a calcium concentration in the terminal cisternae of about 50 mmoles/kg dry wt.

## Summary

Experimental procedures have been developed to allow analysis of localized concentrations of intracellular Ca in the terminal cisternae of mammalian skeletal muscle. Na oEDTA has been synthesized and has been shown to diffuse into the T-tubule. Experiments currently are being performed with CoEDTA as a T-tubule marker, which thus allows for accurate identification of the triadic region and accounts for the contribution of T-tubular Ca to the triadic Ca measurements. This approach should allow accurate testing of the hypothesis that all necessary Ca for contraction in mammalian skeletal muscle resides in the terminal cisternae.<sup>7</sup>

## References

1. M. Endo, "Calcium release from the sarcoplasmic reticulum," *Physiol. Rev.* 57: 71,
2. S. Winegrad, "The intracellular site of calcium activation of contraction in frog skeletal muscle," *J. Gen. Physiol.* 55: 77-88,
3. A. V. Somlyo, H. Gonzalez-Serratus, H. Shuman, G. McClellan, and A. P. Somlyo, "Calcium release and ionic changes in the sarcoplasmic reticulum of tetanized muscle: An electron probe study," *J. Cell Biol.* 90: 577-594,
4. J. H. B. Bridge, M. M. Bersohn, F. Gonzalez, and B. Bassingthwaighte, "Synthesis and use of radiocobaltic EDTA as an extracellular marker in rabbit heart," *Am. J. Physiol.* 242: H671-H676,
5. H. Shuman, A. V. Somlyo, and A. P. Somlyo, "Quantitative electron probe microanalysis of biological thin sections: Methods and validity," *Ultramicroscopy* 1: 317-339,
6. B. R. Eisenberg, A. M. Kuda, J. B. Peter, "Stereological analysis of mammalian skeletal muscle, I Soleus muscle of adult guinea pig," *J. Cell Biology* 60: 732-754,
7. The author would like to acknowledge the guidance and technical assistance provided by Dr. Dale E. Johnson, Dr. J. B. Bassingthwaighte, Dr. T. E. Hutchinson, Eunice Wang, and Alice Lee.

## QUANTIFICATION OF MERCURY LOSSES DURING BIOLOGICAL SPECIMEN PREPARATION AND X-RAY MICROANALYSIS

A. R. Crooker, D. E. Johnson, and N. K. Mottet

The environmental mercury problem and the toxicity of mercury and its compounds are widely recognized. Mercury is widespread in the environment, accumulates in fish and wildlife, and poses real and potential hazards to the human population. In humans, the principal toxic effects of inorganic mercury involve the liver and kidney. Organic mercurials such as methylmercury have a more pronounced effect on the central nervous system.

Mercury is often present in extremely small amounts in biological samples. X-ray microanalytical, histochemical, and autoradiographical studies of subcellular mercury distribution have typically utilized conventional preparation procedures, i.e., chemical fixation, dehydration, and embedding. Although these studies have yielded useful information, conventional processing is likely to elute a considerable portion of the heavy metal and may also cause its translocation. Mercury may be undetectable because of processing losses.

Researchers have often noted the diminution of mercury x-ray signal during microanalysis of test specimens, sediments, or organisms environmentally or experimentally exposed to mercury.<sup>1,2</sup> This elemental mass loss varies somewhat depending on the form of mercury present. Since mercury is volatile under vacuum and in the electron beam, and because low concentrations of mercury are common in samples, analysis is often unsatisfactory.

The present investigation was undertaken to examine ways to minimize mercury loss during processing of biological samples for microscopy and during examination of these samples in the electron microscope. Radioactive mercury and electron microscope x-ray microanalysis were used to monitor mercury losses and mercury-cell interaction. Organ cultured rat cerebellum was used as a model system for the studies.

### *Mercury Losses During Processing for Microscopy*

Cerebella from 20-day fetal rats were cultured in serum-free media by a modified Trowell technique.<sup>3</sup> Methylmercury hydroxide was added to the culture medium (Waymouth's MB 752/1 with l-glutamine supplemented with albumin, insulin, thyroxine, and transferrin) to give a final concentration of 1.0 ppm and cultured for 2 days at 35.5-36.0°C.

The external granular layer of the cerebellum, as seen in conventional thin sections, shows typical signs of methyl mercury exposure (Fig. 1). The chromatin of the nucleus is clumped and organelles have completely dissolved; the cell sap is expanded and pale. Mercury cannot be detected by x-ray microanalysis because of low initial concentrations and losses during processing.

<sup>203</sup>Hg (<sup>203</sup>Hg methylmercury chloride) added to the culture media (1  $\mu$ l <sup>203</sup>Hg/10 ml media, specific activity 0.5 mCi/mg, concentration 0.3 mCi/ml) was used to monitor mercury loss during preparation of cultured cerebellum for conventional microscopy. Results are presented in Fig. 2. Each step in the preparation procedure contributes to loss of labeled mercury. The steps involved in fixation contribute approximately 25% of the loss; dehydration, 30%; and embedding, 15%. The embedded sample contains only approximately 30% of the <sup>203</sup>Hg label originally present in the specimen. These results are roughly similar to information obtained by De Filippis for mercury losses in corn leaf tissue.<sup>4</sup>

In contrast to the conventionally prepared cerebellum, cultured cerebellum labeled with <sup>203</sup>Hg and cryofixed by a rapid plunge into Freon 22 cooled to -165°C with liquid nitrogen retained 90-95% or more of the initial label after freeze drying. Mercury can be demonstrated by x-ray microanalysis (in this case, of a lysosome in the external granular layer)

---

Authors Crooker and Mottet are with the Department of Pathology (SM-30); author Johnson with the Center for Bioengineering (WD-12), University of Washington, Seattle, WA 98195. Supported by NIEHS grants ES07032 (training), ES02190 (center), and ES0677 (research).

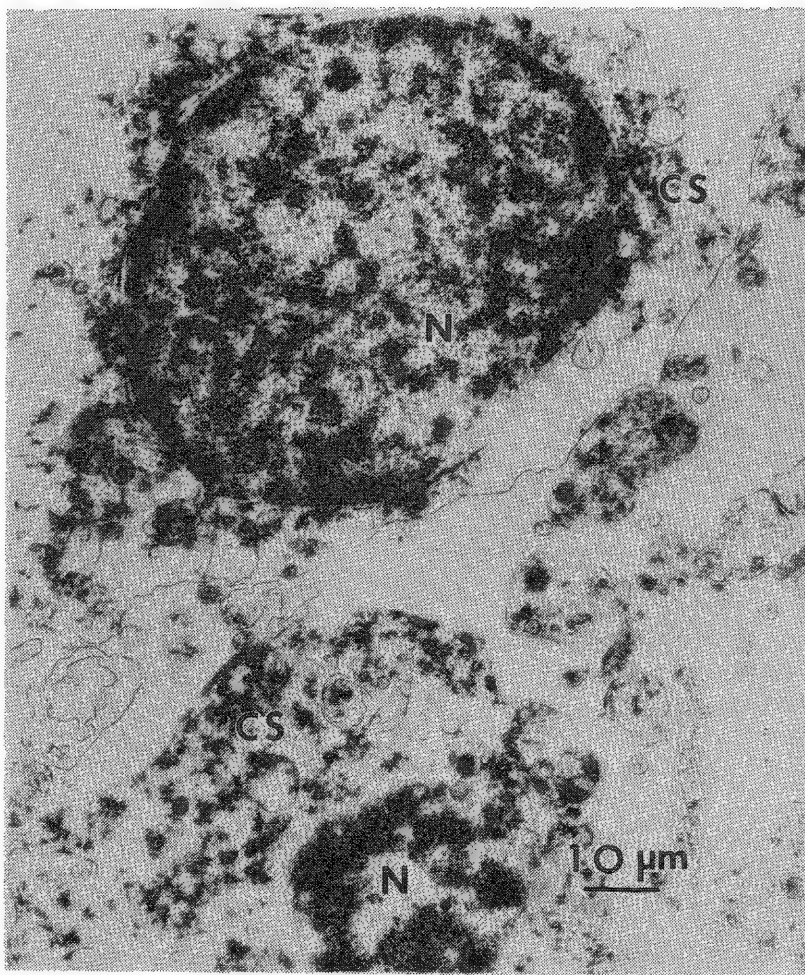


FIG. 1.--External granular layer cells of organ cultured rat cerebellum after treatment with methylmercury hydroxide. Chromatin of the nucleus (N) is clumped and organelles have completely dissolved; the cell sap (CS) is expanded and pale.

cooled cold stage. The following experiments were performed with a cold stage to evaluate the effects of lower specimen temperature on mercury mass loss.

Specimens were prepared from aqueous solutions of 1000 ppm methylmercury hydroxide which was pipetted onto 75 mesh carbon-coated Formvar grids and air dried before examination in the electron microscope.

Specimens were analyzed in a JEOL 100C scanning transmission electron microscope equipped with an energy dispersive x-ray system. A computer program was used to control acquisition and analysis of sequential x-ray spectra, which allowed any number of elements or x-ray energy regions to be monitored for changes in elemental composition with time. Count rate information provided data on element specific specimen changes. This procedure for mass loss determination was developed by Jay Hecker, Department of Pediatrics, University of Virginia, while working at the Microprobe Facility, University of Washington.<sup>6</sup>

Mercury mass loss was pronounced during analysis at room temperature, but much reduced at the cold stage temperature of approximately  $-180^{\circ}\text{C}$  (Fig. 3). The solid and dashed lines represent the model used--a linear least-squares fit to an exponential decay with offset. The count rate at room temperature decreased from an initial rate of approximately 450 counts/5 s to less than 50% of the initial count rate during the exposure period. In contrast, the count rate for the same exposure showed a barely perceptible drop from initial levels when the cold stage was used. The results shown are typical of four trials.

of the cryofixed material which has been cryosectioned dry at  $-100^{\circ}\text{C}$  and examined unstained after freeze drying (Fig. 4). The mercury peaks are well resolved above background. For example, for  $\text{Hg}_{1\alpha}$  at 10 keV, the peak is 600 counts above a background of 1000 counts.

#### *Mercury Loss During Examination in the Electron Microscope*

Mercury loss under conditions encountered during x-ray microanalysis in a scanning electron microscope operated at 30 KV and 150  $\mu\text{A}$  emission current has been quantified by Bistricki using  $^{203}\text{Hg}$ .<sup>1</sup> Fast scans and small diameter probes showed the least decrease in gamma counts with specimen supports of the same conductivity. When support conductivity was varied, count rate dropped as resistance was increased.

Bistricki's data indicate that even with careful instrumental manipulation, significant mercury loss may still occur, especially with the long counting times often necessary for samples containing low concentrations of mercury.

Cryo electron microscopy is often cited as a promising plan for protection against radiation damage.<sup>5</sup> The most readily available instrumentation for this purpose is the conventional electron microscope equipped with a cooling accessory such as a liquid nitrogen-

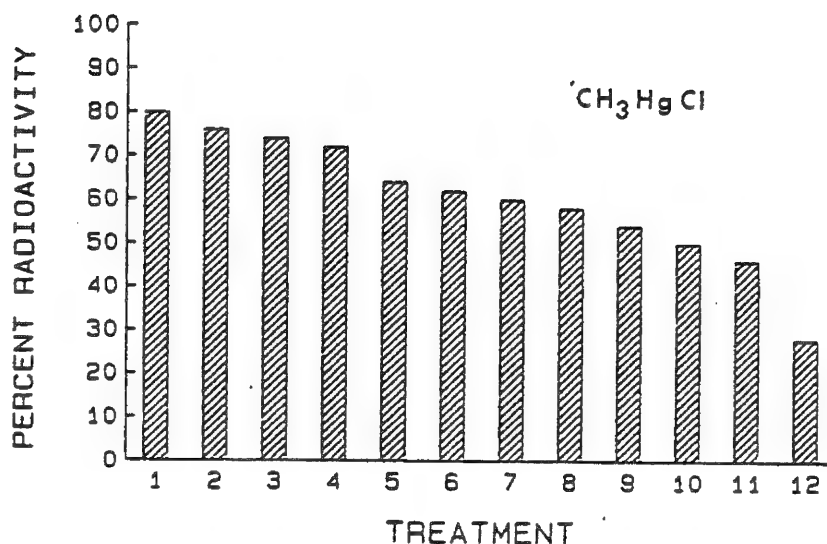


FIG. 2.--Percentage loss of  $^{203}\text{Hg}$  from organ cultured rat cerebellum during conventional processing for electron microscopy. Each result is average of 3 experiments involving 6 pieces of cultured cerebellum per experiment. Losses of radioactivity are expressed as percentage loss of initial radioactivity per piece of tissue. Treatment numbers refer to particular stages in preparation procedure: (1) 3% cacodylate buffered glutaraldehyde fixation, 1 hr; (2) buffer rinse, 1 hr; (3) buffer rinse, 1 hr; (4) 2% osmium tetroxide in distilled water post-fixation, 1 hr; (5) distilled water rinse, 0.5 hr; (6) 30% ethanol, 0.25 hr; (7) 50% ethanol, 0.25 hr; (8) 70% ethanol, 0.25 hr; (9) 90% ethanol, 0.25 hr; (10) 100% ethanol, 3 changes, 0.5 hr; (11) 50% resin, 50% propylene oxide, 2.0 hr; (12) resin after polymerization, 24 hr.

logically important ions is minimized.

Cryopreparative technique and low temperature observation in the electron microscope will be important in future x-ray microanalytical studies of mercury toxicity.

#### References

1. T. Bistricki, "Quantification of losses during x-ray microanalysis of mercury," *9th Intern. Cong. Electron Microscopy*, 1978, II, 12-13.
2. S. Ramamoorthy, A. Massalski, and T. Bistricki, "Energy-dispersive x-ray microanalysis of mercury in environmental samples," in P. A. Russell and A. E. Hutchings, Eds., *Electron Microscopy and X-Ray Applications to Environmental and Occupational Health Analysis*, Ann Arbor: Ann Arbor Science Publishers, Inc., 1978, 247-254.
3. J. Paul, *Cell & Tissue Culture*, New York: Churchill Livingstone, 1975, 202-204.
4. L. F. De Filippis, "Localization of organomercurials in plant cells," *Z. Pflanzenphysiol.* 88: 133-146, 1978.
5. E. Zeitler, "Cryo electron microscopy," *Ultramicrosc.* 10: 1-5, 1982.
6. J. G. Hecker and T. E. Hutchinson, "Measurement of mass loss during microanalysis: Methods and preliminary results," in T. E. Hutchinson and A. P. Somlyo, Eds., *Microprobe Analysis of Biological Systems*, New York: Academic Press, 1981, 83-98.

#### Conclusions

The present investigation demonstrates the importance of specimen preparation and examination techniques for the analytical electron microscopy of samples containing mercury. Cryofixation of  $^{203}\text{Hg}$  labeled organ cultured rat cerebellum, followed by freeze drying, preserves nearly all the radioactivity initially present in the sample. Because of the high mercury retention, mercury can be detected in freeze dried cryosections (cut dry and not stained) of mercury exposed cultured cerebellum, whereas mercury cannot be detected in similarly exposed, conventionally prepared (fixed, dehydrated, and embedded) material. Mercury loss during examination of samples in the electron microscope can be slowed dramatically by use of a liquid nitrogen-cooled cold stage.

Unstained, freeze-dried cryosections of cryofixed material and low temperature observation techniques have not been used previously in mercury toxicity studies. The techniques are important in preserving the small amounts of mercury often present in environmentally or experimentally exposed organisms. An additional advantage, not examined here, is that translocation of diffusible substances such as unbound mercury and physio-

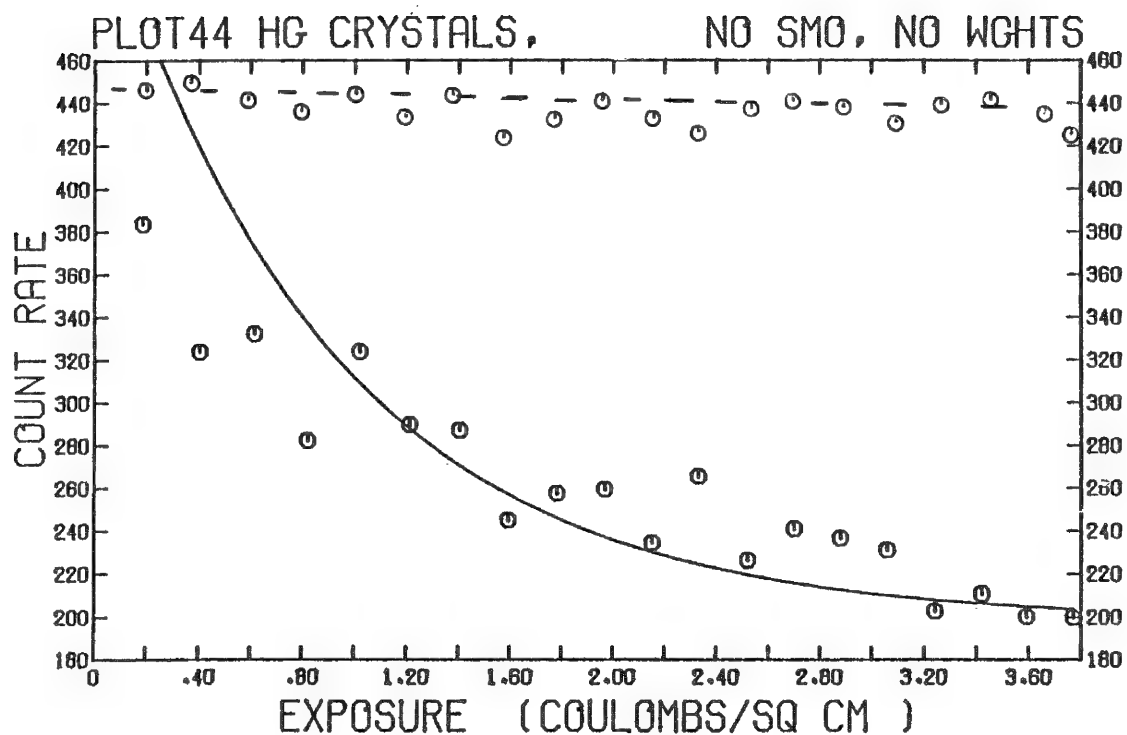


FIG. 3.--Mercury loss with cold stage at room temperature (solid line) and cold stage at liquid nitrogen temperature (dashed line). Count rate (counts/5 s) vs exposure (coulombs/cm<sup>2</sup>). Data shown are from samples analyzed by conventional transmission electron microscopy at 5800 $\times$  with beam current of  $9 \times 10^{-9}$  A, 200s live time, 830s irradiation, specimen tilt 40°. Mercury peak at 2.2 keV is shown.

82-5

PR= S 200SEC 0 INT

V=2048 H=20KEV 1:30 AQ=20KEV 1Q

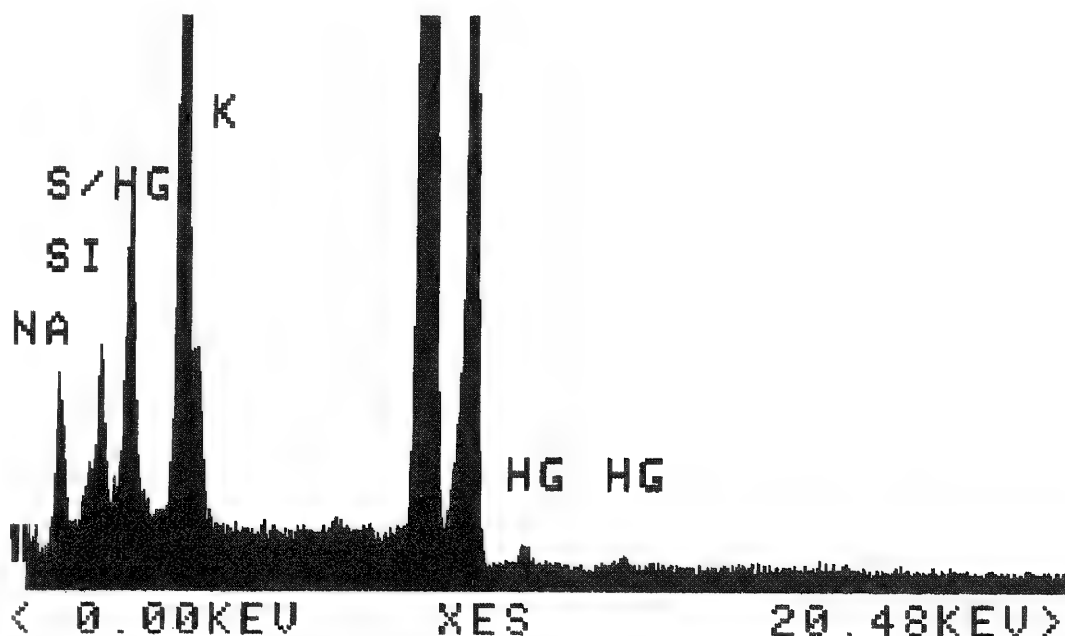


FIG. 4.--X-ray spectrum from lysosome in external granular layer of cryosection from organ cultured rat cerebellum. Mercury peaks are well defined.

## 10 Raman Microbeam Analysis

### RAMAN MICROANALYSIS OF DEFECTS IN INDUSTRIAL MATERIALS

Helgard Boyer

The analysis of defects in industrial material is always related to problems that appear during the production or storage proceedings. The final use of the manufactured product determines whether the defect can be tolerated and what kind of solution has to be found. The infrastructure of the laboratory in charge of examining the defect, and financial and even psychological aspects affect the positive decision for the choice of a real new technique, such as the microanalysis by Raman spectroscopy must still be considered.

One of the aims of our Laboratory is to demonstrate various aspects of the work with this method to help a future customer make a decision. The importance of each aspect varies with the industry in question and even with samples. To illustrate, we select some new applications on samples from the glass, polymer, and metallurgy industries.

#### *General Aspects*

As defects are of a hazardous nature it is a particularly important advantage of Raman microanalysis to provide chemical and physical information about organic and inorganic species.

Most of our examples from glass industry demonstrate the usefulness of in situ analysis for obtaining nonmodified results. It is also of interest simply to put the defect under the microscope stage because it shortens the overall analysis time. If the sample needs preparation, its simplicity remains attractive. But sometimes the possibility of very sophisticated preparation of a sample can save an analysis or greatly improve the quality of the spectrum.<sup>1</sup> Rarely does only one type of analysis bring a complete solution for all problems arising from defects. Since Raman microanalysis is nondestructive, it will be mostly used as the first device in the available analytical sequence.

Other aspects concerning the speed of analysis, fluorescence problems, and the availability of reference spectra will be discussed later. As to reference spectra, up to now each branch of industry has had to build up a great part of its own collection.

#### *Samples from the Glass Industry*

Our first example is related to a problem appearing during the manufacture of glass. The defect appears as a 1-2 mm black trail in the glass. Various samples cut were analyzed in situ. The interesting part of the Raman spectrum is shown in Fig. 1. The lines at 384 and 410  $\text{cm}^{-1}$  are characteristic of molybdenum sulfide  $\text{MoS}_2$ . The molybdenum content indicates the origin of the defect: molybdenum electrodes are used to keep the molten glass at an exact working temperature. They release particles and the machine must be stopped and the defective electrodes changed. That is why this phenomenon is worth a study.

We found that in the samples in which the black trail was completely surrounded by glass, nothing but the  $\text{MoS}_2$  spectrum could be obtained. Even crystals shaped as perfect hexagons inside a bubble were recognized to be  $\text{MoS}_2$ .

Another defect, appearing as a white trail at the surface of glass, was related to the same origin, because here molybdenum was detected in the form of molybdates. Figure 2 shows such a spectrum, with the typical lines of  $\text{Na}_2\text{MoO}_4$  and  $\text{CaMoO}_4$ . These two compounds appeared always together in slightly variable proportions. On the other hand, the same molybdates associated with  $\text{MoS}_2$  were found on a sample where the black trail was in contact with ambient air.

Thus the microanalysis by Raman spectroscopy can follow exactly what products form under specified conditions without further possibility of contamination. So it seems the best method that leads to an understanding why electrodes release particles. In addition

---

The author is at Instruments S.A., 16 rue de Canal, F-91163 Longjumeau Cédex, France.



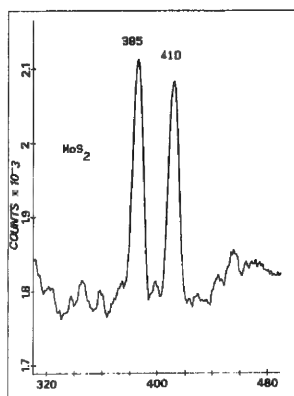


FIG. 1.--Raman spectrum of black trail included in glass.

FIG. 2.--Raman spectrum of white trail at surface of glass.

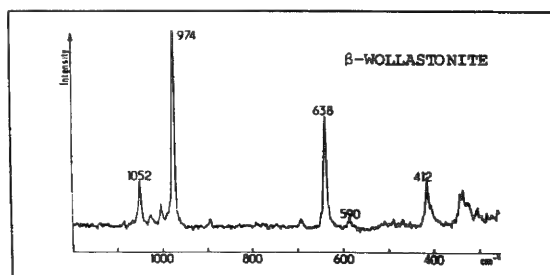
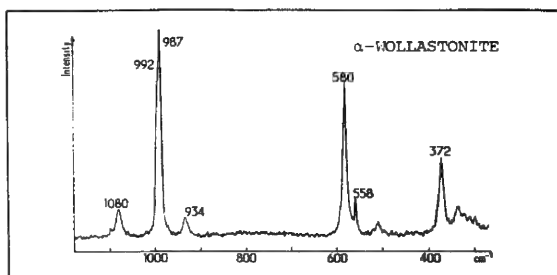
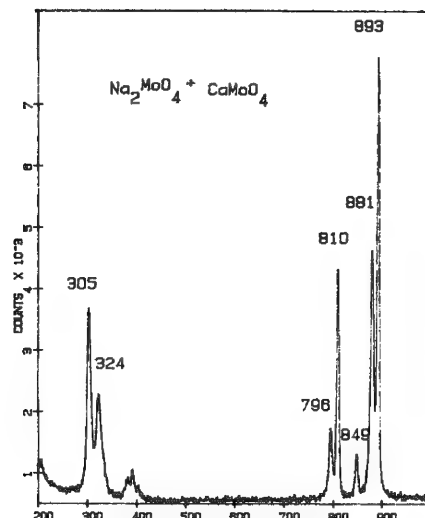


FIG. 3.--Raman spectra of demixtion products in glass.

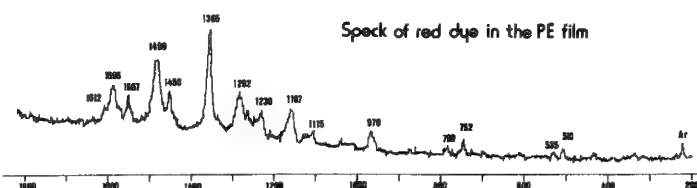
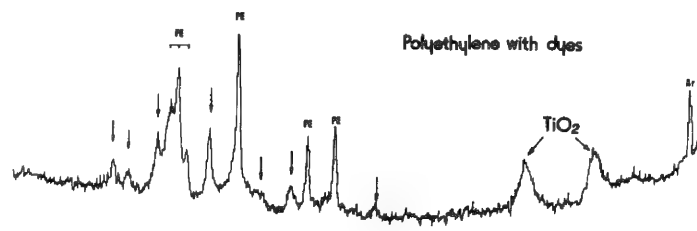


FIG. 4.--Raman spectra of translucent pink polyethylene film and defect.

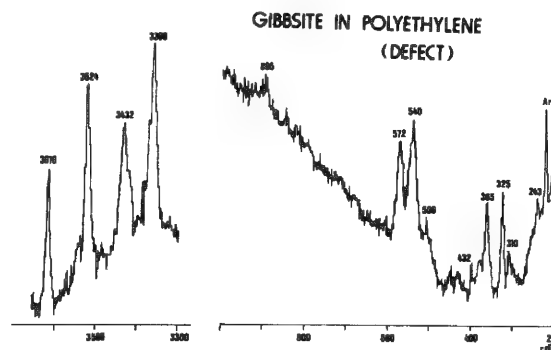


FIG. 5.--Raman spectrum of defect in polyethylene.

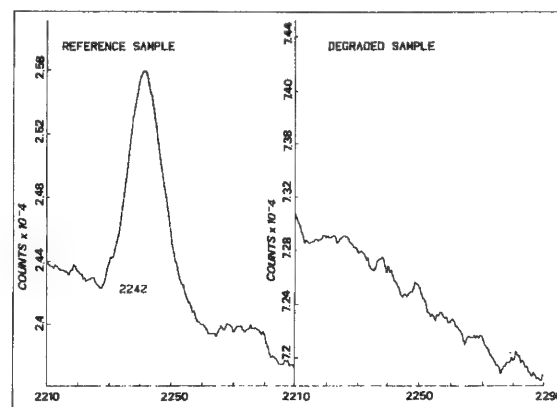


FIG. 6.--Raman spectrum of polymer in  $C \equiv N$  bond range.



to the facility of sample preparation, molybdenum compounds are strong Raman scatterers, so that the study can be carried out rapidly.

Owing to its frequency of occurrence, another important application is the determination of native sulfur in glass bubbles. For the same reasons as previously, the analysis is rapid. The possibility of characterizing native sulfur and not only sulfur containing compounds is useful because the origin of the precipitation of sulfur alone or in association with sodium sulfate is known to be a punctiform lack of balance in the redox conditions of the molten glass.

The analysis is not always so rapid if crystals appear for which no reference spectrum can be found. This was the case with a recently analyzed bubble in which only sulfur precipitated on the upper wall but other nonidentified crystals were laid on the opposite wall. One may regard that as a negative aspect of the technique but in fact even if an exact determination cannot be carried out immediately, the result is not entirely negative. The positive aspects are that a different nature than sulfur of these crystals is assured, some compounds can be eliminated, the hypothesis for a sulfide or perhaps an oxide can be built up, and (since the analysis is nondestructive), other techniques can be applied afterward. Finally, the lack of a reference spectrum is only a question of time.

Demixtion products are defects that create opacities in transparent glass. Fine needles sticking together can be seen under the microscope. They are embedded in the glass matrix so that an analysis in situ becomes necessary. We obtained a spectrum that enabled us to identify alpha wollastonite, a three-member calcium cyclosilicate ( $\text{Ca}_3\text{Si}_3\text{O}_9$ ). At a different temperature beta wollastonite can occur, so that it is important to have a ready means of differentiating between those two allotropic forms. Their spectra are shown in Fig. 3.

#### *Samples from the Polymer Industry*

An application of the micro-Raman technique important to the polymer industry is in the determination of inclusions in polymer fibers or films, as these inclusions can often cause a rupture or other defect. The inclusions can vary considerably in both nature and origin. Calcite and quartz are the most frequently encountered pollutants coming from dust. The presence of polyethylene, Teflon, polystyrene, and cellulose as pollutants are also of external origin such as packing material, etc. The origin of an inclusion can also be carbon black, anatase ( $\text{TiO}_2$ ), or any other additive that is normally finely dispersed.

The matrix of our first example was a film of polyethylene (PE) with a pink translucent tinge. The Raman spectra obtained (Fig. 4) show lines which were characteristic of PE, and two other large bands could be attributed to rutile ( $\text{TiO}_2$ ) and to the red dye responsible for the pink tinge of the sample. Further examination of the sample provided the other spectrum of Fig. 4, which originated from one of the many red particles present through the sample. Raman lines due to PE and rutile are not present. This in situ analysis confirmed the presumed results that the red particles were red dye stuff which had remained agglomerated in the pink matrix as inclusion defects. As the red particles were thermosensitive, the laser beam was defocused to reduce the density of exciting energy.

An "internal" contamination is sometimes present in a degraded form, as illustrated in an example of a gibbsite particle found in a PE injection product. The result of the Raman microanalysis of this sample is shown in Fig. 5. In particular, the four Raman lines in the  $3300\text{--}3700\text{cm}^{-1}$  region identify the included particle as  $\text{Al}(\text{OH})_3$  in its gibbsite form. From this result the manufacturer easily identified the source of origin -- a catalyst that had degraded during processing.

If a defect in a polymer cannot be characterized by a completely different spectrum such as the preceding ones, other aspects become important; in most cases the analysis requires much more time for various reasons. A sample preparation such as microtome slides is suitable, especially if fluorescence occurs, or in order to eliminate part of the matrix spectrum. A defect visible even with the naked eye may affect only a few per cent of the polymer, and that is sometimes not far from the detection limit of the technique. Then high counting times or even accumulated spectra become necessary.

Our third example illustrates these aspects. Here the defect affected the entire sample by a change in color from colorless to red-brown during tempering. The fluorescence level of the degraded sample was too high to permit classical Raman analysis (with macro-chamber). With the microanalysis device the fluorescent volume can be greatly reduced:

all that is needed is to scrape off a few micron-sized particles. After laser illumination for damping out fluorescence, analysis was carried out.

Figure 6 shows the results: In the spectral range of  $C \equiv N$  triple bonds, the colorless sample shows a characteristic line at  $2242\text{ cm}^{-1}$ , whereas in the degraded sample this limit cannot be detected even with 25 accumulations. Tempering affects primarily the  $C \equiv N$  bond.

#### *Samples from the Metallurgy Industry*

Our work on inclusions from the metallurgy industry has only just begun, so that the difficulties that have arisen have not yet been eliminated.

The analyzed inclusions were prepared for other purposes than Raman microanalysis and we found them not as we expected included in the steel matrix but separated as clear precipitates mixed with a black powder, cementite ( $Fe_3C$ ). The microscope stage permits a classification according to the particle size. In the range of  $5\text{ }\mu\text{m}$ , the abundance of particles showing the characteristic calcite spectrum is striking. Here calcite ( $CaCO_3$ ) arises as the classical degradation product of calcium oxide ( $CaO$ ). This circumstance is very favorable for Raman analysis because  $CaO$  has the  $NaCl$  structure, which means no first-order Raman activity, so that no narrow lines can be used for identification purposes.

Other particles have to be reexamined; in a first approach, their spectra were not clear and contained no well-defined lines. The observed slight fluorescent background is a hindrance.

Silicates and aluminates were expected, and we did record spectra permitting the identification of quartz and orthoclase, an alkali feldspar ( $KAlSi_3O_8$ )<sup>2</sup>.

#### *References*

1. M. E. Anderson and R. Z. Muggli, "Microscopical techniques with the molecular optics laser examiner Raman microprobe," *Anal. Chem.* 53: 1772-1777, 1981.
2. W. B. White, "Structural interpretation of lunar and terrestrial minerals by Raman spectroscopy," in *IR and Raman Spectroscopy of Lunar and Terrestrial Minerals*, New York: Academic Press, 1975, 325-348.

## RAMAN MICROPROBE CHARACTERIZATION OF POLYMERIC FIBERS: ORIENTATION, CRYSTALLINITY, AND SKIN-CORE EFFECTS

Fran Adar and Herman Noether

The mechanical characteristics of textile fibers are determined by physical properties such as degree of orientation, degree of crystallinity, and skin-core effects. Examples of Raman microprobe spectra that document the ability to monitor these properties in polyethylene terephthalate and carbon filaments are presented.

Spectra of cross sections of heavy filaments of polyethylene terephthalate treated by drawing through dimethyl formamide (DMF) show that this treatment crystallizes the outer skin. Examination of a series of PET fibers, spin-oriented at speeds between 500 and 5500 m/min, shows that as the take-up speed is increased, the polymer initially orients, and at high speed also crystallizes. The sample originally spun at 500 m/min and subsequently drawn to 5 times its original length over heated pins is somewhat more oriented than the sample taken up at 5500 m/min.

Raman microprobe spectra of carbon fibers fabricated from polyacrylonitrile (PAN) and from pitch show intensity patterns consistent with the electron micrograph descriptions of the orientation of the microcrystallites in these samples. Incomplete extinction of the Raman bands of the pitch fiber when it was oriented with the fiber direction perpendicular to the E vector of the laser and to the direction of the laser propagation implies that the graphite planes are not all oriented along precise radial directions.

### *Background*

*PET.* The method of production of textile fibers is known to affect the relative content of the crystalline and amorphous phases as well as their orientation. Increasing the extrusion velocity increases the orientation of the polymer; at high extrusion velocity the polymer crystallizes as well. Subsequent to spinning, fibers are often drawn (stretched), which can also cause orientation and crystallization.

The effects of crystallinity on the Raman spectra of PET have been well documented. Melveger<sup>1</sup> noted that the width of the carbonyl band correlates well with density and crystalline order, most likely due to resonance stabilization of the C=O with the aromatic ring.

More recently Stokr et al.<sup>2</sup> reported entire spectra of totally unoriented amorphous, semicrystalline, and crystalline (obtained by spectral subtraction) PET. Inspection of these spectra show the presence of the  $1097\text{cm}^{-1}$  band and absence of a background between 800 and  $900\text{cm}^{-1}$  in crystalline PET. Purvis and Bower<sup>3</sup> and Boerio and Bailey<sup>4</sup> consider the effects of orientation on the Raman spectra. Cook and Ogilvie<sup>5</sup> demonstrate the usefulness of a Raman microprobe to monitor crystallinity in PET.

*Graphite.* The Raman spectrum of crystalline and disordered graphite was first reported by Tuinstra and Koenig.<sup>6</sup> Single crystal graphite has one fundamental band at  $1575\text{cm}^{-1}$  that broadens as the crystalline order decreases. Disorder is also monitored by the appearance of a second band at  $1360\text{cm}^{-1}$ .

In an orientation/polarization study Brillson and Burstein<sup>7</sup> have confirmed the assignment of the  $1575\text{cm}^{-1}$  band to an  $E_g$  mode that can only appear for laser and Raman photons polarized perpendicular to the c-axis.

### *Skin-core Effect in PET*

A cross section of a coarse PET fiber that had been subjected to treatment with DMF at  $80^\circ\text{C}$  is shown in Fig. 1. The skin of the fiber is readily distinguishable optically

---

Author Adar is with Instruments SA, Inc., Metuchen, NJ 08840; author Noether is with The Textile Research Institute, Princeton, NJ 08540.

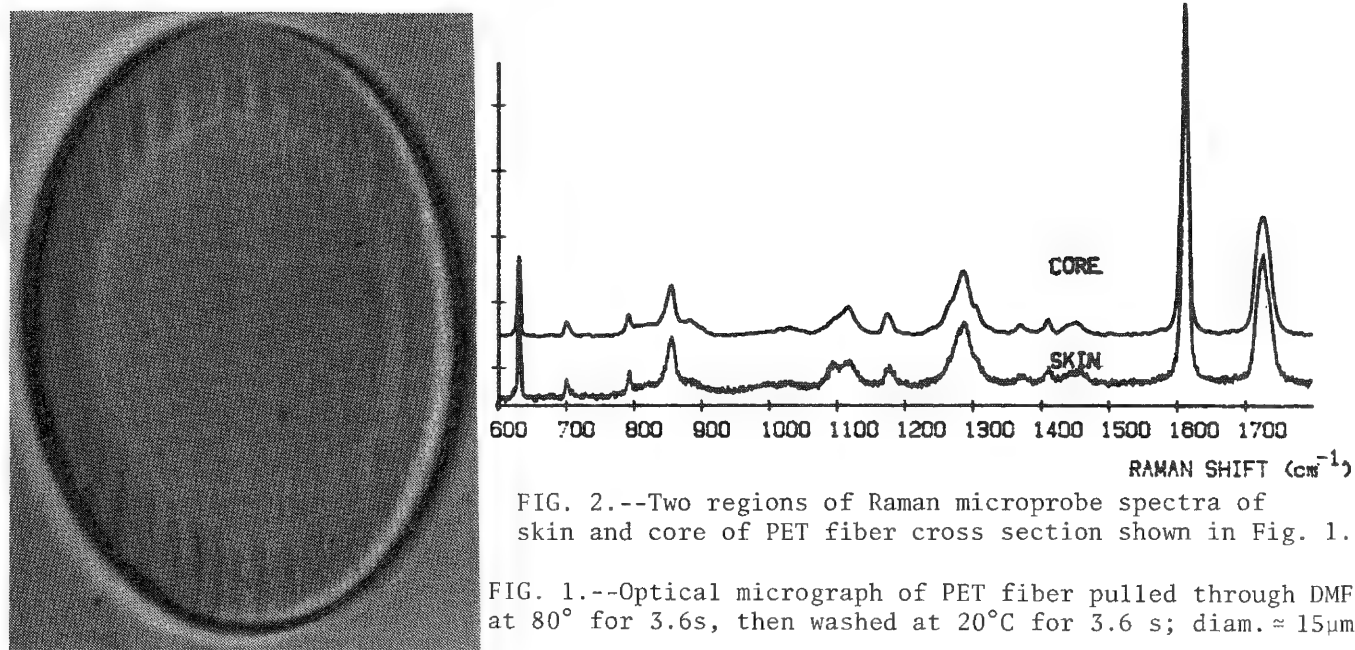


FIG. 2.--Two regions of Raman microprobe spectra of skin and core of PET fiber cross section shown in Fig. 1.

FIG. 1.--Optical micrograph of PET fiber pulled through DMF at 80° for 3.6s, then washed at 20°C for 3.6 s; diam.  $\approx$  15 $\mu$ m.

from the core. Raman microprobe spectra of the skin and core are shown in Fig. 2. The presence of a sharp band at 1097  $\text{cm}^{-1}$  and decreased linewidth of the carbonyl band at 1727  $\text{cm}^{-1}$  are due to the increased crystallinity in the skin. These results are consistent with the results in Refs. 1, 2, and 5 and confirm that the DMF-exposed skin has been crystallized.

#### *Effects of Spin Velocity on Orientation and Crystallinity*

Figure 3 shows spectra of a PET filament examined radially. The appearance of the sharp band at 1097  $\text{cm}^{-1}$ , the intensification of the shoulder at 1270-1280  $\text{cm}^{-1}$ , and the sharpening of the carbonyl band at 1727  $\text{cm}^{-1}$  demonstrate the onset of crystallization at high speed (5500 m/min).

Figure 4 superimposes Raman spectra of PET filaments (spun at 5500  $\mu\text{m}/\text{min}$ ) examined radially and axially in the microprobe. The spectra are displayed with the 1614  $\text{cm}^{-1}$  band at full scale intensity.

Table 1 presents the integrated peak intensities for some bands relative to the 1614  $\text{cm}^{-1}$  band in the axial and radial geometries. These data have been calculated for fibers spin-oriented at 1500, 5500, and 500 m/min; this latter fiber was subsequently drawn to five times its initial length over heated pins.

Differences in relative intensities of the Raman bands of PET fibers examined radially and in cross section are a good indicator of molecular orientation due to spin orientation or drawing. According to Boerio and Bailey<sup>4</sup> all modes have  $A_g$  symmetry (in the  $C_{2h}$  point group) except the  $B_g$  band at 800  $\text{cm}^{-1}$ . In our spectra all bands show a higher intensity in axial observation with the exception of the 800  $\text{cm}^{-1}$  band. It is interesting to note that the subsequently drawn sample seems to have a higher axial/radial ratio than the high speed spin-oriented material (5500 m/min). More work is required to elucidate the molecular structural reasons for these observations.

#### *Orientation of Graphite Fibers*

Graphite fibers prepared from pitch and PAN both have c-axes perpendicular to the fiber axis, but the configuration of the graphite planes transverse to the fiber are quite different. Electron micrographs indicate that the graphite planes wrap around the PAN fibers like onion skins, whereas the planes are more or less radial in the pitch fibers. Because the Raman band requires both the incident and scattered polarization to be perpendicular to the c-axis, the two types of fibers are expected to exhibit different polarization/orientation behavior. The scattering from the PAN fibers should be more or less independent of the orientation of a fiber on a microscope slide. However, when a pitch fiber is oriented with its axis perpendicular to the laser E vector, the Raman signal is

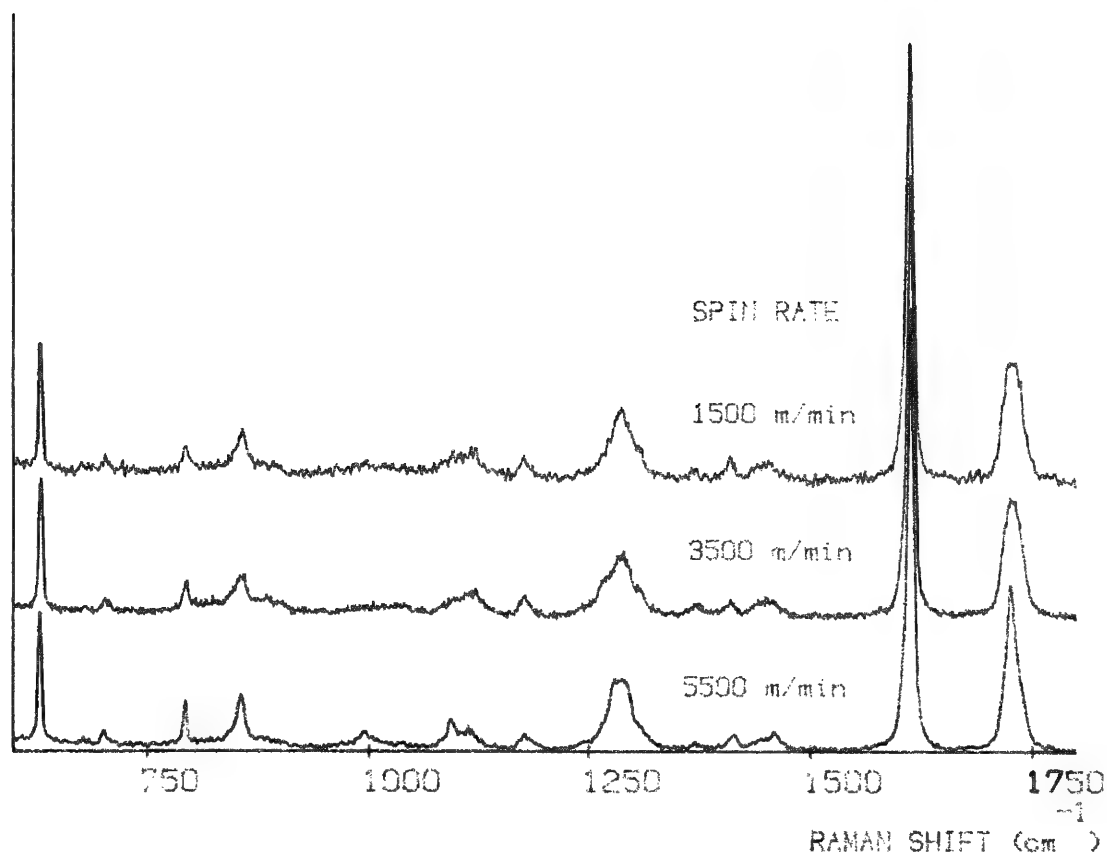


FIG. 3.--Raman microprobe spectra of PET filaments spun at speeds between 1500 and 5500 m/min.

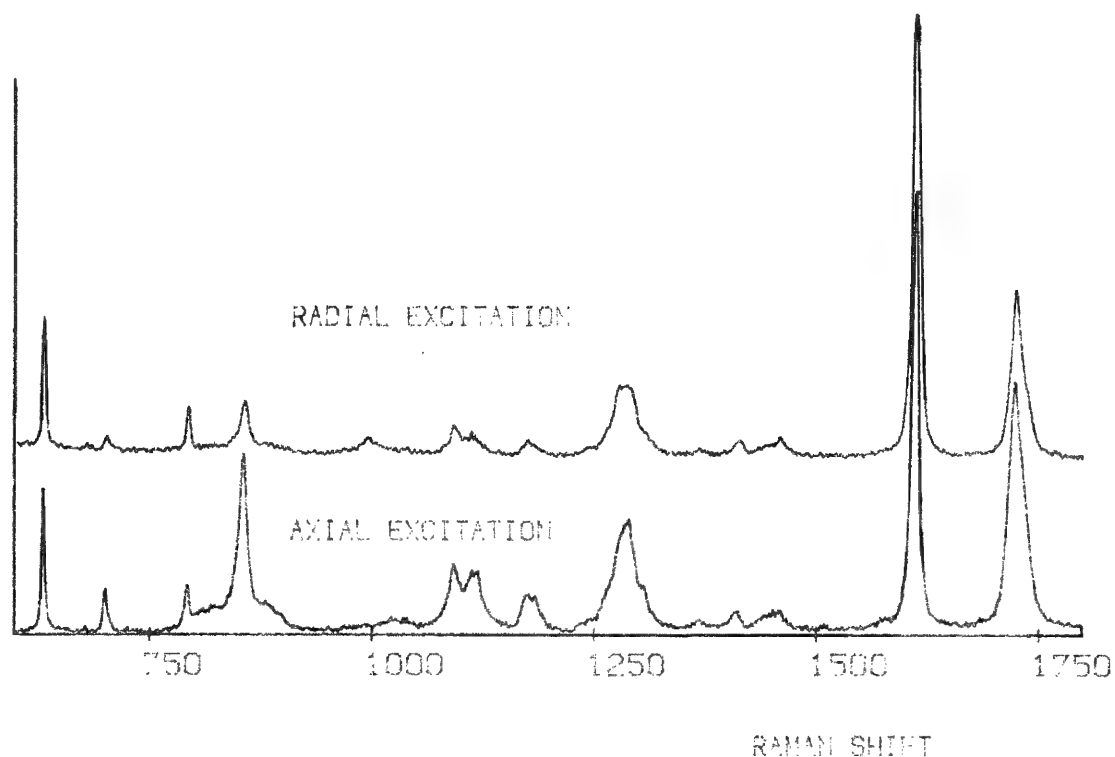


FIG. 4.--Raman microprobe spectra of PET filaments spun at 5500 m/min and examined radially and axially. (Spectra are displayed such that intensity at  $1614 \text{ cm}^{-1}$  is full scale.)

TABLE 1.--Integrated peak intensities relative to 1614cm<sup>-1</sup> band.

Spin Conditions		1727 cm <sup>-1</sup>	1285 cm <sup>-1</sup>	1095 cm <sup>-1</sup>	855 cm <sup>-1</sup>	796 cm <sup>-1</sup>	631 cm <sup>-1</sup>
1500 m/min	Axial	.895	.892	-	.199	.030	.135
	Radial	.574	.482	-	.058	.021	.120
	Axial/Radial	1.56	1.85	-	3.43	1.43	1.12
5500 m/min	Axial	.971	.767	.057	.354	.041	.139
	Radial	.607	.540	.028	.090	.042	.127
	Axial/Radial	1.60	1.40	2.04	3.93	.976	1.09
500 m/min	Axial	1.12	.901	.130	.483	.054	.184
	Radial	.599	.544	.040	.123	.044	.138
	Axial/Radial	1.87	1.66	3.25	3.93	1.23	1.33

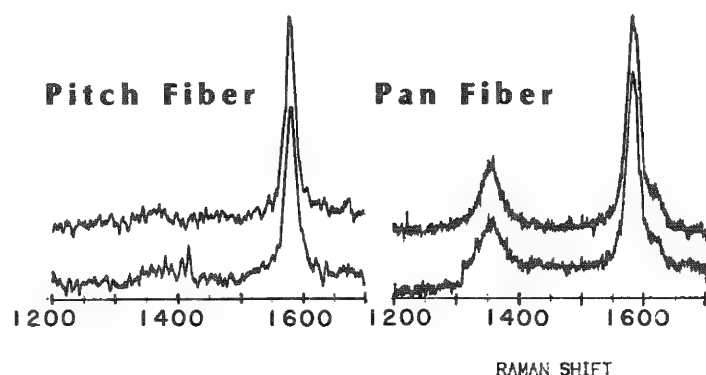


FIG. 5.--Raman microprobe spectra of graphite fibers prepared from pitch (A) and polyacrylonitrile (B); fiber axis parallel to laser E vector (upper trace), perpendicular to laser E vector (lower trace).

not expected to be excited. The spectra shown in Fig. 5 confirms these expectations. The intensity of the Raman band from the PAN fiber is identical in both orientations whereas the intensity of the Raman band of the pitch fiber is reduced by about 15% in the forbidden orientation (fiber axis perpendicular to laser E vector). The fact that the band has significant intensity in the forbidden geometry implies that the crystallites have finite size and a significant proportion of the graphite planes are not precisely radial.

Inspection of the data from the PAN fibers also shows bands at 1360 and 1620 cm<sup>-1</sup> in addition to the principal band at 1582 cm<sup>-1</sup>. The 1360cm<sup>-1</sup> is a consistent indicator of disorder.<sup>6</sup> The 1620cm<sup>-1</sup> band has also been associated with disorder; it is proposed that fine

particles of carbon could have significant quantities of carbonyl at the crystallite edges.<sup>8</sup> However, a band at this region has also been associated with intercalated graphite.<sup>9,10</sup>

### Conclusions

The Raman microprobe spectra of individual PET and carbon fibers enable the measurement of orientation and extent of crystallinity in these materials.

### References

1. A. J. Melveger, "Laser-Raman study of crystallinity changes in poly(ethylene terephthalate)," *J. Poly Sci.*, A-2, 10; 317-322, 1972.
2. J. Stokr et al., "Conformational structure of poly(ethylene terephthalate): Infra-red, Raman and NMR spectra," *Polymer* 23: 714-721, 1982.
3. J. Purvis and D. I. Bower, "Molecular orientation in poly(ethylene terephthalate)

- by means of laser-Raman spectroscopy," *J. Polymer Sci. Polymer Physics* 14: 1461-1484, 1976.
4. F. J. Boerio and R. A. Bailey, "Polarized Raman scattering from polyethylene terephthalate fibers," *Polym. Lett. Ed.* 12: 433-437, 1974.
  5. B. W. Cook and G. D. Ogilvie, "Microanalysis of industrial polymers by Raman spectroscopy," *Microbeam Analysis--1982*, 294-300.
  6. Tuinstra and J. L. Koenig, "Raman spectrum of graphite," *J. Chem. Phys.* 53: 1126-1130, 1970.
  7. L. Brillson, E. Burstein, A. A. Maradudin, and T. Stark, "Frequencies of long wavelength optical vibration modes of graphite," in Carter and Bate, Eds., *Physics of Semimetals and Narrow Gap Semiconductors*, New York: Pergamon Press, 1971, 187-193.
  8. M. Nakamizo, H. Honda, and M. Inagaki, "Raman spectra of ground natural graphite," *Carbon* 16: 281-283, 1978.
  9. S. Y. Leung, G. Dresselhaus, and M. S. Dresselhaus, "Lattice dynamics of graphite intercalation compounds," *Synthetic Metals* 2: 89-98, 1980.
  10. S. A. Solin, "Phonons in graphite intercalation compounds," *J. de Physique* C6: 283-288, 1981.



## CHARACTERIZATION OF COMPOSITE MATERIALS BY MEANS OF THE RAMAN MICROPROBE

Michel Couzi, Francis Cruège, Philippe Martineau, Catherine Mallet, and René Pailier

The recent development of the Raman microprobe has considerably increased the range of applications of Raman spectroscopy. Since areas as small as  $1 \mu\text{m}^2$  can be analyzed and their Raman spectra recorded, composite materials represent an obvious target for this instrument. As a matter of fact, this technique has already been applied with success to in situ and nondestructive characterization of carbon-carbon composite materials,<sup>1,2</sup> as well as of pyrocarbon-silicon carbide codeposits.<sup>3</sup>

In this paper, we present the first results we have obtained on filaments made of silicon carbide deposited by CVD on carbon filament and on tungsten-wire substrates. Structural and chemical inhomogeneities within such composite filaments are detected and analyzed; preliminary results are also presented, concerning the influence of heat treatments on the structure and composition of these filaments inserted in a titanium matrix.

### *Experimental*

Composite materials made of SiC filaments inserted in a titanium matrix have been prepared by hot pressing, as described previously.<sup>4</sup> Various types of SiC filaments have been used. SiC(1) (about  $100 \mu\text{m}$  in diameter) elaborated by SNPE corresponds to SiC deposited by CVD on a tungsten substrate. SiC(2), SiC(3), and SiC(4) (about  $140 \mu\text{m}$  in diameter) are from AVCO and correspond to SiC deposited on carbon monofilament substrates. In all cases, the deposition temperature is of about  $1200^\circ\text{C}$ . In order to improve the mechanical properties of the filament, the CVD procedures used are rather complex and imply, in particular, that inhomogeneities exist within the deposit from the core to the surface of the filament. Thus, the "SiC" filament by itself can be seen as a composite.

The SiC/Ti composite materials were cut perpendicular to the filament direction and polished (Fig. 1). In a first step, we have examined such cross sections of the SiC filaments and recorded the Raman spectra corresponding to various areas situated at various distances from the core. In a second step, the same samples have been analyzed after heat treatments.

The spectra have been recorded with the micro-Raman spectrometer MOLE from JOBIN-YVON equipped with a SPECTRA-PHYSICS model 164 argon ion laser. We always used the  $5145\text{\AA}$  emission line with an incident power not exceeding 20-30 mW at the surface of the sample. Detection was made with a RCA cooled photomultiplier coupled with a photon-counting system. In our experiments, the maximum spatial resolution (about  $1 \mu\text{m}^2$ ) was used; the spectral resolution was of about  $8 \text{ cm}^{-1}$ .

### *Results and Discussion*

Figure 2 represents the Raman spectra of SiC deposits recorded at different distances from the core of the filaments. The Raman spectra of the titanium matrix were featureless.

For the SiC(1) filaments (Fig. 2a), the spectrum of SiC first deposited on the tungsten core is characterized by two strong and narrow lines at  $800$  and  $970 \text{ cm}^{-1}$ ; they are assigned respectively to the TO and LO Raman active modes expected for cubic SiC (zinc blende structure) which is the low-temperature  $\beta$  form. Note the complete absence of additional sidebands that would be observed for the  $\alpha$ -SiC polytypes.<sup>5</sup> Note also that these strong lines are superimposed on broad features centered at about  $800$  and  $500 \text{ cm}^{-1}$ . With increasing distances from the core toward the filament surface, we observe that the two narrow lines are progressively displaced by the broad features at  $800$  and  $500 \text{ cm}^{-1}$  (Fig. 2a). The

---

Authors Couzi and Cruège are at the Laboratoire de Spectroscopie Infrarouge (LASIR), Université de Bordeaux I; authors Martineau, Mallet, and Pailier are at the Laboratoire de Chimie du Solide du CNRS, Université de Bordeaux I, F-33405 Talence Cédex, France.

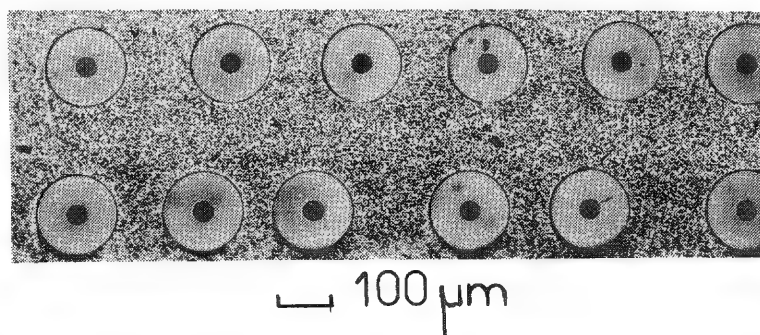


FIG. 1.--SiC/Ti composite material: cross section perpendicular to SiC filament direction.

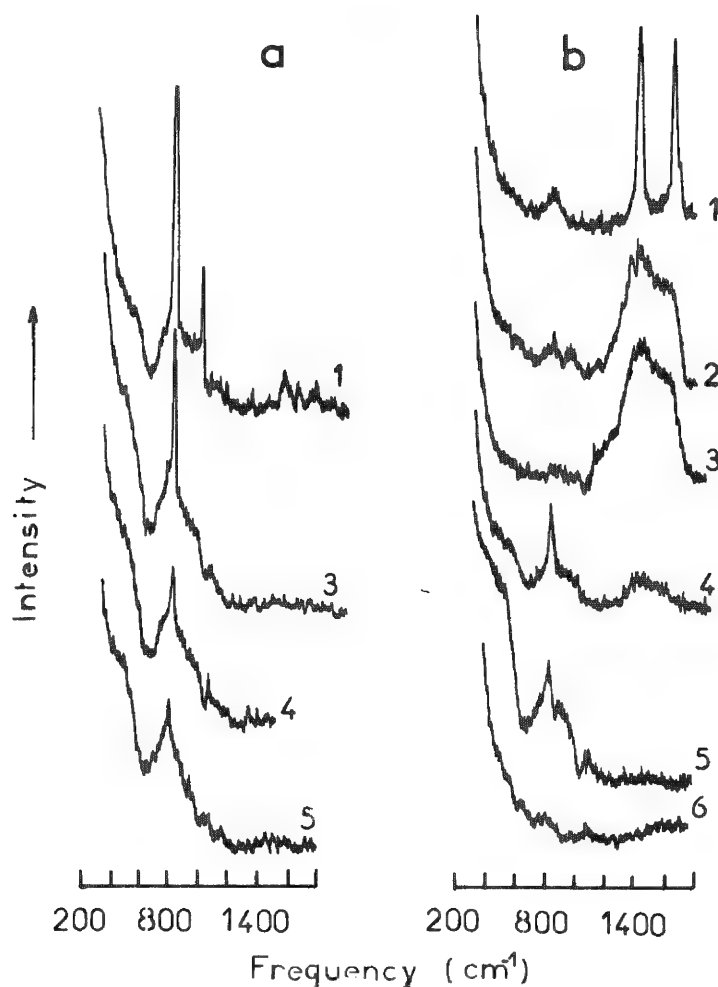
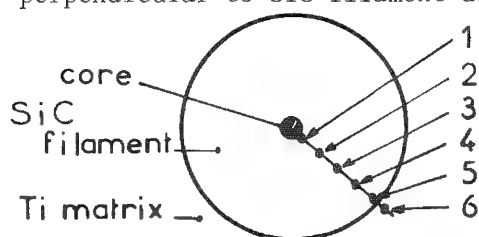


FIG. 2.--Raman spectra of SiC filaments recorded at various positions from core: (a) SiC(1); (b) SiC(2).

latter are assigned to another form of SiC, since microanalysis have shown the presence of stoichiometric SiC only.<sup>6</sup> This new form of SiC, the amount of which increases as the surface of the filament is approached, probably exhibits an important degree of disorder, judging from the width of the observed Raman lines. This spectrum, however, is different from that reported for carbon-deficient sputtered amorphous SiC films.<sup>7</sup>

The results of similar experiments made on SiC(2) filaments are shown in Fig. 2(b). At the core-deposit boundary, we observe strong lines at 1600 and 1350  $\text{cm}^{-1}$  due to the carbon filament substrate,<sup>1,2</sup> as well as a weak band near 800  $\text{cm}^{-1}$  previously assigned to a disorganized form of SiC. On going into the deposit at increasing distances from the core, we first notice an important broadening of the 1600-1350  $\text{cm}^{-1}$  bands and then the disappearance of these lines in favor of the broad features at 800 and 500  $\text{cm}^{-1}$  due to disordered SiC. This spectral evolution shows the presence of highly disorganized carbon<sup>8</sup> as well as SiC close to the core, and the progressive disappearance of this carbon on going close to the surface of the filament, where SiC alone is detected. The results obtained with SiC(3) and SiC(4) filaments show only slight differences with those of Fig. 2(b), and are generally interpreted in a similar way.

In a preliminary experiment, SiC(1) filaments have been analyzed after heat treatment of the SiC/Ti composite at 1100°C during 5 hr. The spectra clearly show the presence of crystallized  $\beta$ -SiC only throughout the filament cross section. The study of diffusion phenomena and/or chemical reactions between the SiC filaments and the Ti matrix is in progress.

### Conclusions

The preliminary results reported here illustrate the interesting possibilities offered by the Raman microprobe in the study of synthetic metal matrix composites, and in particular those containing SiC filaments. We believe that this technique could be successfully

applied to the study of most of the inorganic fibers or filaments that are used for the elaboration of composite materials.

#### References

1. A. Marchand, P. Lespade, and M. Couzi, *Proc. 15th Intern. Conf. on Carbon*, Philadelphia, 1981, 282.
2. P. Lespade, thesis, Bordeaux, 1982.
3. C. Mallet, thesis, Bordeaux, 1982.
4. R. Pailler, P. Martineau, M. Lahaye, and R. Naslain, *Rev. Chim. Min.* 18: 520, 1981.
5. D. W. Feldman, J. H. Parker Jr., W. J. Choyke and L. Patrick, *Phys. Rev.* 173: 787, 1968.
6. P. Martineau and R. Pailler, unpublished.
7. M. Gorman and S. A. Solin, *Solid State Comm.* 15: 761, 1974.
8. P. Lespade, R. Al-Jishi, and M. S. Dresselhaus, *Carbon* 20: 427, 1982.

## MICRO-RAMAN ANALYSIS OF THREE MILE ISLAND SAMPLES

T. E. Doyle and J. L. Alvarez

Using a Raman microprobe, we have analyzed samples from Three Mile Island Unit 2 (TMI-2). The purpose of examining TMI-2 samples is threefold: to determine the various chemical species resulting from a nuclear release accident; to explain the presence, transport, and consequences of release to the environment of specific chemical species; and to clarify and define the accident scenario. One result from the work is discussed in this paper: the positive identification of zirconium oxide, and particles that produce spectra characteristic of  $ZrO_2$ , in the TMI-2 purification system. Spectra of the latter particles reveal differences from the  $ZrO_2$  in crystalline structure that may provide information about processes that occurred in the TMI-2 core.

The samples in which the  $ZrO_2$  was found were obtained from Filter MU-F-5B, one of the two make-up and purification demineralizer filters. Since the sample stage is a conventional light microscope, no special preparation was needed to examine the particles beyond mounting the sample on a glass slide.

Monoclinic zirconium oxide was first discovered as a light gray, oval particle,  $6 \times 8 \mu m$ . The particle's spectrum closely matched a reference spectrum, with nine of the 13 peaks positively resolved. The four unresolved peaks coincided with the plasma lines of the 488.0nm blue line of the argon laser.

A second particle, white, rectangular,  $6 \times 8 \mu m$ , produced a spectrum (Fig. 1) identifying  $ZrO_2$ , but not initially in a monoclinic crystalline state. The first spectrum taken of the particle (Fig. 1, top) displayed weak, broad lines at 256, 465, and  $628 \text{ cm}^{-1}$ , suggesting a strained cubic<sup>1</sup> or tetragonal<sup>2</sup> crystalline structure. The 180 and  $192 \text{ cm}^{-1}$  lines of the monoclinic phase were missing. Subsequent spectra (Fig. 1, middle and bottom) showed the particle undergoing a phase transformation. The monoclinic phase became more dominant with successive spectra. Heating from the laser induced this phase transformation. The final spectrum (Fig. 1, bottom) was not entirely monoclinic but showed a disparity in the relative heights of the 337 and  $476 \text{ cm}^{-1}$  line, and a weak line at  $216 \text{ cm}^{-1}$  was not found in the standard spectrum. In addition, the major monoclinic lines of the intermediate spectrum (Fig. 1, middle) were shifted to higher frequencies (lower wave numbers). The  $180 \text{ cm}^{-1}$  line was shifted to  $173 \text{ cm}^{-1}$ , the  $192 \text{ cm}^{-1}$  line to  $186 \text{ cm}^{-1}$ , and the  $476 \text{ cm}^{-1}$  line to  $465 \text{ cm}^{-1}$ . The intermediate spectrum also showed a strong peak at  $255 \text{ cm}^{-1}$ , not a monoclinic line.

The origin of these particles is of considerable interest. Since  $ZrO_2$  is insoluble in either cold or hot water, the particles most likely originated in the TMI-2 core and were transported by suspension. The existence of monoclinic  $ZrO_2$  in the purification system is not a surprise, since a large portion of the zircaloy fuel-rod cladding is believed to have oxidized, and the most stable form of  $ZrO_2$  below  $1000^\circ\text{C}$  is monoclinic. However,  $ZrO_2$  in a cubic or tetragonal phase has also been discovered. Cubic and tetragonal  $ZrO_2$  are unstable at low temperatures; the  $ZrO_2$  must be locked into the cubic or tetragonal state by the presence of an impurity (e.g.,  $Y_2O_3$  or  $CaO$ ) or rapid cooling (quenching). Stabilizing the tetragonal phase in  $ZrO_2$  by quenching is uncommon, however. Four possible explanations were considered to account for the results.

1. The particles are fragments of the cubic  $ZrO_2$  ceramic spacers in the core. The fragments have been subjected to stresses (i.e., heat and pressure) that have caused phase changes.

2. The  $ZrO_2$  in the particles is in a solid solution. Eutectics may have formed from

---

The authors are at EG&G Idaho, Inc., Idaho Falls, ID 83415. Supported by the U.S. Department of Energy under DOE Contract DE-AC07-76ID01570.

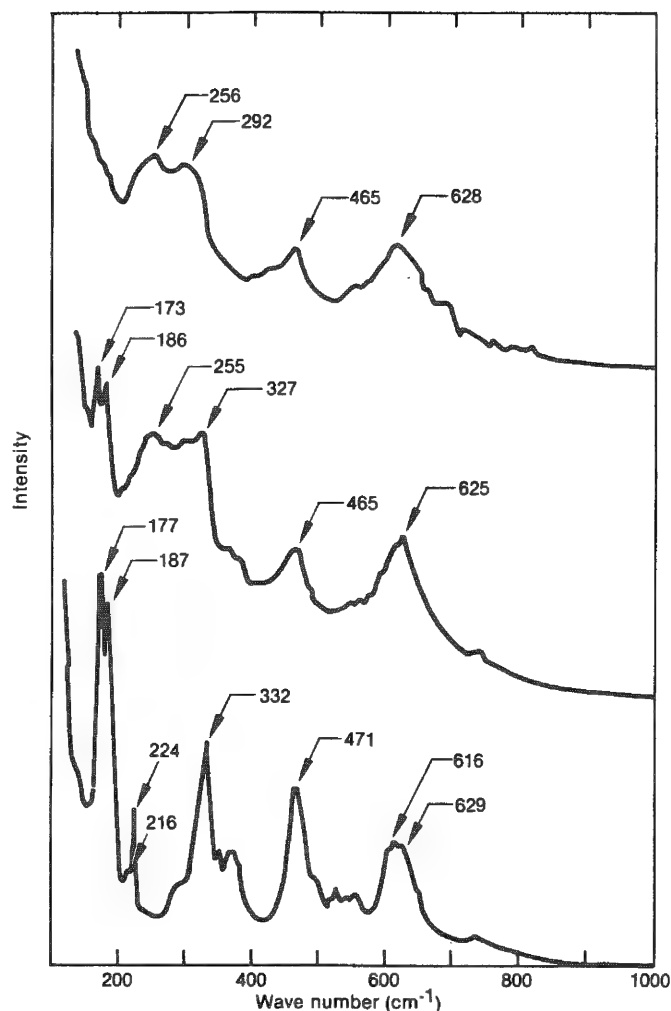


FIG. 1.--Raman spectrum of particle No. 2.

SEM is not capable of detecting these trace quantities, and we do not believe that they would have stabilized the  $ZrO_2$  in the tetragonal phase. Heating from laser irradiance transformed the particles to the monoclinic phase; this phenomenon has not been reported for free particles or ceramic grains stabilized in the tetragonal phase by impurities. Also, it has not been the experience of zirconia researchers that trace impurities stabilize the tetragonal phase.

Raman spectra of slowly oxidized zircaloy display similar line shifts and peak intensity differences as are observed on spectra of some  $ZrO_2$  particles. The gradual formation of monoclinic  $ZrO_2$  on the zircaloy creates stress in the crystalline structure. The monoclinic lattice tries to conform to the atomic spacings of the underlying zircaloy. Similarly, nonstoichiometries in the zirconium oxide of some particles (from the MU-F-5B sample) would also create stress or decrease the lattice dimensions in the monoclinic crystalline structure.<sup>3</sup> The nonstoichiometries would result from incomplete oxidation of the zircaloy.

Below a critical grain or crystal size, the tetragonal phase in  $ZrO_2$  is stable at room temperatures.<sup>4</sup> This research has been done for grains within ceramics, but it can also apply to free particles.<sup>5</sup> Another effect of particle size is the degree of phase transformation that occurs. Microscopic crystals or grains of  $ZrO_2$  transform completely from the tetragonal to monoclinic phase; there is no gradual transformation or intermediate phase for small, single crystals.<sup>5</sup> The  $ZrO_2$  particles from the MU-F-5B sample gradually transformed, evidencing that they are a conglomerate of smaller particles or crystals. SEM micrographs do indeed show transformed particles to be conglomerates.

zirconium and constituents from the fuel and control rods, subsequently oxidizing or forming in the oxidized state, and thereby stabilizing the tetragonal phase.

3. Oxidized zircaloy samples that have been studied show two types of  $ZrO_2$  spectra, corresponding to slowly oxidized and rapidly oxidized zircaloy. Slowly oxidized samples displayed a monoclinic spectrum with lines shifted to lower wave numbers and some differences in peak intensities. Rapidly oxidized samples produced the standard monoclinic spectrum. The spectral differences in the two oxidation rates probably result from a nonstoichiometric oxide which causes crystal strains. However, tetragonal structure was not indicated in either case.

4. Particle size influences the phase transformation of tetragonal  $ZrO_2$  to monoclinic  $ZrO_2$ . The observed tetragonal phase may have been metastable because the particles were smaller than a critical size.

To test these explanations, we analyzed the  $ZrO_2$  particles on the scanning electron microscope (SEM). The ceramic spacers in the TMI-2 core contained 15% (mol.) calcia to stabilize the  $ZrO_2$  in the cubic phase. The presence of calcium, as revealed by SEM analysis, would determine whether the  $ZrO_2$  particles are fragments of ceramic spacers or oxidized fuel-rod cladding. Calcium was not detected by the SEM on any of the  $ZrO_2$  particles.

SEM analysis also did not indicate the presence of eutectics. The  $ZrO_2$  in the particles is either pure or, most likely, contains trace amounts of impurities. The

The absence of calcium strongly suggests that the  $\text{ZrO}_2$  particles are from oxidized cladding. Eutectics were not detected, and we doubt that impurities stabilized the observed tetragonal phase. Also, the initial spectra (before laser heating caused crystal-line phase changes) of some  $\text{ZrO}_2$  particles are very similar to spectra of pure  $\text{ZrO}_2$  raised to  $1200^\circ\text{C}$ .<sup>2,6</sup> An explanation which corresponds to the results is that fuel-rod cladding was oxidized and elevated to at least  $1200^\circ\text{C}$ . Such heating would cause a transition to the tetragonal phase, which is unstable at lower temperatures. The size of the particles (less than  $10\text{ }\mu\text{m}$ ) and perhaps quenching metastably locked the  $\text{ZrO}_2$  into the tetragonal phase.

We have identified zirconium oxide in the TMI-2 purification system. Some  $\text{ZrO}_2$  particles were originally in a tetragonal phase and subsequently transformed to the monoclinic phase. SEM analysis revealed that they were not fragments of the ceramic spacers; we conclude from the Raman data that they were pieces of oxidized fuel-rod cladding elevated to at least  $1200^\circ\text{C}$  in the TMI-2 core. Particle size and possibly quenching stabilized the  $\text{ZrO}_2$  in the tetragonal phase until laser irradiance transformed the  $\text{ZrO}_2$ . Stress or a decrease in lattice dimensions caused by nonstoichiometries would explain the nonstandard Raman spectrum of the subsequent monoclinic phase.

### References

1. C. M. Phillippi and K. S. Mazdidasni, "Infrared and Raman spectra of zirconia polymorphs," *J. Am. Ceramic Soc.* 54: 254-258, 1971.
2. A. Feinberg and C. H. Perry, "Structural disorder and phase transitions in  $\text{ZrO}_2\text{-Y}_2\text{O}_3$  system," *J. Phys. Chem. Solids* 42: 513-518, 1981.
3. S. C. Carniglia, S. D. Brown, and T. F. Schroeder, "Phase equilibria and physical properties of oxygen deficient zirconia and thoria," *J. Am. Ceramic Soc.* 54: 13-17, 1971.
4. F. F. Lange and D. J. Green, "Effect of inclusion size on the retention of tetragonal  $\text{ZrO}_2$ : Theory and experiments," *1st Intern. Conf. Sci. and Tech. of Zirconia*, Cleveland, Ohio, 1980.
5. D. R. Clarke, Rockwell International Science Center, Thousand Oaks, Calif., private communication, 1982.
6. M. Ishigame and T. Sakurai, "Temperature dependence of the Raman spectra of  $\text{ZrO}_2$ ," *J. Am. Ceramic Soc.* 60: 367-369, 1977.

## MICRO-RAMAN ANALYSIS WITH THE USE OF MULTICHANNEL INTENSIFIED PHOTODIODE ARRAY DETECTOR

J. Barbillat and M. Delhay

The first Raman microprobes instruments specially designed for microanalysis,<sup>1,2</sup> which availed themselves of the techniques of conventional Raman spectrometry (scanning monochromators and monochannel detection), permitted successful explorations in many domains of applications such as analysis of inclusions in rocks, identification of defects in industrial materials of various origins (semiconductors, synthetic fibers, etc.), and analysis of biological samples. However, some investigators quickly realized the benefits to be gained from multichannel detection. Thus, for instance, the MOLE microprobe was fitted with multichannel detection (image intensifier tube and TV camera) in addition to conventional PM detection in order to record selective micrographic images of the distribution of chemical species in an heterogeneous sample. The same detection scheme was also used to observe simultaneously all the spectral elements in a small segment of the Raman spectrum of the sample. Nevertheless, some specific applications revealed the limitations of these instruments--limitations due to the lack of sensitivity to detect the Raman spectrum of very weak scatterers or of unstable samples that do not sustain the high irradiation of the laser beam without degradation and so require too low a laser power. There are also the limitations due to the difficulty of obtaining well-contrasted selective images owing to the way the microscope and the spectrometer are coupled. But at about the same time new low-light-level photoelectrical detectors with better characteristics (microchannel plate image intensifier tube, solid-state photodiode array detector) became available with fast detection capabilities that permitted the simultaneous recording of a large number of spectral elements. As a result a new generation of Raman microprobe was developed in which this kind of detector was used and which thus allowed the full benefit of the advantages of multichannel spectral acquisition. As early as 1982 many communications were presented at the MAS meeting that described either laboratory prototypes or commercial instruments.<sup>3-7</sup> In a way it is a return to the origin of spectroscopy, since the emission or absorption spectrographs with photographic plates used at the beginning were the first multichannel instruments. Of course techniques have advanced: the old prisms are replaced by holographic gratings and a good rejection of the stray light is achieved by grating foremonochromators. In the present paper, we describe work done in close collaboration with the DILOR company that led to the commercialization of a new microspectrometer specially built to benefit from the advantages of an intensified photodiode array detector: the Microdil 28.

### *The Microdil 28 Microprobe*

*Multichannel Detection.* The purpose of intensifying the photodiode array is to increase its capability for use at low light levels. Increase in the number of photons available under low-light-level conditions can be achieved with an image intensifier tube that serves as the input to the photodiode array detector. It has been shown that the useful range of the photodiode array may be extended several orders of magnitude by this technique. In order to intensify the photodiode array optically, the following device (one of the best for this purpose) was used. It was a miniature distortionless electrostatic proximity-focused microchannel plate image intensifier tube. Because of the size of the available photodiode array and of the intensifier, a 18mm active diameter tube (RTC) with fiber-optic input and output windows was used in this device. The bounding of the intensifier is

---

The authors are at the Laboratoire de Spectrochimie Infrarouge et Raman CNRS, Université des Sciences et Techniques de Lille I, bât. C.5, 59655 Villeneuve d'Ascq Cédex, France. The authors thank F. X. Sauvage for providing thin films of phthalocyanine and P. Y. Noel for providing crustacean pigment.



accomplished with a nonpermanent oil coupling that needs mechanical clamps to keep the array and the intensifier lined up properly. The Reticon 512 S photodiode array contains a row of 512 diode sensor elements on 25  $\mu\text{m}$  centers, corresponding to an overall length of 12.8 mm. The height of the sensor elements is 2.5 mm. This unit is mounted in a package (Fig. 1) cooled at  $-20^{\circ}\text{C}$  by a Peltier element that increases performance by allowing a possible integration time of as long as 100 s without saturation. A part of the electronics (specially built to detect very weak signals<sup>8</sup>) is included in the same package. Analog information is extracted from the photodiode array successively for each diode, sampled for 12 bits digital conversion in real time (9  $\mu\text{s}$  per diode), and then sent into a fast computer. In this mode of acquisition, integration time can be as short as 10 ms. If the computer is not fast enough, real-time data from A/D converter are stored into two memory blocks (one for signal and the other for background) and an arithmetic unit performs background subtraction. In this mode of acquisition the shortest integration time is about 60 ms, depending on the time the computer needs to get data.

Compared with the conventional scanning technique, multichannel detection means better utilization of the time devoted to spectrum analysis. For instance, for a Raman spectrum of  $N$  spectral elements, a conventional spectrometer receives at its detector only one spectral element during a time  $t = T/N$ , where  $T$  is the total recording time. The  $N - 1$  spectral data dispersed during the same time are lost. This problem is the origin of the degradation of the signal-to-noise ratio. Multichannel techniques enable the simultaneous recording of all  $N$  spectral elements during the same time  $t = T/N$  with the same sensitivity. Thus, if the two spectra are recorded in the same total time  $T$ , the signal-to-noise ratio for the "multichannel spectrum" would be superior by a factor  $\sqrt{N}$ .

Multichannel intensified photodiode detection also makes it possible to reduce routine spectral acquisition time from the few tens of minutes required in scanning spectrometers to typically a few seconds. As a result one can turn this gain in time to profit for detecting very weak Raman signals by accumulating a great number of spectra.

*Spectrometer.* The Microdil 28 comprises a zero-dispersion foremonochromator with two plane holographic grating which disperse the radiation in opposite directions (Fig. 2). It is used to select a spectral band in the spectrum and to reject the exciting line. The center of this band is selected by the rotation of the gratings and its width is determined by the width of the intermediate slit, adjustable from 0 to 20 mm. The band pass is recombined on the exit slit of the foremonochromator and dispersed by a stigmatic grating spectrograph on the multichannel detector. To vary the dispersion and the spectral coverage, the spectrograph is fitted with two plane holographic gratings mounted in a turret. Band pass is about  $1500\text{ cm}^{-1}$  with the 600gr/mm grating and about  $500\text{ cm}^{-1}$  with the 1800gr/mm grating at  $5000\text{ \AA}$ . The maximum resolution, limited by the discrete structure of the detector, is about  $1\text{ cm}^{-1}/\text{diode}$  at  $5000\text{ \AA}$  with the 1800gr/mm grating and is quite sufficient for the majority of applications. The foremonochromator can be automatically converted to a conventional scanning monochromator with a photon counting detection.

*Illuminator and Coupling Optics.* The Microdil 28 is equipped with an Olympus microscope (BHM) that allows one to observe the sample with white-light illumination and to focus the laser beam on a microscopic spot (about  $1\text{ }\mu\text{m}$ ) on the sample. The same objective collects the scattered light at this point. The focusing and coupling optics are specially designed to enable the operator to explore the whole observed area of the sample without moving the stage of the microscope (Fig. 3).<sup>9</sup> To achieve this goal the laser beam is focused into the back focal plane of the microscope objective by a lens. This lens, optically conjugate to the back aperture of the objective, can be moved in two orthogonal directions perpendicular to the laser beam. By moving this lens one can focus the laser beam on any point in the field of the microscope and therefore on any point of the sample. At any point located off center, there is a corresponding scattered beam off the spectrometer axis (Fig. 4). That is why a second moving lens mechanically coupled to the first is placed on the scattered beam to balance any shift in the image of the probed area and bring it to the entrance slit of the spectrometer. After passing through this lens, the scattered beam is always centered on the optical axis, so that it is possible to place, on an intermediate image, an iris diaphragm that eliminates the radiation not directly issuing from the probed area. This optical arrangement rigorously couples the pupils of the microscope and the spectrometer. Thus the whole observed area can be analyzed without any loss of light. This optical arrangement has proved to be most convenient for a variety

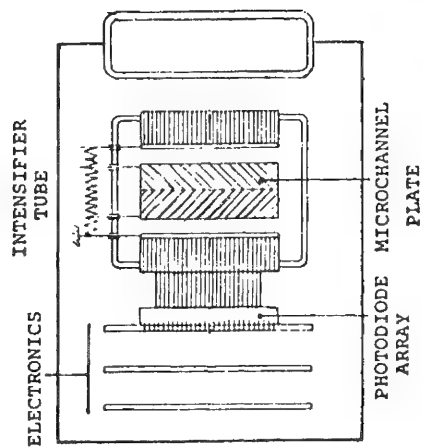


FIG. 1.--Multichannel intensified photodiode array detector.

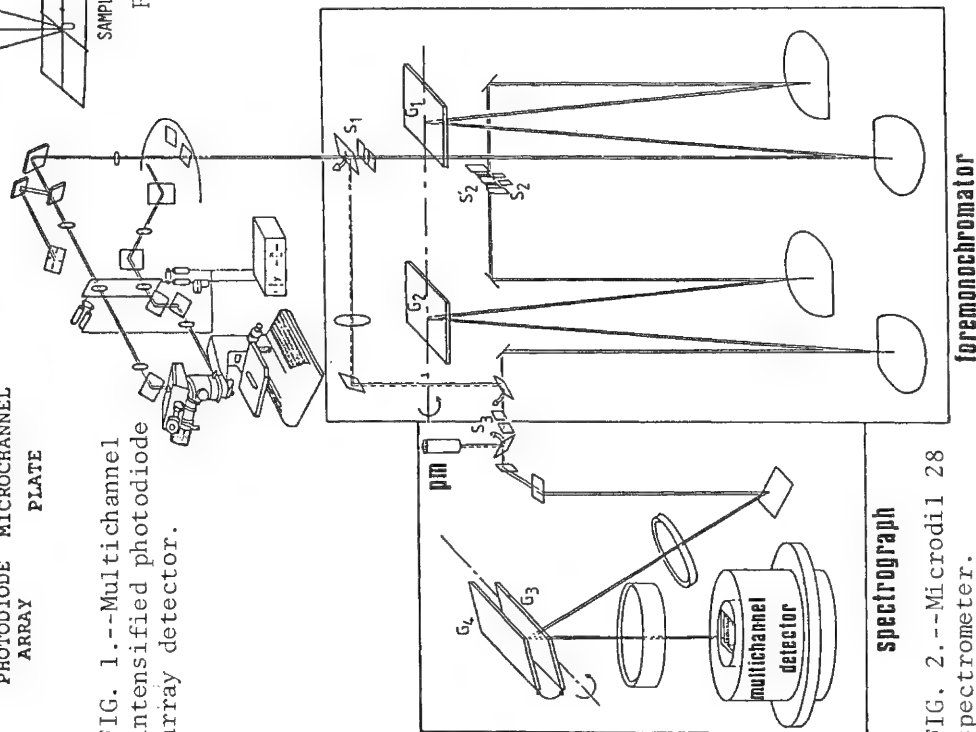


FIG. 2.--Microdi 128 spectrometer.

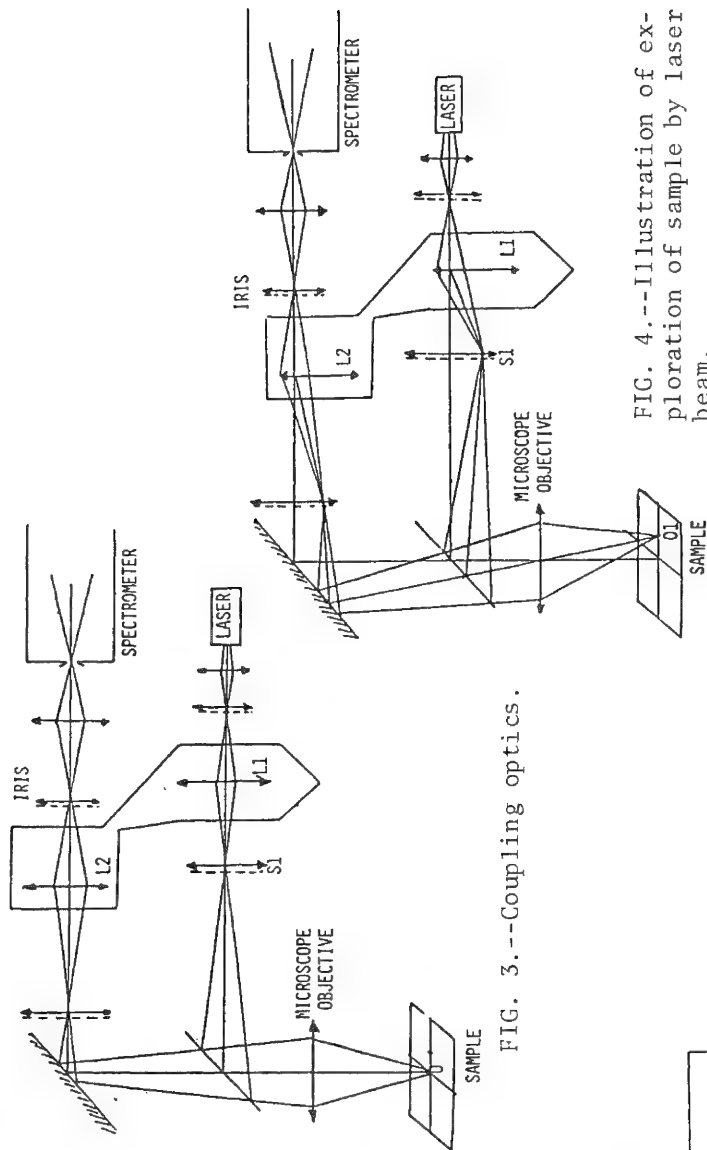


FIG. 3.--Coupling optics.

FIG. 4.--Illustration of exploration of sample by laser beam.

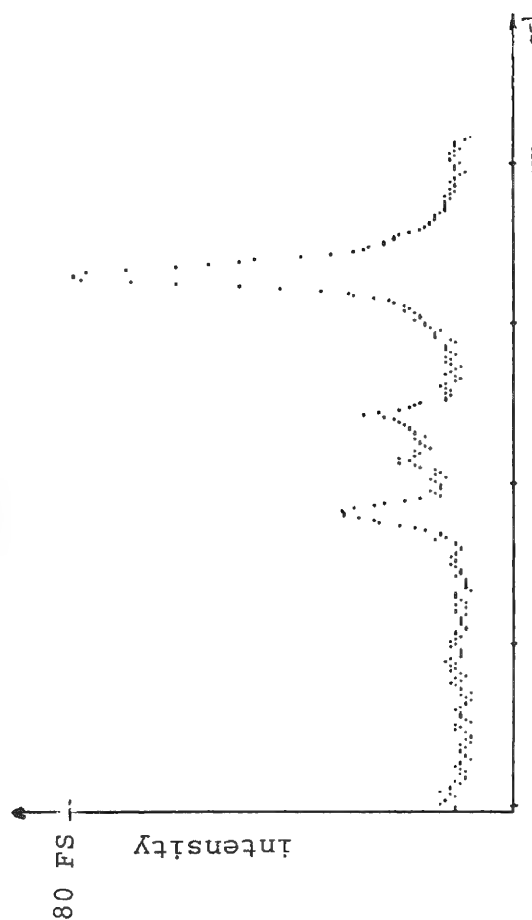


FIG. 5.--Raman spectrum of solid film of  $\alpha$ -copper phthalocyanine:  $\lambda_{exc} = 514.5 \text{ nm}$  (5 mW).

of cumbersome samples or accessories (variable temperature or pressure stages). As the exploration by the laser beam is performed in the back image space of the microscope it profits from the magnification of the objective, and the sample can be analyzed with high spatial accuracy without difficulty.

Instead of focusing the laser beam on a single spot in the sample it is also possible, by means of an oscillating mirror on the path of the laser beam, to illuminate a large number of points along a straight line across the sample and to focus this line on the slit of the monochromator. We describe some applications of this device in the following section.

### *Applications*

*Raman Spectrum of  $\alpha$  Copper Phthalocyanine.* Copper phthalocyanines (CuPc) are commercially important as a pigment system. They exist under two polymorphic forms:  $\alpha$  CuPc and  $\beta$  CuPc. Heating  $\alpha$  CuPc at 300°C changes it into  $\beta$  CuPc. As these compounds are colored, they strongly absorb the laser radiation and can be destroyed with too high a laser power. Raman spectra of  $\alpha$  CuPc and  $\beta$  CuPc published in the literature seem to be the same,<sup>10,11</sup> perhaps because  $\alpha$  CuPc changes into the  $\beta$  CuPc form during the recording time. In order to confirm the Raman spectrum of  $\alpha$  CuPc we have recorded several spectra with various laser powers. The samples were prepared by vacuum evaporation of  $\alpha$  CuPc on a glass slide. In order to prevent the degradation of the sample by the laser beam we used the scanner to focus the laser on a  $1 \times 50 \mu\text{m}$  straight line and reduced the laser power to a very small value (about 0.5 mW at the sample) with a neutral glass filter. Under the conditions we obtained the spectrum shown in Fig. 5, which corresponds to the  $1350\text{--}1550\text{cm}^{-1}$  domain. The sample observed in white-light illumination after the analysis does not exhibit any degradation. By increasing the laser power we observe some modifications in the spectrum (Fig. 6): the bands in the range  $1350\text{--}1550\text{ cm}^{-1}$  become broader and shift (from about  $6\text{ cm}^{-1}$ ) toward the lower wave numbers. At the same time the coloration of the sample changes to indicate a modification in the structure of  $\alpha$  CuPc.

This example points out the capability of the Microdil 28 to record good Raman spectra of unstable samples without degradation even with very low laser power. Focusing the laser beam on a line also prevents thermal decomposition of the sample.

In some other cases, for instance with homogeneous samples at the microscopic level, the method of focusing the laser beam on a line can be used to increase the scattered light by increasing the volume to be analyzed. Under these conditions the laser power can be also increased to improve the signal-to-noise ratio. The increase of the laser power is not generally proportional to the increase in volume, but depends strongly on the nature of the sample and its thermal contact with the support; attention must be paid to the thermal relaxation of the sample that does not generally allow one to increase the laser power by more than a factor of 2-3.

*Raman Spectrum of Crustacean Pigments.* The spectrum of the black pigment of pure melanin from cephalopod was recorded, for the first time, for comparison with the spectra of black pigments of various melanophores. The observed spectrum (Fig. 7) exhibits two bands in the  $1300\text{--}1650\text{cm}^{-1}$  region, which is similar to the spectrum of graphite. But the two bands of graphite are not at the same position. This spectrum, which is less intense than the spectrum of graphite (under the same conditions: acquisition time, 200 s), is a good illustration of the ability of the multichannel technique to detect very weak signals by long-time accumulation.

*Raman Intensity Profiles.* There are two possible ways of obtaining Raman intensity profiles along a straight line across a sample by use of the Microdil 28. In the first one the laser beam is focused point by point along the chosen line and for each point the computer stores the entire Raman spectrum. Then the computer can restore as many intensity profiles as there are spectral elements. The multichannel technique is the only one that enables us to obtain so many data points in so little time. Conventional scanning techniques would require several hours of operation, whereas one can obtain the same amount of information with multichannel detection in a few minutes. The same technique can be extended to record two-dimensional maps, to yield the distribution of several chemical species in the entire observed area. It only requires larger memory capacity and more time.

The second way to obtain Raman intensity profiles is to deflect the laser beam on the sample (with the scanner) rapidly and to project this line on the entrance slit of the

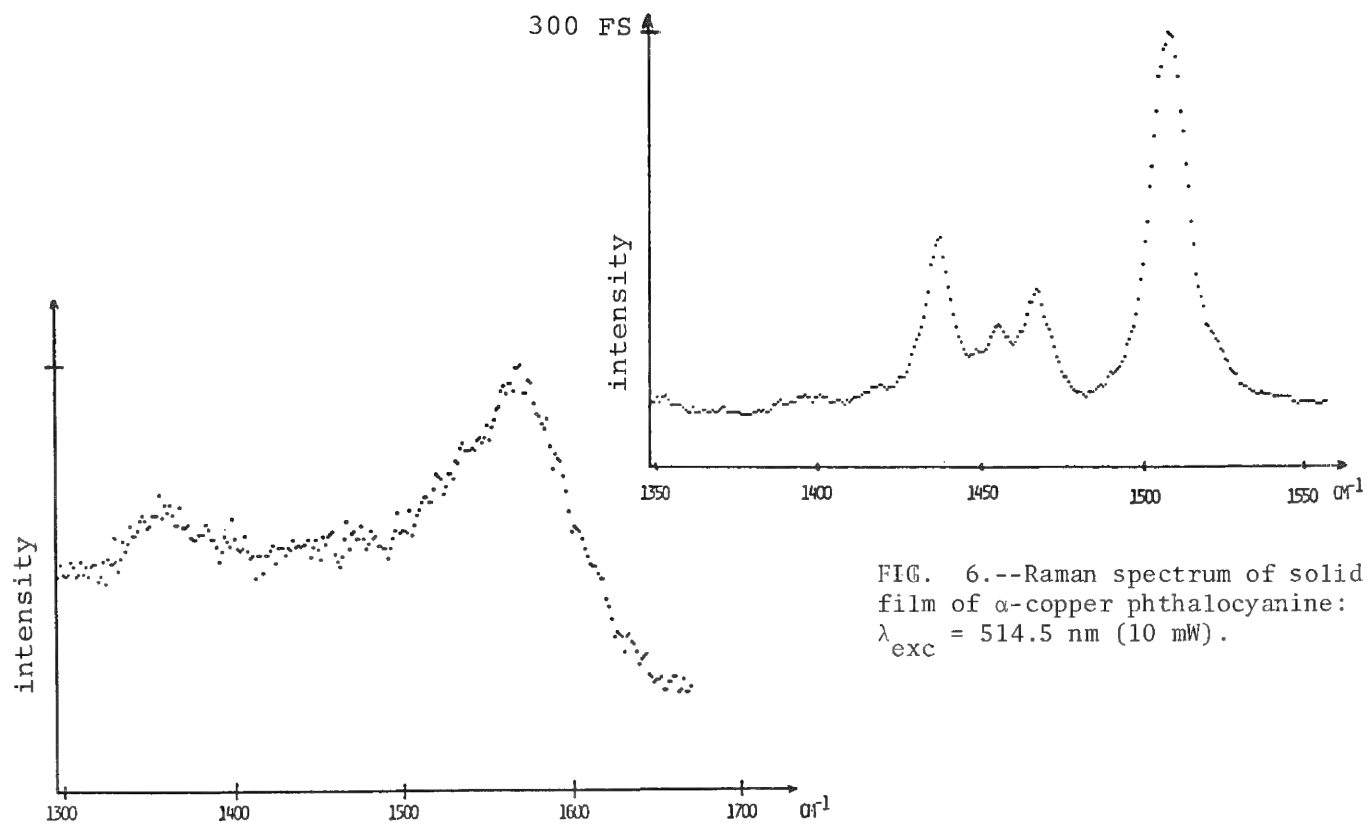


FIG. 6.--Raman spectrum of solid film of  $\alpha$ -copper phthalocyanine:  $\lambda_{\text{exc}} = 514.5 \text{ nm}$  (10 mW).

FIG. 7.--Raman spectrum of pure melanin.

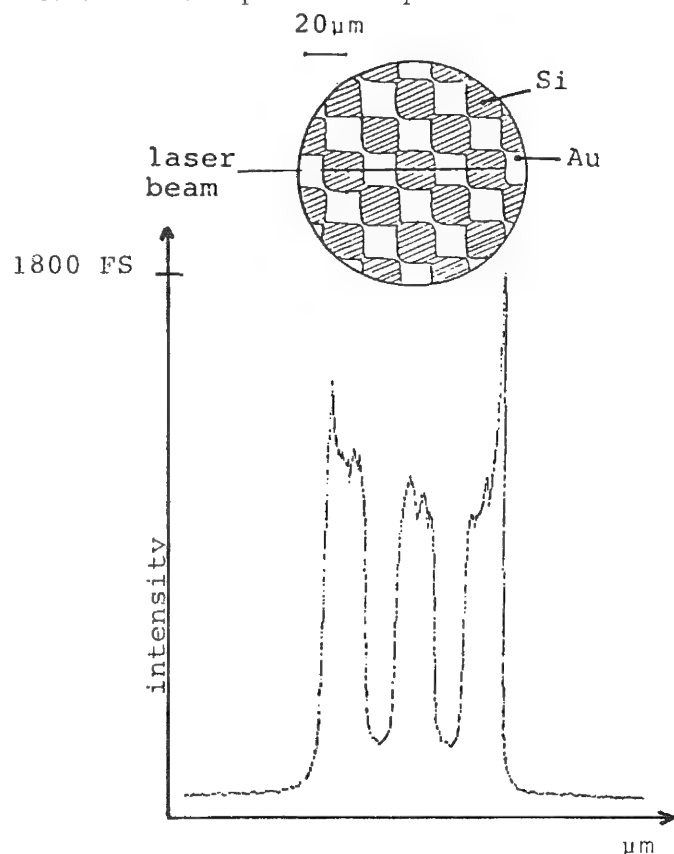


FIG. 8.--Intensity profile on silicon test specimen ( $\bar{\nu} = 525 \text{ cm}^{-1}$ ).

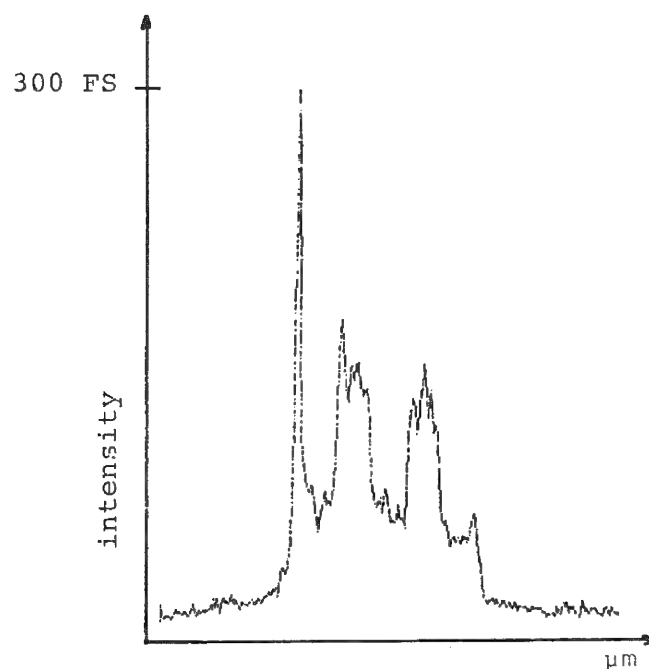


FIG. 9.--Intensity profile on silicon test specimen ( $\bar{\nu} = 545 \text{ cm}^{-1}$ ).

spectrometer, which must be stigmatic. Then if the multichannel detector is placed perpendicular to the dispersion of the spectrum it is possible to focus on it a filtered image of the illuminated line of the sample. Thus one obtains, simultaneously, the intensity profile of the entire line at a given wave number.

Here we present the profile recorded on a silicon test specimen, a silicon chip bearing 1600 thin gold layer squares  $20 \times 20 \mu\text{m}$  arranged in a checkerboard pattern (Fig. 8) that allows highly precise measurements. If the spectrometer is centered on the  $525\text{cm}^{-1}$  line of silicon one obtains directly the intensity profile that gives the distribution of silicon across the sample (Fig. 8). This profile, obtained with an integration time of 40 s, is in good agreement with the white-light image. By tuning the spectrometer to another frequency at which silicon does not scatter, one obtains the distribution of Fig. 9, which is not flat because of the different reflective powers of silicon and gold. It does not correspond to a Raman profile but merely to the stray-light repartition across the sample that acts as a mirror and reflects much of the exciting laser line into the monochromator.

Here again one can extend this technique to the recording of two-dimensional maps that give a cartography of the sample at a single frequency by moving the laser line across the entire observed area.

### Conclusions

The few applications presented here illustrate the gain in sensitivity that can be routinely obtained with the new generation of multichannel microprobe, Microdil 28. One might expect that sample reputed to be difficult a few years ago will be routinely recorded in the future with multichannel photodiode instruments. We have already illustrated this point with graphite, whose weak spectrum it was quite impossible to record with conventional scanning spectrometers. The first generation of Raman microprobes, which had the advantages of collecting the scattered light with a large aperture optical system, delivered sufficiently good spectra of graphite in a few tens of minutes. At present, with Microdil 28, this sample serves as a routine test and its spectrum is recorded in a few seconds without difficulty.

### References

1. G. J. Rosasco et al., "The analysis of discrete fine particles by Raman spectroscopy," *Appl. Spectrosc.* 29: 396, 1975.
2. M. Delhayé and P. Dhamelincourt, "Raman microprobe and microscope with laser excitation," *J. Raman Spectrosc.* 3: 33, 1975.
3. W. R. Steinbach et al., "Analytical applications of a multiplex detector laser Raman microprobe," *Microbeam Analysis--1982*, 279-285.
4. F. J. Purcell and E. S. Etz, "A new spectrograph with a multichannel optical detector for the Raman characterization of microparticles," *Microbeam Analysis--1982*, 301-306.
5. F. P. Milanovich et al., "The Lawrence Livermore National Laboratory Raman microprobe," *Microbeam Analysis--1982*, 270-274.
6. D. O. Landon, "Optical spectroscopy by microprobes with diode array systems," *Microbeam Analysis--1982*, 315-317.
7. M. Delhayé et al., "A new generation of laser Raman microspectrometer: Microdil 28," *Microbeam Analysis--1982*, 275-278.
8. H. Surbeck et al., "The direct recording of Raman spectra with solid state detectors," *Optics Communications* 38: 57-60, 1981.
9. M. Delhayé et al., *Dispositif optimisant le couplage de deux systèmes optiques pour l'observation et l'analyse d'objets*, French patent application 812 332, 1981.
10. R. Aroca et al., "Raman spectra of solid films: (I) metal free phthalocyanine," *J. Phys. Chem. Solids* 43: 707-711, 1982.
11. J. A. Nimmo et al., "The effect of silver on the Raman spectrum of  $\alpha$ -copper phthalocyanine," *Chem. Phys. Letters* 92: 212-214, 1982.

## RAMAN MICROPROBE SPECTROSCOPY AND STUDY OF THE RETENTION OF AIR PARTICLES BY THE HUMAN RESPIRATORY SYSTEM

P. Pineau, M. Audebrand, P. Fréour, J. F. Tessier, and J. G. Faugère

Raman microscopy has been used by certain authors to study the nature of atmospheric particles.<sup>1-6</sup> We use the same instrument, along with infrared interferometry, in order to contribute to the study of the deposit of inhaled particles in the human respiratory system. In this paper we present our method, which consists of comparing the Raman and the infrared spectra of air particles from the air that is exhaled by a person. We also present our preliminary results.

### *The Experimental Phase*

The atmospheric particles were collected with a six-stage cascade impactor (Fig. 1). The averages of the diameters of the particles deposited on the disks of each stage are given in Table 1. We used two impactors. With the smallest, the flow of air was 1.5 l/min. It was possible to take two samples. We first collected the particles in the atmosphere and then the particles in the air exhaled by a subject. The time of each sample-taking was approximately 15 min.

The Raman spectra were recorded with a Raman microprobe, the MOLE made by Jobin-Yvon. The ion argon laser is Model 164, produced by Spectra-Physics. We used the 514.5nm emission line. The power of the beam did not exceed a few milliwatts at the surface of the particle. A cooled RCA photomultiplier was coupled to a photon-counting system. Spectral resolution was approximately  $10\text{ cm}^{-1}$ . When the particles were deposited on shiny aluminum disk, the spectrum was recorded by using a system that is normally used for reflectance measurements.

### *Results and Discussions*

Some samples were taken in Bordeaux. The mineral compounds most frequently detected with Raman microscopy were  $\text{NaNO}_3$ ,  $\text{KNO}_3$ ,  $\text{CaSO}_4$ ,  $(\text{NH}_4)_2\text{SO}_4$ ,  $\text{PbSO}_4$ ,  $\text{SiO}_2$ .<sup>7,8</sup> In the majority of cases, the spectrum of a particle is that of one compound only. For instance, the spectrum of Fig. 2 shows that the greatest part of the particle is sodium nitrate.

We frequently observed the fluorescence of a sample under study, and we often saw carbon bands near  $1350$  and  $1600\text{ cm}^{-1}$  when the power of the laser beam was larger than  $10\text{ mW}$ .<sup>1,2</sup> However, we have detected only few organic compounds due to the lack of sufficient sensitivity of our instrument.

We tried to take a census of particles of the same type (sulfates or nitrates) from some samples. Count taking was very slow and proved to be inaccurate. Nevertheless, there is a correlation between the number of sulfate particles and the total sulfur quantity as determined by x fluorescence measurements.<sup>9</sup> In addition, we observed significant variations in the quantities of some compounds among samples collected in a variety of different places. Furthermore, we found that small particles of calcium sulfate having a diameter of less than  $2\text{ }\mu\text{m}$  are widely deposited in the respiratory system.<sup>9</sup>

Figure 3 shows the infrared spectrum of particles deposited on a silver chloride disk at impactor stage number 4. Only 200 liters of air were pumped into the impactor. There are few particles, and the diameter of the total deposit on the disk was not quite  $2\text{ mm}$ . Nevertheless, with the use of an interferometer, we easily observe ammonium bands (near

---

Authors Pineau and Audebrand are at the Laboratoire de Spectroscopie Infrarouge, Université de Bordeaux I, 351 cours de la Libération, F-33405 Talence Cédex, France; authors Fréour and Tessier are at the Laboratoire de Santé Publique, 3 ter, place de la Victoire, F-33706 Bordeaux Cédex, France; author Faugère is at the Laboratoire Municipal, F-33000 Bordeaux, France.

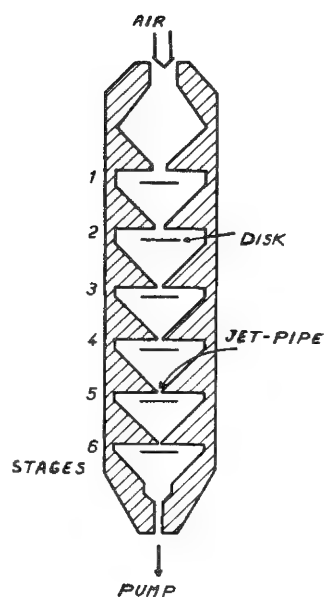


FIG. 1.--Cascade impactor.

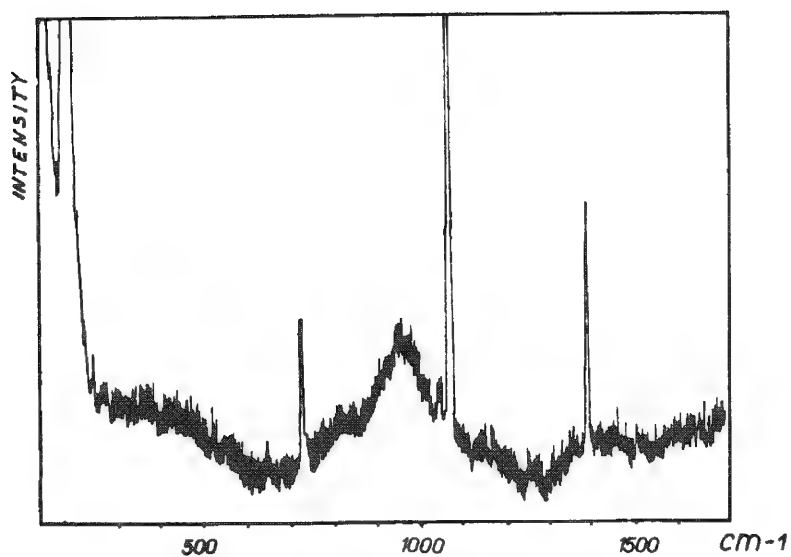


FIG. 2.--Raman spectrum of atmospheric particle containing sodium nitrate.

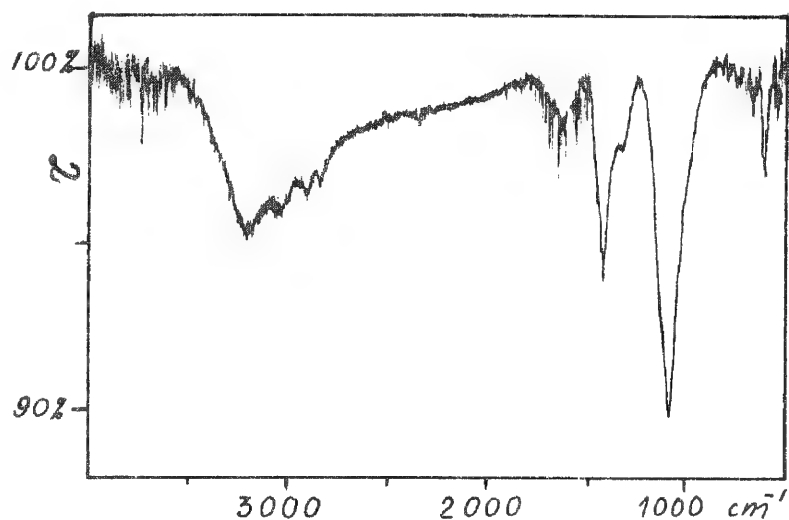


FIG. 3.--Infrared spectrum of particles collected on a silver chloride disk in impactor stage number 4. Volume of air injected: 200 liters.

TABLE 1.--Average diameter of particles deposited on impactor disks.

Stage	Diameter ( $\mu\text{m}$ )
1	6
2	3
3	1.5
4	0.75
5	0.35

1415 and  $3000\text{ cm}^{-1}$ ), sulfate bands (near  $620$  and  $1090\text{ cm}^{-1}$ ), and a nitrate band (near  $1360\text{ cm}^{-1}$ ).

### Conclusion

The interest of our method resides in giving the researcher two types of information related to particle analysis. First, it gives him qualitative information for each particle that has a Raman spectrum. Second, it enables him to follow the evolution of quantities of some of the particle constituents which absorb infrared light. Proceeding from our preliminary results, we show that this method can be useful in the study of certain physical-chemical problems and, in particular, in the analysis of atmospheric particles retained by the human respiratory system.



## References

1. G. J. Rosasco, *Adv. IR & Raman Spectroscopy*, London: Heyden, 1980, 223-282.
2. E. S. Etz and J. J. Blaha, *Characterization of Particles*, NBS Publication 533, 153-197, 1980.
3. E. S. Etz, G. J. Rosasco, and J. J. Blaha, "Observation of the Raman effect from single particles," in Toribara et al., *Environmental Pollutants*, New York: Plenum, 1978, 413-456.
4. W. C. Cunningham, E. S. Etz, and W. H. Zoller, "Raman microprobe characterization of South Pole aerosol," *Microbeam Analysis--1979*, 148-154.
5. M. Delhaye and P. Dhamelincourt, "Raman microprobe and microscope with laser excitation," *J. Raman Spectrosc.* 3: 33-43, 1975.
6. A. Goypiro, R. Foglizzo, J. P. Forgerit, C. de Lozé, C. Lambert, and R. Chesselet, *2nd Intern. Congress on Analytical Techniques in Environmental Chemistry*, Barcelona, 1981.
7. P. Pineau, R. Bernard, and M. Audebrand (with M. Fréour, J. F. Tessier, and J. G. Faugère), *Proc. 8th Conf. Raman Spectrosc. (Linear and Non-linear)*, London: Heyden, 1982, 813-814.
8. P. Pineau, M. Audebrand, P. Fréour, J. F. Tessier, and J. G. Faugère, *VIe Congrès Mondial pour la Qualité de l'Air*, Communication C-I-20, Paris, 1983.
9. P. Fréour, J. F. Tessier, P. Pineau, M. Audebrand, and J. G. Faugère, *ibid.*, Comm. C-II-3.

## A RAMAN MICROPROBE STUDY OF PHASE-SEPARATED MINERALS

F. J. Purcell and W. B. White

Feldspars are the most common minerals in the earth's crust and are thus of great importance to mineralogy, petrology, and geochemistry. The feldspars are three-dimensional framework structures of corner-sharing  $\text{SiO}_4$  and  $\text{AlO}_4$  tetrahedra. Charge neutrality is maintained in the crystals by large cations in the interstitial sites of the aluminosilicate framework. Three end members

$\text{NaAlSi}_3\text{O}_8$	albite
$\text{KAlSi}_3\text{O}_8$	orthoclase
$\text{CaAl}_2\text{Si}_2\text{O}_8$	anorthite

describe the compositions of most terrestrial feldspars, although barium and strontium substitutions also occur, as does  $\text{Fe}^{3+}$  substitution for  $\text{Al}^{3+}$ .

Feldspar mineralogy is very complex because:

1. There are several variants on the feldspar structure based on small distortions of the structural framework. Most feldspars are triclinic,  $\text{P}\bar{1}$  or  $\text{C}\bar{1}$ ; a few are monoclinic,  $\text{C2/m}$ . The structural variations show up well in the K-feldspars where sanidine (high temperature,  $\text{C2/m}$ ), orthoclase (intermediate temperature,  $\text{C2/m}$ ) and microcline (low temperature,  $\text{C}\bar{1}$ ) appear as distinct minerals.

2. There is a continuous variation in the degree of Al/Si order over the tetrahedral sites, depending on thermal history. The graduation between low albite and high albite appears to be mainly one of Al/Si order. Al/Si order is also linked to the structural variants of the K-feldspars.

3. At temperatures near the liquidus, there is a continuous solid solution between the three feldspar components. Below  $600\text{--}700^\circ\text{C}$ , a solvus develops which causes phase separation in the  $\text{KAlSi}_3\text{O}_8\text{--NaAlSi}_3\text{O}_8$  series but not in the plagioclase ( $\text{NaAlSi}_3\text{O}_8\text{--CaAl}_2\text{Si}_2\text{O}_8$ ) series. Many igneous rocks contain two feldspars: a potassium feldspar and a member of the albite-anorthite solid solution. However, phase separation continues down to lower temperatures and on a very fine scale. Most feldspar crystals are complex intergrowths of lamellae with different chemical compositions and different structural states.

The microstructure of feldspars and the structure and composition of individual lamellae record much about the thermal history of the minerals and thus about the evolution of the rocks from which they came. Although much has been learned about composition of the lamellae from electron microprobe studies, information on structural states has been difficult or impossible to obtain. It is the purpose of the present paper to apply micro-Raman spectroscopy to the feldspar problem. Micro-Raman spectroscopy has the great advantage that it can probe individual feldspar grains in a polished section without disturbing the microstructure, and supply the spatial resolution to discriminate between neighboring compositions and structural states.

### *Experimental*

Figure 1 shows an optical diagram of the micro-Raman illuminator, the Spex MICRAMATE, coupled to a 0.85m double Czerny-Turner spectrometer, the Spex 1403. The MICRAMATE consists of a modified research-grade microscope that focuses the laser radiation onto the sample to a spot size on the order of  $1\text{ }\mu\text{m}$ , and the necessary optics to couple the microscope to the spectrometer. The resulting scattered radiation is collected back through the microscope objective and focused onto the entrance slit of the spectrometer. The

---

Author Purcell is with Spex Industries, Inc., Metuchen, NJ 08840; author White is with the Materials Research Laboratory of Pennsylvania State Univ., University Park, PA 16802.

Fig. 1. -- Optical schematic of MICRAMATE and Spex 1403 Double Spectrometer showing how objective both focuses laser beam and collects scattered radiation, which is then passed on to spectrometer entrance slit.

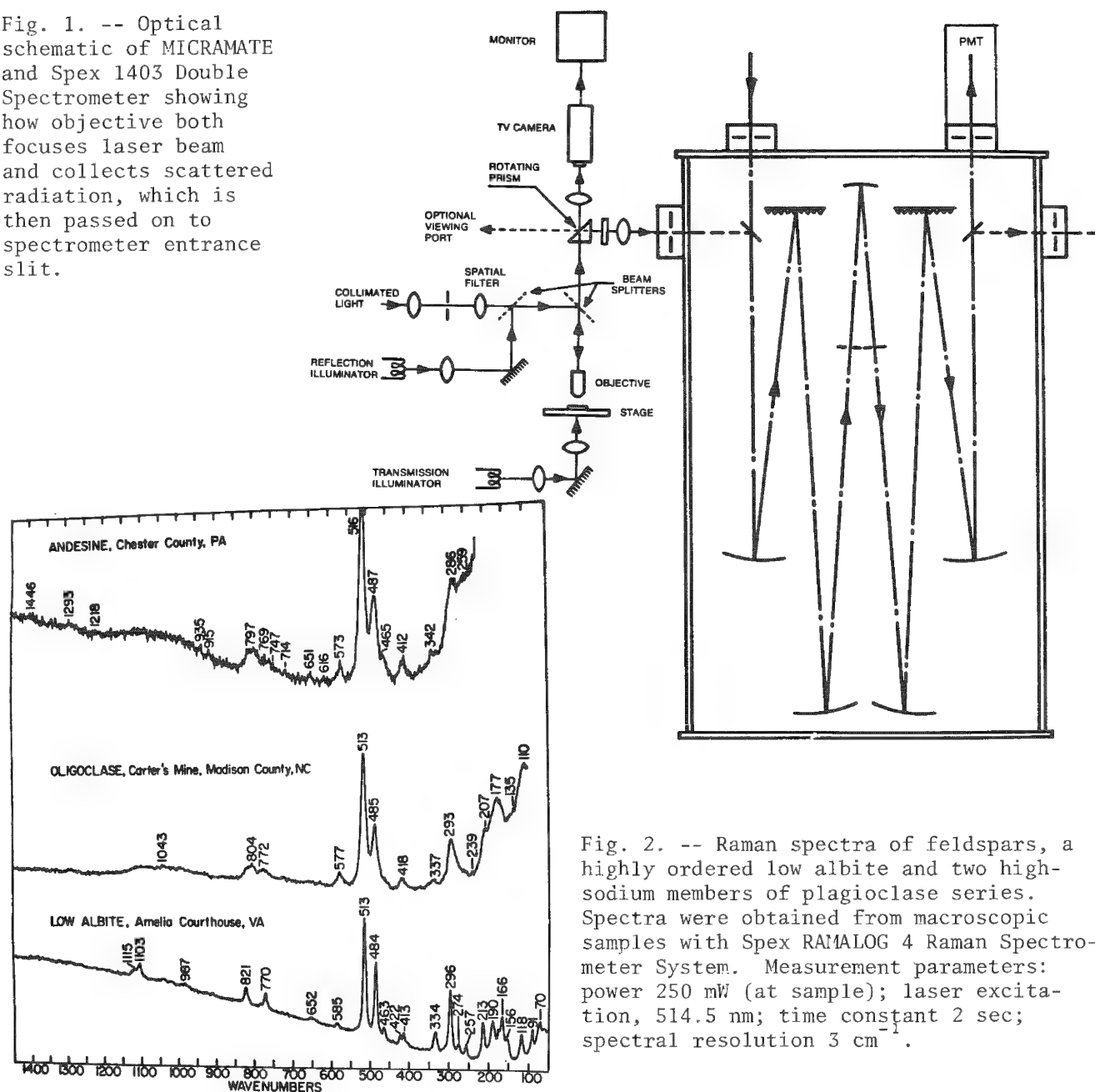


Fig. 2. -- Raman spectra of feldspars, a highly ordered low albite and two high-sodium members of plagioclase series. Spectra were obtained from macroscopic samples with Spex RAMALOG 4 Raman Spectrometer System. Measurement parameters: power 250 mW (at sample); laser excitation, 514.5 nm; time constant 2 sec; spectral resolution 3 cm<sup>-1</sup>.

minimum spot size is achieved with a 40× microscope objective. There is also a 10× objective for initial viewing of the sample. The spectrometer is equipped with 1800 groove/mm holographic gratings, and a Hamamatsu R928 multialkali photomultiplier detector.

#### *Interpretation of the Vibrational Spectra of Feldspars*

The main features observed in the normal, macro-Raman spectra of feldspars are illustrated in Fig. 2, which shows a highly ordered low albite and two high sodium members of the plagioclase series. The spectra may be divided into three regions: from 700 to 1200 cm<sup>-1</sup>, which encompasses the tetrahedral (T-O) stretching modes; the region from 400 to 700 cm<sup>-1</sup>, which includes the intense, sharp band at 510-520 cm<sup>-1</sup>; and the region below 400 cm<sup>-1</sup>.

Unlike most other silicate structures, the T-O stretching bands of framework structures are very weak. They are sharp and weak in the albite spectrum. Here bands appear as high

as  $1115\text{ cm}^{-1}$  due to the complete polymerization of the silica tetrahedra and in spite of mixing with alumina tetrahedra. The low intensity and low frequency are in accordance with a crude normal coordinate analysis of the framework structural unit.<sup>1</sup> In the solid solutions, the T-O stretching region is smeared out and only a broad band is observed in the oligoclase and andesine spectra.

The strong bands at  $515$  and  $485\text{ cm}^{-1}$  are a mixed Si-O-Si (or Si-O-Al) bend/stretch. The mode would be a pure ether-like stretching motion if the interband angle were  $180^\circ$  (linear bridge) and a pure bending mode if the angle were  $90^\circ$ . Because the bond angle in feldspars averages about  $140^\circ$ ,<sup>2</sup> these modes are of a mixed stretching-bending form. There is a pronounced broadening of these bands from the pure albite end member to the andesine solid solution.

The low-frequency region contains complex motions of the tetrahedral framework and also motions of the large cation within their structural cages. Of interest here is the loss of detail that occurs in the spectra of the disordered solid solutions compared with the ordered  $\text{NaAlSi}_3\text{O}_8$ .

#### *Micro-Raman Spectra of Mixed Phase Feldspars*

Figure 3 shows Raman spectra of a microcline from the Wilcox Mine, Hybla, Ontario. Like most feldspars, it is perthitic; that is, it consists of intergrown lamellae of different feldspar composition. Although the bulk composition of this specimen is a potassium feldspar, it is clearly phase-separated and the volumetrically small albite content is easily identified by the Raman spectrum of a  $80 \times 20\mu\text{m}$  section (Fig. 3B). The nominal microcline (or amazonite), which makes up the major portion of the sample, is a mixture of more highly ordered microcline and ordered albite. The spectrum of a  $120 \times 60\mu\text{m}$  region of microcline is shown in Fig. 3A. The slight variations in frequency positions for

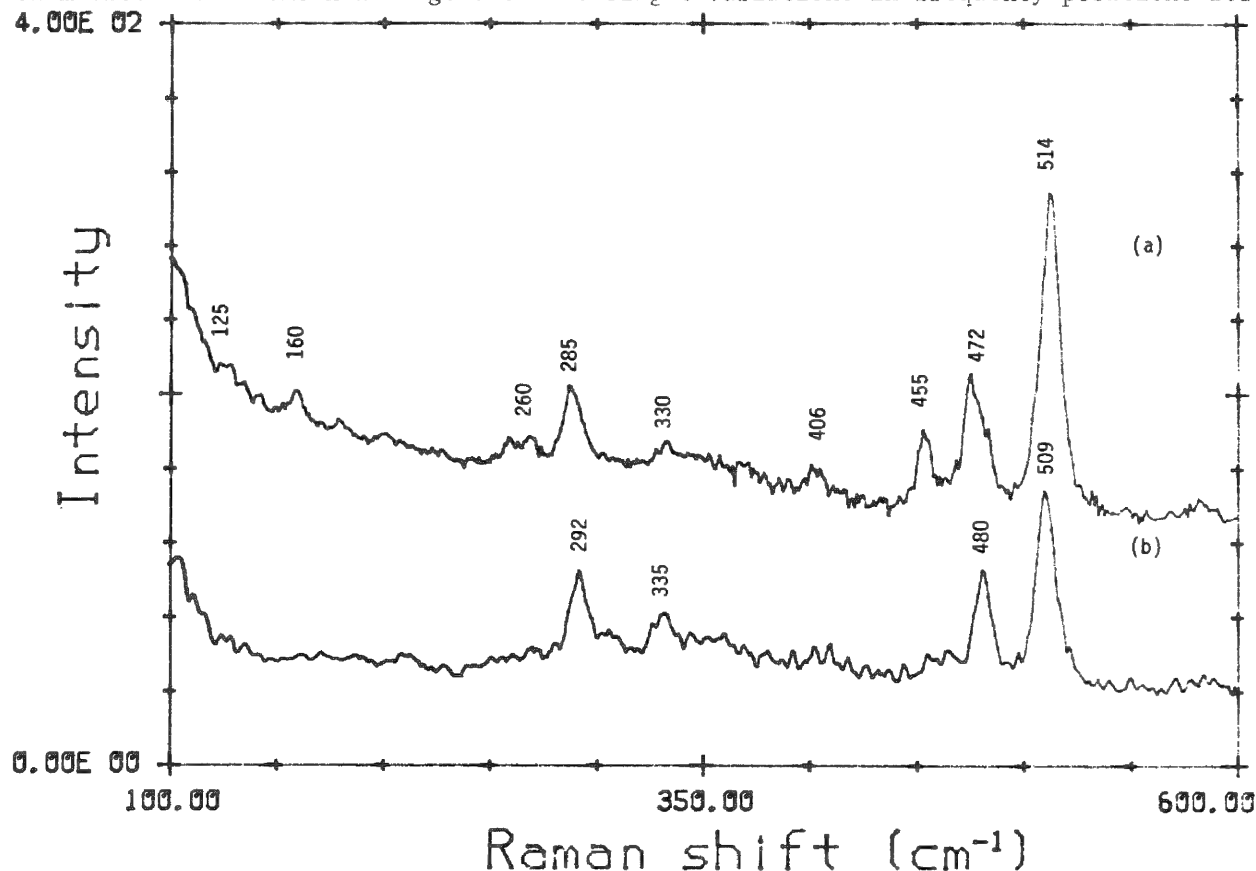


Fig. 3. -- Micro-Raman spectra of microcline from Wilcox Mine, Hybla, Ont.: (a) microcline, (b) low albite. Measurement parameters: (a) specimen size,  $120 \times 60\mu\text{m}$ ; power 25 mW (at sample); laser excitation, 514.5 nm; beam spot, about  $2\mu\text{m}$ ; integration time, 15 s; spectral resolution,  $5\text{ cm}^{-1}$ ; (b) specimen size,  $80 \times 20\mu\text{m}$ ; power, 25 mW (at sample); laser excitation, 514.5 nm; beam spot, about  $2\mu\text{m}$ ; integration time, 15 s; spectral resolution,  $5\text{ cm}^{-1}$ .

these samples from those reported in the literature<sup>1</sup> can be explained by differences in the bulk composition caused by different thermal histories.

Thus, micro-Raman spectroscopy can clearly distinguish phase differences in a mineral specimen on the microscopic level.

### References

1. T. Furukawa et al., "Raman spectroscopic investigation of the structure of silicate glasses: III. Raman intensities and structural units in sodium silicate glasses," *J. Chem. Phys.* 75: 3226, 1981.
2. J. V. Smith, *Feldspar Minerals: 1. Crystal Structure and Physical Properties*, New York: Springer-Verlag, 1973.

## RAMAN MICROPROBE MEASUREMENTS OF LOCAL STRESS IN LASER RECRYSTALLIZED LATERAL EPITAXIAL SILICON FILMS OVER SILICON DIOXIDE

Fran Adar and Paul Zorabedian

Raman microprobe measurements of stress have been performed on a laser-recrystallized, seeded, lateral epitaxial silicon film on silicon dioxide. The direction-averaged, planar tensile stress increased from  $1.9 \times 10^9$  dyn/cm<sup>2</sup> in the seed region to  $4.7 \times 10^9$  dyn/cm<sup>2</sup> in the silicon-on-insulator region at distances greater than 20  $\mu$ m from the seed/oxide boundary. Grain-boundary nucleation observed by optical Nomarski microscopy occurred approximately 11  $\mu$ m from the seed edge in this film. Illumination of the sample by an unfocused laser beam revealed contour-like features that correlated with deviations from smooth variations in stress. Depth variations of the stress were observed by comparisons of measurements at 457.9nm and 514.5nm excitation wavelengths, from which it was inferred that there is relaxation of stress on the top surface.

Laser-induced, seeded lateral epitaxial recrystallization of polysilicon films on oxidized silicon substrates is a promising technique for producing islands of single crystal silicon-on-insulator (SOI) for integrated-circuit device fabrication. In many applications, the complete elimination of all grain boundaries from these islands is highly desirable, yet all published results show the development of grain boundaries at varying distances, typically 10-50  $\mu$ m, from the edge of the seed region. This distance depends on laser beam shape, intensity, scanning technique, and the substrate temperature. For given sets of conditions, however, we have found that the distance is uniform along the edge of the seed region to within  $\pm 2$   $\mu$ m. This observation suggests a well-defined mechanism for grain-boundary formation.

Pinizzotto and coworkers have proposed that stress causes the formation of grain boundaries.<sup>1</sup> Because mobility in n-channel MOSFETS has been shown to be affected by stress in recrystallized SOI,<sup>2</sup> studies of stress in laser-recrystallized lateral epitaxial SOI are useful both for an understanding of the basic mechanisms involved in the recrystallization and for process evaluation and development.

The Raman spectrum of silicon is sensitive to the strain in the lattice and can be used to measure the stress in crystalline samples.<sup>3,4</sup> Recently, the Raman microprobe technique has been employed to map the local stresses in patterned islands of laser-crystallized silicon on bulk glass and in epitaxial silicon on sapphire substrates.<sup>5,6</sup> In what follows we report the first application of the Raman microprobe technique to the measurement of local stresses in the seed and SOI regions of lateral epitaxial, laser-crystallized silicon.

### *Experimental*

The samples examined here were fabricated and laser processed at Hewlett-Packard Laboratories. Polycrystalline silicon films 0.55  $\mu$ m thick were deposited by low pressure chemical vapor deposition (LPCVD) at 625°C on <100> silicon substrates on which 1.4 $\mu$ m-thick, 480 $\mu$ m square islands of SiO<sub>2</sub> had been grown by local oxidation of silicon (LOCOS). The islands were 260  $\mu$ m apart and had their edges aligned along <110> directions. A 6nm-thick LPCVD silicon nitride encapsulation layer was deposited over the polysilicon. The substrates were held at 500°C during recrystallization, and an 11W, 80 $\mu$ m-diameter Gaussian argon-ion laser beam was scanned across the sample at 25 cm/s with a 10 $\mu$ m raster step.

Author Adar is at Instruments SA, Inc., Metuchen, NJ 08840; author Zorabedian is with Hewlett-Packard, Palo Alto, CA 94304. The authors thank B. Perrulli (Instruments SA) for initiating the collaboration between the authors. One of them (P.Z.) would also like to acknowledge many helpful discussions with T. I. Kamins, T. R. Cass, C. I. Drowley, and D. Ilic.

In the areas between the LOCOS islands, recrystallization seeded vertically from the underlying crystal substrate. The seed was pulled laterally over the oxide by the moving, molten-silicon zone under the laser beam.

The Raman spectra were recorded with a Ramanor U-1000 double grating spectrometer, optically conjugated to a research-grade microscope attachment for focusing the excitation laser to a 1 $\mu$ m beam waist. A single objective served to excite the Raman signal and collect the scattered light which was imaged onto the spectrometer entrance slit. Laser lines at 457.9nm and 514.5nm from an argon ion laser were selected for excitation of the sample. The 6nm nitride encapsulation layer remained over the silicon film during the Raman measurements.

### Results and Discussion

Spatially resolved Raman spectra were obtained at 1-5 $\mu$ m intervals along lines perpendicular to the seed/SOI boundary extending from the seed region to a distance 20-30  $\mu$ m from the boundary in the SOI region. The peak frequencies of the Raman spectra were found automatically by the Raman system. The peak phonon frequencies for three sets of sampled points with 514.5nm excitation taken along different lines are shown in Fig. 1. The instrument could reproduce the Raman peak to 0.1  $\text{cm}^{-1}$ . The considerable scatter seen in the data greatly exceeds the instrument precision. However, the general trend is clear. The peak frequency decreases abruptly at the boundary and then continues to decrease gradually over a distance of approximately 20-25  $\mu$ m adjacent to the boundary. The peak frequencies were averaged for points in the seed region and in the SOI at distances >20  $\mu$ m from the seed edge and fit to a linear function of position for points between those regions (Fig. 1).

The peak frequency of the Raman spectrum corresponds to the frequency of the  $k = 0$  optical phonons in the silicon lattice. The changes in phonon frequency due to strain are derived from the dynamical lattice equations. To solve this problem, a model for the stress tensor is required. The form of this tensor is not known exactly for the laser-recrystallized sample, but we have assumed that the stress in the silicon is two-dimensional and isotropic in the plane of the wafer.

In the backscattered geometry used in our Raman measurements, only the singlet phonon mode polarized perpendicular to the film surface is active under these assumptions. In this case, the relationship between plane stress and phonon frequency is

$$(\sigma_x + \sigma_y)/2 = -2.49 \times 10^9 \Delta\nu \text{ dyn/cm}^2$$

which is identical to the expression in Ref. 4 if the stress is assumed to be isotropic. This expression is used to convert the phonon frequencies to the stresses indicated on the right scale of Figs. 1 and 2. A calculation of thermal stress due to the heat cycle involved in laser melting and subsequent cooling to the substrate temperature of 500°C gives a value of  $6 \times 10^9 \text{ dyn/cm}^2$ , compared to the measured maximum stress of  $4.7 \times 10^9 \text{ dyn/cm}^2$  at a distance > 20  $\mu$ m from the interface. Within the accuracy of the measurements, this

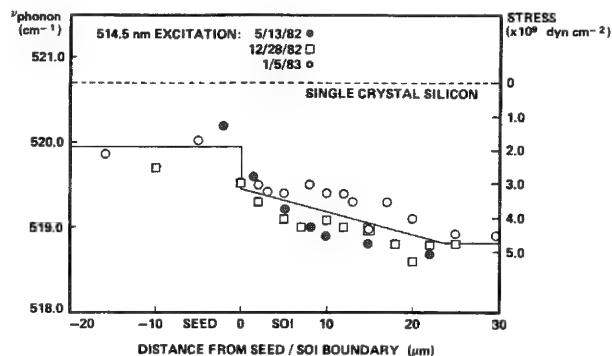


FIG. 1.--Phonon frequencies and stresses for 514.5 nm excitation wavelength along 3 lines perpendicular to the seed/silicon-on-insulator (SOI) boundary.

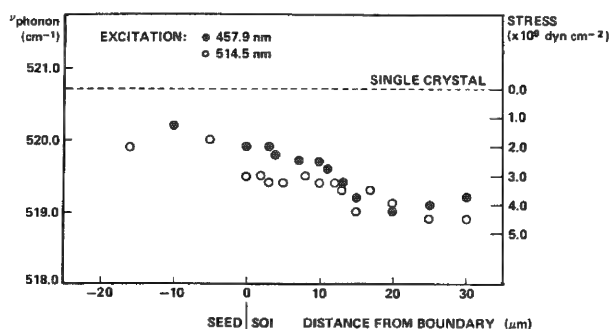


FIG. 2.--Phonon frequencies and stresses for two different excitation wavelengths along single line perpendicular to the seed/silicon-on-insulator (SOI) boundary.



indicates that approximately 20% of the thermal stress is relaxed, possibly by viscous flow of the underlying oxide or by undercooling of the melt prior to solidification.

In order to clarify the considerable scatter observed in the phonon frequencies (which was not instrumental), spectra at two excitation wavelengths, 457.9 and 514.5 nm, were obtained along the same track in the sample. The phonon frequencies and corresponding stress values are shown in Fig. 2. From silicon absorption at 457.9 and 514.5 nm and their respective Raman-shifted wavelengths,<sup>7</sup> the ratio of Raman signal intensities from the back surface of the silicon film to those from the front surface are 0.13 at 457.9 nm and 0.37 at 514.5 nm. In addition, contributions to the signals from the silicon substrate are considered minimal because similar calculations show that reflectivity losses will decrease the substrate signal by an additional factor of 0.6. The observed smaller stress-induced frequency shift for the 457.9nm wavelength thus implies that stress relaxation occurs toward the top surface of the silicon film. This conclusion is consistent with our observation that the variations in the Raman linewidth measured at 457.9 nm are more than the linewidth variations observed with 514.5nm excitation. Since the linewidth in the SOI increases with distance from the boundary, it is implied that a range of phonon frequencies is being detected.

Inspection of Fig. 2 indicates a point in the 514.5 nm data corresponding to 15  $\mu\text{m}$  from SOI interface that deviates from the others. This point was reproduced after the total set was completed and is therefore considered not to be an instrumental artifact. The micrograph shown in Fig. 3 was recorded under illumination of the sample by an unfocused laser beam. The origin of the contour pattern of the micrograph is not well understood at present, but the deviating point was recorded from the point denoted by the asterisk.

After the Raman measurements, the nitride layer was stripped in hydrofluoric acid and the sample was treated with Wright etch<sup>8</sup> to delineate grain boundaries. An optical Nomarski micrograph of the etched sample is shown in Fig. 4. The arrow indicates to within  $\pm 5 \mu\text{m}$  the line along which the points in Fig. 2 were measured.

From previous transmission electron microscopy (TEM),<sup>9</sup> the observed line defects starting about 11  $\mu\text{m}$  from the edge of the seeding region are known to be low-angle grain boundaries with approximately  $1^\circ$  misorientation between adjacent grains. Note that this

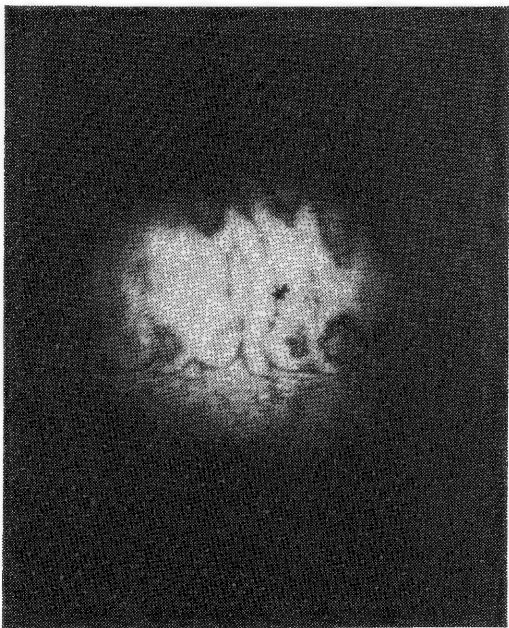


FIG. 3.--Optical micrograph taken from the ground glass screen of the Raman microprobe illuminated with unfocused laser beam; spot indicated by \* corresponds to the anomalous point from the 514.5nm series in Fig. 2.

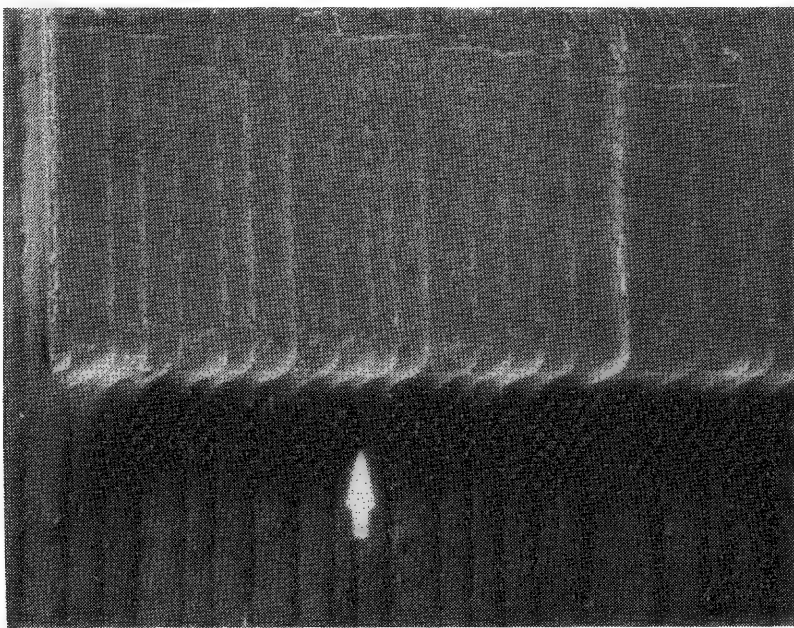


FIG. 4.--Optical Nomarski micrograph of lateral epitaxial silicon film (after chemical delineation of grain boundaries with Wright etch); arrow is over seed region with tip at seed/silicon-on-insulator boundary and points along line sampled in Fig. 2.

distance corresponds to a change in the slope of the phonon frequency in Fig. 2. We conjecture that the change in stress gradient is associated with stress fields around the tips of grain boundaries. (The point in Fig. 3 that produced an anomaly in the Raman data did not correspond to any obvious feature in the Nomarski micrograph.)

Published data on yield stress vs temperature differ widely,<sup>10-12</sup> but the measured stress appears to be less than the yield stress at the substrate temperature during recrystallization. A linear extrapolation to zero stress at the melting point indicates that the film stress would exceed the yield stress for temperatures above approximately 1000°C. The production of defects with sufficient mobility to coalesce into grain boundaries would require a high temperature and is consistent with the appearance of dislocations near the grain boundary tips seen with TEM.

### Conclusions

In conclusion, we have reported the first application of Raman-microprobe stress measurement to a laser-recrystallized, lateral epitaxial silicon film. The stress increases over a distance of approximately 20  $\mu\text{m}$  adjacent to the seed/SOI boundary. The highest stress is comparable to the calculated thermal stress between silicon and silicon dioxide resulting from differential thermal contraction between the silicon and the substrate during recrystallization. Relaxation of stress toward the top surface was observed.

### References

1. R. F. Pinizzotto, H. W. Lam, and B. L. Vaandrager, *J. Electron. Mater.* 11: 413, 1981.
2. B.-Y. Tsaur, J. C. C. Fan, and M. W. Geis, *Appl. Phys. Lett.* 40: 322, 1982.
3. E. Anastasakis, A. Pinczuk, E. Burstein, F. H. Pollak, and M. Cardona, *Solid State Commun.* 8: 133, 1970.
4. T. Englert, G. Abstreiter, and J. Pontcharra, *Solid State Electron.* 23: 31, 1980.
5. S. A. Lyon, R. J. Nemanich, N. M. Johnson, and D. K. Biegelsen, *Appl. Phys. Lett.* 40: 316, 1982.
6. S. R. J. Brueck, B.-Y. Tsaur, J. C. C. Fan, D. V. Murphy, T. F. Deutsch, and D. J. Silversmith, *Appl. Phys. Lett.* 40: 895, 1982.
7. *Physical/Electrical Properties of Silicon*, Durham, N.C.: Research Triangle Institute, vol. 5 of *Integrated Silicon Device Technology*, 1964, 148-149.
8. M. Wright Jenkins, *J. Electrochem. Soc.* 124: 757, 1977.
9. P. Zorabedian, C. I. Drowley, T. I. Kamins, and T. R. Cass, paper presented at Materials Research Society Meeting, Boston, 82, to be published in *Laser-Solid Interactions and Transient Thermal Processing of Materials*, North-Holland, 1983.
10. W. D. Sylwestowicz, *Phil. Mag.* 7: 1825, 1962.
11. T. R. Anthony and H. E. Cline, *J. Appl. Phys.* 49: 5774, 1978.
12. R. B. Fair, *J. Electrochem. Soc.* 125: 923, 1978.

## RAMAN MICROSCOPY THROUGH TRANSPARENT MATERIALS

D. R. Tallant, K. L. Higgins, and C. L. Stein

Applications of the Raman microprobe have generally concentrated on exploiting high spatial resolution in the identification of small defects or particulates.<sup>1</sup> Raman microscopy is also ideally suited to examining particulates, defects, and inclusions that are under millimeter thicknesses of optically transparent materials because the Raman microprobe utilizes a focused *optical* beam and exploits 180° scattering geometry, and because microscope objectives of long working distance are commercially available. Of course the "window" material, in addition to being transparent, should be Raman inactive (such as sodium chloride) or weakly Raman active (such as many common glasses).

This paper describes three applications of Raman microscopy to the study of particulates and inclusions under millimeter thicknesses of transparent materials. These applications include the identification of particulates freezing out of silicone oil inside a device with a glass case; the identification of chromium-oxygen compounds in an air-sensitive mixture under a sodium chloride window; and the quantification of sulfate ( $\text{SO}_4^{=}$ ) concentrations in brine inclusions in Delaware Basin halite.

### *Experimental*

The 514.5nm line from an Argon ion laser (Coherent CR-4) was passed through a line filter and into the incident illumination port of a Zeiss microscope (standard 20T) which had been modified (by Spex Industries) for use in micro-Raman spectroscopy. Scattered light collected by the microscope was dispersed by a double monochromator (Spex 1404) equipped with holographic gratings. Dispersed photons were detected by a photomultiplier tube (RCA C31034), counted by a photometer, and stored in a digital computer. The most commonly used objective was a 10×, 0.30 N.A. (numerical aperture) with a 4mm working distance, 40× objectives with numerical apertures of 0.95, 0.85, and 0.60 and working distances of 0.09, 0.23, and 1.5 mm were also used.

### *Identification of a Frozen Particulate in Silicone Oil*

An electromechanical switch, sealed in a glass case nearly filled with silicone oil, had been found to have intermittent high contact resistance when cooled below -20°C. At this temperature and below, particulates (typically several hundred micrometers in diameter) were observed to form in the "bubble" or void above the oil (Fig. 1) and were thought to be the cause of the contact-resistance problem.

A silicone oil-filled device was cooled to -70°C in a refrigerator until particulate crystals formed on the void bubble, leaving the bulk silicone oil in a liquid state. The device was then immersed in dry ice/methanol in an insulated cup so that the top surface of the device was covered with a thin film of methanol. The bulk silicone oil in the device froze upon immersion in the dry ice/methanol.

The entire bath was then placed under the microscope of the Raman microprobe and spectra were obtained by focusing of the laser beam through the methanol and the glass case onto the inside of the void bubble (Fig. 1). Spectra were obtained of a frozen particulate crystal on the void bubble (Fig. 2a), of an area on the void bubble containing no obvious particulate (Fig. 2b), and of the edge of the frozen particulate after some melting had occurred due to laser heating (Fig. 2c). All three spectra show bands due to the borosilicate glass case and the methanol covering it. In addition, the spectra show bands due to frozen silicone oil and ice ( $3100\text{--}3500\text{ cm}^{-1}$ ). Note that the  $3100\text{ cm}^{-1}$  band of ice is

---

The authors are at Sandia National Laboratories (a U. S. Department of Energy facility), Albuquerque, NM 87185. Supported by DOE under Contract DE-AC04, 76DP00789.

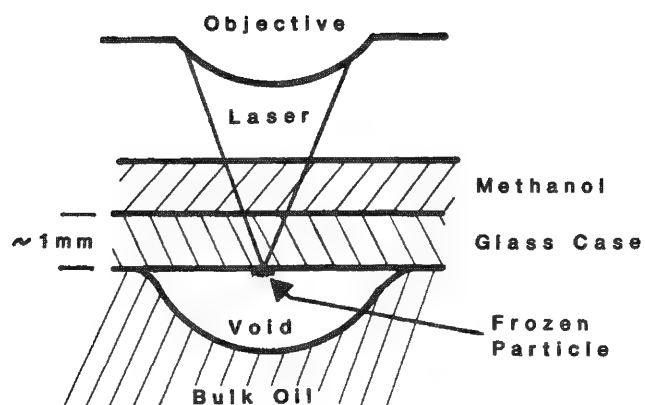


FIG. 1.--Micro-Raman examination of particulate freezing out inside silicone oil-filled electromechanical device with glass case.

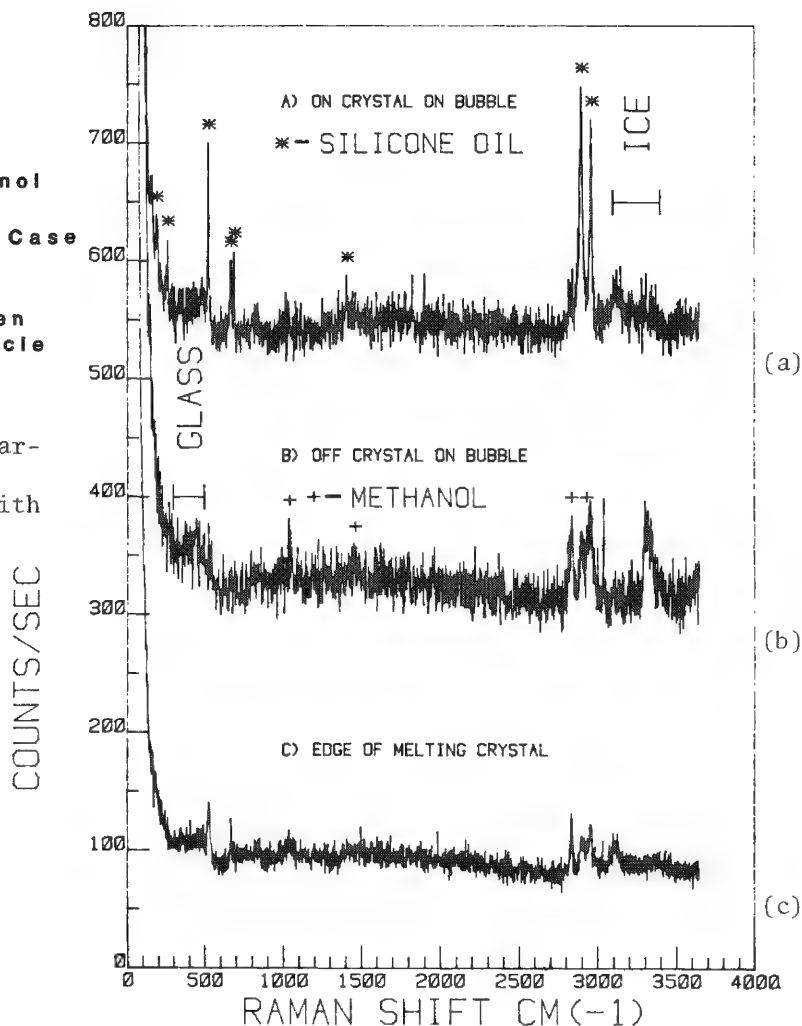


FIG. 2.--Micro-Raman spectra of frozen particulate and background inside glass case of electromechanical device.

highly polarized, which may account for the variation of relative intensity in the ice bands. Figure 2(b) shows relatively weak silicone oil bands, which are probably due to bulk silicone oil below the void bubble. The band near  $3400\text{ cm}^{-1}$  is believed to be due to a thin, highly oriented film of ice, which occasionally has been seen visually. The much greater intensity of the silicone oil bands in Fig. 2(a) compared to Fig. 2(b) suggests that the frozen particulate is a mixture of the silicone oil and water. Figure 2(c) suggests that the melting edge of the particulate crystal contains relatively more water than the bulk of the particulate (compare with Fig. 2a). The most likely explanation for the formation of the frozen particulates above the liquid silicone oil is a reaction between water and the silicone oil to form a small amount of a silanol. The silanol then binds the water and the silicone oil into a mixture which freezes at a temperature between that of the water and the silicone oil. The results suggest that greater care is required in the manufacture of these devices to exclude water.

#### *Identification of Chromium Compounds in an Air-sensitive Mixture*

Certain types of high-temperature batteries use calcium chromate ( $\text{CaCrO}_4$ ) as the oxidant in a molten  $\text{LiCl/KCl}$  eutectic. A silica binder is also present. The Raman microprobe is being used to identify the chromium species present after the battery reaction has occurred. This information helps elucidate the electrochemical processes occurring

in the battery and helps in optimizing battery performance. Since some of the chromium reaction products and the eutectic mixture are sensitive to moisture in the air, the samples were examined in a special fixture consisting of a small aluminum disk into which a depression 0.5 mm deep by 3 mm diameter has been drilled. The reaction mixture is loaded into the depression in a dry atmosphere. Then a ring of vacuum grease is applied to the top of the fixture and a NaCl window is pressed over the depression to seal it from the atmosphere. Chromium-containing particles (identifiable by their color) are illuminated through the NaCl window by means of the 10× objective. Reference spectra of Cr(VI), Cr(V), Cr(IV), and Cr(III) species have been obtained to aid in the identification of particles found in the eutectic mixture.

Figure 3 shows the spectrum of a chromium-containing particle in the eutectic mixture (sealed in the fixture previously described) obtained by use of the Raman microprobe. The broadest band in the spectrum is due to Cr(V), probably present as  $\text{Ca}_5(\text{CrO}_4)_3\text{Cl}$ . Other bands in the spectrum indicate the presence of Cr(VI) species (probably  $\text{CaCrO}_4$ ) which are intimately intermixed with the Cr(V) compound. Cr(III), Cr(IV), and mixed iron-chromium species are also expected to be present in reacted battery mixtures but have not yet been detected.

#### *Quantification of Sulfate in Brine Inclusions*

The Waste Isolation Pilot Plant (WIPP) is a proposed nuclear-waste storage facility intended to demonstrate the feasibility of nuclear-waste storage in bedded (geological) salt deposits. The facility is to be located in halite of Permian age from the Delaware Basin in southeastern New Mexico. A study of fluid inclusions in the halite was undertaken to determine whether the inclusions have migrated over geologic time and their relationship, if any, to the large brine reservoirs found in the salt during preliminary drilling. Sulfate concentrations in the fluid inclusions in the halite were analyzed by Raman microscopy.

Previous such analyses (e.g., Dubessy et al.<sup>2</sup>) took the ratio of Raman intensities of the sulfate  $\nu_1$  band to the  $\nu_2$  bending mode of water as a measure of the sulfate concentration. In this work we used the ratio of the intensity of the  $\nu_1$  sulfate band ( $\sim 980 \text{ cm}^{-1}$ )

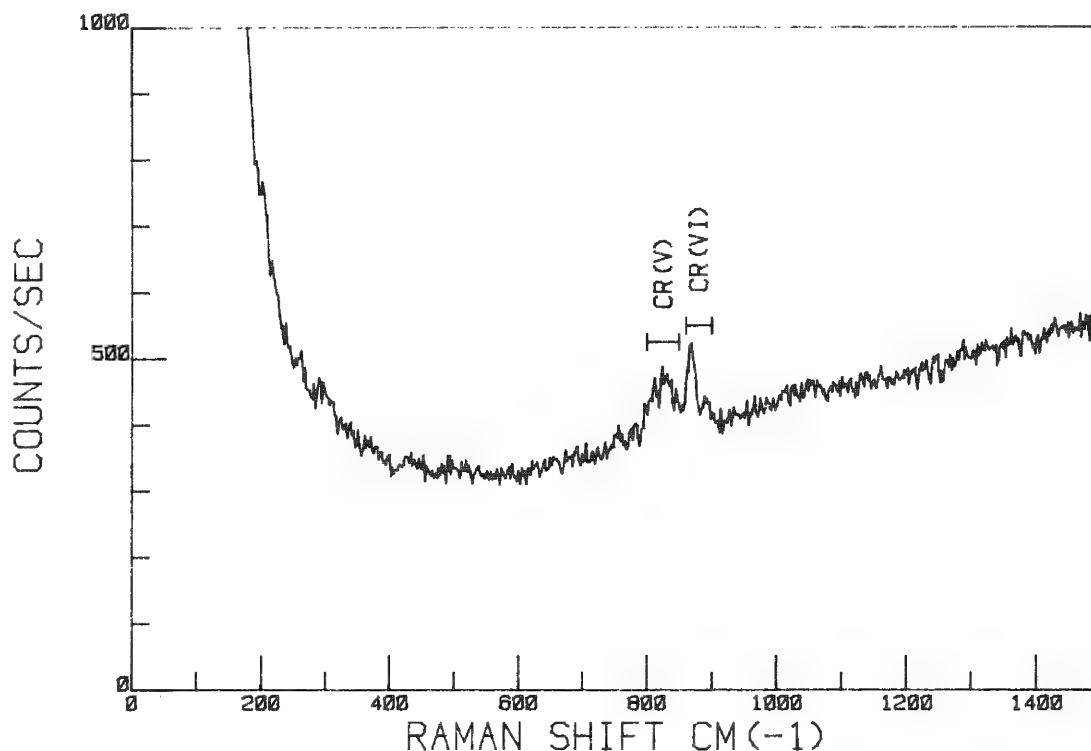


FIG. 3.--Spectrum of chromium-containing particle sealed under NaCl chip, showing presence of Cr(V) and Cr(VI) species.

to the  $\nu_1$  water band ( $3400\text{--}3500\text{ cm}^{-1}$ ), whose greater relative intensity aided in the analysis of very small inclusions. Standard solutions, containing 0, 1400, 2800, 4200, 5600, and 14000 ppm of sulfate in saturated brine (placed in a small beaker and illuminated through a covering sapphire disk) were analyzed. The sulfate concentrations relate linearly to the sulfate/water band intensity ratios over the concentration range of the standard solutions. Linear regression analysis yields the equation  $[\text{SO}_4^{=}] \text{ ppm} = 9.8 \times 10^4 (\text{ratio}) - 450$  with a correlation coefficient of 0.99.

The inclusions analyzed were found in halite core samples from 1100–4000 ft depths. They ranged from tens of micrometers to 1 mm in size and also in depth below the surface of the halite. Figure 4 shows the sulfate concentrations of the inclusions as a function of the sample depth.

The stratigraphic formations can best be dealt with as three lithologic categories (Fig. 4): the Castile Formation, composed of laminated halite ( $\text{NaCl}$ ) - anhydrite ( $\text{CaSO}_4$ ); the Salado Formation below the McNutt Potash zone, containing primarily halite with minor anhydrite layers; and the Salado Formation above the McNutt Potash zone, consisting of massive halite. The sulfate concentrations in the Castile Formation appear to follow a bimodal distribution similar to that found by Dubessy<sup>2</sup> for inclusions in Keuper halite. By this analogy the highest sulfate concentration grouping ( $\sim 10\,000$  ppm) consists of primary inclusions relatively unchanged from the primordial brine from which they formed; the lower sulfate concentration grouping represents inclusions affected by fracturing and annealing of the halite and possible chemical interaction with adjacent mineralogies. In the Salado Formation below the McNutt Potash zone, there appears to be a local increase in the sulfate concentration, possibly resulting from a cessation of anhydrite deposition. The sulfate concentrations in the Salado Formation above the McNutt Potash zone are consistent with late-stage evaporative mineralization; the lowest sulfate values perhaps represent seawater from which virtually all sulfate species have previously precipitated. The data appear to reflect changing seawater compositions in the Delaware Basin over geologic time. Furthermore, they indicate that migration of the fluid inclusions in these formations has been minimal.

#### References

1. G. J. Rosasco and E. S. Etz, "The Raman microprobe: A new analytical tool," *Research/Development* 28(6): 20, 1977.
2. J. Dubessy et al., "The determination of sulphate in fluid inclusions using the MOLE Raman microprobe: Application to a Keuper halite and geochemical consequences," *Geochimica et Cosmochimica Acta* 47: 1, 1983.

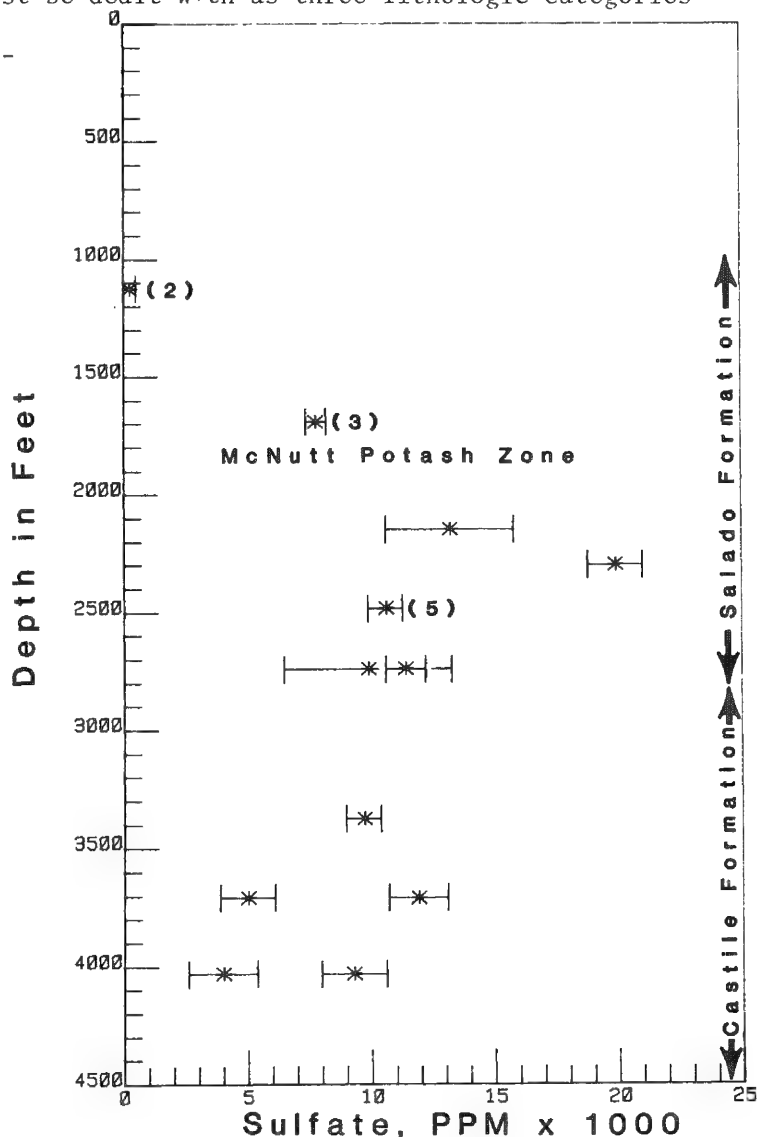


FIG. 4.--Sulfate concentrations in brine inclusions in Delaware Basin Halite. Parentheses indicate that sulfate values from several inclusions were averaged to give data point. Error bars were determined by counting statistics for single analysis on given sample or by variation in results when multiple inclusions in a sample have been analyzed.

## APPENDIX

### LASER MASS SPECTROMETRY OF SOLIDS: A BIBLIOGRAPHY 1963-1982

R. J. Conzemius, D. S. Simons, Zhao Shankai, and G. D. Byrd

The use of lasers as an ionization source for solid samples in mass spectrometry has proliferated in recent years. The main reasons for this increased attention are twofold--the availability of commercial instruments that use the laser as a microprobe, primarily for the analysis of inorganic species, and the increased emphasis in organic mass spectrometry on "soft" ionization sources for the analysis of thermally labile materials. The laser is unique as an ionization source for solids because of the spatial and temporal characteristics of the laser beam and because the ionization mechanism can be altered by a change in the power density.

The following bibliography is a best-effort attempt to include all papers published in the open literature through the end of 1982 where a laser is used as an ionization source in mass spectrometry for a solid-phase sample. It is organized chronologically by year, and alphabetically by first author within each year. A comprehensive cross-reference index by subject is included as an aid in locating references on a specific aspect of laser mass spectrometry.

#### Reference

R. J. Conzemius, D. S. Simmons, Zhao Shankai, and G. D. Byrd, "Laser mass spectrometry of solids: A bibliography 1963-1982," in Ron Gooley, Ed., *Microbeam Analysis--1983*, San Francisco: San Francisco Press, 1983, 301-328.

## INDEX

#### General Articles:

(1964): 6; (1965): 7, 10; (1966): 10, 21, 22; (1967): 11, 32; (1968): 15; (1969): 5, 22; (1970): 15; (1971): 14, 18, 28, 33, 43; (1972): 24, 43; (1973): 4, 14, 23; (1974): 13, 17; (1975): 24, 30; (1976): 11, 33; (1977): 2, 34, 37, 45; (1978): 35, 37, 38, 52; (1979): 4, 13, 25; (1980): 8, 22, 47; (1981): 8, 10, 51, 62; (1982): 26, 44.

#### Instrumentation:

General and Miscellaneous: (1964): 9; (1965): 2; (1966): 14, 22, 24, 25; (1967): 5, 16, 35; (1968): 2, 3, 18, 21, 29, 44; (1969): 20; (1970): 20, 26, 42; (1971): 2, 12, 19, 30, 48; (1972): 13, 14, 23, 29, 54; (1973): 6, 9, 15, 17, 26, 29, 30, 33; (1974): 3, 14, 15, 18, 19, 26, 32; (1975): 14, 15, 22, 25, 30, 38, 45, 48, 53, 54; (1976): 4, 22, 23, 36, 44, 45, 46, 52; (1977): 18, 20, 36, 48, 53, 58; (1978): 6, 13, 23, 25, 40, 41, 42, 46, 60, 61; (1979): 2, 9, 13, 26, 35, 41, 42; (1980): 3, 7, 21, 27, 33, 38, 54; (1981): 13, 18, 21, 33, 46, 62; (1982): 7, 11, 13, 15, 16, 20, 25, 28, 30, 42, 55.

Ion Source: (1963): 3; (1966): 2, 8, 13, 39; (1967): 7, 15, 18, 33; (1968): 16, 17, 21, 35; (1969): 19, 20, 29, 30; (1970): 38, 41; (1971): 11, 12, 36, 39; (1972): 6, 13, 14, 15, 26, 28, 29; (1973): 6, 19, 21, 33, 34; (1974): 6, 22, 23; (1975): 33, 43; (1976): 4, 5, 10, 14, 18, 19, 20; (1977): 5, 12, 23, 51; (1978): 8, 13, 14, 19, 20, 24, 55, 59; (1979): 6, 13, 23, 39; (1980): 2, 9, 33, 55, 56; (1981): 18, 29; (1982): 13, 28, 42, 44, 47, 48.

Mass Spectrometer: (1964): 9; (1965): 2, 13; (1966): 5, 6, 14, 16, 17, 24, 32; (1967): 8, 17, 19; (1968): 8, 12, 16, 17, 18, 20, 31; (1969): 14, 19, 29; (1970): 13, 42; (1971): 9, 10, 11, 16, 31, (1972): 9, 11, 15, 20, 21, 28, 40, 41, 51; (1973): 2, 8, 17, 19, 21, 22, 29, 34; (1974): 10, 17, 18, 22, 23; (1975): 5, 33, 39, 41, 43, 53; (1976): 7, 10, 18, 23, 29, 43, 47, (1977): 5, 8, 12, 23, 34, 44, 53; (1978): 2, 8, 13, 14, 19, 24, 42, 46, 60; (1979): 7, 13, 27, 43; (1980): 3, 7, 33, 38; (1981): 18, 29, 33, 71; (1982): 3, 13, 39, 55, 58.

Author Conzemius is with the Ames Laboratory operated for the U.S. Department of Energy by Iowa State University, Ames, IA 50011, under contract W-7405-ENG-82; author Zhao is with the Analysis and Test Center of Zhongshan University in Quangzhou, China; and authors Simons and Byrd are with the National Bureau of Standards, Washington, DC 20034.



Detectors: (1965): 5; (1966): 8, 13; (1967): 7, 16; (1970): 42; (1971): 12, 19; (1972): 30; (1973): 17, 29, 33; (1975): 28; (1976): 37, 41, 47; (1977): 5, 41, 42; (1978): 23, 24, 53, 60; (1979): 6; (1980): 1, 9, 12, 38; (1981): 42; (1982): 13.

Electronics and Miscellaneous: (1966): 6, 7, 39; (1967): 15, 19; (1969): 29, 30; (1972): 28; (1974): 5, 22; (1975): 32, 33; (1976): 10.

Commercial Instruments: (1970): 28; (1977): 17; (1978): 32, 34, 45, 68, 69, 70, 71; (1979): 12, 13, 17, 43; (1980): 23; (1981): 18, 65; (1982): 13.

#### Analytical Features:

General and Miscellaneous: (1968): 42; (1969): 33; (1972): 36; (1976): 41; (1977): 7; (1978): 13; (1979): 33; (1980): 58; (1982): 3, 4, 8, 11, 39, 41.

Relative Sensitivity Coefficients: (1969): 23, 33; (1971): 11; (1972): 11, 15; (1973): 7, 8, 34; (1974): 10; (1976): 4, 5, 6, 7, 13; (1978): 10, 11, 12, 14; (1981): 18; (1982): 17, 28, 44, 54.

Quantification: (1969): 23, 33; (1970): 30; (1972): 11, 51; (1973): 7, 9, 13, 26, 28, 34; (1974): 10, 17, 33; (1975): 14, 15; (1976): 4, 5, 6, 7, 13, 41, 52; (1977): 9, 12, 48; (1978): 11, 12, 14; (1979): 2, 18, 42, 49; (1981): 11, 27, 55, 58, 59, 66; (1982): 1, 17, 28, 58, 60.

Detection Sensitivity: (1963): 3, 4; (1968): 17, 21; (1969): 14, 23, 33; (1970): 13, 20, 30; (1971): 11; (1972): 51; (1973): 9, 13, 34; (1974): 10, 17, 18, 33; (1975): 14, 15, 21, 22; (1976): 1, 4, 5, 8, 12, 18, 52; (1977): 17, 34, 48; (1978): 8, 32, 34; (1979): 2, 7, 13, 15, 17, 42, 49; (1982): 1, 13, 28, 42, 54, 56.

#### Laser - Solid Interactions in Laser Mass Spectrometry:

General and Miscellaneous: (1963): 2, 7, 9; (1964): 4, 5, 6, 11; (1965): 4, 10, 13, 14; (1966): 1, 9, 20, 23, 27, 28, 29, 31, 32, 36; (1967): 2, 4, 5, 6, 9, 14, 25, 27, 28; (1968): 19, 25, 26, 28, 30, 40; (1969): 16, 17, 27, 28, 39; (1970): 3, 4, 5, 7, 8, 15, 16, 17, 18, 19, 25, 27, 31, 34; (1971): 3, 5, 6, 17, 21, 23, 29, 35, 37, 38, 41, 46, 47, 49; (1972): 27; (1973): 1, 4, 20, 28, 29, 31, 35; (1974): 2, 20, 23, 24, 30, 31, 34, 36; (1975): 1, 2, 6, 7, 8, 17, 29, 31, 35, 37, 38, 43, 50, 52, 56, 58, 59, 60; (1976): 5, 17, 25, 54; (1977): 2, 4, 6, 13, 14, 21, 26, 27, 29, 31, 33, 40, 43, 44, 46, 49, 54; (1978): 9, 10, 23, 35, 50, 66; (1979): 23, 47; (1980): 6, 12; (1981): 8, 17, 30, 63, 70; (1982): 23, 56.

Plasma Formation: (1963): 1, 7, 8; (1964): 1, 4, 11, 12; (1965): 1, 3, 8, 12, 13; (1966): 1, 3, 4, 7, 8, 9, 11, 12, 19, 20, 23, 27, 28, 30, 32, 33, 38; (1967): 1, 2, 3, 6, 10, 24, 25, 26, 27, 28, 31; (1968): 5, 6, 9, 10, 19, 30, 37, 41; (1969): 1, 2, 11, 12, 13, 15, 17, 27, 28, 31, 36, 39; (1970): 1, 2, 6, 7, 12, 16, 24, 25, 31, 33, 34, 35; (1971): 1, 2, 3, 4, 8, 9, 17, 21, 23, 29, 32, 37, 38, 43, 45, 48, 49; (1972): 1, 2, 3, 5, 7, 8, 12, 19, 20, 25, 38, 39, 42, 45, 46, 47, 48, 50, 52, 53, 55; (1973): 1, 2, 3, 5, 10, 11, 12, 16, 17, 24, 25, 28, 29, 31; (1974): 1, 4, 5, 7, 8, 9, 12, 14, 21, 24; (1975): 1, 2, 3, 13, 16, 26, 27, 28, 29, 34, 35, 36, 37, 41, 42, 43, 44, 46, 47, 55, 56, 58; (1976): 2, 3, 8, 9, 15, 16, 18, 27, 40, 49; (1977): 4, 9, 10, 16, 19, 20, 22, 26, 27, 29, 40, 43, 49, 50, 52, 55; (1978): 2, 9, 16, 21, 23, 24, 41, 43, 44, 46, 57, 58, 65, 66, 67, 72; (1979): 30, 34, 35, 40, 45; (1980): 1, 4, 6, 14, 19, 21, 37, 39, 56, 62; (1981): 23, 42, 49, 63; (1982): 20, 22, 35, 44.

Ion Energy: (1963): 7; (1964): 6, 7, 8; (1965): 2, 5, 8, 13; (1966): 1, 2, 3, 5, 7, 13, 14, 15, 16, 19, 27, 28, 30, 32, 37, 38; (1967): 5, 9, 10, 16, 17, 24, 25, 28, 31; (1968): 4, 5, 6, 12, 19, 29, 30, 36, 37, 41; (1969): 1, 4, 11, 12, 13, 16, 30, 31, 36; (1970): 1, 7, 12, 16, 22, 24, 25, 31, 33, 34, 35, 37; (1971): 1, 2, 5, 9, 15, 19, 29, 30, 37, 43, 45; (1972): 2, 5, 7, 8, 9, 10, 11, 12, 16, 19, 20, 25, 30, 38, 42, 48, 49, 52; (1973): 2, 5, 11, 16, 17, 21, 29, 31, 33; (1974): 1, 5, 7, 20, 21, 23; (1975): 3, 5, 13, 16, 26, 29, 33, 36, 38, 42, 44, 46, 56; (1976): 8, 9, 15, 16, 22, 27, 37, 44, 49; (1977): 3, 9, 16, 18, 19, 20, 25, 26, 38, 44, 55; (1978): 1, 2, 16, 17, 21, 23, 41, 44, 46, 49, 51, 60, 61, 67, 72; (1979): 35, 45; (1980): 3, 12, 14, 37, 38, 39; (1981): 42, 49; (1982): 35.

Ion Charge: (1964): 2; (1965): 2, 8; (1966): 25, 28, 37, 38, 39; (1967): 3, 14, 15, 18; (1968): 12, 25, 26, 28, 36, 37, 44; (1969): 2, 13, 30, 31; (1970): 1, 6, 11, 12, 16, 22, 31, 37, 41; (1971): 1, 9, 15, 29, 30, 36, 38, 43; (1972): 2, 9, 10, 17, 19, 28, 30, 32, 48, 55; (1973): 2, 17, 24, 25, 26, 27; (1974): 7, 8, 9, 22; (1975): 13, 36, 38, 46, 47, 55; (1977): 3, 19, 20, 38, 44, 50; (1978): 2, 10, 23, 41, 44, 46, 51, 60, 61; (1979): 6, 9, 35, 45; (1980): 2, 3, 6, 12, 38, 39; (1981): 49; (1982): 28.

Ionization Efficiency: (1963): 1, 2, 3, 4; (1964): 2, 4, 6; (1965): 1; (1966): 2, 16, 17, 25, 36, 38; (1967): 6, 8, 9, 17; (1968): 17, 19, 29, 44; (1969): 4, 23; (1970): 7, 14, 25, 27, 37; (1971): 5, 17, 30, 48; (1972): 3, 7, 13, 16, 32, 38, 48, 51, 54, 55; (1973): 7, 16, 34; (1974): 7, 10; (1975): 4, 29, 34, 38, 42, 43, 44, 47, 58; (1976): 2, 4, 5, 13, 14, 53; (1977): 3, 9, 20, 50, 54; (1978): 46, 65; (1979): 9, 45, 46; (1980): 2; (1981): 22; (1982): 28, 42.

Angular Effects: (1966): 25; (1967): 31; (1969): 15, 35; (1970): 14, 24; (1971): 8, 9, 15, 30, 43; (1972): 45, 48; (1973): 3; (1974): 7, 9; (1975): 13, 33; (1976): 19, 27, 44, 49; (1977): 16, 21, 27; (1978): 1, 2, 15, 24, 41, 67; (1980): 12; (1982): 22, 35.

Cratering: (1963): 2, 4; (1964): 12; (1965): 15; (1966): 3, 13; (1967): 35; (1968): 21, 24, 44; (1969): 3, 9, 14, 15, 18, 23, 35; (1970): 2, 18, 27; (1972): 4, 53, 54; (1973): 20; (1974): 4, 26, 32, 33; (1975): 9, 10, 56; (1976): 4, 5, 12, 25, 28, 32, 53; (1977): 6, 23, 24; (1978): 17, 19; (1979): 7; (1980): 59; (1981): 11; (1982): 28, 37, 44.

Laser Energy Absorption: (1965): 12; (1966): 29, 30; (1968): 10, 11; (1969): 28, 35; (1971): 7; (1973): 3, 17, 31; (1974): 4, 11, 30; (1975): 6, 11, 37; (1976): 39; (1977): 15, 29; (1978): 28, 51, 58; (1980): 1; (1981): 22.

Temporal Effects: (1963): 8; (1964): 8, 10; (1965): 5, 6, 9; (1966): 14; (1967): 18, 19; (1968): 11, 31; (1969): 29, 36; (1970): 3, 13, 16, 26; (1971): 12; (1972): 4, 28, 47; (1973): 17, 21; (1974): 5, 8, 12; (1975): 33; (1976): 14, 15, 32; (1977): 22, 29; (1978): 17, 23, 44, 53; (1979): 39; (1980): 33, 39.

Ion Formation Processes: (1964): 10; (1965): 6; (1966): 5, 7; (1967): 19; (1968): 31, 39; (1970): 17; (1975): 11; (1978): 27; (1979): 9; (1980): 9, 19, 21, 40, 43, 53; (1981): 12, 15, 23, 35, 37, 40, 56, 64, 71; (1982): 4, 24, 29, 46, 53, 56, 57.

#### Applications:

Biological: (1968): 18, 39; (1973): 13; (1974): 17, 18, 19; (1975): 22, 25; (1976): 48; (1977): 23; (1978): 18, 19, 22, 30, 31, 33, 36, 48; (1979): 7, 10, 13, 15, 17, 18, 19; (1980): 16, 23, 29, 30, 36, 41, 42, 44, 47, 49, 50, 51, 52, 53, 57; (1981): 6, 20, 24, 34, 36, 41, 50, 54, 55, 58, 59, 69; (1982): 1, 6, 9, 21, 26, 27, 30, 31, 34, 36, 40, 47, 49, 50, 59.

Botanical: (1979): 5, 22, 29; (1980): 5; (1981): 9, 38, 39, 43, 44, 45, 60; (1982): 5, 38, 43.

Carbon: (1963): 5; (1964): 2; (1966): 39; (1967): 15, 18, 29; (1968): 24, 30, 44; (1969): 17, 25, 30, 38; (1970): 28, 29; (1971): 25, 32, 40; (1972): 22, 28, 29, 32, 33; (1973): 24, 25, 26, 27, 28; (1974): 5, 22; (1978): 26; (1979): 9, 35; (1980): 17, 18, 28.

Fossil Fuels: (1964): 13, 14; (1966): 34, 35; (1967): 12, 34; (1968): 22, 23; (1969): 24, 40; (1970): 21, 26, 39; (1975): 20; (1976): 24, 50, 51; (1977): 28; (1978): 26; (1980): 46; (1981): 48; (1982): 14.

Gaseous Impurities: (1966): 40; (1967): 17, 21, 35; (1968): 7, 8, 17, 21, 30; (1969): 10, 23; (1970): 8, 20, 40, 43; (1971): 13, 24; (1972): 51; (1973): 11; (1974): 27, 32, 33; (1975): 9, 51; (1976): 18, 38, 52; (1977): 11, 17, 30, 39, 47, 48, 56, 57, 58; (1978): 15, 29; (1979): 2, 23, 42, 48, 49; (1980): 11, 37.

Geological: (1969): 32; (1971): 10, 11, 24, 39; (1972): 15, 31; (1973): 18; (1976): 38; (1977): 30, 39, 47; (1978): 12, 13, 14, 64; (1979): 14; (1980): 17, 26, 28; (1981): 5, 32; (1982): 8, 14.

Inorganic: (1963): 3; (1966): 39; (1967): 8, 13, 14, 15; (1968): 18, 20, 25, 26, 27, 28; (1969): 6, 7, 8, 21, 33, 34, 44; (1970): 4, 5, 23, 30; (1971): 11, 34; (1972): 11, 13, 36, 44, 55; (1973): 4, 19, 24, 25, 26, 27; (1974): 34, 35; (1975): 21, 26, 54; (1976): 4, 13, 20; (1977): 8, 12, 14; (1978): 10, 11, 50; (1979): 1, 13; (1980): 18, 24, 48; (1981): 7, 30, 63; (1982): 28, 29, 48.

Isotopic: (1968): 14, 17; (1969): 19, 20; (1970): 13; (1971): 11; (1972): 15; (1976): 7; (1979): 20, 23; (1980): 15, 52; (1981): 55, 63; (1982): 51, 52.

Metals: (1966): 15; (1968): 16, 30; (1971): 11; (1972): 4, 15, 35, 53; (1974): 29; (1975): 9; (1976): 6, 7, 28; (1977): 21; (1978): 14, 50; (1980): 7, 55; (1981): 11, 17, 23, 28, 49, 66; (1982): 3, 44.

Organo-metallic: (1980): 46; (1981): 47, 48; (1982): 18, 45, 48.

Organics: (1966): 39; (1967): 33; (1968): 39, 43; (1969): 9; (1970): 28, 37, 38, 42; (1971): 42, 44; (1972): 4, 16, 22, 26, 37, 53; (1973): 32; (1975): 9, 21, 23, 40, 51; (1976): 29, 31, 34, 47; (1977): 5, 35, 42; (1978): 7, 20, 27, 28, 36, 39, 45, 48, 54, 55, 63, 64; (1979): 1, 2, 4, 6, 8, 13, 15, 21, 28, 36, 37, 39; (1980): 9, 10, 13, 14, 21, 24, 27, 33, 34, 35, 40, 41, 43; (1981): 2, 3, 4, 12, 13, 14, 16, 18, 19, 21, 29, 30, 31, 53, 54, 56, 71; (1982): 2, 21, 23, 24, 26, 56, 57, 60.

Particles and Aerosols: (1980): 31, 32, 58, 60, 61; (1981): 1, 26, 52, 57, 61, 67, 68, 70; (1982): 10, 12, 32, 33, 54.

Polymers: (1967): 18; (1969): 21; (1970): 23; (1971): 34; (1972): 4, 17; (1973): 6; (1974): 16, 28; (1975): 13, 18, 48, 54; (1976): 26, 35, 46; (1977): 14, 26, 27, 36, 44; (1978): 6, 40, 41, 67; (1979): 26, 47; (1980): 20; (1981): 25; (1982): 19.

Surface Analysis: (1968): 38; (1969): 10; (1971): 11; (1972): 26; (1974): 36; (1976): 12; (1977): 7; (1979): 23, 33, 47; (1980): 33, 43, 54; (1981): 11, 21, 37; (1982): 28.

Others and Miscellaneous: (1969): 10; (1971): 7, 20, 44; (1975): 19, 54; (1976): 46; (1978): 30, 40, 69; (1979): 16, 18, 43; (1980): 21, 25; (1982): 11, 23, 30.

Cratering: (1963): 2, 4; (1964): 12; (1965): 15; (1966): 3, 13; (1967): 35; (1968): 21, 24, 44; (1969): 3, 9, 14, 15, 18, 23, 35; (1970): 2, 18, 27; (1972): 4, 53, 54; (1973): 20; (1974): 4, 26, 32, 33; (1975): 9, 10, 56; (1976): 4, 5, 12, 25, 28, 32, 53; (1977): 6, 23, 24; (1978): 17, 19; (1979): 7; (1980): 59; (1981): 11; (1982): 28, 37, 44.

Laser Energy Absorption: (1965): 12; (1966): 29, 30; (1968): 10, 11; (1969): 28, 35; (1971): 7; (1973): 3, 17, 31; (1974): 4, 11, 30; (1975): 6, 11, 37; (1976): 39; (1977): 15, 29; (1978): 28, 51, 58; (1980): 1; (1981): 22.

Temporal Effects: (1963): 8; (1964): 8, 10; (1965): 5, 6, 9; (1966): 14; (1967): 18, 19; (1968): 11, 31; (1969): 29, 36; (1970): 3, 13, 16, 26; (1971): 12; (1972): 4, 28, 47; (1973): 17, 21; (1974): 5, 8, 12; (1975): 33; (1976): 14, 15, 32; (1977): 22, 29; (1978): 17, 23, 44, 53; (1979): 39; (1980): 33, 39.

Ion Formation Processes: (1964): 10; (1965): 6; (1966): 5, 7; (1967): 19; (1968): 31, 39; (1970): 17; (1975): 11; (1978): 27; (1979): 9; (1980): 9, 19, 21, 40, 43, 53; (1981): 12, 15, 23, 35, 37, 40, 56, 64, 71; (1982): 4, 24, 29, 46, 53, 56, 57.

#### Applications:

Biological: (1968): 18, 39; (1973): 13; (1974): 17, 18, 19; (1975): 22, 25; (1976): 48; (1977): 23; (1978): 18, 19, 22, 30, 31, 33, 36, 48; (1979): 7, 10, 13, 15, 17, 18, 19; (1980): 16, 23, 29, 30, 36, 41, 42, 44, 47, 49, 50, 51, 52, 53, 57; (1981): 6, 20, 24, 34, 36, 41, 50, 54, 55, 58, 59, 69; (1982): 1, 6, 9, 21, 26, 27, 30, 31, 34, 36, 40, 47, 49, 50, 59.

Botanical: (1979): 5, 22, 29; (1980): 5; (1981): 9, 38, 39, 43, 44, 45, 60; (1982): 5, 38, 43.

Carbon: (1963): 5; (1964): 2; (1966): 39; (1967): 15, 18, 29; (1968): 24, 30, 44; (1969): 17, 25, 30, 38; (1970): 28, 29; (1971): 25, 32, 40; (1972): 22, 28, 29, 32, 33; (1973): 24, 25, 26, 27, 28; (1974): 5, 22; (1978): 26; (1979): 9, 35; (1980): 17, 18, 28.

Fossil Fuels: (1964): 13, 14; (1966): 34, 35; (1967): 12, 34; (1968): 22, 23; (1969): 24, 40; (1970): 21, 26, 39; (1975): 20; (1976): 24, 50, 51; (1977): 28; (1978): 26; (1980): 46; (1981): 48; (1982): 14.

Gaseous Impurities: (1966): 40; (1967): 17, 21, 35; (1968): 7, 8, 17, 21, 30; (1969): 10, 23; (1970): 8, 20, 40, 43; (1971): 13, 24; (1972): 51; (1973): 11; (1974): 27, 32, 33; (1975): 9, 51; (1976): 18, 38, 52; (1977): 11, 17, 30, 39, 47, 48, 56, 57, 58; (1978): 15, 29; (1979): 2, 23, 42, 48, 49; (1980): 11, 37.

Geological: (1969): 32; (1971): 10, 11, 24, 39; (1972): 15, 31; (1973): 18; (1976): 38; (1977): 30, 39, 47; (1978): 12, 13, 14, 64; (1979): 14; (1980): 17, 26, 28; (1981): 5, 32; (1982): 8, 14.

Inorganic: (1963): 3; (1966): 39; (1967): 8, 13, 14, 15; (1968): 18, 20, 25, 26, 27, 28; (1969): 6, 7, 8, 21, 33, 34, 44; (1970): 4, 5, 23, 30; (1971): 11, 34; (1972): 11, 13, 36, 44, 55; (1973): 4, 19, 24, 25, 26, 27; (1974): 34, 35; (1975): 21, 26, 54; (1976): 4, 13, 20; (1977): 8, 12, 14; (1978): 10, 11, 50; (1979): 1, 13; (1980): 18, 24, 48; (1981): 7, 30, 63; (1982): 28, 29, 48.

Isotopic: (1968): 14, 17; (1969): 19, 20; (1970): 13; (1971): 11; (1972): 15; (1976): 7; (1979): 20, 23; (1980): 15, 52; (1981): 55, 63; (1982): 51, 52.

Metals: (1966): 15; (1968): 16, 30; (1971): 11; (1972): 4, 15, 35, 53; (1974): 29; (1975): 9; (1976): 6, 7, 28; (1977): 21; (1978): 14, 50; (1980): 7, 55; (1981): 11, 17, 23, 28, 49, 66; (1982): 3, 44.

Organo-metallic: (1980): 46; (1981): 47, 48; (1982): 18, 45, 48.

Organics: (1966): 39; (1967): 33; (1968): 39, 43; (1969): 9; (1970): 28, 37, 38, 42; (1971): 42, 44; (1972): 4, 16, 22, 26, 37, 53; (1973): 32; (1975): 9, 21, 23, 40, 51; (1976): 29, 31, 34, 47; (1977): 5, 35, 42; (1978): 7, 20, 27, 28, 36, 39, 45, 48, 54, 55, 63, 64; (1979): 1, 2, 4, 6, 8, 13, 15, 21, 28, 36, 37, 39; (1980): 9, 10, 13, 14, 21, 24, 27, 33, 34, 35, 40, 41, 43; (1981): 2, 3, 4, 12, 13, 14, 16, 18, 19, 21, 29, 30, 31, 53, 54, 56, 71; (1982): 2, 21, 23, 24, 26, 56, 57, 60.

Particles and Aerosols: (1980): 31, 32, 58, 60, 61; (1981): 1, 26, 52, 57, 61, 67, 68, 70; (1982): 10, 12, 32, 33, 54.

Polymers: (1967): 18; (1969): 21; (1970): 23; (1971): 34; (1972): 4, 17; (1973): 6; (1974): 16, 28; (1975): 13, 18, 48, 54; (1976): 26, 35, 46; (1977): 14, 26, 27, 36, 44; (1978): 6, 40, 41, 67; (1979): 26, 47; (1980): 20; (1981): 25; (1982): 19.

Surface Analysis: (1968): 38; (1969): 10; (1971): 11; (1972): 26; (1974): 36; (1976): 12; (1977): 7; (1979): 23, 33, 47; (1980): 33, 43, 54; (1981): 11, 21, 37; (1982): 28.

Others and Miscellaneous: (1969): 10; (1971): 7, 20, 44; (1975): 19, 54; (1976): 46; (1978): 30, 40, 69; (1979): 16, 18, 43; (1980): 21, 25; (1982): 11, 23, 30.

## 1963

1. F.A. Giori, L.A. MacKenzie, and E.J. McKinney, Laser induced thermionic emission, *Appl. Phys. Lett.* 3(1963)25.
2. R.E. Honig, Laser induced emission of electrons and positive ions from metals and semiconductors, *Appl. Phys. Lett.* 3(1963)8.
3. R.E. Honig and J.R. Woolston, Laser induced emission of electrons, ions, and neutral atoms from solid surfaces, *Appl. Phys. Lett.* 2(1963)138.
4. R.E. Honig and J.R. Woolston, Mass spectrographic microanalysis of solids with a focused laser beam, Paper C1-17 presented at the IUPAC Meeting, London, England, July 1963.
5. J.A. Howe, Observations on the maser induced graphite jet, *J. Chem. Phys.* 39(1963)1362.
6. D. Lichtman and J.F. Ready, Laser beam induced electron emission, *Phys. Rev. Lett.* 10(1963)342.
7. W.I. Linlor, Ion energies produced by laser giant pulse, *Appl. Phys. Lett.* 3(1963)210.
8. J.F. Ready, Development of plume of material vaporized by giant pulse laser, *Appl. Phys. Lett.* 3(1963)11.
9. C.M. Verber and A.H. Adelman, Laser induced thermionic emission, *Appl. Phys. Lett.* 2(1963)220.

## 1964

1. E. Archbold and T.P. Hughes, Electron temperature in a laser heated plasma, *Nature* 204(1964)670.
2. J. Berkowitz and W.A. Chupka, Mass spectrometric study of vapor ejected from graphite and other solids by focused laser beams, *J. Chem. Phys.* 40(1964)2745.
3. M. Bessis and M.M. Ter-Pogossian, Micropuncture of cells by means of a laser beam, *Ann. N.Y. Acad. Sci.* 122(1965) 689. From Conference on the Laser, May 4-5, 1964.
4. T.Y. Chang and C.K. Birdsall, Laser-induced emission of electrons, ions, and neutrals from Ti and Ti-D surfaces, *Appl. Phys. Lett.* 5(1964)171.
5. H.I.S. Ferguson J.E. Mentall, and R.W. Nicholls, Laser excitation of powdered solids, *Nature*. 204(1964)1295.
6. R.E. Honig, On the production of positive ions from solids, Paper 38 presented at 12th Annual Conference on Mass Spectrometry and Allied Topics, Montreal, Canada, June 7-12, 1964.
7. N.R. Isenor, Metal ion emission velocity dependence on laser giant pulse height, *Appl. Phys. Lett.* 4(1964)152.
8. N.R. Isenor, High energy ions from a Q-switched laser, *Can. J. Chem.* 42(1964)1413.
9. K.A. Lincoln, Simple display system for recording time resolved mass spectra, *Rev. Sci. Instrum.* 35(1964)1688.
10. K.A. Lincoln, Flash vaporization of solid materials for mass spectrometry by intense thermal radiation, Paper 79 presented at 12th Annual Conference on Mass Spectrometry and Allied Topics, Montreal, Canada, June 7-12, 1964.
11. W.I. Linlor, Some properties of plasma produced by laser giant pulse, *Phys. Rev. Lett.* 12(1964)383.
12. F. Neuman, Momentum transfer and cratering effects produced by giant laser pulses, *Appl. Phys. Lett.* 4(1964)167.
13. A.G. Sharkey, J.L. Shultz, and R.A. Friedel, Gases from flash and laser irradiation of coal, *Nature (London)* 202(1964)988.
14. A.G. Sharkey, J.L. Shultz, and R.A. Friedel, Mass spectrometric investigation of gases from flash and laser irradiation of coal, Paper 63 presented at 12th Annual Conference on Mass Spectrometry and Allied Topics, Montreal, Canada, June 7-12, 1964.

## 1965

1. J.K. Cobb and J.J. Muray, Laser beam-induced electron and ion emission from metal foils, *Brit. J. Appl. Phys.* 19(1965)271.
2. A.S. Gilmour and F.A. Giori, The use of the quadrupole mass spectrometer for laser-surface studies, Paper 60 presented at 13th Annual Conference on Mass Spectrometry and Allied Topics, St. Louis, MO, May 16-21, 1965.
3. M. Iannuzzi and R. Williamson, Effects of absorption of laser radiation on metals, *Nuovo Cimento* 36(1965)1130.
4. N.R. Isenor, Effect of background gas on laser induced electron emission from metal surfaces, *J. Appl. Phys.* 36(1965)316.
5. S.H. Kahn, F.A. Richards, and D. Walsh, Time resolution of laser induced electron and ion emission, *IEEE J. Quant. Electron.* 1(1965)359.
6. K.A. Lincoln, Flash vaporization of solid materials for mass spectrometry by intense thermal radiation, *Anal. Chem.* 37(1965)541.
7. J. McCormack, The laser microprobe....a new metallurgical tool, *Met. Rev.* 38(1965)6.
8. S. Namba, P.H. Kim, S. Nakayama, and I. Ida, Surface temperature of metals heated with laser, *Jap. J. Appl. Phys.* 4(1965)153.
9. H. Opower and E. Burlefinger, Temperature determination of plasmas produced by giant laser pulses, *Phys. Lett.* 16(1965)37.
10. S. Panzer, Heat effects of laser radiation on materials, CEA-tr-A-1948. Translated from KEM 34-6(1965)37.
11. J.F. Ready, Mechanism of electron emission produced by a giant pulse laser, *Phys. Rev.* 137(1965)A620.
12. J.F. Ready, Effects due to absorption of laser radiation, *J. Appl. Phys.* 36(1965)462.
13. J.F. Ready, E. Bernal G., and L.P. Levine, Mechanisms of laser-surface interactions, AD-477 231, Semiannual Report, November 1965.
14. C.M. Verber and A.H. Adelman, Laser induced thermionic emission from tantalum, *J. Appl. Phys.* 36(1965)1522.

15. K. Vogel and P. Backlund, Application of electron and optical microscopy in studying laser-irradiated metal surfaces, J. Appl. Phys. 36(1965)3697.

1966

1. Yu.V. Afanasyev, O.N. Krokhin, and G.V. Sklizkov, 7A5- Evaporation and heating of a substance due to laser radiation, IEEE J. Quantum Electron. QE-2(1966)483.
2. E.D. Andryukhina and I.S. Shpigel, A titanium plasma source. 11. mass composition, energy spectrum, and purification of plasma, pp. 30-35 of Proceedings (Trudy) of the P.N. Lebedev Physics Institute, Vol. 32, Plasma Physics, D.V. Skobel'tsyn (Ed.). Translated from Russian. Consultants Bureau, New York, 1968. Originally published by Nauka Press, Moscow, 1966.
3. S.I. Anisimov, A.M. Bonch-Breuvich, M.A. El'yashevich, Y.A. Imas, N.A. Pavlenko, and G.S. Romanov, Effect of powerful light fluxes on metals, Sov. Phys.-Tech. Phys. 11(1967)945. Translated from Zh. Tekh. Fiz. 36(1966)1273.
4. G.A. Askar'yan and M.S. Rabinovich, Ionization and plasma generation by laser radiation, D.V. Skobel'tsyn (Ed.), Proceedings (Trudy) of the P.N. Lebedev Physics Inst., Vol. 32, Plasma Physics, pp. 76-83. Translated from Russian for Consultants Bureau, New York, 1968. Originally published by Nauka Press, Moscow, 1966.
5. E. Bernal G., J.F. Ready, and L.P. Levine, Adsorbed ion emission from laser irradiated tungsten, Phys. Lett. 19(8)(1966)645.
6. E. Bernal G., L.P. Levine, and J.F. Ready, Time-of-flight spectrometer for laser surface interaction studies, Rev. Sci. Instrum. 37(1966)938.
7. E. Bernal G., J.F. Ready, and L.P. Levine, Ion emission from laser irradiated tungsten, IEEE J. Quant. Electron. QE-2(1966)480.
8. C. Bourrabier, T. Consoli, and L. Slama, Intense pulsed sources of laser produced ions and electrons, Phys. Lett. 23(1966)236.
9. A. Caruso, B. Bertotti, and P. Giupponi, Ionization and heating of solid material by means of a laser pulse, Nuovo Cimento 45B(1966)176.
10. D. Damoth, Laser microprobe sampling and other new time- of-flight mass spectrometer developments, Mod. Aspects Mass Spectrom. Proc. NATO Adv. Study Inst. Mass Spectrom., 2nd., 1966, p.49.
11. C.D. David, P.V. Avizonis, H. Weichel, C. Bruce, and K.D. Pyatt, Density and temperature of a laser induced plasma, IEEE J. Quantum Electronics, QE-2(1966)493.
12. A.W. Ehler, Plasma formed by a laser pulse on a tungsten target, J. Appl. Phys. 37(1966)4962.
13. J.F. Eloy and J.L. Dumas, Study of ions produced by laser impact in a mass spectrometer source, Methodes Phys. Anal. 2(1966)251.
14. C.W. Erickson, Determination of plasma potentials and ion energies by ion extraction and energy analysis, Rev. Sci. Instrum. 37(1966)1308.
15. N.C. Fenner, Ion energies in the plasma produced by a high power laser, Phys. Lett. 22(1966)421.
16. N.C. Fenner and N.R. Daly, Laser used for mass analysis, Rev. Sci. Instrum. 37(1966)1068.
17. N.C. Fenner, R.G. Ridley, R.W.D. Hardy, and N.R. Daly, Application of laser to mass spectrometry, Paper 25 presented at 14th Annual Conference on Mass Spectrometry and Allied Topics, Dallas, TX, May 22-27, 1966.
18. V.J. Fowler and J. Schlafer, A survey of laser beam deflection techniques, Proc. IEEE 54(1966)1437.
19. D.W. Gregg and S.J. Thomas, Kinetic energies of ions produced by laser giant pulses, J. Appl. Phys. 37(1966)4313.
20. D.W. Gregg and S.J. Thomas, Momentum transfer produced by focused laser giant pulses, J. Appl. Phys. 37(1966)2787.
21. O.S. Heavens, Recent applications of lasers, Brit. J. Appl. Phys. 17(1966)287.
22. R.E. Honig, Mass spectroscopy as an analytical tool, Ann. N.Y. Acad. Sci. 137(1966)262.
23. W.L. Knecht, Surface temperature of laser heated metal, Proc. IEEE 54(1966)692.
24. B.E. Knox and F.J. Vastola, Mass spectrometer uses laser microprobe. Ability to vaporize thin surface layers makes combination a powerful tool for studying polymer structures, Chem. Eng. News 44(1966)48.
25. P. Langer, G. Tonon, F. Floux, and A. Ducauze, Laser induced emission of electrons, ions, and x-rays from solid targets, IEEE J. Quantum Electron. 1(1966)499.
26. B.A. Lengyel, Evolution of masers and lasers, Am. J. Phys. 34(1966)903.
27. S. Namba, P.H. Kim, T. Itoh, T. Arai, and H. Schwarz, Ion emission from metal surface irradiated by giant pulse laser beam, Sci. Papers Inst. Phys. Chem. Res. (I.P.C.R.) (Tokyo) 60(1966)101.
28. S. Namba, P.H. Kim, and A. Mitsuyama, Energies of ions produced by laser irradiation, J. Appl. Phys. 37(1966)3330.
29. S.S. Penner and O.P. Sharma, Interaction of laser radiation with an absorbing semi-infinite solid bar, J. Appl. Phys. 37(1966)2304.
30. S.A. Ramsden, R. Benesch, W.E.R. Davies, and P.K. John, Observation of cooperative effects and determination of electron and ion temperatures in a plasma from scattering of a ruby laser beam, IEEE J. Quantum. Electron. QE2(1966)267.
31. J.F. Ready, Effects of laser radiation, Ind. Res. 7(1966)44.
32. J.F. Ready, E. Bernal G., L.P. Levine, and G. Levine, Mechanisms of Laser-surface Interactions, AD-636 680, Honeywell Research Center, 1966, NTIS.
33. J.E. Rizzo and R.C. Klieve, Optical breakdown in metal vapors, Brit. J. App. Phys. 17(1966)1137.
34. A.G. Sharkey, J.L. Shultz, and R.A. Friedel, Gases from flash and laser irradiation of coal, Adv. Chem. Ser. 55(1966)643.
35. A.G. Sharkey, J.L. Shultz, and R.A. Friedel, Comparison of products from high temperature irradiation and carbonization of coal, U.S. Bureau of Mines Report Invest. No. 6868, 1966.
36. D.M. Stevenson, Evaporation and ionization of laser heated tungsten, Proc. IEEE 54(1966)1471.

37. G. Tonon, Energy spectra of ions emitted by beryllium, carbon, and molybdenum under the effects of a laser beam, *Compt. Rend., Ser. B.* 262(1966)706.
38. G.F. Tonon and P. Langer, Laser induced emission of electrons, x-rays and ions from solid target, *IEEE J. Quantum. Electron.* QE2(1966)296.
39. F.J. Vastola, A.J. Pirone, and B.E. Knox, The production of vapor species in a mass spectrometer ionization chamber by laser heating, Paper 24 presented at 14th Annual Conference on Mass Spectrometry and Allied Topics, Dallas, TX, May 22-27, 1966.
40. H.F. Winters and E. Kay, Gas content of sputtered Ni films using laser induced flash evaporation and mass spectrometry, *J. Vac. Sci. Technol.* 3(1966)312. Abstract of paper presented at 13th National Vacuum Symposium, October 1966.

1967

1. Yu.V. Afanas'ev and O.N. Krokhin, Vaporization of matter exposed to laser emission, *Sov. Phys. JETP* 25(1967)639.
2. V.V. Afrosimov and I.P. Gladkovski, Particle diagnostics of a hot plasma (review), *Sov. Phys. Tech. Phys.* 12(1968)1135. Translated from *Zh. Tekh. Fiz.* 37(1967)1557.
3. N.G. Basov, V.A. Boiko, Y.P. Voinov, and E.Y. Kononov, Production of spectra of multiply charged ions by focusing laser radiation on a solid target, *Sov. Phys. JETP* 5(1967)141.
4. A.M. Bonch-Bruевич and Y.A. Imas, Recoil momentum and ejection of metal particles under the action of a giant laser pulse, *Sov. Phys. Tech. Phys.* 12(1968)1407. Translated from *Zh. Tekh. Fiz.* 37(1967)1917.
5. R. Briand, T. Consoli, L. Slama, and P. Grelot, Energy spectrum of ions in a laser-generated aluminum plasma, *Phys. Lett. A* 25A(1967)631.
6. F.V. Bunkin and A.M. Prokhorov, Some features of the interaction between short laser pulses and matter, *Sov. Phys. JETP* 25(1967)1072. Translated from *Zh. Eksp. Teor. Fiz.* 52(1967)1610.
7. J.L. Dumas, Source d'ions pour spectrometre de masse a laser, *Methodes Phys. Anal.* 1(1967)47.
8. N.C. Fenner and N.R. Daly, A laser used for mass analysis, *Lasers Opt. Non Conv.* 8(1967)87.
9. L.I. Grechikhin and L.Y. Min'ko, Similarity between physical processes in a pulsed discharge and in the effect of laser radiation on a metal, *Sov. Phys. Tech. Phys.* 12(1967)846. Translated from *Zh. Tekh. Fiz.* 37(1967)1169.
10. D.W. Gregg and S.J. Thomas, Plasma temperatures generated by focussed laser giant pulses, *J. Appl. Phys.* 38(1967)1729.
11. R.E. Honig, Mass spectrometry of solids: A bibliography for 1966 by Subcommittee VII. Part 2, Sources, General, 15th Annual Conference on Mass Spectrometry and Allied Topics, Denver, CO, May 14-19, 1967.
12. F.S. Karn, R.A. Friedel, and A.G. Sharkey, Distribution of gaseous products from laser pyrolysis of coals of various ranks, *Carbon* 5(1967)25.
13. B.E. Knox, Laser-mass spectrometer microprobe analysis of flux-grown oxide single crystals, Paper 9 presented at 15th Annual Conference on Mass Spectrometry and Allied Topics, Denver, CO, May 14-19, 1967.
14. B.E. Knox, Mass spectrometric study of the laser induced vaporization of selenium and various selenides, in E. Kendrick (Ed.), *Advances in Mass Spectrometry*, Vol. 4, Institute of Petroleum, London, 1968, pp. 491-7. Proceedings of Conference held in Berlin, Germany, September 25-29, 1967.
15. B.E. Knox and F.J. Vastola, Laser microprobe applied to mass spectrometry, *Laser Focus* 3(1967)15.
16. D.W. Koopman, Ion emission from laser produced plasmas, *Phys. Fluids* 10(1967)2091.
17. L.P. Levine, J. F. Ready, and E. Bernal G., Gas desorption produced by a giant pulse laser, *J. Appl. Phys.* 38(1967)331.
18. K.A. Lincoln, Mass spectrometric studies applied to laser induced vaporization of polymeric materials, *Pure Appl. Chem., Suppl.* (1969)323. Proceedings of 3rd International Symposium on High Temperature Technology, Asilomar, CA, 1967.
19. K.A. Lincoln and D. Werner, Time resolved mass spectrometry applied to laser induced vaporization, Paper 125 presented at 15th Annual Conference on Mass Spectrometry and Allied Topics, Denver, CO, May 14-19, 1967.
20. H. Malissa and H. Arlt, Discussion on "comparative observations on electron beam microanalysis and laser micro spectral analysis", *Mikrochim. Acta, Suppl.* 2(1967)101.
21. G.H. Megrue, Isotopic analysis of rare gases with a laser microprobe, *Science*, 157(1967)1555.
22. L. Moenke-Blankenburg, Funktion und einsatzmoglichkeit des laser-mikro-spektralanalysators LMA 1, *Mikrochim. Acta (Wien), Suppl.* 2(1967)82.
23. H. Moenke, Comparative observations on electron beam microanalysis and laser micro spectral analysis, *Mikrochim. Acta (Wien), Suppl.* 2(1967)93.
24. S. Namba, P.H. Kim, T. Itoh, T. Arai, and N. Kinoshita, Relation of laser induced ion energy to laser power, *Jap. J. Appl. Phys.* 6(1967)273.
25. S. Namba, P.H. Kim, T. Itoh, T. Arai, and H. Schwarz, Ion emission from metal surface irradiated by giant pulse laser beam, *Lasers Opt. Non Con.* 8(1967)113.
26. H. OPOWER, W. Kaiser, H. Puell, and W. Heinicke, Energetic plasmas produced by laser light on solid targets, *Z. Naturforsch.* 22A(1967)1392.
27. J.F. Ready, E. Bernal, and L. Levine, Mechanisms of laser-surface interactions, AD-666 245, November 1967.
28. G.M. Rubanova and A.P. Sokolov, Metal heating by laser radiation, *Sov. Phys. Tech. Phys.* 12(1968)1226. Translated from *Zh. Tekh. Fiz.* 37(1967)1677.
29. J.L. Shultz and A.G. Sharkey, Gases from laser irradiation of coal. Effect of argon, nitrogen, and other atmospheres, *Carbon* 5(1967)57.
30. L.L. Steinmetz, Laser triggered spark gap, UCID-15199, September 1967.
31. E.W. Sucov, J.L. Pack, A.V. Phelps, A.G. Engelhardt, Plasma production by a high power Q-switched laser, *Phys. Fluids* 10(1967)2035.

32. H. Van Draat, Microanalysis with lasers, Chem. Tech. Rev. 22(1967)133.
33. F.J. Vastola and A.J. Pirone, Ionization of organic solids by laser irradiation, in E. Kendrick (Ed.), Advances in Mass Spectrometry, Volume 4, Institute of Petroleum, London, 1968, pp. 107-111. Presented at 4th International Mass Spectrometry Conference, Berlin, September 1967.
34. F.J. Vastola, A.J. Pirone, P.H. Given, and R.R. Dutcher, The analysis of coal with the laser mass spectrometer, Abstract L-59, Division of Fuel Chemistry. Presented at 154th Meeting of American Chemical Society, Chicago, IL, September 10-15, 1967.
35. H.F. Winters and E. Kay, Gas incorporation into sputtered films, J. Appl. Phys. 38(1967)3928.

1968

1. M.D. Adams and S.C. Tong, Laser-microscope system as a microsampling device, Anal. Chem. 40(1968)1762.
2. N.I. Alinovskii, Flight type mass spectrometers for research on plasma bursts, in V.T. Tolok (Ed.), Recent Advances in Plasma Diagnostics, Vol. 3, Corpuscular, Correlation, Bolometric, and other Techniques, Consultants Bureau, New York and London, 1971, pp.30-42. Translated from Diagnostika Plasmy, Vyp. 2, Atomizdat, Moscow, 1968, pp. 338-443.
3. N.I. Alinovskii, Y.E. Mesterikhin and B.K. Pakhtusov, Device for plasma diagnostics with a multicomponent beam of fast neutral particles, in V.T. Tolok (Ed.), Recent Advances in Plasma Diagnostics, Vol. 3, Corpuscular, Correlation, Bolometric, and other Techniques, Consultants Bureau, New York and London, 1971, pp. 25-29. Translated from Diagnostika Plasmy, Vyp. 2, Atomizdat, Moscow, 1968, pp. 338-443.
4. F.J. Allen, A description of laser produced plasmas. I. Electron and ion temperatures. AD-681904 Dec. 1968.
5. S.I. Andreev, Y.I. Dymshits, L.N. Kaporskii, and G.S. Musatova, Thermionic emission and expansion of a plasma formed by focused single pulse laser radiation on a solid target, Sov. Phys. Tech. Phys. 13(1968)657. Translated from Zh. Tekh. Fiz. 38(1968)875.
6. S.I. Anisimov, Vaporization of a metal absorbing laser radiation, Sov. Phys. JETP USSR (English Trans.) 27(1968)182.
7. L.A. Arbuzova, A.M. Bonch-Bruevich, V.A. Danilkin, Y.A. Molchanov, and A.G. Mileshtkin, Analysis of Hydrogen in aluminum and titanium alloys, Metody Opred. Issled. Sostoyaniya Gazov Metal, 1968, p. 269.
8. L.A. Arbuzova, V.A. Kanilkin, Ya.A. Imas, V.A. Molchanov, and A.G. Mileshtkin, Qualitative analysis of the local distribution of hydrogen in metals, Ind. Lab. USSR 34(1968)1440. Translated from Zavod. Lab. 34(1968)1199.
9. T.U. Arifov, G.A. Askar'yan, and N.M. Tatasova, Ionizing action of radiation due to heating of substance in the focus of a laser beam and production of a plasma with high degree of ionization, JETP Lett. USSR 8(3)(1968) 77. Translated from Zh. Eksp. Teor. Fiz., Pis'ma Red. 8(3)(1968)128.
10. N.G. Basov, V.A. Boiko, O.N. Krokhin, O.G. Semenov, and G.V. Sklizkov, Reduction of reflection coefficient for intense laser radiation on solid surfaces, Sov. Phys. Tech. Phys. USSR 13(1969)1581. Translated from Zh. Tekh. Fiz. 38(11)(1968)1973.
11. A.M. Bonch-Bruevich, Y.A. Imas, G.S. Romanov, M.N. Libenson, and L.N. Mal'tsev, Effect of a laser pulse on the reflecting power of a metal, Sov. Phys. Tech. Phys. 13(1968)640. Translated from Zh. Tekh. Fiz. 38(1968)851.
12. Yu.A. Bykovskii, V.I. Dorofeev, V.I. Dymovich, B.I. Nikolaev, S.V. Ryzhikh, and S.M. Sil'nov, Mass spectrometer investigation of ions formed by interaction between laser radiation and matter, Sov. Phys.-Tech. Phys. 13(1969)986. Translated from Zh. Tekh. Fiz. 38(1968)1194.
13. E. Cerrai and R. Trucco, Laser microprobe sampling for qualitative analysis, Energ. Nucl. (Milan) 15(1968)342.
14. P. Contamin, A. Cornu, J.F. Eloy, and R. Stefani, Routine isotopic surface analysis by simple focusing laser mass spectrometry, Paper 135, presented at 16th Annual Conference on Mass Spectrometry and Allied Topics, Pittsburgh, PA, May 1968.
15. H.W. Drawin, Mass spectrometry of plasmas, in W. Lochte-Holtgreven (Ed.), Plasma Diagnostics, Chap. 13, North Holland Publishing Company, Amsterdam, 1968, pp. 777-841.
16. J.F. Eloy, New experiments with laser source mass spectrometer, Methodes Phys. Anal. 4(1968)161.
17. J.F. Eloy, P. Contamin, R. Stefani, and A. Cornu, Surface isotopic analysis by laser source single focusing mass spectrometer, CEA-CONF-1111, Commissariat a l'energie Atomique, Grenoble, France, Centre d'Etudes Nucleaires, April 1968, 13 pp. CONF-680543-1, Paper 135 presented at 16th Annual Conference on Mass Spectrometry and Allied Topics, Pittsburgh, PA, May 12-17, 1968.
18. N.C. Fenner and N.R. Daly, Instrument for mass analysis using a laser, J. Mater. Sci. 3(1968)259.
19. A.F. Haught, D.H. Polk, and W.J. Fader, Production of plasmas for thermonuclear research by laser beam irradiation of solid particles, NYO-3578-10, Dec (1968).
20. M.O. Hobbs, A.J. Getzkin, and R.A. Meyer, Laser quadrupole mass spectrometer system as applied to analysis of inorganic salts, Paper no. 134 presented at 16th Annual Conference on Mass Spectrometry and Allied Topics, Pittsburgh, PA, May 12-17, 1968.
21. G.F. Ivanovskii, L.M. Blyumkin, S.V. Varnakov, and L.P. Lisovskii, Apparatus for mass spectrographic analysis of distribution of gaseous impurities in materials by probing with a laser beam, Ind. Lab. USSR 34(1968)1524. Translated from Zavod. Lab. 34(1968)1263.
22. W.K. Joy, W.R. Ladner, and E. Pritchard, Laser heating of coal particles in the source of a time-of-flight mass spectrometer, Nature (London) 217(1968)640.
23. F.S. Karn and A.G. Sharkey, Pyrolysis of coal macerals by laser irradiation, Fuel 47(1968)193.
24. F.S. Karn and J. Singer, Photographic study of laser irradiation of coal and graphite, Fuel, 47(1968)235.
25. B.E. Knox, Mass spectrometric studies of laser induced vaporization. I. Selenium, Mater. Res. Bull. 3(1968)329.
26. B.E. Knox and V.S. Ban, Mass spectrometric studies of laser induced vaporization. III. The arsenic-selenium system, Mater. Res. Bull. 3(1968)885.



27. B.E. Knox and V.S. Ban, Mass spectrometric studies of the laser induced vaporization of arsenic and various arsenic selenides, Paper 127, presented at 16th Annual Conference on Mass Spectrometry and Allied Topics, Pittsburgh, PA, May 12-17, 1968.
28. B.E. Knox, V.S. Ban, and J. Schottmiller, Mass spectrometric studies of laser induced vaporization. II. The bismuth-selenium system, *Mater. Res. Bull.* 3(1968)337.
29. P. Langer, B. Pin, and G. Tonon, Utilisation du laser dans l'Analyse isotopique d'un echantillon de DLi, *Rev. Phys. Appl.* 3(1968)405.
30. L.P. Levine, J. F. Ready, and E. Bernal G., Production of high energy neutral molecules in laser-surface interaction, *IEEE J. Quantum Electron.* 4(1968)18.
31. K.A. Lincoln, Instrumentation for time resolved mass spectrometry application to laser vaporization of solid materials, AD-669 453, 1968.
32. M. Margoshes and B.F. Scribner, Emission spectrometry with subsection on lasers and microanalysis, *Anal. Chem.* 40(1968)223R.
33. H. Moenke and L. Moenke-Blankenburg, Laser micro- spectrochemical analysis, Crane, Russak and Co., New York, 1973, 261 pp. Translated from *Einführung in die Laser- Mikro-Emissionsspektralanalyse*, 2. Auflage, Akademische Verlagsgesellschaft geest und protig K.-G., Leipzig, 1968.
34. H. Moenke, L. Moenke-Blankenburg, and W. Quillfeldt, Laser-mikro-emissionsspektralanalyse in verschiedenen wellenlangengereichen, *Mikrochim. Acta (Wien)*, Suppl. 3(1968)221.
35. J.L. Pack, T.V. George, and A.G. Engelhardt, Retracting pedestal apparatus that presents a single solid target to a focused Q-switched laser beam, *Rev. Sci. Instrum.* 39(1968)1697.
36. B.E. Paton and N.R. Isenor, Energies and quantities of ions in laser produced metal plasmas, *Can. J. Phys.* 46(1968)1237.
37. G. Tonon and M. Rabeau, Laser-matter interaction intense source of multicharged ions, CEA-CONF-1342, International Conference on Ion Sources, Saclay, France 1968.
38. F.J. Vastola, Analysis of surfaces by laser vaporization, *Appl. Spectrosc.* 22(1968)374. Abstract No. 172, presented at 7th National Meeting of the Society for Applied Spectroscopy, Chicago, IL, May 13-17, 1968.
39. F.J. Vastola, A.J. Pirone, and R.O. Mumma, Analysis of biological related organic salts by laser ionization, Paper 105 presented at 16th Annual Conference on Mass Spectrometry and Allied Topics, Pittsburgh, PA, May 12-17, 1968.
40. V.P. Veiko, Y.A. Imas, A.N. Kokora, and M.N. Libenson, Metal temperature in interaction region with a laser beam, *Sov. Phys. Tech. Phys.* 12(1968)1410. Translated from *Zh. Tekh. Fiz.* 37(1967)1920.
41. H. Weichel, C.D. David, P.V. Avizonis, Effects of radiation pressure on a laser produced plasma, *Appl. Phys. Lett.* 13(1968)376.
42. A.B. Whitehead and H.H. Heady, Laser spark excitation of homogeneous powdered materials, *Appl. Spectrosc.* 22(1968)7.
43. R.H. Wiley and P. Veeravagu, Focussed, coherent radiation (laser) induced degradation of aromatic compounds, *J. Phys. Chem.* 72(1968)2417.
44. P.D. Zavitsanos, Mass spectrometric analysis of carbon species generated by laser evaporation, *Carbon* 6(1968)731.

1969

1. Yu.V. Afanas'ev, N.G. Basov, O.N. Krokhin, N.V. Morachevskii, and G.V. Sklizkov, Gas-dynamic processes in irradiation of solids, *Sov. Phys.-Tech. Phys.* 14(1969)669.
2. Yu.V. Afanas'ev, E.M. Belenov, O.N. Krokhin, and I.A. Poluektov, Ionization process in a laser plasma, *ZhETF. Pis. Red.* 10(2969)553.
3. A.I. Akimov and L.I. Mirkin, Certain regularities in the effect of laser beams on pure metals, *Sov. Phys.-Dokl.* 13(1969)1162.
4. T.U. Arifov, G.A. Askaryan, and N.M. Tarasova, Ionization by ultraviolet radiation emitted from a laser produced plasma, NP-tr-1790. Translated from *Zh. Eksp. Teor. Fiz.* 56(1969)516.
5. V.S. Ban, Mass spectrometric studies of laser induced vaporization of solids, Thesis, Pennsylvania State University, University Park, March 1969, 136 pp. plus addendum. Univ. Microfilms Order No. 70-655.
6. V.S. Ban and B.E. Knox, Mass spectrometric studies of laser produced vapor species, *Int. J. Mass Spectrom. Ion Phys.* 3(1969)131.
7. V.S. Ban and B.E. Knox, Vaporization of antimony and tellurium in the vicinity of the critical point, *J. Chem. Phys.* 51(1969)524.
8. V.S. Ban and B.E. Knox, Mass spectrometric studies of laser induced vaporization of solids, Paper 22, presented at the 17th Annual Conference on Mass Spectrometry and Allied Topics, Dallas, Texas, May 18-23, 1969.
9. E.S. Beatrice, I. Harding-Barlow, and D. Glick, Electric spark cross-excitation in laser microprobe-emission spectroscopy for samples of 10-25 micron diameter, *Appl. Spectrosc.* 23(1969)257.
10. S.M. Bedair and Harold P. Smith, Jr., Atomically clean surfaces by pulsed laser bombardment, *J. Appl. Phys.* 40(1969)4776.
11. W. Boegershausen and K. Hoenle, Temperature measurements for diagnostics of plasmas produced and heated by laser pulses, *Spectrochim. Acta* 24B(1969)71.
12. W. Boegershausen and R. Vesper, Generation and heating of plasmas through absorption of intensive laser beams, (N-74-32185). Translated from *Spectrochim. Acta*, Part B 24(1969)103. 23 p. (NASA-TT-F-15894).
13. Yu.A. Bykovskii, N.N. Degtyarenko, V.I. Dymovich, V.F. Elesin, Yu.P. Kozyrev, B.I. Nikolaev, S.V. Ryzhikh, and S.M. Sil'nov, Energy distribution of the ions produced by a large laser pulse on a solid target, *Sov. Phys.- Tech. Phys.* 14(1970)1269. Translated from *Zh. Tekh. Fiz.* 39(1969)1694.
14. Yu.A. Bykovskii, V.I. Dorofeev, V.I. Dymovich, B.I. Nikolaev, S.V. Ryzhikh, and S.M. Sil'nov, Mass spectrometer with a laser ion source for determination of microimpurities, *Sov. Phys.-Tech. Phys.*

- 14(1970)955. Translated from Zh. Tekh. Fiz. 39(1969)1272.
15. Yu.A. Bykovskii, A.G. Dudoladov, N.N. Degtyarenko, V.F. Elesin, Yu.P. Kozyrev, and I.N. Nikolaev, Angular distribution of a substance having been vaporized by a laser beam, SC-T-70-4007, Sandia Labs., Albuquerque, NM. Translated from Zh. Eksp. Teor. Fiz. 56(1969)1819, 6pp., CFSTI.
16. A. Caruso and R. Gratton, Interaction of short laser pulses with solid materials, Plasma Phys. 11(1969)839.
17. C.D. David and H. Weichel, Temperature of a laser heated carbon plasma, J. Appl. Phys. 40(1969)3674.
18. J.L. Deming, Profiles of laser created cavities on metal surfaces, Amer. Inst. Chem. Eng. J. 15(1969)501.
19. J.F. Eloy, Surface isotopic analysis by a laser source mass spectrometer, Methodes Phys. Anal. 5(1969)157.
20. J.F. Eloy, Ion source with impact laser for a mass spectrograph: Application to exact isotopic analyses of surfaces, Premiere Conference Internationale sur les Sources d'Ions, Saclay, France, June 18-20, 1969, pp.617-33. I.N.S.T.N. 1970, in French. From International Conference on Ion Sources, CONF-690625.
21. O.F. Folmer and L.V. Azarraga, A laser pyrolysis apparatus for gas chromatography, in A. Zlatkis (Ed.), Adv. Chromatogr., pp. 216-221. Proceedings of 5th International Symposium, Las Vegas, NV, January 20-23, 1969, Preston Technical Abstracts, Evanston, IL, 1969.
22. R.E. Honig, Mass spectrometric studies of the interaction of laser beams with solids, in H.J. Schwarz and H. Hora (Eds.), Laser Interaction and Related Plasma Phenomena, Vol. 1, Plenum Press, New York, 1971, pp.85-108. Proceedings of the 1st Workshop held at Rensselaer Polytechnic Inst., East Windsor Hill, CN, June 9-13, 1969.
23. G.F. Ivanovskii and S.V. Varnakov, Analytical characteristics of the method of laser beam probing, Ind. Lab. USSR 35(1969)1151. Translated from Zavod. Lab. 35(1969)959.
24. W.K. Joy and B.G. Reuben, Laser pyrolysis of coal and related materials in the source of a time-of-flight mass spectrometer, in D. Price and J.E. Williams (Eds.), Dynamic Mass Spectrometry, Vol. 1, Heyden, London, 1970, Chap. 13, pp. 183-97. 2nd European Symposium on the Time-of-Flight Mass Spectrometer, Univ. of Salford, England, July 7-11, 1969.
25. F.S. Karn, R.A. Friedel, and A.G. Sharkey, Coal pyrolysis using laser irradiation, Fuel 48(1969)297.
26. A.S. Ketcham, R.C. Hoyer, and G.C. Riggie, The laser in cancer research, Ann. N.Y. Acad. Sci. 168(1970)634. From 2nd Conference of the Laser, May 2-3, 1969.
27. B.E. Knox and V.S. Ban, Laser-solid interaction phenomena, Bull. Am. Phys. Soc. 14(1969)419.
28. M.N. Libenson, G.S. Romanov, and Y.A. Inas, Temperature dependence of optical constants of metal in heating by laser radiation, Sov. Phys. Tech. Phys. 13(1969)925.
29. K. A. Lincoln, Improved instrumentation for time resolved mass spectrometry with application to laser vaporization of solid materials, Int. J. Mass Spectrom. Ion Phys. 2(1969)75.
30. K.A. Lincoln and F.A. Wodley, Mass spectrometric measurement of the thermal velocities of various species evolved from laser vaporized materials, Paper 21 presented at 17th Annual Conference on Mass Spectrometry and Allied Topics, Dallas, TX, May 18-23, 1969.
31. M. Mattioli and D. Vernon, Electron-ion recombination in laser-produced plasma, Plasma Phys. 11(1969)684.
32. G.H. Megrue, Laser microprobe mass spectrometry with applications to meteorite research, in K. Ogata and T. Hayakawa (Eds.), Recent Developments in Mass Spectroscopy, Univ. of Tokyo Press, Tokyo, Japan, 1970, pp. 654-656, Proceedings of International Conference on Mass Spectroscopy, Kyoto, Japan, September, 8-12, 1969.
33. V.G. Mossotti, D.W. Golightly and W.C. Phillips, Laser assisted spark source mass spectrographic trace analysis of semiconducting and nonconducting materials, 15th Colloquium Spectroscopicum Internationale, Madrid, Spain, May 1969.
34. G.L. Pellett and W.R. Cofer, High temperature decomposition of ammonium perchlorate using carbon dioxide laser mass spectrometry, in D. Price (Ed.), Dynamic Mass Spectrometry, Volume 2, Heyden, London, 1971, Chap. 9, pp. 217-236. Based on a paper presented at the AIAA 7th Aerospace Science Meeting, New York, January 20-22, 1969.
35. O.I. Putrenko and A.A. Yankovskii, Some features of laser induced erosion of materials, J. Appl. Spectrosc. USSR 11(1969)1165. Translated from Zh. Prikl. Spektrosk. 11(1969)617.
36. F.A. Richards and D. Walsh, Time resolved temperature measurement of a laser heated surface, J. Phys. D 2(1969)663.
37. R.J. Rockwell, Designs, and functions of laser systems for biomedical applications, Ann. N.Y. Acad. Sci. 68(1970)459. From 2nd Conference on the Laser, New York, NY, 1969.
38. R. Schaeffer and R.K. Pearson, Reaction of carbon vapor produced by laser evaporation of graphite, J. Am. Chem. Soc. 91(1969)2153.
39. H.J. Schwarz and H. Hora, (Eds.), Laser interaction and related plasma phenomena, Volume 1, Plenum Press, New York, 1971. Proceedings of the 1st Workshop, Rensselaer Polytechnic Institute, Hartford Graduate Center, East Windsor Hill, CT, June 9-13, 1969, 520 pp.
40. A.G. Sharkey, A.F. Logar, and F.S. Karn, Laser irradiation of oxidized coals, Fuel, 48(1969)95.
41. K. Taki, Pil Hyon Kim, and S. Namba, Laser induced chemical reaction. I. Reaction of carbon vapor produced by a pulse ruby laser, Bull. Chem. Soc. Jpn. 42(1969)823.
42. K. Taki, Pil Hyon Kim, and S. Namba, Laser induced chemical reaction. II. Reaction induced by a giant pulse laser, Bull. Chem. Soc. Jpn. 42(1969)2377.
43. P. VonGorlich and L. Moenko-Blankenburg, Laser in der Spektrometrie, Exp. Tech. Phys. 2(1969)105.
44. R.H. Wiley and E. Reich, Mechanistic studies of the decomposition process in focussed laser beams, Ann. N.Y. Acad. Sci. 168(1970)610. From 2nd Conference on The Laser, New York, NY, May 2-3, 1969.

1970

1. F.J. Allen, Method of determining ion temperatures in laser produced plasmas, J. Appl. Phys. 41(1970)3048.
2. S.I. Andreev, I.V. Verzhikovskii, and Y.I. Dymshits, Plasma formation in a solid target by a single shot laser, Sov. Phys.-Tech. Phys. 15(1971)1109. Translated from Zh. Tekh. Fiz. 40(1970)1436.

3. J.P. Babuel-Peyrissac, and C. Fauquignon, Effect of very short laser pulses on a solid target, CEA-R-3970, April 1970, 21 p.
4. V.S. Ban and B.E. Knox, Mass spectrometric study of the laser induced vaporization of compounds of bismuth with the elements of group VIA, J. Chem. Phys. 52(1970)243.
5. V.S. Ban and B.E. Knox, Mass spectrometric study of the laser induced vaporization of compounds of arsenic and antimony with the elements of group-VIA, J. Chem. Phys. 52(1970)248.
6. N.G. Basov, V.A. Boiko, Y.A. Drozhbin, S.M. Zakharov, O.N. Krokhin, G.V. Sklizkov, and V.A. Yakovlev, Study of the initial stage of gas-dynamic expansion of a laser flare plasma, Sov. Phys. Dokl. 15(1970)576. Translated from Dokl. Akad. Nauk SSSR 192(1970)1248.
7. J. L. Bobin, Interactions between a laser beam and a solid target, Onde Electr. 50(1970)577.
8. V.F. Brekhovskikh, Possible influence of gas content in metals on the zone of laser beam action, Sov. Phys. Dokl. 15(1970)124. Translated from Dokl. Akad. NAUK SSSR 190(1970)1059.
9. R.P. Burns, Molecular beam-surface interactions, J. Chem. Phys. 52(1970)2152.
10. R.P. Burns and H.L. Blaz, Molecular beam-surface interactions, in A. Quayle (Ed.), Adv. Mass Spectrom. Vol. 5, The Institute of Petroleum, London, 1971, pp. 462-4. Proceedings of a conference held in Brussels, August 31-Sept. 4, 1970.
11. Yu.A. Bykovskii, N.N. Degtyarenko, V.F. Elesin, Yu.P. Kozyrev, and S.M. Sil'nov, The yield and energy distribution of multiply charged ions which are formed as a result of the action of a focused laser beam on tungsten, Radiophys. Quant. Electron. 13(1970)703. Translated from Izv. Vyssh. Uchebn. Zaved. Radiofiz. 13(1970)891.
12. Yu.A. Bykovskii, N.N. Degtyarenko, V.F. Elesin, Yu.P. Kozyrev, and S.M. Sil'nov, Energy spectra of ions formed by laser irradiation of a solid target, Sov. Phys.-Tech. Phys. 15(1971)2020. Translated from Zh. Tekh. Fiz. 40(1970)2578.
13. Yu.A. Bykovskii, V.I. Dymovich, Yu.P. Kozyrev, V.N. Nevolin, and S.M. Sil'nov, Resolving power and measurement of isotopic abundances by a time-of-flight mass spectrometer with a laser ion source, Sov. phys.-Tech. Phys. 15(1971)1877. Translated from Zh. Tekh. Fiz. 40(1970)2401.
14. A. Caruso, A. DeAngelis, G. Gatti, R. Gratton, and S. Martellucci, Energetic ions produced by subnanosecond laser pulses, Phys. Lett. 33A(1970)336.
15. C. DeMichelis, Laser interaction with solids: A bibliographical review, IEEE J. Quantum Electron. 6(1970)630.
16. W. Demtroder and W. Jantz, Investigation of laser produced plasmas from metal surfaces, Plasma Phys. 12(1970)691.
17. W.W. Duley, CO<sub>2</sub> laser induced thermionic emission from metals. Direct energy conversion, Can. J. Phys. 47(1970)2419.
18. J.L. Dumas, Interaction d'un faisceau laser avec une cible metallique. Premiere Partie, Etude de l'echauffement et de la vaporisation de la cible, Rev. Phys. Appl. 5(1970)795.
19. J.L. Dumas, Etude de la photoionisation des cibles metalliques en vue d'application a la spectrometrie de masse, Thesis, University of Grenoble, France, December 1970, 141 pp.
20. G.D. Glebov, N.A. Iofis, and M.S. Chupina, Study of gaseous impurities in the interior, in the surface layer and on the surface of a solid by means of a laser mass spectrometer, Bull. Acad. Sci. USSR, Phys. Ser. 35(1971)594. Translated from Izv. Akad. Nauk SSSR, Ser. Fiz. 35(1971)644. Transactions of 14th All-Union Conference on Emission Electronics, Tashkent, May 11-16, 1970.
21. A.F. Granger and W.R. Ladner, The flash heating of pulverized coal, Fuel, 49(1970)17.
22. T.S. Green, A spectrograph for the simultaneous measurement of velocity spectra and charge-to-mass ratios of ions, Rev. Sci. Instrum. 41(1970)1533.
23. B.T. Guran, R.J. O'Brien, and D.H. Anderson, Design, construction, and use of a laser fragmentation source in gas chromatography, Anal. Chem. 42(1970)115.
24. A.F. Haught and D.H. Polk, Formation and heating of laser irradiated solid particle plasmas, Phys. Fluids 13(1970)2825.
25. A.F. Haught, D.H. Polk, AND W.J. Fader, Magnetic field confinement of laser irradiated solid particle plasmas, Phys. Fluids 13(1970)2842.
26. W.K. Joy, W.R. Ladner, and E. Pritchard, Laser heating of pulverized coal in the source of a time-of-flight mass spectrometer, Fuel 49(1970)26.
27. I.G. Karasev, V. M. Kirillov, V.E. Norskii, V.I. Samoilov, and P.I. Ulyakov, Disintegration of metals by a laser beam, Sov. Phys.-Tech. Phys. 15(1971)1523. Translated from Zh. Tekh. Fiz. 40(1970)1954.
28. F.S. Karn, R.A. Friedel, and A.G. Sharkey, Gases from laser pyrolysis of organic materials, Chem. Ind. (London) (1970)239.
29. F.S. Karn, A.G. Sharkey, A.F. Logar, and R.A. Friedel, Coal investigations using laser irradiation, PB-190 031. United States Dept. of Interior, Bureau of Mines, January 1970, 32 pp. N70-15659, BM-RI-7328.
30. B.E. Knox, Trace analysis of alkali metals in semiconductor materials by laser mass spectrometry, presented at Triennial International Mass Spectrometry Conference, Brussels, Belgium, August 31-September 4, 1970.
31. B.E. Knox, Molecularly and charge states of laser vaporized materials, Symposium on Thermokinetic Effects in Pulsed Energy Deposition, Albuquerque, NM, October 1970.
32. L. Moenke-Blankenburg, J. Mohr, and W. Quillfeldt, Fortschritte der laser-mikroemissionsspektroanalyse in bezug auf die anwendung in der metallkundlichen analytik, Mikrokchim. Acta (Wien), Suppl. 4(1970)229.
33. B.W. Muller, X-ray temperature measurements of laser produced plasmas, Plasma Phys. 13(1970)73.
34. H. Puell, Heating of laser produced plasmas generated at plane solid targets. I. theory, Z. Naturforsch. 25A(1970)1807.
35. H. Puell, H.J. Neusser, and W. Kaiser, Temperature and expansion energy of laser produced plasmas. II. experiments, Z. Naturforsch. 25A(1970)1815.
36. W.T. Ristau and N.W. Vanderborgh, Simplified laser degradation inlet system for gas chromatography, Anal. Chem. 42(1970)1848.

37. F.J. Vastola, The production of ions by laser irradiation of organic solids, Paper J9 presented at 18th Annual Conference on Mass Spectrometry and Allied Topics, San Francisco, CA, June 14-19, 1970.
38. F.J. Vastola, R.O. Mumma, and A.J. Pirone, Analysis of organic salts by laser ionization, *Org. Mass Spectrom.* 3(1970)101.
39. F.J. Vastola, A.J. Pirone, P.H. Given, and R.R. Dutcher, The analysis of coal with the laser mass spectrometer, in R.A. Friedel (Ed.), *Spectrometry of Fuels*, Plenum Press, New York, 1970, Chap. 3, pp. 29-36.
40. F.F. Vodovatov, G.V. Indenbaum, and A.V. Vanyukov, A study of oxygen diffusion in cadmium telluride by mass spectrometer methods, *Sov. Phys.-Solid State* 12(1970)17. Translated from *Fiz. Tverd. Tela*, 1(1970)22.
41. E.D. Vorob'ev and A.S. Pasyuk, Sources of multicharged ions, JINR-P7-5177, Summary of the 14th All-Union Conference on Emission Electronics, Tashkent, May 1970.
42. D.L. Winter and L.V. Azarraga, The fabrication and application of a low power ruby laser assembly as a vaporizer for a TOF mass spectrometer, Paper J8 presented at 18th Annual Conference on Mass Spectrometry and Allied Topics, San Francisco, CA, June 14-19, 1970.
43. H.F. Winters and E. Kay, Gas analysis in films by laser induced flash evaporation and mass spectrometry, Paper K9 presented at 18th Annual Conference on Mass Spectrometry and Allied Topics, San Francisco, CA, June 14-19, 1970.

1971

1. Yu.V. Afanas'ev, E.M. Belenov, O.N. Krokhin, and I.A. Poluektov, Self-consistent regime of heating of matter by a laser pulse under conditions of nonequilibrium ionization, *Sov. Phys. JETP* 33(1971)42.
2. F.J. Allen, Plane electrostatic analyzer for laser produced plasma studies, *Rev. Sci. Instrum.* 42(1971)1423.
3. U.A. Arifov, V.V. Kazanskii, V.B. Lugovskoi, and Z.A. Kayumova, Laser induced integral and spiked emission, *Bull. Acad. Sci. USSR, Phys. Ser.* 35(1971)550. Translated from *Izv. Akad. Nauk SSSR, Ser. Fiz.* 35(1971)599.
4. N.G. Basov, S.D. Zakharov, O.N. Krokhin, P.G. Kryukov, Y.V. Senat-Skii, E.L. Tyurin, A.I. Fedosimov, S.V. Chekalin, and M.Y. Shchelev, Investigations of a plasma formed by ultrashort laser pulses, *Sov. J. Quant. Electron.* 1(1971)2. Translated from *Kvant. Elektron. (Moscow)* 1(1)(1971)4.
5. J.L. Bobin, Flame propagation and overdense heating in a laser created plasma, *Phys. Fluids* 14(11)(1971)2342.
6. J.L. Bobin and G. Tonon, Interaction of a laser beam with a target, *Bull. Inform. Sci. Tech., Commis. Energ. At. Fr.* 160(1971)23, in French.
7. A.M. Bonch-Bruевич, I.V. Aleshin, Y.A. Imas, and A.V. Pavshukov, Absorption of laser radiation in the surface layer of optical glass, *Sov. Phys. Tech. Phys. USSR* 16(1971)479. Translated from *Zh. Tekh. Fiz.* 41(1971)617.
8. Yu.A. Bykovskii, M.F. Gryukhanov, V.G. Degtyarev, N.N. Degtyarenko, V.F. Elesin, I.D. Laptev, and V.N. Nevolin, Angular distribution of the ions of a laser plasma, *JETP Lett.* 14(1971)157. Translated from *Zh. Eksp. Teor. Fiz. Pis'ma Red.* 14(1971)238.
9. Yu.A. Bykovskii, N.N. Degtyarenko, V.F. Elesin, Yu.P. Kozyrev, and S.M. Sil'nov, Mass spectrometer investigation of a laser plasma, *Sov. Phys.-JETP* 33(1971)706. Translated from *Zh. Eksp. Teor. Fiz.* 60(1971)1306.
10. Yu.A. Bykovskii, V.A. Gridin, V.I. Dymovich, Z.I. Matveeva, and V.N. Nevolin, Mass composition of multicomponent geological rocks vaporized by laser radiation, *Sov. Phys.-Tech. Phys.* 16(1971)338. Translated from *Zh. Tekh. Fiz.* 41(1971)442.
11. J.F. Eloy, Semiquantitative chemical analyses by mass spectrometry with ionization by photon bombardment with a ruby laser, AEC-tr-7239, 1971. Translation from *Int. J. Mass Spectrom. Ion. Phys.* 6(1971)101.
12. M. Friedman, Acceleration of heavy ions from a metallic plasma subjected to high electric field, *IEEE Trans. Nucl. Sci.* 19(1972)184. International Conference on Multiply-Charged Heavy Ion Sources and Accelerating Systems, Gatlinburg, TN, October 25-28, 1971.
13. H.R. Gray, Ion and laser microprobes applied to measurement of corrosion produced hydrogen on a microscopic scale, *Corrosion (Houston)* 28(1972)47. Issued as N72-13470, 1971.
14. O.S. Heavens, Basics of lasers and general applications. History, trends, nature of light, Duckworth, London, 1971, 163 pages.
15. N. Inoue, Y. Kawasumi, and K. Miyamoto, Expansion of a laser produced plasma into a vacuum, *Plasma Phys.* 13(1971)84.
16. V.I. Karataev, B.A. Mamyurin, and D.V. Shmikk, New method of focusing ion bunches in time-of-flight mass spectrometers, *Sov. Phys.-Tech. Phys.* 16(1972)1177. Translated from *Zh. Tekh. Fiz.* 41(1971)1498.
17. V.M. Kirillov and P.I. Ulyakov, Ratio of liquid and gaseous phases during the action of focused laser radiation on metals, N71-36858, NASA-TT-F-13,906, National Aeronautics and Space Administration, Washington, DC, September 1971. Translated from *Sootnosheniye Zhidkoy i Gazobraznoy Faz pri Vozdeystvii Sfokusirovannogo Izlucheniya Okg Na Metally, Fiz. Khim. Orab. Mater.* 1(1971)8.
18. B.E. Knox, Laser probe mass spectrometry, in D. Price (Ed.), *Dynamic Mass Spectrometry*, Vol. 2, Heyden, London, 1971, Chap. 2, pp. 61-96.
19. V.S. Koidan, Multichannel energy analysis of ions and fast charge-exchange atoms in the investigation of a high temperature plasma, *Instrum. Exp. Tech. USSR* 14(1971)725. Translated from *Prib. Tekh. Eksp.* 3(1971)63.
20. V.A. Komotskii, Maximum evaporation rate from a metal surface, *Sov. Phys.-Tech. Phys.* 16(1971)168. Translated from *Zh. Tekh. Fiz.* 41(1971)220.
21. O.N. Krokhin, High-temperature and plasma phenomena induced by laser radiation, *Rend. Scu. Int. Fis. Enrico Fermi* 48(1971)278.
22. V.V. Lyubimov, I.A. Fersman, and L.D. Khazov, "Optical" strength of lenses and prisms, *Sov. J. Quant. Electron.* 1(1971)201. Translated from *Kvant. Elektron. (Moscow)* 1(1971)107.

23. M. Mattioli, Recombination processes during the expansion of a laser produced plasma, *Plasma Phys.* 13(1971)19.
24. G.H. Megrue, Distribution and origin of Helium, Neon, and Argon isotopes in apollo 12 samples by in situ analysis with a laser probe mass spectrometer, *J. Geophys. Res.*, 76(1971)4956.
25. R.T. Meyer, A.W. Lynch, and J.M. Freese, Vapor composition and chemical reactions of laser vaporized carbon, Paper L9 presented at 19th Annual Conference on Mass Spectrometry and Allied Topics, Atlanta, GA, May 2-7, 1971.
26. F.P. Miknis and J.P. Biscar, Q-Switched laser induced reactions of thiophene with oxygen, *High Temp. Sci.* 3(1971)478.
27. F.P. Miknis and J.P. Biscar, Q-Switched laser induced reactions of thiacyclobutane and thiacyclopentane with oxygen, *J. Phys. Chem.* 75(1971)725.
28. C.B. Moore, Lasers in chemistry, *Ann. Rev. Phys. Chem.* 22(1971)387.
29. P. Mulser, Electrostatic fields and ion separation in expanding laser produced plasmas, *Plasma Phys.* 13(1971)1007.
30. A. Perez, Laser production of multiply charged heavy ions, *Bull. Inform. Sci. Tech. (Paris)* 160(1971)39.
31. W. P. Poschenrieder, Multiple-focusing time-of-flight mass spectrometers. Part I. TOFMS with equal momentum acceleration, *Int. J. Mass Spectrom. Ion Phys.* 6(1971)413.
32. H. Puehl, W. Spengler, and W. Kaiser, Time-resolved temperature measurements of a laser produced carbon plasma, *Phys. Lett. A* 37(1971)35.
33. J.F. Ready, Effects of high-power laser radiation, Academic Press, New York, 1971, 443 pp.
34. W.T. Ristau and N.E. Vanderborgh, Laser induced degradation of hydrocarbon compounds analyzed using gas-liquid chromatography, *Anal. Chem.* 43(1971)702.
35. N.N. Rykalin and A.A. Uglov, Bulk vapor production by a laser beam acting on a metal, *High Temp.* 9(1971)522. Translated from *Teplofiz. Vys. Temp.* (USSR) 9(1971)575.
36. H. Schwarz, Linear and nonlinear laser-induced emission of ions from solid targets with and without magnetic field, in *Laser Interaction and Related Plasma Phenomena*, H.J. Schwarz (Ed.), New York, Plenum Publishing Corp. 1971. pp. 207-22.
37. H. Schwarz, Influence of magnetic fields on plasmas produced by laser irradiation from solid targets, *Sov. J. Quant. Electron.* 1(1972)512. Translated from *Kvant. Elektron.* (Moscow) 5(1971)102.
38. J.L. Schwob, W. Seka, and C. Breton, Utilization of the x-ray-uv spectra of multiply charged ions in the study of plasmas produced by the impact of a laser beam on bulk targets, *J. Phys. (Paris), Colloq.* 4(1971)44.
39. R.H. Scott, P.F.S. Jackson, and A. Strasheim, Application of laser source mass spectroscopy to analysis of geological material, *Nature (London)* 232(1971)623.
40. A.G. Sharkey, A.F. Logar, and R.G. Lett, Laser time-of-flight mass spectrometer studies of sorbed species and surface reactions, Paper S4 presented at 19th Annual Conference on Mass Spectrometry and Allied Topics, Atlanta, GA, May 2-7, 1971.
41. G.V. Sklizkov, Kinetic and ionization phenomena in laser-produced plasmas, in *Laser Interaction and Related Plasma Phenomena*, H.J. Schwarz (Ed.), New York, Plenum Publishing Corp., pp. 235-57, 1971.
42. K. Taki, Pil Hyon Kim, and S. Namba, Laser induced chemical reaction. III. Decomposition of metal compounds and reaction of decomposed fragments with organic compounds, *Sci. Pap. Inst. Phys. Chem. Res. (Jpn.)* 65(1971)70.
43. G.F. Tonon, Laser source for multiply charged heavy ions, *IEEE Trans. Nucl. Sci.* 19(1972)172. From International Conference on Multiply charged heavy ion sources and accelerating systems, Gatlinburg, TN, October 25, 1971, CONF-711021.
44. F.J. Vastola and R.O. Mumma, The application of laser ionization mass spectrometry to the identification of organic salts in a polluted water, PB-193 797, Pennsylvania State Univ., University park, Institute for Research on Land and Water Resources, 7 pp., NTIS, 1971.
45. M.B. Wolterbeek and T.S. Green, X-ray temperature measurements of laser produced plasmas, *Plasma Phys.* 13(1971)73.
46. S.D. Zakharov, International conference on laser produced plasmas, Moscow, November 17-21, 1970, *Sov. J. Quant. Electron.* 1(1971)308. Translated from *Kvant. Elektron.* (Moscow) 1(1971)123.
47. S.D. Zakharov, O.N. Krokhin, P.G. Kryukov, and E.L. Tyurin, Role of focusing in heat conduction heating of a plasma by high power laser radiation, *Sov. J. Quant. Electron.* 1(1971)198. Translated from *Kvant. Elektron.* (Moscow) 1(1971)104.
48. V.P. Zakharov, I.M. Protas, and V.N. Chugaev, Mass spectrometric investigation of the plasma formed by laser irradiation of a ferrite, *Sov. Phys.-Tech. Phys.* 16(1971)1019. Translated from *Zh. Tekh. Fiz.* 41(1971)1296.
49. B.M. Zhiryakov, N.N. Rykalin, A.A. Uglov, and A.K. Fannibo, Metal Destruction caused by focused laser radiation, *Sov. Phys. Tech. Phys.* 16(1971)815. Translated from *Zh. Tekh. Fiz.* 41(1971)1037.

#### 1972

1. Yu.V. Afanas'ev, E.M. Belenov, O.N. Krokhin, and I.A. Poluektov, Kinetic processes in a laser plasma, *Sov. Phys. JETP* 36(1973)64. Translated from *Zh. Eksp. Teor. Fiz.* 63(1972)121.
2. Yu.V. Afanas'ev and V.B. Rozanov, Energy spectrum of multicharged ions in a laser plasma, *Sov. Phys. JETP* 35(1972)13. Translated from *Zh. Eksp. Teor. Fiz.* 62(1972)247.
3. E.V. Aglitsky, N.G. Basov, V.A. Boiko, V.A. Gribkov, S.A. Zakhorov, O.N. Krokhin, and G.V. Sklizkov, Determination of electron density, velocity, and gas-dynamic pressure in laser plasma, in R.N. Franklin (Ed.) 10th International Conference on Phenomena in Ionized Gases, Donald Parsons and Co., Ltd., Oxford, 1972. pp.229 Conference held in Oxford, England, Sept. 13-18, 1971.
4. C.D. Allemand, Spectroscopy of single-spike laser generated plasmas, *Spectrochim. Acta* 27B(1972)185.

5. F.J. Allen, Production of high-energy ions in laser produced plasmas, *J. Appl. Phys.* 43(1972)2169.
6. M. Bajard (Univ. Lyon, Villeurbanne, France), A. Chabert, T. Tauth, A. Perez, G. Tonon, Laser ion source: Some possibilities for improvement, CONF-720948 11 Sept. (1972).
7. V.A. Batanov, F.V. Bunkin, A.M. Prokhorov, and V.B. Fedorov, Gasodynamic structure of a plasma flare produced by evaporation of metals by intense optical radiation, *Sov. Phys. JETP* 36(1973)654. Translated from *Zh. Eksp. Teor. Fiz.* 63(1972)1240.
8. A. Bonnier and J. Martineau, Temperature laws for laser created plasmas from thin targets, *Phys. Lett.* 38A(1972)199.
9. Yu.A. Bykovskii, V.G. Degtyarev, N.N. Degtyarenko, V.F. Elesin, I.D. Laptev, and V.N. Nevolin, Ion energies in a laser produced plasma, *Sov. Phys.-Tech. Phys.* 17(1972)517. Translated from *Zh. Tekh. Fiz.* 42(1972)658.
10. Yu.A. Bykovskii, N.M. Vasil'ev, N.N. Degtyarenko, V.F. Elesin, I.D. Laptev, and V. N. Nevolin, Formation of the energy spectrum of the ions of a laser plasma, *JETP Lett.* 15(1972)217. Translated from *Zh. Eksp. Teor. Fiz. Pis'ma Red.* 15(1972)308.
11. Yu.A. Bykovskii, N.M. Vasil'ev, N.N. Degtyarenko, and V.N. Nevolin, Possible determination of stoichiometric composition on mass spectrometer with laser ion sources, *Sov. Phys.-Tech. Phys.* 17(1973)1397. Translated from *Zh. Tekh. Fiz.* 42(1972)1749.
12. D. Colombant, A. Perez, and G. Tonon, Ionization processes in heavy ion plasmas created by laser impact, CONF-720948 (1972)586-596.
13. H.J. Dietze and H. Zahn, Eine Ionenquelle für massenspektrographischen Laser-Mikroanalyse an Festkörpern mit dem Laser-Mikrospektroskop LMA-1 (An ion source for mass spectrographic laser microanalysis on solids using the LMA-1 laser microspectral analyzer), *Exp. Tech. Phys.* 20(1972)389. IS-Trans-101, Iowa State University, Ames Laboratory, DOE, Ames, IA, 20 pp.
14. H.J. Dietze and H. Zahn, An ion source for mass spectrographic laser microanalysis on solids using the LMA-1 laser microspectral analyzer, *Exp. Tech. Phys.* 20(1972)389.
15. J.F. Eloy, G. Nief, and A. Cornu, Analytical photon impact mass spectrography using direct ionization by a laser, presented at 2nd International Symposium on Analytical Chemistry, Ljubljana, Yugoslavia, June 12-17, 1972.
16. R.G. Evans and P.C. Thoneman, Laser produced dissociation and ionisation of residual hydrocarbons in a high vacuum system, *Phys. Lett. A* 38(1972)398.
17. D.L. Fanter, R.L. Levy, and C.J. Wolf, Laser pyrolysis of polymers, *Anal. Chem.* 44(1972)43.
18. A. Felske, W.D. Hagenah, and K. Laque, Über Einige Erfahrungen bei der makrospektrographischen Analyse mit Laserlichtquellen. I. Durchschnittsanalyse Metallischer Proben, *Spectrochim. Acta*, Part B 27(1972)1.
19. F.E. Irons, N.J. Peacock, and R.S. Pease, Plasma produced by laser irradiation of solid targets as a source of highly stripped ions, *Sov. J. Quant. Electron.* 2(1972)13. Translated from *Kvant. Elektron.* (Moscow) 1(1972)20.
20. H.B. Kang, T. Yamanaka, K. Yoshida, M. Waki, and C. Yamanaka, Ion temperature of laser-produced plasma, *Jap. J. Appl. Phys.* 11(1972)765.
21. V. I. Karataev, B. A. Mamyrin, and D. V. Shmikk, New method for focusing ion bunches in time-of-flight mass spectrometers, *Soviet Phys.-Tech. Phys.* 16(1972)1177.
22. F.S. Karn, R.A. Friedel, and A.G. Sharkey, Studies of solid and gaseous products from laser pyrolysis of coal, *Fuel* 51(1972)113.
23. R. Kaufmann, F. Hillenkamp, and E. Remy, Die Lasermikrosonde, *Microscopica Acta* 73(1972)1 (in German).
24. B.E. Knox, Laser ion source analysis of solids, in A.J. Ahearn (Ed.), *Trace Analysis by Mass Spectrometry*, Academic Press, New York, 1972, Chap. 14, pp. 423-44.
25. D.W. Koopman, Precursor ionization fronts ahead of expanding laser plasmas, *Phys. Fluids* 15(1)(1972)56.
26. M. Kumar and L. J. Rigby, Laser volatilization of surface layers, in D. Price (Ed.), *Dynamic Mass Spectrometry*, Vol. 3, Heyden, London, 1972, Chap. 14, pp. 283-290.
27. W.F. Leising, Laser prepulse vaporization of aluminum wire targets, Thesis, Ph.D., University of Rochester, New York, 1972, 168 pp., Univ. Microfilms Order No. 73-14,822.
28. K.A. Lincoln, Investigation of laser induced vaporization processes by a new mass spectrometer system, Paper T-5 presented at 20th Annual Conference on Mass Spectrometry and allied Topics, Dallas, TX, June 4-9, 1972.
29. K.A. Lincoln, Laser mass spectrometer, NASA Tech Brief B72-10571, September 1972, 2pp.
30. T. Matoba, Measurements of laser produced plasmas from lithium targets by retarding potential probe, *Japan. J. Appl. Phys.* 11(1972)760.
31. G.H. Megrue and F. Steinbrunn, Classification and source of lunar soils; clastic rocks; and individual mineral, rock, and glass fragments from Apollo 12 and 14 samples as determined by the concentration gradients of the helium, neon, and argon isotopes, *Geochim. Cosmochim. Acta*, Suppl. 3, 36(1972)1899. From Proceedings of 3rd Lunar Science Conference, MIT Press, 1972.
32. R.T. Meyer, J.M. Freese, and A.W. Lynch, Relative partial pressures of carbon vapor species from laser heated graphite, Paper D-3 presented at 20th Annual Conference on Mass Spectrometry and Allied Topics, Dallas, TX, June 4-9, 1972.
33. R.T. Meyer and A.W. Lynch, On mechanism of particle emission from graphites during pulsed laser heating, *High Temp. Sci.* 4(1972)283.
34. F.P. Miknis and J.P. Biscar, High temperature laser induced reactions between sulfur and hydrocarbons, *High Temp. Sci.* 4(1972)48.
35. H. Moenke and L. Moenke-Blankenburg, Mass spectrographic laser microanalysis and emission spectrographic laser microanalysis in inert gas, with the help of the laser microspectral analyzer -- LMA 1, *Mikrochim. Acta* (Wien), Suppl. 5, (1974)377. Presented at 6th Kolloquium Metallkundliche Analyse Berücksichtigung der Elektronenstrahl-Mikroanalyse, October 23-25, 1972.
36. R.O. Mumma and F.J. Vastola, Analysis of organic salts by laser ionization mass spectrometry. Sulfonates, sulfates, and thiosulfates, *Org. Mass Spectrom.* 6(1972)1373.
37. S. Namba, P.H. Kim, and K. Taki, Laser induced chemical reaction -- thermochemical reaction by laser



- heating, in C. Yamanaka (Ed.), Proceedings of the Japan-U.S. Seminar on Laser Interaction with Matter, Japan Society for the Promotion of Science, Japan, pp. 443-54. Conference held in Kyoto, Japan, September 24-29, 1972.
38. R.A. Olstad, Mass spectrometric investigation of laser induced vaporization of binary solid compounds, LBL-1177, Thesis, California University, Berkeley, Lawrence Berkeley Lab., December 1972, 198 pp., NTIS.
  39. H. Pepin, K. Dick, J. Martineau, and K. Parbhaker, Plasma produced by irradiation of thin foils of aluminum by a CO<sub>2</sub>-Tea laser, Phys. Lett. 38A(1972)203.
  40. W. P. Poschenrieder, Multiple-focusing time-of-flight mass spectrometers. Part II. TOFMS with equal energy acceleration, Int. J. Mass Spectrom. Ion Phys. 9(1972)357.
  41. W. P. Poschenrieder and G. H. Oetjen, New directional and energy focusing time-of-flight mass spectrometers for special tasks in vacuum and surface physics, J. Vac. Sci. Technol. 9(1972)212.
  42. H. Puell, H.J. Neusser, and W. Kaiser, Theoretical and experimental investigations of the electron temperature in laser produced plasmas, Sov. J. Quant. Electron. 2(1972)536. Translated from Kvant. Elektron. (Moscow) 6(1972)56.
  43. L.J. Rigby and M. Kumar, Laser volatilization of surface layers, in D. Price (Ed.), Dynamic Mass Spectrometry, Volume 3, Heyden, London, 1972, Chap. 14, pp. 283-90.
  44. W.T. Ristau and N.E. Vanderborgh, Effect of carbon loading upon product distribution of laser induced degradations, Anal. Chem. 44(1972)359.
  45. D. Schirmann, M. Rabeau, G. Tonon, and P. Grelot, Interferometric study of the expansion of a plasma created by a laser, CEA-R-4299, 65 pp., April 1972.
  46. H.J. Schotzau, H.J. Mahler, and F.K. Kneubuhl, Mass Spectroscopy of HCN-laser plasmas with H<sub>2</sub> & D<sub>2</sub>, Phys. Lett. 38A(1972)286.
  47. C.R. Stumpf, J.L. Robitaille, and H.J. Kunze, Investigation of the early phases of plasma production by laser irradiation of plane solid targets, J. Appl. Phys. 43(1972)902.
  48. G. Tonon, A. Perez, C. Faure, D. Parisot, and B. Aveneau, Study of highly multiply charged heavy ions produced in laser plasma, In R.N. Franklin (Ed.), 10th International Conference on Phenomena in Ionized Gases, Donald Parsons and Co., Ltd., Oxford, 1972, pp. 232, held in Oxford, England, September 13, 1971.
  49. G. Tonon, D. Schirmann, and M. Rabeau, Electron and ion temperature measurements of a laser produced plasma, in R.N. Franklin (Ed.), 10th International Conference in Ionized Gases, Donald Parsons and Co., Ltd., Oxford, 1972, pp. 225, held in Oxford, England, September 13, 1971.
  50. M. Waki, T. Yamanaka, H.B. Kang, K. Yoshida, and C. Yamanaka, Properties of plasma produced by high power laser, Japan. J. Appl. Phys. 11(1972)420.
  51. H.F. Winters and E. Kay, Gas analysis in films by laser induced flash evaporation followed by mass spectrometry, J. Appl. Phys. 43(1972)789.
  52. C. Yamanaka, T. Yamanaka, H. Kang, T. Sasaki, K. Yoshida, K. Ueda, M. Hongyo, and M. Waki, Plasma generation and heating by lasers, Sov. J. Quant. Electron. 2(1972)127. Translated from Kvant. Elektron. (Moscow) 2(1972)45.
  53. T. Yamane and S. Matsushita, Influences of a spark plasma on a sample surface in laser emission microspectral analysis, Spectrochim. Acta 27B(1972)27.
  54. H. Zahn and H.J. Dietze, Die massenspektroskopische bestimmung von plasma-parametern in laser mikroplasmen von feststoffen und ihr gesetzmässiger zusammenhang (Mass spectroscopic determination of plasma parameters in laser microplasmas of solids and their mathematical relationships), Exp. Tech. Phys. 20(1972)401. IS-Trans-99, Iowa State University, Ames Laboratory, DOE, Ames, IA, 14 pp.
  55. V.P. Zakharov and I.M. Protas, Mass spectrometric analysis of evaporation of semiconducting A(III)B(V) compounds by a laser, Sov. Phys.-Tech. Phys. 17(1972)528. Translated from Zh. Tekh. Fiz. 42(1972)670.

#### 1973

1. S.I. Anisimov and A.KH. Rakhmatulina, The dynamics of the expansion of a vapour when evaporated into a vacuum, Sov. Phys. JETP 37(1973)441. Translated from Zh. Eksp. Teor. Fiz. 64(1973)869.
2. U.A. Arifov, M.R. Bedilov, T.G. Tsoi, D. Kuramatov, and Kh. Beisenbaeva, Temperature of laser plasma, Dokl. Akad. Nauk Uzb. SSR; No.5(1973)19.
3. A.A. Bakeev, Y.M. Vas'kovskii, N.N. Vorob'eva, V.K. Orlov, and R.E. Rovinskii, Role of a plasma jet in the energy balance of the interaction between laser radiation and matter, Sov. J. Quant. Electron. 3(1973)139. Translated from Kvant. Elektron. (Moscow) 2(1973)77.
4. E.C. Beahm, An investigation of the laser source mass spectrometer, Thesis, Pennsylvania State University, University Park, April 1973, 87 pp. University Microfilms Order No. 74-4215.
5. V.I. Bergel'son, A.P. Golub', I.V. Nemchinov, and S.P. Popov, Formation of a plasma in a vapor layer produced by the action of laser radiation on a solid, Sov. J. Quant. Electron. 3(1974)288. Translated from Kvant. Elektron. (Moscow) 4(1973)20.
6. S.G. Colloff and N.E. Vanderborgh, Time resolved laser induced degradation of polystyrene, Anal. Chem. 45(1973)1507.
7. G.G. Devyatikh, N.V. Larin, G.A. Maksimov, and A.I. Suchkov, The capacity of chemical elements for ionization under the influence of laser radiation, Russ. J. Phys. Chem. 47(1973)1638. Translated from Zh. Fiz. Khim. 47 (1973)2917.
8. J.F. Eloy and R. Stefani, Microanalyses des solides par spectrographie de masse a faisceau laser ionisant, Paper 178, Colloquium Spectroscopium Internationale XVII, Firenze, September 16-22, 1973, Volume 1, pp. 310-15.
9. J.F. Eloy and R. Stefani, Microanalysis of solids by mass spectrometry using an ion laser beam, N75-13058/3SL, Council for Scientific and Industrial Research Pretoria, South Africa, December 1973, 9pp. SCI-T-AER-R-S1304 Report-1134.
10. V.B. Fedorov, V.A. Batanov, V.A. Bogatyrev, and N.K. Sukhodrev, Spectral diagnostics of plasma plume



- produced in intense metal evaporation under laser radiation, *Sov. phys. JETP* 37(1973)419. Translated from *Zh. Eksp. Teor. Fiz.* 64(1973)825.
11. R.R. Goforth and D.W. Koopman, Reflection of background ions by an expanding laser-produced plasma, AD-766893-2 Apr. (1973).
  12. V.K. Goncharov, L.Y. Min'ko, E.S. Tyunina, and A.N. Chumakov, Experimental investigation of the optical properties of laser erosion plasma in the interaction zone, *Sov. J. Quant. Electron.* 3(1973)29. Translated from *Kvant. Elektron. (Moscow)* 1(1973)56.
  13. I. Harding-Barlow and R.C. Rosan, Application of the laser microprobe to the analysis of biological materials, in C.A. Anderson (Ed.), *Microprobe Analysis*, John Wiley, New York, 1973, Chap. 14, pp.477-87.
  14. I. Harding-Barlow, K.G. Snetsinger, and K. Keil, Laser microprobe instrumentation, in C.A. Anderson (Ed.), *Microprobe Analysis*, John Wiley, New York, 1973, Chap. 12, p.423-55.
  15. F. Hillenkamp, R. Kaufmann, and E. Remy, Investigations toward a laser microprobe, *Modern Techniques in Physiological Sciences*, J. F. Gross, R. Kaufmann, and E. Wetterer (Eds.), Academic Press, London/New York, 1973, p. 225.
  16. A.A. Kalmykov and G.N. Rozental, Ionizing properties of radiation emitted from dielectric and metallic surfaces illuminated with a ruby laser beam, *Sov. J. Quant. Electron.* 3(1973)93. Translated from *Kvant. Elektron. (Moscow)* 2(1973)12.
  17. H.B. Kang, M. Waki, K. Yoshida, Y. Sakagami, and T. Yamanaka, Heating of high-z plasma by laser, *J. Phys. Soc. Jap.* 34(1973)504.
  18. K. Keil and K.G. Snetsinger, Applications of the laser microprobe to geology, in C.A. Anderson (Ed.), *Microprobe Analysis*, John Wiley, New York, 1973, Chap. 13, pp. 457-76.
  19. B.E. Knox and E.C. Beahm, Investigation of solid inorganic materials with the laser mass spectrometer, Paper G-9 presented at 21st Annual Conference on Mass Spectrometry and Allied Topics, San Francisco, CA, May 20-25, 1973.
  20. G.R. Levinson and V.I. Smilga, Mechanism of the damage of thin metal films by focused laser radiation, *Sov. J. Quant. Electron.* 3(1973)220. Translated from *Kvant. Elektron. (Moscow)* 3(1973)72.
  21. K.A. Lincoln, Mass spectrometric determination of molecular velocities in laser produced vapor plumes, Paper W-10 presented at 21st Annual Conference on Mass Spectrometry and Allied Topics, San Francisco, CA, May 20-25, 1973.
  22. B.A. Mamyrin, V.I. Karataev, D.V. Shmikk, and V.A. Zagulin, The mass-reflectron, a new nonmagnetic time-of-flight mass spectrometer with high resolution, *Sov. Phys.-JETP* 37(1973)45. Translated from *Zh. Eksp. Teor. Fiz.* 64(1973)82.
  23. M. Margoshes, Application of laser microprobe to the analysis of metals, in C.A. Andersen (Ed.), *Microprobe Analysis*, John Wiley, New York, 1973, Chap. 15, pp. 489-505.
  24. R.T. Meyer, Pulsed laser induced vaporization of graphite and carbides, Paper W-9 presented at 21st Annual Conference on Mass Spectrometry and Allied Topics, San Francisco, CA, May 20-25, 1973.
  25. R.T. Meyer, Pulsed-laser induced vaporization of graphite and carbides, SLA-73-5233, Sandia Labs., Albuquerque, NM, 1973, 2pp., NTIS. CONF-730601-1. Presented at 11th Biennial conference on Carbon, Gatlinburg, TN, June 4-8, 1973.
  26. R.T. Meyer, A.W. Lynch, and J.M. Freese, Chemical reactions of carbon atoms and molecules from laser induced vaporization of graphite and tantalum carbide, *J. Phys. Chem.* 77(1973)1083.
  27. R.T. Meyer, A.W. Lynch, and J.M. Freese, Vapor Composition and chemical reactions of carbon atoms and molecules from graphite and from tantalum carbide heated by laser radiation, LSA-73-57, Sandia Labs., Albuquerque, NM, February 1973, 43 pp., NTIS.
  28. R.T. Meyer and A.W. Lynch, Reevaluation of carbon vapor pressures and third law heats of formation: triatomic carbon, *High Temp. Sci.* 5(1973)192.
  29. J.N. Olsen, G.W. Kuswa, and E.D. Jones, Ion expansion energy spectra correlated to laser plasma parameters, *J. Appl. Phys.* 44(1973)2275.
  30. M. Oron and Y. Paiss, A dynamic mass spectrometer for the study of laser produced plasmas, *Rev. Sci. Instrum.* 44(1973)1293.
  31. A.M. Prokhorov, V.A. Batanov, F.V. Bunkin, and V.B. Fedorov, Metal evaporation under powerful optical radiation, *IEEE J. Quant. Electron.* QE-9(1973)503.
  32. K. Taki, Pil Hyon Kim, and S. Namba, Reactions of hydrocarbons with atomic oxygen produced by laser irradiation of metal oxides, *Sci. Pap. Inst. Phys. Chem. Res. (Jpn.)* 67(1973)82.
  33. G. Tonon and M. Rabeau, Plasma characteristics with TEA-CO<sub>2</sub> laser and wavelength scaling law, *Plasma Phys.* 15(1973)871.
  34. V.P. Zakharov and I.M. Protas, Modification of a spark mass spectrometer with double focusing for investigation the interaction of laser radiation with solids, *Instrum. Exp. Tech. (USSR)* 16(1973)846. Translated from *Prib. Tekh. Eksp.* 3(1973)162.
  35. B.M. Zhiryakov, N.N. Rykalin, A.A. Uglov, and A.K. Fannibo, Some relationships governing the ejection of matter from the zone of interaction with laser radiation, *Sov. J. Quant. Electron.* 3(1973)70. Translated from *Kvant. Elektron. (Moscow)* 1(1973)119.

1974

1. A.V. Antonov, A.R. Zaritskii, and S.D. Zakharov, Collector probe measurements of the parameters of a laser plasma at long distances, *Sov. J. Quant. Electron.* 4(1974)342. Translated from *Kvant. Elektron. (Moscow)* 1(1974)615.
2. C. Bar-Isaac and U. Korn, Moving heat source dynamics in laser drilling processes, *Appl. Phys.* 3(1974)45.
3. C. Bar-Isaac, U. Korn, and S. Shtrikman, Thermoelectric temperature measurements in laser pulsed heating of metals, *Appl. Phys.* 3(1974)285.
4. V.A. Batanov, I.A. Bufetov, S.G. Lukishova, and V.B. Fedorov, Intensive evaporation of germanium and

- silicon by millisecond laser radiation pulses, *Sov. J. Quant. Electron.* 4(1974)248. Translated from *Kvant. Elektron. (Moscow)* 1(1974)436.
5. E. Bernal G., J.F. Ready, and F.J. Allen, Energy spectra of laser produced ions, *J. Appl. Phys.* 45(1974)2980.
  6. V.A. Boiko, O.N. Krokhin, and G.V. Sklizkov, Investigation of the parameters and dynamics of a plasma obtained by sharp focusing of laser radiation on solid targets, in N.G. Basov (Ed.), *Proceedings of the P.N. Lebedev Physics Institute, Vol. 76, Lasers and their Applications*, pp. 183-223, Consultants Bureau, New York and London, 1976. Translated from *Trudy P.N. Lebedev Fizicheskii Institut, Vol. 76, Lazery i ikh Primenenie, Nauka, Moscow*, 1974.
  7. V.A. Boiko, O.N. Krokhin, and G.V. Sklizkov, Study of the parameters and dynamics of a laser plasma, *JPRS-61638*. 2 Apr. 1974.
  8. Yu.A. Bykovskii, N.N. Degtyarenko, V.F. Elesin, V.E. Kondrashov, E.E. Lovetskii, A.N. Polyanchikov, and V.S. Fetisov, Recombination in an expanding plasma, *Sov. Phys.-Tech. Phys.* 19(1974)43. Translated from *Zh. Tekh. Fiz.* 44(1974)73.
  9. Yu.A. Bykovskii, Yu.P. Kozyrev, S.M. Sil'nov, and B.Yu. Sharkov, Spatial structure of an expanding laser plasma consisting of aluminum ions and nuclei, *Sov. J. Quant. Electron.* 4(1974)405. Translated from *Kvant. Elektron. (Moscow)* 1(1974)709.
  10. G.G. Devyatykh, N.V. Larin, G.A. Maksimov, and A.I. Suchkov, Analysis of solids on a time-of-flight mass spectrometer, *J. Anal. Chem. USSR* 29(1974)1313. Translated from *Zh. Anal. Chem.* 29(1974)1516.
  11. I.P. Dobrovolskii and A.A. Uglov, Analysis of the heating of solids by laser radiation allowing for the temperature dependence of the absorptivity, *Sov. J. Quant. Electron.* 4(1974)788. Translated from *Kvant. Elektron. (Moscow)* 1(1974)1423.
  12. H.W. Drawin and F. Emard, Influence of laser radiation on the collisional-radiative recombination and ionization coefficients, *Z. Phys.* 266(1974)257.
  13. W.W. Duley, CO lasers: Effects and applications, Academic Press, New York, 1976, Chaps. 7 and 8.
  14. N.P. Egorov, V.N. Komarov, S.E. Kypriyanov, E.A. Trubacheev, and V.I. Volchenok, Apparatus for mass spectroscopic analysis of plasma in gas-discharge lasers, *Instrum. Exp. Tech. USSR* 17(1974)1743. Translated from *Prib. Tekh. Eksp.* 6(1974)159.
  15. J.F. Friichtenicht, Laser generated pulsed atomic beams, *Rev. Sci. Instrum.* 45(1974)51.
  16. F.T. Greene and G. Radolovich, Mass spectrometric studies of laser plumes formed at atmospheric pressure, Paper L-8 presented at 22nd Annual Conference on Mass Spectrometry and Allied Topics, Philadelphia, PA, May 19-24, 1974.
  17. I. Harding-Barlow, Quantitative laser microprobe analysis, in M.L. Wolbarsht (Ed.), *Laser Applications in Medicine and Biology, Vol. 2*, Plenum Press, New York, 1974, Chap. 4, pp.133-49.
  18. F. Hillenkamp, R. Kaufmann, R. Nitsche, E. Remy, and E. Unsold, Recent results in the development of a laser microprobe, in T. Hall, P. Echlin and R. Kaufmann (Eds.), *Microprobe Analysis as Applied to Cells and Tissues. Proceedings of Conference at Battelle Seattle Research Center, Seattle, Washington, April 30-May 2, 1973*, Academic Press, London and New York, 1974, pp.1-14.
  19. R. Kaufmann, F. Hillenkamp, R. Nitsche, and E. Unsold, The laser microprobe mass analyzer (LAMMA). A new approach in microanalysis of biological materials, *Proceedings of "Micro" 74, Annual Meeting of the Royal Microscopical Society, London, July 8-12, 1974*.
  20. F.F. Kormendi, Laser induced surface temperature rise measurement by field emission technique, *J. Phys. E* 7(1974)1004.
  21. A.R. Larson, Calculations of laser-induced spall in aluminum targets, LA-5619-MS(Rev.), Nov. 1974.
  22. K.A. Lincoln, A new mass spectrometer system for investigating laser induced vaporization phenomena, *Int. J. Mass Spectrom. Ion Phys.* 13(1974)45.
  23. K.A. Lincoln and M.A. Covington, Dynamic sampling of laser induced vapor plumes by mass spectrometry and allied topics, Philadelphia, PA, May 19-24, 1974.
  24. Y.N. Lokhov, V.S. Mospanov, and Y.D. Fifeiskii, Adsorption of laser radiation in a surface layer of a transparent dielectric, *Sov. J. Quant. Electron.* 4(1974)214. Translated from *Kvant. Elektron. (Moscow)* 1(1974)385.
  25. K.W. Marich, Laser microprobe emission spectroscopy biomedical applications, in T. Hall, P. Echlin and R. Kaufmann (Eds.), *Microprobe Analysis as Applied to Cells and Tissues*, Academic Press, New York, 1974, pp. 15-31. *Proceedings of Conference at Battelle Seattle Research Center, Seattle, Wash., April 30-May 2, 1973*.
  26. K.W. Marich, W.J. Treytl, J.G. Hawley, N.A. Peppers, R.E. Meyers, and D. Glick, Improved Q-switched ruby laser microprobe for emission spectroscopic element analysis, *J. Phys. E.* 7(1974)830.
  27. V.V. Mel'nikov, G.A. Maksimov, B.S. Kaverin, G.A. Domrachev, N.V. Larin, and G.G. Devyatykh, Composition and structure of coatings deposited from the vapor phase in thermal decomposition of bis-arene-chromium complexes, *Dokl. Chem. Technol.*, 219(1974)216. Translated from *Dokl. Akad. Nauk SSSR*, 219(1974)929.
  28. C. Merritt, R.E. Sacher, and B.A. Petersen, Laser pyrolysis-gas chromatographic-mass spectrometric analysis of polymeric materials, *J. Chromatogr.* 99(1974)301.
  29. H. Moenke and L. Moenke-Blankenburg, Mass spectrographic laser microanalysis and emission spectrographic laser microanalysis in inert gas, with the help of the laser microspectral analyzer, *Mikrochim. Acta.* 5(1974)577.
  30. D.A. Reilly and P.S. Rostler, Pre-breakdown laser target vaporization and enhanced thermal coupling, AD-A009 297/3SL, 49 p., August 1974.
  31. A.A. Samokhin, Some aspects of the intense evaporation of condensed media by laser radiation, *Sov. J. Quant. Electron.* 4(1975)1144. Translated from *Kvant. Elektron. (Moscow)* 1(1974)2056.
  32. R.A. Savinkov, A.A. Kiselev, and O.P. Obukhov, Localized determination of oxygen, nitrogen, and hydrogen in titanium and niobium alloys by means of a laser, *J. Anal. Chem. USSR* 29(1974)663. Translated from *Zh. Anal. Khim.* 29(1974)779.
  33. V.S. Talaev and V.A. Danilkin, Determination of hydrogen in aluminum alloys by means of a focused laser

- probe, *J. Anal. Chem. USSR* 29(1974)658. Translated from *Zh. Anal. Khim.* 29(1974)773.
34. V.P. Zakharov and I.M. Protas, Mass-spectroscopy investigations of the conditions of formation of amorphous semiconducting films upon condensation from the vapor phase, *Sov. Phys. Dokl.* 19(1974)138.
  35. V.P. Zakharov and I.M. Protas, Mass spectrometry of ionic emission during evaporation of complex substances by activity of laser radiation, *Bull. Acad. Sci. USSR, Phys. Ser.* 38(1974)51. Translated from *Izv. Akad. Nauk SSSR. Ser. Fiz.* 38(1974)238.
  36. V.P. Zakharov and I.M. Protas, Mass spectrometric study of the conditions of semiconductor amorphous film formation in the condensation from the vapour phase, *Sov. Phys. Dokl.* 19(1974)138. Translated from *Dokl. Akad. Nauk SSSR* 215(1974)562.

#### 1975

1. S.I. Anisimov, V.A. Gal'burt, and V.I. Fisher, Structure of the absorption band of a metal subjected to laser radiation, *Sov. Tech. Phys. Lett.* 1(1975)153. Translated from *Pis'ma Zh. Tekh. Fiz.* 1(1975)321.
2. V.V. Apollonov, A.I. Barchukov, N.V. Karlov, A.M. Prokhorov, and E.M. Shefter, Thermal action of high power laser radiation on the surface of a solid, *Sov. J. Quant. Electron.* 5(1975)216. Translated from *Kvant. Elektron. (Moscow)* 2(1975)380.
3. V.I. Bergel'son, T.V. Loseva, I.V. Nemchinov, and T.I. Orlova, Propagation of plane supersonic radiation waves, *Sov. J. Plasma Phys.* 1(1975)498. Translated from *Fiz. Plazmy* 1(1975)912.
4. T.T. Bykova, Y.P. Efimov, and A.M. Tyutikov, Emission of positive ions from the surface of lithium fluoride subject to laser radiation, *Sov. Tech. Phys. Lett.* 1(1975)380. Translated from *Pis'ma Zh. Tekh. Fiz.* 1(1975)872.
5. Y.A. Bykovskii, S.M. Sil'nov, B.Y. Sharkov, and S.M. Shuvalov, Laser plasma electrons, *Sov. J. Quant. Electron.* 5(1975)538. Translated from *Kvant. Elektron. (Moscow)* 2(1975)989.
6. J.C. Couturaud, M. Decroisette, C. Faure, J.C. Griesemann, M. Louis Jacquet, J. Martineau, B. Meyer, C. Batou, M. Rabreau, and A. Saleres, Interaction d'un faisceau laser avec de la matiere, *Bull. Inform. Sci. Tech. (Paris)* 204(1975)17.
7. J. Desserre and J.F. Eloy, Interaction d'un faisceau de lumiere coherente pulsee avec une cible complexe. Application a l'elaboration de composes en couches minces (Interaction of light laser beam pulses with complex targets. Application in case of thin-films compounds), *Bull. Inform. Sci. Tech.*, 204(1975)71.
8. J. Desserre and J.F. Eloy, Interaction d'un faisceau de lumiere coherente pulsee avec une cible complexe: Application a l'elaboration de composes en couches minces, *Thin Solid Films*, 29(1975)29.
9. G.G. Devyatikh, G.A. Maksimov, A.I. Suchkov, and N.V. Larin, Layer-by-layer analysis of solids on a time-of-flight mass spectrometer using a laser ion source, *J. Anal. Chem. USSR* 30(1975)560. Translated from *Zh. Anal. Khim* 30(1975)664.
10. G.G. Devyatikh, B.A. Nesterov, G.A. Maksimov, and N.V. Larin, Structure of the halo produced by laser pulses on a target surface, *Sov. Tech. Phys. Lett.* 1(1975)152. Translated from *Pis'ma Zh. Tekh. Fiz.* 1(1975)318.
11. V.A. Dlugunovich, V.A. Zhdanovskii, and V.N. Snopko, Measuring the reflection capacity of dielectrics during the laser heating of their surfaces, *J. Appl. Spectrosc. USSR* 23(1975)1563. Translated from *Zh. Prikl. Spektrosk.* 23(1975)969.
12. Y.I. Dymshitz and V.G. Neverov, Experimental observation of shielding by a laser produced plasma, *Sov. Tech. Phys. Lett.* 1(1975)253. Translated from *Pis'ma Zh. Tekh. Fiz.* 1(1975)558.
13. A.W. Ehler, High energy ions from a CO<sub>2</sub> laser produced plasma, *J. Appl. Phys.* 46(1975)2464.
14. J.F. Eloy, Application of laser ion sources to the analysis of solids using mass spectrometry (Applications des sources d'ions a laser a l'analyse des solides par spectrometrie de masse), in A. Cornu (Ed.), *Precis de Spectrometrie de Masse Analytique*, Presses Universitaires, Grenoble, France, 1975, ISBN 2706100516, Chap.9, pp. 381-409.
15. J.F. Eloy, Sensibilite du spectrographe de masse a source laser pour la microanalyse des solides, presented at XVIII Colloquium Spectroscopicum Internationale, Grenoble, France, September 15-19, 1975.
16. A.P. Gagarin, V.V. Druzhinin, N.A. Raba, and S.V. Maslenikov, Destructive action of thermal radiation of a laser erosion plasma under "well-shielded" conditions, *Sov. Tech. Phys. Lett.* 1(1975)149. Translated from *Pis'ma Zh. Tekh. Fiz.* 1(1975)311.
17. G.P. Golubev, I.Y. Ivantsov, A.M. Pavlov, A.K. Semenov, and V.P. Filippov, Investigation of pressure in metals acted upon by laser radiation, *Sov. Tech. Phys. Lett.* 1(1975)312. Translated from *Pis'ma Zh. Tekh. Fiz.* 1(1975)711.
18. F.T. Greene and G. Radolovich, Molecular beam mass spectrometric studies of laser plumes formed at atmospheric pressure, Paper N-4 presented at 23rd Annual Conference on Mass Spectrometry and Allied Topics, Houston, TX, May 25-30, 1975.
19. F.T. Greene and G. Radolovich, A mass spectrometric investigation of atmospheric pressure laser plumes, *J. Electrochem. Soc.* 122(1975)261C, Abstract No. 206. Presented at the Electrochemical Society Meeting, Dallas, TX, October 5-9, 1975.
20. R.L. Hanson, N.E. Vanderborgh, and D.G. Brookins, Characterization of oil shales by laser pyrolysis-gas chromatography, *Anal. Chem.* 47(1975)335.
21. F. Hillenkamp, E. Unsold, R. Kaufmann, and R. Nitsche, Laser microprobe mass analysis of organic materials, *Nature (London)* 256(1975)119.
22. F. Hillenkamp, E. Unsold, R. Kaufmann, and R. Nitsche, A high sensitivity laser microprobe mass analyser, *Appl. Phys.* 8(1975)341.
23. J.L. Hirshfield, Laser initiated vacuum arc for heavy ion sources, *IEEE Trans. Nucl. Sci.* 23(1976)1006. International Conference on Heavy Ion Sources, Gatlinburg, TN, October 27, 1975.
24. H. Hora and Y. Ksander, *Laser plasmas and nuclear energy*, Plenum Press, New York, 1975, 454 pp.
25. R. Kaufmann, F. Hillenkamp, R. Nitsche, M. Schurmann, and E. Unsold, Biomedical applications of laser

- microprobe analysis, *J. Microscopie et Biol. Cell.* 22(1975)389.
26. I.D. Kovalev, N.V. Larin, and G.A. Maksimov, Mass spectrometric investigation of ion acceleration in the expansion of a laser plasma of binary compounds, *Sov. Tech. Phys. Lett.* 1(1975)348. Translated from *Pis'ma Zh. Tekh. Fiz.* 1(1975)798.
27. B.M. Kozlov, A.A. Samokhin, and A.B. Uspenskii, Numerical analysis of pulsating evaporation of condensed matter under the action of laser radiation, *Sov. J. Quant. Electron.* 5(1975)1120. Translated from *Kvant. Elektron.* (Moscow) 2(1975)2061.
28. N.N. Kozlova, A.I. Petrukhi, and V.A. Sulyaev, Experimental investigation of beginning of evaporation and appearance of plasma layer on exposure of metals in different gases to laser radiation, *Sov. J. Quant. Electron.* 5(1975)747. Translated from *Kvant. Elektron.* 2(1975)1390.
29. P. Krehl, F. Schwirzke, and A.W. Cooper, Correlation of stress wave profiles and the dynamics of the plasma produced by laser irradiation of plane solid targets, *J. Appl. Phys.* 46(1975)4400.
30. G.W. Kuswa, Experimental studies of collective ion acceleration, *Ann. New York Acad. Sci.* 251(1975)514.
31. T.N. Lee and D.J. Nagel, X-ray emission from laser produced magnesium plasmas, *J. Appl. Phys.* 46(1975)3784.
32. K.A. Lincoln, A modular electronic output system for improved fast response time-of-flight mass spectrometric measurements, Paper I-1 presented at 23rd Annual Conference on Mass Spectrometry and Allied Topics, Houston, TX, May 25-30, 1975.
33. K.A. Lincoln and M.A. Covington, Dynamic Sampling of laser induced vapor plumes by mass spectrometry, *Int. J. Mass Spectrom. Ion Phys.* 16(1975)191.
34. K.A. Lincoln, M.A. Covington, and G.N. Liu, Vaporization response of high temperature materials exposed to pulsed laser radiation, *J. Electrochem. Soc.*, 122(1975)261C Abstract No. 205. Presented at the Electrochemical Society Meeting, Dallas, TX, October 5-9, 1975.
35. V.D. Lokhnygini and A.A. Samokhin, Shielding of a metal surface subject to laser radiation, *Sov. Tech. Phys. Lett.* 1(1975)327. Translated from *Pis'ma Zh. Tekh. Fiz.* 1(1975)749.
36. E.E. Lovetskii, A.N. Polyanichev, and V.S. Fetisov, Ion recombination and acceleration in a laser produced plasma, *Sov. J. Plasma Phys.* 1(1975)422. Translated from *Fiz. Plazmy* 1(1975)773.
37. S. Marcus, J.E. Lowder, S. Malief, and D.L. Mooney, Laser-heating of metallic surfaces, *IEEE J. Quant. Electron.* 11(1975)49.
38. E.S. Marmar, J.L. Cecchi, and S.A. Cohen, System for rapid injection of metal atoms into plasmas, *Rev. Sci. Instrum.* 46(1975)1149.
39. T. McGee, Laser flash photolysis-TOF mass spectrometer system for investigation of gas phase reactions involving polyatomic free radicals, presented at American Chemical Society National Meeting, Philadelphia, PA, April 6-11, 1975.
40. J.C. Means, and E.G. Perkins, Combined laser pyrolysis GC/MS analysis of organic compounds. III. Neutral lipids - a comparison of fragmentation in inert and oxidizing atmospheres, *J. Am. Oil Chem. Soc.* 52(1975)124A. Abstract only.
41. D.R. Olander, Evaporation of solids by laser pulses, Paper N-7 presented at 23rd Annual Conference on Mass Spectrometry and Allied Topics, Houston, TX, May 25-30, 1975.
42. D.R. Olander, Laser vaporization of solids, Paper COLL 48, *Abstr. Papers Am. Chem. Soc.* 170(1975)48.
43. R.A. Olstad and D.R. Olander, Evaporation of solids by laser pulses. I. Iron, *J. Appl. Phys.* 46(1975)1499.
44. R.A. Olstad and D.R. Olander, Evaporation of solids by laser pulses. II. Zirconium hydride, *J. Appl. Phys.* 46(1975)1509.
45. M. Oron, A study of the analogy between ion and light spectrometry leading to the development of a new dynamic mass spectrograph, Thesis, University of Rochester, Rochester, NY, 1975, 118 pp., Univ. Microfilms Order No. 76-24, 018.
46. J.F. Ready, Interaction of high intensity laser radiation with solid surfaces, *J. Electrochem. Soc.* 122(1975)259C.
47. S.A. Reshetnyak and L.A. Shelepin, Kinetics of the formation of multiply charged ions, *Sov. J. Quant. Electron.* 4(1975)969. Translated from *Kvant. Elektron.* (Moscow) 1(1974)1752.
48. E.J. Rolinski, C.J. Oblinger, and C.R. Thomas, Time-resolving mass spectra produced by laser vaporization of solids, Paper N-5 presented at 23rd Annual Conference on Mass Spectrometry and Allied Topics, Houston, TX, May 25-30, 1975.
49. T.E. Romesser and J.T. Tang, Mass analysis of plasma in a laser initiated negative ion source, *Bull. Am. Phys. Soc.* 20(1975)1366.
50. M. Salvat, Model for laser heating of solid targets, N76-20985/7SL, 22 pp., January 1975.
51. F. Schwirzke, H. Brinkschulte, and M. Hashmi, Laser induced desorption of gas from metallic surfaces, *J. Appl. Phys.* 46(1975)4891.
52. D.F. Steverson, E.J. Rolinski, C.J. Oblinger, and M. Hoch, Laser damage evaluation studies of composites, *J. Electrochem. Soc.* 122(1975)259C, Abstract No 193. Presented at Electrochemical Society Meeting, Dallas, TX, October 5-9, 1975.
53. C.R. Thomas, A method of time-resolving the mass spectra produced by laser vaporization of solids, AD-A008 655/3SL, Air Force Institute of Technology, Wright-Patterson Air Force Base, OH, March 1975, 45 pp, NTIS, GNE/PH/75-12.
54. K.R. Thompson, Laser source mass spectroscopy of inclusions in solids, Paper N-6 Presented at 23rd Annual Conference on Mass Spectrometry and Allied Topics, Houston, TX, May 25-30, 1975.
55. A.V. Vinogradov, I.Y. Skobelev, and E.A. Yukov, Determination of plasma density from spectra of helium-like ions, *Sov. J. Quant. Electron.* 5(1975)630. Translated from *Kvant. Elektron.* (Moscow) 2(1975)1165.
56. Nguyen Tho Vyong, Phenomenological mechanism of metal breakdown under the action of laser radiation, *J. Appl. Spectrosc. USSR*, 23(1975)1306. Translated from *Zh. Prikl. Spektrosk.* 23(1975)586.
57. V.P. Vyzhelevskii, I.N. Dernova, V.V. Panteleev, M.L. Petukh, O.I. Putrenko, O.F. Troshin, and A.A. Yankovskii, "Korrall-1", a Laser for Atomic Spectral Analysis, *J. Appl. Spectrosc. USSR* 23(1975)1260. Translated from *Zh. Prikl. Spektrosk.* 23(1975)515.

58. P.S.P. Wei, D.J. Nelson, and R.B. Hall, Laser induced evaporation of solid surfaces, *J. Chem. Phys.* 62(1975)3050.
59. E.F. Zapechel'nyuk, B.S. Mikhailov, and R.B. Tagirov, Emission of neutral molecules and electrons from the surface of an insulator by laser radiation, *Sov. J. Quant. Electron.* 5(1975)1427. Translated from *Kvant. Elektron. (Moscow)* 2(1975)2614.
60. B.M. Zhiryakov, N.I. Popov, A.A. Samokhin, and A.K. Fannibo, Fluctuating metal evaporation under laser radiation, *Sov. Tech. Phys. Lett.* 1(1975)320. Translated from *Pis'ma Zh. Tekh. Fiz.* 1(1975)731.

1976

1. M.L. Aleksandrov, N.A. Konovalova and N.S. Pliss, Determination of the degree of sensitivity of mass spectrometers to microimpurities, *Sov. At. Energy* 41(1976)740. Translated from *At. Energ.* 41(1976)128.
2. I. Apostol, E. Cojocaru, I.N. Mihailescu, I.G. Morjan, and I.M. Popescu, Charge collection measurements of TEA CO<sub>2</sub> laser produced plasma on metallic targets, *Rev. Roum. Phys.* 21(1976)1009.
3. U.A. Arifov, V.V. Kazanskii, V.B. Lugovskoi, and V.A. Makarenko, Emission of negatively charged particles in laser irradiation of tungsten, *Sov. Phys.-Tech. Phys.* 21(1976)239. Translated from *Zh. Tekh. Fiz.* 46(1976)417.
4. R.A. Bingham and P.L. Salter, Materials analysis by laser-probe mass spectrometry, *Int. J. Mass Spectrom. Ion Phys.* 21(1976)133.
5. R.A. Bingham and P.L. Salter, Analysis of solid materials by laser-probe mass spectrometry, *Anal. Chem.* 48(1976)1735.
6. Yu.A. Bykovskii, T.A. Basova, V.I. Belousov, V.M. Gladskoi, V.V. Gorshkov, V.G. Degtyarev, I.D. Laptev, and V.N. Nevolin, Possibility of standard-free quantitative analysis of solid bodies on mass spectrometer with laser ion source, *Sov. Phys.-Tech. Phys.* 21(1976)761. Translated from *Zh. Tekh. Fiz.* 46(1976)1338.
7. Yu.A. Bykovskii, T.A. Basova, V.I. Belousov, V.M. Gladskoi, V.V. Gorshkov, V.G. Degtyarev, I.D. Laptev, and V.N. Nevolin, Resolution and accuracy of mass spectrometric analysis of solids by means of a laser plasma ion source, *J. Anal. Chem. USSR* 31(1976)1528. Translated from *Zh. Anal. Khim.* 31(1976)2092.
8. Yu.A. Bykovskii, S.M. Sil'nov, B.Yu. Sharkov, S.M. Shuvalov, and G.A. Sheroziya, Effect of initial dimension of laser produced plasma on ionization and recombination, *Sov. J. Plasma Phys.* 2(1976)136. Translated from *Fiz. Plazmy* 2(1976)248.
9. D. Colombant and N. Winsor, Fast ions in laser-produced plasmas, *Bull. Am. Phys. Soc.* 21(1976)597.
10. R.J. Conzemius and H.J. Svec, A new laser-arc milliprobe mass spectrometer, Paper M-10, presented at 24th Annual Conference on Mass Spectrometry and Allied Topics, San Diego, CA, May 9-13, 1976.
11. C. Cuna, D. Ianoviciu, and S. Cuna, Spectrometria de masa dubla focalizare folosita in analiza solidelor (double focusing mass spectrometry used in the analysis of solids), *Stud. Cercet. Fiz.* 28(1976)481.
12. G.G. Devyatykh, S.V. Gaponov, I.D. Kovalev, N.V. Larin, V.I. Luchin, G.A. Maksimov, L.I. Pontus, and A.I. Suchkov, Possible chemical analysis of microscopic regions with a laser mass spectrometer, *Sov. Tech. Phys. Lett.* 2(1976)356. Translated from *Pis'ma Zh. Tekh. Fiz.* 2(1976)906.
13. G.G. Devyatykh, I.D. Kovalev, N.V. Larin, and G.A. Maksimov, Determination of binary compound stoichiometry using mass spectrometer with laser source of ions, *Dokl. Phys. Chem.* 226(1976)4. Translated from *Dokl. Akad. Nauk SSSR* 226(1976)109.
14. H.J. Dietze, H. Zahn, and W. Schmidt, Über die form von Ionenimpulsen aus einer Laser Ionenquelle (The shapes of ion impulses from a laser ion source), *Int. J. Mass Spectrom. Ion Phys.* 21 (1976)231. IS-Trans-100, Iowa State University, Ames Laboratory, DOE, Ames, IA, 13 pp.
15. M.G. Drouet, R. Bolton, P. Kieffer, G. Saint-Hilaire, and Z. Szili, Spatial correlation between 1.06  $\mu$ m laser irradiation and emitted current for a plane target, *Phys. Lett.* 59A(1976)210.
16. P.E. Dyer, S.A. Ramsden, J.A. Sayers, and M.A. Skipper, The interaction of CO<sub>2</sub> laser radiation with various solid targets, *J. Phys. D* 9(1976)373. [Correction, 9(1976)1181].
17. J.F. Eloy, Phenomenes resultant de l'interaction laser- materiaux solides et leurs applications, CEA-R-4777, CEA Centre d'Etudes Nucleaires de Fontenay-aux-Roses, Dept. de Chimie Appliquee, France, November 1976, 54 pp.
18. J.F. Eloy and J.P. Zirheld, Possibility of on-line analysis of very short lived nuclei with the aid of a spectrograph equipped with a laser ion source, *Nucl. Instrum. Methods*, 135(1976)111.
19. J.F. Friichtenicht, N.G. Utterback, and J.R. Valles, Intense accelerated metal ion beam utilizing laser blowoff, *Rev. Sci. Instrum.* 47(1976)1489.
20. C.M. Fu and R.P. Burns, A mass spectrometric investigation of chemical reactions between adsorbed species on an alumina surface, *High Temp. Sci.* 8(1976) 353.
21. E. Giovannini, G.B. Principato, and F. Rondelli, Standards for iron, cobalt, nickel, copper, and zinc in laser microprobe emission spectrometry of biological material, *Anal. Chem.* 48(1976)1517.
22. S.S. Glaros, K.G. Tirsell, V.C. Rupert, H.C. Catron, and V.W. Slivinsky, Measurement of high energy ions, UCRL-78427 (Rev. 1) 9 Nov (1976).
23. R.R. Goforth, A multichannel ion mass spectrometer in laser produced plasma studies, *Rev. Sci. Instrum.* 47(1976)548.
24. R.L. Hanson, D.G. Brookins, and N.E. Vanderborgh, Stoichiometric analysis of oil shales by laser pyrolysis-gas chromatography, *Anal. Chem.* 48(1976)2210.
25. W.C. Ho, A.F. Leung, Y.T. Fung, and C.C. Chang, Surface effect on laser induced damage in thin metal films, *Thin Solid Films* 38(1976)L9.
26. D.O. Hummel, Structure and degradation behaviour of synthetic polymers using pyrolysis in combination with field ion mass spectrometry, in C.E.R. Jones and C. A. Cramers (Eds.), *Analytical Pyrolysis*, Elsevier, Amsterdam, 1977, pp. 117-38. Proceedings of 3rd International Symposium on Analytical Pyrolysis, Amsterdam, September 7-9, 1976.
27. J.F. Kephart, Measurements of angular distribution of energetic ions from laser-produced plasmas, *Bull. Am.*

- Phys. Soc. 21(1976)11.
28. R. Kirchheim, U. Nagorny, K. Mair, and G. Tolg, Laser microprobe spectrometry of single crystal metals and alloys, *Anal. Chem.* 48(1976)1505.
  29. P.G. Kistemaker, A.J.H. Boerboom, and H.L.C. Meuzelaar, Laser pyrolysis mass spectrometry: Some aspects and applications to technical polymers, in D. Price and J.F.J. Todd (Eds.), *Dynamic Mass Spectrometry*, Vol. 4, Heyden, London, 1976, Chap. 9, pp. 139-52.
  30. P.G. Kistemaker, H.H. Tuithof, A.J.H. Boerboom, B. Neering, and H.L.C. Meuzelaar, Laser pyrolysis-mass spectrometry of biopolymers, in C.E.R. Jones and C.A. Cramers (Eds.), *Analytical Pyrolysis*, Elsevier, Amsterdam, 1977, p. 420. Proceedings of 3rd International Symposium on Analytical Pyrolysis, Amsterdam, September 7-9, 1976.
  31. R.D. Macfarlan and D.F. Torgerson, 252Cf-Plasma desorption time-of-flight mass spectrometry, *Int. J. Mass Spectrom. Ion Phys.* 21(1976)81.
  32. W.E. Maher and R.B. Hall, Experimental study of effects from two laser pulses, *J. Appl. Phys.* 47(1976)2486.
  33. G.A. Maksimov and N.V. Larin, Mass spectrometric analysis of solids using laser ion sources, *Russ. Chem. Rev.* 45(1976)1091. Translated from *Usp. Khim.*, 45(1976)2121.
  34. J.C. Means and E.G. Perkins, Laser pyrolysis GC/MS of membrane components, in Jones, C.E.R., and Cramers, C.A. (Eds.), *Proceedings of 3rd International Symposium on Analytical Pyrolysis*, Elsevier Scientific Publishing Co. Amsterdam, Oxford, and New York, pp. 249, held in Amsterdam, Sept. 7, 1976.
  35. C. Merritt, M.L. Bezinet, R.E. Sacher, and J. Sprouse, Laser pyrolysis-gas chromatographic-mass spectrometric analysis of epoxy composites, in C.E.R. Jones and C.A. Cramers (Eds.), *Analytical Pyrolysis*, Elsevier Scientific Publishing Co., Amsterdam, 1977. Proceedings of 3rd International Symposium on Analytical Pyrolysis, September 7-9, 1976.
  36. M. Oron, Static-field mass spectrograph for laser produced plasma experiments, *Nucl. Instrum.* 139(1976)235.
  37. I. Pelah, Diagnosis of laser produced plasma with charge collectors, *Phys. Lett. A*, 59(1976)348.
  38. T. Plieninger and O.A. Schaeffer, Laser probe Ar(39)- Ar(40) ages of individual mineral grains in lunar basalt 15607 and lunar breccia 15465, Proceedings of the 7th Lunar Science Conference, Houston, TX, March 15-19, 1976. Volume 2, *Petrogenetic Studies of Mare and Highland Rocks*, Pergamon Press, New York, 1976, pp. 2055-66. *Geochim. Cosmochim. Acta*, Suppl. 7.
  39. J.F. Ready, Change of reflectivity of metallic surfaces during irradiation by CO<sub>2</sub>-TEA laser pulses, *IEEE J. Quant. Electron.* 12(1976)137.
  40. T.E. Romesser and J.T. Tang, Mass analysis of plasma in a laser initiated negative ion source, *J. Appl. Phys.* 47(1976)1929.
  41. T.E. Sharp and B.A. Watson, Intensity calibration of ion spectrograph for laser plasmas, *Bull. Am. Phys. Soc.* 21(1976)1173. Abstract of paper presented at 18th Annual Meeting of the Division of Plasma Physics of the American Physical Society, San Francisco, CA, November 15-19, 1976.
  42. D.H. Sliney, W.J. Marshall, P.F. Del Valle, J.K. Franks, and T.L. Lyon, Laser hazard classification guide, PB-266497, Army Environmental Hygiene Agency, Aberdeen Proving Ground, MD, July 1976, 213 pp., NTIS.
  43. R. Stefani, Mass spectrometry: a versatile aid to inorganic analysis, in N.R. Daly (Ed.), *Advances in Mass Spectrometry*, Volume 7A, Heyden for the Institute of Petroleum, London, 1978, pp. 729-50. Proceedings of 7th International Mass Spectrometry Conference, Florence, Italy, August 30-September 3, 1976.
  44. S.P. Tang and J.F. Friichtenicht, Studies of laser generated atomic beams and metal oxide chemiluminescent reactions, *Prog. Astronaut. Aeronaut.* 51(1977)1061. presented at 10th International Symposium on Rarefied Gas Dynamics, Aspen, CO, July 19-23, 1976.
  45. S.P. Tang, N.G. Utterback, and J.F. Friichtenicht, Measurement of chemiluminescent reaction cross sections for B + N<sub>2</sub> yields BO\* + N<sub>2</sub> and Ho + N<sub>2</sub> yields HoO + N<sub>2</sub>, *J. Chem. Phys.* 64(1976)3833.
  46. K.R. Thompson, Mass spectrometry of inclusions in solids by laser vaporization, *Anal. Chem.* 48(1976)696.
  47. H.H. Tuithof, A.J.H. Boerboom, P.G. Kistemaker, and H.L.C. Meuzelaar, A magnetic mass spectrometer with simultaneous ion detection and variable mass dispersion in laser pyrolysis and collision induced dissociation studies, in N.R. Daly (Ed.), *Advances in Mass Spectrometry*. Volume 7B, Heyden for Institute of Petroleum, London, 1978, pp. 838-45. Proceedings of 7th International Mass Spectrometry Conference, Florence, Italy, August 30-Sept. 3, 1976.
  48. E. Unsold, F. Hillenkamp, and R. Nitsche, Laser microprobe mass analysis of biological tissues, *Analysis* 4(1976)115.
  49. N.G. Utterback, S.P. Tang, and J.F. Friichtenicht, Atomic and ionic beam source utilizing pulsed laser blow-off, *Phys. Fluids* 19(1976)900.
  50. N.E. Vanderborgh, Laser induced pyrolysis techniques, LA-UR-76-1952, Los Alamos Scientific Laboratory of the University of California, Los Alamos, NM, 1976, 15 pp., CONF-7609821-1. Presented at 3rd International Symposium on Analytical Pyrolysis, Amsterdam, September 7-9, 1976.
  51. N.E. Vanderborgh, Laser induced pyrolysis techniques, in C.E.R. Jones and C.A. Cramers (Eds.), *Analytical Pyrolysis*, Elsevier, Amsterdam, 1977, pp. 235-48. Proceedings of 3rd International Symposium on Analytical Pyrolysis, Amsterdam, September 7-9, 1976.
  52. V.P. Velyukhanov, G.V. Mikhailova, L.L. Kunin, and Y.A. Kulakov, Determination of gaseous impurities in metal films by laser-mass spectrometry, *J. Anal. Chem. USSR* 31(1976)768. Translated from *Zh. Anal. Khim.* 31(1976)946.
  53. H. Zahn and H.J. Dietze, Die bestimmung der anzahl der ionen, elektronen, und atome in lasermikroplasmen von feststoffen (Determining the number of ions, electrons, and atoms in laser microplasmas from solids), *Int. J. Mass Spectrom. Ion Phys.*, 22(1976)111. IS-Trans-98, Iowa State University, Ames Laboratory, DOE, Ames, IA, 12 pp.
  54. E.F. Zapechel'nyuk, B.S. Mikhailov, and R.B. Tagirov, Emission of neutral molecules and electrons from the surface of an insulator by laser radiation, *Sov. J. Quant. Electron.* 5(1976)1427.



1. V.S. Antonov, I.N. Knyazer, V.S. Letokhov, V.M. Matyuk, V.G. Movshev, and V.K. Potapov, Selective stepwise photoionization of molecules by laser radiation in a mass spectrometer, *Sov. Tech. Phys.* 3(1977)531.
2. N.G. Basov (Ed.), Temporal characteristics of laser pulses and interaction of laser radiation with matter, Volume 84 in the Lebedev Inst. Series, Plenum, New York, 1977, 200 pp. Translated from the Russian.
3. V.V. Berezovskii, Yu.A. Bykovskii, S.M. Sil'nov, A.I. Suslov, B.Yu. Sharkov, and S.M. Shuvalov, Ion composition in the plasma produced by a CO<sub>2</sub> laser, *Sov. Tech. Phys. Lett.* 3(1977)126. Translated from *Pis'ma Zh. Tekh. Fiz.* 3(1977)310.
4. J.L. Bobin, W. Woo, and J.S. Degroot, Force ponderomotrice, champs magnetiques et hydrodynamique des plasmas produits par laser, *J. Phys. (Paris)* 38(1977)769.
5. A.J.H. Boerboom, P.G. Kistemaker, M.A. Posthumus, and H.L.C. Meuzelaar, Simultaneous opto-electrical ion selection of submicrosecond laser induced desorption processes, in D. Price and J.F.J. Todd (Eds.), *Dynamic Mass Spectrometry*, Vol. 5, Chap. 9, Heyden, London, 1978 pp. 114-118. International Symposium held at the University of Salford, England, July 5-7, 1977.
6. A.F. Bokhonov, V.S. Burakov, V.V. Zhukovskii, and A.A. Stavrov, Erosion due to radiation activity of lasers in the mode-locked regime, *J. Appl. Spectrosc.* 26(1977)588. Translated from *Zh. Prikl. Spektrosk.* 26(1977)821.
7. G. Brochard and J.F. Eloy, Identifications analytiques de differentes peintures de carrosserie automobile par spectrographie de masse a sonde laser (Analytical identification of different automobile paints using laser probe mass spectrography), *Analysis* 5(1977)242.
8. G. Brochard and J.F. Eloy, Applications of a laser probe mass spectrograph to localized microanalysis in forensic science, Paper MC-1 presented at 25th Annual Conference on Mass Spectrometry and Allied Topics, Washington, DC, May 29-June 3, 1977.
9. A.I. Busygin, Quantitative analysis of solids in a mass Lett. 3(1977)459. Translated from *Pis'ma Zh. Tekh. Fiz.* 3(1977)1116.
10. A.I. Busygin, Residual ionization in the expansion of a laser produced plasma, *Sov. Tech. Phys. Lett.* 3(1977)468. Translated from *Pis'ma Zh. Tekh. Fiz.* 3(1977)1137.
11. T.T. Bykova, E.F. Lazneva, and A.F. Tavasiev, Laser stimulated desorption of oxygen from cadmium selenide films, *Sov. Tech. Phys. Lett.* 3(1977)189. Translated from *Pis'ma Zh. Tekh. Fiz.* 3(1977)467.
12. Yu.A. Bykovskii, L.M. Babenkov, T.A. Basova, V.I. Belousov, V.M. Gladskoi, V.V. Gorshkov, V.G. Degtyarev, I.D. Laptev, and V.N. Nevolin, High yield laser ion source with plasma focusing for mass spectrometric analysis of solids, *Instrum. Exp. Tech. USSR* 20(1977)508. Translated from *Prib. Tekh. Eksp.* 2(1977)163.
13. Yu.A. Bykovskii and Yu.P. Kozyrev, Multicharged ions in a laser plasma, *Priroda, Moscow* 5(1977)54, in *Russian Chem. Abstr.*, 87-76121.
14. Yu.A. Bykovskii, S.M. Sil'nov, B.Yu. Shrkov, G.A. Sheroziya, and S.M. Shuvalov, Laser produced plasma of two component mixtures, *Sov. J. Plasma Phys.* 3(1977)639. Translated from *Fiz. Plasmy* 3(1977)1153.
15. P.W. Chan, Y.W. Chan, and H.S. Ng, Reflectivity of metals at high temperatures heated by pulsed laser, *Phys. Lett.* 61A(1977)151.
16. C.T. Chang, M. Hashmi, and H.C. Pant, Study of a laser produced plasma by Langmuir probes, *Plasma Phys.* 19(1977)1129.
17. N.R. Daly and R.E. Powell, Use of a new type of plasma- ion analyzer to determine the hydrogen content of metals, *Rev. Sci. Instrum.* 48(1977)1336.
18. R. Decoste and B.H. Ripin, High energy ion analyzer for laser produced plasma studies, *Rev. Sci. Instrum.* 48(1977)232. AD-A038 174/9SL.
19. R. Decoste and B.H. Ripin, High energy ions from a Nd laser produced plasma, *Appl. Phys. Lett.* 31(1977)68. AD-A046 799/3SL. NRL-MR-3549.
20. C. Denus, J. Farny, Z. Wereszczynski, J. Wolowski, and E. Woryna, Application of ion diagnostics for the study of plasma produced by a laser beam focused on Z greater than 5 targets, *J. Tech. Phys., Warsaw* 18(1977)25.
21. G.A. Doschek, U. Feldman, P.G. Burkhalter, and T. Finn, Highly directional expansion of laser-produced plasmas, *J. Phys. B (London)* 10(1977)L745.
22. M.G. Drouet, Duration of the source of the current in laser produced plasmas, *Phys. Lett.* 63A(2)(1977)99.
23. J.F. Eloy, Chemical analysis of biological materials with the laser probe mass spectrograph, in *Microscopica Acta*, Suppl. 2. Microprobe Analysis in Biology and Medicine, pp. 307-17. Echlin, P. and Kaufmann, R. (Eds.), S. Hirzel Verlag, Stuttgart, 1978. From International Conference, Muenster, Germany, Sept. 4-8, 1977.
24. H. Endert, D. Malz, and K. Vogler, Materialabtrag und plasmaanregung bei bestrahlung von festkorper targets mit CO<sub>2</sub>-TEA laserstrahlung. I. Materialabtrag und verdampfung. (Material excavation and plasma excitation by irradiation of solid targets with focused CO<sub>2</sub>-TEA laser radiation. I. Material excavation and evaporation), *Exp. Tech. phys.* 25(1977)27.
25. F.S. Felber and R. Decoste, Fast ions from laser plasmas: Analytic solution and scaling laws, AD-A047 399/1SL, Naval Research Laboratory, Washington, DC, September 1977, 11 pp, NRL-MR-3578.
26. J.R. Greig, Molecular emissions from laser-solid target interactions, *J. Appl. Phys.* 48(12)(1977)5382.
27. J.R. Greig and R.E. Pechacek, Disintegration and vaporization of plastic targets irradiated by high- power laser-pulses, *J. Appl. Phys.* 48(2)(1977)596.
28. R.L. Hanson, N.E. Vanderborgh, and D.G. Brookins, Characterization of coal by laser pyrolysis-gas chromatography, *Anal. Chem.* 49(1977)390.
29. R.J. Harrach, Theory for laser induced breakdown over a vaporizing target surface, UCRL-52389, Lawrence Livermore, Lab., Univ. of Calif., Livermore, CA, December 1977, NTIS.
30. J.B. Hartung, T. Plieninger, H.W. Muller, and O.A. Schaeffer, Helium, neon, and argon on sunlit and shaded surfaces of lunar rock 12054, *Proc. Lunar Sci. Conf. 8th*, 8650881, 1977. From Proceeding of the 8th Lunar



- Science Conference, Houston, TX, March 14-18, 1977, Vol. 1. The Moon and the Inner Solar System, Pergamon Press, New York, 1977.
31. H. Hora and H.J. Schwarz, Fourth International Workshop on Laser Interaction and Related Plasma Phenomena at RPI, Troy, November 8-12, 1976. *Laser-plasma-interaction*, Atomkernenergie 30(1977)70.
  32. B.A. Huber, T.M. Miller, P.C. Cosby, H.D. Zeman, R.L. Leon, J.T. Moseley, and J.R. Peterson, Laser-ion coaxial beams spectrometer, *Rev. Sci. Instrum.* 48(1977)1306.
  33. J.C. Koo, Laser induced explosion of solid material, *J. Appl. Phys.* 48(1977)618.
  34. J.D. Kovalev, G.A. Maksimov, and A. Suchkov, Analytical characteristics of laser mass spectrometers, *Poluck. Anal. Chist. Veshchestv* 2(1977)71 (Russ.).
  35. F.R. Krueger, Mechanism of fission-fragment induced desorption (Zum mechanismus der spaltfragment-induzierten desorption), *Z. Naturforsch. Teil A* 32(1977)1084.
  36. R.M. Lum, Direct analysis of polymer pyrolysis using laser microprobe techniques, *thermochim. Acta* 18(1977)73. Paper presented at 6th North American Thermal Analysis Society Conference, Princeton, NJ, June 20-23, 1976.
  37. T.H. Maiman, Laser applications, *Phys. Today* July(1977)24.
  38. E.A. McLean, R. DeCoste, B.H. Ripin, J.A. Stamper, H.R. Griem, J.M. McMahon, and S.E. Bodner, Spectroscopic observation of fast ions from laser produced plasmas, *Appl. Phys. Lett.* 31(1977)9.
  39. H.W. Muller, T. Plieninger, O.B. James, and O.A. Schaeffer, Laser probe Ar39 Ar40 dating of materials from consortium breccia 73215. Proceedings of the 8th Lunar Science Conference, Houston, TX, March 14-18, 1977, pp. 2551-65. Volume 2. Petrogenetic Studies of Mare and Highland Rocks, Pergamon Press, New York, 1977.
  40. G.L. Payne, J.D. Perez, T.E. Sharp, and B.A. Watson, Effects of recombination in expansion of laser produced plasmas, *B. Amer. Phys. Soc.* 22(1977)1181.
  41. J.S. Pearlman, Faraday cups for laser plasmas, *Rev. Sci. Instrum.* 48(1977)1064.
  42. M.A. Posthumus, P.G. Kistemaker, H.L.C. Meuzelaar, and M.C. Ten Noever de Brauw, Laser desorption mass spectrometry of polar nonvolatile bio-organic molecules, preprint of paper presented in part at 4th International Symposium on Mass Spectrometry in Biochemistry and Medicine, Riva del Garda, Italy, June 20-22, 1977 and at International Mass Spectrometry Symposium on Natural Products, Rehovot, Israel, August 28-September 2, 1977.
  43. A.T. Prengel, J. DeHaven, E.J. Johnson, and P. Davidovits, Production of neutral atoms by pulsed laser heating, *J. Appl. Phys.* 48(1977)3551.
  44. J.F. Ready, An investigation of laser interactions, AD-A050 049, Final Progress Report, December 15, 1972-September 30, 1977, November 1977, 67 pp., AFOSR-TR-78-0070, NTIS.
  45. M. Ross (Ed.), Laser applications, Volume 3, Academic Press, New York, 1977.
  46. A.V. Savchenko, P.N. Sairkunov, and V.V. Smirnov, Emission of ions as a result of laser heating of electrolyte drops, *Sov. J. Quant. Electron.* 7(1977)1248. Translated from *Kvant. Elektron.* (Moscow) 4(1977)2182.
  47. O.A. Schaeffer, H.W. Muller, and T.L. Grove, Laser Ar-39 Ar-40 study of Apollo 17 basalts, Volume 2, Petrogenetic Studies of Mare and Highland Rocks, Pergamon Press, New York, 1977, pp. 1489-1499, *Geochim. Cosmochim. Acta*, Suppl. 8. Proceedings of the 8th Lunar Science Conference, Houston, TX, March 14-18, 1977, pp. 1489-99.
  48. J. Smalley, The remote measurement of sulphur in steels by mass spectrometry, *Vacuum* 27(1977)555.
  49. D.C. Smith, Gas breakdown initiated by laser radiation interaction with aerosols and solid surfaces, *J. Appl. Phys.* 48(1977)2217.
  50. C. Stenz, C. Popovics, E. Fabre, J. Virmont, A. Poquerusse, and C. Garban, Correlation entre le rayonnement X et l'émission d'ions rapides dans l'interaction laser CO<sub>2</sub>-cible, *J. Phys. (Paris)* 38(1977)761.
  51. K. Toyoda, P. H. Kim, Y. Okabe, and S. Namba, Ion sources utilizing TEA carbon dioxide laser irradiation, *Rikagaku Kenkyusho Hokoku* 53(1977)70.
  52. M.H. Tuillier and B. Lacour, Soft X-ray emission from picosecond laser plasmas, *J. Phys. B* 10(1977)1407.
  53. P. Waegli, A wide energy range mass spectrograph for measurements of the ion energy and mass distributions of fast pulsed sources, *Z. Angew. Math. Phys. (J. Math. Phys. Appl.)* 29(1978)358. From Rapport de la Societe Suisse de physique, Berne, Switzerland, October 7-8, 1977. Abstract only.
  54. P.S.P. Wei, A spectroscopic study of the evaporation of aluminum as irradiated by a long pulse Nd laser, *J. Appl. Phys.* 48(1977)4196.
  55. C. Yamabe, E. Setoyama, A. Thein, M. Yokoyama, and C. Yamanaka, Interaction of TEA CO<sub>2</sub> laser light with laser produced plasma, *Jpn. J. Appl. Phys.* 16(1977)131.
  56. B.K. Zuev, G.N. Kasatkin, and G.V. Mikhailova, Laser mass spectrometric study of hydrogen distribution in the region of sulfide inclusions in steel 30KhNM, *Metody Opredeleniya Nemegal. Dr. Vred. Primesei Prom. Materialakh.* 12-17, 1977.
  57. B.K. Zuev (Zouev), Yu.A. Kulakov (Koulakov), L.L. Kunin (Kounin), and G.V. Mikhailova, L'Analyse de la distribution de l'Hydrogene selon les composants de la structure et pour macrodefauts des corps solides en utilisant la methode de mass spectrometrie a laser (The investigation of the distribution of the hydrogen on the structural components and on the macrodefects of solid states by using the laser mass spectrometer), Paper 1F4 of Hydrogen in Metals, Volume 7, Pergamon Press, NY, 1977. From 2nd International Congress, Paris, France, June 1977, CONF-770613-P7.
  58. B.K. Zuev, Yu.A. Kulakov, L.L. Kunin, G.V. Mikhailova, examining hydrogen distribution in chromium plated steel, *Ind. Lab. USSR* 43(1977)539. Translated from *Zavod. Lab.* 43(1977)456.

1978

1. C.L. Allyn, T. Gustafsson, and E.W. Plummer, Analyzer system capable of determining energy and direction of charged particles in ultrahigh vacuum, *Rev. Sci. Instrum.* 49(1978)1197
2. J.P. Anthes, M.A. Gusinow, and K. Matzen, Experimental observation and numerical simulations of laser

- driven ablation, *Phys. Rev. Lett.* 41(1978)1300.
3. V.S. Antonov, I.N. Knyazev, V.S. Letokhov, V.M. Matiuk, V.G. Movshev, and V.K. Potapov, Stepwise laser photoionization of molecules in a mass spectrometer: A new method for probing and detection of polyatomic molecules, *Opt. Lett.* 3(1978)37.
4. F. Aussenegg (Ed.), *Laserspektroskopie: Neue Entwicklungen und Anwendungen*, Acta Phys. Austriaca, Suppl. XI, 1979. Springer-Verlag, Wien and New York, 1979, 300 pp. Vorträge der 3rd Fachtagung des Fachausschusses Elektrodynamik und Optik der Österreichischen Physikalischen Gesellschaft an der Universität Graz, June 19-21, 1978.
5. R.M. Barnes, Emission spectroscopy (review)/with subsection on laser analysis, *Anal. Chem.* 50(1978)100R.
6. R.A. Beyer, Molecular beam sampling mass spectrometry of high heating rate pyrolysis: Description of data acquisition system and pyrolysis of HMX in a polyurethane binder, AD-A054328. Memorandum report ARBRL-MR-02816, U.S. Army Armament Research and Development Command, Ballistic Research Laboratory, Aberdeen Proving Ground, MD, March 1978.
7. C.R. Blakely, M.J. McAdams, and M.L. Vestal, Crossed-beam liquid chromatograph-mass spectrometer combination, *J. Chromatogr.* 158(1978)261. Presented at 13th International Symposium on Advances in Chromatography, St. Louis, MO, October 16-19, 1978.
8. A.I. Busygin and B.Sh. Ul'masbaev, Laser ion source for mass spectrometer MI-1309, *Instrum. Exp. Tech. USSR*, 21(1978)171. Translated from *Prib. Tekh. Eksp.* 1(1978)164.
9. Yu.A. Bykovskii, Yu.A. Kozyrev, K.I. Kozlovskii, and A.S. Tsybin, Effect of collision between laser produced plasma flows in conical targets on plasma parameters in final states of expansion, *Kvant. Elektron. (Moscow)* 5(1978)337.
10. Yu.A. Bykovskii, G.I. Zhuravlev, V.I. Belousov, V.M. Gladskoi, V.G. Degtyarev, Yu.N. Kolosov, and V.N. Nevolin, Yield of various ions from a laser produced plasma, *Sov. J. Plasma Phys.* 4(1978)180. Translated from *Fiz. Plazmy* 4(1978)323.
11. Yu.A. Bykovskii, G.I. Zhuravlev, V.I. Belousov, V.M. Gladskoi, V.G. Degtyarev, and V.N. Nevolin, Laser mass spectrometric method for the noncalibrated determination of the elementary composition of solids, *Ind. Lab. USSR* 44(1978)799. Translated from *Zavod. Lab.* 44(1978)701.
12. Yu.A. Bykovskii, G.I. Zhuravlev, V.M. Gladskoi, V.G. Degtyarev, and V.N. Nevolin, Element analysis of geological and extraterrestrial samples with a laser mass spectrometer, *Sov. Phys.-Tech. Phys.* 23(1978)225. Translated from *Zh. Tekh. Fiz.* 48(1978)382.
13. R.J. Conzemius and H.J. Svec, A scanning laser mass spectrometer milliprobe, Paper RB-13 presented at 26th Annual Conference on Mass Spectrometry and Allied Topics, St. Louis, MO, May 28-June 2, 1978.
14. R.J. Conzemius and H.J. Svec, Scanning laser mass spectrometer milliprobe, *Anal. Chem.* 50(1978)1854.
15. J.P. Cowin, D.J. Auerbach, C. Becker, and L. Wharton, Measurement of fast desorption kinetics of D<sub>2</sub> from tungsten by laser induced thermal desorption, *Surf. Sci.* 78(1978)545.
16. R. Decoste and B.H. Ripin, High energy ion expansion in laser-plasma interactions, *Phys. Rev. Lett.* 40(1978)34.
17. P.E. Dyer, J.A. Sayers, and G. Salvetti, Plasma production experiments using a pulsed HF laser, *Appl. Phys. Lett.* 32(1978)457.
18. P. Echlin and R. Kaufmann (Eds.), *Microprobe analysis in Biology and medicine*, *Microsc. Acta*, Suppl. 2, 1978. From International Conference, Munster, Germany, September 4-8, 1977.
19. J.F. Eloy, Chemical analysis of biological materials with the laser probe mass spectrograph, *Microsc. Acta*, Suppl. 2, (1978)307.
20. V.I. Faerman and I.L. Agafonov, Mass spectrometer system for analyzing surface contamination, *Ind. Lab. USSR* 44(1978)816. Translated from *Zavod. Lab.* 44(1978)715.
21. F.S. Felber and R. Decoste, Fast expansions of laser-heated plasmas, *Phys. Fluids* 21(1978)520.
22. E. Gabriel, R. Wechsung, H. G. Klinger, and H. Gerhard, Laser microprobe mass analysis LAMMA of element distribution in dental hard tissue with special respect to fluorine, 25th Symposium of the Organization for Caries Research (ORCA), Turku, Finland, June 28-July 1, 1978.
23. W. Gekelman, V. Vanek, and A.Y. Wong, Characterization of a laser-produced negative-hydrogen-ion plasma, *J. Appl. Phys.* 49(1978)3049.
24. S.J. Gitomer and H. Brysk, Space charge effects on particle diagnostics of laser produced plasmas, *Appl. Phys. Lett.* 32(1978)616.
25. S.F. Hahn, D.B. Van Hulsteyn, and M.F. Becker, Multiple species ion energy analyzer applied to laser induced plasma experiments, *Rev. Sci. Instrum.* 49(1978)473.
26. R.L. Hanson, Plasma quenching reactions with laser pyrolysis of graphite and coal in helium and hydrogen, *Carbon* 16(1978)159.
27. H. Hartwig and P. Mioduszewski, Studies on laser induced thermal desorption, *Ber. Kernforschungsanlage Juelich*, Juel 1530(1978)43.
28. H. Hartwig and P. Mioduszewski, Investigation of the laser-induced thermal desorption, *JUEL-1530 Aug* (1978).
29. H. Hartwig, P. Mioduszewski, and A. Pospieszczyk, Laser induced desorption experiments with technical metal surfaces, *J. Nucl. Mater.* 76(1978)625. Proceedings of the 3rd International Conference on Plasma Surface Interactions in Controlled Fusion Devices, Abingdon, Oxfordshire, UK, April 3-7, 1978.
30. H. J. Heinen, R. Wechsung, H. Vogt, F. Hillenkamp, and R. Kaufmann, Laser-Mikrosonden-Massen-Analysator LAMMA, *Biotechnische Umschau* 2(1978)346 (in German).
31. R. Kaufmann, Advances in microbeam analysis (electron beam-, laser beam-, ion beam-) techniques as applied to ion measurement in tissues, *Arzneim.-Forsch. (Drug Research)* 28(1978)705.
32. R. Kaufmann, F. Hillenkamp, R. Nitsche, M. Schurmann, H. Vogt, and R. Wechsung, The LAMMA instrument, a new laser microprobe mass analyzer for biomedical purposes, Proceedings of the 13th Annual Conference of the Microbeam Analysis Society, Ann Arbor, Michigan, June 19-23, 1978, p.16A.
33. R. Kaufmann, F. Hillenkamp, R. Nitsche, M. Schurmann, and R. Wechsung, The laser microprobe mass analyzer

- (LAMMA): biomedical applications, *Microscopica Acta*, Supplement 2 (1978)297.
34. R. Kaufmann, F. Hillenkamp, and R. Wechsung, Laser microprobe mass analysis, *Eur. Spectrosc. News*, 20(1978)41.
  35. F.C. Khanna, Laser-matter interaction, AEC-6343, Chalk River Nuclear Laboratories, Atomic Energy of Canada Ltd., Chalk River, Ontario, September 1978, 148 pp.
  36. P.G. Kistemaker, M. Lens, and H.L.C. Meuzelaar, Laser- induced desorption and ionization of bio-polymers, Paper FB1 presented at 26th Annual Conference on Mass Spectrometry and Allied Topics, St. Louis, MO, May 28-June 2, 1978.
  37. I.D. Kovalev, G.A. Maksimov, A.I. Suchkov, and N.V. Larin, Analytical capabilities of laser probe mass spectrometry, *Int. J. Mass Spectrom. Ion Phys.* 27(1978)101.
  38. H. Liebl, Mass spectrometry of solids-with special emphasis on probe sampling, *Mikrochim. Acta (Wien)*, (1978)241.
  39. E.R. Lory, B.G. Dawkins, P.J. Arpino, P.A. Hoffman, and F.W. McLafferty, Laser enhanced ionization of low volatility samples in solution, Paper RE-4 presented at 26th Annual Conference on Mass Spectrometry and Allied Topics, St. Louis, MO, May 28-June 2, 1978.
  40. R.M. Lum, Microanalysis of trace contaminants by laser probe pyrolysis, *Am. Lab.* 10(1978)47.
  41. M.W. McGeoch, Electrostatic analyzer for laser-produced plasmas. Ion spectra for polythene at 10.6  $\mu$ m, CLM-R-186, April (1978).
  42. S.S. Medley, Energetic ion mass analysis using a radio- frequency quadrupole filter, *Rev. Sci. Instrum.* 49(1978)698.
  43. S.L. Motylev and P.P. Pashinin, Experimental investigations of spontaneous magnetic fields in a laser-induced plasma, *Sov. J. Quant. Electron.* 8(1978)700. Translated from *Kvant. Electron. Moscos* 5(1978)1230.
  44. M.S. Mussetto, M. Krishnan, P. Avivi, J.L. Hirschfield, and D. Segal, Ion confinement in pulsed laser-produced plasmas, *Phys. Rev. Lett.* 40(1978)321.
  45. R. Nitsche, R. Kaufmann, F. Hillenkamp, E. Unsold, H. Vogt, and R. Wechsung, Mass spectrometric analysis of laser induced microplasmas from organic samples, *Israel J. Chem.* 17(1978)181.
  46. G.L. Payne, J.D. Perez, T.E. Sharp, and B.A. Watson, Recombination effects in an expanding laser produced plasma, *J. Appl. Phys.* 49(1978)4688.
  47. M.L. Petukh and A.A. Yankovskii, Atomic emission spectral analysis using lasers, *J. Appl. Spectrosc. USSR* 29(1978)1527 Translated from *Zh. Prikl. Spektrosk.* 29(1978)1109.
  48. M.A. Posthumus, P.G. Kistemaker, H.L.C. Meuzelaar, and M.C. Ten Noever de Brauw, Laser desorption-mass spectrometry of polar nonvolatile bio-organic molecules; *Anal. Chem.* 50(1978)985.
  49. G. Rankin, N. Abt, A. Lilly, and W. Kunkel, Experimental- determination of ion energy scaling in a laser-produced plasma, *B. Am. Phys. S.* 23(1978)879.
  50. J.F. Ready, Laser produced shocks and their relation to material damage, *IEEE J. Quant. Electron.* 14(1978)79, AD-A053 974 or AFOSR-TR-78-0763, NTIS.
  51. J.F. Ready, Coupling of CO<sub>2</sub> laser energy into ionized blowoff material, *Opt. Lett.* 2(1978)130.
  52. J.F. Ready, Industrial applications of lasers, New York, Academic Press, 1978.
  53. S. Sarraf and D.M. Woodall, Resolving the positive, negative, and neutral fluxes of an expanding laser produced plasma, *Rev. Sci. Instrum.* 49(1978)1147.
  54. H.-R. Schulten, Laser assisted field desorption mass spectrometry, Paper TA-9 presented at 26th Annual Conference on Mass Spectrometry and Allied Topics, St. Louis, MO, May 28-June 2, 1978.
  55. H.-R. Schulten, W.D. Lehmann, and D. Haaks, Laser assisted field desorption mass spectrometry, *Org. Mass Spectrom.* 13(1978)361.
  56. R.H. Scott and A. Strasheim, Laser emission excitation and spectroscopy, in E.L. Grove (Ed.), *Applied Atomic Spectroscopy*, Volume 1, Plenum Press, New York, 1978, Chap. 2, pp. 73-118.
  57. H.D. Shay, R.A. Haas, W.L. Kruer, M.J. Boyle, D.W. Phillion, V.C. Rupert, H.N. Kornblum, R. Rainer, V.W. Slivinsky, L.N. Kopperl, L. Richards, and K.G. Tirsell, Interaction of 1.06  $\mu$ m laser radiation with variable z targets, *Phys. Fluids* 21(1978)1634.
  58. V.H. Shui, B. Kivel, and G.M. Weyl, Effect of vapor plasma on the coupling of laser-radiation with aluminum targets, *J. Quant. Spectros.* 20(1978)627.
  59. G. Sidenius, Ion sources for low energy accelerators, *Nucl. Instrum. Methods* 151(1978)349.
  60. D.C. Slater, Thomson parabola ion analyzer for laser plasma studies, *Rev. Sci. Instrum.* 49(1978)1493.
  61. G.J. Tallents, The operation of a 45 degree parallel-plate electrostatic analyser in laser produced plasma studies, *J. Phys. E* 11(1978)769.
  62. J.C. Travis, G.C. Turk, and R.B. Green, Laser enhanced ionization for trace metal analysis in flames, *ACS Symp. Ser.* 85(1978)91-3855.
  63. E. Unsold, G. Renner, F. Hillenkamp, and R. Nitsche, Investigation of organic materials using a laser microprobe mass analyzer, *Adv. Mass Spectrom.*, Volume 7, N. R. Daly (Ed.), Institute of Petroleum, London, 1978, p. 1425.
  64. N.E. Vanderborgh and M.A. Fletcher, Laser pyrolysis- gas chromatography: a modern source rock assay technique, *METC/SP-78/6(Vol.2)*, pp. 151-163, Oct. 1978.
  65. E.K. Vul'fson, V.I. Dvorkin, and A.V. Karayakin, The problem of vaporization of a substance in a laser jet, *J. Appl. Spectrosc. USSR*, 29(1978)1293. Translated from *Zh. Prikl. Spektrosk.* 29(1978)781.
  66. P. Waegli and T.P. Donaldson, Measurements of the ion emission from laser generated plasma, *Z. Angew. Math. Phys.* 29(1978)358.
  67. P. Waegli, T.P. Donaldson, and P. Ladrach, Scaling of nonthermal ion energy in laser generated plasma, *Appl. Phys. Lett.* 32(1978)638.
  68. R. Wechsung, Laser microprobe mass analysis - new method for biological research, *Chimia* 32(1978)444 (in German).
  69. R. Wechsung, F. Hillenkamp, R. Kaufmann, R. Nitsche, and H. Vogt, LAMMA - a new laser microprobe mass analyzer, *Scanning Electron Microscopy/1978/I*, SEM Inc., AMF O'Hare, Illinois, 1978, p. 611.

70. R. Wechsung, F. Hillenkamp, R. Kaufmann, R. Nitsche, and H. Vogt, Laser microprobe mass analyzer "LAMMA": a new analysis method for research and technology, *Mikroskopie* (Wien) 34(1978)47 (in German).
71. R. Wechsung, F. Hillenkamp, R. Kaufmann, R. Nitsche, E. Unsold, and H. Vogt, LAMMA - a new laser microprobe mass analyzer, *Microscopica Acta*, Supplement 2 (1978)281.
72. L.M. Wickens, J.E. Allen, and P.T. Rumsby, Ion emission from laser produced plasmas with two electron temperatures, *Phys. Rev. Lett.* 41(1978)243.
73. O.K.T. Wu and R.P. Burns, Molecular binding states on clean oxidized surfaces: SiO[g] + W[clean] and SiO[g] + W[oxidized], *Surf. Sci.* 77(1978)626.

1979

1. I.L. Agafonov and V.I. Faerman, Influence of laser irradiation of a mass-spectrometer ion-field source emitter on the magnitude of the ion current, *Instrum. Exp. Tech. USSR* 22(1979)1116.
2. I.L. Agafonov and A.I. Kuzmiche, Device for mass- spectroscopic analysis of micorconcentrations of gaseous impurities in non-conducting materials, *Instrum. Exp. Tech. USSR* 22(1979)797.
3. Yu.K. Al'tudov, T.A. Basova, Yu.A. Bykovskii, V.G. Degtyarev, Yu.N. Kolosov, I.D. Laptev, and V.N. Nevolin, Laser-plasma source for ion implantation in solids, *Sov. Phys. Tech. Phys.* 24(1979)1077.
4. H.D. Beckey, Experimental techniques in field ionization and field desorption mass spectrometry, *J. Phys. E. Sci. Instrum.* 12(1979)72.
5. H. P. Bochem and B. Sprey, Laser microprobe analysis of inclusions in *Dunaliella salina*, *Z. Pflanzenphysiol.* 95(1979)179.
6. Yu.A. Blykovskii, Yu.P. Kozyrev, V.B. Lagoda, A.I. Suslov, and G.A. Sheroziya, Effect of secondary electron emission on the efficiency with which the ions emitted by a laser plasma are detected, *Sov. Phys. Tech. Phys.* 49(1979)1368.
7. P. Chibon and J.F. Eloy, Local analysis of the composition of amphibian and shark teeth using laser probe mass spectrometry, *Jour. Biol. Buccale.* 7(1979)263.
8. G.D. Daves, Jr., Mass spectrometry of involatile and thermally unstable molecules, *Mass Spectrom.* 12(1979) 359.
9. N. Furstenau, F. Hillenkamp, and R. Nitsche, Laser induced positive and negative molecular ions from thin carbon foils, *Int. J. Mass Spectrom. Ion Phys.* 31(1979)85.
10. E. Gabriel, S. Neumeyer, and K. J. Klink, Fluoridwirkung auf Loslichkeit, Abriebfestigkeit und Fluoreszenz von Rattenzahnen und Fluoridnachweis mit dem LAMMA-Verfahren, *Dtsch. zahnarztl. Z.* 34(1979)716 (in German).
11. E. Gabriel, R. Wechsung, H.G. Klinger, and H. Gerhard, Laser microprobe mass analysis of element distribution in dental hard tissue with special reference to fluorine, *Caries Res.* 13(1979)118. Abstract of paper presented at 25th ORCA Congress.
12. H. J. Heinen, The application of a laser microprobe mass analyzer (LAMMA) in organic and inorganic chemistry, *Chemie* 8(1979)35.
13. H.J. Heinen, R. Wechsung, H. Vogt, F. Hillenkamp, and R. Kaufmann, Laser-mikrosonden-massen-analysator LAMMA, *Acta Phys. Austriaca*, Suppl. XX (1979)257.
14. C.E.R. Jones and N.E. Vanderborgh, Elucidation of geomatrics by laser pyrolysis-gas chromatography and pyrolysis-mass spectrometry, *J. Chromatogr.* 186(1979)831.
15. R. Kaufmann, H. J. Heinen, M. Schurmann, and R. Wechsung, Recent advances of laser microprobe mass analysis (LAMMA) as applied to biological and engineering specimens, *Microbeam Analysis-1979*, D. E. Newbury (Ed.), San Francisco Press, San Francisco, 1979, p.63.
16. R. Kaufmann and F. Hillenkamp, LAMMA and its applications, *Industr. Res. Dev.* April(1979)145.
17. R. Kaufmann, F. Hillenkamp, and R. Wechsung, The laser microprobe mass analyzer (LAMMA), a new instrument for biomedical microprobe analysis, *Med. Prog. Technol.* 6(1979)109.
18. R. Kaufmann, F. Hillenkamp, R. Wechsung, H. J. Heinen, and M. Schurmann, Laser microprobe mass analysis: achievements and aspects, *Scanning Electron Microscopy/1979/II*, SEM Inc., AMF O'Hare, Illinois, 1979, p. 279.
19. R. Kaufmann, F. Hillenkamp, and R. Wechsung, Biomedical applications of the laser microprobe mass analyzer (LAMMA), *Symposium of Ernst Leitz GmbH (Wetzlar)*, Moscow, May, 1979.
20. M.S. Kaviladze, T.A. Melashvili, and M.S. Kviriya, Determination of isotopic composition of elements in microvolumes of a solid, *Instrum. Exp. Tech. USSR*, 20(1970)512. Translated from *Prib. Tekh. Eksp.* 2(1979)166.
21. P.G. Kistemaker, M.M.J. Lens, G.J. Q. van der Peyl, and A.J.H. Boerboom, Laser induced desorption mass spectrometry, in *Advances in Mass Spectrometry*, Vol. 8A. A. Quayle (Ed.). Heyden and Son Ltd. 1979. Proceedings of the 8th International Mass Spectrometry Conference, Oslo, 1979.
22. P. Klein and J. Bauch, On the localization of ions in cell wall layers of treated wood based on a laser microprobe mass analyzer (LAMMA), *Holzforsch.* 33(1979)35.
23. V.N. Kotikov, S.V. Oshemkov, A.A. Petrov, G.V. Skvortso, and A.S. Cheremuk, Use of lasers for spectral-isotopic determination of nitrogen in the surface-layer of steel, *Ind. Lab. R.* 45(1979)998.
24. H.S. Kwong and R.M. Measures, Trace element laser microanalyzer with freedom from chemical matrix effect, *Anal. Chem.* 51(1979)428.
25. K. Laqua, Analytical spectroscopy using laser atomizers, in *chemical analysis*, Vol. 50, *Analytical Laser Spectroscopy*, John Wiley, New York, 1979, Chap. 2, pp. 47-118.
26. R.M. Lum, Thermal decomposition of poly(butylene terephthalate), *J. Polym. Sci., Polym. Chem. Ed.* 17(1979)203.
27. B.A. Mamyrin and D. V. Shmikk, The linear mass reflectron, *Sov. Phys.-JETP* 49(1979)762.
28. R.P. Mariella, Jr., A study of laser-assisted surface ionization of lithium, *J. Chem. Phys.* 71(1979)94.
29. A. Mathey, Contribution a l'etude de la famille des tryptetheliacees (lichens pyrenomycetes), *Nova Hedwigia* 31(1979)917 (in French).

30. M.K. Matzen and J.S. Pearlman, Impact of nonequilibrium ionization and recombination processes on the evaluation of laser produced plasmas, *Phys. Fluids*, 22(1979)449.
31. R.M. Measures and H.S. Kwong, TABLASER: trace (element) analyzer based on laser ablation and selectively excited radiation, *Appl. Opt.* 18(1979)281.
32. Hk. Mueller-Buschbaum and H. Pausch, A new preparation technique in solid state chemistry. I. High temperature reactions with CO<sub>2</sub> laser. II. High pressure-high temperature reactions with CO<sub>2</sub> lasers, *Z. Naturforsch., Teil B*, 34(1979)371, 375.
33. V. Y. Munblit and L. N. Grigorov, Use of laser flash-desorption method with mass-spectrometric analysis for studying intermediates from heterogeneous-catalytic reactions, *Tr. Mosk. Fiz.-tekhn. In-t* 11(1979)205 (in Russian).
34. I.I. Opzchko, Interaction of the multiply charged ions of a laser-induced plasma with a solid surface, *Sov. Phys. Tech. Phys.* 24(1979)985.
35. R.A. Phaneuf and R.H. Hughes, Laser plasma ion-source for low-energy charge-transfer cross-section measurements, *B. Am. Phys. S.* 24(1979)1179.
36. W.D. Reynolds, Field desorption mass spectrometry, *Anal. Chem.* 51(1979)283A.
37. B. Schueler and F.R. Krueger, Spectra of quaternary ammonium salts taken by fission fragment and laser induced desorption, *Org. Mass Spectrom.* 14(1979)439.
38. M.S. Slutsky and T.F. George, Laser stimulated migration of adsorbed atoms on solid surfaces, *J. Chem. Phys.* 70(1979)1231.
39. R. Stoll and F. W. Roellgen, Laser desorption mass spectrometry of thermally labile compounds using a continuous wave carbon dioxide laser, *Org. Mass Spectrom.* 14(1979)642.
40. R.G. Tomlinson, W.J. Fader, D.H. Polk, and J.H. Stufflebeam, Magnetic mirror confinement of laser produced LiH plasmas, *Phys. Fluids* 22(1979)566.
41. P. Waegli, Wide energy range mass spectrograph, *Rev. Sci. Instrum.* 50(1979)165.
42. C.M. Ward and L.E. Bergquist, Mass spectrometer determination of argon contents in laser fusion target pellets, *J. Nucl. Mater.* 85 & 86(1979)117.
43. R. Wechsung, H. J. Heinen, F. Hillenkamp, and R. Kaufmann, Laser microprobe mass analyzer LAMMA. Principle and description of a new instrument, Symposium of Ernst Leitz GmbH (Wetzlar), Moscow, May, 1979.
44. M. Wittmer, W. Luthy, and M. Von Allmen, Laser induced reaction of magnesium with silicon, *Phys. Lett. A* 75(1979)127.
45. H. Yasuda and T. Sekiguchi, Computational studies on ionization processes of laser-produced high-z plasmas, *Jap. J. Appl. Phys.* 18(1979)2245.
46. L. Zandee and R.B. Bernstein, Laser ionization mass spectrometry: extensive fragmentation via resonance enhanced multiphoton ionization of a molecular benzene beam, *J. Chem. Phys.* 70(1979)2574.
47. P.D. Zavitsanos, J.A. Golden, and W.G. Browne, Study of laser effects on heat shield materials, AD-A066 068/BSL, General Electric Co., Philadelphia, PA, Reentry and Environmental Systems Div. and Army Research Office, Research Triangle Park, NC, 37 pp. January 1979.
48. B.K. Zuev, G.N. Kasatkin, Yu.A. Kulakov, L.L. Kunin, and G.V. Mikhailova, Investigation of hydrogen distribution in the region of nonmetallic inclusions in steel by laser mass spectrometry, *J. Anal. Chem. USSR* 34(1979)1330. Translated from *Zh. Anal. Khim.*
49. B.K. Zuev, V.P. Velyukhanov, Yu.A. Kulakov, L.L. Kunin, and G.V. Mikhailov, Separate determination of surface and volume content of oxygen and hydrogen in metal films, *J. Anal. Chem. USSR*, 34(1979)727. Translated from *Zh. Anal. Khim* 34(1979)940.

#### 1980

1. F. Amman, G.P. Banfi, P.G. Gobbi, S. Morosi, and G.C. Reali, Absorption in metallic targets irradiated by 50 ps laser pulses at intensities below 10E12 W/cm<sup>2</sup> *Plasma Phys.* 22(1980)453.
2. H. Bader, K. Rohr, and H. Weber, Space-charge effects in electrostatic ion analyzers for laser-produced plasma detection, *J. Phys. D* 13(8)(1980)L149.
3. L. Bertalot, H. Herold, U. Jager, A. Mozer, T. Oppenlan, M. Sadowski, and H. Schmidt, Mass and energy analysis and space-resolved measurements of ions from plasma-focus devices, *Phys. Lett. A* 79(5-6)(1980)389.
4. A.V. Bessarab, V.N. Novikov, D.V. Pavlov, and A.I. Funtikov, Laser-wavelength dependence of the threshold for plasma generation at metal surfaces the range 1-10  $\mu$ m, *Sov. Phys. Tech. Phys.* 25(1980)534.
5. A. Chamel and J.F. Eloy, Application of laser probe mass-spectrography to study of variations of mineral-content in woody tissues, *J. Plant. Nut.* 2(1980)445.
6. R.M. Clement, R.A. Davies, H.T. Miles, and S.K. Sethuram, Influence of charge-transfer on energy measurements of ions expanding from laser-produced plasmas, *J. Phys. D* 13(9)(1980)1643.
7. R.B. Cody, R.C. Burnier, W.D. Reents, Jr., T.J. Carlin, D.A. McCrery, R.K. Lengel, and B.S. Freiser, Laser ionization source for ion cyclotron resonance spectroscopy. Applications to atomic metal ion chemistry, *Int. J. Mass Spectrom. Ion Phys.* 33(1980)37.
8. R.J. Conzemius and J.M. Capellen, A review of the applications to solids of the laser ion-source in mass-spectrometry, *Int. J. Mass Spectrom. Ion Phys.* 34(1980)197.
9. R.J. Cotter, Laser desorption chemical ionization mass- spectrometry, *Anal. Chem.* 52(11)(1980)1767.
10. R.J. Cotter, Mass spectrometry of nonvolatile compounds desorption from extended probes, *Anal. Chem.* 52(1980)1589A.
11. P.L. Cowan and J.A. Golovchenko, Laser surface treatment studies in ultrahigh vacuum, *J. Vac. Sci. Technol.* 17(5)(1980)1197.
12. R. Dinger, K. Rohr, and H. Weber, Ion distribution in laser-produced plasma on tantalum surfaces at low irradiances, *J. Phys. D* 13(1980)2301.
13. W. Drachsel, S. Nishigak, and J.H. Block, Photo-induced field-ionization mass-spectroscopy, *Int. J. Mass Spectrom. Ion Phys.* 32(1980)333.

14. W. Ehler, F. Begay, T.H. Tan, J. Hayden, and J. McLeod, Effect of target purity on laser-produced plasma expansion, *J. Phys. D* 13(2)(1980)L29.
15. P. Englert and U. Herpers, Isotopic anomalies of osmium from different deposits determined by the laser microprobe mass analyzer LAMMA, *Inorg. Nucl. Chem. Lett.* 16(1980)37.
16. T.N. Filip'skii and P.N. Pasha, Some possible uses of laser mass spectrometry in element analysis of biological substances, in *Metody Radiobiol. Sel. Genet. S-kh. Rast.* (1980) pp. 115-19 (Russ) Ed. by T.N. Filip'skii, Kishinev. S-kh. Inst.: Kishinev, USSR.
17. F. Freund, H. Kathrein, H. Wengeler, R. Knobel, and H. J. Heinen, Carbon in solid solution in forsterite- a key to the untractable nature of reduced carbon in terrestrial and cosmogenic rocks, *Geochim. Cosmochim. Acta* 44(1980)1319.
18. F. Freund, H. Wengeler, H. Kathrein, and H. J. Heinen, Atomic carbon in magnesium oxide, Part II: Laserflash- induced mass spectrometry, *Mat. Res. Bull.* 15(1980)1019.
19. N. Furstenau and F. Hillenkamp, Laser induced cluster ions from foils of metals and semiconductors and thermodynamic properties of the phase transition, *Proc. of the Symposium on Sputtering*, P. Varga, G. Bets, and F. P. Viehbock (Eds.), *Inst. Angew. Physik, Techn. Univ. Wien*, 1980, p. 707.
20. J. A. Gardella, D. M. Hercules, and H. J. Heinen, Mass spectrometry of molecular solids: Laser microprobe mass analysis (LAMMA) of selected polymers, *Spectrosc. Lett.* 13(1980)347.
21. L.N. Grigorov, V.B. Kazanski, and V.Ya. Mumblit, Laser flash desorption and its application in research on heterogeneous catalysis. I. Basic features of surface heating by laser radiation and certain problems in the kinetics of laser thermal desorption. II. Products in Unit for laser flash desorption with mass spectrometric analysis of products in microsecond range, *Kinet. Catal.* 21(2,2)(1980)363. Translated from *Kinet. Katal.*
22. E. Gulari, Chemical and biochemical applications of lasers. Volume IV, Edited by C. Bradley Moore, *J. Am. Chem. Soc.* 102(5)(1980)1762.
23. H. J. Heinen, F. Hillenkamp, R. Kaufmann, W. Schroder, and R. Wechsung, LAMMA: a new laser microprobe mass analyzer for biomedical and biological materials analysis, *Recent Developments in Mass Spectrometry in Biochemistry and Medicine*, Volume 6, A. Frigerio and M. McCamish (Eds.), Elsevier, Amsterdam, 1980, p. 435.
24. H. J. Heinen, S. Meier, H. Vogt, and R. Wechsung, Laser induced mass spectrometry of organic and inorganic compounds with a laser microprobe mass analyzer, *Adv. Mass Spectrom.*, Volume 8, A. Quayle (Ed.), Institute of Petroleum, London, 1980, p. 942.
25. H. J. Heinen, S. Meier, H. Vogt, and R. Wechsung, Recent advances of organic and inorganic analysis with the laser microprobe LAMMA, *Proceedings of the 8th International Vacuum Congress*, Cannes, September 1980, Suppl., *Le Vide, Les Couches Minces*, No. 201, F. Abeles and M. Croset (Eds.), Volume 1, p.263.
26. S. Henstra, E. B. A. Bisdorf, A. Jongerius, H. J. Heinen, and S. Meier, Microchemical analysis of thin sections of soils with the laser microprobe mass analyzer LAMMA-500, *Beitr. Elektronenmikroskop. Direktabb. Oberfl.* 13(1980)63 (in German).
27. F. Heresh, E.R. Schmid, and J.F.K. Huber, Repetitive laser desorption mass spectrometry for nonvolatile organic compounds, *Anal. Chem.* 52(1980)1803.
28. W. Herr, P. Englert, U. Herpers, E. A. Watts, and A. G. Whittaker, A contribution to the riddle about the origin of certain glassy spherules, *Meteoritics* 15(1980)300.
29. B. Kaduk, K. Metze, P. F. Schmidt, and G. Brandt, Secondary atrophic cardiomyopathy - heart damage due to Wilson's disease, *Virchows Archiv. A Path. Anat. and Histol.* 387(1980)67.
30. R. Kaufmann, Recent LAMMA studies of physiological cation distributions in retina tissues, *Scanning Electron Microscopy/1980/II*, SEM Inc., AMF O'Hare, Illinois, 1980, p. 641.
31. R. Kaufmann and P. Wieser, Laser microprobe mass analysis (LAMMA) in particle analysis, in *Characterization of Particles*, K. F. J. Heinrich (Ed.), NBS Spec. Pub. 533, Washington, 1980, p.199.
32. R. Kaufmann, P. Wieser, and R. Wurster, Application of the laser microprobe mass analyzer LAMMA in aerosol research, *Scanning Electron Microscopy/1980/II*, SEM Inc., AMF O'Hare, Illinois, 1980, p. 607.
33. G.L. Kellogg and T.T. Tsong, Pulsed-laser atom-probe field-ion microscopy, *J. Appl. Phys.* 51(1980)1184.
34. P. G. Kistemaker, M. M. J. Lens, G. J. Q. van der Peyl, and A. J. H. Boerboom, Laser induced desorption mass spectrometry, *Adv. Mass Spectrom.*, Volume 8, A. Quayle (Ed.), Institute of Petroleum, London, 1980, p. 928.
35. P.G. Kistemaker, G.J.Q. van der Peyl, A.J.H. Boerboom, and J. Haverkamp, Laser desorption mass spectrometry of organic molecules, Presented at 28th Conference on Mass Spectrometry, New York, NY, May 25-30, 1980.
36. P. G. Kistemaker, G. J. Q. van der Peyl, and J. Haverkamp, Laser desorption mass spectrometry, *Soft Ionization Biological Mass Spectrometry*, H. R. Morris (ed.), Heyden, London, 1981, p. 120.
37. I.D. Kovalev, N.V. Larin, G.A. Maksimov, and A.I. Suchkov, Energy distributions of the ions in a laser plasma, *Sov. Phys. Tech. Phys.* 25(1980)259.
38. M. Krishnan and J.L. Hirshfield, Fast high-resolution ion energy and momentum spectrometer, *Rev. Sci. Instrum.* 51(1980)911.
39. M. Krishnan and J.L. Hirshfield, Mass-spectrometric investigation of laser-initiated vacuum arcs, *B. Am. Phys. S.* 25(1980)101.
40. F. R. Krueger and B. Schueler, Organic mass spectra obtained by fission-fragment and pulsed laser-induced desorption, *Adv. Mass Spectrom.*, Volume 8, A. Quayle (Ed.), Institute of Petroleum, London, 1980, p.918.
41. K. D. Kupka, F. Hillenkamp, and Ch. Schiller, Laser induced mass spectrometry of bio-organic compounds, *Adv. Mass Spectrom.*, Volume 8, A. Quayle (Ed.), Institute of Petroleum, London, 1980, p.935.
42. K. D. Kupka, W. W. Schropp, Ch. Schiller, and F. Hillenkamp, Laser-micro-mass analysis (LAMMA) of metallic and organic ions in medical samples, *Scanning Electron Microscopy/1980/II*, SEM Inc., AMF O'Hare, Illinois, 1980, p. 635.
43. J.-T. Lin and T.F. George, Quantum-stochastic approach to laser-stimulated desorption dynamics and population distributions of chemisorbed species on solid surfaces, *J. Chem. Phys.* 72(1980)2554.
44. A.D. Macknigh, Comparison of analytic techniques -- chemical, isotopic, and micro-probe analyses, *Fed.*



- Proc. 39(1980)2881.
45. W.E. Maher and R.B. Hall, Pulsed laser heating profile width and changes in total coupling with pulse length and pressure, *J. Appl. Phys.* 51(1980)1338.
  46. J. F. Muller, J. M. Magar, and D. Cagniant, Etude de substances modeles susceptibles de complexes les metaux de transition dans les fractions lourdes du petrole, I- Caracterisation par ESCA et LAMMA de complexes au nickel, cobalt et rhodium avec des ligandes sulfures, *J. Organomet. Chem.*, 186(1980)389 (in French).
  47. G.D.J. Phillies, Chemical and biochemical applications of lasers. Volume III., Ed. by C. Bradley Moore, (Book Review), *J. Am. Chem. soc.* 102(1980)1478.
  48. L. Salvati, Jr., D. M. Hercules, and H. Vogt, Laser microprobe mass analysis of  $\text{NH}_4\text{ReO}_4$ ,  $\text{AgReO}_4$ , and  $\text{Al(ReO}_4)_3$ , *Spectrosc. Lett.* 13(1980)243.
  49. P. F. Schmidt, Einsatzmöglichkeiten des LAMMA-Verfahrens bei der Analyse von biologischmedizinischen Proben, *Beitr. Elektronenmikroskop. Direktabb. Oberfl.* 13(1980)51 (in German).
  50. P. F. Schmidt, H. G. Fromme, and G. Pfefferkorn, LAMMA investigations of biological and medical specimens, *Scanning Electron Microscopy/1980/II*, SEM Inc., AMF O'Hare, Illinois, 1980, p. 623.
  51. P. F. Schmidt, H. G. Fromme, and G. Pfefferkorn, Use of LAMMA (laser microprobe mass analyzer) in the analysis of biological medical tests, *Mikroskopie (Wien)* 36(1980)297 (in German).
  52. W. H. Schroeder, D. Frings, and H. Stieve, Measuring Ca uptake and release of avertebrate photoreceptor cells by laser microprobe mass spectrometry, *Scanning Electron Microscopy/1980/II*, SEM Inc., AMF O'Hare, Illinois, 1980, p. 647.
  53. B. Schueler and F. R. Krueger, Comparative study of pulsed laser and fission fragment induced desorption with nucleotic compounds, *Org. Mass Spectrom.* 15(1980)295.
  54. B. Schueler, R. Nitsche, and F. Hillenkamp, Possibilities for a laser-induced micro-mass-analysis of bulk surfaces, *Scanning Electron Microscopy/1980/II*, SEM Inc., AMF O'Hare, Illinois, 1980, p. 597.
  55. H. R. Schulten, R. Mueller, and D. Haaks, Laser assisted field desorption mass spectrometry. 2. Metals and alloys, *Z. Anal. Chem.* 304(1980)15.
  56. D.W. Scudder and H.C. Praddaud, Laser-produced plasmas and radiation sources, AD-A084 201/3, 169 pp., January 1980.
  57. U. Seydel and H. J. Heinen, First results on fingerprinting of single mycobacteria cells with LAMMA, Recent Developments in Mass Spectrometry in Biochemistry and Medicine, Volume 6, A. Frigerio and M. McCamish (Eds.), Elsevier, Amsterdam, 1980, p. 489.
  58. D. S. Simons, Ion microprobe, ion microscope, and laser microprobe mass analysis of particulates, *Microbeam Analysis-1980*, D. B. Wittry (Ed.), San Francisco Press, San Francisco, 1980, p. 178.
  59. A.Ya. Vorob'ev and V.M. Kuz'michev, Absorption of laser radiation in craters on metal targets, *Sov. J. Quant. Electron.* 10(1980)103.
  60. P. Wieser, R. Wurster, and H. Seiler, Identification of airborne particles by laser induced mass spectrometry, *Atmos. Environ.* 14(1980)485.
  61. P. Wieser, R. Wurster, and H. Seiler, Analysis of microparticles by means of electron microprobe and laser microprobe mass analyzer, *Electron Microscopy-1980*, Volume 3, P. Brederoo and V. E. Cosslett (Eds.), 7th European Congress on Electron Microscopy, 1980, p. 56.
  62. E.J. Yoffa, Dynamics of dense laser-induced plasmas, *Phys. Rev. B* 21(1980)2415.

1981

1. F. Adams, P. Bloch, D. F. S. Natusch, and P. Surkyn, Microscopical analysis for source identification in air chemistry and air pollution, *Proceedings, International Conference on Environmental Pollution, Thessalonika, Greece*, Sept. 21-25, 1981, p. 122.
2. K. Balasamugam, T. A. Dang, R. J. Day, and D. M. Hercules, Some cation and anion attachment reactions in laser desorption mass spectrometry, *Anal. Chem.* 53(1981)2296.
3. P. Bernsen, L. Reimer, and P. F. Schmidt, Investigation of electron irradiation damage of evaporated organic films by laser microprobe mass analysis, *Ultramicroscopy* 7(1981)197.
4. P. Bernsen, P. F. Schmidt, and L. Reimer, LAMMA analysis of crystalline organic films damaged by 100 keV electron irradiation, *Z. Anal. Chem.* 308(1981)309.
5. E. B. A. Bisdorf, S. Henstra, A. Jongerius, H. J. Heinen, and S. Meier, Chemical element detection in thin sections of soils with the laser microprobe mass analyzer (LAMMA 500), *Neth. J. Agric. Sci.* 29(1981)23.
6. R. Bohm, Sample preparation technique for the analysis of vegetative bacteria cells of the genus bacillus with the laser microprobe mass analyzer (LAMMA), *Z. Anal. Chem.* 308(1981)258.
7. A.A. Boitsov and Kh.I. Zil'bershtein, Optical emission laser microprobe analysis of synthetic oxide monocrystals, *Spectrochim. Acta* 36B(1981)1201.
8. P.K. Carrol and E.T. Kennedy, Laser produced plasmas, *Contemp. Phys.* 22(1981)61.
9. A.R. Chamel, A.M. Andreani, and J.F. Eloy, Distribution of Foliar-applied boron measured by spark-source mass- spectrometry and laser-probe mass-spectrography, *Plant Physiol.* 67(1981)457.
10. J.W. Coburn and W.W. Harrison, Plasma sources in analytical mass spectrometry, *Appl. Spectrosc. Rev.* 17(1981)95.
11. R.J. Conzemius, F.A. Schmidt, and H.J. Svec, Scanning laser mass spectrometry for trace level solute concentration profiles, *Anal. Chem.* 53(1981)1899.
12. R.J. Cotter, Cationized species in laser desorption mass spectrometry, *Anal. Chem.* 53(1981)719.
13. R.J. Cotter, Timing circuitry for pulsed laser desorption on a scanning mass-spectrometer, *Chem. B. Env.* 11(1981)57.
14. R. J. Day, A. L. Forbes, and D. M. Hercules, Laser desorption mass spectrometry of some organic acids, *Spectrosc. Lett.* 14(1981)703.
15. R. J. Day and D. M. Hercules, Ionization processes in laser desorption, *Proceedings, 29th Annual Conference*



- on Mass Spectrometry and Allied Topics, Minneapolis, May 24-29, 1981, p. 523.
16. R. J. Day, J. Zimmerman, and D. M. Hercules, Laser desorption mass spectrometry of underivatized bile acids, *Spectrosc. Lett.* 14(1981)773.
17. H.J. Dietze, S. Becker, I. Opauszky, L. Matus, I. Nyary, and J. Frecska, Studies on the formation of molecular ions in laser plasmas, *ZfI-Mitt.* 48(1981)48.
18. T. Dingle, B.W. Griffiths, and J.C. Ruckman, LIMA - A laser induced ion mass analyzer, *Vacuum* 31(10-12)(1981)571.
19. P. K. Dutta and Y. Talmi, Desorption and fragmentation studies of organic molecules by laser-induced mass spectrometry, *Anal. Chim. Acta* 132(1981)111.
20. L. Edelmann, Selective accumulation of Li<sup>+</sup>, Na<sup>+</sup>, K<sup>+</sup>, Rb<sup>+</sup>, and Cs<sup>+</sup> at protein sites of freeze-dried embedded muscle detected by LAMMA, *Z. Anal. Chem.* 308(1981)218.
21. B.K. Furman and C.A. Evans, Jr., Direct-imaging laser mass analyzer, *Microbeam Anal.* 16(1981)336.
22. N. Furstenau, Investigation of laser induced damage, evaporation, and ionization with homogeneous inorganic target foils, *Z. Anal. Chem.* 308(1981)201.
23. N. Furstenau and F. Hillenkamp, Laser induced cluster ions from thin foils of metals and semiconductors, *Int. J. Mass Spectrom. Ion Phys.* 37(1981)135.
24. E. Gabriel, Y. Kato, and P. J. Rech, Preparation methods and LAMMA analysis of dental hard tissue with special respect to fluorine, *Z. Anal. Chem.* 308(1981)234.
25. J. A. Gardella and D. M. Hercules, Mass spectrometry of molecular solids. II. Laser microprobe mass analysis (LAMMA) of selected polymers, *Z. Anal. Chem.* 308(1981)297.
26. A. J. Gay, A. P. von Rosensteil, and P. J. van Duin, Investigation of fly ash particles with respect to the morphology and surface enrichment of matrix and trace elements, *Microbeam Analysis-1981*, R. H. Geiss (Ed.), San Francisco Press, San Francisco, 1981, p. 229.
27. U. Haas, P. Wieser, and R. Wurster, A quantitative interpretation of LAMMA spectra based on a local thermodynamic equilibrium (LTE) model, *Z. Anal. Chem.* 308(1981)270.
28. E. Hamer, W. Gerhard, and C. Plog, LAMMA and SIMS/AES measurements on Fe-Ti alloys, *Z. Anal. Chem.* 308(1981)287.
29. E.D. Hardin and M.L. Vestal, Laser ionization mass spectrometry of nonvolatile samples, *Anal. Chem.* 53(1981)1492.
30. H. J. Heinen, On ion formation in laser desorption mass spectrometry with LAMMA, *Int. J. Mass Spectrom. Ion Phys.* 38(1981)309.
31. H. J. Heinen, S. Meier, H. Vogt, and R. Wechsung, Laser desorption mass spectrometry with LAMMA, *Z. Anal. Chem.* 308(1981)290.
32. S. Henstra, E. B. A. Bisdorf, A. Jongerius, H. J. Heinen, and S. Meier, Microchemical analysis of thin sections of soils with the laser microprobe mass analyzer (LAMMA), *Z. Anal. Chem.* 308(1981)280.
33. F. Heresch, E. R. Schmid, and J. F. K. Huber, Repetitive pulsing laser-desorption mass spectrometry, a technique suitable for scanning-type instruments, *Anal. Chem. Symp. Ser.* 7(1981)351.
34. F. Hillenkamp, Laser induced micro-mass-spectrometry (LAMMA) of bioorganic molecules and biological specimens, *Quant. Electron.* 8(1981)2655 (in Russian).
35. F. Hillenkamp, R. Kaufmann, and R. Florian, Laser induced ion formation from nonvolatile organic molecules, *Proceedings of the 7th International Vavilov Conference on Nonlinear Optics*, Novosibirsk, USSR, June 22-25, 1981.
36. H. Hirsche, J. Heinrichs, H. E. Schaefer, and M. Schramm, Preparation and analysis of heart and skeletal muscle specimens with LAMMA, *Z. Anal. Chem.* 308(1981)224.
37. G.L. Kellogg, Pulsed laser stimulated field desorption of hydrogen from molybdenum, *J. Chem. Phys.* 74(1981)1479.
38. P. Klein and J. Bauch, Studies concerning the distribution of inorganic wood preservatives in cell wall layers based on LAMMA, *Z. Anal. Chem.* 308(1981)283.
39. P. Klein and J. Bauch, On the determination of wood preservatives in the cell wall of treated wood by a laser microprobe mass analyzer (LAMMA), *Wood and Fiber* 13(1981).
40. F. R. Krueger, Ion formation from organic solids by laser or swift ion irradiation, related to their acidity and basicity scale, *Proceedings, 29th Annual Conference on Mass Spectrometry and Allied Topics*, Minneapolis, May 24-29, 1981, p.25.
41. K. D. Kupka, W. W. Schropp, Ch. Schiller, and F. Hillenkamp, Identification of atoms and molecules in human skin after long-term medical treatment, *Z. Anal. Chem.* 308(1981)229.
42. J.L. Lachambre and C.R. Neufeld, Interaction of long-pulse CO<sub>2</sub> laser radiation with solid targets, *Phys. Fluids* 24(1981)2336.
43. D. W. Lorch and H. Schafer, Localization of lead in cells of *Phymatodocis nordstedtiana* (chlorophyta) with the laser microprobe analyzer (LAMMA 500), *Z. Anal. Chem.* 308(1981)246.
44. A. Mathey, LAMMA: new perspective for lichenology?, *Z. Anal. Chem.* 308(1981)249.
45. A. Mathey, J. Gatzmann, and J. F. Muller, TEM and LAMMA investigation of the microlichen *Phaeographina chrysocarpa* (Radii) Redinger, *Beitr. Elektronenmikroskop. Direktabb. Oberfl.* 14(1981)631 (in German).
46. I. Matsumoto, Laser micro-probe mass-spectrometer (LAMMS), *Seikagaku* 53(1981)108.
47. J. F. Muller, C. Berthe, and J. M. Magar, LAMMA analysis of organo-metallic compounds, *Z. Anal. Chem.* 308(1981)312.
48. J. F. Muller, J. M. Magar, D. Cagniant, and J. M. Mouchot, Etude de substances modeles susceptibles de complexes les metaux de transition dans les fractions lourdes du petrole, *Partie II- Caracterisation par ESCA et LAMMA de complexes du vanadium avec des ligandes sulfures. Comparaison avec les asphaltenes*, *J. Organomet. Chem.* 205(1981)329 (in French).
49. M. Newstein and N. Solimene, Laser metal interaction in vacuum, *IEEE J. Quant. Electron.* QE-17(1981)2085.
50. A. Orsulakova and R. Kaufmann, Cation distribution of the cochlea wall (stria vascularis), *Z. Anal. Chem.* 308(1981)221.

51. C.K. Rohdes, Atomic, molecular, and condensed-matter studies using ultraviolet excimer lasers, *Novel Mater. Tech. Condens. Matter, Proc. Midwest Solid State Conference*, 29th Pub. 1982(1981)151.
52. A. P. von Rosenstiel, A. J. Gay, and P. J. van Duin, Investigation of fly ash particles with respect to the morphology and surface enrichment of matrix and trace elements, *Beitr. Elektronenmikroskop. Direktabb. Oberfl.* 14(1981)153 (in German).
53. Ch. Schiller, K. D. Kupka, and F. Hillenkamp, Laser induced mass spectrometry of amino acids and peptides, *Proceedings of the 7th International Symposium on Mass Spectrometry in Biochemistry, Medicine, and Environmental Research*, Milan, Italy, June 16-18, 1980, *Anal. Chem. Symp. Ser.*, Volume 7, ACS Press, Washington, 1981, p. 287.
54. Ch. Schiller, K. D. Kupka, and F. Hillenkamp, Investigation of the biologically relevant amino acids and some small peptides by laser induced mass spectrometry, *Z. Anal. Chem.* 308(1981)304.
55. W. H. Schroeder, Quantitative LAMMA analysis of biological specimens. I. Standards, II. Isotope labelling, *Z. Anal. Chem.* 308(1981)212.
56. B. Schueler, P. Feigl, F. R. Krueger, and F. Hillenkamp, Cationization of organic molecules under pulsed laser induced ion generation, *Org. Mass Spectrom.* 16(1981)502.
57. H. Seiler, U. Haas, I. Rentschler, H. Schreiber, P. Wieser, and R. Wurster, Einige Untersuchungen an atmosphärischen Aerosolpartikeln, *Optik* 58(1981)145 (in German).
58. U. Seydel and B. Lindner, Application of the laser microprobe mass analyzer (LAMMA) to qualitative and quantitative single cell analysis, *Int. J. Quant. Chem.* 20(1981)505.
59. U. Seydel and B. Lindner, Qualitative and quantitative investigations of mycobacteria with LAMMA, *Z. Anal. Chem.* 308(1981)253.
60. B. Sprey and H. P. Bochem, Uptake of uranium into the alga *dunaliella* detected by EDAX and LAMMA, *Z. Anal. Chem.* 308(1981)239.
61. K. R. Spurny, J. Schormann, and R. Kaufmann, Identification and microanalysis of mineral fibers by LAMMA, *Z. Anal. Chem.* 308(1981)274.
62. R. Stefani, Trace analysis by mass spectrometry -- potential applications of the spark source and laser probe, *Trends Anal. Chem.* 1(1981)84.
63. C.H. Tsai, The kinetics of laser pulse vaporization of uranium dioxide by mass spectrometry, Thesis, University of California, Berkeley, CA USA, 1981, 191 pp. Univ. Microfilms Int., Order No. DA8212131.
64. G.J.Q. van der Peyl, K. Isa, J. Haverkamp, and P.G. Kistemaker, Gas phase ion/molecule reactions in laser desorption mass spectrometry, *Org. Mass Spectrom.* 16(1981)416.
65. H. Vogt, H. J. Heinen, S. Meier, and R. Wechsung, LAMMA 500 principle and technical description of the instrument, *Z. Anal. Chem.* 308(1981)195.
66. P. Wieser and R. Wurster, Investigation of bulk material by means of the laser microprobe mass analyzer, *Beitr. Elektronenmikroskop. Direktabb. Oberfl.* 14(1981)59 (in German).
67. P. Wieser, R. Wurster, and U. Haas, Application of LAMMA in aerosol research, *Z. Anal. Chem.* 308(1981)260.
68. P. Wieser, R. Wurster, and L. Phillips, Laser microprobe mass analysis: a powerful tool in aerosol research, *Proceedings of the International Symposium on Aerosols in the Mining and Industrial Work Environment*, Minneapolis, November 1-6, 1981, p. 1169.
69. G. Wilhelm and K. D. Kupka, Identification of amino citric acid in biological peptides, *FEBS Letters* 123(1981)141.
70. R. Wurster, U. Haas, and P. Wieser, Electronmicroscopical investigations of laser irradiated foils and particles, *Z. Anal. Chem.* 308(1981)206.
71. D. Zakett, A.E. Schoen, R.G. Cooks, and P.H. Hemberger, Laser-desorption mass spectrometry/mass spectrometry and the mechanism of desorption ionization, *J. Am. Chem. Soc.* 103(1981)1295.

1982

1. I.M. Aref'ev, A.I. Boriskin, A.S. Bryukhanov, Yu.A. Bykovskii, A.A. Komleva, I.D. Laptev, and R.I. Utyamyshev, Determination of element composition of bloodstains on metal by laser mass spectrometry, *Sud.-Med. Ekspert.* 25(3)(1982)35 (Russ).
2. K. Balasanmugam and D. M. Hercules, Laser microprobe mass analysis of zwitterionic quarternary ammonium salts, *Microbeam Analysis-1982*, K. F. J. Heinrich (Ed.), San Francisco Press, San Francisco, 1982, p. 389.
3. R. C. Burnier, G. D. Byrd, T. J. Carlin, M. B. Wise, R. B. Cody, and B. S. Freiser, Study of atomic metal ions generated by laser ionization, *Lect. Notes Chem.* 31(1982)98.
4. K. L. Busch, S. E. Unger, A. Vincze, R. G. Cooks, and T. Keough, Desorption ionization mass spectrometry: sample preparation for secondary ion mass spectrometry, laser desorption, and field desorption, *J. Am. Chem. Soc.* 104(1982)1507.
5. A. Chamel and J. F. Eloy, Some applications of the laser microprobe mass spectrograph (L. P. M. S.) in plant biology, *Scanning Electron Microscopy/1982*, SEM Inc., AMF O'Hare, Illinois, 1982.
6. A. J. Chaplin, P. R. Millard, and P. F. Schmidt, The use of a laser microprobe to identify calcium oxalate in histological material, *Histochemistry* 75(1982)259.
7. R. Conzemius, Scanning laser mass spectrometry, *Microbeam Analysis-1982*, K. F. J. Heinrich (Ed.), San Francisco Press, San Francisco, 1982, p. 369.
8. E. Deloule and J. F. Eloy, Improvements of laser probe mass spectrometry for the chemical analysis of fluid inclusions in ores, *Chem. Geol.* 37(1982)191.
9. S. DeNollin, W. Jacob, and M. Borgers, Detection of calcium by laser microprobe mass analysis (LAMMA), *Janssen Research News* 7(1982)4.
10. E. Denoyer, T. Mauney, D. F. S. Natusch, and F. Adams, Laser microprobe mass analysis of coal and oil fly ash particles, *Microbeam Analysis-1982*, K. F. J. Heinrich (Ed.), San Francisco Press, San Francisco, 1982, p. 191.
11. E. Denoyer, R. Van Grieken, F. Adams, and D. F. S. Natusch, Laser microprobe mass spectrometry 1: Basic

- principles and performance characteristics, *Anal. Chem.* 54(1982)26A.
12. J. DeWaele, P. Van Espen, E. Vansant, and F. Adams, Study of asbestos by laser microprobe mass analysis, *Microbeam Analysis-1982*, K. F. J. Heinrich (Ed.), San Francisco Press, San Francisco, 1982, p. 371.
13. T. Dingle, B. W. Griffiths, J. C. Ruckman, and C. A. Evans, Jr., The performance of a laser-induced ion mass analyzer system for bulk samples, *Microbeam Analysis-1982*, K. F. J. Heinrich (Ed.), San Francisco Press, San Francisco, 1982, p. 365.
14. P. K. Dutta and Y. Talmi, Compositional and structural study of a coal surface using a laser microprobe mass detector, *Fuel* 61(1982)1241.
15. B. K. Furman and C. A. Evans, Jr., Applications of a combined direct imaging laser ionization-secondary ionization mass spectrometer to materials analysis, *Microbeam Analysis-1982*, K. F. J. Heinrich (Ed.), San Francisco Press, San Francisco, 1982, p. 222.
16. B. K. Furman and C. A. Evans, Jr., A combined direct-imaging laser ionization secondary ionization mass spectrometer, *Secondary Ion Mass Spectrometry-SIMS III*, A. Benninghoven et. al. (Eds.), Springer-Verlag, Berlin, 1982, p. 88.
17. R. Gijbels, P. Verloot, and S. Tavernier, Anionic surfactant films as standards for quantitative laser microprobe mass analysis, *Microbeam Analysis-1982*, K. F. J. Heinrich (Ed.), San Francisco Press, San Francisco, 1982, p. 378.
18. S. W. Graham, P. Dowd, and D. M. Hercules, Laser desorption mass spectrometry of some cobalamins, *Anal. Chem.* 54(1982)649.
19. S. W. Graham and D. M. Hercules, Laser desorption mass spectra of biomedical polymers: Avcothane, Biomer, polyether, polyurethane, *Spectrosc. Lett.* 15(1982)1.
20. A.V. Gurevich and A.P. Meshcherkin, Runaway ions in an expanding plasma, *Fiz. Plazmy* (Moscow) 8(3)(1982)502.
21. E.D. Hardin, Laser desorption mass spectrometry of nonvolatile biomolecules, Thesis, Univ. Houston, Houston, TX USA. 1981, 104 pp. Univ. Microfilms Int., Order No. DA8208693.
22. M.J. Herbst, P.G. Burkhalter, J. Grun, R.R. Whitlock, and M. Fink, Spot spectroscopy: Local spectroscopic measurements within laser produced plasmas, *Rev. Sci. Instrum.* 53(1982)1418.
23. D. M. Hercules, R. J. Day, K. Balasubramanian, T. A. Dang, and C. P. Li, Laser microprobe mass spectrometry 2. Applications to structural analysis, *Anal. Chem.* 54(1982)280A.
24. F. Hillenkamp, Laser desorption techniques of non-volatile organic substances, *Int. J. Mass Spectrom. Ion Phys.* 45(1982)305.
25. F. Hillenkamp, P. Feigl, and B. Schueler, Laser micro mass analysis of bulk surfaces, *Microbeam Analysis-1982*, K. F. J. Heinrich (Ed.), San Francisco Press, San Francisco, 1982, p. 359.
26. F. Hillenkamp and R. Kaufmann, Laser microprobe mass analysis (LAMMA): a new approach in biomedical microanalysis and analytical mass spectrometry, *Laser Applications in Medicine and Biology*, Volume 4, M. L. Wolbarsht (Ed.), Plenum Press, New York/London, 1982.
27. W. Jacob, S. De Nollin, R. Hertsens, and P. Dockx, Antimycotic activity of econazole on *Aspergillus fumigatus* as revealed by cytochemistry, elemental analysis, and freeze-fracturing, 10th International Congress on Electron Microscopy, Hamburg, August 17-24, 1982.
28. J.A.J. Jansen and A.W. Witmer, Quantitative inorganic analysis by Q-switched laser mass spectroscopy, *Spectrochim. Acta* 37B(1982)483.
29. B. Jost, B. Schueler, and F. R. Krueger, Ion formation from alkali halide solids by high power pulsed laser irradiation, *Z. Naturforsch.* 37a(1982)18.
30. R. Kaufmann, Laser microprobe mass analysis (LAMMA). Current state of the art with special emphasis on biomedical applications, *Microbeam Analysis-1982*, K. F. J. Heinrich (Ed.), San Francisco Press, San Francisco, 1982, p. 341.
31. R. Kaufmann, Laser microprobe mass analysis (LAMMA) as applied to soft biological tissues, *Z. Anal. Chem.* 311(1982)345 (in German).
32. R. Kaufmann, G. Barths, G. Schmitz, K. Spurny, and J. Bruch, LAMMA studies in mineral fibres and coal mine dust particles, Proceedings of the 12th Annual Symposium on the Analytical Chemistry of Pollutants, Amsterdam, April 14-16, 1982.
33. R. Kaufmann and P. Wieser, Laser microprobe mass analysis in particle analysis, *Modern Methods of Fine Particle Characterization*, Volume III, I. Beddow and A. Vetter (Eds.), CRC Press, Boca Raton, 1982.
34. R. Lehmann, H. Sluka, and P. F. Schmidt, Unerwartete intrazelluläre Ablagerungen von TiO<sub>2</sub> im Pulpagewebe, *Die Quintessenz* 3(1982)613 (in German).
35. C.L.S. Lewis, P.F. Cunningham, L. Pina, A.K. Roy, and J.M. Ward, Characteristics of ion flows from laser irradiated plane targets, *J. Phys. D: Appl. Phys.* 15(1982)69.
36. R. W. Linton, J. D. Shelburne, D. S. Simons, and P. Ingram, Correlative electron, ion, and laser microprobe analysis of particle-laden alveolar macrophages, 40th Annual Proceedings of the Electron Microscopy Society of America, G. W. Bailey (Ed.), Washington, 1982, p. 370.
37. J.M. Liu, Simple technique for measurements of pulsed Gaussian-beam spot sizes, *Opt. Lett.* 7(1982)196.
38. A. Mathéy, J. Gatzmann, and J. F. Müller, TEM- and LAMMA-investigation of the orange pigment of the microlichen *phaeographina chrysocarpa* (radii) redinger, 10th International Congress on Electron Microscopy, Hamburg, August 17-24, 1982.
39. D. A. McCrery, E. B. Ledford, Jr., and M. L. Gross, Laser desorption Fourier transform mass spectrometry, *Anal. Chem.* 54(1982)1435.
40. S. Meier, Laser microprobe mass analysis and its application in physiological and biological research, *Z. Anal. Chem.* 311(1982)338.
41. E. Michiels, A. Celis, and R. Gijbels, Atomic and molecular ion emission from silica in laser mass spectrometry, *Microbeam Analysis-1982*, K. F. J. Heinrich (Ed.), San Francisco Press, San Francisco, 1982, p. 383.
42. C.M. Miller, J.B. Cross, and N.S. Nogar, Single photon photoionization mass spectroscopy via autoionizing

- resonances, *Opt. Commun.* 40(1982)271.
43. P. Moesta, U. Seydel, B. Lindner, and H. Grisebach, Detection of glyceollin on the cellular level in infected soybean by laser microprobe mass analysis, *Z. Naturforsch.* 37c(1982)748.
  44. I. Opauszky, Lasers in solid state mass spectrometry, *Pure Appl. Chem.* 54(1982)879.
  45. J. L. Pierce, K. L. Busch, R. G. Cooks, and R. A. Walton, Desorption ionization mass spectrometry: secondary ion and laser desorption mass spectra of transition-metal complexes of beta-diketones, *Inorg. Chem.* 21(1982)2597.
  46. B. Schueler, P. Feigl, and F. R. Krueger, Kinetics of ion formation from inorganic and organic salts by pulsed laser irradiation, *Proceedings of the 30th Annual Conference on Mass Spectrometry and Allied Topics*, Honolulu, June 6-11, 1982, p. 569.
  47. H. R. Schulten, T. Komori, K. Fujita, A. Shinoda, T. Imota, and T. Kawasaki, Laser-assisted field-desorption mass spectrometry. Part IV. Laser-assisted field-desorption mass spectrometry of cyclomalto-hexaose and -heptaose and some 6-alkylthio derivatives, *Carbohydr. Res.* 107(1982)177.
  48. H. R. Schulten, P. B. Monkhouse, and R. Mueller, Laser-assisted field desorption mass spectrometry of inorganic and organometallic compounds, *Anal. Chem.* 54(1982)654.
  49. U. Seydel, B. Lindner, and K. Brandenburg, New possibilities from single cell mass analysis in the field of mycobacterial infections, *Recent Developments in Mass Spectrometry in Biochemistry and Medicine*, Volume 8, A. Frigerio and M. McCamish (Eds.), Elsevier, Amsterdam, 1982.
  50. U. Seydel, B. Lindner, J. K. Seydel, and K. Brandenburg, Detection of externally induced impairments in single bacterial cells by laser microprobe mass analysis, *Int. J. Leprosy* 50(1982)90.
  51. D. S. Simons, Isotopic analysis with the laser microprobe mass analyzer, *Proceedings of the 30th Annual Conference on Mass Spectrometry and Allied Topics*, Honolulu, June 6-11, 1982, p. 482.
  52. D. S. Simons, Isotopic analysis with the laser microprobe mass analyzer, *Microbeam Analysis-1982*, K. F. J. Heinrich (Ed.), San Francisco Press, San Francisco, 1982, p. 390.
  53. R. Stoll and F. W. Rollgen, Cationization by alkali ion attachment in laser desorption mass spectrometry, *Z. Naturforsch.*, 37A(1982)9.
  54. P. Surkyn and F. Adams, Laser microprobe mass analysis of glass microparticles, *J. Trace and Microprobe Techniques* 1(1982)79.
  55. T.T. Tsong, S.B. McLane, and T.J. Kinkus, Pulsed-laser time-of-flight atom-probe field ion microscope, *Rev. Sci. Instrum.* 53(1982)1442.
  56. G.J.Q. Van der Peyl, J. Haverkamp, and P.G. Kistemaker, Thermal aspects of laser desorption mass spectrometry, *Int. J. Mass Spectrom. Ion Phys.* 42(1982)125.
  57. G.J.Q. Van der Peyl, K. Isa, J. Haverkamp, and P.G. Kistemaker, Cationization in laser desorption mass spectrometry, *Nucl. Instrum. Methods Phys. Res.* 198(1982)125.
  58. J. Volovski, E. Voryna, S. Denus, A.A. Erokhin, Yu.A. Zakharenkov, W. Mroz, G.V. Sklizkov, J. Farny, and A.S. Shikanov, Thomson mass spectrograph for the study of laser plasma, *Zh. Tekh. Fiz.* 52(1982)366.
  59. H. Wakasugi, T. Kimura, W. Haase, A. Kribben, R. Kaufmann, and I. Schulz, Calcium uptake into acini from rat pancreas: evidence for intracellular ATP-dependent calcium sequestration, *J. Membrane Biol.* 65(1982)205.
  60. P. Wieser, R. Wurster, and H. Sella, Laser microprobe mass analysis of doped epoxy resin standards, *Scanning Electron Microscopy/1982*, SEM Inc., AMF O'Hare, Illinois, 1982.

## Author Index

- Adar, 269, 293  
 Aden, 195  
 Albee, 177  
 Aliotta, 131  
 Allen, 51  
 Alvarez, 277  
 Andrejko, 19  
 Audebrand, 286  
 Barbillat, 280  
 Bardin, 15  
 Bieg, 168  
 Bolon, 11, 125  
 Boyer, 265  
 Bradley, J. G., 177  
 Bradley, J. P., 187  
 Brewer, 5  
 Brown, 89  
 Brownlee, 187  
 Buseck, 85, 182, 195  
 Byrd, 301  
 Calvo, 65  
 Cameron, 237  
 Chambers, 109  
 Chao, 27  
 Chapman, 215  
 Coane, 131  
 Conley, 177  
 Conzemius, 301  
 Couzi, 274  
 Crooker, 261  
 Cruège, 274  
 Cvikevich, 79  
 Davidson, 121  
 Delhay, 280  
 Dingle, 101  
 Doyle, 277  
 Dulong, 27  
 Echlin, 243  
 Elin, 233  
 Ellis, 156  
 Ensign, 257  
 Evans, 101  
 Farrow, 143  
 Faugère, 286  
 Fiori, 233  
 Frèour, 286  
 Friday, 115  
 Fritz, 1  
 Giffin, 177  
 Goddard, 257, 259  
 Griffith, 252  
 Griffiths, 101  
 Grubb, 125  
 Guilemany, 65  
 Hale, 97  
 Hare, 111  
 Hayes, 243  
 Higgins, 297  
 Hinthorne, 54  
 Hook, 233  
 Huggins, 22  
 Hunter, 237  
 Ingram, F. D., 229  
 Ingram, M. J., 229  
 Isaacs, 202  
 Izutsu, 257  
 Jenson, 128  
 Johnson, D. E., 261  
 Johnson, K. A., 171  
 Johnson, S. G., 5  
 Jones, 151  
 Joy, 143  
 Knowles, 61  
 Kortemeier, 43  
 Kruit, 247  
 Kuptsis, 79  
 Landon, 151  
 Larson, 27  
 Laudale, 1  
 Launspach, 47  
 Leapman, 163  
 Lindner, 106  
 Long, 57  
 McConnell, 11, 125  
 McCormick, 39  
 McKenzie, 204  
 McKoon, 243  
 Mallet, 274  
 Martineau, 274  
 Minkin, 27  
 Mosley, 117  
 Mottet, 261  
 Murata, 79  
 Myers, 211  
 Myklebust, 148, 168, 174  
 Neuzil, 27  
 Newbury, 148, 168  
 Nicholson, 215  
 Ninham, 101  
 Noether, 269  
 Norris, 209  
 Olson, 5  
 Packwood, 88, 97  
 Pailer, 274  
 Pearson, 85  
 Pineau, 286  
 Post, 182  
 Pun, 156  
 Purcell, 289  
 Raymond, 15  
 Reeves, 171  
 Remond, 89  
 Rez, 153  
 Romig, 168  
 Rosencwaig, 137  
 Russ, 111  
 Seydel, 106  
 Shankai, 301  
 Sheridan, 35, 39, 43  
 Shuman, 247  
 Sicignano, 115  
 Simons, 301  
 Small, 148, 209  
 Smith, D. G. W., 47  
 Smith, N. K. R., 237  
 Snyder, 22  
 Somlyo, 247  
 Southan, 101  
 Staudhammer, 171  
 Stein, 297  
 Strope, 51, 57  
 Swyt, 163  
 Tallant, 297  
 Tamarin, 257  
 Taylor, D. A., 211  
 Taylor, D. M., 11  
 Tessier, 286  
 Thomas, 70  
 Thompson, 27  
 Tomassian, 177  
 Tong, 11  
 Tormey, 221  
 Vander Wood, 85  
 Vesser, 171  
 Wang, 257  
 Wandless, 27  
 Ward, 5  
 Warner, 211, 230  
 Warren, 31  
 Wells, 131  
 White, 289  
 Wirfel, 231  
 Wohletz, 35  
 Zorabedian, 293

# Notes

# Notes



# Notes